

AMERICAN UNIVERSITY OF BEIRUT

PROBABILISTIC CHARACTERIZATION OF THE
VISCOELASTOPLASTIC BEHAVIOR OF ASPHALT-
AGGREGATE MIXTURES

by

HUSSEIN AMINE KASSEM

A dissertation

submitted in partial fulfillment of the requirements
for the degree of Doctor of Philosophy
to the Department of Civil and Environmental Engineering
of the Faculty of Engineering and Architecture
at the American University of Beirut

Beirut, Lebanon

July, 2017

AMERICAN UNIVERSITY OF BEIRUT

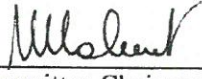
PROBABILISTIC CHARACTERIZATION OF THE
VISCOELASTOPLASTIC BEHAVIOR OF ASPHALT-
AGGREGATE MIXTURES

by


HUSSEIN AMINE KASSEM

Approved by:

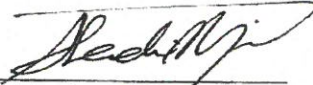
Dr. Mounir Mabsout, Professor
Department of Civil and Environmental Engineering


Committee Chairperson

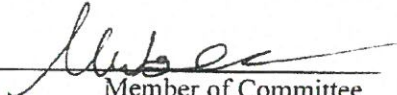
Dr. Ghassan R. Chhab, Associate Professor
Department of Civil and Environmental Engineering


Advisor

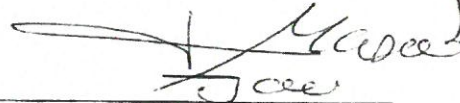
Dr. Shadi Najjar, Associate Professor
Department of Civil and Environmental Engineering


Member of Committee

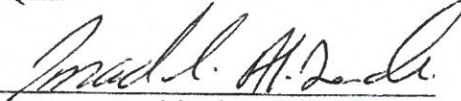
Dr. Mutasem Shehadeh, Associate Professor
Department of Mechanical Engineering


Member of Committee

Dr. Eyad Masad, Professor
Zachry Department of Civil Engineering, Texas A&M University
Mechanical Engineering Program, Texas A&M at Qatar


Member of Committee

Dr. Imad Al-Qadi, Founder Professor
Department of Civil and Environmental Engineering
University of Illinois at Urbana-Champaign


Member of Committee

Date of dissertation defense: July 24, 2017

AMERICAN UNIVERSITY OF BEIRUT

THESIS, DISSERTATION, PROJECT RELEASE FORM

Student Name:

_____ Kassem _____ Hussein _____ Amine
Last First Middle

Master's Thesis Master's Project Doctoral Dissertation

I authorize the American University of Beirut to: (a) reproduce hard or electronic copies of my thesis, dissertation, or project; (b) include such copies in the archives and digital repositories of the University; and (c) make freely available such copies to third parties for research or educational purposes.

I authorize the American University of Beirut, to: (a) reproduce hard or electronic copies of it; (b) include such copies in the archives and digital repositories of the University; and (c) make freely available such copies to third parties for research or educational purposes after: **One ---- year from the date of submission of my thesis, dissertation, or project.**
Two ---- years from the date of submission of my thesis, dissertation, or project.
Three ---- years from the date of submission of my thesis, dissertation, or project.

Signature

Date

This form is signed when submitting the thesis, dissertation, or project to the University Libraries

ACKNOWLEDGMENTS

The achievement of this work was simply impossible without the guidance, support, and assistance of many individuals and institutions whose contributions are greatly appreciated.

First, I would like to express my utmost gratitude to my advisor, Dr. Ghassan R. Chehab, for his infinite effort in making my PhD experience enthusiastic, productive, and successful. He has been always there as the motivator who kept me strong during tough times and as the facilitator who helped me go the extra mile. He was confident in my potential and believed in my ambitions throughout the past five years. He taught me the norms of being an ethical and successful researcher supported me to achieve my goals, and provided me the valuable advice for my career at the post-graduate level. I was fortunate to work with him as he provided me with a great exposure to top scholars and practitioners in the field of pavement engineering and materials. Moreover, he pushed me to present my research work at international conferences and meetings. Dr. Chehab was the tough advisor yet the very kind person whose efforts, time, and investment paved the way for me to achieve this moment.

Also, I would like to thank to Dr. Shadi Najjar for supporting my research work over the past years. His Course “Reliability Based Design of Civil Engineering Systems” stimulated my research interests towards the application of the concepts of probabilistic modeling in the field of pavements which, become my favorite research domain. Dr. Najjar door was always open to answer my questions, help me solve the many problems I faced, and provide me with valuable feedback. Most importantly, I appreciate all that effort and the positive energy that he provided me with.

I would like to extend my gratitude and thank Dr. Mounir Mabsout, Dr. Mutasem Shehadeh, Dr. Eyad Masad, and Dr. Imad Al-Qadi for serving on my doctoral committee. Thank you for the valuable time and the effort of reviewing my dissertation and the constructive feedback provided. In addition, I would like to thank Dr. George Saad, Dr. Issam Srour, Dr. Majdi Abou Najm, and Dr. Mohamad Abiad for sharing with me their research experience on the many research projects that I undertook.

Moreover, I want to extend my regards to the staff of the Civil and Environmental Engineering Laboratories at AUB. I would like to thank them not only for helping me technically, but also for providing me with the emotional support during my study years. Also, I am particularly grateful all the support that I got from the Department of Civil and Environmental Engineering at AUB and all help by Mrs. Zakiya Deeb.

My recognition and gratitude are addressed to the Lebanese National Council for Scientific Research for its financial support through CNRS-L/AUB PhD Scholarship. Also, part of this work was made possible by the financial support provided by Qatar National Research Fund (QNRF) through the National Priority Research Program project NPRP 5-506-2-203. All statements are those of the authors and do not represent QNRF.

I would like to acknowledge all my friends, classmates, and colleagues whose support provided with the strength needed to finish my PhD. I could not but thank the members of my research group members and especially all the undergraduate lab assistants who helped me in getting my lab work perfectly done. I want to specifically thank Noor Alhuda Saleh,

Ali Zalghout, Jad Khalil, and Bassel Zalzali for being there to help me whenever I needed wishing them the best of luck in their endeavors.

Yara Hamdar, my friend and colleague, thanks for your generous support and for being always there for me whenever I need any help. Our work together will always make me look forward for future collaborations.

I would like also to thank Mr. Helmi Khatib for being my trusted advisor in this journey. my interaction with him evolved from him being the lab manager to him becoming a mentor during the past year. I appreciate all the advice and talks he provided me with.

My family, thank you for being there for me at every step during my PhD studies. Your care, encouragement, sacrifices, and patience were my strength to reach where I am today. Thanks for believing in me and I hope I will make you proud.

Finally, I want to express my deep gratitude and appreciation to Dima Al Hassanieh. Dima thanks for undertaking this journey with me. You were always by my side in my best moments and my most stressful times. Your endless love, and support made my PhD possible.

AN ABSTRACT OF THE DISSERTATION OF

Hussein Amine Kassem for Doctor of Philosophy
Major: Civil and Environmental Engineering

Title: Probabilistic Characterization of the ViscoElastoPlastic Behavior of Asphalt-Aggregate Mixtures

The objective of this work is to provide accurate and realistic characterization of different types of asphalt concrete mixtures using advanced material modeling within a probabilistic framework. The methodology adopted builds on and enhances a viscoelastoplastic continuum damage (VEPCD) material model by utilizing a suite of associated experimental testing protocols and incorporating the uncertainties associated with the different material properties. The developed framework is then applied to assess the behavior of different types of unconventional asphalt concrete mixtures such as Warm Mix Asphalt (WMA), Fiber-Reinforced Asphalt Concrete (FRAC), and those containing Reclaimed Asphalt Pavement materials (RAP).

The modeled uncertainties address the variabilities and errors associated with the linear viscoelastic (LVE) functions achieved from the complex modulus test and damage characteristic curves obtained from constant crosshead rate testing. A probabilistic scheme using First Order approximations and Monte Carlo simulations is developed to characterize the inherent uncertainty of each of the LVE functions (dynamic modulus $|E^*|$, relaxation modulus $E(t)$, and creep compliance $D(t)$) over the time domain of their mastercurves. The results show that the quantified uncertainties are significant especially at high temperatures and/or slow loading rates. Based on the results of several investigated mixtures, the inherent uncertainty of LVE properties of asphalt concrete becomes higher for mixtures with a larger nominal maximum aggregate size, mixtures with modified binders, and/or mixtures with WMA additives. At small reduced times, the uncertainty in $|E^*|$, $E(t)$, and $D(t)$ are similar in magnitude; however, differences become significant at large reduced times implying that modeling the uncertainty of either of these functions is not enough to represent that of the other ones. The sources of uncertainty in these functions are categorized and their influence are tested where fitting techniques yield uncertainty unlike machine loading, testing instrumentation, and data acquisition. In addition, the effect of uncertainties in the time-temperature shift factors and phase angle are shown to be minimal and thus can be neglected in any probabilistic analysis.

For damage characteristic curves, the uncertainty in normalized pseudostiffness (C) increases as the level of damage (S) becomes larger. This uncertainty, quantified by the coefficient of variability, does not exceed a value of 0.2 for a drop of C from 1 to 0.5. The conducted analysis shows that the uncertainty in C can be modeled directly as a function of the input stress without the need of developing two distinct models for C versus S and S versus stress. The uncertainties of LVE properties are propagated along with those of C versus stress curves to yield a probabilistic viscoelastic continuum damage model (P-VECD). The P-VECD not only predicts the average viscoelastic response to a given loading input, but it can also provide its distribution, which is essential for a reliability-based pavement design. For the case of a loading ramp, the uncertainty of the predicted probabilistic viscoelastic strains is

mainly due to initial uncertainty of the response just after the application of the load. Based on the results of the P-VECD model, it is recommended to minimize the effort of the current practice in developing the VECD model by determining the C versus stress curve based on conducting the constant crosshead rate test for only one replicate per asphalt concrete mixture. In addition, the data used in the development of the P-VECD model is utilized to develop a generic C versus stress curve which can be used as an alternative for the development of mixture specific C versus stress curves. Thus, a simplified VECD model with the generic C versus stress curve can be used for predicting the response of asphalt concrete mixtures due to compression loading. Such model requires only the determination of the LVE properties of the investigated mixture. The model is validated and verified for a suite of seven asphalt mixtures with components different than those used for its calibration. The developed generic C versus stress curve could be recalibrated using the data of more asphalt concrete mixtures but so far it is verified in this research that this approach is applicable for cases of assessing a variety of asphalt mixtures incorporating different additives, modifiers, and production technologies.

CONTENTS

ACKNOWLEDGMENTS.....v

ABSTRACT vii

ILLUSTRATIONS..... xvi

TABLES xxv

Chapter

1. INTRODUCTION.....1

1.1. Warm Mix Asphalt..... 1

1.1.1. WMA Technologies 1

1.1.2. Performance and Durability of WMA.....2

1.2. Advanced Material Characterization.....4

1.3. Uncertainty Quantification in Asphalt Materials 6

1.4. Research Objective.....8

1.5. Dissertation Roadmap9

2. LITERATURE REVIEW ON UNCERTAINTIES IN MATERIAL BEHAVIOUR 11

2.1. Types Of Uncertainty 11

2.2. Uncertainty In Dynamic Modulus $|E^*|$ Data 11

2.3. Uncertainty In Relaxation Modulus And Creep Compliance 14

2.4. Uncertainty In Advanced Mechanistic Models	16
3. THEORETICAL BACKGROUND ON ASPHALT MATERIALS CHARACTERIZATION	19
3.1. Introduction	19
3.2. Overview of Modeling Approach	20
3.3. Linear Viscoelastic Characterization	22
3.3.1. Complex Modulus	24
3.3.2. Relaxation Modulus	25
3.3.3. Creep Compliance	25
3.4. Conversion Among LVE Response Functions	25
3.4.1. Analytical Representation of $E(t)$ and $D(t)$	26
3.4.2. Conversion Methods	27
3.5. Time-Temperature Superposition	29
3.5.1. Case of LVE Behavior	29
3.5.2. Case of Growing Damage State	30
3.6. Modeling of Viscoelastic Behavior	30
3.6.1. Elastic-Viscoelastic Correspondence Principle.....	30
3.6.2. Pseudostrain Calculation	31
3.6.3. Uniaxial Constitutive Modeling Using Work Potential Theory	32
3.6.4. C vs S Approach.....	34
3.7. Modeling of Viscoplastic Behavior	35
3.8. ViscoElastoPlastic Model	36
4. EXPERIMENTAL PROGRAM	37

4.1. Materials.....	37
4.1.1. Aggregates	37
4.1.2. Asphalt Binder	39
4.1.3. WMA Additives.....	41
4.1.4. Fibers.....	43
4.2. Mix Design of HMA and WMA	43
4.2.1. Mixes with Unmodified Binder and 25.0 mm Gradation	45
4.2.2. Mixes with Modified Binder and 19.0 mm Gradation.....	48
4.2.3. Mixes with Unmodified Binder and 19.0 mm Gradation	50
4.3 Testing Program	51
4.3.1. Testing System	51
4.3.2. Testing Methods.....	53
4.4 Sample Preparation	59
4.4.1. Mixing and Compaction.....	59
4.4.2. Conditioning and Curing.....	60
4.4.3. Volumetrics	61
5. RESULTS ON ASPHALT MATERIALS CHARACTERIZATION	63
5.1. Linear ViscoElastic Functions	63
5.1.1. Effect of WMA Additives on Mixes with Unmodified Binder.....	64
5.1.2. Effect of WMA Additives on Mixes with Modified Binder	66
5.1.3. Statistical Analysis to Test Effect of WMA Additive on $ E^* $	68
5.1.4. $E(t)$ and $D(t)$ of HMA and WMA mixes	73
5.2. Viscoelastic modeling	76
5.3. Viscoplastic Modeling	80

5.4. Comparison of HMA and WMA Mixes Based on Random Stress Profile.....	82
5.5. Assessing Effect of Fibers on $ E^* $ of HMA and WMA	92
5.6. Conclusions and Recommendations	100
6. MODELING OF THE INHERENT UNCERTAINTY IN THE COMPONENTS OF the VECD MODEL	102
6.1. Introduction	102
6.2. Experimental Program	102
6.3. Probabilistic Modeling Methodology	105
6.3.1. First Order Approximation.....	105
6.3.2. Monte Carlo Simulations	106
6.3.3. Probabilistic Modeling Strategy.....	108
6.4. Inherent Uncertainty in LVE Functions	109
6.4.1. Inherent Uncertainty in $ E^* $	109
6.4.2. Inherent Uncertainty in $E(t)$ and $D(t)$	140
6.4.3. Probability Distribution of LVE Functions.....	155
6.5. Inherent Uncertainty in Damage Characteristic Curve, C vs. S	159
6.5.1. Introduction	159
6.5.2. Inherent Uncertainty in C vs. S	160
6.5.3. Damage as a function of Stress	168
6.5.4. C as a Function of Lebesgue Norm of Stress	173
7. PREDICTION OF PROBABILISTIC VISCOELASTIC STRAINS	178
7.1. Propagation Methodology	178

7.2. Input Data: Stress History and Material Properties.....	178
7.3. Predicted Viscoelastic Strains: Deterministic and Probabilistic solutions.....	182
7.3.1. Results of the P-VECD Model Predictions.....	182
7.3.2. Probability Distribution of Predicted Probabilistic Viscoelastic Strains.....	185
7.3.3. Number of Realizations Required for P-VECD Model.....	186
7.4. Comparison of Results of Deterministic VECD AND P-VECD Results.....	189
7.5. Use of Global Damage Characteristic Curve for Predicting Viscoelastic Strains ..	194
7.5.1. Development of Global Damage Characteristic Curve.....	194
7.5.2. Verification of Using a Global Damage Characteristic Curve.....	196
7.5.3. Validation of Using a Global C vs Stress Relationship.....	199
7.6. Effect of Number of Replicates of Crosshead Test on The Predicted Viscoelastic Strains.....	205

8. MODELING OF THE INHERENT UNCERTAINTY IN LVE FUNCTIONS FROM FIELD and MULTI-LABORATORY DATA 210

8.1. Introduction.....	210
8.2. Inherent Uncertainty in $ E^* $	210
8.2.1. Dynamic Modulus Data.....	210
8.2.2. Probabilistic Model of $ E^* $ Master Curve.....	215
8.2.3. Modeling of Uncertainty In $ E^* $	217
8.2.4. Results.....	217
8.2.5. Rut Depth Prediction.....	221
8.2.6. Conclusions.....	224
8.3. Inherent Uncertainty in $E(t)$ and $D(t)$	225
8.3.1. $E'(w)$, $E(t)$, $D(t)$ Data.....	225

8.3.2. Probabilistic Model of E' , $E(t)$ and $D(t)$	227
8.3.3. Modeling of Uncertainty	231
8.3.4. Probability Distribution of $E(t)$ and $D(t)$	240
8.3.5. Case Study.....	242
8.3.6. Conclusions	245
8.4. Effect of Plant-Mixing and Multi-Laboratory Testing on Uncertainty in LVE Functions.....	245
9. CONCLUSIONS AND FUTURE WORK	252
9.1. Summary and Conclusions.....	252
9.2. Recommendations for Future Work.....	256
REFERENCES	258
APPENDIX	267
1- Specimen Preparation Protocols And Data Log Sheets	267
Batching Sheet	267
Batching	268
Mixing.....	269
Short Term Aging	272
Mixing And Short Term Aging Sheet.....	273
Compaction.....	274
General Notes.....	276
Compaction Sheet.....	277
Gmm Testing Sheet.....	278
Gmb Testing Sheet/Volumetric Samples.....	279
Gmb Testing Sheet/ E^* Samples.....	280
Mixing, Short Term Aging, and Compaction Sheet	281
Complex Modulus Testing.....	282
PID Tuning Parameters for E^* Testing.....	283
2- R Codes	284

Calculation of PseudoStrains/ PieceWise Linear Method	284
Calculation of PseudoStrains/ State Variables Method	285
Calculation of Viscoelastic Strains	287
Calculation of Probablistic Viscoelastic Strains	288
Code for Monte Carlo Simulations: Case of C vs S	290
3- Assessing the Effect of the Addition of RAP on $ E^* $ of WMA	293
Reclaimed Asphalt Pavement	293
Design of Mixes with RAP	293
Dynamic Modulus Testing.....	294
4- Complex Modulus Data	296

ILLUSTRATIONS

Figure

1. (a) Variation of COV of $ E^* $ with reduced frequency (b) Average universal $ E^* $ master curve with 96% confidence-bounds.....	14
2. Probabilistic damage characteristic curve (after Singh and Swamy 2017).....	18
3. Complex modulus graphical representation.....	24
4. 19.0 mm gradation used for mixes with Gabbro aggregates.	37
5. 25.0 mm gradation used for mixes with Gabbro aggregates.	38
6. Viscosity vs. temperature for: (a) unmodified binder, (b) modified binder.....	41
7. Mix of aramid and polyolefin fibers.	43
8. Volumetric properties of 25.0 mm mix with unmodified binder.	46
9. Universal testing machine.....	52
10. Gluing jig for mounting studs on asphalt samples.....	53
11. Complex modulus testing setup.....	54
12. Constant crosshead rate results showing the difference between crosshead and on specimen LVDT strains (Chehab 2002).....	57
13. $ E^* $ mastercurves curves for HMA and WMA mixes having an unmodified binder and a 25.0 mm aggregate gradation constructed at a reference temperature of 25°C: a) semi-log scale and b) log-log scale.....	65
14. Time-Temperature shift factor for HMA and WMA mixes with unmodified binder and 25.0 mm gradation as used to construct E^* master curve at 25°C.....	66
15. $ E^* $ mastercurves for HMA and WMA mixes with modified binder and a 19.0 mm aggregate gradation at a reference temperature of 25°C in a) semi-log scale and b) log-log scale.....	67
16. Time-Temperature shift factors for HMA and WMA mixes with modified binder and a 19.0mm aggregate gradation as used to construct the mastercurves of different LVE functions.....	68
17. Residual analysis of linear model representing ANOVA analysis of $\log(E^*)$ vs. reduced frequency*type of mix.....	70

18. Boxplot showing variation of E^* between HMA and WMA mixes at different selected frequencies for the group of modified binder.	72
19. Boxplot showing variation of E^* between HMA and WMA mixes at different selected frequencies for the group of unmodified binder.	73
20. $D(t)$ calculated by the Approximate method for HMA and WMA U25 mixes at a reference temperature of 5°C	74
21. $E(t)$ calculated by the Approximate and Exact methods for HMA and WMA U25 mixes at a reference temperature of 5°C	75
22. $D(t)$ calculated by the Approximate method for HMA and WMA M19 mixes at a reference temperature of 5°C	75
23. $E(t)$ calculated by the Approximate and Exact methods for HMA and WMA M19 mixes at a reference temperature of 5°C	76
24. Predicted and measured VE strains vs. time at 5°C for crosshead test rates used to develop and calibrate VE model of WMA with Sasobit and unmodified binder.	77
25. Damage characteristic curves for VECD modeling for HMA and WMA U25 mixes.	78
26. Damage characteristic curves for VECD modeling for HMA and WMA M19 mixes.	79
27. Measured and predicted strains for AC sample subjected to cyclic loading.	82
28. Investigated stress profile for prediction of strains for HMA and WMA mixes.	83
29. Predicted viscoelastic strain for the different HMA and WMA M19 mixes in response to the investigated random stress profile at a temperature of a) 5°C and b) 35°C	85
30. Predicted viscoelastic strain for the different HMA and WMA U25 mixes in response to the investigated random stress profile at a temperature of a) 5°C and b) 35°C	86
31. Predicted viscoplastic strains for the different HMA and WMA M19 mixes in response to the investigated random stress profile at a temperature of a) 5°C and b) 35°C	88
32. Predicted viscoplastic strains for the different HMA and WMA U25 mixes in response to the investigated random stress profile at a temperature of a) 5°C and b) 35°C	89
33. Predicted total (viscoelastic + viscoplastic) strains for the different HMA and WMA M19 mixes in response to the investigated random stress profile at a temperature of a) 5°C and b) 35°C	90

34. Predicted total (viscoelastic + viscoplastic) strains for the different HMA and WMA U25 mixes in response to the investigated random stress profile at a temperature of a) 5°C and b) 35°C.	92
35. Average $ E^* $ mastercurves for control and fiber- reinforced mixes with unmodified binder and a 19.0 mm aggregate gradation at a reference temperature of 25°C.	93
36. Time-Temperature shift factor for HMA and WMA mixes with unmodified binder and a 19.0 mm aggregate gradation as used to construct the mastercurves of different LVE functions.....	94
37. $D(t)$ calculated by the Approximate method for HMA and WMA U19 mixes with and without fibers at a reference temperature of 5°C.	94
38. $E(t)$ calculated by the Approximate and Exact methods for HMA and WMA U19 mixes with and without fibers at a reference temperature of 5°C.	95
39. Damage characteristic curves of U19 mixes with and without fibers.	96
40. Predicted viscoelastic, viscoplastic, and total strains in response to random stress profile at 5°C and 35°C.	99
41. Schematic showing material testing and properties required for VECD and P-VECD modeling.	103
42. Flowchart showing the methodology followed for modeling of uncertainty in viscoelastic continuum damage model.	110
43. Best fit sigmoidal functions for $ E^* $ of replicates in (a) U19-HMA (b) M19-HMA (c) U19-WMA-SonneWarmix (d) U25-HMA.	113
44. Average $ E^* $ mastercurves at a reference temperature of 25°C as obtained from ten tested replicates, First Order Approximation, and Monte Carlo Simulations for each of the four mixes.	116
45. $ E^* $ mastercurves obtained by First Order Approximation, Monte Carlo Simulations, and Experimental Data in the region of 10^{-6} to 10^{-1} Hz.....	117
46. $ E^* $ mastercurves obtained by First Order Approximation, Monte Carlo Simulations, and Experimental Data in the region of 10^{-1} to 10^{+3} Hz.	117
47. $ E^* $ mastercurves obtained by First Order Approximation, Monte Carlo Simulations, and Experimental Data in the region of 10^2 to 10^5 Hz	118

48. Realizations of $ E^* $ mastercurves from Monte Carlo simulations for a) U19-HMA, b) M19-HMA, c) U19-WMA-SonneWarmix, and d) U25-HMA.....	119
49. COV of $ E^* $ as a function of reduced frequency using Monte Carlo Simulations and First Order Approximation.....	120
50. Time-temperature shift factor curves of the replicates of a) U19-HMA, b) M19-HMA, c) U19-WMA-SonneWarmix, and d) U25-HMA.	124
51. $ E^* $ mastercurves from Monte Carlo simulations with deterministic and probabilistic time-temperature shift factors for a) U19-HMA, b) M19-HMA, c) U19-WMA-SonneWarmix, and d) U25-HMA.....	127
52. COV of reduced frequencies at different E^* testing temperatures.	128
53. Effect of uncertainty in shift factor model parameters on the COV of $ E^* $	129
54. $ E^* $ mastercurves fitted using three models for the U19-HMA, M19-HMA, U19-WMA-SonneWarmix, and U25-HMA.	134
55. COV of $ E^* $ mastercurve fitted using three different models for a) U19-HMA and U25-HMA, and b) M19-HMA and U19-WMA-SonneWarmix.	135
56. COV of applied load at different frequencies and temperature of E^* testing.....	137
57. Hollow steel sample used for checking the effect of LVDTs and their mounting setup on the uncertainty in E^* testing.	139
58. COV of measured displacement using on-specimen mounted LVDTs for a hollow steel sample.	140
59. Mastercruves of $E(t)$ replicates and averages for a) U19-HMA, b) M19-HMA, c) U19-WMA-SonneWarmix, and d) U25-HMA.	142
60. Mastercruves of $D(t)$ replicates and averages for a) U19-HMA, b) M19-HMA, c) U19-WMA-SonneWarmix, and d) U25-HMA.	142
61. COV of storage modulus mastercurve as a function of reduced angular frequency for the four mixes.	149
62. COV of $ E^* $ mastercurve as a function of reduced angular frequency for the four mixes.	150
63. (a) Average and COV of phase angle and b) Average and COV of cosine of phase angle.	151

64. COV quantified by using First Order Approximation and Monte Carlo	153
65. COV of $D(t)$ as a function of reduced time quantified based on First Order Approximation and Monte Carlo Simulations.	154
66. a) Slope of $E(t)$ as a function of reduced time and b) COV of slope of $E(t)$ as a function of reduced time.....	155
67. Probability distribution of $ E^* $ for different reduced frequencies at a reference temperature of 25°C for the four mixes U19-HMA, M19-HMA, U19-WMA-SonneWarmix, and U25-HMA.	157
68. Probability distribution of $E(t)$ for different reduced times at a reference temperature of 25°C for the four mixes U19-HMA, M19-HMA, U19-WMA-SonneWarmix, and U25-HMA.	158
69. C vs. S plots of replicates tested for each of the ten replicates.	161
70. Mean C vs S curves determined by First Order Approximation and Monte Carlo Simulations.	165
71. COV of C as a function of S determined by First Order Approximation and Monte Carlo Simulations.	166
72. COV of C as a function of its mean determined by First Order Approximation and Monte Carlo Simulations.....	167
73. Simulated C vs S curves by Monte Carlo for a) U19-HMA, b) M19-HMA, c) U19-WMA-SonneWarmix, and d) U25-HMA.....	168
74. S vs. Lebesgue norm of stress for replicated of the four mixes a) U19-HMA, b) M19-HMA, c) U19-WMA-SonneWarmix, and d) U25-HMA.....	169
75. Mean S curves obtained using First Order Approximation and Monte Carlo simulations.	172
76. COV of S as a function of Lebesgue norm of stress calculated using First Order Approximation and Monte Carlo simulations.....	173
77. Mean of C vs. Lebesgue Norm of Stress evaluated by the First Order Approximation and Monte Carlo Simulation for the four mixes.	176
78. COV of C as a function of Lebesgue norm of stress evaluated using First Order Approximation and Monte Carlo simulations for the four mixes.....	176

79. Different investigated stress inputs as a function of actual time at 5°C, 25°C, and 35°C.	179
80. Lebesgue norm of the investigated stress profile as a function of time at 5°C for the cases of U19-HMA, M19-HMA, U19-WMA-SonneWarmix, and U25-HMA.	180
81. Lebesgue norm of the investigated stress profile as a function of time at 25°C for the cases of U19-HMA, M19-HMA, U19-WMA-SonneWarmix, and U25-HMA.....	180
82. Lebesgue norm of the investigated stress profile as a function of time at 35°C for the cases of U19-HMA, M19-HMA, U19-WMA-SonneWarmix, and U25-HMA.....	180
83. A sample of simulated D(t) mastercurves from Monte Carlo Realizations plotted as a function of reduced time at 5°C and extracted for the prediction of probabilistic viscoelastic strains.	181
84. Predicted probabilistic viscoelastic strain means and COVs for case of stress input at 5°C for M19-HMA, U19-HMA, U19-WMA-SonneWarmix, and U25-HMA.	183
85. Predicted probabilistic viscoelastic strain means and COVs for case of stress input at 25°C for M19-HMA, U19-HMA, U19-WMA-SonneWarmix, and U25-HMA.....	183
86. Predicted probabilistic viscoelastic strain means and COVs for case of stress input at 5°C for M19-HMA, U19-HMA, U19-WMA-SonneWarmix, and U25-HMA.	184
87. COV of predicted viscoelastic strains across the 10,000 simulations of the P-VECD model for U19-HMA.	188
88. COV of predicted viscoelastic strains across the 10,000 simulations of the P-VECD model for M19-HMA.....	188
89. COV of predicted viscoelastic strains across the 10,000 simulations of the P-VECD model for U19-WMA-SonneWarmix.	188
90. COV of predicted viscoelastic strains across the 10,000 simulations of the P-VECD model for U19-WMA-SonneWarmix.	189
91. Predicted viscoelastic strains in response to the investigated stress profile at 5°C calculated using deterministic VECD and P-VECD model along with its 68% and 95% confidence intervals for a) M19-HMA, b) U19-HMA, c) U25-HMA, and d) U19-WMA- SonneWarmix.	190
92. Predicted viscoelastic strains in response to the investigated stress profile at 25°C calculated using deterministic VECD and P-VECD model along with its 68% and 95%	

confidence intervals for a) M19-HMA, b) U19-HMA, c) U19-WMA-SonneWarmix and d) U25-HMA.....	192
93. Predicted viscoelastic strains in response to the investigated stress profile at 35°C calculated using deterministic VECD and P-VECD model along with its 68% and 95% confidence intervals for a) M19-HMA, b) U19-HMA, c) U25-HMA, and d) U19-WMA-SonneWarmix.	193
94. Mix-specific and global C vs S curves calculated based on the four mixes: U19-HMA, M19-HMA, U19-WMA-SonneWarmix, and U25-HMA.	195
95. Mix-specific and global S vs Lebesgue Norm of Stress curves calculated based on the four mixes: U19-HMA, M19-HMA, U19-WMA-SonneWarmix, and U25-HMA.	195
96. Predicted viscoelastic strains calculated using Global damage characteristic curve in response for the investigated stress profile at 5°C for a) M19-HMA, b) U19-HMA, c) U19-WMA-SonneWarmix, and d) U25-HMA.	197
97. Predicted viscoelastic strains calculated using Global damage characteristic curve in response for the investigated stress profile at 25°C for a) M19-HMA, b) U19-HMA, c) U19-WMA-SonneWarmix, and d) U25-HMA.	198
98. Predicted viscoelastic strains calculated using Global damage characteristic curve in response for the investigated stress profile at 35°C for a) M19-HMA, b) U19-HMA, c) U19-WMA-SonneWarmix, and d) U25-HMA.	199
99. Viscoelastic strains calculated in response to the investigated stress profile at 5°C for different mixes using both the damage characteristic curves specific to each mix and the developed global relations for a) Time = 25 second, b) Time = 50 second, c) Time = 100 second, and d) Time = 150 second.	202
100. Measured and predicted viscoelastic strains using global damage vs. stress relationships for tested replicates of U25-WMA-Sasobit-RAP at 5°C and rates of a) 0.000025 ε/sec and b) 0.00005 ε/sec.	204
101. Viscoelastic strains in response to random stress profile predicted using mix-specific and global C vs stress relationships.	205
102. Predicted viscoelastic strains in response to the investigated stress profile at 5C using damage characteristic curves calculated based on one, two, and three tested replicates at a) time = 25 second, b) time = 50 second, c) time = 100 second, and d) time = 150 second.	207
103. Binder content of different batches of 19.0 mm FR mix of Set I.	212

104. Best fit sigmoidal functions for $ E^* $ of replicates in (a) Set I and (b) Set II mixes.	215
105. Cumulative distribution functions for the parameters: δ , α , γ , and β	216
106. (a) COV of $ E^* $ as a function of reduced frequency for mixes of Set I compacted at a level of 4.0% air voids, (b) COV of $ E^* $ as a function of reduced frequency for prefabricated mixes of Set II compacted at a level of 7.0% air voids.	219
107. Correlation between COV of $ E^* $ and NMAS at very low reduced frequencies.....	219
108. Histograms of simulated $ E^* $ values compared to theoretical distributions for the 25mm mix.	221
109. Probabilistic Simulation of Rut Depth for hot climate case with slow moving, normal, and fast-moving traffic (a) 19mm FR mix (b) 25mm mix.....	224
110. E(t) and D(t) mastercurves for mixes of Set I and Set II at 20°C.	226
111. Cumulative distribution functions of sample parameters referring to E(t) and D(t) of 19mm-FR Mix of Set I: a) E1 having normal distribution as best fit, b) E11 having log normal as best fit, c) E7 having the 5th order Hermite polynomial as the best fit, d) D0 having normal distribution as best fit, e) D7 having log normal as best fit, and f) D1 having the 5th order Hermite polynomial as the best fit.....	229
112 (a) COV of E' as a function of reduced time for mixes of Set I, (b) COV of E' as a function of reduced time for mixes of Set II.....	233
113 (a) COV of E(t) calculated using the Approximate Method for mixes of Set I as a function of reduced time, (b) COV of E(t) calculated using the Exact Method for mixes of Set I as a function of reduced time.....	235
114. (a) COV of E(t) calculated using the Approximate Method for mixes of Set II as a function of reduced time, (b) COV of E(t) calculated using the Exact Method for mixes of Set II as a function of reduced time.	235
115. (a) COV of D(t) for mixes of Set I as a function of reduced time, (b) COV of D(t) for mixes of Set II as a function of reduced time.	238
116. The COV of the slope of E(t) at reduced times of 10^4 and 10^6 sec for the mixes of Set I and Set II.....	240
117. Probability distribution functions of simulated data for a) E(t) and b) D(t) at for selected mixes and reduced times.....	242

118. Illustration of the case study used for the calculation of the tensile strains under the load at the bottom of AC layer within a three-layered pavement system.....	242
119. COV of $ E^* $ as a function of reduced frequency at 20°C based on Monte Carlo Simulations for the 19.0 mm mixes that are plant and laboratory mixed.....	246
120. COV of $ E^* $ as a function of reduced frequency at 20°C based on Monte Carlo Simulations for the 25.0 mm mixes that are plant and laboratory mixed.....	247
121. COV of $E(t)$ as a function of reduced frequency at 20°C based on Monte Carlo Simulations for the 19.0 mm mixes that are plant and laboratory mixed.....	249
122. COV of $D(t)$ as a function of reduced frequency at 20°C based on Monte Carlo Simulations for the 19.0 mm mixes that are plant and laboratory mixed.....	250

TABLES

Table

1. Advantages and benefits of using WMA (Button et al. 2007, Chowdhury and Button 2008, D'Angelo et al. 2008, Kassem et al. 2015, Zaumanis 2014).....	2
2. Illustration of the time dependence of the behavior of asphalt concrete using different tests.	22
3. Bailey Conformity equations for 19.0 and 25.0 mm gradations.....	39
4. WMA additives used in this research with the type, supplier, recommended dosage, and image for each.....	43
5. Description of HMA and WMA mixes.....	44
6. Superpave design requirements.	45
7. Summary of mix design results of mixes with unmodified binder and 25.0 mm gradation.	48
8. Mix design results of HMA with modified binder.....	49
9. Summary of mix design results for mixes with modified binder and 19.0 mm gradation. .	50
10. Summary of mix design results for mixes with unmodified binder and 19.0mm gradation.	51
11. Complex modulus testing information showing testing temperatures, frequencies, and number of cycles at each combination.....	55
12. Calculation of testing temperature for State of Qatar.	58
13. Testing conditions for VE and VP model development and validation.	58
14. Coefficients of sigmoidal function and time-temperature shift factors for a reference temperature of 25°C to predict $ E^* $ of the HMA and WMA mixes at any combination of temperature and loading frequency.....	63
15. TukeyHSD test results for multiple comparisons of means of $ E^* $ mastercurves of HMA and WMA mixes at a 95% family-wise confidence level.....	71
16. Fitting Parameters of damage characteristic curve for all the mixes in the study.	77
17. Predicted viscoelastic strains for HMA and WMA mixes after 100 creep and recovery cycles.....	80

18. Results of crosshead testing at 35°C and slow rates showing the portion of VP strain for HMA and WMA mixes.	81
19. Predicted Viscoelastic Strains for U19 mixes at 35C after 100 creep and recovery cycles.	97
20. Asphalt concrete mixes selected for probabilistic analysis.....	104
21. Testing conditions for probabilistic analysis of VECD model.....	105
22. Relationships used for the First Order Approximation of $ E^* $	113
23. Components of the mean vector, standard deviation vector, and correlation matrices for the fitting coefficients of $ E^* $ for the four mixes under study.	114
24. p-values by Shapiro-Wilk Normality Test for Parameters Describing $ E^* $ Fits.....	115
25. Relationships used for the First Order Approximation of $ E^* $ with probabilistic time-temperature shift factors.	125
26. Components of the mean vector, standard deviation vector, and correlation matrices for the fitting coefficients parameters describing the time-temperature shift factors for the four mixes under study where $\log(a_T)=aT^2+bT+c$	126
27. Relationships used for the First Order Approximation of $ E^* $ fitted using the Generalized Logistic Function (5 parameters model).	131
28. Relationships used for the First Order Approximation of $ E^* $ fitted using the Sigmoidal Function with 6 parameters.....	131
29. AIC of the three $ E^* $ fitting models for four mixes.	133
30. Components of the Mean Vector, Standard Deviation Vector, and Correlation Matrices For the Fitting Coefficients of $E'(w)$	143
31. Mean, standard deviation, and part of correlation matrix between the Prony Coefficients of $E(t)$ for the four investigated mixes.....	145
32. Distribution of the Prony Coefficients of $E(t)$ for the four investigated mixes.	145
33. Mean, standard deviation, and part of correlation matrix between the Prony Coefficients of $D(t)$ for the four investigated mixes.	147
34. Distribution of the Prony Coefficients of $D(t)$ for the four investigated mixes.....	147

35. Relationships for First Order Approximation of $E(t)$ and $D(t)$	148
36. p-values from Shapiro-Wilk Normality test for $D(t)$ at different reduced times at a reference temperature of 25°C.....	159
37. Mean and COV of maximum slope of $ E^* $ curve based on 10 tested replicates for each mix.	162
38. Mean, standard deviation, probability distribution, and correlation coefficients of parameters fitting the C vs. S curves.	163
39. Relationships to conduct First Order Approximation for C vs. S.....	164
40. Mean, standard deviation, distribution, and correlation coefficients of the parameters fitting S vs. Lebesgue norm of stress for the four mixes.	171
41. Relationships required for First Order Approximation of S vs. Lebesgue Norm of Stress.	172
42. Correlation coefficients of fitting parameters of C vs. S and S vs. Lebesgue norm of stress.....	174
43. Relationships required for First Order Approximation of C vs. Lebesgue norm of stress.	175
44. p-values by Shapiro-Wilk Normality Test for predicted viscoelastic strains for the investigated stress input at 5°C for the four mixes.	186
45. p-values by Shapiro-Wilk Normality Test for predicted viscoelastic strains for the investigated stress input at 35°C for the four mixes.	186
46. p-values from statistical analysis results for predicted viscoelastic strains using damage characteristic curves calculated from one, two, and three replicates.	209
47. Properties of the mixes used to quantify the inherent uncertainty of $ E^* $	211
48. Components of the mean vector, standard deviation vector, and correlation matrices for the fitting coefficients of $ E^* $ for the mixes under study.	217
49. The averages and COVs for Prony coefficients for $E(t)$ calculated using the Approximate method at 20°C for mixes of Set I and Set II.	227
50. Components of the mean vector, standard deviation vector, and correlation matrices for the fitting coefficients of storage modulus for the mixes under study.....	228

51. Mean, Standard Deviation, Distribution, and Part of Correlation Matrix Between the Prony Coefficients of Each of E(t) and D(t) for Two of The Investigated Mixes.	231
52. Predicted tensile strains and corresponding number of cycles to failure in fatigue using deterministic and probabilistic analyses.	244

To my parents....

CHAPTER 1

INTRODUCTION

1.1. Warm Mix Asphalt

Pursuing sustainable development has become a basic and common goal across various industries worldwide. This goal has received a significant share of attention and effort in the construction sector, where various stakeholders are enacting initiatives and regulations to render the industry more sustainable by introducing green concepts into this sector's practices. These new concepts minimize the depletion rate of natural resources and lessen the negative social and environmental impacts. For the roadway construction sector, in particular, tremendous efforts are being placed to render its practices more sustainable. One of these measures include the utilization of warm mix asphalt (WMA) additives to reduce the production and paving temperatures used in the case of traditional hot mix asphalt (HMA).

WMA can be considered as an eco-friendly and cost effective technology that is becoming commonly used in the pavement industry. Initially developed in Europe, WMA is gaining interest as an alternative to HMA all over the world. Its signature feature is the reduction of the asphalt binder's viscosity and/or increase of the mixture's workability at lowered temperatures (Chowdhury and Button 2008). Thus, the use of WMA allows for a significant reduction in the production (mixing), transportation, and paving (compaction) temperatures as compared to the traditional HMA mixes. It is worth noting, however, that the use of WMA in asphalt pavement construction has many advantages and benefits that exceed the direct gain of reducing production and compaction temperatures, as summarized in Table 1.

1.1.1 WMA Technologies

The reduction of production temperatures is achieved through widely developed commercial products that employ mechanisms involving microstructural, physiochemical, and mechanical changes to asphalt binders. As such, different WMA technologies exist:

- 1) Wax-based organic additives that reduce the binder's viscosity at mixing temperatures while maintaining or slightly increasing the viscosity at operational temperatures,
- 2) Chemical additives that reduce the surface tension of the binder to improve the wettability of aggregates, and

- 3) Water-based or water-foaming technologies that provide better coating of aggregates and aid in compaction by the injection of water which causes the formation of small bubbles that decrease the binder's viscosity (Rubio et al. 2012).

Table 1. Advantages and benefits of using WMA (Button et al. 2007, Chowdhury and Button 2008, D'Angelo et al. 2008, Kassem et al. 2015, Zaumanis 2014).

Category	Advantages and Benefits
Environment	<ul style="list-style-type: none"> • Decreases fuel or energy consumption in the range of 20-75% or 2-3% reduction for every 6°C reduction in temperature. • Reduces CO₂ emission (up to 40%) because of lower WMA production temperatures and lower fuel consumption. • Reduces SO₂ emission (20 to 35%) • Reduces nitrous oxides emissions (up to 70%) • Provides better working conditions for the plant/paving workers due to the reduction in visible and invisible emissions, fumes, smoke, dust, and odor. • Decreases dust production due to the short heating time and lower temperatures.
Production	<ul style="list-style-type: none"> • Uses a higher percentage of reclaimed asphalt pavement (RAP). • Extends paving season and increases productivity as a result of the ability to pave under cooler temperatures compared to HMA. • Provides greater acceptance of presence of plant sites in urban areas due to lower emission, dust, and noise. • Uses less-aged binder, which reduces the fatigue cracking and extending the pavement life.
Paving	<ul style="list-style-type: none"> • Improves workability. • Reduces paving time, especially for pavements with thick lifts. • Extends haul distance due to the lower thermal gradient between the ambient temperature and the mix's temperature. • Provides quicker opening of paved roadways to traffic. • Creates a healthier working environment compared to the HMA placing conditions for paving crew. • Reduces thermal segregation in the asphalt concrete mat.
Economic	<ul style="list-style-type: none"> • Decreases the production cost due to reduction in fuel and energy consumption (30% to 50% of HMA's producers overhead cost) • Reduces wear and maintenance needs of the plant due to lower mixing temperatures.

1.1.2 Performance and Durability of WMA

With the increased interest and use of WMA, products are continuously improved, refined, and developed (Chowdhury and Button 2008). Thus, the evaluation of WMA

additives has gained momentum to ensure performance and durability requirements of asphalt mixes are met or exceeded (Button et al. 2007, Prowell et al. 2011).

The durability and performance of WMA mixes need to be assessed because of the lower mixing and compaction temperatures. Thus, the resistance to moisture sensitivity is becoming an important factor for WMA due to two major reasons: 1) the aggregates might not completely dry during mixing due to lower temperatures and thus part of the moisture might be entrapped in the mix leading to an increased susceptibility to moisture damage, 2) foaming-based WMA technologies may cause possible residual moisture beyond the microscopic foaming process leading to reduced moisture resistance. This retained moisture may affect the adhesive bond between the aggregates and the binder leading to moisture damage (Zaumanis 2014). This is considered as a major concern for WMA and it has been investigated and evaluated by many researchers (Alavi et al. 2012, Buss et al. 2016, Cucalon et al. 2015, Martin et al. 2016, Mogawer et al. 2011). For the case of cracking, the lower production temperature of WMA implies a binder that is less aged than the case of HMA. In this case, the WMA will not have a major negative impact on the cracking resistance whether it is the case of fatigue cracking or thermal cracking (Das et al. 2012, Haggag et al. 2011, Sadeq et al. 2016). However, the lower stiffness of the binder in WMA that might be due to less aging during mixing and compaction may cause earlier rutting in comparison to pavements with HMA (Bower et al. 2016, Chowdhury and Button 2008, Prowell et al. 2011, Zaumanis 2014). WMA mixes with wax additives have shown an exception of that because the wax stiffens the binder at in-service temperatures and thus induces a higher resistance to rutting.

With the rapid implementation of WMA, many research studies have been conducted to evaluate and support its use, taking into consideration durability and long-term performance. In the United States, many research projects have been initiated by the National Cooperative Highway Research Program (NCHRP), Federal Highway Administration (FHWA) and state highway agencies aiming to provide recommendations on mixture design practices for WMA, moisture susceptibility of WMA technologies, short term laboratory conditioning of WMA, and field performance of WMA (Bonaquist 2011, Martin et al. 2014, Newcomb et al. 2015, West et al. 2014). The continued worldwide implementation of WMA depends on the ability to produce mixtures with similar or better durability and performance than traditional HMA used in the region of interest. One of the major challenges in providing effective recommendations for mixture design and long-term performance evaluation for WMA is the large amount of technological modifications that can be categorized under WMA technologies. Thus, it is of a high importance to understand the effect of the various WMA

technologies at a mixture level and to check whether WMA mixes are acceptable in terms of performance as a replacement of HMA or not.

1.2. Advanced Material Characterization

Ultimately, this research will feed into the implementation of WMA in Qatar and the Gulf Region as this work is part of the National Priority Research Program (NPRP) project 5-506-2-203 entitled “Design and Performance Evaluation of Warm Asphalt Mixtures in Qatar” supported by Qatar National Research Fund (QNRF). The main objective of this project is to develop WMA and to evaluate the engineering, economical, and environmental benefits of implementing it in Qatar by considering locally available materials and evaluate its performance in Qatar. It should be noted that the WMA technology has not yet been explored in Qatar or in the Gulf region before the project at hand. Part of this dissertation will feed into this project through the assessment and realistic prediction of the performance of HMA and WMA mixes using advanced and accurate asphalt material characterization models.

The realistic prediction of the performance of asphalt pavements will be carried out mechanistically through structural response models. Such models predict the stresses and strains in a given pavement structure based on its traffic loading and environmental conditions. These models require accurate and advanced material properties that are provided through material characterization models, which are addressed through this particular research for different HMA and WMA mixes used and/or recommended for Qatar and the Gulf region. The modeling of pavement performance will be conducted based on macro-scale continuum damage theories. This approach ignores the physical interactions at micro-scale level and thus models the behavior based on parameters that can be obtained on a macro-scale level (Underwood et al. 2010). It takes into account the fact that asphalt concrete mixes behave differently based on temperature and load rate. This behavior can extend from elastic and linear viscoelastic at low temperatures and fast loads to nonlinear viscoelastic and viscoplastic at high temperatures and slow loads. Therefore, the adopted modeling strategy aims at modeling each component, separately, referred to as the viscoelastic (VE) strain, combining both elastic and VE strains, and the viscoplastic (VP) strain that combines both the plastic and VP strains. These are combined together, resulting in the ViscoElastoPlastic Continuum Damage (VEPCD) Model (Chehab et al. 2003).

The VEPCD model provides the ability of predicting the performance of asphalt concrete with a reasonable accuracy which assures the better understanding of the behavior of HMA and WMA mixes under realistic loading and environmental conditions (Underwood et al. 2010). In this research, this model will be utilized to assess the rate dependent behavior of

WMA mixes compared to HMA under compressive loading which is responsible for the rutting of pavements. This characterization method takes into account the micro-crack induced damage and its role in accelerating the development of permanent deformation in asphalt material used in the upper bound layers of a pavement structure. In compression, those cracks are oriented vertically in the pavement structure in a direction parallel to the loading. Consequently, this will cause a reduction in the overall mixture modulus, which promotes higher total strain for a given load. Thus, at conditions of slow loading, high temperature, and/or high loads the asphalt mix will have a lower stiffness and thus a lower resistance to rutting. The VEPCD model used in this study was developed by researchers at North Carolina State University where it has gained the interest of researchers and practitioners of the paving industry worldwide. It has been developed in tension and compression as part of NCHRP Project 9-19 and other projects where it was shown to be capable of describing the behavior of asphalt concrete (and particularly HMA) in both loading states (Chehab et al. 2003, Gibson 2006, Underwood et al. 2010, Yun et al. 2009, Zhao 2002).

Advanced material characterization of WMA is needed to provide a better understanding of its behavior as compared with that of the corresponding HMA mixes. This is needed in order to know the effect of different WMA additives on the behavior of a given mix at different environmental and loading conditions. It has been shown by previous researchers that the used VEPCD model is capable of predicting the stress-strain behavior of HMA mixes under different conditions; thus, it is selected for the assessment and comparison of the behavior of HMA and WMA mixes. It is believed that this will provide an insight of whether there is any need to change or recalibrate the models and transfer functions that are being currently used in existing pavement design and analysis methods and which were originally built based on various HMA mixes.

The comparison of the performance of WMA to HMA mixes has been carried out by several studies of which only few have relied on the mechanical characterization of the viscoelastic behavior of these mixes. Such studies have focused more on the assessment of the fatigue cracking rather than asphalt rutting of WMA mixes. One of these studies was conducted by Sadeq et al. (2015) where the Superpave rutting factor was used to compare the performance of an HMA and WMA asphalt binders. This factor was assessed based on the binder's performance in the linear VE region. The results showed that the wax-based additive "Sasobit" stiffened the binder more than the foaming-based additive "Advera" which showed almost the same behavior as the original binder (Sadeq et al. 2015). Another study that was also conducted by Sadeq et al. (2016) focused on using the viscoelastic continuum

damage analysis to assess the resistance of warm fine aggregate mix (W-FAM) to fatigue cracking imposed by applying damaging shear stress oscillations. This study investigated W-FAM with three different additives (Advera, Sasobit, and Rediset) where it showed that there is not significant difference between the W-FAM and the control mix in terms of the number of cycles to failure (Sadeq et al. 2016). In addition, a study was conducted by Safaei et al. (2014) on the performance of HMA and WMA binders with a chemical based additive “Evotherm” and with foaming by water injection. This study focused on determining the effect of various ageing levels on the fatigue behavior of HMA and WMA binders and mixes using a simplified viscoelastic continuum damage analysis. It showed that the difference in the fatigue performance between WMA and HMA become insignificant after long-term aging (Safaei et al. 2014).

1.3. Uncertainty Quantification in Asphalt Materials

Mechanistic approaches, such as the VEPCD model, have been developed to be used instead of the state-of-practice empirical and mechanistic-empirical analysis approaches in order to yield more realistic prediction of the performance of asphalt pavements, (Gibson 2006). Despite the advantage of these models in providing accurate and advanced material characterization, it is needed to be improved from being purely deterministic towards being probabilistic (Gudipudi and Underwood 2016). Such a need exists because of the industry’s drive towards the adoption of reliability-based design principles. Basically, through uncertainty quantification, reliability principles provide a set of tools to characterize and account for the precision/consistency of the measurements involved in the different inputs required for pavement performance prediction. In other words, uncertainty quantification and reliability-based analysis cannot assess whether a prediction model is accurate, but it can tell that if the validity of a model is accepted to some quantified degree, then the validity of certain conclusions should be accepted to some quantified degree too (Sullivan 2015). Therefore, modeling and quantifying the uncertainties of the material’s properties are becoming of high interest to the practitioners in the pavement industry (Castillo and Caro 2014, Kalita and Rajbongshi 2015). It will allow for assessing the probabilities of unsatisfactory performance of asphalt concrete pavements.

The field of uncertainty quantification in the paving industry is about making safer bets in different aspects that include foreseeing experimental results in the lab, making bids for pavement maintenance by service companies, determining asphalt material specifications by departments of transportation, and investing in the manufacturing of new asphalt technologies by the industry (Ghanem 2013). Uncertainty quantification aims at the characterization of the

proximity between predictions and observations. It is a field that produces the methodology, tools, and research to connect computational models to the actual physical systems they simulate by combining concepts of applied mathematics, engineering, computational science, and statistics (Ghanem et al. 2016). A major trigger for the need of uncertainty quantification is make predictions of complex systems that are credible and useful for decision making and requires computational and statistical models to improve the odds of their bets and not only experience, better understanding of physical principles, and laboratory observations. Such systems include random heterogeneous media and composite materials such as asphalt concrete mixtures. Ignoring statistical analysis in formulating the properties of such materials might lead to false conclusions jeopardizing the functionality and economy of built engineering systems (Simsiriwong et al. 2014).

The heterogeneous nature of asphalt concrete, induced by the microstructure of asphalt mixtures and its spatial distribution, along with the wide range of testing conditions (loading rates and testing temperatures) that are required to fully present its properties can be considered as major factors of inherent uncertainty. Also, testing is carried out within protocols that exhibit high variability in instrumentation and equipment from one lab to another (Aguiar-Moya et al. 2011). Therefore, uncertainties in the measured properties might be due to several factors related to sample preparation and testing methods, data analysis techniques, and errors by the operators. This might include (Mehrez et al. 2014):

- Inability to replicate the same mixing and compaction temperatures,
- Variation in aggregate properties and their distribution between one replicate and the other,
- Slight variations in vertical pressure during compaction,
- Difference in the height and diameter of samples during sawing and coring,
- Variabilities encountered in the collection of data and temperature control during testing,
- Spatial variability in air void distribution and its connectivity,
- Inability to add the same amount of asphalt binder during the production of asphalt mixtures.

These challenges result in some uncertainty for the measured values of different material properties within the same mix. Even if the same sample is tested different times, the measurements would exhibit a certain level of variability (Mehrez et al. 2014).

1.4. Research Objective

The main objective of this dissertation is providing a framework for accurate and realistic characterization of HMA and WMA mixes using advanced material models and a probabilistic approach. This is carried out mechanistically through the modeling of the viscoelastic and viscoplastic behavior of asphalt concrete in the compression state. In addition, the viscoelastic continuum damage modeling approach is developed to provide more realistic predictions through the incorporation of the uncertainties in material properties rendering the current state purely deterministic models towards becoming probabilistic. The scope of this work includes a variety of HMA and WMA mixes which are used to achieve the following objectives:

- Assessing the effect of using various WMA technologies (Sasobit, Rediset, Advera, and Sonnewarmix) on mixes with Gabbro aggregates and two types of asphalt binders (unmodified and polymer-modified).
- Assessing the effect of using aramid and polyolefin fibers on the viscoelastic and viscoplastic properties of WMA and their corresponding HMA mixes.
- Modeling and quantification of the inherent uncertainties in different linear viscoelastic characteristics of asphalt concrete mixes with different components.
- Evaluating the effect of various factors involved in mixture composition, testing conditions, data fitting and analysis, temperature and loading rate on the inherent uncertainty of linear viscoelastic functions.
- Studying the effect of field versus lab mixing and production conditions on the uncertainty in linear viscoelastic functions.
- Modeling and quantification of the inherent uncertainties of damage characteristic properties developed in compression state for a variety of asphalt concrete mixes.
- Developing the deterministic viscoelastic continuum damage models towards being probabilistic, referred to as probabilistic viscoelastic continuum damage (P-VECD) model, through the forward propagation of the inherent uncertainties of each of the material properties required as an input characterizing the behavior of asphalt mixes.
- Modeling and quantification of the uncertainties in predicted viscoelastic strains in response to different input stress profiles.

1.5. Dissertation Roadmap

This dissertation consists of nine different chapters. Chapter 1 briefly introduces the main aspect of each of the areas in context with the objectives of this dissertation. In addition, it provides a review of the existing literature on the performance of WMA, use of advanced material characterization models to characterize WMA mixes, and the efforts in assessing uncertainties in the field of pavement engineering. Chapter 2 presents a synthesis of the work related to the uncertainties in material properties of asphalt concrete. Chapter 3 presents the theoretical background necessary for understanding and the development of the viscoelastic continuum damage model and viscoplastic model aggregated as the viscoelastoplastic model. This chapter also presents methods for determining and inter-converting of linear viscoelastic material response functions, which are the building blocks of any representative characterization model.

Chapter 4 illustrates the different types of materials used in this research including aggregates, asphalt binders, WMA additives, and fibers. It covers the methodology followed for selection of aggregate gradations, mix designs of HMA and WMA mixes, and sample preparation protocols followed in this research. In addition, this chapter presents the experimental program, test methods, testing systems, and the instrumentation used for testing the samples of the investigated types of asphalt concrete mixes. Chapter 5 is dedicated to present the tested properties of all HMA, WMA, and Fiber-reinforced mixes. These properties include the linear viscoelastic functions, developed viscoelastic continuum damage models, and the viscoplastic models characterizing the behavior of each of the mixes. In addition, this chapter provides the assessment of the performance of these different WMA mixes and fiber-reinforced mixes as compared to the control HMA mixes.

All efforts in the roadway towards the quantification and modeling of the uncertainties in the mechanical properties of asphalt concrete mixes are presented in Chapters 6, 7, and 8. While chapter 6 presents a framework for modeling the inherent uncertainty in the components of the viscoelastic damage model, Chapter 7 presents the methodology required for the development of a probabilistic viscoelastic continuum damage model (P-VECD) along with probabilistic viscoelastic strains predicted in response to various stress profiles for a suit of different types of mixes. Chapter 6 provides the detailed methodology followed to assess uncertainties in properties acquired using complex modulus and constant crosshead rate testing models. However, Chapter 7 presents the results of the developed P-VECD model with suggested simplifications for the development of the VECD model without effecting the accuracy nor the precision of its predictions. All the work presented in these chapters is based on a single-laboratory prepared and fabricated asphalt concrete samples. Thus, Chapter 8

provides a step further in the assessment of uncertainties in asphalt concrete mixtures, and basically linear viscoelastic functions, by the investigations of data of 6 different mixes with a large number of samples per mix. This chapter provides an insight of variability that could be incurred due to plant mixing conditions and multi-laboratory testing which is the case discretizing issues related to the actual conditions of the production and testing of asphalt concrete mixes in the field.

Finally, the dissertation is concluded by Chapter 9 representing an overview of the conclusions and major findings of the work presented in Chapters 5, 6, 7, and 8. This chapter also highlight the scope and suggestions for future work. Also, a set of appendices is included at the end of this dissertation presenting sample preparation and protocols, laboratory data sheet forms, codes written for carrying out the different required computations especially those related to the VECD model and algorithms used for uncertainty modeling. In addition, a dataset with the complex modulus test results for the samples of all mixes is presented. The advantage of such a dataset is not only providing fundamental properties of a variety of asphalt concrete mixes that could be used by other researchers and projects but also provides the complex modulus data from big number of tested replicates per mix.

CHAPTER 2

LITERATURE REVIEW ON UNCERTAINTIES IN MATERIAL BEHAVIOUR

2.1 Types Of Uncertainty

As any other engineering applications, the uncertainty in asphalt characterization is unavoidable where the available invariable contains variability and insufficient or incomplete information for fully characterizing the behavior of asphalt. In addition, performance predictions are yielded from asphalt characterization models with unknown degrees of imperfections relative to reality which involve additional uncertainties. These uncertainties can be classified under two categories as the following (Tang and Ang 2007):

- Aleatory Uncertainty: It refers to uncertainty about inherently variable phenomena. Such phenomena are characterized by field or laboratory experiments and observations that possesses a significant level of variability describing its natural randomness. Thus, the variability inherent in such data will be statistical in nature and thus its realizations will involve probability.
- Epistemic Uncertainty: It refers to uncertainty arising from lack of knowledge and associated with idealized models that could be an imperfect representation of the real world. These models could be mathematical or simulation models where their analysis, predictions, or estimations might have some degree of error and thus contain uncertainty.

In this research, the two types of uncertainties will be combined and their aggregate effects will be estimated accordingly.

2.2 Uncertainty In Dynamic Modulus $|E^*|$ Data

Quantifying the uncertainty of $|E^*|$ is important due to its influence on the predicted performance of asphalt pavements. The most reliable approach to evaluate $|E^*|$ is through experimental testing whereby mastercurves of $|E^*|$ are determined using a minimum of three temperatures and three frequencies. $|E^*|$ is affected by the HMA mix properties, the test frequency, the test temperature, experimental setup, and the specimen geometry (Daniel et al. 2004, Tashman and Elangovan 2008). Since asphalt is a viscoelastoplastic material, the $|E^*|$ testing protocol is quite complex and may include uncertainties due to experimental setups, sample preparation methods, data analysis techniques, and human error.

For field applications involving large quantities of asphalt mixtures that are constructed over several days, additional uncertainties in material properties are expected due to variations in the asphalt production activities other than that due to the nature of asphalt mixture and sample preparation and testing. Although the aim of any mixing plant is to produce a target mix that is exactly the same from one day to another (or even from one batch to another), this aim might not be achieved due to uncertainties in the plant operations and variabilities in raw materials. Since the mixing plant activities are supervised and bound by the mix and construction specifications, these variabilities are generally limited and lie within an acceptable tolerance. For example, commonly specified acceptable ranges for the variations of the asphalt content and air voids are $\pm 0.2-0.3\%$ and $\pm 0.5\%$, respectively (Hamdar et al. 2015, Mahoney et al. 2000). Production specifications and tolerances vary from one agency to another and from one project to the other. Despite the level of control that is practiced in the production of large quantities of asphalt mixtures in the field, the uncertainty in $|E^*|$ due to inherent variability between batches in a given project is expected to be of importance in determining the reliability of an asphalt pavement performance.

The literature is currently lacking information about the uncertainty in $|E^*|$ due to the inherent variability resulting from production of large volumes of asphalt mixes in practical field pavement operations. There is an urgent need for quantifying this uncertainty due to two main reasons. First, information about inherent variability in $|E^*|$ is needed for adopting realistic QA/QC measures, especially that critical minimum $|E^*|$ values have been recommended as potential QA/QC parameters in the field (Azari et al. 2007). Second, proper quantification of the magnitude of the uncertainty in $|E^*|$ due to inherent variability is important from a design perspective since it will allow for separating this source of uncertainty from other sources of uncertainty that affect the prediction of $|E^*|$. These other sources of uncertainty are primarily related to the empirical models used to predict $|E^*|$ (example: Witzak, Hirsch, Kahil et al., among others) (Kahil et al. 2015). Since model uncertainties are generally evaluated from statistical analyses involving databases of measured and predicted $|E^*|$ values, the evaluation of model uncertainty could be flawed by the inherent variability that could exist in the measured values of $|E^*|$ for the cases included in the database. This could result in estimates of model uncertainty that are larger than expected, falsely indicating that the available models are ineffective at predicting $|E^*|$.

Limited research studies on pavement reliability problems using $|E^*|$ indicate that the variability in the resilient modulus is generally adopted to represent the uncertainty in $|E^*|$ (Aguiar-Moya and Prozzi 2011, Dilip et al. 2013, Kim and Lee 2002, Maji and Das 2008). Additionally, the statistical properties of the asphalt modulus and its probability distribution

are normally adopted from existing literature on the resilient modulus yielding a coefficient of variation (COV) in the range of 0.1 to 0.4 (Timm et al. 1999). Aguiar-Moya and Prozzi reported that the modulus of the HMA layer has a significant impact on the performance of a given layer even when using a COV less than 10% (Aguiar-Moya and Prozzi 2011). Alternatively, many studies use the probability distributions of the input parameters of the Witczak or Hirsh predictive models for $|E^*|$ to determine the distribution of $|E^*|$ through Monte Carlo simulations or other reliability based analyses (Aguiar-Moya et al. 2012, El-Basyouny and Jeong 2010, Jeong 2010, Thyagarajan et al. 2011).

The degree of uncertainty in $|E^*|$ depends on the method used to determine $|E^*|$. If $|E^*|$ is being measured in the laboratory using conventional testing protocols, the main source of uncertainty will be the inherent variability due to the different factors described earlier. If $|E^*|$ is being predicted using available empirical models, the main sources of uncertainty stem from uncertainty associated with the predictive model and the inherent variability that is expected to exist in practical field conditions. All of the previous attempts to characterize the uncertainty in $|E^*|$ fall short of providing a realistic quantification of the sources of uncertainty in $|E^*|$. The study done by Kahil et. al. constituted the first attempt to determine a priori realistic probability distribution for $|E^*|$ at any reduced frequency (Kahil et al. 2015). The approach provided a realistic universal probability model for $|E^*|$ regardless of the properties of the asphalt concrete mix being used. Although no attempt was made to separate the different sources of uncertainty, the study showed that an accurate representation of the average $|E^*|$ master curve can be obtained using the mathematical expressions of the sigmoidal function. The main finding of the study is that the universal coefficient of variation (COV) of $|E^*|$ varies significantly with reduced frequency, with the COV increasing from a relatively small value of 0.55 for high reduced frequencies to a high value of 1.55 for the very low reduced frequencies. Based on the statistical characterization of $|E^*|$, 96% confidence bounds about the mean master curve were determined as shown in Figure 1. These confidence intervals are indicative of the level of uncertainty in $|E^*|$ predictions for a given reduced frequency.

The probabilistic $|E^*|$ model presented by Kahil et al. represents the universal uncertainty in $|E^*|$. The COVs that are reflected in the model (Figure 1 a) include the contributions of model uncertainty (sigmoidal model) and uncertainty due to inherent variability (for measured $|E^*|$ in database). There is a need for quantifying the contribution of the inherent variability to the universal uncertainty in $|E^*|$. Typically, specifications and standards require testing only two or three samples for $|E^*|$ to assess the variability in the $|E^*|$ master curve of a given mix. Testing a larger number of samples is prohibitive due to the fact

that the testing needed to measure $|E^*|$ is complex, expensive, and time consuming. Thus, it is difficult to assess the inherent variability of a certain mix based on the typical practice due to the small number of tested specimens.

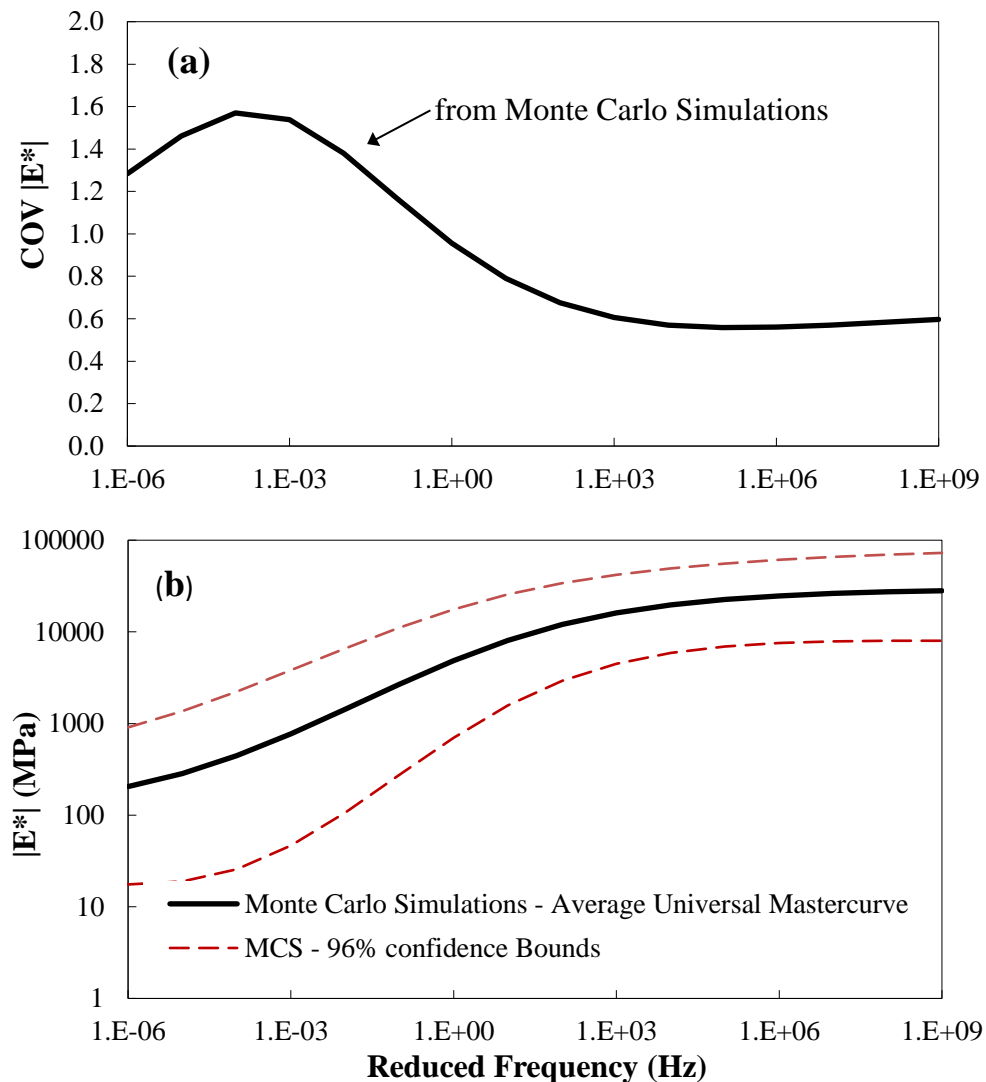


Figure 1. (a) Variation of COV of $|E^*|$ with reduced frequency (b) Average universal $|E^*|$ master curve with 96% confidence-bounds.

2.3 Uncertainty In Relaxation Modulus And Creep Compliance

$|E^*|$ serves as a key input parameter for the design and analysis of the performance of pavements in terms of rutting and fatigue cracking using the mechanistic-empirical pavement design guide (recently known as Pavement ME or DARWin-ME). However, $E(t)$ and $D(t)$ serve as two fundamental input parameters for the development of advanced VEPCD model of asphalt concrete. Also, $D(t)$ serves as a major parameter for the characterization of the thermal cracking behavior of asphalt concrete mixes (Jamrah and Kutay 2015). The analysis of the viscoelastic behavior of asphalt concrete by finite element analysis requires the shear modulus ($G(t)$) and bulk modulus ($K(t)$) as fundamental properties presenting the time and temperature dependency of asphalt mixes (Azari et al. 2007, Elseifi et al. 2006, Kim et al.

2010). $G(t)$ and $K(t)$ are typically calculated based on $E(t)$ and Poisson's ratio. This shows that $E(t)$ and $D(t)$ are key parameters for different problems and methods related to the analysis of pavement performance which implies the necessity of accurately presenting these properties by characterizing the uncertainties associated with them. This is required to serve as an input to robust reliability analysis for the performance of asphalt pavements. Given the uncertainties quantified for $|E^*|$ and the fact that the common practice requires the use of interconversion methods to obtain $E(t)$ and $D(t)$ from measured E^* data, it is believed to be necessary to quantify the inherent uncertainties associated with $E(t)$ and $D(t)$ as a function of reduced time. Thus, the inherent uncertainty of E^* presented by $E'(w)$ will be propagated forward to quantify that of $E(t)$ and $D(t)$ in terms of each function's Prony coefficients. The Prony representation of $E(t)$ and $D(t)$ of any asphalt concrete mix will be a probabilistic model that can be used as an input for any analysis method requiring any of these properties. It allows the calculation of $E(t)$ and $D(t)$ with the associated uncertainty at any required reduced time.

Limited research is available in the literature on quantifying the uncertainty associated with $E(t)$ and $D(t)$. Hilton et al. studied the effect of using each of the Gaussian and Beta distributions to present the probability distributions of the creep and relaxation functions (Hilton et al. 1991). The relaxation modulus data was found to be dispersed over an interval of six standard deviations around the mean, with standard deviations modeled as a function of time. A study conducted by Simsiriwong et al. has stated that viscoelastic material properties generally exhibit a large degree of scatter in the order of 50-100% and ignoring statistical analysis in the formulation of viscoelastic functions lead to false conclusions (Simsiriwong et al. 2014). This study focused on determining the variability of short-term creep compliance curves fitted by Prony series for a thermoset vinyl ester resin. The conducted statistical analysis showed that Weibull distribution with two parameters can be used for fitting $D(t)$ at any time. In addition, a study conducted by Mehrez et. al has addressed the modeling of the components of $D(t)$ for AC: storage and loss compliances ($D'(w)$ and $D''(w)$) within a stochastic identification framework that accounts for different sources of uncertainty such as noisy measurements, model inadequacy, inherent material variability, and scarcity of available testing data presented by only two replicates for each mix (Mehrez et al. 2014). The proposed probabilistic framework has the ability to overcome the shortcomings of typically used deterministic calibration methods where the averaging of available data does not account for uncertainties imposed by the data, calibration process, and modeling approach.

2.4 Uncertainty In Advanced Mechanistic Models

The VEPCD model requires several material properties that need to be determined using different test methods (complex modulus test, crosshead test, creep and recovery test...) at different loading conditions and temperatures. Test results might be used directly or after being converted mathematically to determine other needed properties such as: 1) using complex modulus (E^*) data to determine creep compliance ($D(t)$) and relaxation modulus ($E(t)$), and 2) using data from monotonic tests to determine damage evolution curves. Such mathematical formulations and computations might induce further uncertainties in the material properties which will propagate forward towards the predicted viscoelastic and viscoplastic strains. Thus, it is needed to consider the inherent uncertainty associated with each of the required material properties and to propagate them within a probabilistic framework towards the achievement of a probabilistic VEPCD model.

The common practice in developing and calibrating VEPCD model considers all these properties to be deterministic as calculated by averaging the results of testing two or three replicates of each test. However, a larger number of replicates for each test is needed for conducting a meaningful statistical analysis. This is not a common practice due to the complex, expensive, and time-consuming preparation and testing of asphalt concrete specimens. In this research, mixes with at least eight replicates for each required test will be investigated to model and quantify the inherent variability in each of the input material properties. These uncertainties will be forward propagated to provide a probabilistic model for the predicted viscoelastic strains.

In general, limited research has been conducted on probabilistic modeling of the inherent uncertainties in asphalt material properties and specifically on advanced asphalt material characterization models. A study conducted by Mehrez et al. (2014) addressed the stochastic modeling and propagation of creep compliance within a probabilistic framework coupled with finite element analysis to provide a spectral representation and statistical analysis of strain response which can be used for reliability based analysis of pavement performance. (Mehrez et al. 2014). Another studies have addressed the modeling of the uncertainty in material properties of asphalt pavements in terms of randomized air void fields and the incorporation of the random distribution of these voids into macro-mechanical modeling of flexible pavements using finite element methods (Caro et al. 2013, Castillo and Caro 2014). Also, this heterogeneity in asphalt concrete mixtures was incorporated using stochastic techniques to simulate the response of asphalt concrete layers subjected to moisture diffusion and mechanical loading (Caro et al. 2015).

Recently, research initiatives have taken place to provide probabilistic approaches for modeling the mechanistic behavior of asphalt concrete and namely the prediction of the viscoelastic and viscoplastic strains. Lee et al. (2015) developed a probabilistic approach for modeling the fatigue crack growth for asphalt concrete (Lee et al. 2015). A research conducted by Sadek (2015) provided a novel probabilistic framework for predicting, as accurate as possible, the fatigue life of asphalt mixes using the viscoelastic continuum damage approach (Sadek 2015). In this study, the number of cycles to failure by fatigue cracking has been modeled by considering the material properties from three tested replicates where these properties are considered as normally-distributed random variables. This probabilistic analysis provided more consistent and reliable fatigue life results than those of the deterministic analysis (Sadek et al. 2016).

Research by Gudipudi and Underwood (2016) studied the reliability of the fatigue life of asphalt concrete with the simplified-VECD model. The method considered the uncertainty and variability of the input parameters related to the linear viscoelastic characterization, damage characteristic curve, and failure criterion through MonteCarlo Simulations (Gudipudi and Underwood 2016). The presented work examined only a single mix, a single laboratory, and a limited number of replicates that could induce some errors in the probability distribution of the input parameters used in the prediction models. This framework has been expanded to improve the reliability of predicting the fatigue life predictions by using data from the fine aggregate matrix phase rather than the asphalt concrete data (Gudipudi and Underwood 2017).

Sharma and Swamy (2016) and Singh and Swamy (2017) presented a probabilistic approach to describe the scatter in damage characteristic curves used for the prediction of fatigue cracking based on VECD mechanics. This research shows that a significant scatter is found in the damage characteristic curves even under well-controlled laboratory conditions as shown in Figure 2 (Sharma and Swamy 2016, Singh and Swamy 2017). This is done by testing eight replicates of the investigated asphalt concrete mix: four replicates to determine the linear viscoelastic properties and other four used for damage-inducing tests to determine fatigue properties of asphalt concrete. Then, 16 damage characteristic curves were calculated, fitted, and used to characterize the scatter by fitting the distribution of the damage parameter values obtained at particular values of normalized pseudostiffness.

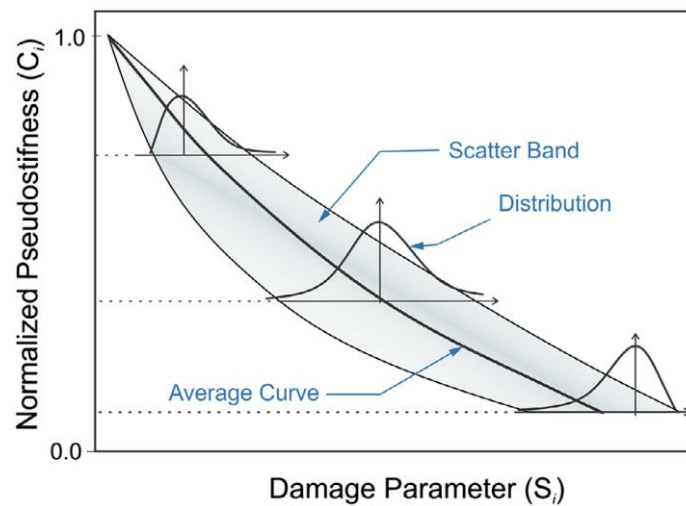


Figure 2. Probabilistic damage characteristic curve (after Singh and Swamy 2017).

The available studies in literature aim at providing probabilistic approaches for predicting the resistance of asphalt concrete mixes to fatigue cracking that is based on testing asphalt mixes either in tension state or tension/compression state. A recent study by Bai et al. (2016) presented a stochastic viscoelastic-viscoplastic model to analytically investigate the modification effect of fine and coarse crumb rubber using the dry-process on asphalt mixtures under uniaxial compression state. The presented model is based on Schapery's nonlinear viscoelastic model and Schwartz's viscoplastic model. The total strain of a deformed asphalt mix is considered to be decomposed of viscoelastic strain and a viscoplastic component multiplied by a time-independent random parameter to representing sample dispersion. The scatter of the viscoelastic strain is neglected as assumed that it is much smaller than the viscoplastic strain (Bai et al. 2016). This parameter has a lognormal distribution and calculated based on the realization of four creep tests and five repeated stress creep and recovery tests conducted in compression state at 15°C.

Many of these studies are novel yet more work is required towards rendering asphalt characterization from being deterministic towards being fully probabilistic. Such work needs to be conducted under the condition of fully understanding the concepts of probability and statistics associated with the problem in hand. It is needed to make a proper use of such concepts to properly characterize and quantify the uncertainties associated with the various parameters being investigated.

CHAPTER 3

THEORETICAL BACKGROUND ON ASPHALT MATERIALS CHARACTERIZATION

3.1 Introduction

Material characterization models can provide accurate and advanced material properties that account for the inherent behavior of the different HMA and WMA mixes utilized in this research. These are mathematical models that idealize the real mechanical or/and engineering behavior of asphalt mixes. Such models are based on historically developed theories and have different levels of complexity.

Asphalt concrete can be considered a unique material whose mechanics differ from that of other commonly used materials. This uniqueness is imposed by different factors related to its composition, production process, environmental conditions and performance which is dictated by its different modes of failure. Asphalt concrete is a composite material basically made up of aggregates, asphalt binder, and air voids along with other constituents that might be added to improve any of the previously mentioned aspects. These include but are not limited to WMA additives, fibers, fillers, recycled materials, modifiers, and antistripping agents. Mixes with these additives have a complex behavior due to the variability presented in the composition, properties, stiffness, distribution, localization, and interaction between each of its components which varies from one source to another. Even though the asphalt binder constitutes only about 3% to 7% by weight of the asphalt concrete mix, its sensitivity to temperature and loading rate makes the behavior of asphalt concrete more complex and challenging. This might be even more complicated due to the incorporation of additives having different functions and interactions with the other components of the mix.

The behavior of asphalt concrete may vary from elastic and linear VE at low temperatures and/or fast loading rates to non-linear VE, VP and plastic at high temperatures or slow loading rates (Chehab 2002). The nonlinear VE behavior might be also experienced at service loading conditions due damage presented by micro-cracking. In this case, the complexity will be encountered by the need to account for the VE hereditary effects of the asphalt along with the evolution of damage (Park et al. 1996). Thus, a comprehensive material characterization model has to include the different behaviors of asphalt concrete i.e. both the VE and VP components.

Constitutive models represent the mathematical relationship between the changes in stress and strains in asphalt mixtures based on experimentally obtained results. Such models are based on two approaches in the field of mechanics of materials:

1) Micromechanical Approach is based on the discretization of the asphalt concrete and characterizing the properties of its constituents. The state of damage is characterized by the measurement and evaluation of the defects that compose it and how the distribution of these microdefects affect the macroscopic constitutive parameters (Abbas et al. 2007, Kim 2008, Shakiba et al. 2013). The complexity of the microstructure, micromechanics, and the interactions among the microdefects require certain assumptions and simplifications that might lead to compromising the realistic characterization of the macroscopic behavior of asphalt (Kim 2008, Park et al. 1996).

2) Macromechanical Approach considers the asphalt mixture as a homogenous continuum without modeling its individual constituents where the model is based on experimental measurements of representative samples of the asphalt concrete composite. This model is independent of the mixture's specific properties where it ignores the physical interactions at micro-scale level. It models the behavior based on parameters that can be obtained on a macro-scale level (Underwood et al. 2010). This approach quantifies damage by internal state variables within the context of thermodynamics of irreversible processes (Lee and Kim 1998).

3.2 Overview of Modeling Approach

In this research, the continuum macro-scale damage model is utilized in order to characterize the mechanical behavior of asphalt concrete with growing damage. Based on continuum damage mechanics, the strain constitutive equations for damaged materials may be derived in the same way for a virgin material except for the effective stiffness of the material which takes into account the reduction of the material's stiffness due to damage (Lemaitre 2012). In other words, the damaged body is considered as an undamaged body with reduced stiffness. Thus, this approach acquires the modeling of the material's net effect of microstructural changes through observational properties of this material, thus taking into account the fact that asphalt concrete behaves differently at various temperatures and loading rates. Based on the strain decomposition principle, the strain response of an asphalt mix has several components as presented in Equation 1 (Chehab et al. 2003, Saadeh et al. 2007).

$$\varepsilon_{Total} = \varepsilon_e + \varepsilon_{ve} + \varepsilon_p + \varepsilon_{vp} \quad \text{Equation 1}$$

where:

ε_{Total} = total strain response, ε_e = elastic strain which is recoverable and instantaneous, ε_{ve} = viscoelastic strain which is recoverable and time dependent, ε_p = plastic strain which is irrecoverable and instantaneous, and ε_{vp} = viscoplastic strain which is irrecoverable and time dependent.

The behavior of asphalt concrete can extend from VE at low temperatures and fast loads to VP at high temperatures and slow loads. The adopted modeling strategy aims at modeling each component separately referred to as the VE strain combining both elastic and VE strains (both the linear and nonlinear components); and the VP strain which combines both the plastic and VP strains. These are combined together to yield the material's response by the VEPCD model (Chehab 2002). This model is selected because it is applicable for the characterization of the behavior of asphalt concrete under complex loading conditions and different temperatures without the need to deal with the complicated physical interactions at the microscale level. In addition, the needed testing protocol is simple where it requires complex modulus testing and constant crosshead rate tests at low and high temperatures (Yun and Kim 2011).

The used VE modeling approach is based on Schapery's continuum damage model. The model, originally developed for modeling solid rocket propellant and then developed by Kim and Little for asphalt concrete (Kim and Little 1990, Kim et al. 1997, Lee and Kim 1998a), is based on a thermodynamic formulation. This theory presents the structural changes with the growth of damage using internal state variables. For the VP component, the strain hardening model from Uzan's work has been adopted for this purpose (Uzan et al. 1985). This model is needed because the VE model is not able to realistically characterize the behavior of asphalt concrete at conditions of high temperature and/or slow loading rates at which the VP component becomes significant (Chehab 2002).

The adopted strategy for the VEPCD modeling requires a stepwise approach such that the experimental program systematically evaluates the different strain components from the simplest state of linear viscoelasticity (LVE) without cracking and permanent deformation to states with complex mechanisms including the cases of nonlinear viscoelasticity due to microcracking damage and the case of viscoplasticity (Kim 2008). First, the VE model is developed based on experimental testing for cases of low temperatures and/or high testing rates where the effect of viscoplasticity is minimal. Then, the experimental data of tests at

high temperature and/or slow loading rates is used for the development of the VP model. The VEPCD is based on the following four principles:

- Elastic-Viscoelastic correspondence principle
- Work potential theory and continuum damage mechanics
- Strain hardening viscoplastic model
- Time-temperature superposition with growing damage

3.3 Linear Viscoelastic Characterization

As mentioned earlier, asphalt concrete is a viscoelastic material that exhibits a time/rate dependency. For a system to be linear, it must satisfy the conditions of both homogeneity and superposition:

- Homogeneity:

$$R(cI) = cR(I) \quad \text{Equation 2}$$

- Superposition:

$$R(I_1 + I_2) = R(I_1) + R(I_2) \quad \text{Equation 3}$$

where: I, I₁, and I₂ = input histories, R=response, and c= arbitrary constant.

The response is a function of the input history as illustrated through simple examples presented in Table 2. Homogeneity requires that the response is proportional to the input and the superposition implies that the response to the sum of n inputs is equal to the sum of the responses of the n individual inputs.

Table 2. Illustration of the time dependence of the behavior of asphalt concrete using different tests.

EXPERIMENT	STRAIN	STRESS
CREEP	Increase (R)	Constant (I)
RELAXATION	Constant (I)	Decrease (R)
CYCLIC	Sinusoidal/Haversine (R)	Sinusoidal/Haversine (I)
	R has the same shape as I but with a shift lag (Stress precedes strain by phase angle)	
CONSTANT RATE	Constant rate of increase (I)	Increases till maximum (R)

The response of the material is a function of both current and past input history. The mathematical formulation of the LVE theory presenting the relationship between the input and response (i.e. constitutive equations for stress-strain relationship) is expressed through the convolution integral (also known as hereditary, superposition, Boltzman integral) as

presented in Equation 4. This integral is built on the principle of superposition to determine the response of an input history consisting of an infinite number of increments over the time domain.

$$R = \int_{-\infty}^t R_H(t, \tau) \frac{dI}{d\tau} d\tau \quad \text{Equation 4}$$

where: R_H = unit response function, I = input history, R = response, t = time of interest, and τ = integration parameter.

Equation 4 allows the calculation of the response to any input history for an aging LVE system in which the prediction at any time is a function of time of fabrication and time of loading. In this research, asphalt concrete is assumed to behave as a non-aging system in which Equation 4 reduces as the following:

$$R = \int_{-\infty}^t R_H(t - \tau) \frac{dI}{d\tau} d\tau \quad \text{Equation 5}$$

The lower bound of integration can be reduced to 0 instead of $-\infty$ if the input starts at time 0 and both the response and input are equal to 0 at $t < 0$. The designation 0 represent time 0 which in fact account for any possible discontinuity in the input at $t = 0$. Thus, Equation 5 reduces to:

$$R = \int_0^t R_H(t - \tau) \frac{dI}{d\tau} d\tau \quad \text{Equation 6}$$

For uniaxial loading, the non-aging, linear viscoelastic stress-strain relationships are:

$$\sigma = \int_0^t E(t - \tau) \frac{d\varepsilon}{d\tau} d\tau \quad \text{Equation 7}$$

$$\varepsilon = \int_0^t D(t - \tau) \frac{d\sigma}{d\tau} d\tau \quad \text{Equation 8}$$

where: $E(t)$ and $D(t)$ are unit response functions presenting the relaxation modulus and creep compliance, respectively.

The characterization of LVE behavior of asphalt concrete is done through a set of experimental uniaxial tests that are able to take into consideration the time dependency of the material's response. The tests done to determine these properties of asphalt concrete are non-damage-inducing tests performed in the LVE range in order to determine the unit response functions being: complex modulus (E^*) in frequency domain, and relaxation modulus ($E(t)$) and creep compliance ($D(t)$) in time domain.

These response functions are fundamental for characterizing the behavior of asphalt concrete in the LVE; however, they are required as fundamental input for the development of the VEPCD model. Moreover, they are used as the viscoelastic fingerprints to assess the specimen-to-specimen variability in experimental testing of asphalt concrete (Kim 2008). The

relaxation modulus is needed for the calculation of pseudostrains and the creep compliance is required to calculate the strains beyond the LVE range.

3.3.1 Complex Modulus

The complex modulus E^* is a response function that relates stress to strain in the LVE range upon application of a sinusoidal/haversine loading. It is composed of two components: 1) dynamic modulus $|E^*|$ presenting the ratio of stress amplitude to strain amplitude and 2) phase angle presenting the time lag between stress and strain. Being a complex number, E^* has both real and imaginary parts, the storage and loss moduli respectively as shown in Equation 9.

$$E^* = E' + iE'' \quad \text{Equation 9}$$

where:

E' = Storage Modulus,

E'' = Loss Modulus, and

$i = \sqrt{-1}$.

Therefore, the magnitude of the E^* i.e. $|E^*|$ is defined as shown in Equation 10:

$$|E^*| = \sqrt{E'^2 + E''^2} \quad \text{Equation 10}$$

The storage and loss moduli are related to the dynamic modulus as shown in Equation 11 and Equation 12, respectively. This relation is represented by Figure 3. The phase angle (ϕ) presents the delay between stresses and strains where ϕ decreases as the material tends to be more elastic reaching a value of zero for a pure elastic material. Similarly, the more the material is viscous the more the phase angle tends to increase, thus a pure viscous material has $\phi=90^\circ$.

$$E' = |E^*| \cos \phi \quad \text{Equation 11}$$

$$E'' = |E^*| \sin \phi \quad \text{Equation 12}$$

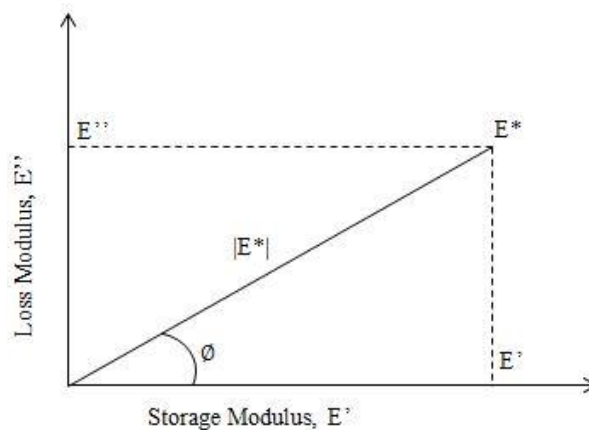


Figure 3. Complex modulus graphical representation.

3.3.2 Relaxation Modulus

The relaxation modulus $E(t)$ is the time dependent stress response to a unit uniaxial strain input. In the LVE range, $E(t)$ can be obtained at different strain levels by defining it as:

$$E(t) = \frac{\sigma(t)}{\varepsilon_0} \quad \text{Equation 13}$$

where: $\sigma(t)$ = time dependent stress and ε_0 = constant applied strain

At short times, the $E(t)$ follows a high asymptotic plateau level referred to as the glassy or elastic modulus where it falls to reach the equilibrium (rubbery) modulus presented by a low asymptotic plateau at longer times (Katicha 2007).

3.3.3 Creep Compliance

The creep compliance $D(t)$ is the time dependent strain response to a unit uniaxial stress input. In the LVE range, $D(t)$ can be obtained at different stress levels defined as:

$$D(t) = \frac{\varepsilon(t)}{\sigma_0} \quad \text{Equation 14}$$

where: $\varepsilon(t)$ = time dependent strain and σ_0 = constant applied stress.

If asphalt concrete is purely elastic, $D(t)$ and $E(t)$ will be the reciprocal of each other. However, since asphalt is a viscoelastic material then the constitutive equation relating $D(t)$ to $E(t)$ will be determined by substituting the ε presented by Equation 8 in Equation 7 which yields:

$$1 = \int_0^t E(t - \tau) \frac{dD(\tau)}{d\tau} d\tau \quad \text{Equation 15}$$

3.4 Conversion Among LVE Response Functions

Researchers have shown that these three LVE response functions are mathematically equivalent and each has essentially the same information regarding the creep and relaxation behavior of asphalt concrete (Park and Kim 1999). This indicates that measuring one of these responses experimentally allows it to be converted using mathematical formulations to determine the other two responses (Mun et al. 2007). The need for interconversion arises from several factors that can be summarized through the following points:

- 1) E^* and $D(t)$ can be measured easily in lab, while the mechanical testing of $E(t)$ requires robust and high capacity testing machines
- 2) If the three functions are to be measured experimentally, then more samples are needed implying experimental programs that require more time
- 3) It is not always possible to conduct $E(t)$ and $D(t)$ over a wide range of time domain such as at very short times

4) Risk of exceeding the LVE range in mechanical tests of E(t) and D(t).

Therefore, E* test is conducted and converted mathematically to determine E(t) and D(t) as presented below.

3.4.1 Analytical Representation of E(t) and D(t)

Whether E(t) and D(t) are measured through mechanical testing or converted from E*, the data of those response functions should be fitted to representative analytical models to be used for modeling the VE and VP behaviors. Several analytical representations were investigated by previous researchers such as: pure power law, generalized power law, modified power law, and Prony series (Kim 2008). The Prony series representation will be used for E(t) and D(t). These series have been shown to have the ability of modeling a wide range of LVE response and the ease in computations of integrals of VEPCD. This is due to their relatively simple and rugged computation efficiency associated with their exponential basis. The use of Prony series for the characterization of LVE properties is based on the theory of mechanical models presented by linear springs and dashpots.

The Prony series representation of E(t) is physically related to the Wiechert (or Generalized Maxwell) model consisting of M Maxwell models connected in parallel with an individual spring of stiffness E_∞ whose mathematical formulation is presented by the following form:

$$E(t) = E_\infty + \sum_{m=1}^M E_m e^{-t/\rho_m} \quad \text{Equation 16}$$

where:

E_∞ = long time equilibrium modulus which can be determined from the storage modulus at a very small non negative radial frequency (Mun et al. 2007),

ρ_m = relaxation time, and

E_m = Prony regression coefficients.

The relaxation times are usually assumed and thus the regression coefficients can be determined by collocation for certain points of time. The relaxation coefficients can be determined by defining the following set of matrices:

$[B]$ = Square Matrix of size $m \times n$ ($m=n$) whose entries are calculated using Equation 17

$$B_{n,m} = \sum_{m=1}^M e^{-t_n/\rho_m} \quad \text{Equation 17}$$

$[A]$ = Column vector of size n where $A_n = E(t_n) - E_\infty$

$[C]$ = Column vector of size m with non-negative coefficients presenting the relaxation coefficients. The condition that the coefficients are non-negative is not necessary but preferable.

Having $E(t_n)$, E_∞ , t_n , and ρ_m as known factors, then the relaxation coefficients can be solved by performing the following matrix multiplication:

$$[C] = [B]^{-1} \times [A] \quad \text{Equation 18}$$

The Prony series representation of $D(t)$ is physically related to the Kelvin (or Generalized Voigt) model consisting of M Kelvin models connected in series with an individual spring whose mathematical formulation is presented by the following form:

$$D(t) = D_o + \sum_{m=1}^M D_m [1 - e^{-t/\tau_m}] \quad \text{Equation 19}$$

where:

D_o = Glassy compliance = Initial creep compliance, it can be calculated as the storage compliance at a very large angular frequency (Mun et al. 2007),

D_m = regression coefficients, and

τ_m = Retardation time.

As in the case of $E(t)$, the collocation method is used in order to determine the regression coefficients for $D(t)$ where:

$$A_n = D(t_n) - D_o \quad \text{Equation 20}$$

$$B_{n,m} = \sum_{m=1}^M (1 - e^{-\frac{t_n}{\tau_m}}) \quad \text{Equation 21}$$

3.4.2 Conversion Methods

The conversion between LVE response functions in frequency and time domains has been illustrated through different methods and approaches (Chehab and Kim 2009, Mun et al. 2007, Park and Kim 1999, Schapery and Park 1999). The basics of these approaches will be introduced briefly in the following sections:

3.5.2.1 E^* to $E(t)$: Approximate Method

An approximate relationship exists for the calculation of $E(t)$ using the storage modulus ($E'(\omega)$) which can be formulated using the following set of equations:

$$E(\xi) \cong \frac{1}{\lambda} E'(\omega) \Big|_{\omega = (\frac{1}{\xi})} \quad \text{Equation 22}$$

where: ξ = Reduced time, ω = reduced frequency, and λ = adjustment function defined as:

$$\lambda = \Gamma(1 - n) \cos\left(\frac{n\pi}{2}\right) \quad \text{Equation 23}$$

where: Γ is a gamma function and n is local log-log slope of $E'(\omega)$.

3.5.2.2 E^* to $E(t)$: Exact Method

The Exact Method is derived from the Generalized Maxwell model where the Fourier transform is used along with the elastic-viscoelastic correspondence principle. E^* is expressed through the following equation:

$$E^* = E_\infty + \sum_{m=1}^M \frac{i\omega_n \rho_m E_m}{i\omega_n \rho_m + 1}, n = 1, \dots, N \quad \text{Equation 24}$$

In Equation 24, E^* is presented by a complex number whose real component is the storage modulus ($E'(\omega)$) and hence presented as:

$$E'(\omega_n) = E_\infty + \sum_{m=1}^M \frac{\omega_n^2 \rho_m^2 E_m}{\omega_n^2 \rho_m^2 + 1}, n = 1, \dots, N \quad \text{Equation 25}$$

where: ρ_m = Relaxation time and ω_n = Reduced angular frequency

The Prony series coefficients E_m will be solved by the collocation method of the $E'(\omega)$ data calculated from the results of E^* testing. These coefficients will be used to calculate $E(t)$ for asphalt concrete mixes.

3.5.2.3 E^* to $D(t)$: Direct Conversion

This conversion method is based on the following relationship for LVE systems:

$$D^* \cdot E^* = 1 \quad \text{Equation 26}$$

where: D^* = complex compliance and E^* = complex modulus.

Equation 26 is used to calculate the storage compliance D' which is based on the mechanical testing of E^* presented as:

$$D' = \frac{E'}{(E')^2 + (E'')^2} = \frac{\cos(\phi)}{|E^*|} \quad \text{Equation 27}$$

The storage modulus will be presented by the Prony series whose coefficients will be determined using the collocation method. Thus, D' will be presented as the following:

$$D' = D_o + \sum_{n=1}^N \frac{D_n}{\omega_R^2 \tau_n^2 + 1} \quad \text{Equation 28}$$

The coefficients of D' will be used in order to determine $D(t)$ through Prony series presented by:

$$D(\xi) = D_o + \sum_{n=1}^N D_n (1 - e^{-\frac{\xi}{\tau_n}}) \tau \quad \text{Equation 29}$$

3.5.2.4 E^* to $D(t)$: Through $E(t)$

After determining $E(t)$ using any of the aforementioned methods, it can be converted into $D(t)$ through an approximate method based on the relation between $E(t)$ and $D(t)$ in the LVE presented as:

$$E(t)D(t) = \frac{\sin(m\pi)}{m\pi} \quad \text{Equation 30}$$

where: m is the power determined from fitting $E(t)$ to power law as presented in Equation 31.

$$E(t) = E_1 t^{-m} \quad \text{Equation 31}$$

The power law is not able to present $E(t)$ or $D(t)$ over the entire time domain because it is not able to capture the short or long time asymptote. Therefore, the $E(t)$ over the entire time domain will be presented by a set of local power law representations and thus $D(t)$ will be calculated using Equation 30. From the converted data, the collocation method will be used to determine the regression coefficients required to fit the Prony series of $D(t)$.

3.5 Time-Temperature Superposition

3.5.1 Case of LVE Behavior

The behavior of asphalt concrete is highly dependent on the temperature and time/frequency of loading. In the LVE range, it is well known to be a thermorheologically simple (TRS) material; i.e. the effects of time or frequency are dependent and thus can be jointly expressed through one parameter. The time-temperature superposition can be used to characterize the dependency of asphalt concrete in the LVE range. For example, the same $|E^*|$ can be obtained at different combinations of temperature and loading rate.

The LVE properties (E^* , $E(t)$, or $D(t)$) as a function of time or frequency at different temperatures, can be shifted horizontally along the time or frequency axis in the log scale to build a single mastercurve of the investigated LVE property. This mastercurve will be developed for a given arbitrary reference temperature towards which the data at different temperatures will be shifted and a shift factor (a_T) will be associated with each temperature. For example, $|E^*|$ is commonly expressed as $|E^*|(f_R)$ instead of $|E^*|(frequency, Temperature)$ where f_R presents the reduced frequency that is a joint factor of both frequency and temperature. In frequency domain, the reduced frequency (f_R) is expressed as:

$$f_R = f \times a_T \quad \text{Equation 32}$$

$$\log(f_R) = \log(f) + \log(a_T) \quad \text{Equation 33}$$

For case of time domain, reduced time can be expressed as:

$$t_R = \frac{t}{a_T} \quad \text{Equation 34}$$

$$\log(t_R) = \log(t) - \log(a_T) \quad \text{Equation 35}$$

3.5.2 Case of Growing Damage State

The development of constitutive models for the characterization of asphalt concrete beyond the LVE range requires conducting experimental tests that extend to the case of damage. Therefore, researchers have investigated the applicability of the time-temperature superposition principle for cases of damage to reduce the required experimental testing. This helps in having economic and efficient experimental programs for the development of such advanced models. The applicability of this principle namely for hot mix asphalt (HMA), in the cases of growing damage and viscoplastic straining in both tension and compression states was valid (Chehab et al. 2002, Schwartz et al. 2002, Yun et al. 2009, Zhao and Kim 2003). These studies have shown that the same shift factors used for developing the $|E^*|$ mastercurves in the undamaged LVE state can be used for damage state analysis. For example, the VE strain at high temperatures can be determined by applying the time-shift factors obtained from the E^* testing to the VE model to be developed at low temperatures (Chehab et al. 2003, Yun et al. 2009). Moreover, these shift factors have been shown to be applicable at high levels of damage and permanent deformation regardless of the loading type (monotonic or repetitive creep and recovery) given that all tests are to be unconfined or done at the same confining pressure.

3.6 Modeling of Viscoelastic Behavior

The LVE model is extended to include the damage induced by microcracking using the work-potential theory and the elastic-viscoelastic correspondence principle to establish the viscoelastic continuum damage (VECD) model (Chehab et al. 2003, Daniel and Kim 2002, Kim and Daniel 1997, Yun et al. 2009).

3.6.1 Elastic-Viscoelastic Correspondence Principle

The elastic-viscoelastic correspondence principle was developed by Schapery in order to eliminate the time dependence and thus simplify a viscoelastic problem into a mathematically equivalent elastic problem (Schapery 1984). For non-aging and linear systems, the correspondence occur between the constitutive equations of the viscoelastic and elastic domains. Stresses and strains are not necessarily physical quantities in the viscoelastic body but pseudo variables in the form of convolution integrals. More theoretical background of this concept can be found elsewhere (Chehab 2002, Schapery 1984).

According to Schapery, the uniaxial pseudostrain (ε^R) can be defined as:

$$\sigma = \varepsilon^R \times E_R \quad \text{or} \quad \varepsilon^R = \frac{\sigma}{E_R} \quad \text{Equation 36}$$

where: E_R = Reference modulus set as an arbitrary constant (taken as 1 MPA in this study),

ε^R = Dimensionless pseudostrain; and

σ = Uniaxial stress.

Substituting the stress in Equation 36 with its corresponding stress-strain constitutive equation presented in Equation 7 yields:

$$\varepsilon^R = \frac{1}{E_R} \int_0^t E(t - \tau) \frac{d\varepsilon}{d\tau} d\tau \quad \text{Equation 37}$$

The pseudostrain accounts for all the hereditary effects of the material through the convolution integral. It allows for the separation of the viscoelastic behavior from any accumulated damage. In simple words, pseudostrain can be considered as the stress response to any strain input in the LVE range. By continuum damage principles, any reduction in stiffness is related to damage. Any reduction in the slope of the stress-pseudostrain curve is directly related to the accumulation of damage especially that the time effect is eliminated by the pseudo. In the LVE range, the slope of the stress-pseudostrain curve known as pseudostiffness is typically 1.0.

3.6.2 Pseudostrain Calculation

Based on previous studies, the pseudostrain can be calculated through two different methods:

- Linear piecewise method: it presents the development of the analytical equation of pseudostrain presented by Equation 34 which can be reduced as the following:

$$\varepsilon^R = \frac{1}{E_R} \left[\int_0^{t_1} E(t - \tau) \frac{d\varepsilon_1}{d\tau} d\tau + \int_{t_1}^{t_2} E(t - \tau) \frac{d\varepsilon_2}{d\tau} d\tau + \dots + \int_{t_{n-1}}^{t_n} E(t - \tau) \frac{d\varepsilon_n}{d\tau} d\tau \right]$$

$$\text{Equation 38}$$

Considering the case of constant crosshead testing that is strain controlled:

$$\frac{d\varepsilon_n}{d\tau} = c_n \quad \text{Equation 39}$$

where c_n presents a constant at each time step.

Equation 38 can be solved by change of variables through setting ($u = t - \tau$) and considering the Prony series representation of $E(t)$ as shown in Equation 16. This will reduce the pseudostrain equation as:

$$\varepsilon_R = c_1 \left[E_{\infty} u - \sum_{m=1}^M \rho_m E_m e^{-\frac{u}{\rho_m}} \right]_{t-t_1}^t + c_2 \left[E_{\infty} u - \sum_{m=1}^M \rho_m E_m e^{-\frac{u}{\rho_m}} \right]_{t-t_2}^{t-t_1} + \dots + c_n \left[E_{\infty} u - \sum_{m=1}^M \rho_m E_m e^{-\frac{u}{\rho_m}} \right]_0^{t-t_n}$$

$$\text{Equation 40}$$

- **State Variable Approach:** This approach was developed by Simo and Hughes where it constitutes the transformation of the convolution integral into an algebraic operation (Simo and Hughes 1998). This method requires the association of a variable with each Maxwell element of the Prony series representation of E(t) as presented in Equation 16. This variable tracks the behavior of each element throughout the loading and thus the pseudostrain will be formulated as:

$$\varepsilon^{R(n+1)} = \frac{1}{E_R} [\eta_0^{n+1} + \sum_{i=1}^m \eta_i^{n+1}] \quad \text{Equation 41}$$

$$\eta_0^{n+1} = E_\infty (\varepsilon^{n+1} - \varepsilon^0) \quad \text{Equation 42}$$

$$\eta_i^{n+1} = e^{-\Delta t / \rho_i} \eta_i^n + E_i e^{-\Delta t / 2\rho_i} (\varepsilon^{n+1} - \varepsilon^n) \quad \text{Equation 43}$$

where: η_0 and η_i are internal state variables for Maxwell elements i at time step n+1, respectively.

The algorithms for the two methods are coded and checked where they provide exactly the same curve for pseudostrains as a function of time. However, the linear piecewise approach is inefficient when analyzing large amounts of data because it requires analyzing the data for all the time steps before the time of interest. This results in a higher analysis time as more data needs to be analyzed. However, the state variables method has been shown to be more efficient where the analysis time is significantly smaller in comparison to the piecewise linear method (Kim 2008).

3.6.3 Uniaxial Constitutive Modeling Using Work Potential Theory

As mentioned earlier, internal state variables (ISV) will be used to quantify the state of damage in asphalt concrete. In this context, the term damage is defined as all structural changes, except linear viscoelasticity, that result in the reduction of stiffness or strength as the material is loaded (Chehab 2002). When damage occurs in a certain system, the energy applied to this system will not be totally stored but part of it will be consumed by causing the damage to the system (Park et al. 1996). This amount of consumed energy will be expressed by ISV. The work potential theory for the behavior of elastic media with growing damage was developed by Schapery based on the method of thermodynamics of irreversible processes and the observed phenomenon of path dependence of work. The elements of this theory in terms of strain energy formulation are represented through the following equations:

- Strain energy density function: $W = W(\varepsilon_{ij}, S_m)$ **Equation 44**

- Stress-strain relationship: $\sigma_{ij} = \frac{\partial W}{\partial \varepsilon_{ij}}$ **Equation 45**

- Damage evolution law: $-\frac{\partial W}{\partial S_m} = \frac{\partial W_S}{\partial S_m}$ **Equation 46**

where:

ε_{ij} = strains, σ_{ij} = stresses, S_m = ISV or damage parameter, W = available thermodynamic force from loading, and W_S = dissipated energy due to damage growth.

These relationships are developed in order to account for viscoelasticity through the application of the elastic-viscoelastic correspondence principle and the replacement of the physical strain with pseudostrain that will now govern the viscoelastic damage. However, the correspondence principle has been shown insufficient to translate the damage evolution law of elastic material for viscoelastic material because the material's resistance to growth is rate dependent too (Kim 2008). Therefore, researchers have shown the applicability of the use of the well-known power crack growth laws for viscoelastic material as developed by Schapery in 1975. Thus, the relationships for the work potential theory for viscoelastic material with rate dependent evolution law will be as the following:

- Pseudotrain energy density function: $W^R = W^R(\varepsilon^R, S_m)$ **Equation 47**

- Stress-pseudostrain relationship: $\sigma_{ij} = \frac{\partial W^R}{\partial \varepsilon^R}$ **Equation 48**

- Damage evolution law: $\dot{S}_m = \left(-\frac{\partial W^R}{\partial S_m}\right)^\alpha$ **Equation 49**

where:

α = material-dependent constant related to viscoelasticity of the material.

In damage inducing tests, the slope of stress vs. pseudostrain curve decreases due to the reduction in stiffness resulting from the accumulation of damage. This slope is presented by the pseudostiffness (S^R) defined as:

$$S^R = \frac{\sigma}{\varepsilon_R} \quad \text{Equation 50}$$

The calculation of the pseudostrain requires determining $E(t)$ which is converted from E^* . The samples used for damage characterization tests such as the crosshead test are different from those used for E^* . The $E(t)$ for the crosshead samples might not be the same as those of the samples used for E^* even though both sets of samples are representative of the asphalt concrete mix under investigation. This is basically due to specimen-to-specimen variability and different uncertainties associated with the testing of each single specimen of both tests. To account for that, $E(t)$ of monotonic testing is normalized by determining a fingerprint of

every crosshead sample. This is done by testing the sample for $|E^*|$ prior to its damage test at the same temperature of the latter but using a limited number of frequency sweeps. The ratio of the $|E^*|$ fingerprint to that of the $|E^*|$ determined from the entire E^* testing is used to normalize $E(t)$ and get the one specific to the crosshead sample.

In addition, the specimen-to-specimen variability in the pseudostiffness is corrected using the initial pseudostiffness “I” whose value varies around 1.0. The normalized pseudostiffness (C) becomes:

$$C = \frac{S^R}{I} \quad \text{Equation 51}$$

The following uniaxial constitutive equations are presented for linear elastic and linear viscoelastic systems with and without damage. It shows the correspondence where both the viscoelastic and the elastic equations have the same form with pseudostrain replacing the physical strain:

- Elastic body without damage: $\sigma = E\varepsilon$ **Equation 52**
- Elastic body with damage: $\sigma = C(S^*)E\varepsilon$ **Equation 53**
- Viscoelastic body without damage: $\sigma = E_R\varepsilon^R$ **Equation 54**
- Viscoelastic body with damage: $\sigma = C(S^*)E_R\varepsilon^R$ **Equation 55**

where: E = Young’s modulus, C = Normalized pseudostiffness, and S = Internal state variable.

The constitutive equation for the uniaxial stress-strain behavior of asphalt concrete is based on the damage parameter (S) and presented as:

$$W^R = \frac{I}{2} C(S)(\varepsilon^R)^2 \quad \text{Equation 56}$$

The damage parameter has been shown to be simplified from S to S for cases of the uniaxial loading as developed by Park and Kim (Park et al. 1996). S is defined as the Lebesgue norm of pseudostrain as presented by the following equation:

$$S = \left[\int_0^\xi |\varepsilon^R|^{2\alpha} d\xi \right]^{1/2\alpha} \quad \text{Equation 57}$$

where: α is a material constant presenting the inverse of the maximum slope of LVE functions in log-log scale.

3.6.4 *C vs S Approach*

In order to predict the viscoelastic strain for a given stress input at a given reduced time, the relationships relating C to S , and S to stress should be determined. This will be conducted

for each mix at fast loading rates and cold temperatures to ensure the absence of viscoplasticity where the C vs S curves should collapse on top of each other. The experimental results will be used to fit these relationships to serve as the basis corresponding for the prediction of the viscoelastic strain of every mix.

For each test, S can be calculated using the pseudostrain at each data point as obtained from corresponding time and strain of the test. Mathematically, C(S) can be fitted using the C vs S data for any mix using the following model:

$$C(S) = ae^{b(S)^c} \quad \text{Equation 58}$$

where: a, b, and c are fitting parameters.

When the strain history is unknown with only stress and time are given, S can be determined as a function of the Lebesgue norm of stress as shown by (Park et al. 1996) as:

$$S = f \left[\int_0^t \sigma^{2\alpha} dt \right]^{1/2\alpha} \quad \text{Equation 59}$$

S can be related to the Lebesgue norm of stress (LS) using the data of crosshead testing conducted at low temperature and fast loading rates. The relationship between S and LS is obtained by fitting the testing data to 5-term exponential series function:

$$S = a_1 e^{a_2 \times LS(\sigma)} + a_3 e^{a_4 \times LS(\sigma)} + a_5 e^{a_6 \times LS(\sigma)} + a_7 e^{a_8 \times LS(\sigma)} + a_9 e^{a_{10} \times LS(\sigma)} \quad \text{Equation 60}$$

where: $a_1 \dots a_{10}$ are fitting parameters.

Using the inverse of ε^R and expressing it as a function of C(S) and σ , the VE strain can be expressed as:

$$\varepsilon_{ve} = E_R \int_0^t D(t - \tau) \frac{d(\frac{\sigma}{C(S)})}{d\tau} d\tau \quad \text{Equation 61}$$

3.7 Modeling of Viscoplastic Behavior

Many studies have been conducted in order to develop viscoplastic models that are able to predict the permanent strains in HMA. One of these models for uniaxial loading is assumed to follow a strain-hardening model based on fundamental relationships proposed by Uzan and Schapery (Schapery and Park 1999, Uzan 1996, Uzan et al. 1985). This model was shown to predict the viscoplastic strain in both cases of compression and tension under monotonic loading (Chehab et al. 2003, Gibson 2006, Zhao 2002). This can be expressed by:

$$\dot{\varepsilon}_{vp} = \frac{g(\sigma)}{\eta_{vp}} \quad \text{Equation 62}$$

where: $\dot{\varepsilon}_{vp}$ =VP strain rate; η_{vp} = material's coefficient of viscosity, and $g(\sigma)$ is uniaxial stress loading function.

Assuming that η_{vp} follows a power law in strain, the VP strain rate equation reduces to:

$$\dot{\varepsilon}_{vp} = \frac{g(\sigma)}{A\varepsilon_{vp}^p} \quad \text{Equation 63}$$

which can be rearranged and integrated as:

$$\varepsilon_{vp} = \left(\frac{p+1}{A}\right)^{1/p+1} \left(\int_0^t g(\sigma) dt\right)^{1/p+1} \quad \text{Equation 64}$$

Assuming power law of the form $g(\sigma) = B\sigma^q$ in which B and q are material constants, the VP model reduces to:

$$\varepsilon_{vp} = \left(\frac{p+1}{Y}\right)^{1/p+1} \left(\int_0^t \sigma^q dt\right)^{1/p+1} \quad \text{Equation 65}$$

where: ε_{vp} is total viscoplastic strain; q, p, and Y are model parameters.

3.8 ViscoElastoPlastic Model

Crosshead tests are conducted at high temperatures and slow loading rates in order to determine the VP model coefficients. The response of those testes are shifted using the LVE shift factors to a reference temperature in order to obtain a stress-reduced time history which is used as an input to the VE model. The predicted VE strains are subtracted from the total measured strains and the resulting response is attributed to viscoplasticity and used to determine A, q, and Y of the VP model. The separately developed VE and VP models can be integrated together to present the total strain response for a given stress history:

$$\varepsilon = E_R \int_0^t D(t - \tau) \frac{d(\frac{\sigma}{G(S)})}{d\tau} d\tau + \left(\frac{p+1}{Y}\right)^{1/p+1} \quad \text{Equation 66}$$

CHAPTER 4

EXPERIMENTAL PROGRAM

4.1 Materials

4.1.1 Aggregates

The work herein is part of QNRF-NPRP No: 5-506-2-203, therefore the used materials represent what is locally used for paving projects in Qatar. Gabbro aggregates from Fujairah in the United Arab Emirates (UAE) are used. This type of aggregates is an igneous rock that is commonly used in the asphalt pavement industry in the countries of the Arabian Gulf Region including Qatar. These aggregates have higher resistance to degradation, higher texture level, and more skid resistance than the locally available limestone aggregates of Qatar (Masad et al. 2011).

Two aggregate gradations were selected to present the conventional dense graded mixtures that are used for asphalt surface course (ASC) and asphalt base course (ABC). These two gradations have nominal maximum aggregate sizes (NMAS) of 19.0 mm and 25.0 mm presenting an ASC and ABC mixes, respectively as presented in Figure 4 and Figure 5. These gradations were selected after checking that they pass the Superpave criteria and the Bailey Conformity Equations from a set of investigated gradations that are commonly used by local contractors in Qatar.

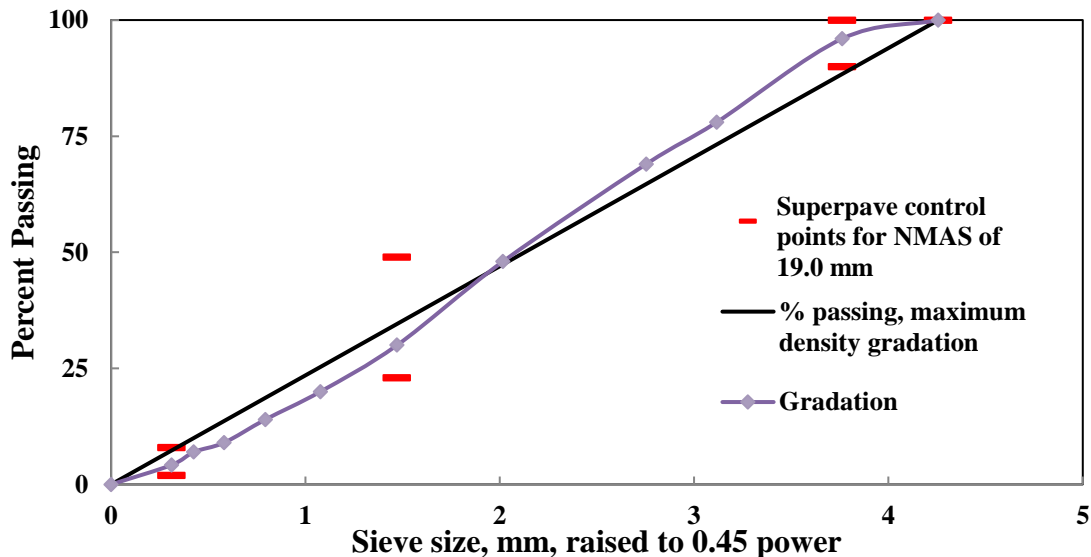


Figure 4. 19.0 mm gradation used for mixes with Gabbro aggregates.

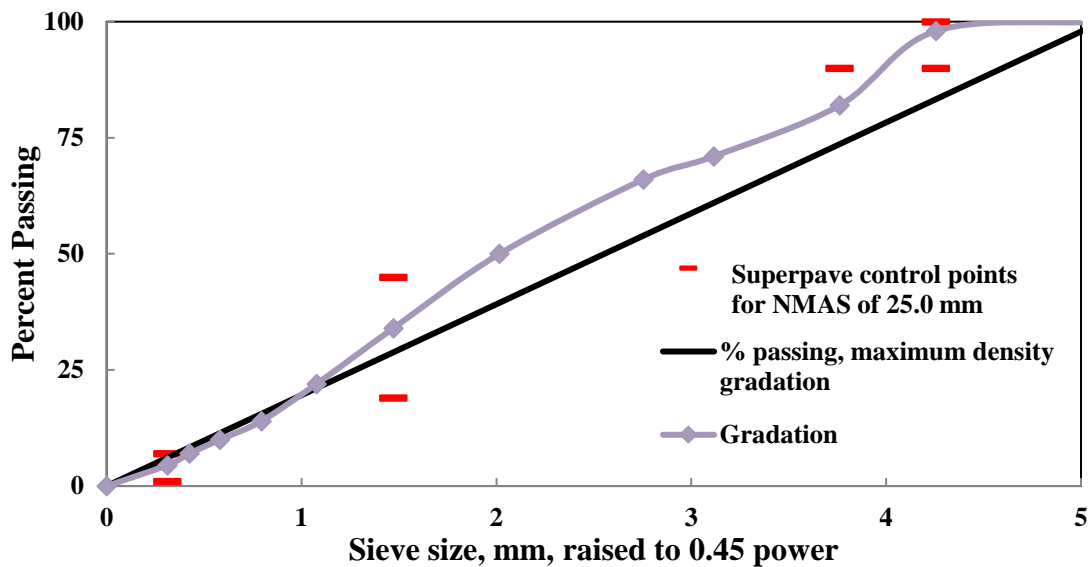


Figure 5. 25.0 mm gradation used for mixes with Gabbro aggregates.

The Bailey method was selected for the assessment of the aggregate gradations to ensure a good packing and interlock of aggregates so that the mix will be resistant to rutting while maintaining the required volumetric properties to ensure the mix's durability (Vavrik 2002). This method provides a better understanding of the combination of aggregates used in asphalt mixtures by redefining fine and coarse aggregates depending on the NMAS. In this context, fine aggregates are those that fill the voids created in between the coarse aggregates when placed in a unit volume. This method is carried out through the establishment of several control sieves summarized as the following:

- Primary Control Sieve (PCS) = $0.22 \cdot \text{NMAS}$ = Break sieve between coarse and fine aggregates
- Secondary Control Sieve (SCS) = $0.22 \cdot \text{PCS}$ = Break sieve between the coarse and fine portion (i.e. coarse sand) of the fine aggregates (i.e. fine sand)
- Tertiary Control Sieve (SCS) = $0.22 \cdot \text{SCS}$ = Break sieve for coarse and fine portions of the fine sand
- Half Sieve = $0.5 \cdot \text{NMAS}$ = Break sieve for interceptors which are the portion of coarse aggregates that cannot fill the voids between the large coarse aggregates and thus spread them apart

The gradation is analyzed by determining three ratios that represent the packing of the different portions of the aggregate gradation as presented in the following conformity equations:

- Coarse Aggregate Ratio (CA Ratio) = $\frac{\% \text{ passing Half seive} - \% \text{ passing PCS}}{100 \% - \% \text{ passing Half seive}}$
- Fine Aggregate Coarse Ratio (FA_C Ratio) = $\frac{\% \text{ passing SCS}}{\% \text{ passing PCS}}$
- Fine Aggregate Fine Ratio (FA_F Ratio) = $\frac{\% \text{ passing TCS}}{\% \text{ passing SCS}}$

For every NMAS, researchers have set ranges for each of these ratio to be passed in order to be considered passing the Bailey method as shown in Table 3 (Vavrik 2002).

Table 3. Bailey Conformity equations for 19.0 and 25.0 mm gradations.

	19.0 mm Gradation		25.0 mm Gradation	
	Control Sieve or Aggregate Ratio	Recommended Ranges of Aggregate Ratios	Control Sieve or Aggregate Ratio	Recommended Ranges of Aggregate Ratios
PCS	4.75		4.75	
Half Sieve	9.5		12.5	
SCS	1.18		1.18	
TCS	0.30	0.30		
CA	0.68	0.6-0.75	0.72	0.7-0.85
FA_C	0.42	0.35-0.5	0.44	0.35-0.5
FA_F	0.45	0.35-0.5	0.45	0.35-0.5
Superpave Status (Based on min and max control points)	Passing		Passing	
Bailey Status	Passing		Passing	

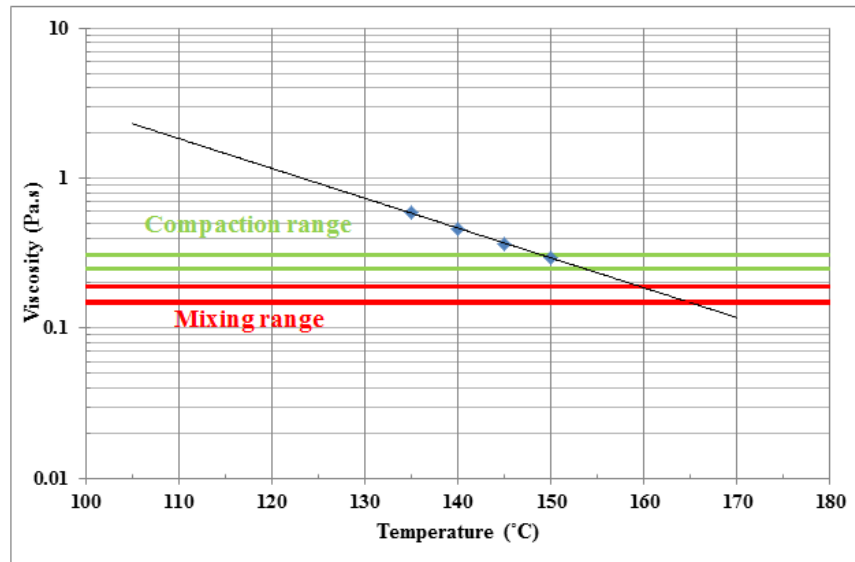
4.1.2 Asphalt Binder

Two asphalt binders that are commonly used in the pavement construction industry in Qatar are used. The first is an unmodified Pen 60/70 which corresponds in the Superpave Performance Grading (PG) to PG 64-22. The second type of binder is a PG 76-22 which is a polymer modified binder supplied by Woqood. The unmodified binder was originally imported from Bahrain and it constitutes the base binder which is modified by styrene butadiene styrene (SBS) to produce the modified binder. The latter was further characterized through the multiple stress creep and recovery (MSCR) test as a PG76E binder according to AASHTO TP70-10.

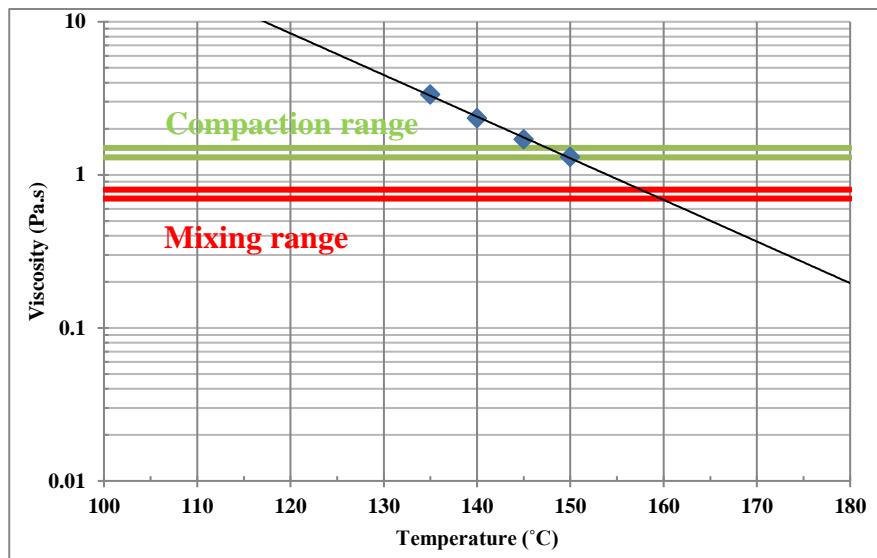
For each of the two binders, the viscosity was measured for three replicates at temperatures higher than 135°C in accordance to ASTM D4402. This was carried out to determine the mixing and compaction temperatures of each of the binders for the cases of the control HMA mixes. For the unmodified binder, the Asphalt Institute Equi-Viscous Method was used where the mixing and compaction temperatures correspond to a viscosity of

0.17±0.02 Pa.s and 0.28±0.03 Pa.s, respectively as shown in Figure 6 (a). Results yielded a mixing range of 158-164°C and a compaction range of 148-153°C. Thus, a mixing and a compaction temperature of 160°C and 150°C, respectively, will be used in this study for the PG 64 binder.

For the case of the modified binder, mixing and compaction temperatures correspond to a viscosity of 0.75±0.05 Pa.s and 1.4±0.1 Pa.s, respectively, based on the Equi-Viscous method and the recommendations of NCHRP Report 459 as shown in Figure 6(b) (Bahia et al. 2001). Results yielded mixing and compaction temperature ranges of 157-159 °C and 147-149 °C, respectively. Thus, for this study the mixing and compaction temperatures of HMA mixes with modified binder were selected to be 160°C and 150°C, respectively.



(a)



(b)

Figure 6. Viscosity vs. temperature for: (a) unmodified binder, (b) modified binder.

4.1.3 WMA Additives

As stated earlier, a variety of products and technologies are developed and implemented in the pavement construction industry with the ultimate goal being the reduction of production temperatures. In this research, different WMA additives are selected to present the three major categories of WMA based on their composition and functionality. The additives selected in this study are Advera, Rediset, Sasobit, and SonneWarmix which are classified as the following:





- **Foaming:** Typically, these techniques incorporate the addition of moisture/water to the asphalt binder producing small bubbles that decrease its viscosity. A commonly used foaming product is Advera®. It has about 20% moisture bonded to zeolite chemically

and structurally. The zeolite releases this moisture over a sustained period of time, causing lasting micro-foaming. The steam that improves the workability of the mix will be compressed out during compaction and any residual moisture remaining in the mix will be reabsorbed by Advera® and get bounded in place (Smith 2007). Once in place, Advera behaves as a mineral filler knowing that it is a free flowing inorganic powder passing the No. 200 sieve. According to PQ corporation, Advera does not change the PG of the binder used and does not imply any need for changing the mix design. It can be added to the mix at a dosage range of 0.25% by weight of the mix, allowing the reduction in production temperatures by 50-70°F as compared to HMA (Smith 2007).

- Chemical additives: Generally, these additives reduce the friction between the aggregate and the asphalt binder that is coating it. Rediset LQ® can be considered as an easy-to-use liquid that not only is a WMA additive, but it also provides an active adhesion that enhances the coating of aggregates (Hamzah et al. 2015).
- Organic additives: These additives use long chain aliphatic hydrocarbons that can modify the asphalt binder to have lower viscosity values at elevated temperatures compared to traditional asphalt. A widely-used additive of this family is Sasobit® which is a Fisher-Tropsch wax produced by the treatment of hot coal with steam in the presence of a catalyst. When added to asphalt binder, it can melt at a temperature of binder exceeding 115°C to internally lubricate the mix so that it can be handled easier (Wax 2005). Also, SonneWarmix was selected as an organic WMA additive made up of paraffinic wax. It is typically heated to a temperature of 90-120°C before blending it with the binder to achieve a reduction in temperature of approximately 30°C.

The used WMA additives are presented in Table 4.

Table 4. WMA additives used in this research with the type, supplier, recommended dosage, and image for each.

WMA Additive	Advera®	Sasobit®	Rediset LQ1102CE®	SonneWarmiX®
Category	Foaming	Organic	Chemical	Organic
Supplier	PQ Corporation	Sasol	AkzoNobel	SonneBorn
Supplier's Recommended Dosage	0.25% by weight of mix	1.5% by weight of binder	0.4-0.6% by weight of binder	0.5-1.5% by weight of binder
Image				

4.1.4 Fibers

The asphalt reinforcing fibers used were supplied by Forta Corporation in pre-prepared small bags to be added to the different mixes/batches in the study. They are provided in proprietary blends of aramid and polyolefin fibers of length 19.0 mm as shown in Figure 7. These fibers are chemically inert and they are designed for a working temperature of 100°C and higher. The polyolefin fibers are made of polypropylene in the form of twisted fibrillated fibers with a tensile strength of 483 MPa. However, the aramid fibers are of the form of monofilaments with a tensile strength of 3000 MPa (Kaloush et al. 2008). It is recommended by the supplier to use these fibers at a rate of 0.5 kg per metric ton of asphalt mixture.



Figure 7. Mix of aramid and polyolefin fibers.

4.2 Mix Design of HMA and WMA

For the gradations presented in Figure 4 and Figure 5, 14 different HMA and WMA mixes were designed incorporating both unmodified and modified binders. These mixes are

classified into three different categories based on the combination of the binder type and the NMAS of the gradations. The labels “U25”, “M19”, and “U19” are used commonly in this document where they are designated as the following:

- U25: mix with unmodified binder (PG 64-22) and the 25.0 mm aggregate gradation.
- M19: mix with modified binder (PG 76-22) and the 19.0 mm aggregate gradation.
- U19: mix with unmodified binder (PG 64-22) and the 19.0 mm aggregate gradation.

The research has covered 14 different mixes with selected combinations of different gradations, binder type, WMA technologies, fibers, and RAP. These mixes are summarized in Table 5.

Table 5. Description of HMA and WMA mixes.

Mix Category	Aggregate Gradation	Binder Type	Mix Type
U25	Gabbro, dense-graded, 25mm	PG 64-22 unmodified	HMA
			WMA-Sasobit
			WMA-Advera
			WMA-Rediset
			HMA+ RAP
M19	Gabbro, dense-graded, 19mm	PG76-22 SBS Modified	WMA-Sasobit + RAP
			HMA
			WMA-Sasobit
			WMA-Advera
			WMA-Rediset
U19	Gabbro, dense-graded, 19mm	PG 64-22 unmodified	HMA
			HMA with Fibers
			WMA-SonneWarmix
			WMA-SonneWarmix with Fibers

The mix designs of the control HMA mixes in the three aforementioned categories were conducted to determine the optimum asphalt content that gives a design air void level of 4.0%. Then, the corresponding WMA mixes of each category were designed by validating the optimum asphalt content that was determined for each of the control HMA mixes. In order to design a WMA mix with a targeted level of air voids, three different variables can be varied: 1) compaction temperature, 2) asphalt content, and/or 3) WMA additive dosage. The supplier of each of the WMA additives recommends a range for the dosages to be used and a range for the temperature reduction during production and compaction. In this study, the same temperature reduction is proposed for both the mixing and compaction of the WMA mixes. The highest possible level of temperature reduction is targeted satisfying the condition that it gives a full coating of the aggregates and a 4.0% air voids for the same compaction effort

used for HMA. For each category of mixes, the optimum asphalt content of the control HMA mix was used for the corresponding WMA mix in order to achieve the same volumetric properties so that a comparable performance will be achieved between HMA and its corresponding WMA mix (Bonaquist 2011). For each WMA mix, different WMA additive dosages were used such that they fall within the ranges recommended by the suppliers in order to determine the appropriate dosage for each combination of binder type and WMA technology. It is recommended in this study to have the same temperature reduction in mixing and compaction for all WMA mixes regardless of the type of additive and without changing the asphalt content.

All the mixes in this study were designed based on the Superpave Mix Design Method with a compaction effort corresponding to case of medium to high traffic with 3 to 30 million ESALs (Superpave 1996). This is represented by the following compaction parameters:

- Initial number of gyrations (N_{ini}) = 8
- Design number of gyrations (N_{des}) = 100
- Maximum number of gyrations (N_{max}) = 160

For each mix, the mix design was conducted by preparing and testing three specimens compacted to N_{des} and three loose samples at each of the tested asphalt contents. The compacted specimens were used to measure the bulk specific gravity (G_{mb}) according to ASTM 2726 and the loose ones were used for the theoretical maximum specific gravity (G_{mm}) according to ASTM 2041. For each mix, the optimum asphalt content was determined and the Superpave criteria, as shown in Table 6, was checked for voids in mineral aggregates (VMA), voids filled with asphalt (VFA), air voids at N_{ini} , and the dust proportion. Then two specimens were mixed and compacted to N_{max} to ensure that the percentage of air voids is larger than 2%.

Table 6. Superpave design requirements.

Design ESALs (million)	Required Density (% of theoretical G_{mm})			Minimum VMA (%)		VFA (%)
	N_{ini}	N_{des}	N_{max}	NMAS, mm		
				25	19	
10 to < 30	≤ 89.0	96.0	≤ 98.0	12.0	13.0	65-75

4.2.1 Mixes with Unmodified Binder and 25.0 mm Gradation

For the U25-HMA mix, volumetric properties were investigated at four different asphalt contents: 3.0%, 3.5%, 4.0%, and 4.5% of the total weight of the mix. The optimum

asphalt content of this HMA mix was determined as 3.6% for a target air voids of 4.0% with a VMA of 12.4%, a VFA of 69%, % air voids at N_{ini} of 12.8%, and % air voids at N_{max} of 2.6% as presented in Figure 8. The final mix design passes all the Superpave criteria except for the dust proportion which is 1.3 that exceeds the Superpave maximum limit of 1.2. However, this maximum limit is recommended to be increased to 1.6 as per the guidelines of Superpave Lead States and AASHTO MP2 (Solaimanian et al. 1999).

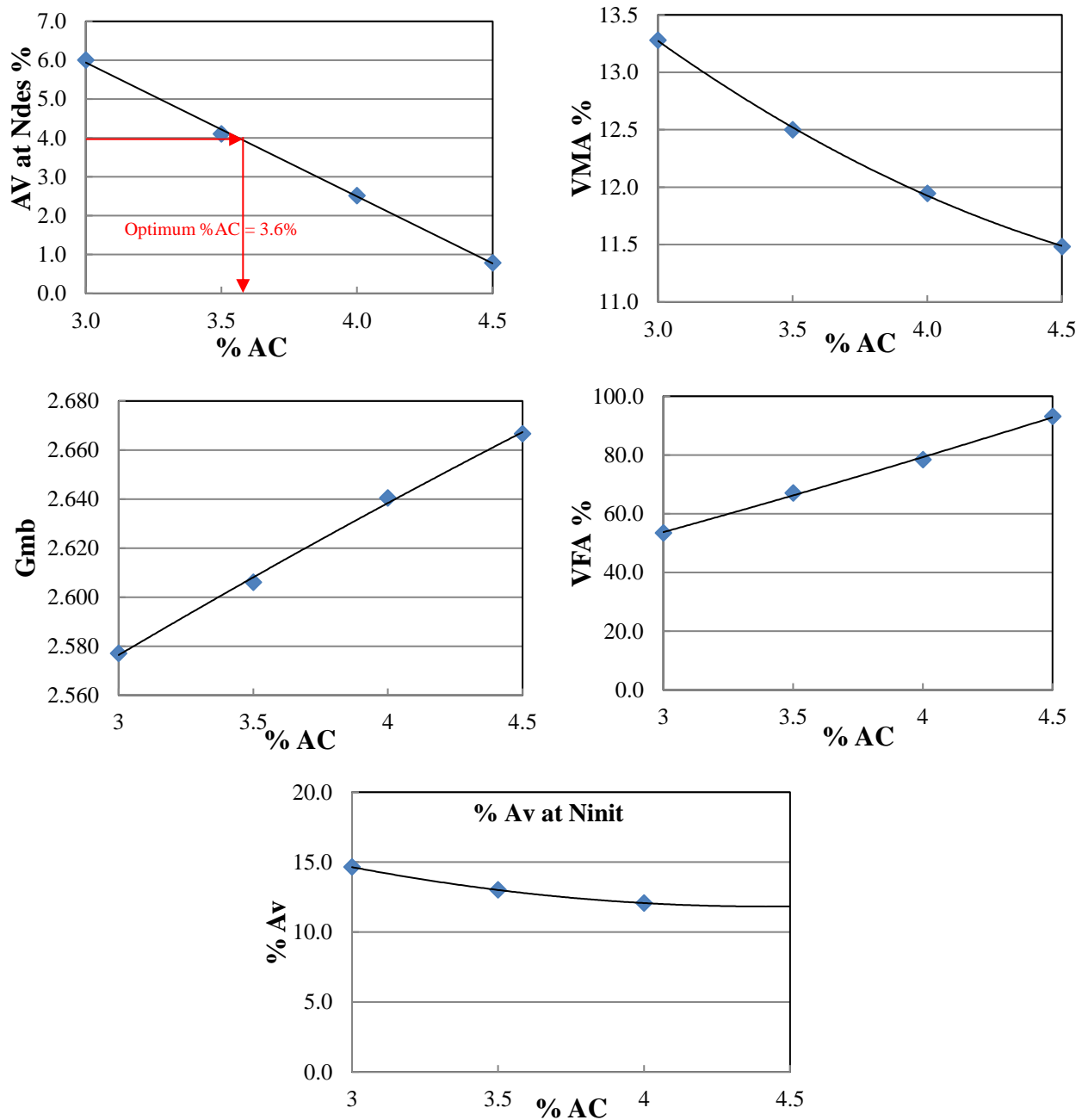


Figure 8. Volumetric properties of 25.0 mm mix with unmodified binder.

For WMA mixes with unmodified binder, the reduction of temperature was selected to be 35°C implying a mixing and compaction temperatures of 125°C and 115°C, respectively. This reduction in temperature is accepted because full coating of aggregates is

achieved during mixing for all WMA additives investigated. The mix designs of WMA mixes of this category are summarized as the following:

- **U25-WMA-Advera Mix:** Considering the optimum asphalt content (% AC) of 3.6% for the control HMA, WMA mixes with Advera were prepared having different dosages. The testing results showed an average air void level of 3%, 3.7%, and 3.9% for mixes with Advera dosages of 0.25%, 0.125%, and 0.1% of the total weight of the mix, respectively. Thus, WMA mixes with 0.1% dosage of Advera is adopted for the remaining of the study. Also, this mix was checked for air voids at N_{ini} and N_{max} where it passed the required criteria by being 13.2% and 2.5%, respectively.
- **U25-WMA-Sasobit Mix:** Sasobit was added at a rate of 2% and 1% by weight of the binder at the optimum %AC of 3.6%. These dosages yielded similar levels of %AV of 3.1% and 3.2%, respectively. Since the supplier's minimum recommended rate is 1%, the % AC was reduced by 0.1% and 0.2% and samples at these two levels were prepared and tested. This step indicated that WMA with Sasobit requires a decrease of %AC by 0.1% to yield a % AV level of 3.9%. This mix was checked for air voids at N_{ini} and N_{max} where it passed the required criteria by being 13.4% and 3.2%, respectively.
- **U25-WMA-Rediset Mix:** The same strategy was followed for WMA mixes with Rediset which yielded a dosage rate of 0.5% by weight of binder with an optimum %AC of 3.5% for a target %AV of 4.0%. This mix was checked for air voids at N_{ini} and N_{max} where it passed the required criteria by being 13.4% and 3.0%, respectively.

A summary of the mix design of all mixes with unmodified binder is presented in Table 7. These results show that the incorporation of the WMA additives for mixes with target of 4.0% air void does not imply a change of the volumetric properties of the mixes where still they pass the Superpave criteria (VMA>12%, VFA in range of 65-75%, %AV at N_{ini} > 11.0%, and %AV at N_{max} > 2.0%). It is noticed that the %AV at N_{ini} is almost higher by 0.5% for all WMA mixes in comparison with that of the control HMA.

Table 7. Summary of mix design results of mixes with unmodified binder and 25.0 mm gradation.

	U25-HMA	U25-WMA-Advera	U25-WMA-Rediset	U25-WMA-Sasobit
Binder Content, % (by weight of mix)	3.6	3.6	3.5	3.5
Gmm	2.716	2.717	2.718	2.718
AV (%)	4.0	3.9	4.0	4.0
VMA (%)	12.4	12.4	12.4	12.3
VFA (%)	68.8	69.5	68.0	68.9
% AV at N_{ini}	12.8	13.2	13.4	13.4
% AV at N_{max}	2.7	2.5	3.0	3.2
WMA Additive Dosage	N/A	0.1% by weight of mix (1 kg/ton of mix)	0.5% by weight of binder (0.175 kg/ton of mix)	(1% by weight of binder (0.35 kg/ton of mix)
Mixing Temperature (°C)	160	125		
Compaction Temperature (°C)	150	115		

4.2.2 Mixes with Modified Binder and 19.0 mm Gradation

The mix designs of mixes with modified binder and 19.0 mm gradation were conducted with the same additives that were used in the case of unmodified binder. However, different dosages were required for each WMA additive due to the difference of the binder's stiffness and viscosity. For WMA, trial mixes were done and a difficulty was presented when trying to achieve a decrease in mixing and compaction temperature of 35°C similar to the case of unmodified binder. For a decrease of 35°C in the mixing temperature, the binder was observed to be stiff enough so that it was difficult to add the WMA additive and mix it. So, the binder needs to be heated to a higher temperature in order to be able to mix it with the WMA additives. Upon different trials, it was decided that for WMA mixes with modified binder the mixing and compaction temperatures will be decreased by 20°C i.e. 140°C and 130°C, respectively. These temperatures were fixed for all the WMA mixes and the variables to achieve a 4.0% AV are the additive dosage and then the % AC. The designs of the mixes of this category are summarized as the following:

- **M19-HMA**: The mix design was conducted by preparing samples at three different %AC of 3.5, 4, and 4.5% by total weight of the mix as presented in Table 8. The optimum %AC is 3.9% for a target air void of 4.0% yielding a VMA of 14.0%, a VFA of 70.5%, dust proportion of 1.08, and %AV at N_{ini} of 13.2% which are all within the Superpave volumetric mix design Requirements.

Table 8. Mix design results of HMA with modified binder.

%AC	%AV at N _{comp}	%VMA	%VFA	%AV at N _{ini}	G _{mb}	G _{mm}
3.5	5.1	13.8	63.1	14.4	2.575	2.713
4.0	3.8	14.0	72.8	12.9	2.581	2.683
4.5	1.9	13.8	86.5	11.9	2.602	2.651

- **M19-WMA-Sasobit**: For 3.9% AC, WMA with Sasobit was tested with a dosage of 2% by weight of binder which yielded an average % AV of 4.5%. Thus, a higher dosage of 3% was considered that yielded a %AV of 4.0% at N_{des} and 3.3% at N_{max}.
- **M19-WMA-Rediset**: A dosage rate of 0.5% by weight of binder yielded a %AV of 4.0% with a %AC of 3.9%.
- **M19-WMA-Advera**: A dosage of Advera of 0.25% by weight of the mix yielded the design %AV of 4.0% without any change in the optimum %AC.

The addition of WMA additive with modified binder requires a lower reduction in production temperatures. It can be concluded that for WMA with Sasobit, Rediset, and Advera the modified binder requires a higher additive dosage with a lower reduction in the mixing and compaction temperatures than that of HMA with unmodified binder without the need to reduce the asphalt content as it is the case of mixes with unmodified binder. The results showed that the same volumetric properties were obtained for all WMA mixes with modified binder and their corresponding control HMA mix. A summary of the mix design results of HMA and WMA mixes with modified binder and 19.0 mm aggregate gradation is presented in Table 9.

Table 9. Summary of mix design results for mixes with modified binder and 19.0 mm gradation.

	M19-HMA	M19-WMA-Advera	M19-WMA-Rediset	M19-WMA-Sasobit
Binder Content, % (by weight of mix)	3.9	3.9	3.9	3.9
Gmm	2.689	2.687	2.669	2.688
AV (%)	4.0	4.0	4.0	4.0
VMA (%)	14.0	14.0	14.5	14.0
VFA (%)	70.1	71.2	72.8	71.2
% AV at Nini	13.2	13.3	13.2	13.4
% AV at Nmax	3.0	3.1	3.1	3.3
WMA Additive Dosage	N/A	0.25% by weight of mix (2.5 kg/ton of mix)	0.5% by weight of binder (0.195 kg/ton of mix)	3% by weight of binder (1.17 kg/ton of mix)
Mixing Temperature (°C)	160	140		
Compaction Temperature (°C)	150	130		

4.2.3 Mixes with Unmodified Binder and 19.0 mm Gradation

For mixes with unmodified binder and 19.0 mm gradation, the mix design results showed that HMA mixes require an optimum asphalt content of 3.7% to achieve 4.0% air voids. In comparison with the HMA mix with same gradation but modified binder, a 0.2% reduction by weight of asphalt is needed due to use of unmodified binder that is less stiff given that both binders have the same mixing and compaction temperatures. The use of Sonnewarmix as a WMA additive and the addition of fibers has no effect on the optimum asphalt content. HMA, HMA with Fibers, WMA with Sonnewarmix, and WMA with Sonnewarmix and fibers were designed with the volumetric properties as summarized in Table 10.

Table 10. Summary of mix design results for mixes with unmodified binder and 19.0mm gradation.

	U19-HMA	U19-HMA- Fi	U19-WMA- SonneWarmix	U19-WMA- SonneWarmix-Fi
Binder Content, % (by weight of mix)	3.7	3.7	3.7	3.7
Gmm	2.686	2.685	2.683	2.687
AV (%)	4.0	4.0	4.0	4.0
VMA (%)	13.8	13.7	13.9	13.8
VFA (%)	71	70.8	71.2	70.5
% AV at Nini	13.0	13.1	12.9	13.2
% AV at Nmax	3.0	3.3	3.1	3.2
WMA Additive Dosage	N/A	N/A	0.185 kg per ton	0.185 kg per ton
Mixing Temperature (°C)	160		125	
Compaction Temperature (°C)	150		115	

4.3 Testing Program

In this section, a brief summary of the testing system, temperature control, and data acquisition system utilized in this research will be provided. Moreover, an overview of the conducted test methods will be presented.

4.3.1 Testing System

4.3.1.1 Testing Machine

A UTM-25 servo-hydraulic universal testing machine is used. It has a 25 kN capacity and is manufactured by Industrial Process Controls (IPC) from Australia as shown in Figure 9. It is based on a loading frame consisting of two vertical columns and two heavy duty crossheads. It is robustly manufactured to limit the deflections and vibrations which might affect the accuracy of measurement during dynamic load testing scenarios. This machine has a Ram displacement of 50.0 mm span with a maximum speed of 1200 mm/min. This closed loop machine allows conducting sophisticated material testing due to its ability to apply precisely controlled rates of forces or deformation and its ability to accurately measure the resulting responses through its various mounted transducers and data acquisition system. It is capable of applying static and dynamic loads at a wide range of temperatures and loading rates/frequencies.

4.3.1.2 Temperature Control

The UTM-25 is equipped with an environmental chamber for controlling the temperature during testing. The temperature control system is refrigeration based with a heating element

for achieving high temperatures. It has the capability of temperature control in the range of -15°C to 60°C which falls within the requirements of the mechanical tests required in this research. An asphalt dummy specimen is prepared for each mix to account for the variability in thermal properties induced by different types of binders, aggregates gradations, and the effect of WMA additives if any. For each dummy specimen, two k-type thermocouples are embedded at the center and mounted on the surface of the specimen. The second thermocouple is added for all dummy specimens in this research to ensure that the temperature is homogeneous between the specimen's surface and its center. Each specimen is accompanied by its corresponding dummy specimen during the curing time of the epoxy glue to mount the studs and then these specimens are conditioned at different testing temperatures together. During testing, the sample is set for a period of time to reach equilibrium after reaching the required testing temperature.

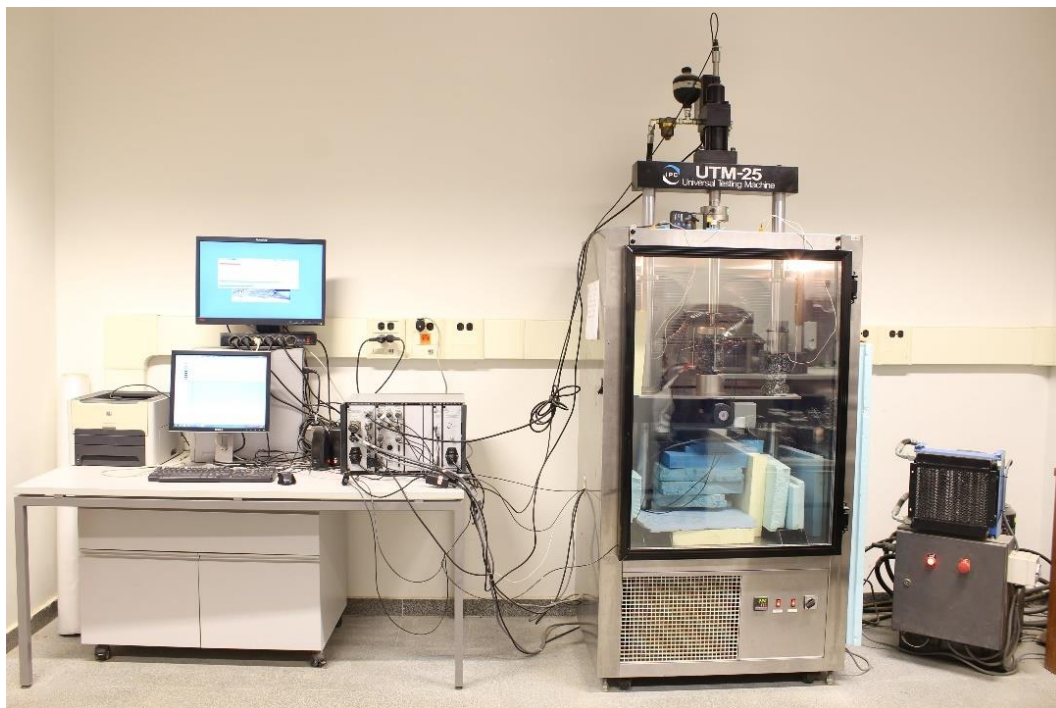


Figure 9. Universal testing machine.

4.3.1.3 Measurement System

The measurement system for UTM-25 is fully computer controlled and capable of the acquisition of data through eight channels simultaneously. These channels are assigned to various sensors. Two of these channels are dedicated for the load cell and the actuator's LVDT (linear variable differential transformer). The other six channels are connected to various sensors, including three on-specimen vertical spring LVDTs and a temperature probe.

For data acquisition, a 20-bit Integrated Multi-Axis Control System (IMACS) manufactured by IPC is used. Several data acquisition programs are provided by IPC to be

used for test control and raw data collection. The rate of data acquisition is 50 data points per cycle for sinusoidal/haversine loading. However, for constant rate tests the data acquisition rate varies between 50 and 1000 data points per second depending on the testing rate ranging. Three D6 05000A spring loaded LVDTs with end axial exit cables are used for measuring the specimen's vertical deformations. They are placed at 120° apart along the circumference and at the middle two-third of the specimen's height with a gage length of 100 mm. The LVDTs are attached to the surface of the specimen using mounting studs. The mounting studs are glued to the surface using Devcon Plastic Steel Putty10110 epoxy by means of an in-house fabricated jig ensuring the alignment and the equal angularity in between them as shown in Figure 10.



Figure 10. Gluing jig for mounting studs on asphalt samples.

4.3.2 Testing Methods

4.3.2.1 Complex Modulus Testing

The complex modulus (E^*) test is conducted in the stress control mode to determine the linear viscoelastic properties and the time-temperature shift factors of all the mixes in the study. It entails the application of a uniaxial sinusoidal/haversine stress to an unconfined asphalt concrete sample and determining the response strains in order to compute the dynamic modulus ($|E^*|$).

The test samples have a diameter of 100 mm and height of 150 mm with a targeted %AV of $7.0 \pm 0.75\%$ and they are cored and cut from gyratory compacted samples of diameter and height of 150 mm and 175 mm, respectively as shown in Figure 11. Typically, three replicates were prepared and each tested for each mix at 24 combinations of temperature and

frequency. A fourth replicate is tested in cases of high variability in testing results especially in the case of mixes with fibers.



Figure 11. Complex modulus testing setup.

A haversine loading in compression that is sufficient to produce a total strain amplitude in the range of 70-75 microstrains is applied at 24 combinations of frequency and temperature as presented in Table 11. The limit of 70-75 microstrains is set in order to ensure that the material is in the linear viscoelastic range (Chehab 2002, King 2004, Underwood and Kim 2012). The load amplitude for each combination of testing frequency and temperature is adjusted based on the material's stiffness and testing conditions such that the 75 microstrains limit is not exceeded. For each temperature, preconditioning loading cycles are applied before applying the testing frequencies to obtain better quality of loading and displacement data during testing. The preconditioning cycles are applied at the highest frequency for each temperature with loads that are 50% the normal load applied at that specific frequency and temperature. The loading frequencies are applied from the fastest to the slowest with a rest period of five minutes between them. This rest period is applied to allow the sample to recover transient strains before the application of the next loading frequency and thus to minimize any possible effect on the measured modulus values (Kim 2008).

Table 11. Complex modulus testing information showing testing temperatures, frequencies, and number of cycles at each combination.

Frequency (Hz)	Temperature (°C)			
	-5	10	25	40
20-Preconditioning	X	X	100	100
20	X	X	200	200
10- Preconditioning	100	100	100	100
10	100	100	100	100
5	100	100	100	100
1	20	20	20	20
0.5	15	15	15	15
0.1	15	15	15	15
0.01	10	10	X	X

During the test, the raw data of the applied load and the measured axial deformation of each of the 3 LVDTs is recorded through an IMACS at a rate of 50 points per cycle. This data is then analyzed by considering the last 5 cycles of each temperature frequency combination. The stress and strain data is fitted to cosine functions shown in Equation 67 and Equation 68 using the least square method. The dynamic modulus is defined as the average peak stress divided by the average peak strain as shown in Equation 69 while the phase angle is the difference between the phase angle of the stress and the strain.

$$\sigma = \sigma_0 \cos(2\pi ft + \phi_1) + \sigma_1 \quad \text{Equation 67}$$

$$\varepsilon = \varepsilon_0 \cos(2\pi ft + \phi_2) + \varepsilon_1 t + \varepsilon_2 \quad \text{Equation 68}$$

where

σ : stress

ε : strain

t : time in sec

f : frequency in Hz

σ_0 , σ_1 , and ϕ_1 = regression constants for stress equation

ε_0 , ε_1 , ε_2 , and ϕ_2 = regression constants for strain equation

$$|E^*| = \frac{\sigma_0}{\varepsilon_0} \quad \text{Equation 69}$$

$$\phi = \phi_2 - \phi_1 \quad \text{Equation 70}$$

where

$|E^*|$: dynamic modulus

ϕ : phase angle

Considering the wide range of temperature changes between different regions and times of the year and the different vehicular speeds that can be encountered, the testing

temperatures need should represent this variation in climatic conditions. Thus, the testing is carried out at low temperatures to represent cold climates and at high temperatures to represent hot climates. In addition, the loading rates are varied to represent fast and slow vehicular speeds. However, conducting the test for each temperature and for all loading rates would be rigorous along with the fact that there is a machine limitation to that. Therefore, the time-temperature superposition principle is used in order to provide the material response under predetermined temperatures and frequencies that can then be shifted to construct the dynamic modulus master curve at a reference temperature. The reference temperature of 25°C is selected in this research. This principle entails that a certain dynamic modulus value at a reference temperature can be measured either at a higher temperature and high frequency, or at a lower temperature and a lower frequency. These measured values can be then shifted by the shift factor a_T that is multiplied by the testing frequency to obtain the reduced frequency at the reference temperature and thus construct the $|E^*|$ master curve of each replicate. The shift factors, a_T , are used to shift the dynamic modulus versus frequency curves at -5, 10, and 40°C along the frequency axis to form a continuous master curve at 25°C are defined as the following:

$$\log(f_R) = \log(f) + \log(a_T) \quad \text{Equation 71}$$

where:

f_R = reduced frequency at the reference temperature (25°C)

f = frequency at a given temperature T before shifting, and

a_T = shift factor for temperature T

The shift factors are determined by first assigning trial initial values and then using the least squares technique to minimize the error between actual and predicted $|E^*|$ values using the log-sigmoidal function as presented by Equation 72.

$$\log(|E^*|) = a + \frac{b}{c + \frac{f}{\exp(d + e \cdot \log(fr))}} \quad \text{Equation 72}$$

where:

$a, b, c, d, e,$ and f : regression coefficients

Also, the shift factor as a function of temperature is fitted as presented in Equation 73.

$$\log(a_T) = a_1 T^2 + a_2 T + a_3 \quad \text{Equation 73}$$

where:

$a_1, a_2,$ and a_3 : regression coefficients

4.3.2.2 Constant Crosshead Rate Compression Test

The constant crosshead rate test, which is also known as monotonic test, is conducted in compression mode at different crosshead rates using the UTM-25 machine. In this test, the

specimens are loaded in compression at different temperatures and rates and are extensively used for the development and calibration of the viscoelastic and viscoplastic models. The tests are conducted until failure or until the machine's capacity of 25 kN is reached in the cases of low temperatures and fast loading rates. This test can be considered as a simple test that can be used for VEPCD based on the findings by previous researches that the behavior of asphalt concrete is independent of the loading mode and thus the monotonic test was selected for this purpose (Daniel and Kim 2002).

Figure 12 shows a typical on-specimen and actuator LVDT strain measurements as well as the stress response in a crosshead compression test. It is observed that the on specimen LVDT measurements follow a nonlinear curve whereas the actuator strain rate is constant. Also, the on specimen LVDT strain is less than the actuator strain during the test where this along with the nonlinearity behavior are due to the machine compliance where different parts of the machine deforms under stresses (Daniel et al. 2004). Thus, the analysis of strains in this entire study will be based on data collected by the on-specimen mounted LVDTs.

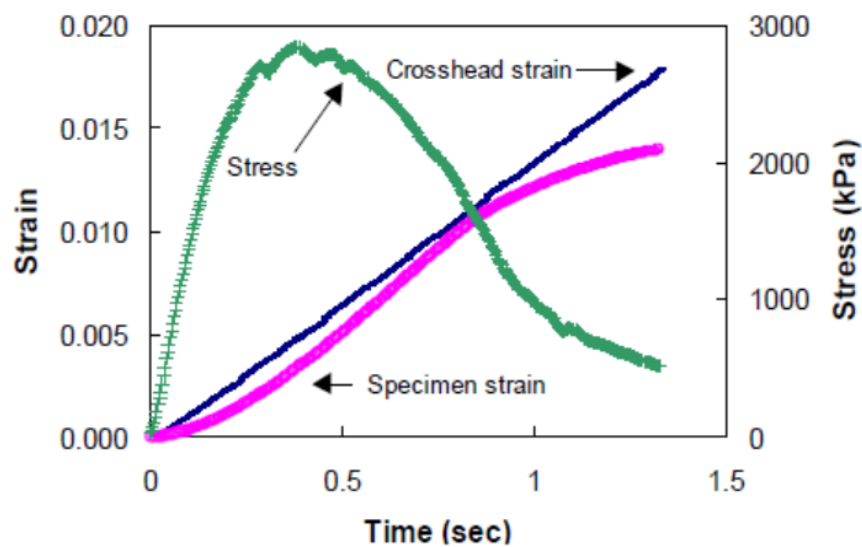


Figure 12. Constant crosshead rate results showing the difference between crosshead and on specimen LVDT strains (Chehab 2002).

Based on previous studies (Chehab et al. 2003, Gibson 2006, Underwood 2011, Zhao 2002), samples tested at 5°C are used for VE modeling. For VP modeling, a high temperature of 35°C is selected and it refers to the mean annual average temperature (MAAT) plus one standard deviation of the mean monthly air temperature as calculated based on the historic climatic data for the State of Qatar calculated for weather data collected between 2000 and 2012 as presented in Table 12.

Table 12. Calculation of testing temperature for State of Qatar.

	Average High Temperature (°C)	Average Low Temperature (°C)	Average Monthly Temperature (°C)
January	22	14	18
February	23	15	19
March	27	17	22
April	33	22	27.5
May	39	27	33
June	42	29	35.5
July	42	31	36.5
August	41	31	36
September	39	29	34
October	35	25	30
November	30	21	25.5
December	25	16	20.5
<i>Mean Average Annual Temperature (°C)</i>			<u>28</u>
<i>Standard deviation of the mean monthly air temperature (°C)</i>			<u>7</u>
<i>Proposed Testing temperature (°C)</i>			<u>35</u>

The constant crosshead testing conditions are summarized in Table 13.

Table 13. Testing conditions for VE and VP model development and validation.

	Linear Viscoelastic Characterization	Viscoelastic Model	Viscoplastic Model
Test	Complex Modulus in Compression mode	Constant Crosshead Rate Compression Test	
Temperature	-5, 10, 25, and 40°C	5°C	35°C
Testing Rate	20, 10, 5, 1, 0.5, 0.1, and 0.01 Hz (3 replicates for each mix)	0.0001 strain/sec, 0.00005 strain/sec, 0.000025 strain/sec, and 0.00001 strain/sec. (1 replicate at each rate for each of the mixes)	0.00025 strain/sec, 0.0001 strain/sec, and 0.00005 strain/sec. (1 replicate at each rate for each of the mixes)

Specimens used for the constant crosshead test are different from those used for the E* testing. The fingerprint of each specimen is determined by conducting the E* at 5°C and 25°C for samples used for VE and VP modeling, respectively. The E* test is done only at 1 temperature and at a limited number of frequency sweeps. The |E*| and E' is determined for these sweeps and temperatures and it can be used to normalize the entire |E*|, E', E(t) and D(t) mastercurves. This accounts for the specimens specific LVE properties without

assuming the average mastercurve to be its property. Fingerprinting based on $|E^*|$ and E' could be done but both give the same normalizing factors based on data of this research. This test precedes every constant crosshead test with at least two hours where the sample can rest for enough time to ensure the recovery of any possible accumulated strain. This fingerprint will be used to account for specimen-to-specimen variability.

For VECD modeling, it should be assured that the stiffness vs. damage curves of the three replicates collapse on top of each other for each mix. Then, the data of the fastest two rate tests are used to develop the model while the third is used to validate the developed model.

4.4 Sample Preparation

4.4.1 Mixing and Compaction

Specimens of the different mixes of this research are prepared based on the standard procedures and protocols. The same mixing and compaction procedures are followed for WMA and HMA mixes taking into account the mixing and compaction temperature of each single mix in light with the recommendations of the Draft Appendix to AASHTO R35 (Bonaquist 2011). All the aggregates are totally dried, sieved, and stored in closed barrels before being used for the preparation of the required batches.

WMA binders are prepared by pre-blending the required dosages of WMA additives with the virgin asphalt binders at the mixing temperature prior to mixing it with aggregates. The WMA additives are mixed with the binder using a laboratory mechanic stirrer to obtain a homogeneous distribution of the additive with the binder. A heating plate is used under the asphalt can in order to maintain the temperature of the sample during mixing. All the used WMA additives are added to the binder except for Advera. According to PQ Corporation, Advera can be added in both ways either by pre-blending it with the binder or by adding it to the mix in the pool of binder after adding this latter to the aggregates. During the pre-blending of Advera with modified binder, the additive could not be blended homogeneously with the binder. Thus, in the research only Advera is added to the mix directly and not by pre-blending it with the asphalt binder.

For the mixes with fibers, same procedures are followed as the control mixes with the pre-prepared fibers spread as widely as possible over the aggregates area. Then, the aggregates are stirred along with fibers for a period of 5 seconds to pre-blend homogeneously distribute the fibers within the aggregate's matrix. After that, a cater is formed in the middle of the aggregates for the asphalt binder to be added. After mixing, all the mixing equipment are scrapped well to make sure of not losing the fibers.

For the mixes incorporating RAP, virgin aggregates and RAP are batched separately. The batch of RAP is placed at the mixing temperature only for 4 hours before mixing to avoid any further aging of the RAP's binder. After that, they are added to that of the virgin aggregates which are typically placed in the oven at the mixing temperature for an overnight.

In this research, all the specimens are compacted using a Superpave Gyratory Compactor which is a byproduct of SHRP project developed for the purpose of mimicking field compaction of asphalt mixtures in the laboratory where it tends to orient the aggregates similar to that observed in the field (Brown et al. 2009). The used compactor is a Rainhart Cat. No. 144 Gyratory Compactor which is in conformity with the requirements of the Superpave Mix Design (Superpave 1996) and the AASHTO T 312 and ASTM D6926 standards which describe the preparation and determination of the relative density of HMA specimens by the Superpave Gyratory Compactor. This compactor is servo-controlled where it applies a static compressive vertical force, while simultaneously applying a gyratory motion to the cylindrical mold.

All the specimens are compacted in a mold of 150.0 mm diameter with a height of 110.0-120.0 mm and 175.0 mm for mix design and mechanical testing specimens, respectively. The weights of these specimens were determined by trial and error which was selected to be 4700 grams for mix design compacted specimens. For G_{mm} testing, the weight of the specimen for all mixes was selected to be 2500 grams in accordance with ASTM D2041 for mixes with NMAS of 19.0 to 25.0 mm.

4.4.2 Conditioning and Curing

Typically, the standard practice requires the short-term aging of the loose asphalt mixtures before compaction to simulate the absorption and short term aging of the binder during construction up to the point of compaction. Since mix design processes of WMA are still under development, different conditioning protocols are recommended by different researchers (Bonaquist 2011, Estakhri et al. 2010, Harrigan 2012, Yin and Cicalon 2011). These protocols include:

- 1) Two hours at compaction temperature
- 2) Four hours at 275°F (135°C)
- 3) Comprehensive conditioning protocol: 2 hours at compaction temperature followed by 16 hours at 140°F (60°C) and two hours at compaction temperature
- 4) Four hours at compaction temperature
- 5) Four hours at 275°F (135°C)

Thus, based on the finding by Yin and Cucalon (2011) and the recommendations of NCHRP Report 691, all mixes will be conditioned for two hours at the compaction temperature for both volumetric and performance testing samples.

Another major concern with WMA is its early age performance. It is expected that WMA might require a longer curing period than conventional HMA mixes so that the asphalt binder regains its apparent viscosity and any entrapped moisture will be evaporated (Al-Qadi et al. 2012). This post construction time-dependent hardening constitutes strength gaining and oxidative hardening. These processes are a function of many factors that include the type of additive used, the type of binder, and aggregates. The study conducted by Al-Qadi et al. (2012) has shown that the variation in mixture properties attributed to the curing time is similar for the cases of HMA and WMA mixes as there is not enough evidence that the curing time has to be prolonged for the case of WMA especially those having Sasobit and Evothorm. In light of these findings and to avoid any effect of curing especially for case of WMA with Advera, all mechanical tests are conducted on the samples after 5 days of mixing and compaction.

4.4.3 Volumetrics

The calculation of %AV of the AC specimens is calculated based on ASTM D3203 as:

$$\%AV = 100\left(1 - \frac{G_{mb}}{G_{mm}}\right)$$

where: G_{mb} = the bulk specific gravity of the compacted specimens, and
and G_{mm} = the theoretical maximum specific gravity of the loose specimens.

For the mix design purposes, the G_{mm} is measured using the flask method as per ASTM D2041 and G_{mb} is measured using the commonly used saturated surface-dry (SSD) technique as per ASTM D2726 which is valid for specimens that do not absorb more than 2.0% of water by volumes.

For the mechanical testing specimens, the cored and sawed gyratory plugs are required to have a target %AV of $7.0 \pm 0.75\%$. The tolerance of air voids in these samples is selected to be 0.75% instead of 0.5% to avoid the potential for specimen rejection. This is in light of the recommendations of NCHRP report 702 that accept a tolerance of 1%. This study showed that there is not a systematic air void effect over 1.0% tolerance range. The G_{mb} of these specimens is measured using the Parafilm Method as per ASTM D1188. This technique is selected rather than the SSD method due to the high level of targeted %AV which makes the specimen's absorption of water exceeds 2.0% and thus ASTM D2041 is not applicable. These specimens are dried using a 30-psi air pressure gun prior to the

measurement of G_{mb} . After ensuring that the sample's %AV is within the targeted range, the specimens are stored in zip-locked bags inside a closed cabinet at room temperature to minimize the potential of aging.

For the sake of achieving the targeted level of %AV in the cored and sawed specimens, the required weights of the gyratory plugs are determined by trial and error:

- Mixes with 19 mm gradations: 7500 grams
- Mixes with 25 mm gradations: 7550 grams
- Mix with 25 mm gradation and 15% RAP replacements: 7300 grams

The weight of the specimen is reduced in the case of having RAP because the used RAP is made up of limestone which is lighter than the virgin Gabbro aggregates. Thus, the 15% replacement by weight will provide aggregates with higher volume occupying more space and leading to a decrease in %AV if considering the same weight and height for the specimens.

CHAPTER 5

RESULTS ON ASPHALT MATERIALS CHARACTERIZATION

5.1 Linear ViscoElastic Functions

For each replicate of the mixes, the $|E^*|$ data is shifted based on the time-temperature superposition to form the mastercurve at a reference temperature of 25°C. The data of $|E^*|$ and the shift factors are fitted using the polynomial equation (Equation 73) and sigmoidal function (Equation 72), respectively. For each mix, the data of the three replicates are averaged and the coefficients defining the mastercurve and the time-temperature shift factors are determined as shown in Table 14.

Table 14. Coefficients of sigmoidal function and time-temperature shift factors for a reference temperature of 25°C to predict $|E^*|$ of the HMA and WMA mixes at any combination of temperature and loading frequency.

Mixture	Shift Function Coefficients			Sigmoidal Coefficients					
	a1	a2	a3	a	b	c	d	e	F
U25-HMA	0.0009	-0.179	3.9079	1.0287	3.3197	0.9125	1.3075	0.4313	1.4435
U25-WMA-Ad	0.0011	-0.1773	3.7362	0.9257	3.4864	0.9548	1.2225	0.4954	1.4719
U25-WMA-Re	0.0017	-0.187	3.6255	1.2940	0.4268	0.1290	2.5264	0.4846	0.8898
U25-WMA-Sa	0.0019	-0.1895	3.6484	0.7336	2.6753	0.7052	1.5382	0.4854	1.2361
U25-WMA-Sa-RAP	0.0019	-0.2212	4.2313	-0.2485	3.1345	0.6529	1.1216	0.3820	0.5305
M19-HMA	0.0013	-0.1969	3.9768	0.7546	4.3507	1.1268	1.2964	0.3740	1.5274
M19-WMA-Ad	0.0012	-0.1897	3.9135	1.7700	0.2265	0.0787	2.8686	0.4094	0.8493
M19-WMA-Re	0.0011	-0.1827	3.8794	1.0355	3.7608	1.0663	1.1529	0.4166	1.5381
M19-WMA-Sa	0.0012	-0.1904	3.9155	1.5545	2.8555	0.9396	1.1162	0.3895	1.3990
U19-HMA	0.0013	-0.188	3.7545	1.6583	0.9605	0.3349	1.2871	0.5727	0.7723
U19-HMA-Fi	0.0014	-0.1884	3.8127	1.0564	0.9979	0.2845	1.7016	0.4554	0.7364
U19-WMA-Sonne	0.0015	-0.1934	3.8879	2.0372	0.8332	0.3367	0.6184	0.6274	0.5878
U19-WMA-Sonne-Fi	0.0009	-0.1652	3.5755	2.0654	0.8903	0.3686	0.6507	0.6108	0.6141

5.1.1 Effect of WMA Additives on Mixes with Unmodified Binder

$|E^*|$ mastercurves and shift factors of all the mixes with unmodified binder are presented in Figure 13 and Figure 14, respectively. In general, the results show that for mixes with unmodified binder, $|E^*|$ is reduced for all WMA mixes as compared with the control HMA mix at both high and low reduced frequencies. This implied that the use of the WMA additives Sasobit, Rediset, and Advera might affect the performance of asphalt concrete where it might improve its resistance to cracking but not rutting.

The mix with Sasobit has a reduced stiffness at the range of reduced frequencies between 0.01 and 100 Hz compared to the control HMA but this reduction is less than the other two WMA mixes with Advera and Rediset. However, at high reduced frequencies the mix with Sasobit shows more reduction in $|E^*|$ than the other two additives when compared to the control HMA mix. This could show that Sasobit might have a better resistance to both rutting and cracking than the other two WMA mixes with Advera and Rediset. The mix with Rediset has an $|E^*|$ lower than that of the control mix in the entire reduced frequency range except at the very low reduced frequency where it can be observed to be approaching and slightly exceeding that of the control U25-HMA mix as shown in Figure 13-b. This implies that U25-WMA with Rediset will affect the rutting resistance of asphalt concrete expect in cases where the effective frequency for rutting happens to be very low.

As shown in Figure 14, the time-temperature shift factors are almost the same for WMA and HMA mixes for low temperatures up to the reference temperature of 25°C. For higher temperatures, the use of Sasobit and Rediset cause an increase in the shift factors as compared to the control HMA. In this case, the WMA mix with Advera still has the same shift factor as the control HMA mix. These results show that WMA mixes with unmodified binder might have a better resistance to fatigue cracking; however, they might be more prone to rutting as compared to the control HMA mix.

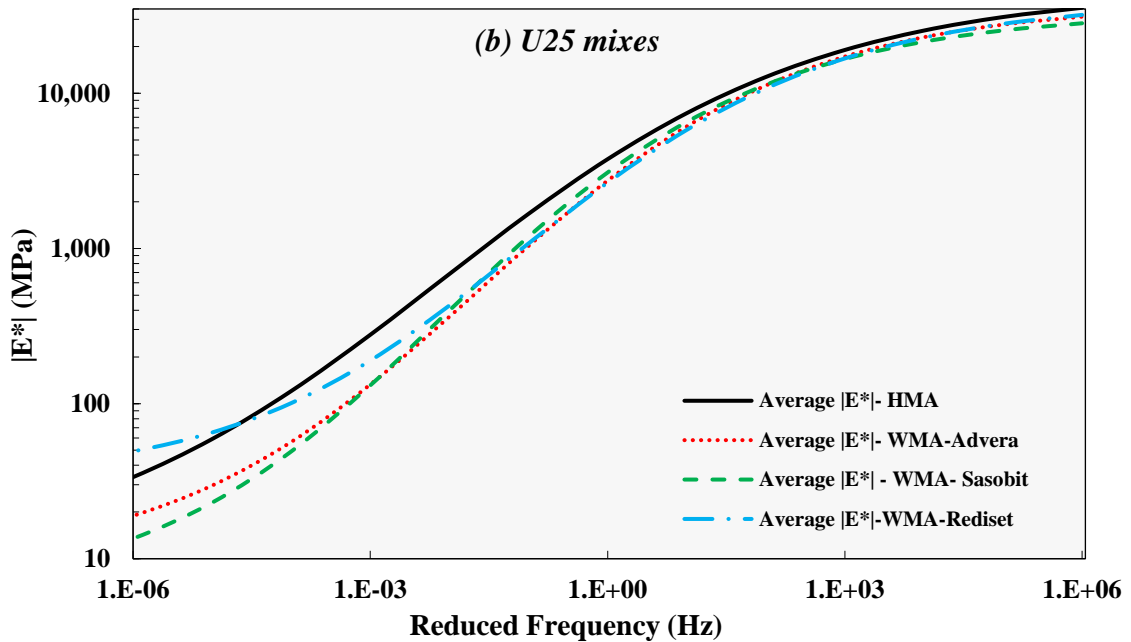
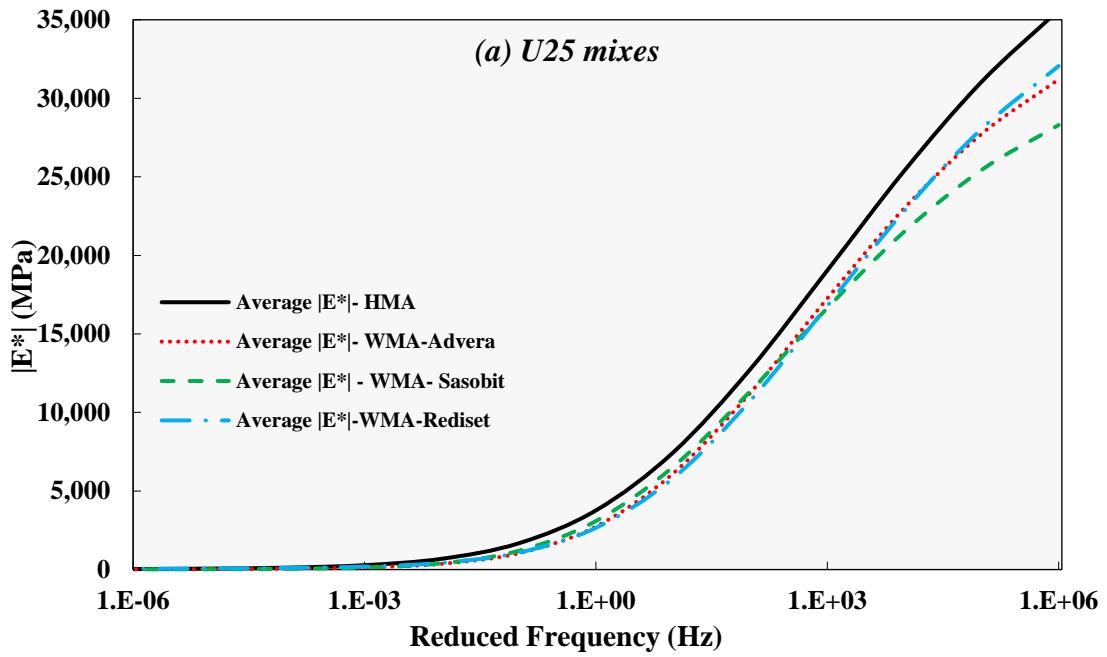


Figure 13. $|E^*|$ mastercurves curves for HMA and WMA mixes having an unmodified binder and a 25.0 mm aggregate gradation constructed at a reference temperature of 25°C: a) semi-log scale and b) log-log scale.

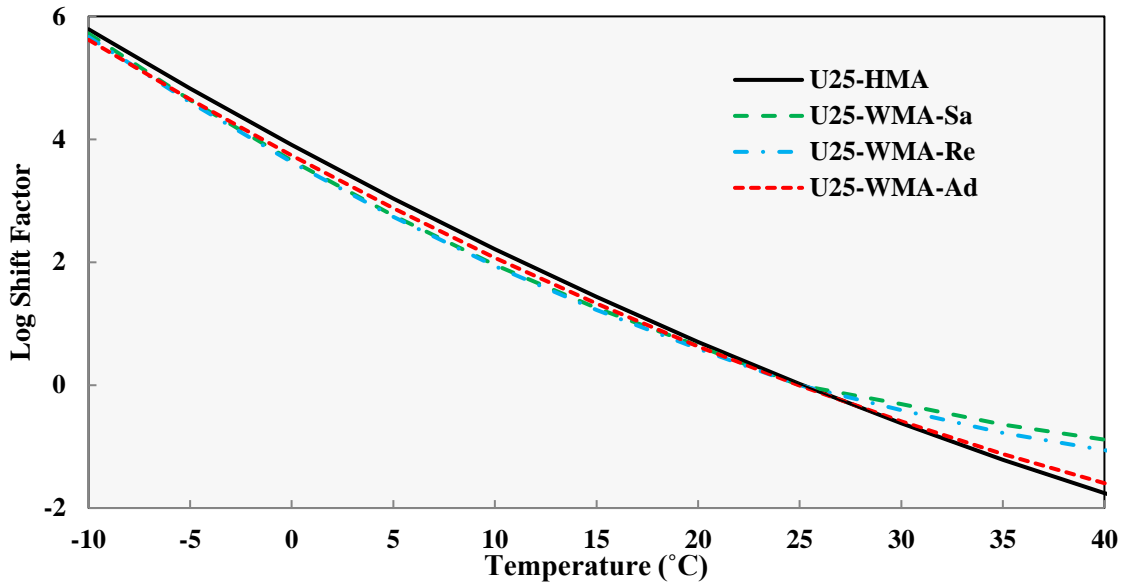


Figure 14. Time-Temperature shift factor for HMA and WMA mixes with unmodified binder and 25.0 mm gradation as used to construct E^* master curve at 25°C.

5.1.2 Effect of WMA Additives on Mixes with Modified Binder

For mixes with modified binder, the $|E^*|$ mastercurves and shift factors are presented in Figure 15 and Figure 16, respectively. The results show that the stiffness of WMA compared to the control HMA mix with a modified binder (PG76-22) is dependent on the WMA additive used unlike the case when having an unmodified PG64-22 asphalt binder. At the time Advera stiffens the mix at high reduced frequency, WMA with Rediset has a lowest stiffness as compared to the control M19-HMA mix. However, Sasobit has a minimal effect in decreasing in $|E^*|$ as compared to the corresponding HMA mix at high reduced frequencies. These results show that WMA mixes with either Sasobit or Rediset might have a better resistance to fatigue cracking when used with modified asphalt binders.

However, the plots in Figure 15-b show that at low reduced frequency, Sasobit and Advera used with modified binder increase the stiffness of the asphalt concrete mixes unlike the case of Rediset which results in a mix with lower stiffness compared to the control HMA. Thus, the usage of Rediset as a WMA additive for mixes with modified binder might lead to the production of asphalt concrete mixes with a lower resistance to rutting as compared to the control HMA mix but the case is opposite when using Sasobit and Advera as WMA additives for this category of mixes. In addition, WMA additives seem to have no effect on the time-temperature shift factors as shown in Figure 16 for the case of mixes with modified binder.

Therefore, the effect of the different types of WMA additives is dependent on the type of additive, the type of base binder used, and the region of temperature/loading rate. In general, the effect of WMA additives would be reduction in $|E^*|$ when having an unmodified base binder, but it might have positive and negative effects in terms of $|E^*|$ when used with

modified binder. It is worth noting that the use of Sasobit with modified binder increases $|E^*|$ at low reduced temperatures and decreases it at high reduced frequencies implying a better performance in resistance to both cracking and rutting when compared to performance of its control mix.

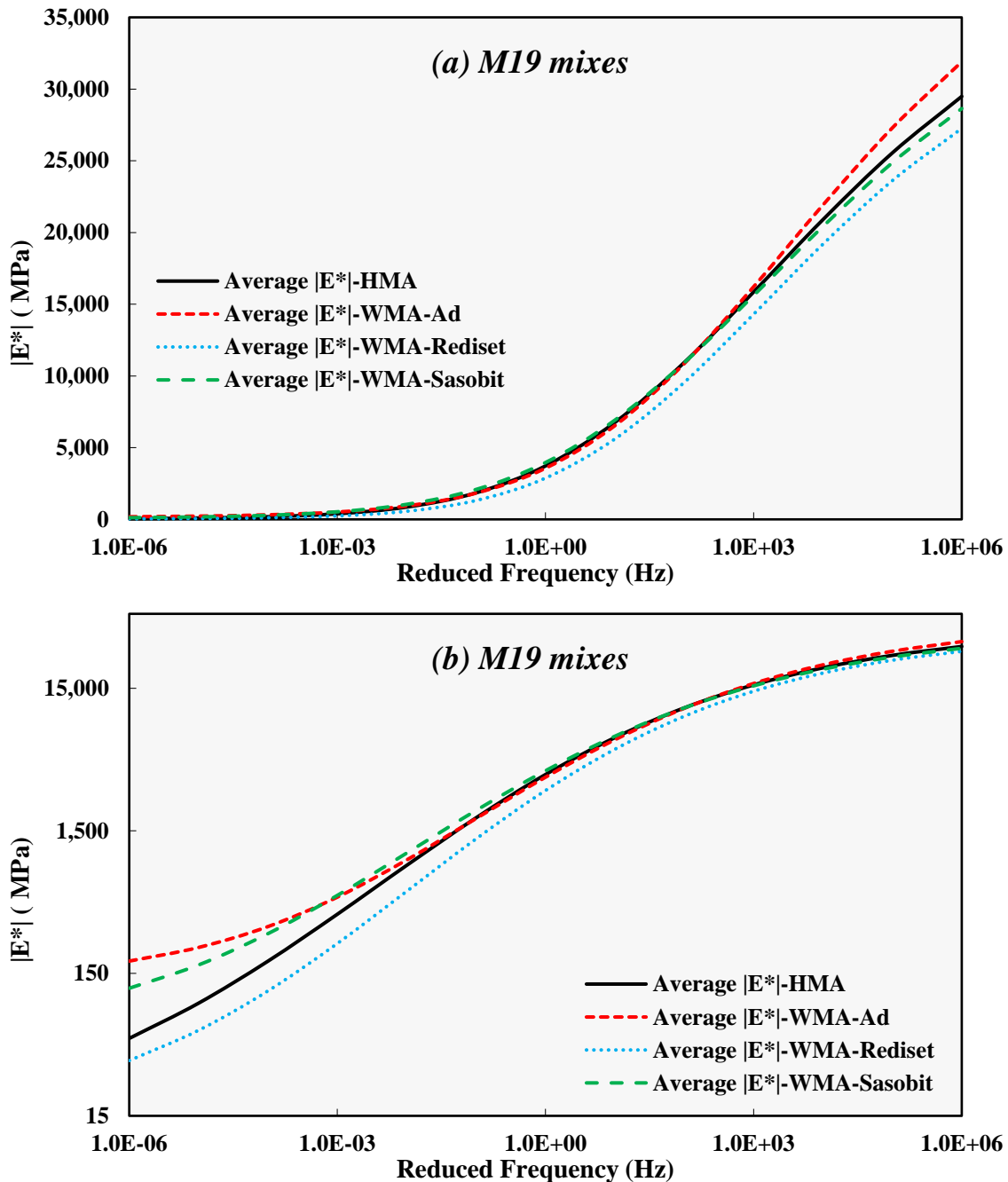


Figure 15. $|E^*|$ mastercurves for HMA and WMA mixes with modified binder and a 19.0 mm aggregate gradation at a reference temperature of 25°C in a) semi-log scale and b) log-log scale.

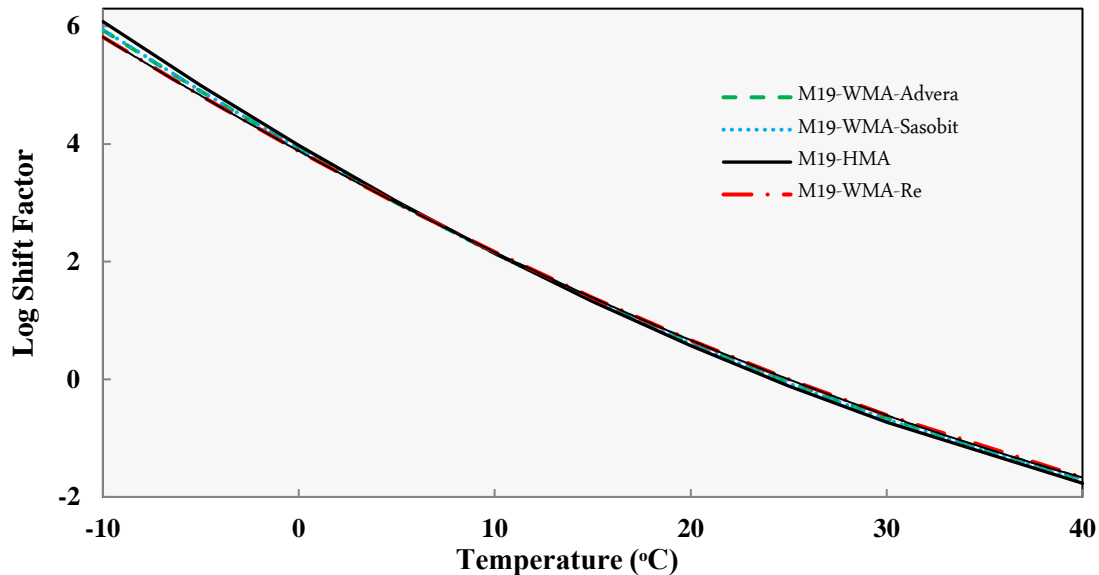


Figure 16. Time-Temperature shift factors for HMA and WMA mixes with modified binder and a 19.0mm aggregate gradation as used to construct the mastercurves of different LVE functions.

5.1.3 Statistical Analysis to Test Effect of WMA Additive on $|E^*|$

The plots of different replicates of each mix show a scatter around the average whose magnitude differs from one mix to another. This might be an indicator that different WMA additives might have different effects on the spatial distribution of the additives within the binder and thus the asphalt matrix. It implies different inherent uncertainties in material properties from one mix to another. However, such an observation needs more investigation as three replicates of each mix is not enough to conduct a probabilistic quantification of inherent variability. Using the available data, a statistical analysis was conducted to study the effect of the WMA additives on the stiffness of the asphalt mixes. This will show whether there is any significant difference between $|E^*|$ of HMA and that of different WMA mixes for the two types of binders (unmodified and modified). Moreover, this will be studied to check whether there is an interaction between the binder types and WMA technology used on the E^* results.

Two-way analysis of variance (ANOVA) is the process of studying more than one factor at a time. ANOVA was conducted for each group of the mixes to indicate whether for a given asphalt binder type there is a difference in the dynamic modulus of HMA and the different WMA mixes. In this case, the two independent variables are the reduced frequency and the type of the mix. For the first predictor, the fitted sigmoidal function was used to calculate the dynamic modulus for each mix at 10^{-3} , 10^{-2} , 10^{-1} , 1, 10, 10^2 , 10^3 , 10^4 , 10^5 , and 10^6 Hz which present a wide range of frequencies used for prediction of

rutting and fatigue cracking (i.e. most frequent distresses in asphalt pavement). Thus, the reduced frequency is tested for ten different levels and the type of mix for four levels/treatments (i.e. HMA, WMA_Rediset, WMA_Sasobit, and WMA_Advera). In this case, the two-way ANOVA has to be used as it is suspected that there might be some kind of interaction between the different levels of reduced frequency and the type of WMA additive used. It was initially expected that certain additives have an effect at high temperature only (i.e. very low reduced frequencies). The two-way ANOVA will be conducted in order to test the following null hypothesis:

- 1- H_0 : Dynamic modulus means for the type of WMA additive are equal.
- 2- H_0 : Dynamic modulus means for reduced frequency are equal.
- 3- H_0 : There is no interaction between reduced frequency and the type of WMA additive.

So, the reduced frequency and the type of WMA additive are considered as factors in the conducted ANOVA. In fact, the interest is studying both null hypothesis 1 and 3 because for the second one it is already known that as reduced frequency increases the dynamic modulus becomes higher regardless of the type of the asphalt concrete mix. It is noted here that the $|E^*|$ values are calculated at each reduced frequency using the fitted model rather than taking the measured values for testing because the measured values for all mixes and even replicates are not at same reduced frequency due to difference of few degrees in testing temperatures.

The tested samples are independent and the groups have the same sample size where each combination of frequency and mix type has three measurements representing the different tested replicates. Based on the findings by Kahil et al., $|E^*|$ at each reduced frequency is lognormally distributed (Kahil et al. 2015). Thus, the log of the $|E^*|$ is used as the response rather than $|E^*|$. Due to the low number of samples (three for each combination), the test for equality of variances will lack a high degree of statistical power. Instead, a linear regression model is fitted for $\log(|E^*|)$ vs. type and reduced frequency and the residuals are checked. The results of the residual analysis (as presented in Figure 17) show that there is no problem with the assumptions of lognormality of $|E^*|$ and equal variances. Thus, ANOVA can be conducted with the satisfaction of these assumptions.

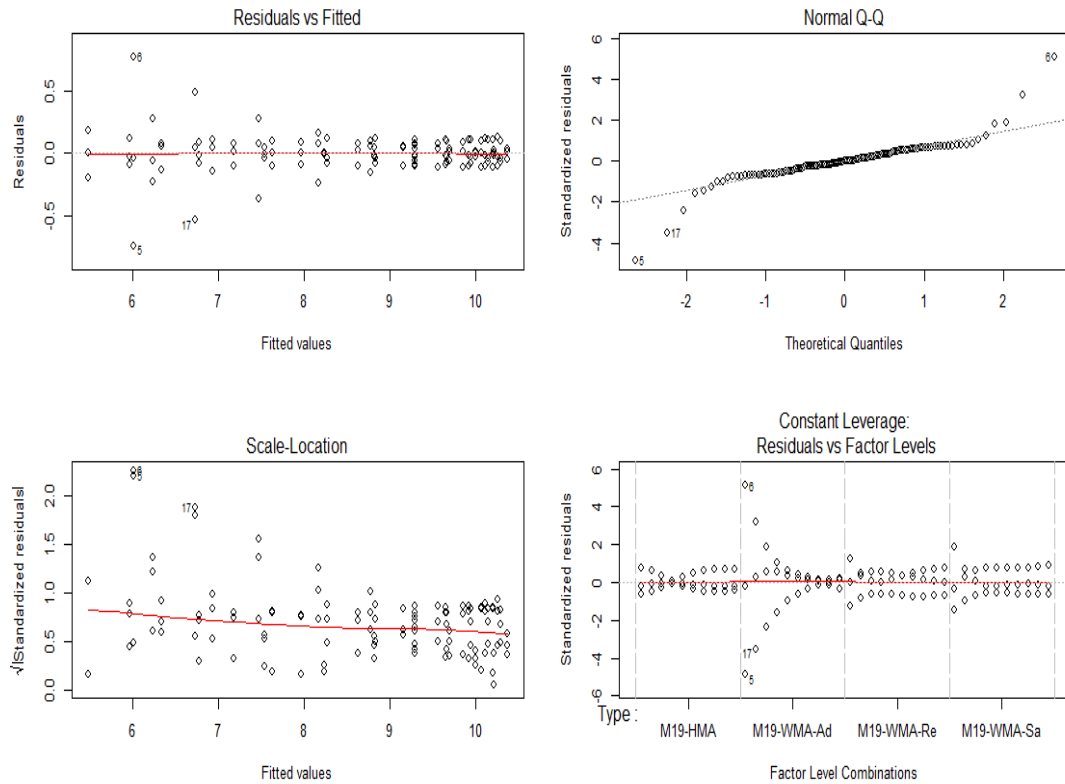


Figure 17. Residual analysis of linear model representing ANOVA analysis of $\log(|E^*|)$ vs. reduced frequency*type of mix.

It is shown that for both cases of unmodified and modified binders, there is not a significant interaction between the reduced frequency and the type of WMA additive used where a p-value of 0.6 is much higher the alpha value of 0.05. Thus, it can be concluded that WMA additives do not have an effect in further modifying the binder at only high temperature and this conclusion is valid at least for the materials used in this research. Thus, the WMA additives have an effect of shifting the entire $|E^*|$ master curve and not only shifting a part of it.

The interaction term was removed and two-way ANOVA was run as an additive model to study the main effect of each factor separately. In both case, and for both factors a p-value $\ll 0.05$ is obtained indicating that the null hypothesis should be rejected. This is expected for the case of reduced frequency and therefore does not require any further analysis. ANOVA indicates that the mix-type has an effect on $|E^*|$ but without telling how the effect of WMA additive varies between one additive and the other. Thus, the Tukey Honest Significant Difference (TukeyHSD) test was conducted to determine how the mixes differ in comparison with each other. The results of the TukeyHSD test, as presented in Table 15, show that for the mixes with modified binder there is not a significant difference between the $|E^*|$ of HMA and WMA with Sasobit and that with Advera but there is a significant

difference between HMA and WMA with Rediset. The test shows that WMA with Rediset has a lower $|E^*|$ than that of the control HMA mix used. However, another trend was obtained from the results of TukeyHSD test for mixes with unmodified binder where it was found that there is not a significant difference between the $|E^*|$ of the WMA mixes regardless of the additive used. The $|E^*|$ of all the WMA mixes is significantly different from the HMA mix where the $|E^*|$ of WMA is always lower than that of HMA. These results can be further visualized in the box plots of Figure 18 and Figure 19. These plots show variability in observations between one sample and the other and thus the effect of the WMA additive has to be very high to show a significance due to the inherent uncertainty processed between one replicate and another of the same mix.

Table 15. TukeyHSD test results for multiple comparisons of means of $|E^*|$ mastercurves of HMA and WMA mixes at a 95% family-wise confidence level.

Compared Pairs of Mixes	Difference Indicator	Adjusted p- value
“M19-WMA-Ad” vs. “M19-HMA”	0.004875	0.99
“M19-WMA-Re” vs. “M19-HMA”	-0.22225	0.00005
“M19-WMA-Sa” vs. “M19-HMA”	0.045389	0.78
“M19-WMA-Re” vs. “M19-WMA-Ad”	-0.22713	0.00004
“M19-WMA-Sa” vs. “M19-WMA-Ad”	0.040514	0.83
“M19-WMA-Sa” vs. “M19-WMA-Re”	0.267639	0.000001
“U25-WMA-Ad” vs. “U25-HMA”	-0.31071	0.0000009
“U25-WMA-Re” vs. “U25-HMA”	-0.27121	0.00002
“U25-WMA-Sa” vs. “U25-HMA”	-0.30084	0.000002
“U25-WMA-Re” vs. “U25-WMA-Ad”	0.039501	0.89
“U25-WMA-Sa” vs. “U25-WMA-Ad”	0.009865	0.99
“U25-WMA-Sa” vs. “U25-WMA-Re”	-0.02964	0.95

The results of the statistical test show that for mixes with modified binder, Sasobit or Advera will not affect the stiffness of the mix but it is lowered when Rediset is used. This can be explained by the fact that Rediset is added in the form of oil and thus as any other oil it might play a role of softening the binder and thus reduces $|E^*|$. However, it is not the case of Sasobit and Advera which are added in the form of pills and powder which might act as a filler in the mix which typically stiffens the asphalt binder/mastic and thus increases $|E^*|$.

In addition, the conducted two-way ANOVA was expanded to a three-way ANOVA where the binder type was added as a factor. Since there is no interaction between the reduced frequency and the WMA additive, then the only interaction tested in this model is that between the type of binder and the type of WMA additive. The results gave a p-value of 0.000103 for the interaction between the type of binder and the type of WMA additive used. This indicates that there is a strong evidence of interaction between these two factors which

explains the two different trends explained earlier based on the results of the couple of two-way ANOVA conducted above.

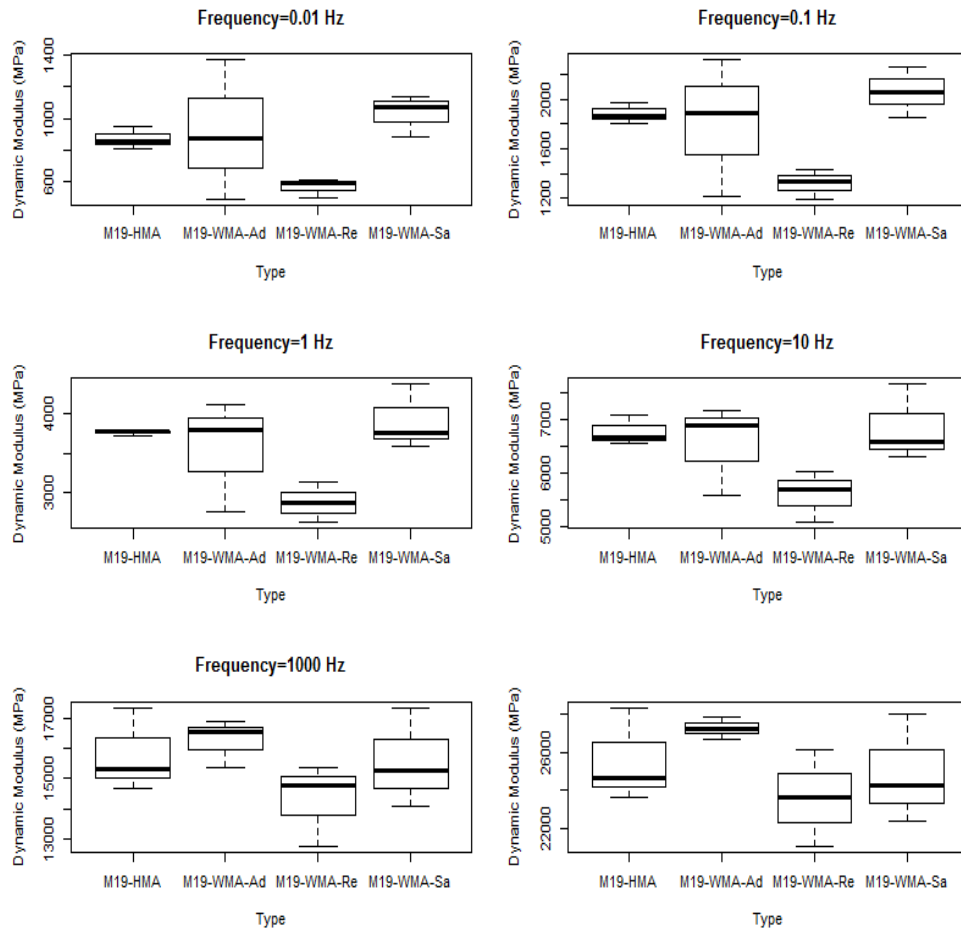


Figure 18. Boxplot showing variation of E^* between HMA and WMA mixes at different selected frequencies for the group of modified binder.

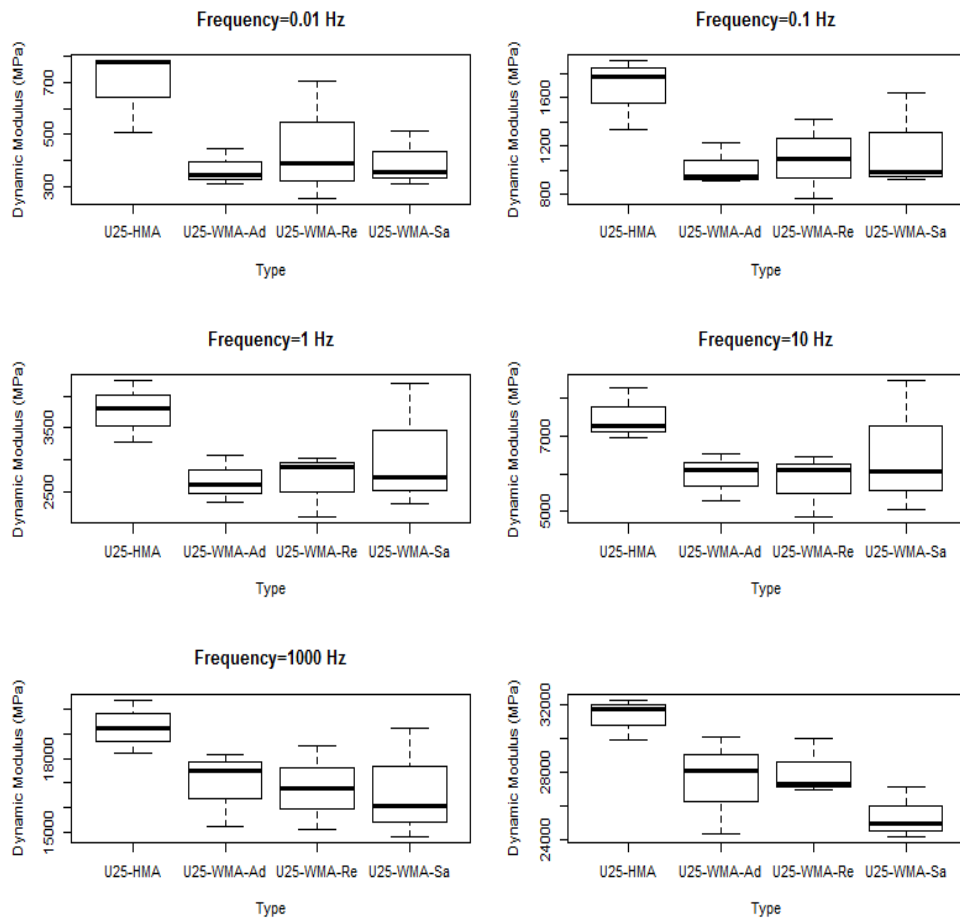


Figure 19. Boxplot showing variation of E^* between HMA and WMA mixes at different selected frequencies for the group of unmodified binder.

Therefore, it has been shown that the effect of WMA additive depends on the additive itself and the type of binder used. For modified binder, the stiffness of mixes with Sasobit and Advera are the same as that of the control HMA mix; however, Rediset is able to soften the binder and thus reduce the stiffness of the mix. However, for the case of unmodified binder the three WMA additives have the same effect in reducing the $|E^*|$ of WMA.

On the other hand, these results provide an evidence that WMA mixes can have the same stiffness as that of HMA. However, this needs to be further investigated and thus the mixes are assessed based on mechanistic modeling of the VE and VP behavior rather than on a single material property such as $|E^*|$.

5.1.4 $E(t)$ and $D(t)$ of HMA and WMA mixes

The $|E^*|$ is used along with phase angle in order to determine the storage and loss moduli which in role are used in order to determine $E(t)$ and $D(t)$. For each tested E^* replicate, $E(t)$ and $D(t)$ are determined using the different interconversion methods that are presented earlier. These response functions are determined at a reference temperature of 25°C where they can be shifted using the time-temperature shift factors for any needed temperature

(example: at 5°C for modelling of the viscoelastic behaviour). The data is fitted for each replicate and presented by Prony series having 18 different coefficients (E1, E2, E3,..., E17 and E_{inf}) which presents the E(t) and D(t) over a reduced time range of 10⁻⁸ to 10⁺⁸ second. The average E(t) and D(t) mastercurves is presented for each of the mixes understudy are in Figure 20 to Figure 23. The mastercurves are presented at a reference temperature of 5°C which is the temperature of the development of the viscoelastoplastic models as stated earlier.

The results show that for every replicate the same E(t) is obtained whether it is calculated using the Exact or the Approximate method. However, variabilities are obtained for some replicates in the case of D(t) calculated using the Direct method or through the interconversion from E(t). For all purposes, D(t) obtained by the Approximate method through the conversion from E(t) is used as it satisfies the constitutive equation relating E(t) to D(t) as shown in Equation 74.

$$1 = \int_0^t E(t - \tau) \frac{dD(\tau)}{d\tau} d\tau \quad \text{Equation 74}$$

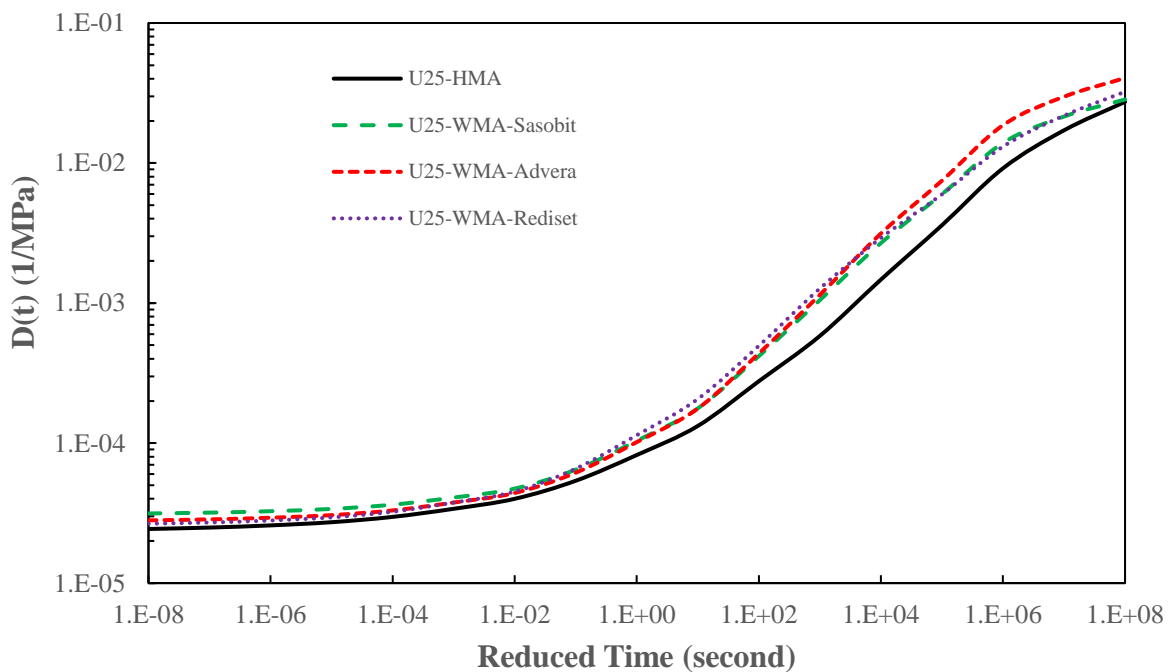


Figure 20. D(t) calculated by the Approximate method for HMA and WMA U25 mixes at a reference temperature of 5°C.

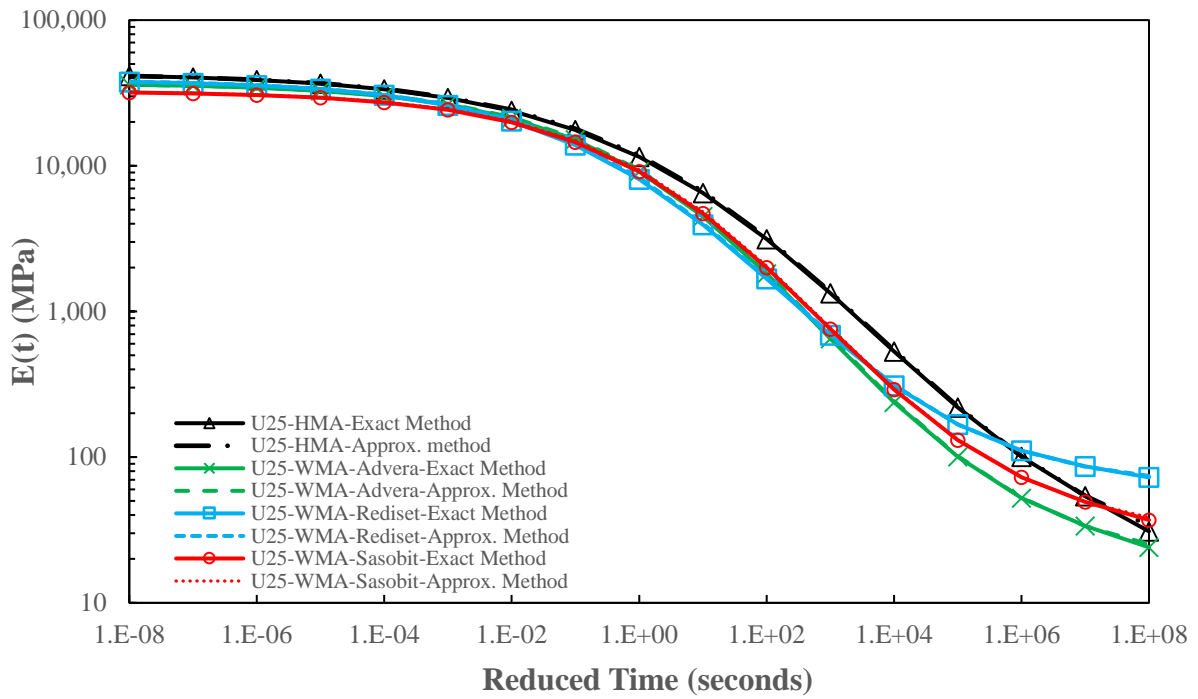


Figure 21. $E(t)$ calculated by the Approximate and Exact methods for HMA and WMA U25 mixes at a reference temperature of 5°C.

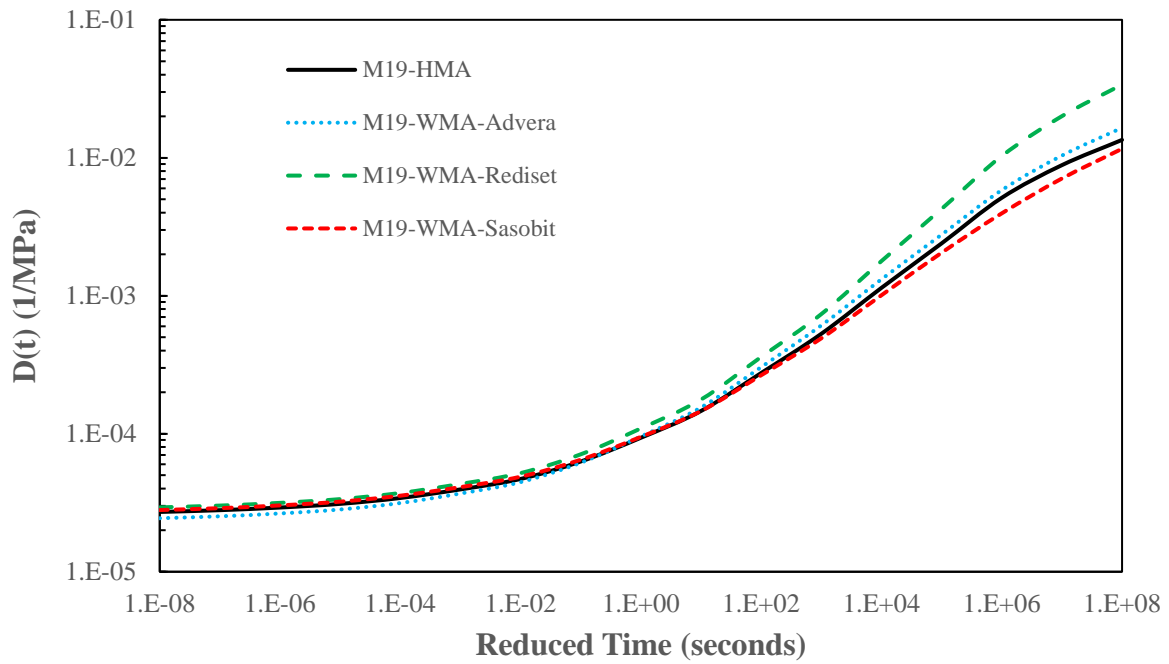


Figure 22. $D(t)$ calculated by the Approximate method for HMA and WMA M19 mixes at a reference temperature of 5°C.

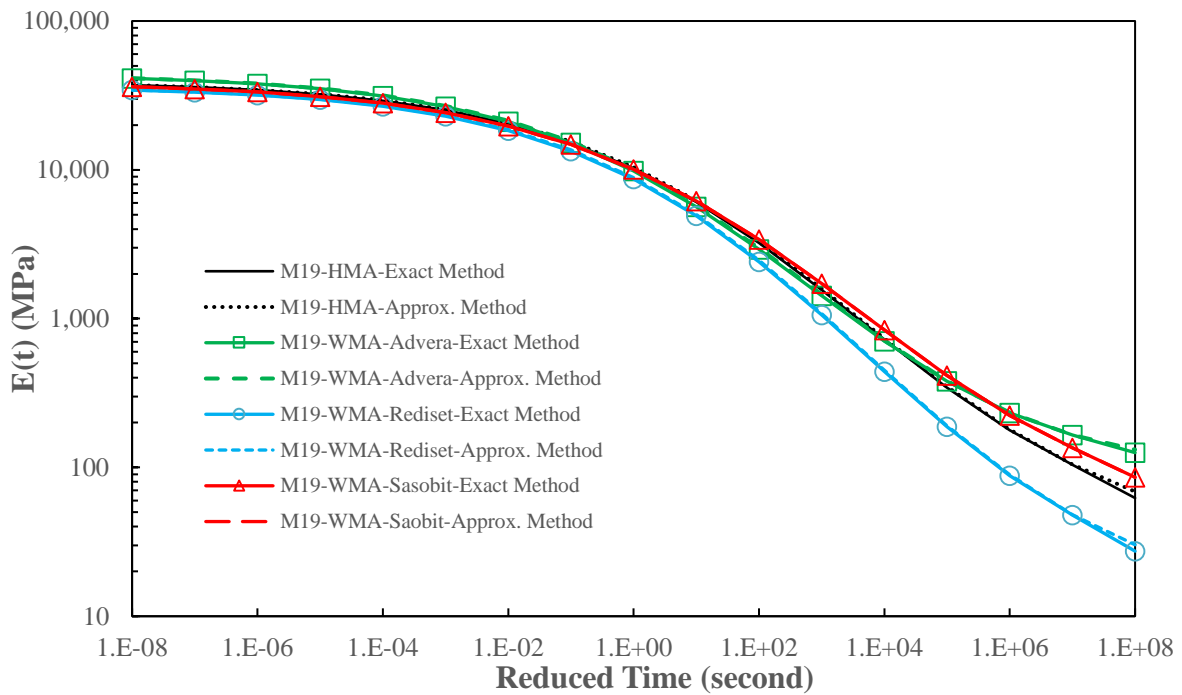


Figure 23. $E(t)$ calculated by the Approximate and Exact methods for HMA and WMA M19 mixes at a reference temperature of 5°C .

5.2 Viscoelastic Modeling

For each of the mixes under study, the constant crosshead tests at 5°C yield normalized pseudostiffness vs damage (C vs S) curves that collapse perfectly on top of each other indicating the absence of viscoplasticity for the investigated testing conditions. Thus, the viscoelastic model for all mixes is developed based on the outputs of tests conducted at 5°C and rates of 0.0001 strain/sec and 0.00005 strain/sec. For each mix, the third replicate tested at 0.000025 strain/sec is used to validate the developed viscoelastic model. The results show that for the developed models are accurate where the predicted viscoelastic strains fit perfectly with the measured on-specimen LVDT strains. The plots in Figure 24 show the VE predictions for which VE strains are predicted for different crosshead rates for WMA with PG64-22 binder and Sasobit as an additive. The VE model is developed for the 12 different mixes under study which shows that the proposed VE modeling is valid for WMA as HMA and for both PG64-22 and PG76-22 binders. However, the fitting parameters of the C vs S curves and S vs. Lebesgue norm of stress vary from one mix to another, as presented in Table 16, showing the model's sensitivity to WMA as well as HMA mixes.

Table 16. Fitting Parameters of damage characteristic curve for all the mixes in the study.

Mix	S(LS) Model										C(S) Model			Alpha
	a1	b1	a2	b2	a3	b3	a4	b4	a5	b5	a	b	c	
U25-HMA	5.26E-01	1.61E-04	-6.67E+03	-4.17E-05	-1.02E+02	3.95E-04	5.54E+02	-2.64E-02	6.61E+03	1.68E-04	1.34	-0.03	0.37	2.37
U25-WMA-Ad	5.26E-01	1.61E-04	-6.67E+03	-1.47E-04	-1.02E+02	1.74E-04	5.54E+02	-2.64E-02	6.61E+03	1.25E-04	1.24	-0.03	0.34	2.03
U25-WMA-Re	5.26E-01	1.52E-04	-1.96E+04	-7.67E-05	1.24E+00	4.90E-04	5.41E+03	-2.91E-04	1.42E+04	7.53E-05	1.41	-0.06	0.29	2.22
U25-WMA-Sa	5.25E-01	1.51E-04	-1.90E+04	-7.86E-05	1.17E+00	1.66E-04	6.70E+03	-2.31E-04	1.24E+04	7.96E-05	1.18	-0.01	0.44	2.13
M19-HMA	7.99E+02	-5.11E+00	1.17E+03	1.43E-04	-2.01E+02	4.46E-04	-5.52E+03	-6.41E-06	4.54E+03	2.16E-04	1.13	-0.01	0.49	2.85
M19-WMA-Ad	1.53E+01	-2.72E-02	-4.36E+05	-7.96E-06	8.91E+04	-5.79E-05	-3.50E+04	-1.00E+04	3.47E+05	8.09E-06	1.25	-0.02	0.42	2.56
M19-WMA-Re	1.53E+01	-2.72E-02	-4.36E+05	-1.27E-05	8.91E+04	-5.79E-05	-3.50E+04	-1.00E+04	3.47E+05	1.58E-06	1.16	-0.01	0.41	2.42
M19-WMA-Sa	-8.57E+00	-1.00E+01	-4.36E+03	-5.52E-05	-3.83E+02	3.61E-04	-7.44E-02	8.21E-06	4.69E+03	2.04E-04	1.04	0.00	0.68	2.40
U19-HMA	1.00E+00	1.04E-05	-9.98E+01	-3.35E-02	-1.93E+04	-8.78E-05	8.35E+03	-2.06E-04	1.09E+04	8.39E-05	1.24	-0.02	0.41	2.19
U19-HMA-Fi	1.53E+01	-2.73E-02	-3.80E+05	-1.55E-05	1.66E+05	-4.40E-05	-3.50E+04	-1.00E+04	2.14E+05	1.06E-05	1.22	-0.01	0.44	2.35
U19-WMA-Sonne	1.52E+01	-2.73E-02	-3.03E+05	4.03E-05	2.63E+05	4.28E-05	-3.50E+04	-1.00E+04	4.10E+04	5.90E-05	1.22	-0.01	0.42	2.17
U19-WMA-Sonne-Fi	1.00E+02	-2.90E+01	-2.23E+05	-5.01E-05	1.50E+05	-7.55E-05	-8.67E+08	-1.55E+00	7.31E+04	1.53E-05	1.23	-0.02	0.38	2.28

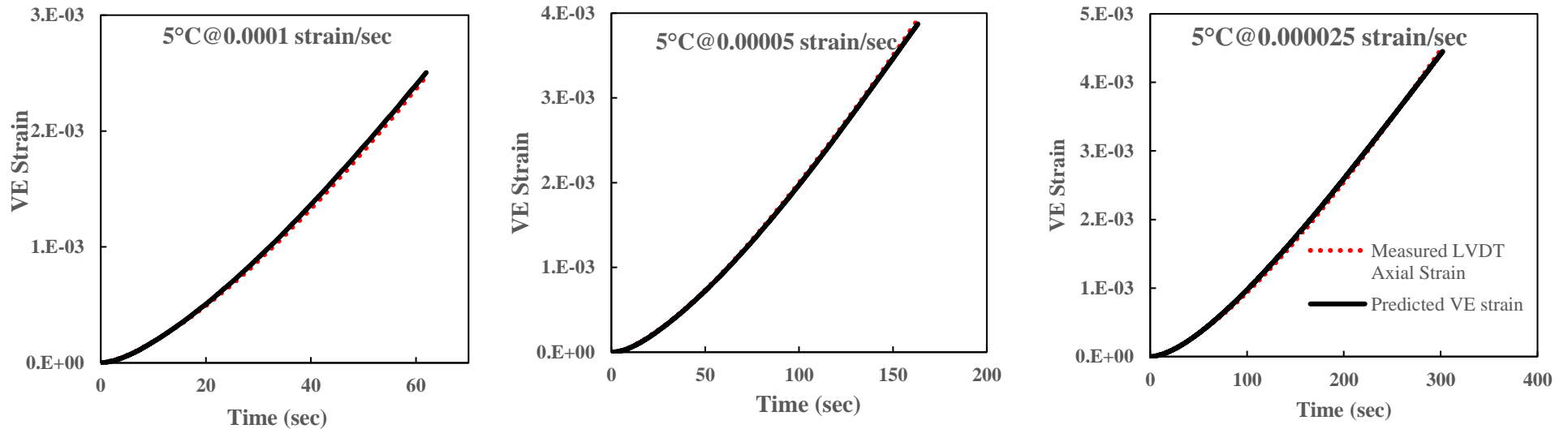


Figure 24. Predicted and measured VE strains vs. time at 5°C for crosshead test rates used to develop and calibrate VE model of WMA with Sasobit and unmodified binder.

In order to compare the viscoelastic damage behavior of HMA and WMA mixes, the C vs S are investigated as plotted in Figure 25 and Figure 26 for the U25 and M19 mixes, respectively. Considering a drop of C from 1 to 0.5 as a failure criteria, then the following conclusions can be made:

- For the U25 mixes with PG64-22 binder and 25 mm gradation: while U25-HMA requires an S value of 17,100 corresponding for a drop in C to 0.5, the S value is 18,500, 19,800, and 22,500 for the U25-WMA-Advera, U25-WMA-Rediset, and U25-Sasobit, respectively. This indicates that the three WMA mixes shows more favorable damage characteristics than HMA.
- For the M19 mixes with PG76-22 binder and 19 mm gradation: For M19-HMA, the S value is 15,555 which is almost similar to that of the M19-WMA-Advera and M19-WMA-Sasobit being 15,450 and 16,050, respectively. However, M19WMA Rediset shows a higher S value of 24,800. Thus, WMA mixes with Advera and Sasobit show almost the same damage characteristics as HMA; however, the damage behavior of WMA with Rediset is more favorable.

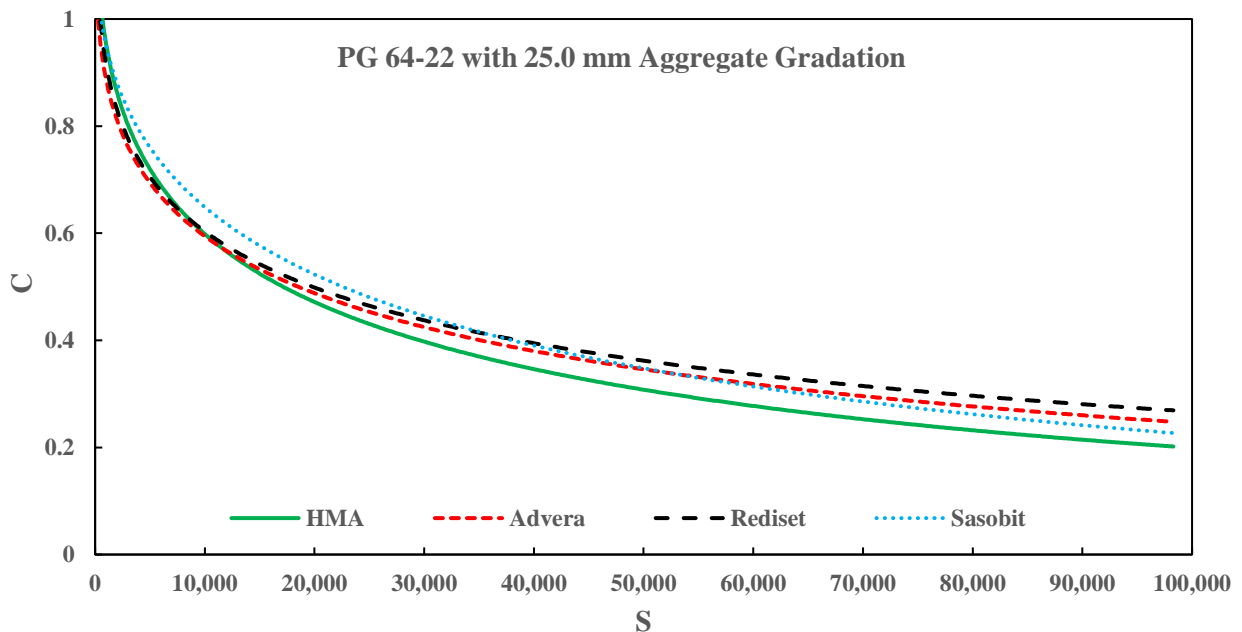


Figure 25. Damage characteristic curves for VECD modeling for HMA and WMA U25 mixes.

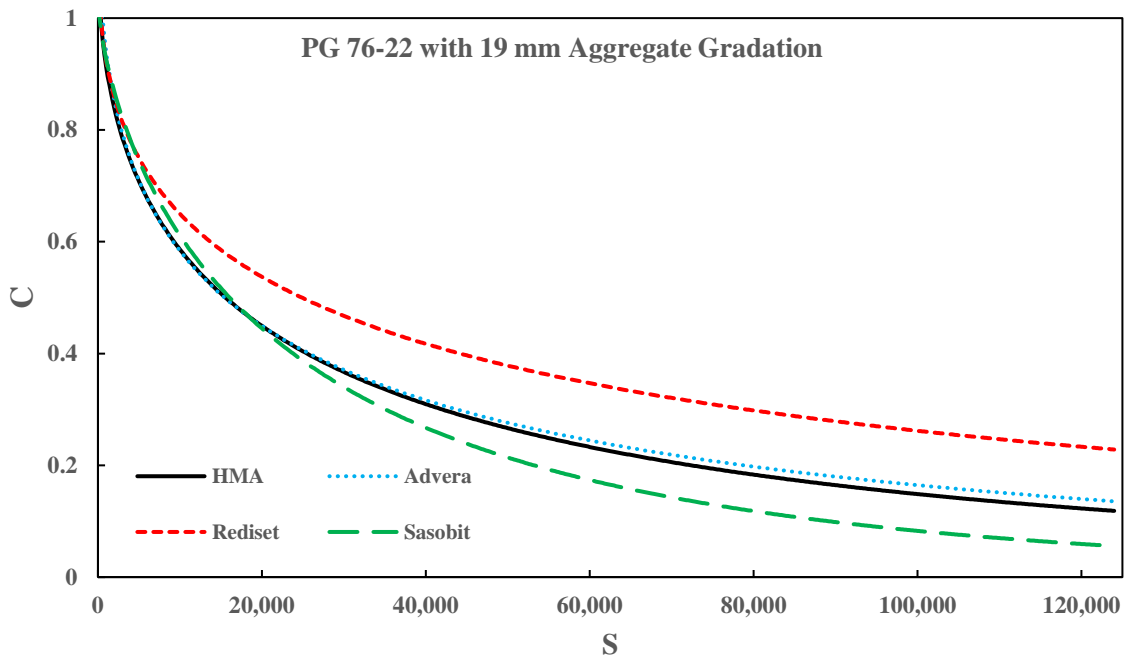


Figure 26. Damage characteristic curves for VECD modeling for HMA and WMA M19 mixes.

It should be noted that the amount of accumulated damage to achieve a certain value of C would give an idea of the behavior of the mixes but that could not be enough to assess the performance of the mix. This could be made clearer especially that S to achieve $C=0.5$ is 17,100 for the U25-HMA mix that is around 10% higher than that of M19-HMA. Even though the U25-HMA requires more damage to get to $C=0.5$ than the M19-HMA but this does not mean that it would have a better performance than the M19-HMA. One point to be highlighted is the fact that the drop in C of 0.5 is relative to the actual stiffness of the mix which differ from one mix to another. On the opposite side, the statistical analysis conducted for the $|E^*|$ results of HMA and WMA with Sasobit, Rediset, and Advera with both modified and unmodified binders shows that the effect of WMA additive depends on the additive itself and the type of binder used. For modified binder, the stiffness of mixes with Sasobit and Advera are the same as that of the control HMA mix; however, Rediset is able to reduce the stiffness of the mix. For the case of unmodified binder the three WMA additives have the same effect in reducing the $|E^*|$ of WMA. Therefore, it is not enough to assess the behavior of HMA and WMA mixes under a certain loading profile based on either C vs S or dynamic modulus results. So, the performance of the mix should take into account the mix's resistance to damage and deformation (Underwood 2011). Based on that the mix are compared using the prediction of viscoelastic strain in response to a given stress profile where damage characteristic curves, LVE properties, and time- temperature shift factors are incorporated.

Such a task is carried out by taking a stress history of 100 creep and recovery tests with a loading and resting period of 0.1 and 0.9 sec, respectively. This is considered with a deviator stress of 600 kPa and at a temperature of 35°C. The VE strain component is predicted for this loading profile for the HMA and WMA mixes which are ranked based on the VE damage strain after 100 cycles as shown in Table 17. WMA with Sasobit shows a better performance than the corresponding HMA mixes. The performance of WMA with Rediset is better than that of HMA in case of unmodified binder but worse in case of the modified binder. However, WMA with Advera has a 15% higher viscoelastic strain for the case of modified binder and almost 80% higher than HMA in case of unmodified binder.

Taking the case of M19 mixes, WMA with Rediset shows more favorable damage properties but lower $|E^*|$ than other mixes; however, based on the predicted viscoelastic strain it has the highest unrecoverable strain at the end of the 100th creep and recovery cycle. On the other side, taking the case of U25 mixes, Sasobit shows the most favorable damage properties but a lower $|E^*|$ than U25-HMA; but, it shows the lowest predicted viscoelastic strains at the end of the 100th creep and recovery cycle as compared to the mixes of its category. Therefore, this shows that $|E^*|$ nor C vs. S alone can characterize the performance of asphalt concrete mixes and thus the full image on this behalf is dictated by the predictions that aggregate the material properties among different levels of characterization.

Table 17. Predicted viscoelastic strains for HMA and WMA mixes after 100 creep and recovery cycles.

Mix Description		VE Strain after 100 Creep and Recovery Cycles	Ranking Within Category
PG76-22, 19mm	HMA	4.11E-04	2
	Sasobit	2.98E-04	1
	Advera	4.70E-04	3
	Rediset	7.65E-04	4
PG64-22, 25mm	HMA	8.36E-04	3
	Sasobit	5.29E-04	1
	Advera	1.52E-03	4
	Rediset	5.98E-04	2

5.3 Viscoplastic Modeling

As discussed earlier, part of the nonlinear damage in the asphalt mixtures is attributed to viscoplasticity. This is modeled by using the results of crosshead testing done at high temperature of 35°C and slow testing rates. It is notable from the testing results that the binder softens during testing and thus the response of the mix will be affected by the aggregate interlock at a certain point just before the peak stress is reached. At this level, the

resistance to deformation will be attributed to the aggregate interlock and not only the binder. Therefore, the viscoplastic strain is modeled for the stress profile before the effect of the aggregate interlock appears. The results, as presented in Table 18, show that the contribution to viscoplasticity is affected by the type of WMA additive used. The use of Sasobit as a wax-based additive increases the contribution of viscoplasticity to total damage significantly regardless of the type of binder. However, the foaming based WMA additive “Advera” reduces the contribution of viscoplasticity for both modified and unmodified binders. It is worth noting that the contribution of viscoplasticity varies between 25 and 35% of the total damage which is thus dominated by nonlinear viscoelasticity for the case of 35°C and the considered testing rates. In addition, it can be observed that the peak stress is higher with a larger corresponding axial strains for case of M19 mixes as compared to the U25 mixes. This indicates the effect of modified binder in increasing the stress and ductility of the asphalt concrete mixes. By comparing the effect of WMA additives, it can be observed that almost mixes with Sasobit show a similar peak stress and corresponding strain compared to the control HMA mixes of each category. For each of the mixes under study, the viscoplastic model is developed where the parameters p , q , and Y as per Equation 65. For example, for M19-HMA the p , q , and Y are 0.47, 0.05, and 4.4E10, respectively; while for U25-HMA they have a value of 0.21, 0.08, and 4.6E9, respectively. The values for the viscoplastic model differs from one mix to another differentiating the viscoplastic behavior of each of the investigated mixes. These developed models allow for the prediction of viscoplastic strains due to any input stress profile.

Table 18. Results of crosshead testing at 35°C and slow rates showing the portion of VP strain for HMA and WMA mixes.

Mix Description		Peak Stress (kPa)	Axial Strain at Peak Stress	Percentage of Viscoplastic Strain
PG76-22, 19mm Gradation	HMA	998.7	0.0148	31.3
	Sasobit	939.9	0.0138	36.6
	Advera	830.6	0.0152	30.3
	Rediset	752.8	0.0130	30.0
PG64-22, 25mm Gradation	HMA	699.2	0.0122	28.8
	Sasobit	610.1	0.0101	33.1
	Advera	557.6	0.0080	24.5
	Rediset	509.5	0.0091	30.8

Even though the VEPCD model is developed, calibrated, and validated based on constant crosshead rate tests, where damage accumulates without any recovery. The model is

further validated for cases with recovery by applying 500 haversine cycles at a frequency of 20 cycles/second, a temperature of 7°C, and an amplitude of 1200 kPa. As seen by the results of the last few cycles as shown in Figure 27, the predicted total strain in response to the described stress profile is almost within 5% of the measured strains.

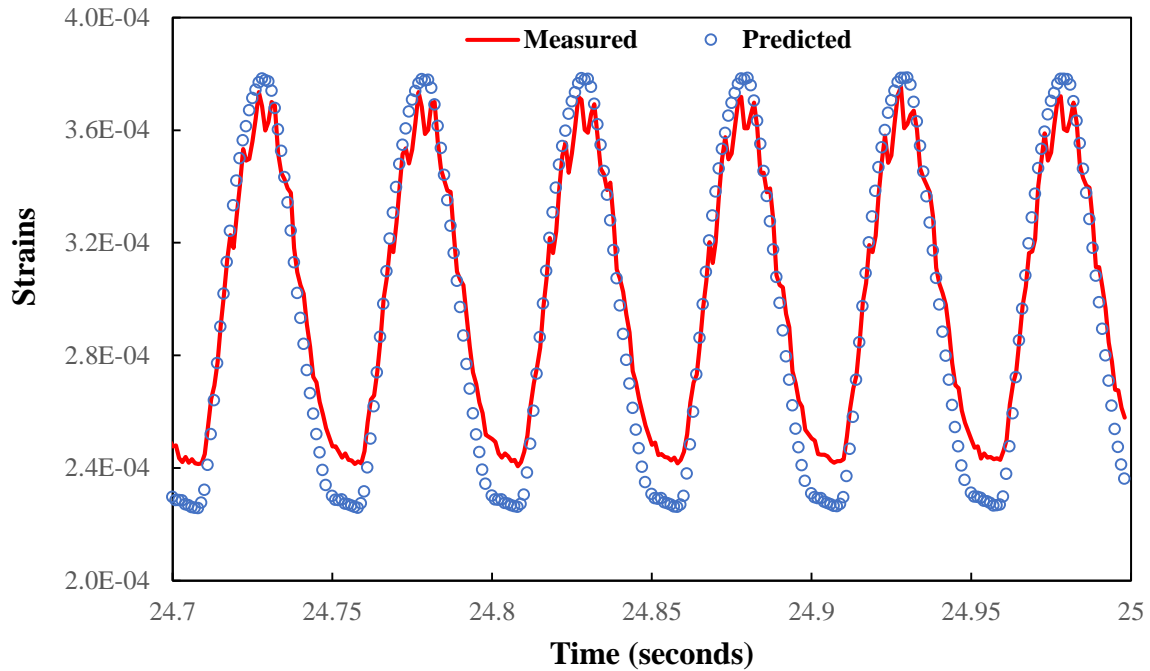


Figure 27. Measured and predicted strains for AC sample subjected to cyclic loading.

5.4 Comparison of HMA and WMA Mixes Based on Random Stress Profile

In order to assess the effect of different WMA additives on the performance of asphalt concrete mixes and based on the previously drawn conclusions, strains are predicted for each of the mixes in response to a random stress profile. A stress profile is selected randomly as shown in Figure 28. The stress profile is chosen randomly to include stress cycles with different magnitudes, different loading durations, and different resting periods. The stress magnitude peaks fall in the range of 100-600 kPa with duration times between 1 and 40 seconds which could represent traffic at a signal that could have different speeds or even stationary for a certain period of time.

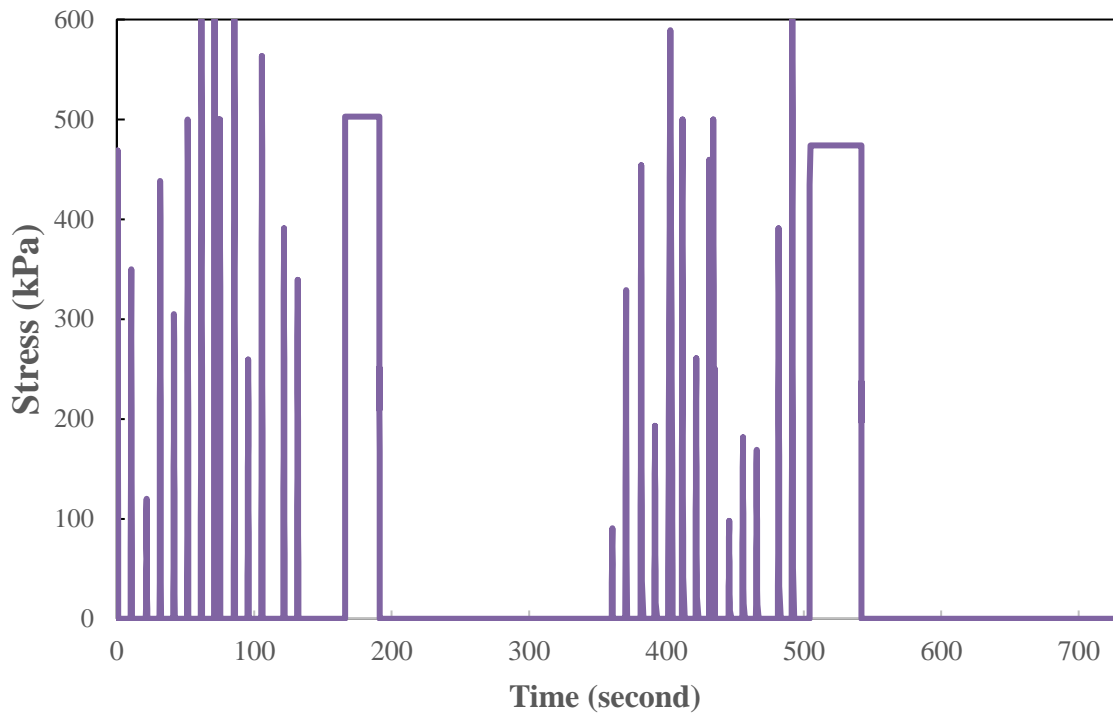


Figure 28. Investigated stress profile for prediction of strains for HMA and WMA mixes.

This random stress profile is used only for illustration to assess the performance of the investigated HMA and WMA mixes knowing that a more realistic traffic profile could be further investigated based on a real traffic count. Both viscoelastic and viscoplastic strains are simulated for each mix using its developed model in the previous parts of this research. For each mix, the components strains are predicted separately and added to constitute the total strain. For each mix, the investigated stress profile is assumed to be at a temperature of 5°C and 35°C. Thus, the total strains are predicted for each mix for the given stress profile at the two different temperatures. The predicted viscoelastic strains in response to the investigated stress profile are presented in Figure 29 and Figure 30, respectively.

For the M19 mixes, it can be shown that the use of Sasobit as a WMA additive shows different effect at the two different investigated temperatures of 5°C and 35°C. This difference appears mainly in the loading regime where the predicted strain for the M19-WMA-Sasobit is almost the same as that of the control HMA mix at 5°C but smaller in the case of higher temperature of 35°C. However, a higher proportion of the accumulated viscoelastic strain instantaneously recovers upon the removal of the load for the case of the M19-HMA as compared to the M19-WMA-Sasobit. This yields that both M19-HMA and M19-WMA-Sasobit have the same magnitude of viscoelastic strains during recovery period just after the removal of load. This indicates that the usage of Sasobit as a WMA additive to asphalt concrete mixes with modified binder will not have any negative effect on the performance when assessed based on the viscoelastic strain in compression state.

For the case of WMA mixes with modified binder and utilizing Rediset and Advera as additives a different behavior is observed. For both temperatures of 5°C and 35°C, mixes with Advera and Rediet show higher predicted viscoelastic strains in both loading and unloading regions as compared to the reference HMA mix. Such a difference become more prominent for the case of 35°C as compared to that of 5°C and this could be due to the softening effect of Rediset as the temperature becomes higher especially that Rediset is an oily-based product unlike Advera which ends up in the mix as a synthesized type of fillers. As this could show and as revealed in the predictions of viscoelastic strains, the difference between the predicted viscoelastic strain compared to that of the reference M19-HMA mix is more significant for the case of M19-WMA-Rediset as compared to that of M19-WMA-Advera. During recovery period, the viscoelastic strain for M19-WMA-Advera approaches that of M19-HMA but it is not the case for M19-WMA-Rediset where it is always higher.

In addition, it can be observed that the recovery is almost similar for all the M19 mixes regardless of the effect of temperature and the type of WMA additive used. The effect of any WMA additive on the recovery properties is mainly overcovered by that of the used modified binder. However, this is not the case of the U25 mixes with unmodified binder as shown for the predicted viscoelastic strains in Figure 30. At 5°C, the unrecovered viscoelastic strains at the end of the analysis is higher for all WMA mixes as compared to the reference HMA mixes which is not the case at 35°C except for U25-WMA-Advera. For this category of mixes, the predicted viscoelastic strains show that at 5°C it is always higher for the WMA mixes as compared to the control HMA mix regardless of the type of WMA additive used. Rediset and Advera has almost the same effect on yielding higher levels of predicted viscoelastic strains more than the case of using Sasobit. At 35°C, a different behavior is obtained especially that U25-WMA-Advera is the only mix to show a higher predicted viscoelastic strain that the control HMA mixes. However, during recovery the strain decreases at a fast rate approaching that of the control HMA. For the case of U25-WMA-Rediset and U25-WMA-Sasobit, the predicted strain is below that of the control HMA during loading where the later has a higher ability of recovery where the unrecovered viscoelastic strain is obtained to be the same at the end of the analysis period for these three mixes. For the U25-WMA-Rediset, these results might be due to the fact that its stiffness is higher than that of U25-HMA at very low reduced frequency. However, for the U25-WMA-Sasobit the result might be governed by the more favorable damage characteristics that it possesses as discussed earlier.

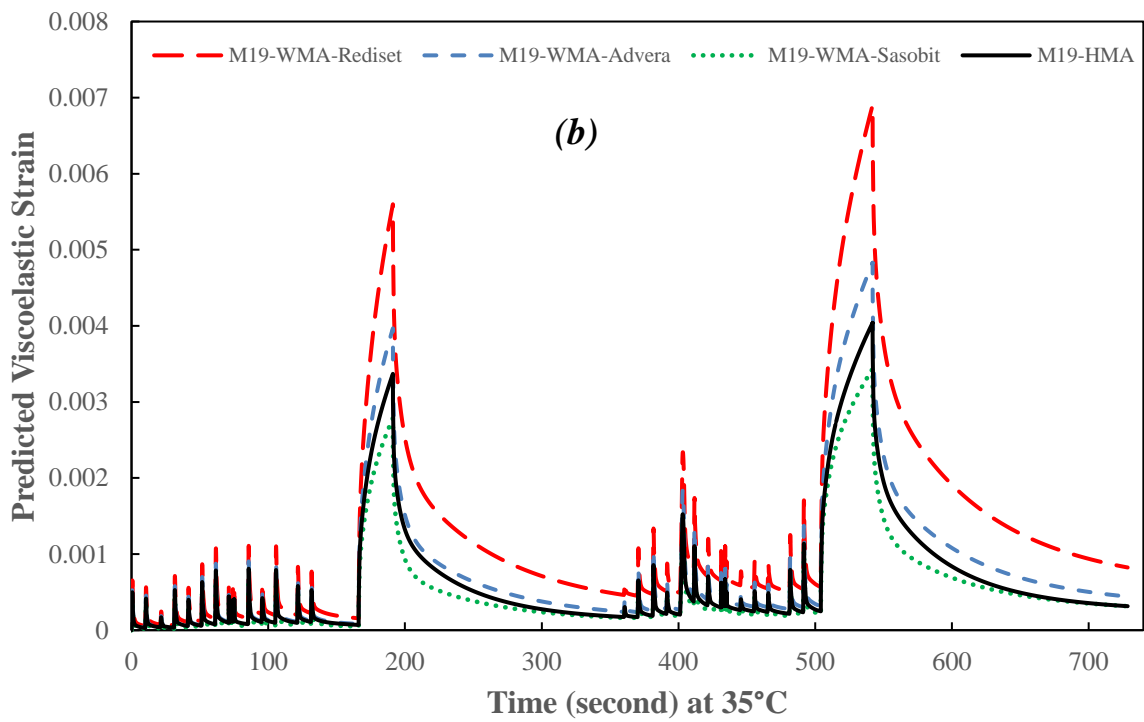
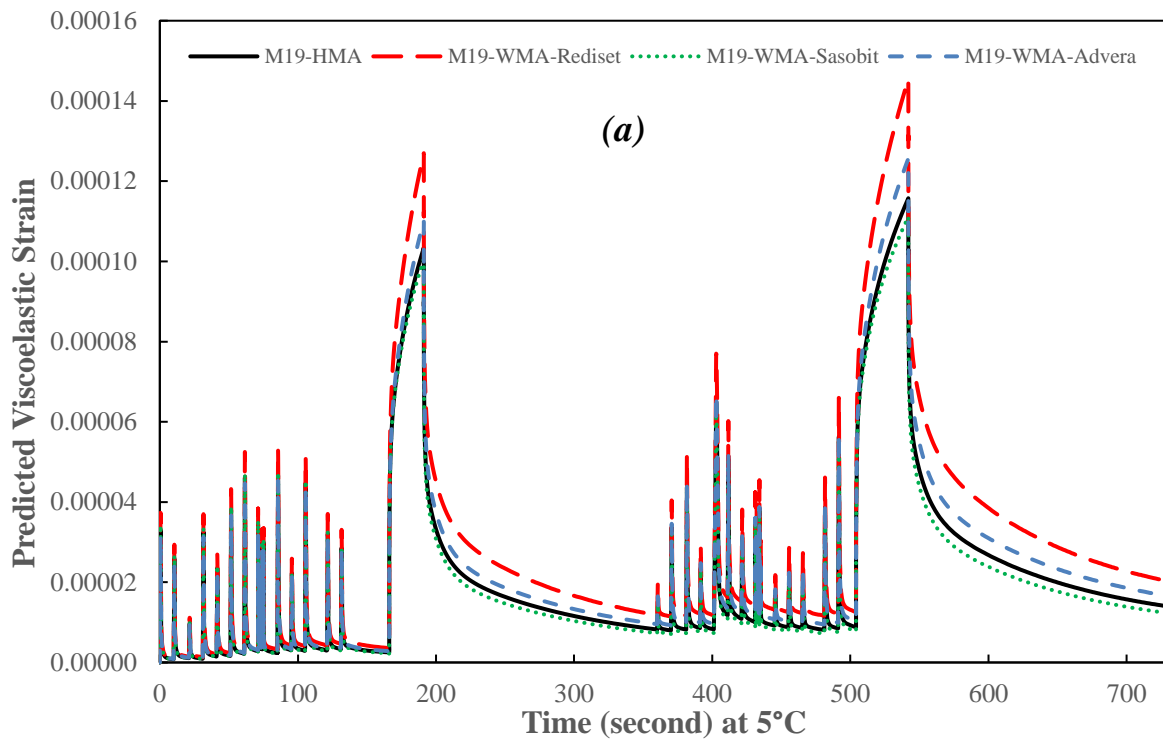


Figure 29. Predicted viscoelastic strain for the different HMA and WMA M19 mixes in response to the investigated random stress profile at a temperature of a) 5°C and b) 35°C.

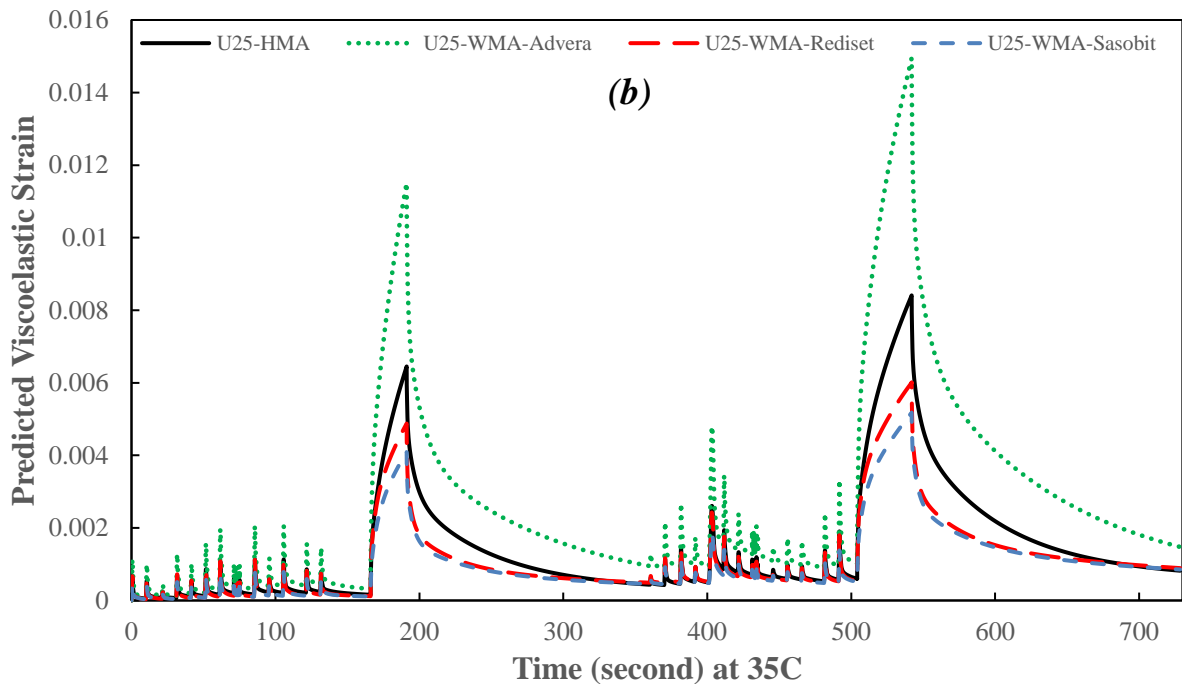
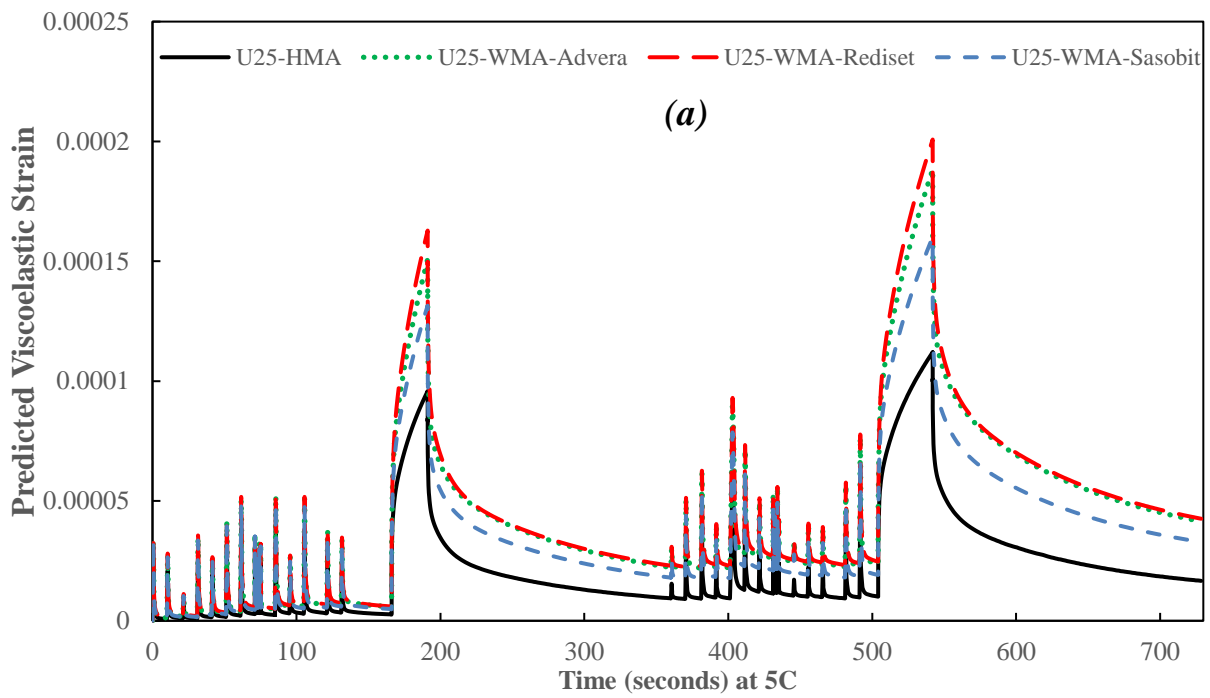
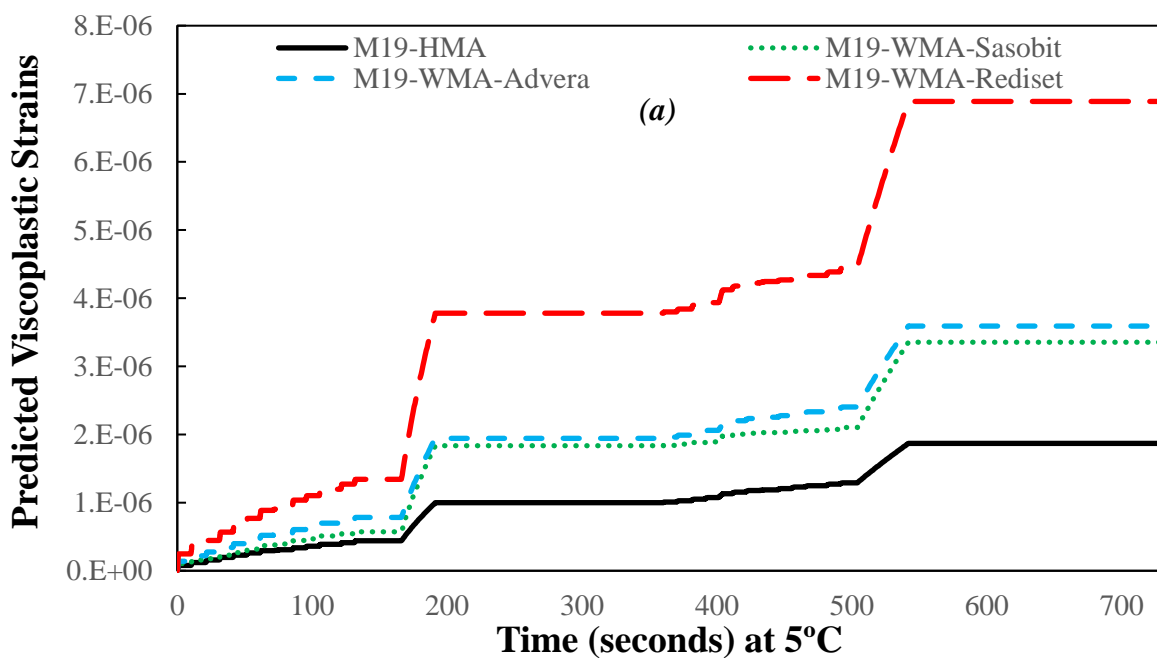


Figure 30. Predicted viscoelastic strain for the different HMA and WMA U25 mixes in response to the investigated random stress profile at a temperature of a) 5°C and b) 35°C.

Since the response of asphalt concrete includes a viscoplastic component, the latter is predicted in response to the investigated stress profile at both temperatures of 5°C and 35°C. It is apriority known that at 5°C the viscoelastic strain will be dominant and thus a little proportion of the total strain will be due to viscoplasticity slow rate of loading for the application of the load for a long period of time. The viscoplastic strains are predicted for M19 and U25 mixes as shown in Figure 31 and Figure 32, respectively. In general, it can be concluded that the use of Advera and Sasobit as WMA additives increases the viscoplastic

strains of asphalt concrete mixes regardless of the type of binder and temperature. For Rediset, the same can be observed in all cases expect the case of using it with a modified binder at a high temperature of 35°C.

For the case of modified binder, at 5°C, the waxy component of Sasobit might be stiff enough unlike the case of 35°C where it might softens adding another factor for softening the binder and triggering higher deformations presented by increased viscoplastic strains. This results in a viscoplastic strain at 35°C higher than that of case of Advera which ends up in the mix as a filler than could resist the deformation of the binder. Similar results could be obtained for Sasobit and Advera for the case of unmodified binder at 35°C. However, the effect of Sasobit in increasing the accumulated viscoplastic strain for mixes with unmodified binder appears significantly at 5°C unlike the case of modified binder. This could be attributed to the fact the for mixes with modified binder, the properties of the binder are dominant over Sasobit especially at low temperatures but it is not the case when having unmodified binder. For each category of mixes, it can be observed that the effect of Sasobit with respect to other mixes of the category differs whether the predicted strain is viscoelastic or viscoplastic. For example, taking the case of M19-WMA-Sasobit at 35°C shows that it has a lower predicted viscoelastic strain but a higher viscoplastic strain as compared to the control M19-HMA. Therefore, it can be concluded that the use of WMA additives with both unmodified and modified binder will have a negative effect on the mix's resistance to deformation in compression state where it is almost expected to have higher predicted viscoplastic strains.



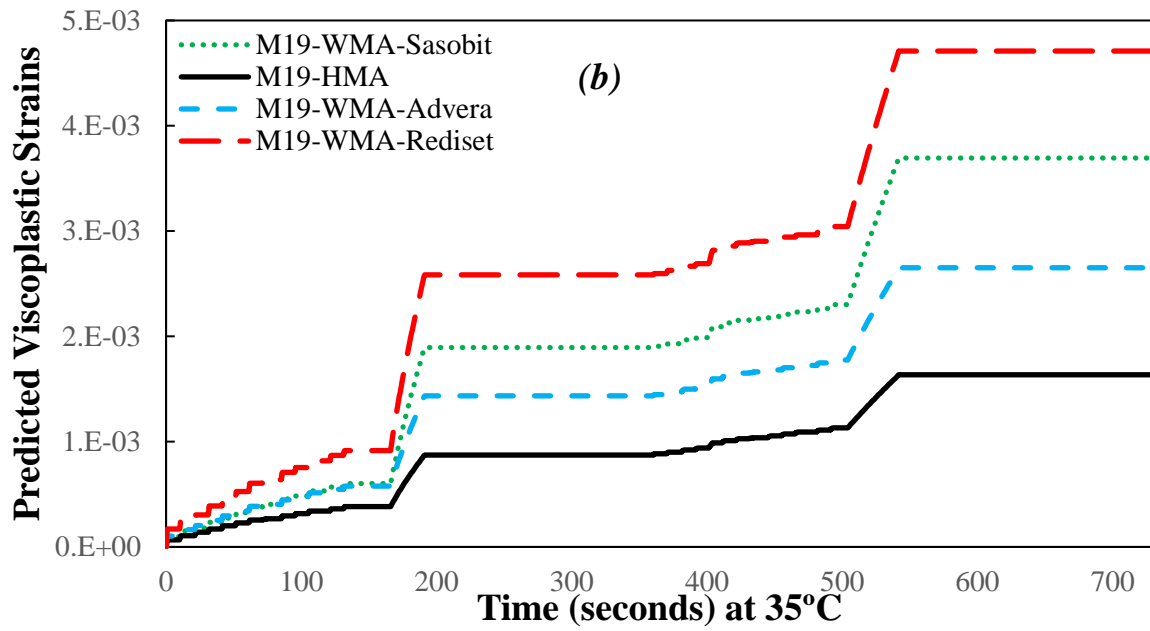
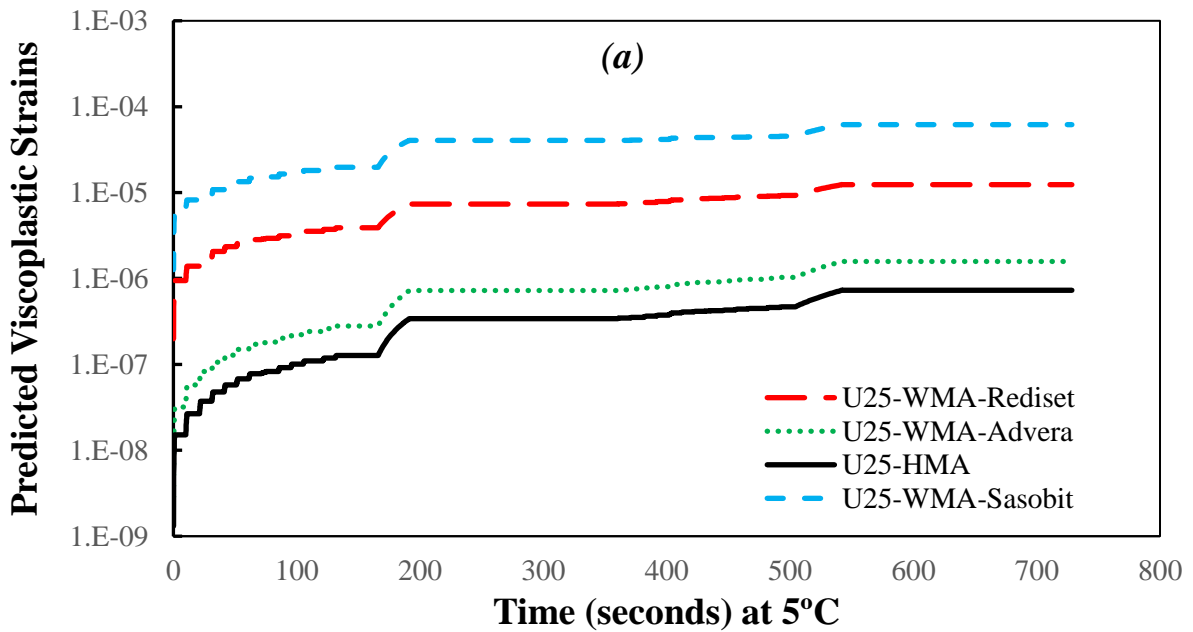


Figure 31. Predicted viscoplastic strains for the different HMA and WMA M19 mixes in response to the investigated random stress profile at a temperature of a) 5°C and b) 35°C.



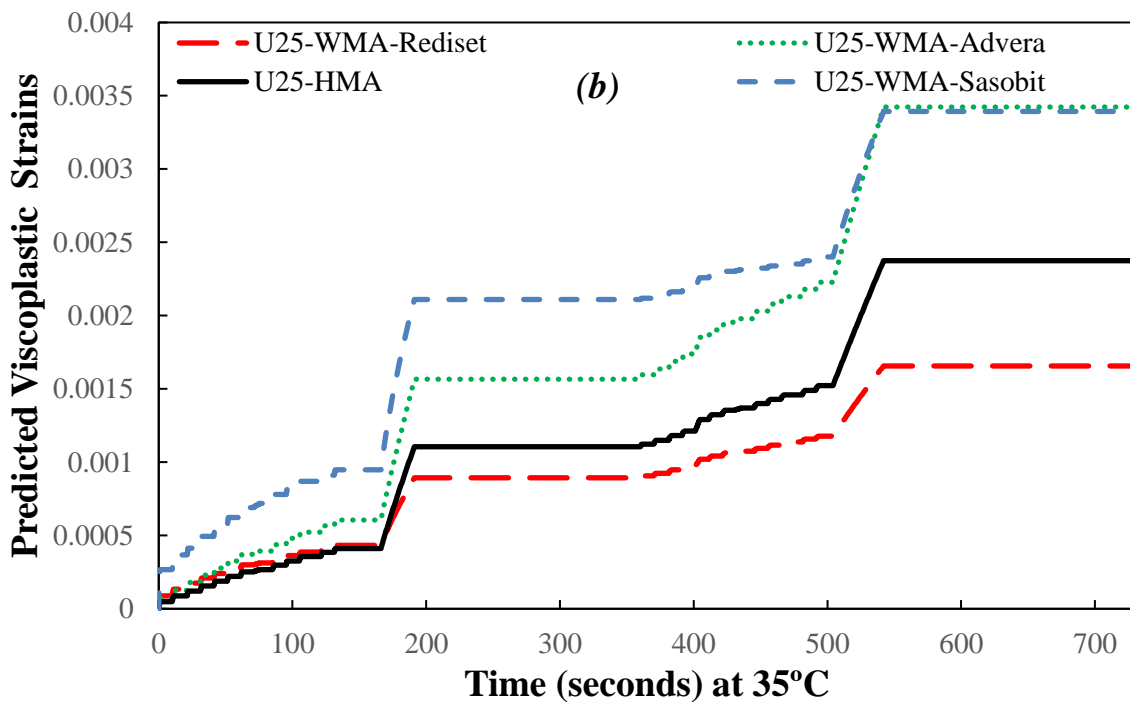


Figure 32. Predicted viscoplastic strains for the different HMA and WMA U25 mixes in response to the investigated random stress profile at a temperature of a) 5°C and b) 35°C.

It is worth noting that for the case of predicted viscoelastic strains, mixes with unmodified binder possess in generally higher strain levels than mixes with modified binders. However, in the case of predicting viscoplastic strains, mixes with both modified and unmodified binder are of the same level of magnitudes. This is basically due to the fact that the used PG76-22 binder is modified with SBS which is an elastomer enhancing the elastic recovery of the asphalt.

As a result of the predicted viscoelastic and viscoplastic strains for the case of every mix at 5°C and 35°C, the total strain in response to the investigated stress profile is determined as the sum of these two components that are already predicted. The total strains are plotted in Figure 33 for the M19 mixes. For the mixes of M19, WMA additives generally leads to an increase in the predicted total strains as compared to the control HMA mix. At low temperature of 5°C, the net effect of Sasobit is null where the strains are the same as that of M19-HMA. The final results show that Rediset leads to the most increase in the predicted total strains when compared to the control HMA at mix. The difference between the total strain of the WMA mixes and HMA becomes larger as the temperature increases. At high temperature, Advera shows the most favorable deformations in compression state among the other WMA additives. At the end of the considered analysis period, the percentage of the viscoplastic strain from the total strain for the stress profile at 35°C is about 85% for M19-HMA, M19-WMA-Rediset, and M19-WMA-Advera and about 92% for the M19-WMA-

Sasobit which shows that although the wax increases stiffness in terms of $|E^*|$ but it have a negative impact on increasing permanent deformation in asphalt mixes when subjected to compression loading.

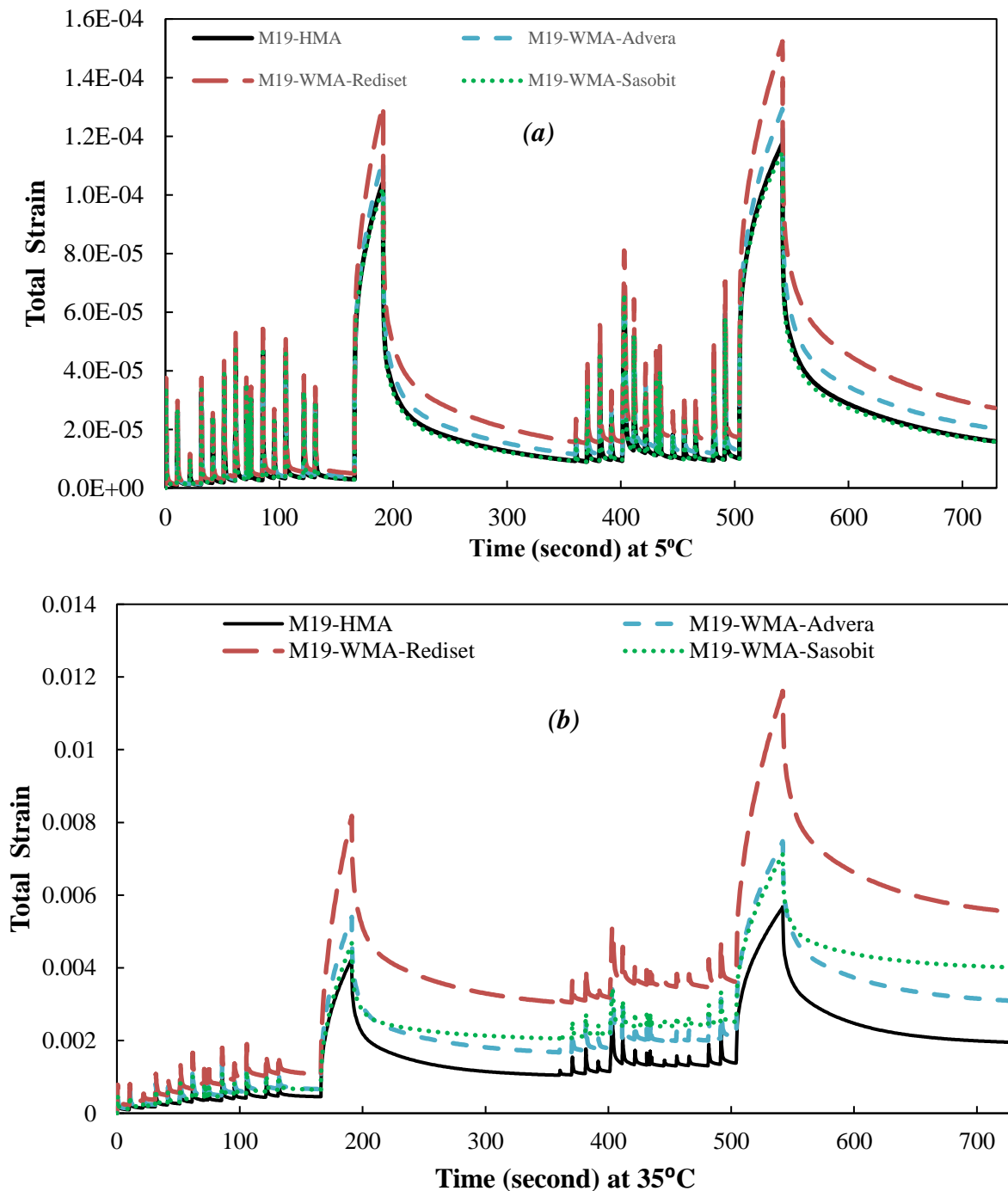
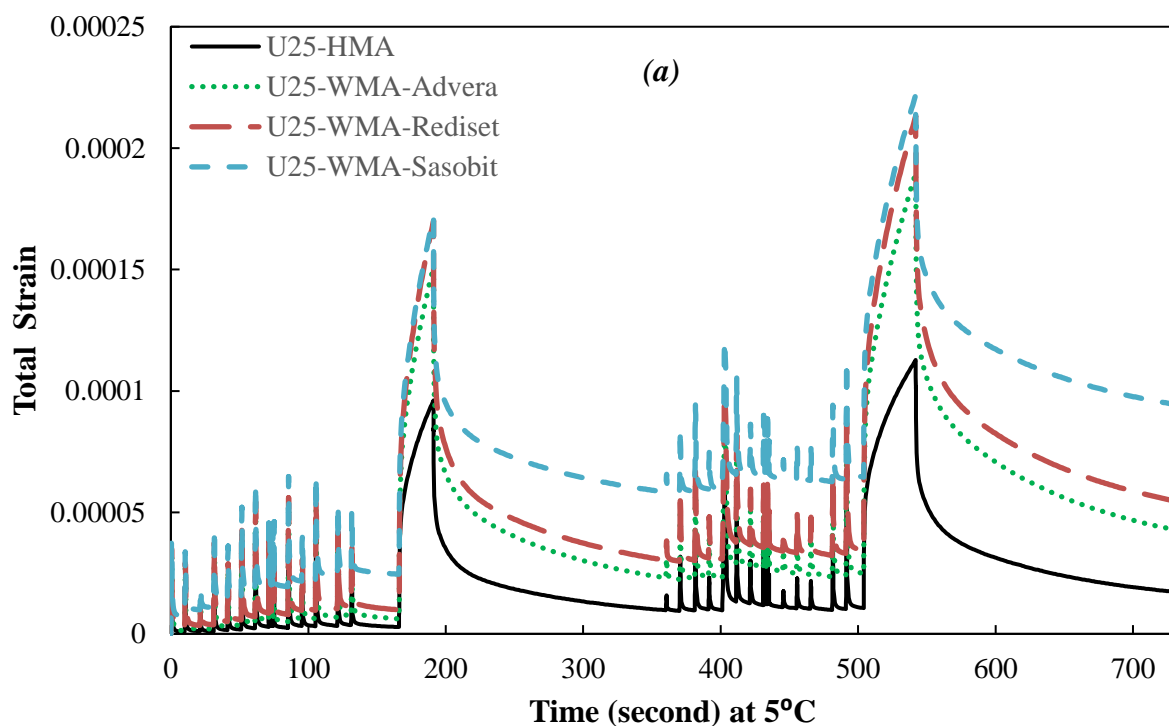


Figure 33. Predicted total (viscoelastic + viscoplastic) strains for the different HMA and WMA M19 mixes in response to the investigated random stress profile at a temperature of a) 5°C and b) 35°C.

Similar to the case of M19 mix, the total strain is determined in response to the investigated stress profile for the U25 mixes as presented in Figure 34. Unlike the case of the M19 mixes, the effect of WMA additive is more significant at 5°C compared to the predictions at 35°C where all additive lead to an increase in the predicted total strain. At 5C,

the total strain of all WMA mixes is higher than that of the control HMA mix with the highest strain predicted for U25-WMA-Sasobit and the least for U25-WMA-Advera. However, at 35°C, U25-WMA-Rediset shows a total strain lower than that of the control HMA mix but Advera and Sasobit yields a total strain that is about 30% higher than that of the control mix. The fact the Rediset yields a lower total strain might be attributed to the fact that its optimum asphalt content is lower than that of the control mix by 0.1% (3.5% for U25-WMA-Rediset vs. 3.6% for U25-HMA).

Based on the viscoelastic and viscoplastic strain predictions, it can be concluded that the effect of WMA additive is dependent on both temperature/loading rate/loading duration and the type of binder with which it is used. In general, WMA additives reduces the mixes resistance to deformation in compression state and this could be due to the fact that they are subjected to less aging and that the additives are able to alter the properties of the binder which leads to the observed differences in the total strain predictions between one mix and the other.



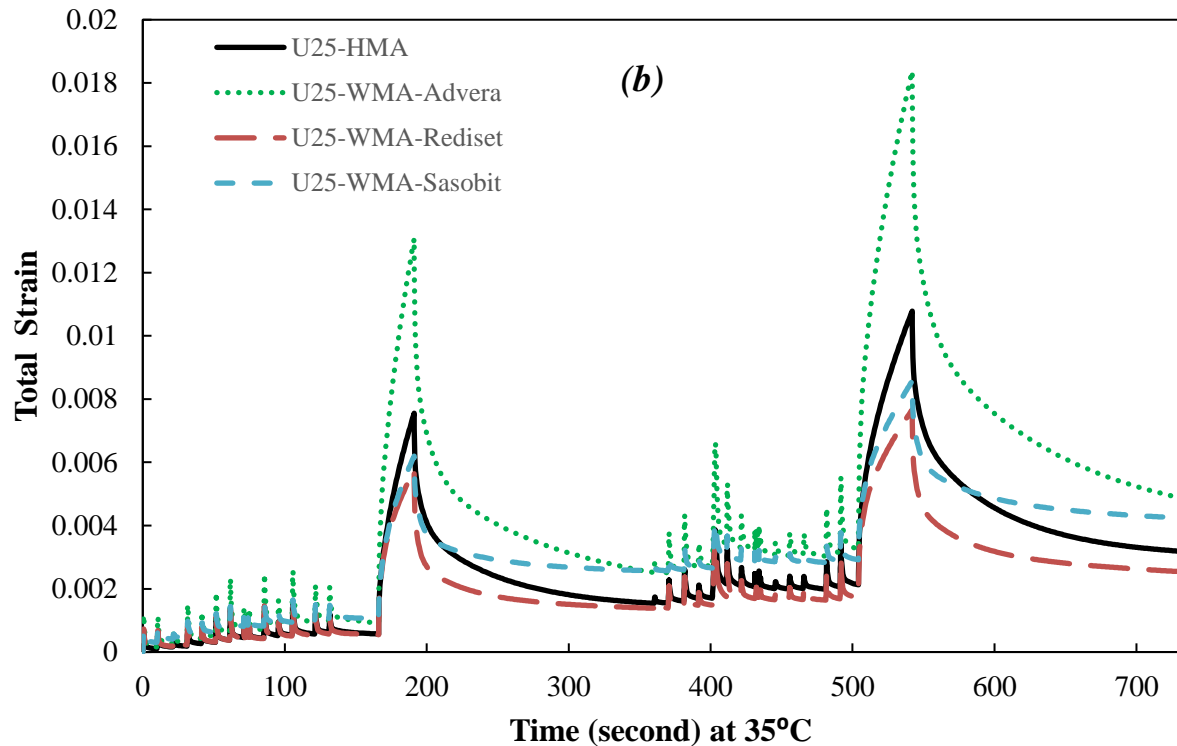


Figure 34. Predicted total (viscoelastic + viscoplastic) strains for the different HMA and WMA U25 mixes in response to the investigated random stress profile at a temperature of a) 5°C and b) 35°C.

5.5 Assessing Effect of Fibers on $|E^*|$ of HMA and WMA

For the category of mixes with unmodified binder and 19.0 mm aggregate gradation referred to as U19 mixes, $|E^*|$, $E(t)$, and $D(t)$ mastercurves are constructed and fitted at a reference temperature of 25°C for each replicate similar to the case of the mixes of categories M19 and U25. The average $|E^*|$ mastercurves and shift factors for the HMA and WMA mixes with and without fibers are presented in Figure 35 and Figure 36, respectively. For these mixes, WMA has a higher $|E^*|$ at low reduced frequencies smaller than 0.01 Hz. This implies that using wax-based WMA additive improves the stiffness of the asphalt mixes at conditions of high temperature and/or slow speeds. For higher reduced frequencies, the WMA has almost the same $|E^*|$ mastercurve as that of the corresponding HMA mix except for a slight decrease of $|E^*|$ at high reduced frequencies similar to the effect of Sasobit with mixes of categories U25 and M19.

The addition of fibers shows that it has an effect on $|E^*|$ which is measured in compression. For HMA mix, the addition of fibers yields a mix that is less stiff especially at low reduced frequencies. In the case of WMA with fibers, $|E^*|$ is decreased at high reduced frequencies as compared to both the corresponding HMA and WMA mix (without fibers). Also, the addition of fibers to WMA causes an increase in $|E^*|$ at low reduced frequencies.

These results show that using aramid and polypropylene fibers with wax-based WMA additive improves the AC mix which might yield a better resistance to both rutting and fatigue cracking. The effect of wax in reducing the viscosity of the binder at the mixing temperature helps in ensuring more dispersion of the fibers within the binder as compared to the case of HMA. This might be a factor which helps in avoiding any possible clumping of fiber that could occur in the case of HMA. Thus, the role of fibers in enhancing the properties of AC is made more efficient in the presence of wax.

For the time-temperature shift factors, only the WMA mix with fibers exhibits a slight reduction in their magnitude at low temperatures. It is worth mentioning that the mixes with fibers show a high variability between the three replicates. Thus, a fourth was tested to better represent the properties of those mixes.

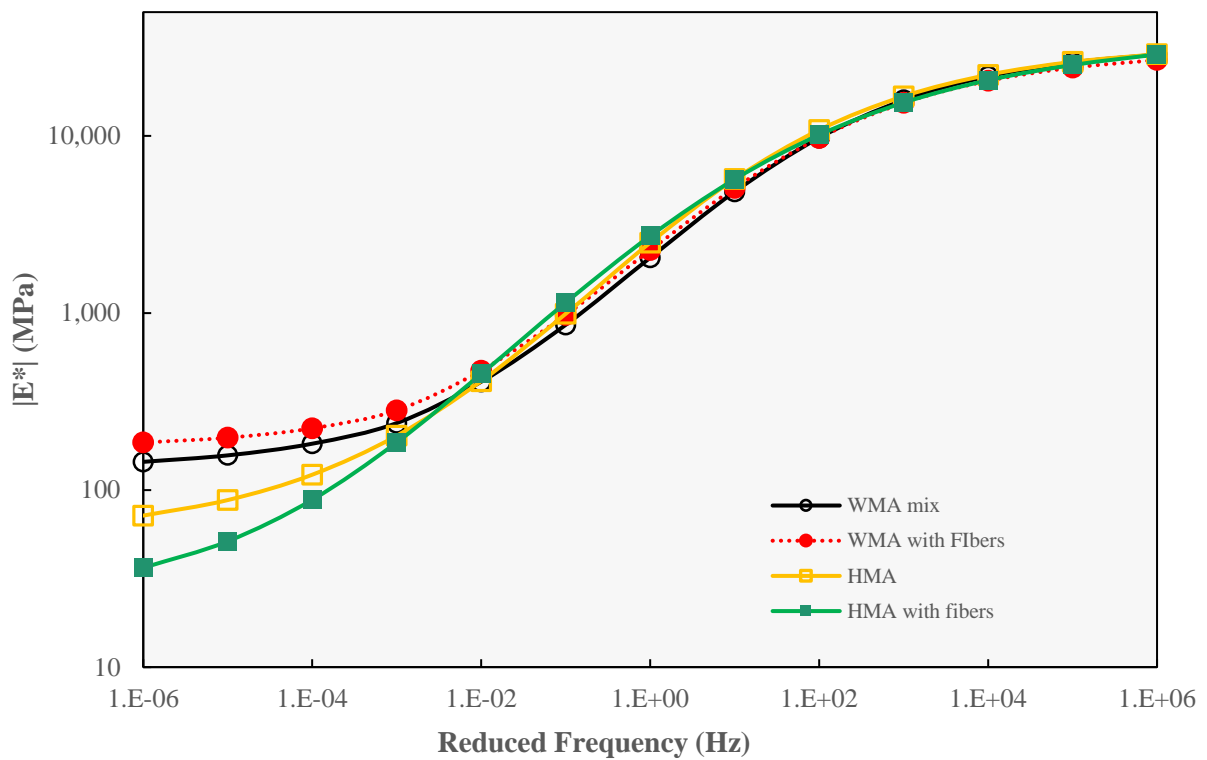


Figure 35. Average $|E^*|$ mastercurves for control and fiber-reinforced mixes with unmodified binder and a 19.0 mm aggregate gradation at a reference temperature of 25°C.

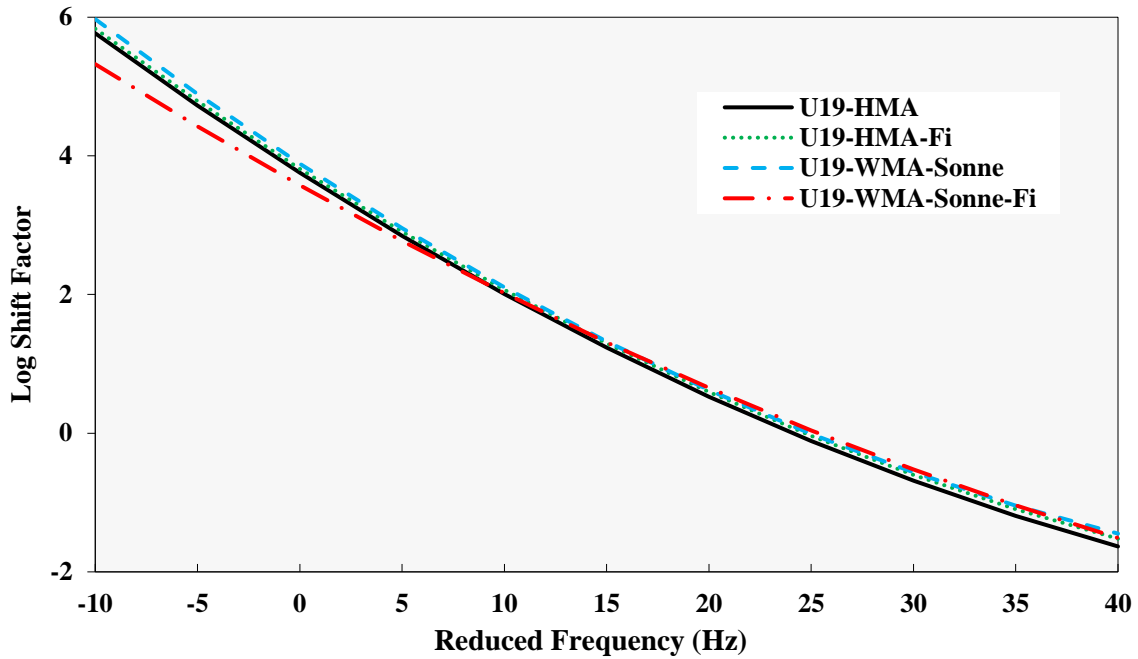


Figure 36. Time-Temperature shift factor for HMA and WMA mixes with unmodified binder and a 19.0 mm aggregate gradation as used to construct the mastercurves of different LVE functions.

In addition, the E^* data is converted for each replicate using both Exact and Approximate methods to determine the $E(t)$ mastercurves of each of these four mixes. Then, the data is converted to determine $D(t)$ using the Approximate method as explained earlier. The $D(t)$ and $E(t)$ plotted at 5°C in Figure 37 and Figure 38 will be used for the development of the viscoelastoplastic models of these mixes.

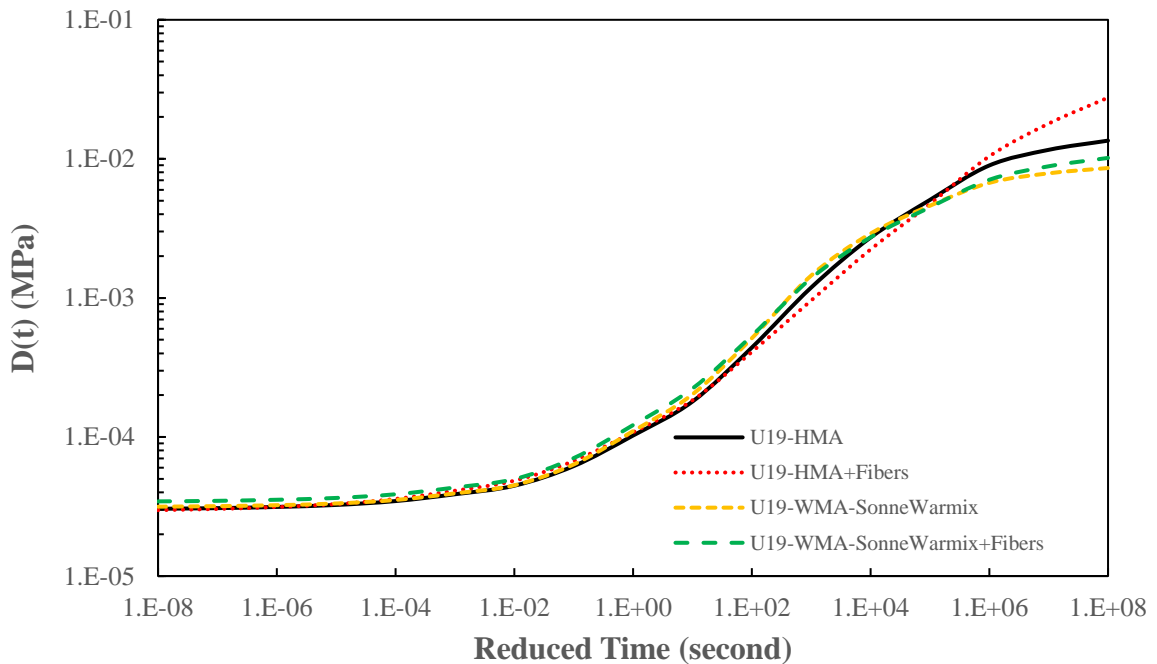


Figure 37. $D(t)$ calculated by the Approximate method for HMA and WMA U19 mixes with and without fibers at a reference temperature of 5°C .

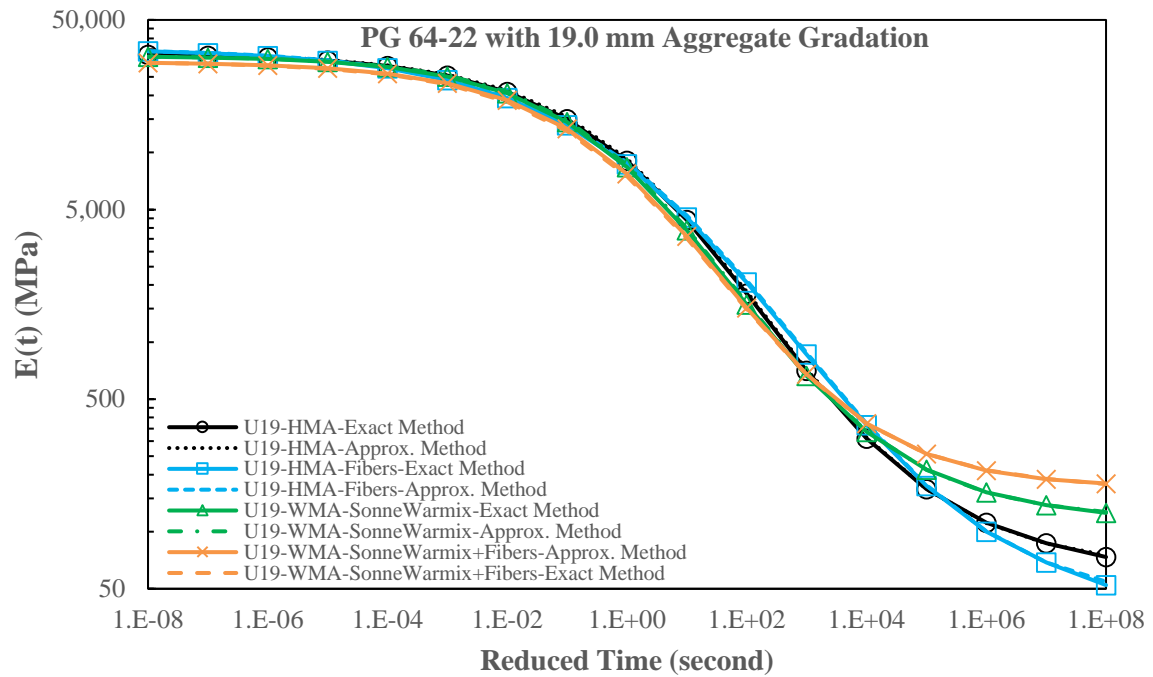


Figure 38. $E(t)$ calculated by the Approximate and Exact methods for HMA and WMA U19 mixes with and without fibers at a reference temperature of 5°C.

For each of the mixes, the conducted constant crosshead tests at 5°C yield C vs S curves collapsed perfectly on top of each other indicating the absence of viscoplasticity. Thus, the viscoelastic model for all mixes was developed based on the outputs of tests conducted at 5°C and rates of 0.0001 strain/sec and 0.00005 strain/sec. For each mix, the third replicate tested at 0.000025 strain/sec was used for validation. The results showed that the developed models are accurate where the predicted viscoelastic strains fit perfectly with the measured-on-specimen strains. The viscoelastic model was developed for the four different mixes under study. This shows that the proposed viscoelastic modeling is valid for WMA as for HMA, and for both mixes with and without fibers. However, the fitting parameters of the C vs. S curves and S vs. Lebesgue norm of stress vary from one mix to another, as presented in Table 16, showing the model’s sensitivity to WMA as well as HMA mixes.

In order to compare the viscoelastic behavior of the investigated HMA and WMA mixes, the C vs S plotted in Figure 39 are investigated. Considering a drop of C from 1 to 0.5 as a failure criteria, it can be concluded that WMA with the SonneWarmix has a better damage behavior than HMA. In addition, incorporating fibers with the WMA mix further improves the mix’s damage behavior. This is not the case with the addition of fibers to the HMA mix which indicates that the stiffening effect of the fibers within WMA might be due to certain interactions between the wax additive and the used synthetic fibers upon their blending.

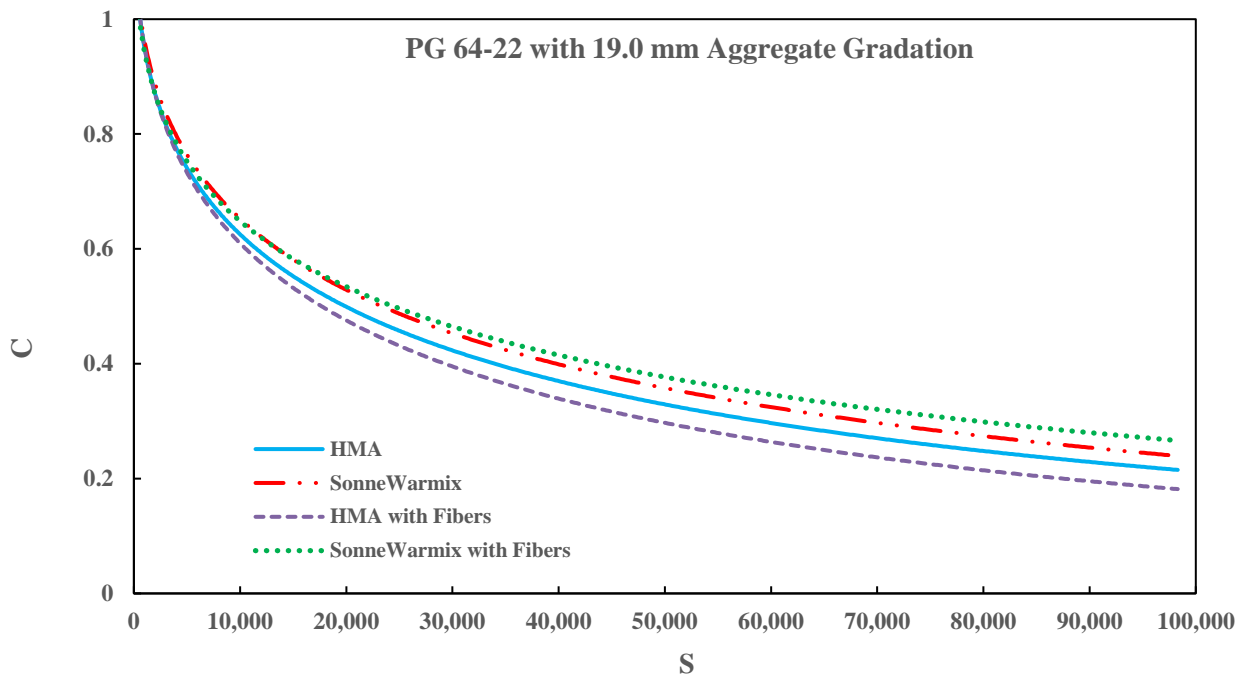


Figure 39. Damage characteristic curves of U19 mixes with and without fibers.

Further and more realistic assessment based on predicted response for a given loading history is conducted, taking into account both the linear viscoelastic properties and damage characteristics. To meet this purpose, a loading history consisting of 100 creep and recovery cycles was considered with a loading and rest period of 0.1 and 0.9 sec, respectively, applied stress of 600 kPa, at a temperature of 35°C. The calibrated viscoelastic model characterizing each mix was used along with the time-temperature shift factors to predict the viscoelastic strain response for the applied stress history. The mixes were ranked based on the calculated viscoelastic strain as shown in Table 19. This strain can be considered nonlinear viscoelastic (long-term recoverable and non-recoverable) strain representing both strain development and recovery properties of HMA and WMA. The WMA shows a better performance than the corresponding HMA mixes. This is further improved upon addition of fibers to WMA mix showing the most favorable performance as compared to the control HMA mix and the WMA mix. Therefore, a wax-based additive and a mix of aramid and polyolefin fibers improves the mechanical properties of AC mixes by possessing a better resistance to deformation due to compressive loading. This improvement might be due to several factors that may include the stiffening of the binder due to wax-based additives and the resistance to microcracking that might be induced by the use of fibers.

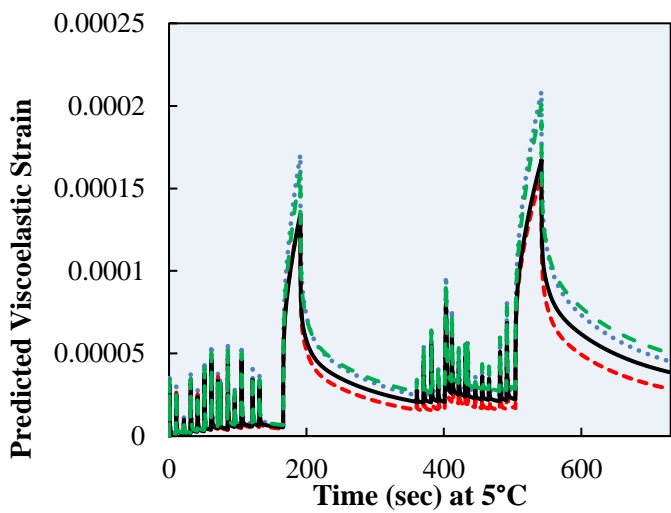
Table 19. Predicted Viscoelastic Strains for U19 mixes at 35C after 100 creep and recovery cycles.

Mix Description		Viscoelastic Strains after 100 Creep and Recovery Cycles	Ranking Within Category
PG64-22, 19mm	HMA	5.98E-04	3
	WMA-SonneWarmix	4.11E-04	2
	HMA with Fibers	6.82E-04	4
	WMA-SonneWarmix with Fibers	3.79E-04	1

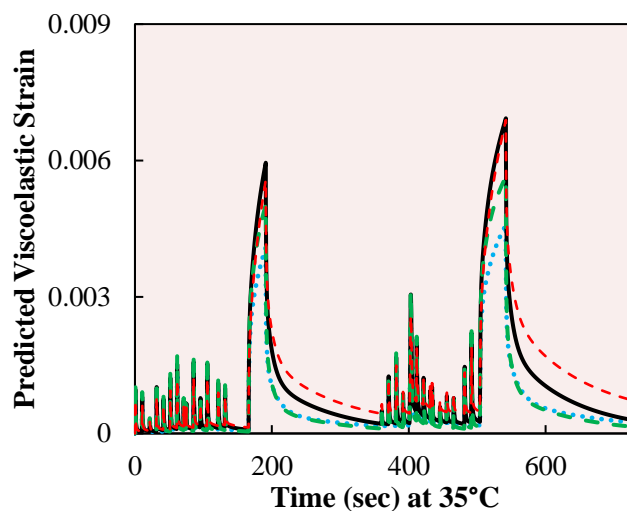
Further, both viscoelastic and viscoplastic strains are simulated for each of the mixtures U19-HMA, U19-HMA-Fi, U19-WMA-SonneWarmix, and U19-WMA-SonneWarmix-Fi using the developed models presented earlier. For each mixture, the components strains are predicted separately and added to constitute the total strain, as presented in Figure 40. The results show that the effect of fibers on the performance of AC in the compression state is dependent on the mode of loading (loading vs. rest period), temperature, and type of behavior (viscoelastic vs. viscoplastic). In regions with dominance of viscoelastic response; i.e., 5°C, U19-WMA-SonneWarmix exhibits higher strain levels in both loading and unloading regimes as compared to the control HMA mix. However, this is not the case at 35°C, where the viscoelastic strain is observed to be lower in both loading and unloading regimes for the U19-WMA-SonneWarmix as compared to the control U19-HMA. The addition of fibers shows no effect on the performance of HMA and WMA mixes in the loading region at 5°C; however, the fibers impose a faster recovery of the viscoelastic strains during rest periods. The effect of fibers is more favorable at 35°C, where WMA yields lower strain levels during loading. The U19-WMA-Fi yields smallest viscoelastic strains at high temperatures. The fibers appear to be more effective with the WMA mix possibly due to the role of the wax in reducing the viscosity of the binder allowing the fibers to be spatially spread within AC without being prone to clumping.

Focusing on viscoplastic response, the wax-based WMA additive yields higher viscoplastic strain compared to that of the control U19-HMA at both 5°C and 35°C. The difference between the viscoplastic strain of the U19-WMA-SonneWarmix and U19-HMA increases as the level of damage becomes larger. The addition of fibers reduces the viscoplastic strain for the cases of both U19-HMA and U19-WMA-SonneWarmix at cold temperature of 5°C. Similar results are obtained for the case of the higher temperature of 35°C except for the case of U19-WMA-SonneWarmix-Fi as the level of damage increases

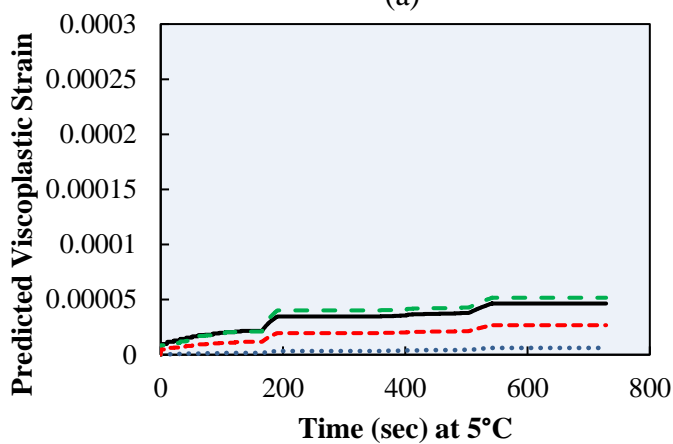
where the effect of the wax-based additive in increasing the viscoplastic strain outweighs the effect of fibers in resisting it. Based on the total predicted strains, fibers improve the performance in terms of the predicted strains in response to a given stress input. This effect is more significant and favorable in cases where viscoelasticity is dominant as shown in Figure 40-e. At conditions of high temperature, fibers show a favorable effect in reducing deformation especially in the loading region when used with a wax-based WMA additive; this implies lower levels of damage which can extend the life of AC pavements. Such effects can not be shown by only comparing single material properties such as $|E^*|$ and/or damage characteristic curves alone. Hence, a combined mechanistic material characterization and mechanistic performance prediction is valuable for the realistic and accurate assessment of new technologies in the industry of asphalt paving.



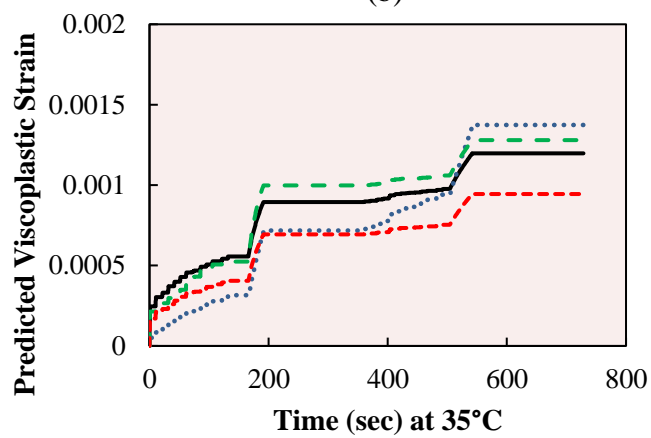
(a)



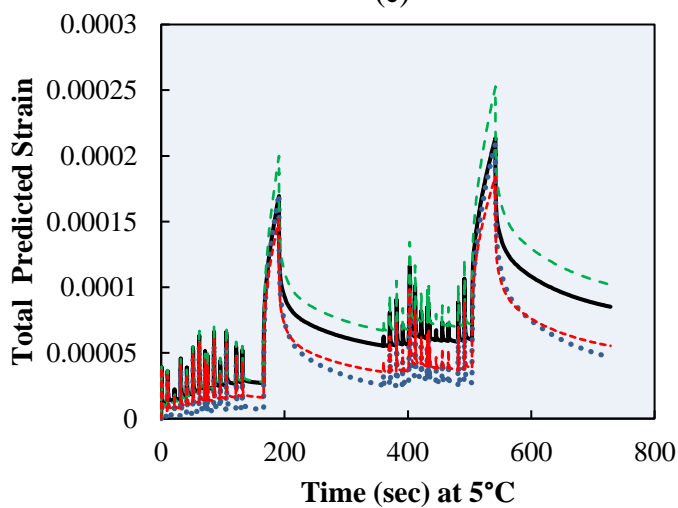
(b)



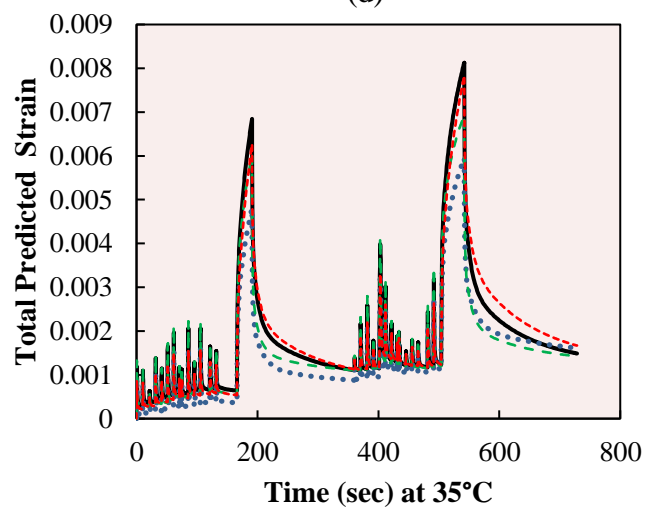
(c)



(d)



(e)



(f)

— U19-HMA U19-WMA-Fi - - - U19-WMA - - - U19-HMA-Fi

Figure 40. Predicted viscoelastic, viscoplastic, and total strains in response to random stress profile at 5°C and 35°C.

5.6 Conclusions and Recommendations

1. The viscoelastic and viscoplastic continuum damage models used for characterization of HMA mixes are applicable for WMA mixes.
2. At a time that LVE properties and damage characteristic curves can be used to assess different types of mixes, the realistic and accurate comparison of different mixes requires the use of all these measured and develop material properties in the prediction of the response of each of the mixes to a given stress profile.
3. The effect of WMA additives on the mechanical properties of asphalt mixes in compression state is dependent on the type of binder used (i.e. unmodified vs. polymer modified binder) and the temperature considered in the analysis.
4. Based on the developed viscoelastoplastic models, the different WMA additives show a light effect on the predicted strains compared to control HMA mixes when used with modified binder at a low temperature of 5°C and with unmodified binder at 35°C.
5. The predicted total strain is significantly higher than control mixes for various types of WMA additives used with modified asphalt binder at high temperature of 35°C and with unmodified asphalt binder a low temperature of 5°C.
6. At time the wax based additive Sasobit shows minimal effect on the performance of asphalt concrete in compression when assessed based on the viscoelastic model, it induced high viscoplastic strains compared to that of the control HMA mixes.
7. Compared to other WMA additives and based on viscoelastoplastic models, Advera shows the most favourable results when used with modified binder; however, the performance of mixes with Sasobit and Rediset is more favourable for the case of unmodified binder.
8. For the materials used in the Arabian Gulf region, it is recommended to use WMA mixes without any change in the asphalt content. The mixing and compaction temperature can be reduced constantly among all contractors by 20°C and 35°C for modified and un-modified binders, respectively.
9. Based on predictions from the develop viscoelastoplastic models, fibers improve the performance in terms of the predicted strains in response to a given stress profile.

10. The effect adding aramid and polypropylene fibers provides an improvement to the mixes' performance in the compression state when used with a wax based WMA additive.
11. The improvement of the performance of mix due to the introduction of aramid and polypropylene fibers with SonneWarmix has to be further investigated and validated among the other WMA additives in study.

CHAPTER 6

MODELING OF THE INHERENT UNCERTAINTY IN THE COMPONENTS OF THE VECD MODEL

6.1 Introduction

The modeling of the inherent uncertainties associated with the components of the VECD model is done on a component basis. This includes modeling the inherent uncertainty of the different material properties that are involved in the prediction of the viscoelastic strain. Basically, the uncertainties to be modeled address the variabilities and errors associated with the properties achieved from the complex modulus and the constant crosshead rate testing. The uncertainty of the E^* is propagated into $|E^*|$, E' , $E(t)$, and $D(t)$. In addition, the uncertainty associated with crosshead testing is propagated through the prediction of stiffness due to any stress profile input which is basically through the models of C vs S and S vs. Lebesgue Norm of stress. Further, these uncertainties are jointly taken into consideration and propagated into the prediction models of the viscoelastic strains at different conditions of input stress profiles and temperatures.

6.2 Experimental Program

The modeling of the viscoelastoplastic behavior of asphalt concrete requires experimental data obtained from two different tests: E^* and monotonic testing. As shown in Figure 41, the inherent variability determined from E^* testing is propagated through $E(t)$ and $D(t)$ that serves as key parameters for the calculation of the viscoelastic strains. In addition, $E(t)$ data is used to calculate the slope of this curve in its linear portion as it is a key parameter for the calculation of the damage parameter S . The monotonic testing is required to determine the damage characteristic properties (C vs S curve) of asphalt concrete. Therefore, after quantifying the inherent variabilities in $E(t)$ and $D(t)$ from E^* testing, other samples are required to be tested in order to model the probabilistic distribution of the parameters presenting the C vs. S and S vs. Lebesgue Norm of Stress ($LS(\text{stress})$) curves. As a result, the inherent variabilities in $D(t)$ and $C(LS(\text{stress}))$ (which is jointly $C(S)$ and $S(LS(\text{stress}))$) is modeled and thus forward propagated through the convolution integral to yield a probabilistic viscoelastic strain prediction model.

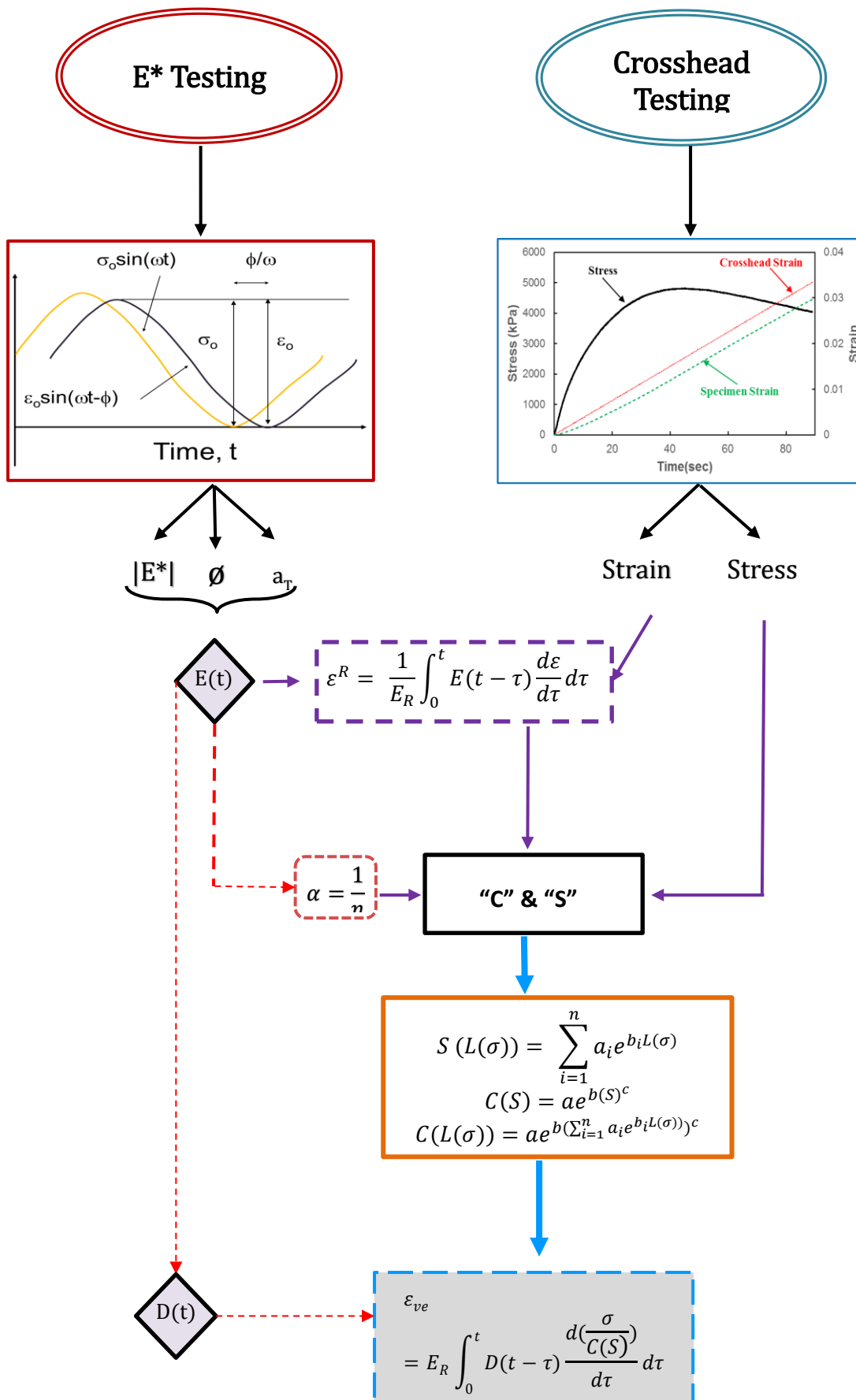


Figure 41. Schematic showing material testing and properties required for VECD and P-VECD modeling.

For achieving this purpose, four mixes from those designed in the previous tasks of the research as summarized in Table 5 are selected for a full probabilistic investigation. The inherent uncertainty is quantified and modeled for every single material property and thus propagated forward to yield probabilistic VECD model for each mix. The mixes selected for this purpose are presented in Table 20. These mixes are selected to show whether the binder type (unmodified vs polymer-modified binders), use of WMA additives, and aggregate gradation (mainly NMAS) influence the inherent variability in the material measured properties or not.

Table 20. Asphalt concrete mixes selected for probabilistic analysis.

Asphalt Concrete Mix Type	Assessed Factor
U19-HMA	-
M19-HMA	Modified Binder
U19-WMA-SonneWarmix	WMA additive
U25-HMA	Aggregate NMAS

For each mix, E^* samples are prepared and tested to have a total of ten replicates for each mix. These samples are prepared and tested following the same protocols used for testing the first three replicates that are used in the typical deterministic characterization as presented earlier. For each replicate, E^* data is used to determine $E(t)$ and $D(t)$ which are required for VECD modeling. Thus, a probabilistic analysis is conducted to quantify the inherent uncertainty of these response functions through the Prony coefficients defining each of them. Like the case of E^* , constant crosshead rate compression tests are conducted at 5°C and fast loading rates so that the total number of samples of this test is at least ten for each mix as presented in Table 21. In this case, the samples can be tested at different rates but the same temperature under the condition that the behavior is purely viscoelastic. The number of replicates is selected as a practical lower bound to the number of tests that would allow for meaningful statistical analyses to be conducted.

Table 21. Testing conditions for probabilistic analysis of VECD model.

	Linear Viscoelastic Characterization	Viscoelastic Model
Test	Complex Modulus in Compression mode	Constant Crosshead Rate Compression Test
Temperature	-5, 10, 25, and 40°C	5°C
Testing Rate	20, 10, 5, 1, 0.5, 0.1, and 0.01 Hz (10 replicates for each mix)	0.0001 strain/sec, (4 replicates for each mix) 0.00005 strain/sec, (4 replicates for each mix) and 0.000025 strain/sec. (3 replicates for each mix)
Total Number of Replicates Per Mix	10	11

6.3 Probabilistic Modeling Methodology

6.3.1 First Order Approximation

First order approximation has been used for decades as a tool for reliability analysis where it transforms the problem in hand into an approximate optimization problem (Tang and Ang 2007). The expected value of a function of many random variables is called a mathematical expectation. For $Y = g(X_1, X_2, \dots, X_n)$, the mathematical expectation is given by Equation 75 which can be used in order to derive the moments of Y.

$$E(Y) = \int_{-\infty}^{\infty} \dots \int_{-\infty}^{\infty} g(X_1, X_2, \dots, X_n) f_{X_1, X_2, \dots, X_n}(X_1, X_2, \dots, X_n) dX_1 dX_2 \dots dX_n$$

Equation 75

The function $g(X_1, X_2, \dots, X_n)$ is expanded in a Taylor series about the mean values $(\mu_{X_1}, \mu_{X_2}, \dots, \mu_{X_n})$ to obtain the approximate mean and variance of Y. This will yield Equation 76 which can be truncated at its linear terms given an approximation of Y as given in Equation 77.

$$Y = g(\mu_{X_1}, \mu_{X_2}, \dots, \mu_{X_n}) + \sum_{i=1}^n (X_i - \mu_{X_i}) \frac{\partial g}{\partial X_i} + \frac{1}{2} \sum_{i=1}^n \sum_{j=1}^n (X_i - \mu_{X_i})(X_j - \mu_{X_j}) \frac{\partial^2 g}{\partial X_i \partial X_j}$$

Equation 76

$$Y \cong g(\mu_{X_1}, \mu_{X_2}, \dots, \mu_{X_n}) + \sum_{i=1}^n (X_i - \mu_{X_i}) \frac{\partial g}{\partial X_i} \quad \text{Equation 77}$$

The first-order mean and variance of Y are reduced as shown in Equation 78 and Equation 79, respectively.

$$E(Y) \cong g(\mu_{X_1}, \mu_{X_2}, \dots, \mu_{X_n}) \quad \text{Equation 78}$$

$$Var(Y) \cong \sum_{i=1}^n \sigma_{X_i} \left(\frac{\partial g}{\partial X_i} \right)^2 + \sum_{i,j=1}^n \sum_{i \neq j} \rho_{ij} \sigma_{X_i} \sigma_{X_j} \frac{\partial g}{\partial X_i} \frac{\partial g}{\partial X_j} \quad \text{Equation 79}$$

where all derivatives are evaluated at $\mu_{X_1}, \mu_{X_2}, \dots, \mu_{X_n}$

This can be simplified by solving the relationship:

$$C_Y = AC_xA^T \quad \text{Equation 80}$$

where:

- C_x : Covariance matrix of X_i s where $C_{xij} = \rho_{ij}\sigma_{X_i}\sigma_{X_j}$
- C_Y : Covariance of $Y = \text{Variance of } Y$
- $A = \left[\frac{\partial g}{\partial X_1} \quad \frac{\partial g}{\partial X_2} \quad \dots \quad \frac{\partial g}{\partial X_n} \right]$ Evaluated at $\mu_{X_1}, \mu_{X_2}, \dots, \mu_{X_n}$
- ρ_{ij} : Correlation coefficient =
$$\frac{n(\sum x_i x_j) - (\sum x_i)(\sum x_j)}{\sqrt{[n \sum x_i^2 - (\sum x_i)^2][n \sum x_j^2 - (\sum x_j)^2]}}$$

6.3.2 Monte Carlo Simulations

The first order estimates of the mean and COVs of the response variable could suffer from inaccuracies especially in the case of problems with a highly nonlinear mathematical form such as the case of sigmoidal functions (Ching 2011, Kahil et al. 2015). In addition, the first order approximation does not provide any feedback regarding the mathematical form of the probability distribution of the response of interest which is a necessity for conducting a reliability-based analysis. To cater for the above limitation, a robust statistical analysis that is based on Monte Carlo simulations is conducted to provide more realistic estimates of the mean, COV, and probability distribution of the response and to check the accuracy of the results of the First Order Approximation.

The Monte Carlo method is a simulation technique that relies on computational algorithms to model the probabilities of different outcomes depending on the intervention of different random variables. It allows the generation of quantitative results based on results of previous tests without further conducting any physical testing (Nowak and Collins 2012). The information on probability distributions of the parameters in hand is used to generate large samples of numerical data. This method provides an edge where it can be applied to complex problems with extremely difficult closed-form solutions such as probabilistic problems with complicated non-linear models. Further, it yields realistic solutions without the need for simplified assumptions. Monte Carlo simulations can reproduce random variables while preserving their specified probabilistic distributions and correlation relationships (Chang et al. 1994).

For a given problem to be simulated by Monte Carlo, the response of interest Y (e.g. $|E^*|$, $E'(w)$, $E(t)$, $D(t)$, $C(S)$, $S(\text{Leb}(\text{stress}))\dots$) is presented by:

$$Y = g(\vec{X}) \quad \text{Equation 81}$$

where: $\vec{X} = [X_1, X_2, \dots, X_n]$ is the vector of input variables (e.g. α , γ , β , and δ for $|E^*|$ and $E'(w)$ and Prony Coefficients for $E(t)$ and $D(t)$).

An estimate of the cumulative distribution function for Y which is equal to $P(Y < y)$ can be obtained by simulating N realizations, and then counting the number of realizations (n) that give $g(\vec{x}_k) \leq y$:

$$F_y(Y) \approx \frac{n}{N}$$

Also, the moments of Y can be estimated where the mean of Y ($E(Y)$) is calculated by simulating “ Equation 81” N times, and taking the average of Y .

The, the second moment of Y is calculated as:

$$\text{VAR}(Y) \approx \frac{1}{N-1} \sum_{k=1}^N (g(\vec{x}_k) - E(Y))^2 \quad \text{Equation 82}$$

The basis for simulating the realizations of \vec{X} by Monte Carlo method is to:

- Generate a vector of statistically independent, uniformly distributed random variables between 0 and 1 designated by $\vec{\mu}_k$.
- Transform $\vec{\mu}_k$ into \vec{X}_k by assuming μ_k to be the value of the cumulative distribution function of X_k . This is a more complicated process for correlated random variables where it requires the transformation of $\vec{\mu}_k$ to independent standard normal random variables \vec{X}'_k instead of transforming it directly to \vec{X}_k .
- Perform a linear transformation to transform the independent standard normal random variables \vec{X}'_k to correlated random variable \vec{X}_k as the following:

$$\vec{X}_k = [A]\vec{X}'_k + \vec{b} \quad \text{Equation 83}$$

where:

- \vec{b} = mean vector of X
- $[A]$ = a transformation lower triangular matrix obtained from the covariance matrix of the input variables X such that: $C_X = AC'_X A^T$
- C_X = Covariance matrix of X
- C'_X = Identity matrix

The transformation matrix $[A]$ can be determined using different matrix decomposition techniques: eigenvalue decomposition, singular value decomposition, and Cholesky decomposition. The Cholesky method is the fastest and commonly used in Monte Carlo simulations and it presents a useful mathematical technique that can be used for the

decomposition of symmetric and definite matrices like C_X into an upper and a lower triangular matrices (like [A]). Applying [A] to a vector of uncorrelated sample $\overrightarrow{X'_k}$, generates a sample vector $[A]\overrightarrow{X'_k}$ having the same covariance properties as the problem/system being modeled. The elements a_{ii} and a_{ij} of the matrix [A] are defined in Equation 84 and Equation 85, respectively.

$$a_{ii} = \sqrt{\text{Covariance}(X_i, X_i) - \sum_{j=1}^{i-1} a_{ij}^2} \quad \text{Equation 84}$$

$$a_{ji} = \frac{\text{Covariance}(X_i, X_j) - \sum_{h=1}^{i-1} a_{ih}a_{jh}}{a_{ii}}, j > 1 \quad \text{Equation 85}$$

To obtain a reasonable accuracy of the estimated response, large number of realizations has to be simulated. Simulating 500,000 realizations is believed to provide accurate results for the simulated responses which implies large computational efforts. In this research, the Monte Carlo simulations are carried out using both Microsoft Excel spreadsheets and R-codes/scripts.

6.3.3 Probabilistic Modeling Strategy

The purpose of this part of the research is the propagation of the uncertainties in material properties into VECD model. This is carried out on a component basis by modeling the inherent uncertainty of each material property and forward propagating it to yield a probabilistic prediction of viscoelastic strains. This requires modeling the uncertainty in the LVE functions from the E^* testing and in the damage characteristic curves based on the constant rate crosshead tests as summarized in Figure 42. Thus, the aim is to model the uncertainty in $|E^*|$ as a function of reduced frequency/time, $E(t)$ as a function of reduced time, $D(t)$ as a function of reduced time, and C as a function of any value of Lebesgue Norm of stress ($LS(\text{stress})$). For the case of C , it is presented as a function of $LS(\text{stress})$ directly but considering the uncertainties of both functions: $C(S)$ and $S(LS(\text{Stress}))$. To achieve this, the uncertainty of every material property ($|E^*|$, $E(t)$, $D(t)$, $C(S)$, $S(LS(\text{stress}))$, and $C(LS(\text{stress}))$) is modeled by forward propagation of the uncertainties in the parameters of the model describing that property over its domain as described in the following sections. For each mix, realizations from Monte Carlo simulations for $D(t)$ and $C(LS(\text{stress}))$ will be used to forward

propagate their uncertainties into the prediction of the viscoelastic strain for given stress profiles and temperatures.

6.4 Inherent Uncertainty in LVE Functions

6.4.1 Inherent Uncertainty in $|E^*|$

E^* serves as an important and basic material characterization test to be used for VECD in terms of converted $E(t)$ and $D(t)$ and into other commonly used pavement design and analysis methods like the mechanistic-empirical design methods. Even though $|E^*|$ is not used directly in the prediction of the viscoelastic strain, its uncertainty will be modeled because it serves a key parameter in the characterization of asphalt concrete. Also, the uncertainty in $|E^*|$ is required to provide a better understanding of that in $E(t)$ and $D(t)$. Throughout this section, a preliminary quantification of the uncertainty due to inherent variability in $|E^*|$ is introduced and presented where it can serve as an input to any probabilistic pavement design method. The primary objective of this section is to characterize the inherent variability in $|E^*|$ across the full spectrum of the $|E^*|$ master curve (i.e. at different reduced frequencies). This objective is achieved by analyzing the $|E^*|$ data of 10 replicates of each of the four mixes.

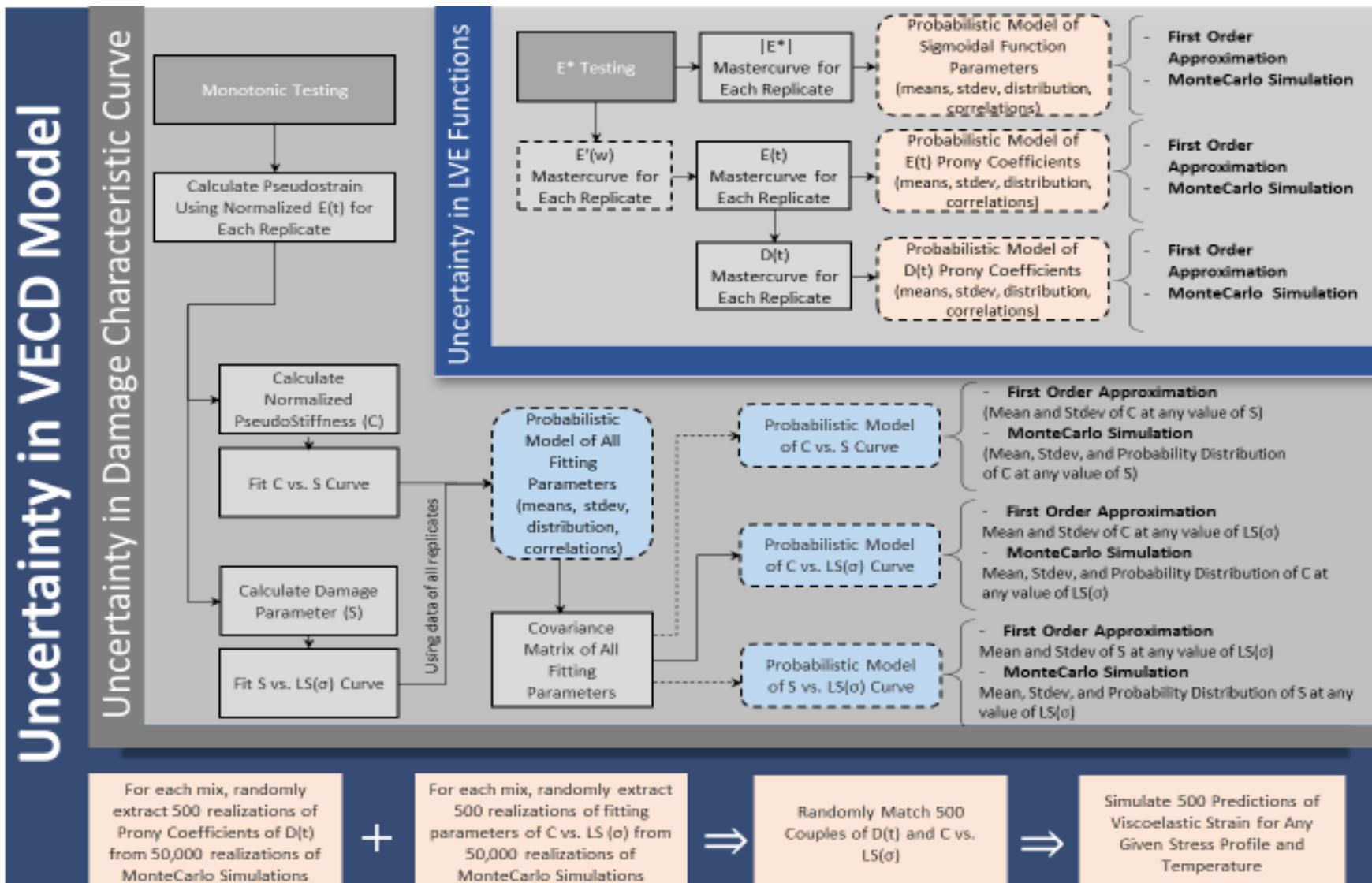


Figure 42. Flowchart showing the methodology followed for modeling of uncertainty in viscoelastic continuum damage model.

6.4.1.1 $|E^*|$ Mastercurve

The $|E^*|$ mastercurve is determined by fitting the sigmoidal function to the measured $|E^*|$ data as indicated in Equation 86 and Equation 87. The sigmoidal function relates $|E^*|$ to the reduced frequency which is calculated as a function of temperature and frequency. It is remarkable that the sigmoidal function used in this part of the research is based on four fitting parameters; while in the previous sections all $|E^*|$ mastercurves are fitted to sigmoidal function with six parameters as shown in Equation 72. This is done at this level, for both $|E^*|$ and $E'(w)$, in order to simplify and reduce the number of parameters involved in the quantification of the uncertainties. It is worth noting that many forms of the sigmoidal function can be used to fit $|E^*|$ mastercurves. The effect of the sigmoidal function form on the uncertainty in $|E^*|$, and basically the epistemic part, is studied in the following sections.

$$\log |E^*| = \delta + \frac{\alpha}{1+e^{\beta+\gamma \log(f_r)}} \quad \text{Equation 86}$$

$$|E^*| = 10^{\delta + \frac{\alpha}{1+e^{\beta+\gamma \log(f_r)}}} \quad \text{Equation 87}$$

where:

$|E^*|$: dynamic modulus (MPa)

a, b, c, δ , α , β , and γ : fitting parameters

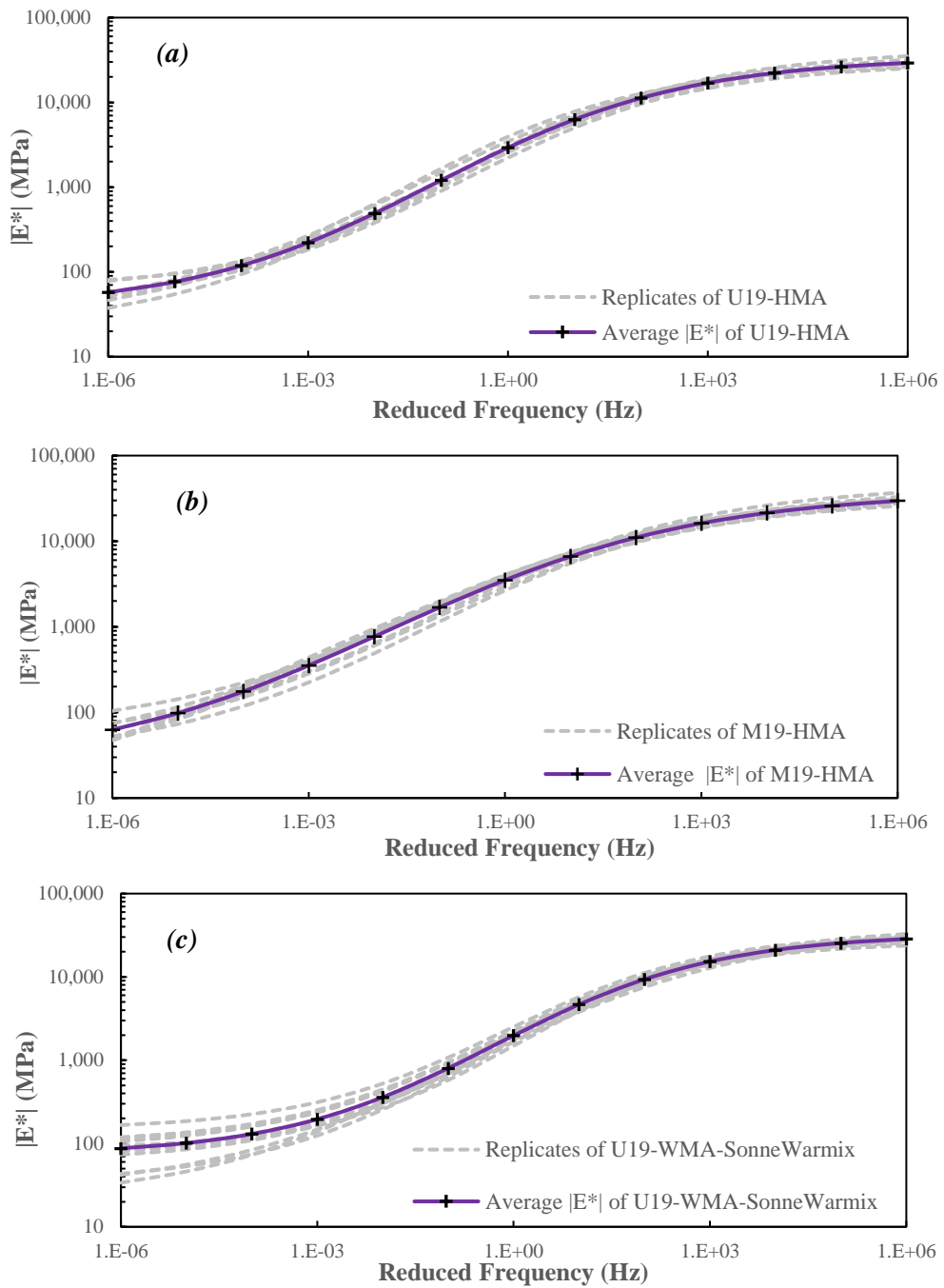
f_r : Reduced frequency (Hz) at a reference temperature T_0

The relation between $|E^*|$ and f_r is governed by four parameters (δ , α , β , and γ), and that between f_r and temperature by three other parameters (a, b, and c) as presented earlier in Equation 32, Equation 33, and Equation 73, resulting in a total of seven model parameters.

6.4.1.2 $|E^*|$ Data

For each replicate of the four mixes, $|E^*|$ mastercurve is constructed at a reference temperature of 25°C as presented in Figure 43. For each replicate, the parameters α , γ , β , and δ are determined along with the shift factors. For each mix, an average $|E^*|$ mastercurve that represents the average of the replicates is also presented. Irrespective of the mix properties, results in Figure 43 indicate that there exists scatter/variability that is clearly exhibited in the $|E^*|$ curves of the different replicates around the average curve of any given mix. The scatter is minimal at relatively high values of reduced frequency and increases systematically as the reduced frequency decreases. This implies that the inherent variability of $|E^*|$ is expected to be higher in the lower range of reduced frequencies. Visual observation of the scatter indicates that the magnitude of the variability in $|E^*|$ at relatively small reduced frequencies changes and seems to depend on the components of the mix. For the mix with WMA additive, the inherent variability in $|E^*|$ seems to be higher than the variability exhibited in the

U19-HMA mix. Also, the inherent variability in $|E^*|$ seems to increase as the NMAS of the mix becomes larger as it is the case of the U25-HMA compared with U19-HMA.



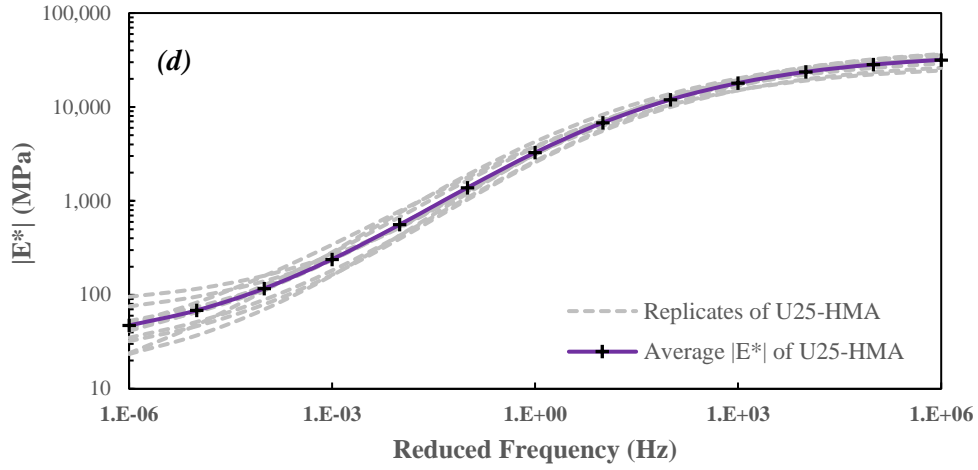


Figure 43. Best fit sigmoidal functions for $|E^*|$ of replicates in (a) U19-HMA (b) M19-HMA (c) U19-WMA-SonneWarmix (d) U25-HMA.

6.4.1.3 Probabilistic Model of $|E^*|$ Mastercurve

$|E^*|$ can be considered as a random variable because it is a function of the random variables: γ , α , δ , and β . However, the derivation of the probability distribution of $Y = E^*$ (γ , α , δ , β) has to take into account that Y and X_i s are governed by the sigmoidal fit which has a nonlinear nature. The uncertainties in the parameters a , b , and c of the shift factor are neglected given that the contribution of these parameters to the total uncertainty of $|E^*|$ was found to be negligible as per Kahil et al. (2015) and as confirmed in the following sections.

The first order approximation method will be used in order to determine the mean and covariance of the nonlinear function $Y = E^*$ (γ , α , δ , β) from the first and second moments of each of the X_i s through the relations presented in Table 22.

Table 22. Relationships used for the First Order Approximation of $|E^*|$.

$Y =$	$ E^* = 10^{\delta + \frac{\alpha}{1 + e^{\beta + \gamma \log(fr)}}}$
X_i s =	$\gamma, \alpha, \delta, \text{ and } \beta$
$E(Y) =$	$E(E^*) = 10^{\mu_\delta + \frac{\mu_\alpha}{1 + e^{\mu_\beta + \mu_\gamma \log(fr)}}}$
$\frac{\partial E^*}{\partial \delta} =$	$\ln(10) \cdot 10^{\left(\delta + \frac{\alpha}{1 + \exp(\beta + \gamma \log(fr))}\right)}$
$\frac{\partial E^*}{\partial \alpha} =$	$\frac{\ln(10) \cdot 10^{\left(\delta + \frac{\alpha}{1 + \exp(\beta + \gamma \log(fr))}\right)}}{\exp(\beta + \gamma \log(fr)) + 1}$
$\frac{\partial E^*}{\partial \beta} =$	$-\frac{\ln(10) \cdot \alpha \cdot \exp(\beta + \gamma \log(fr)) \cdot 10^{\left(\delta + \frac{\alpha}{1 + \exp(\beta + \gamma \log(fr))}\right)}}{(\exp(\beta + \gamma \log(fr)) + 1)^2}$
$\frac{\partial E^*}{\partial \gamma} =$	$-\frac{\ln(10) \cdot \alpha \cdot \exp(\beta + \gamma \log(fr)) \cdot \log(fr) \cdot 10^{\left(\delta + \frac{\alpha}{1 + \exp(\beta + \gamma \log(fr))}\right)}}{(\exp(\beta + \gamma \log(fr)) + 1)^2}$

For each of the replicates under study, the parameters of the sigmoidal function are determined. The mean and standard deviation for each parameter is consequently calculated for any given mix. The results show that β has the highest uncertainty for all mixes as indicated by comparing its COV (ratio of standard deviation to mean) with that of the other three parameters. The correlation coefficients that define the covariance structure between the different pairs of parameters are also determined. The mean vector, standard deviation vector, and correlation matrix of the four parameters are presented in Table 23 for all the four mixes analyzed in this part of the study. Results indicate that the correlation coefficients between the different pairs of the four parameters vary in magnitude and sense. It can be observed that γ and α exhibit strong positive correlations irrespective of the mix. Also, the couples “ δ - γ ”, “ β - γ ”, and “ β - α ” are observed to be negatively correlated for all mixes.

Table 23. Components of the mean vector, standard deviation vector, and correlation matrices for the fitting coefficients of $|E^*|$ for the four mixes under study.

Mix		U19-HMA	M19-HMA	U19-WMA-SonneWarmix	U25-HMA
δ	Mean	4.542	4.583	4.521	4.573
	Std Dev.	0.054	0.046	0.055	0.078
α	Mean	-3.035	-3.260	-2.728	-3.171
	Std Dev.	0.184	0.366	0.311	0.434
β	Mean	0.597	0.744	0.187	0.666
	Std Dev.	0.174	0.191	0.126	0.213
γ	Mean	0.533	0.432	0.593	0.508
	Std Dev.	0.040	0.049	0.059	0.055
Correlation Coefficient	δ - δ	1.00	1.00	1.00	1.00
	δ - α	-0.36	-0.08	-0.75	-0.57
	δ - β	-0.30	-0.01	0.57	0.20
	δ - γ	-0.49	-0.25	-0.78	-0.59
	α - α	1.00	1.00	1.00	1.00
	α - β	-0.61	-0.94	-0.79	-0.87
	α - γ	0.87	0.94	0.87	0.89
	β - β	1.00	1.00	1.00	1.00
	β - γ	-0.40	-0.92	-0.83	-0.83
	γ - γ	1.00	1.00	1.00	1.00

The statistical data presented in Table 23 defines the first two moments (mean and covariance) of the model parameters. To complete the probabilistic model for the inherent variability in $|E^*|$, knowledge about the probability distributions of the parameters is required. This is done by conducting the Shapiro-Wilk Normality Test which has a good power for a given level of significance. This is conducted using R-Studio where the null hypothesis: “ H_0 : Data comes from a normal distribution” is tested where the obtained p-value is compared to a

significance level of 0.05. Also, a log transformation is performed to check whether the normal or lognormal distribution best fits the tested data set. The results of the test, as presented in Table 24, show p-values higher than 0.05 for all the parameters in the case of the four mixes. This indicates that the normal distribution provides a realistic fit of all the model parameters and thus it has been adopted to model the probability distribution of each of α , γ , β , and δ .

Table 24. p-values by Shapiro-Wilk Normality Test for Parameters Describing $|E^*|$ Fits.

	δ	α	β	γ
U19-HMA	0.272	0.709	0.583	0.436
M19-HMA	0.911	0.075	0.361	0.474
U19-WMA-SonneWarmix	0.988	0.280	0.468	0.833
U25-HMA	0.352	0.191	0.216	0.860

6.4.1.4 Modeling of Uncertainty in $|E^*|$

The probabilistic model describing the uncertainty in the parameters of the sigmoidal function allows for the quantification of the inherent variability in $|E^*|$ for each mix by Monte Carlo Method and First Order Approximation. Monte Carlo Simulations consisting of 500,000 realizations of each parameter in the sigmoidal function are conducted to provide realistic estimates of the mean and COV of $|E^*|$ at specified values of reduced frequencies ranging from 10^{-6} to 10^6 Hz.

As expected, the average $|E^*|$ mastercurves that are determined from the Monte Carlo simulations for each of the four mixes are found to be identical to the average mastercurves of the different test replicates shown in Figure 44. For the average mastercurves obtained from the First Order Approximation, the same pattern can be observed with respect to the average mastercurves of the different test replicates with a slight variation especially at reduced frequencies smaller than 10^{-3} Hz. This finding is significant indicating that the probabilistic model of the sigmoidal function is realistic and representative of the data analyzed in the four mixes.

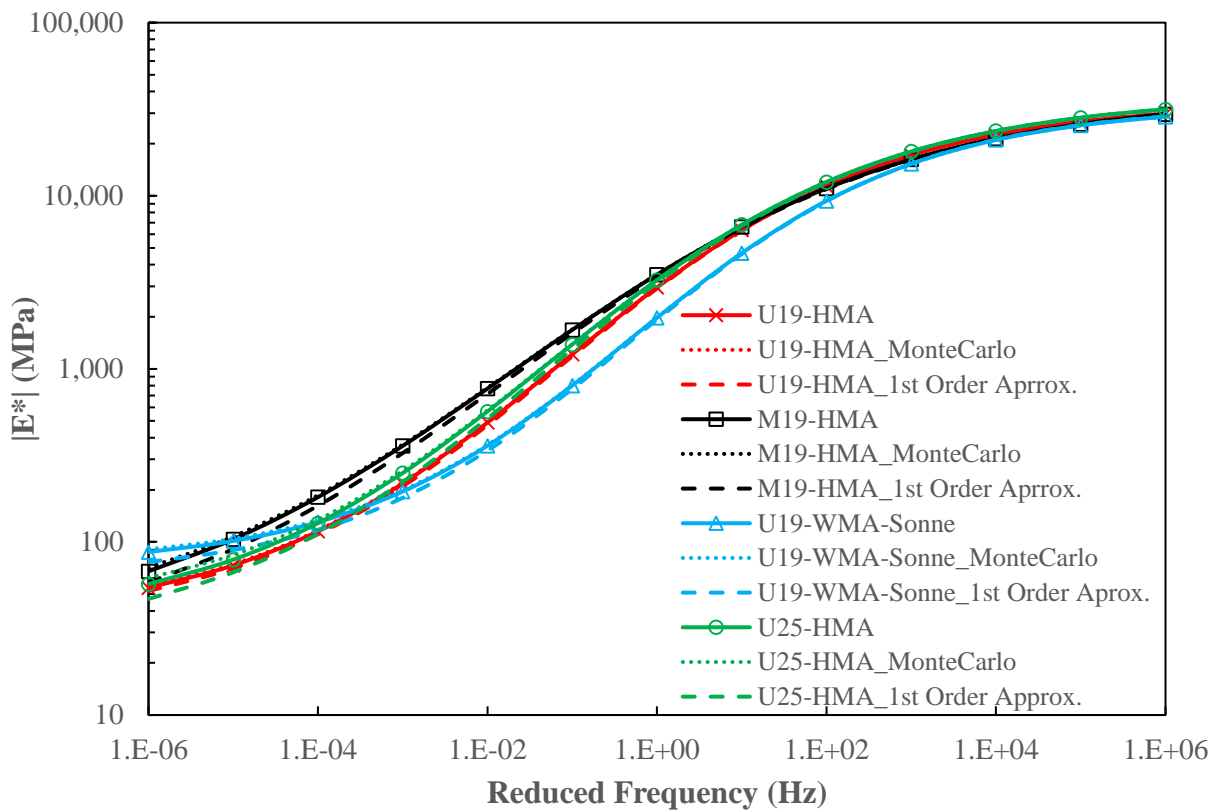


Figure 44. Average $|E^*|$ mastercurves at a reference temperature of 25°C as obtained from ten tested replicates, First Order Approximation, and Monte Carlo Simulations for each of the four mixes.

A further analysis of the obtained $|E^*|$ mastercurves requires a closer look at each of curves for the four mixes. Thus, $|E^*|$ mastercurves at different domains of reduced frequencies is extracted from the entire domain as shown in Figure 45, Figure 46, and Figure 47 for $[10^{-6}-10^{-1}]$ Hz, $[10^{-1}-10^3]$, and $[10^2-10^5]$ Hz, respectively. The entire region of reduced frequencies is divided into these three domains to represent regions of interest for acquiring $|E^*|$ representing conditions for the calculation of different types of pavement performance predictions. In the range of reduced frequency smaller than 1.0 Hz in which $|E^*|$ corresponds for the assessment of rutting, Monte Carlo simulations give the same $|E^*|$ mastercurve as that of the average of the replicates of the experimental data. However, the First Order Approximation underestimate the magnitude of $|E^*|$ in this region as shown in Figure 45. Thus, using the $|E^*|$ mastercurve resulting from the First Order Approximation will yield higher rut depths as the asphalt concrete's stiffness is underestimated. This will be least obtained for the case of U19-HMA but might yield higher differences for the other three mixes with highest difference appear for the case of U25-HMA and U19-WMA-SonneWarmix.

In addition, the comparison of the $|E^*|$ mastercurves is done in the regions of $10^{-1}-10^3$ Hz and 10^2-10^5 Hz which correspond to $|E^*|$ required for the prediction of fatigue and thermal

cracking, respectively. As shown in Figure 46 and Figure 47, both $|E^*|$ mastercurves determined by Monte Carlo Simulations and First Order Approximation lie on top of that obtained as the average of the replicates from experimental data. This indicates that the use of $|E^*|$ mastercurve from either Monte Carlo Simulations or First Order Approximation doesn't have an effect on the accuracy of predictions of pavement performance under fatigue and thermal cracking. Therefore, $|E^*|$ mastercurve from Monte Carlo simulation can be always used to predict pavement performance. However when using the $|E^*|$ mastercurve obtained from First Order Approximation precautions should be taken as it yields higher predicted rut depth. The significance of this difference could be investigated in future studies.

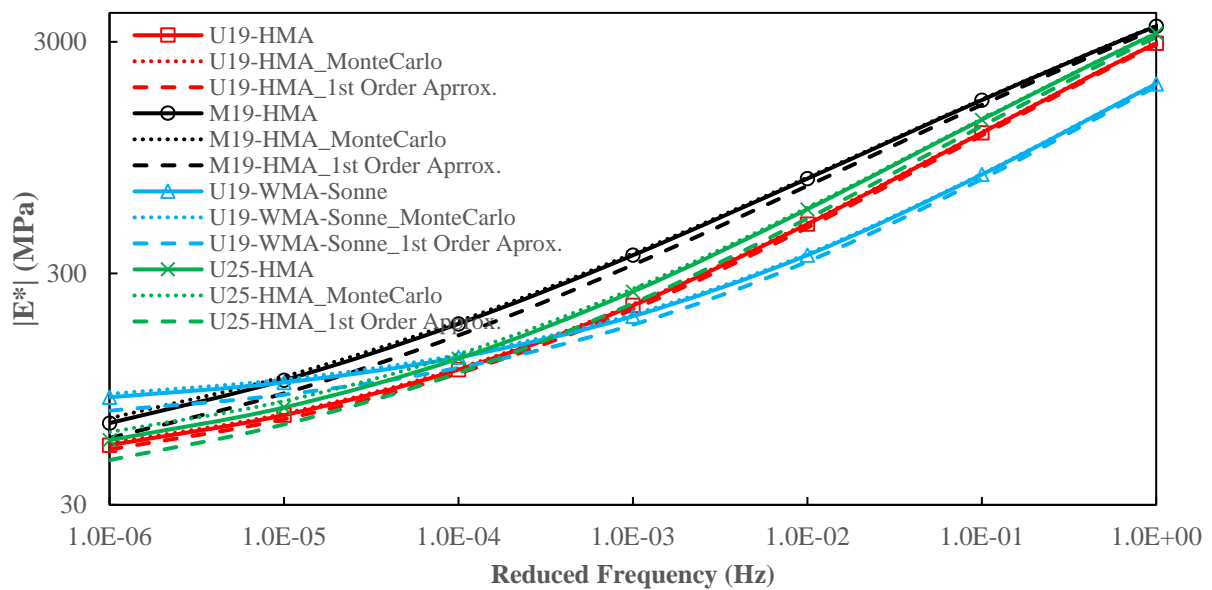


Figure 45. $|E^*|$ mastercurves obtained by First Order Approximation, Monte Carlo Simulations, and Experimental Data in the region of 10^{-6} to 10^{-1} Hz.

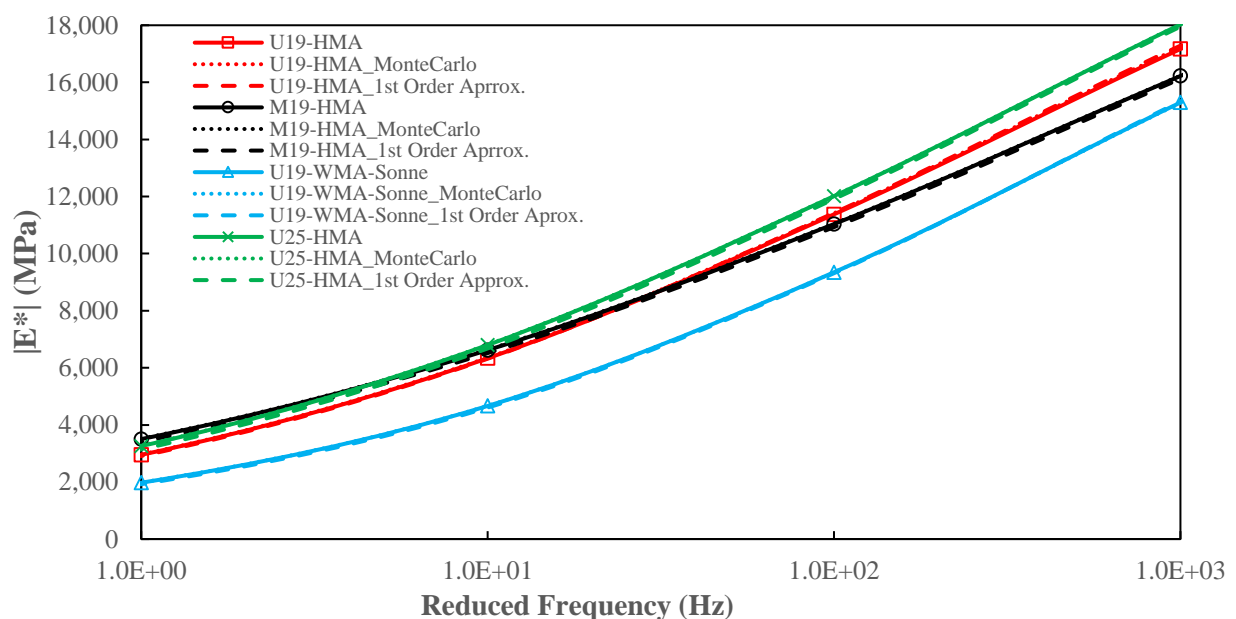


Figure 46. $|E^*|$ mastercurves obtained by First Order Approximation, Monte Carlo Simulations, and Experimental Data in the region of 10^{-1} to 10^3 Hz.

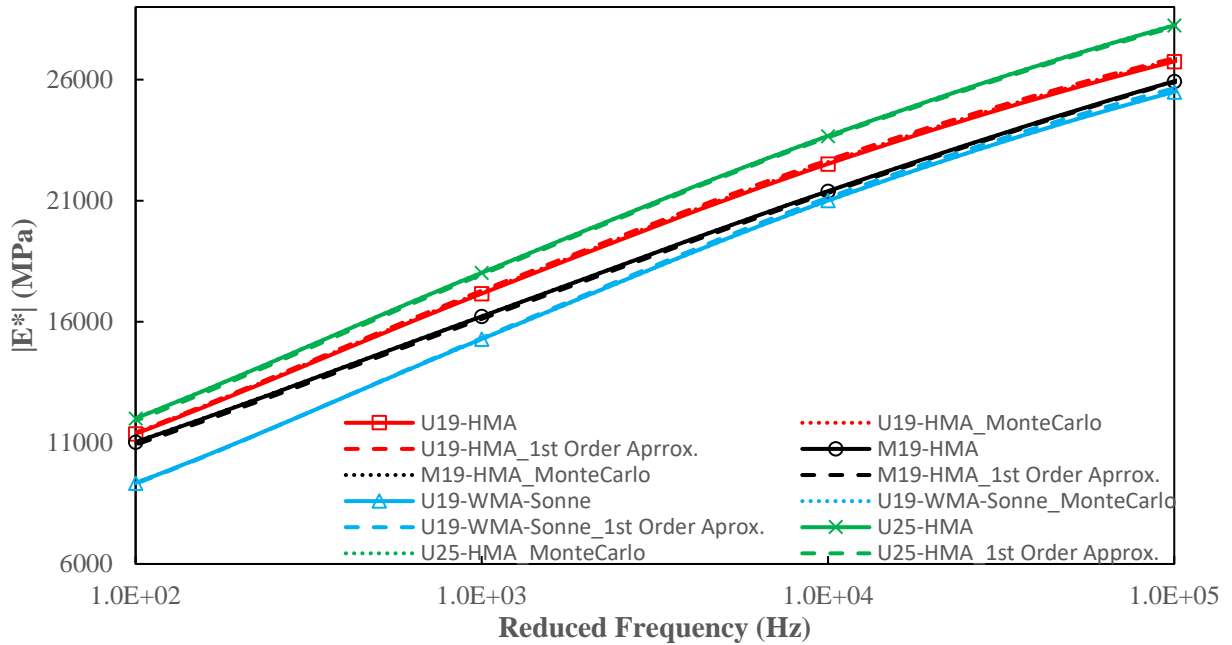


Figure 47. $|E^*|$ mastercurves obtained by First Order Approximation, Monte Carlo Simulations, and Experimental Data in the region of 10^2 to 10^5 Hz

A sample of the realizations of $|E^*|$ mastercurves from the Monte Carlo simulations are presented in Figure 48 which shows a scatter around the $|E^*|$ mean. This scatter is presented as a bound around the mean where it becomes wider as the reduced frequency decreases like the case of the experimental data as shown in the plots of Figure 43. The scatter appears to be higher for the U19-WMA-SonneWarmix and the U25-HMA mix as compared to that of the U19-HMA and M19-HMA mixes. This can be revealed by the values of $|E^*|$ at a reduced frequency of 10^{-6} Hz where it falls in the range of 30 to 120 MPa, 30 to 180 MPa, 20 to 240 MPa, and 20 to 250 MPa for the U19-HMA, M19-HMA, U19-WMA-SonneWarmix, and U25-HMA; respectively.

On the other hand, the inherent uncertainty in $|E^*|$ is reflected by the COVs calculated using the Monte Carlo simulations and First Order Approximation at different reduced frequencies. The variation of the COV of $|E^*|$ with reduced frequency is plotted in Figure 49 for the four mixes. The results indicate that the COV of $|E^*|$ increases as the reduced frequency decreases indicating that the inherent variability of $|E^*|$ is governed by the asphalt temperature and loading frequency.

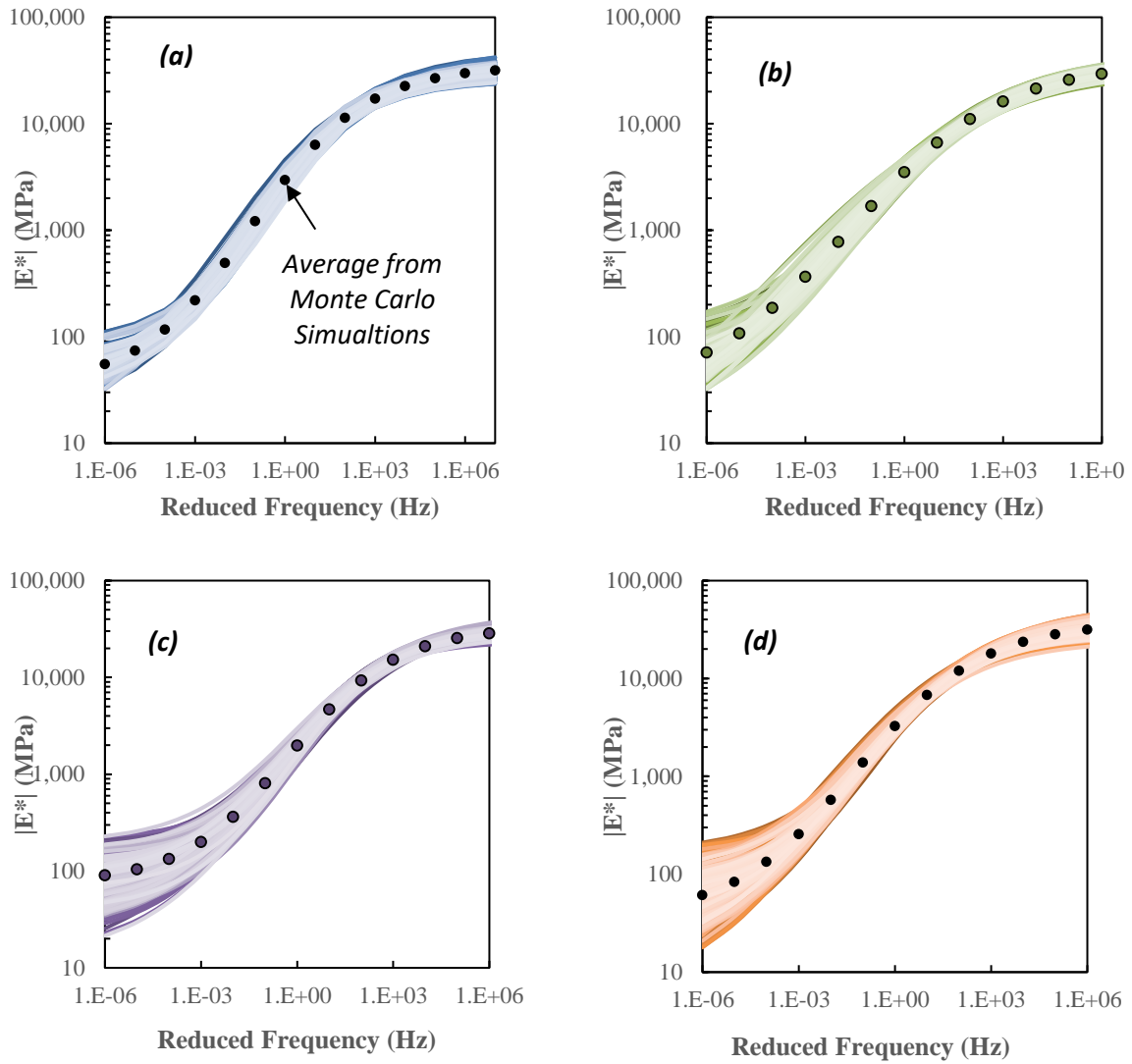


Figure 48. Realizations of $|E^*|$ mastercurves from Monte Carlo simulations for a) U19-HMA, b) M19-HMA, c) U19-WMA-SonneWarmix, and d) U25-HMA.

By comparing the results from Monte Carlo and First Order Approximation as shown in Figure 49, it can be observed that the COVs of $|E^*|$ obtained from both methods are the same for all mixes at reduced frequencies smaller than 0.1 Hz. As the reduced frequency decreases, the COV obtained from the First Order Approximation deviates lower than that from the Monte Carlo Simulations with a difference becoming larger as the reduced frequency becomes smaller. This is the case for all mixes except the case of U19-HMA where both methods yield the same COV over the range of reduced frequencies between 10^{-6} and 10^6 Hz. It can be observed that both methods provide the same COV when it is smaller than or equal to 0.25 which is the case for U19-HMA in the range of 10^{-6} - 10^6 Hz and the case of the three other mixes for reduced frequencies larger than 0.1 Hz. This shows that the First Order Approximation might not be efficient especially for levels of COV higher than 0.25 due the high non-linearity of the sigmoidal function. It might be useful as a simple method to

conduct but caution should be taken when analyzing results since the uncertainty is underestimated especially when having values of COV higher than 0.25.

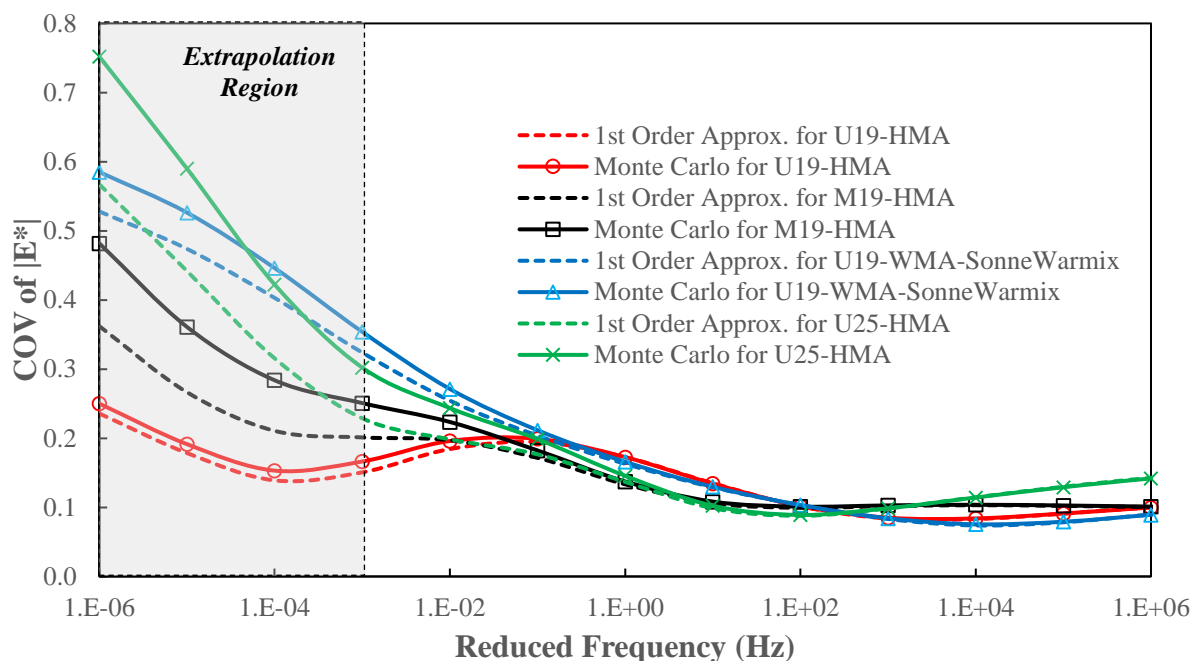


Figure 49. COV of $|E^*|$ as a function of reduced frequency using Monte Carlo Simulations and First Order Approximation.

For all the asphalt mixes, the COV of $|E^*|$ at high reduced frequencies (10^2 to 10^6 Hz) seems to vary in the narrow range around 0.1 for all mixes except U25-HMA. These COV values are small and indicate a low degree of inherent variability in $|E^*|$. The COV of $|E^*|$ for the U25-HMA reaches a value of 0.15 for larger reduced frequencies. This mix is the only one with a nominal maximum aggregate size (NMAS) of 25.0 mm while all the other three mixes with a NMAS of 19.0 mm have the same COV of 0.1. At high reduced frequencies corresponding to high frequency and/or low temperature, the binder is stiff and thus it has a minimal effect on the COV of $|E^*|$. For reduced frequencies that are smaller than 100 Hz, the uncertainty in $|E^*|$ increases with the decrease in the reduced frequency, reaching maximum COV values of 0.75 for one of the mixes at the lowest analyzed reduced frequency. These observations indicate high inherent uncertainty levels in $|E^*|$ at high temperatures and low frequencies where asphalt has a lower stiffness and thus prone to higher levels of deformation.

A thorough analysis of the COVs in Figure 49 indicates that the magnitude of the inherent variability in $|E^*|$ in the medium to low reduced frequency range (i.e. below 100 Hz) is a function of the components of the mix. At time U19-HMA has a COV of $|E^*|$ varying in the range of 0.1-0.25, the COV of $|E^*|$ for the three other mixes increases at different magnitudes with a difference between one mix and the other observe at reduced frequencies below 0.01 Hz. At 10^{-6} Hz, U25-HMA has the highest COV of 0.75 followed by U19-WMA-

SonneWarmix with a value of 0.6 and then M19-HMA with a COV of 0.5 which are all highest than the reference mix U19-HMA having a highest COV of 0.25. The increase of the inherent uncertainty with the decrease in the reduced frequency is expected to be due to the dominance of the aggregates' influence and the decrease in the number of loading cycles at low reduced frequencies (i.e. 100 cycles at 10 Hz versus 15 cycles at 0.1 Hz). For the lower frequencies, steady state may not be fully achieved in the last 5 or 6 cycles of testing at 0.1 Hz.

In addition, the investigated mixes show that its composition might be a factor influencing the inherent uncertainty in $|E^*|$ especially at low reduced frequencies (i.e. high temperatures and/or slow loading rates). This can be classified under two major categories: 1) Aggregate gradation presented by the NMAAS, and 2) Binder type dictated by the modification of the binder. Both the M19-HMA and the U19-WMA-SonneWarmix show a higher COV in $|E^*|$ at low reduced frequencies as compared to U19-HMA. Those three mixes have the same aggregate type and gradation but different types of asphalt binders with different modes of modification. U19-HMA has the raw unmodified binder; however, U19-WMA-SonneWarmix has the same binder type but modified in the lab with SonneWarmix which is a wax-based WMA additive. M19-HMA have a polymer modified binder produced by blending the unmodified binder with polymers at high tech-specialized plants. This indicates the modification of the binder and the type of this modification could be sources that further increase the uncertainty in $|E^*|$ of asphalt mixes. In general, the uncertainty is increased due to the modification of the binder and the spatial dispersion of the additives/modifiers within the asphalt binder. Such additives soften under high temperatures where they can be easily added and blended in which they will be dispersed within the binder to improve its properties at the desired conditions. The uncertainty of U19-WMA-SonneWarmix is the highest in this category and this might be due to many possibilities including: additive is not fully dispersed in the asphalt mix, wax might be conglomerated spatially within the mix increasing its level of heterogeneity, part of the additive might not be dissolved, and the dispersed particles of the wax might have different sizes... For M19-HMA, the COV of $|E^*|$ at low reduced frequencies is higher than that of U19-HMA because the polymer modification might be a source of heterogeneity that increases the inherent uncertainty; however, it is lower than that of U19-WMA-SonneWarmix as the modification process is done a specialized manufacturing facility under controlled conditions and processes. The level of compatibility of the modifier with the binder affecting its dispersion and thus the heterogeneity of the asphalt mix.

The COV of $|E^*|$ at low reduced frequencies is much higher for U25-HMA mix reaching a value of 0.75 at 10^{-6} Hz that is almost three times that of the U19-HMA. Both

mixes are of the same binder type, level of air voids, aggregate type, aggregate source, mixing and compaction temperatures but a different aggregate gradation and NMA. The mix with a larger NMA of 25.0 mm has a higher level of inherent uncertainty in $|E^*|$. The sensitivity of the inherent uncertainty in $|E^*|$ to the NMA at small reduced frequencies could be due to the reduction that occurs in the binder's stiffness rendering the response of the mix more sensitive to the properties of the aggregate components (Mohammad et al. 2013). As such, $|E^*|$ might become more susceptible to the variation of the aggregate's skeleton: distribution, orientation, and interlock within the replicates, thus affecting the load distribution within the sample. This is coupled with the fact that as the aggregates become larger, an increase in the sizes of the air voids in the specimen could occur resulting in a higher variability in the response of the mix. For a constant volume, the larger the aggregates, the larger the space filled with binder and thus a region weaker especially at slow rate and/or high temperatures leading to a higher effect of aggregates on the COV of $|E^*|$. Thus, the COV of $|E^*|$ is affected by both binder type and NMA at low reduced frequencies but only large NMA influences the COV of $|E^*|$ at large reduced frequencies. It is worth noting that even though these components have an effect at both regions, this effect is more dominant at low reduced frequencies. Large NMA imposes uncertainty in $|E^*|$ at low and high reduced frequencies which implies that it is better to have mixes with smaller NMA; however, this needs to be further confirmed in future work.

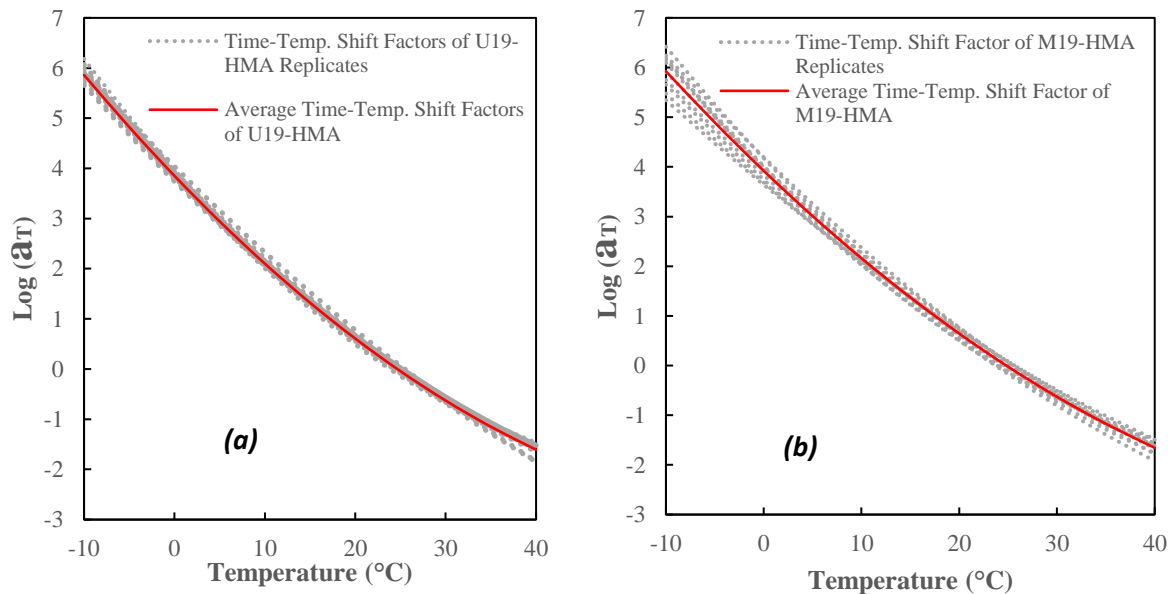
Moreover, the E^* testing conditions require applying the tests at four different temperatures in the range of -5-40°C as summarized in Table 11. The temperature-frequency combination that gives the smallest reduced frequency ($\sim 10^{-3}$ Hz) is 40°C and 0.1 Hz. Thus, the portion of the $|E^*|$ mastercurve for reduced frequencies in the range of 10^{-6} - 10^{-3} Hz is not fitted based on experimental data but an extrapolation of the fitted sigmoidal function. Hence, the unavailability of data in this region, shaded in grey in Figure 49, and the nature of the used sigmoidal function might be other sources contributing to the uncertainty of $|E^*|$ as reflected by the calculated COVs. The effect of uncertainty due to the fitting of the sigmoidal function might be more influential on the COV of $|E^*|$ in the region of 10^{-6} - 10^{-3} Hz as compared to that in 10^{-3} - 10^2 Hz in which experimental data is available.

6.4.1.5 Effect of Probabilistic Time-Temperature Shift Factors on Uncertainty in $|E^*|$

In the previous section, the analysis of the uncertainty is conducted assuming the time-temperature shift factors to be deterministic to simplify the solution process. Only the four parameters (α , β , γ , and δ) of the sigmoidal function are taken probabilistic while the parameters (a, b, and c) are considered deterministic. This could reduce the need to develop

the probabilistic models of each of the parameters a, b, and c and to find the correlation in-between them and between them and the parameters of the sigmoidal function. In addition, probabilistic time-temperature shift factors will yield probabilistic reduced frequencies which complicates the analysis of the uncertainty in the mastercurve of $|E^*|$ i.e. COV of $|E^*|$ as a function of any reduced frequency. In such a case, the uncertainty of $|E^*|$ will be quantified at any combination of temperature and loading frequency.

The time-temperature shift factors as a function of temperature for each replicate of the four mixes are presented in Figure 50. It is observed that the time-temperature shift factors show a scatter around the mean with high magnitude especially at regions of low and high temperatures. Visually, this scatter is shown to be larger for the M19-HMA, U19-WMA-SonneWarmmix, and U25-HMA as compared to the U19-HMA. So, the time-temperature shift factors have an inherent uncertainty that could be affected by temperature and the components of the mix in hand similar to the case of $|E^*|$. Thus, it is needed to study if the time-temperature shift factors contribute to the inherent uncertainty in $|E^*|$ and whether it is valid to assume them deterministic in any probabilistic analysis of any material property of asphalt concrete.



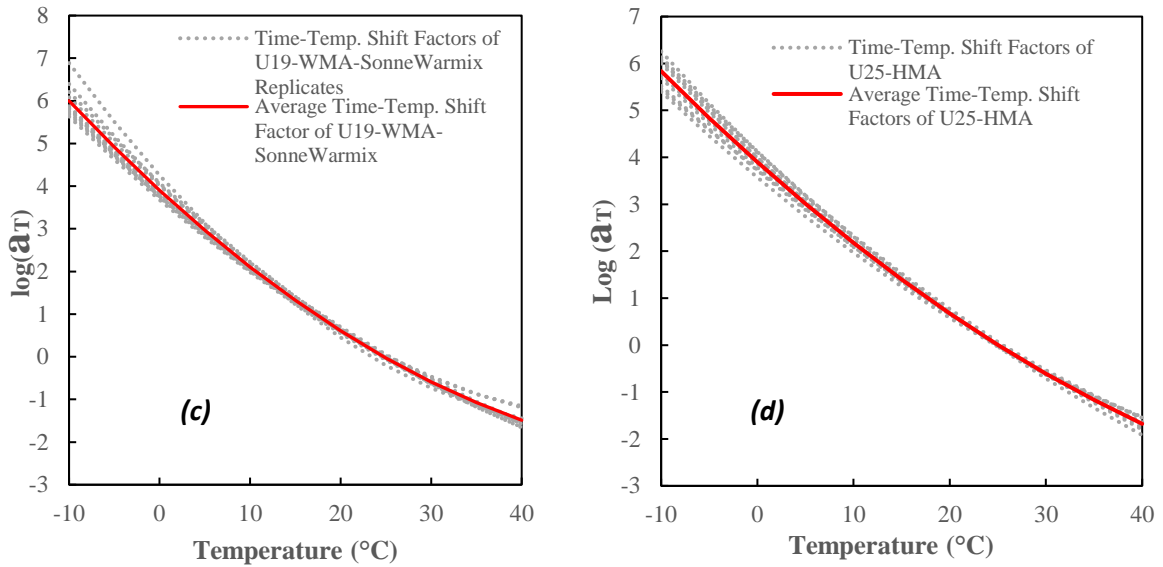


Figure 50. Time-temperature shift factor curves of the replicates of a) U19-HMA, b) M19-HMA, c) U19-WMA-SonneWarmmix, and d) U25-HMA.

Since the three parameters of the shift factor are also uncertain, they are expected to contribute to the total uncertainty in $|E^*|$ and may increase the previously calculated COVs of E^* which were presented or reflected in Figure 49. $|E^*|$ is considered as a random variable because where it is a function of the random variables: γ , α , δ , β , a , b , and c . The derivation of the probability distribution of $Y = E^*$ (γ , α , δ , β , a , b , c) has to take into account that Y and X_i s are governed by the sigmoidal fit and second degree polynomial for the shift factors. Both the First Order approximation and Monte Carlo simulations are used to quantify the uncertainty in $|E^*|$ with a probabilistic time-temperature shift factors through the relationships presented in Table 25. To limit the mathematical computations, the analysis is conducted for cases involving combinations of real frequency of 0.01, 0.1, 0.5, 1, 10, and 20 Hz with temperatures of -10°C, 0°C, 10°C, 25°C, and 40°C.

For each mix, the probabilistic model of the parameters a , b , and c is developed as presented in Table 26 to complement those of the parameters of the sigmoidal function as presented earlier in Table 23. The results show that the parameters a , b , and c follow a normal distribution for the four mixes. The analysis of the correlation coefficients show that there is not any strong correlation between the parameters of the time-temperature shift factors and the fitting parameters of the sigmoidal function. The magnitude of almost all these correlation coefficients fall in the range of -0.5 to 0.5 without any clear pattern with respect to either couples of parameters or mixes. However, a strong negative correlation is found for the parameters “ a ” and “ b ” for the four mixes. Also, a strong negative correlation exists for the parameters b and c for all mixes except U19-HMA.

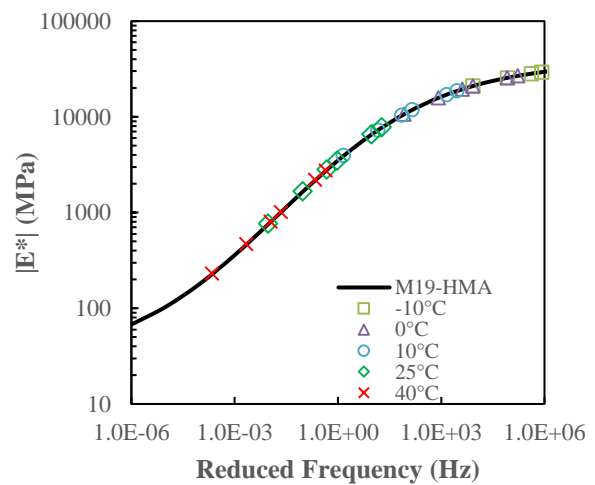
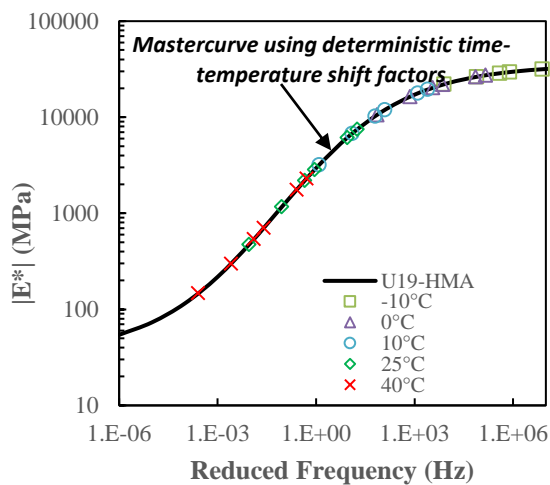
Table 25. Relationships used for the First Order Approximation of $|E^*|$ with probabilistic time-temperature shift factors.

$Y =$	$ E^* = 10^{\left(\delta + \frac{\alpha}{1 + \exp(\beta + \gamma (a.T^2 + b.T + c + \log(f)))}\right)}$
$X_{is} =$	$\alpha, \delta, \gamma, \beta, a, b, \text{ and } c$
$E(Y) =$	$E(E^*) = 10^{\mu_\delta + \frac{\mu_\alpha}{1 + e^{\mu_\beta + \mu_\gamma \log(\mu_a.T^2 + \mu_b.T + \mu_c + \log(f))}}}$
$\frac{\partial E^* }{\partial \alpha} =$	$\frac{\ln(10) \cdot 10^{\left(\delta + \frac{\alpha}{1 + \exp(\beta + \gamma (a.T^2 + b.T + c + \log(f)))}\right)}}{\exp(\beta + \gamma (a.T^2 + b.T + c + \log(f))) + 1}$
$\frac{\partial E^* }{\partial \beta} =$	$-\frac{\ln(10) \cdot \alpha \cdot \exp(\beta + \gamma (a.T^2 + b.T + c + \log(f))) \cdot 10^{\left(\delta + \frac{\alpha}{1 + \exp(\beta + \gamma (a.T^2 + b.T + c + \log(f)))}\right)}}{(\exp(\beta + \gamma (a.T^2 + b.T + c + \log(f))) + 1)^2}$
$\frac{\partial E^* }{\partial \gamma} =$	$-\frac{\ln(10) \cdot (a.T^2 + b.T + c + \log(f)) \cdot \alpha \cdot \exp(\beta + \gamma (a.T^2 + b.T + c + \log(f))) \cdot 10^{\left(\delta + \frac{\alpha}{1 + \exp(\beta + \gamma (a.T^2 + b.T + c + \log(f)))}\right)}}{(\exp(\beta + \gamma (a.T^2 + b.T + c + \log(f))) + 1)^2}$
$\frac{\partial E^* }{\partial \delta} =$	$\ln(10) \cdot 10^{\left(\delta + \frac{\alpha}{1 + \exp(\beta + \gamma (a.T^2 + b.T + c + \log(f)))}\right)}$
$\frac{\partial E^* }{\partial a} =$	$-\frac{\ln(10) \cdot T^2 \cdot \alpha \cdot \gamma \cdot \exp(\beta + \gamma (a.T^2 + b.T + c + \log(f))) \cdot 10^{\left(\delta + \frac{\alpha}{1 + \exp(\beta + \gamma (a.T^2 + b.T + c + \log(f)))}\right)}}{\exp(\beta + \gamma (a.T^2 + b.T + c + \log(f))) + 1)^2}$
$\frac{\partial E^* }{\partial b} =$	$-\frac{\ln(10) \cdot T \cdot \alpha \cdot \gamma \cdot \exp(\beta + \gamma (a.T^2 + b.T + c + \log(f))) \cdot 10^{\left(\delta + \frac{\alpha}{1 + \exp(\beta + \gamma (a.T^2 + b.T + c + \log(f)))}\right)}}{(\exp(\beta + \gamma (a.T^2 + b.T + c + \log(f))) + 1)^2}$
$\frac{\partial E^* }{\partial c} =$	$-\frac{\ln(10) \cdot \alpha \cdot \gamma \cdot \exp(\beta + \gamma (a.T^2 + b.T + c + \log(f))) \cdot 10^{\left(\delta + \frac{\alpha}{1 + \exp(\beta + \gamma (a.T^2 + b.T + c + \log(f)))}\right)}}{(\exp(\beta + \gamma (a.T^2 + b.T + c + \log(f))) + 1)^2}$

For the four mixes, the results of Monte Carlo simulations show that taking the time-temperature shift factors to be either deterministic or probabilistic yields no differences on the simulated $|E^*|$ mastercurves as shown in Figure 51. The results are based on 500,000 realizations of $|E^*|$ at each combination of loading temperature and frequency where the plots are based solely on “average” reduced frequency determined for plotting purposes and was calculated as a bi-product of the Monte Carlo analysis. The same results are obtained for $|E^*|$ mastercurves obtained from First Order Approximation with both deterministic and probabilistic time-temperature shift factors. The results are applicable for $|E^*|$ predicted at all combinations of temperatures and frequencies similar to the conditions of E^* testing. Thus, the uncertainty presented in the time-temperature shift factors seems to have no effect on the simulated $|E^*|$ mastercurves regardless of the temperature or the type of the mix.

Table 26. Components of the mean vector, standard deviation vector, and correlation matrices for the fitting coefficients parameters describing the time-temperature shift factors for the four mixes under study where $\log(a_T)=aT^2+bT+c$.

Mix		U19-HMA	M19-HMA	U19-WMA-SonneWarmmix	U25-HMA
a	Mean	1.31E-03	1.22E-03	1.50E-03	1.09E-03
	Std Dev.	2.20E-04	3.16E-04	4.02E-04	2.13E-04
	Distribution	Normal	Normal	Normal	Normal
b	Mean	-0.189	-0.188	-0.195	-0.183
	Std Dev.	0.008	0.016	0.017	0.011
	Distribution	Normal	Normal	Normal	Normal
c	Mean	3.850	3.920	3.903	3.898
	Std Dev.	0.064	0.192	0.176	0.193
	Distribution	Normal	Normal	Normal	Normal
Correlation Coefficient	a-δ	0.12	-0.48	0.23	-0.02
	a-α	-0.27	0.31	-0.39	0.18
	a-β	-0.08	-0.15	0.23	-0.42
	a-γ	-0.12	0.17	-0.48	0.40
	a-b	-0.91	-0.92	-0.94	-0.80
	a-c	-0.04	0.56	0.67	0.44
	b-δ	-0.16	0.33	-0.35	-0.39
	b-α	0.27	-0.03	0.50	0.28
	b-β	0.21	-0.15	-0.29	0.06
	b-γ	0.13	0.16	0.62	0.05
	b-c	-0.32	-0.80	-0.87	-0.88
	c-δ	0.49	-0.09	0.50	0.58
	c-α	-0.11	-0.13	-0.60	-0.55
	c-β	-0.39	0.28	0.33	0.23
c-γ	-0.09	-0.31	-0.68	-0.40	



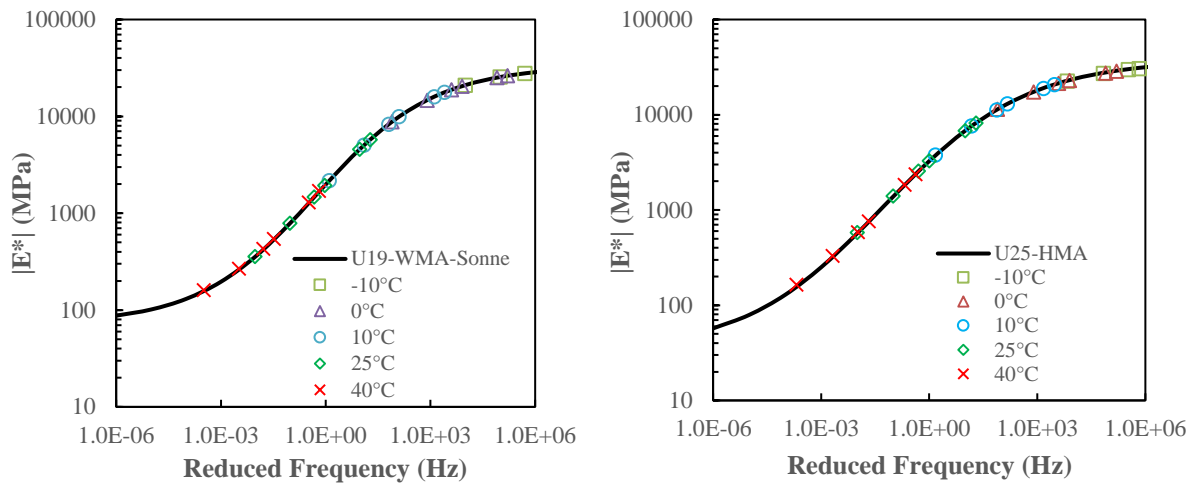


Figure 51. $|E^*|$ mastercurves from Monte Carlo simulations with deterministic and probabilistic time-temperature shift factors for a) U19-HMA, b) M19-HMA, c) U19-WMA-SonneWarmix, and d) U25-HMA.

For every temperature, the COV of the reduced frequency is shown in Figure 52. It is constant and independent of the loading frequency because the shift factors are modeled as a function of only temperature. At any temperature, the COV of reduced frequency of U19-HMA is significantly lower than that of the three other mixes. At a low temperature of -10°C , the probabilistic reduced frequencies fall in the range of 7×10^3 - 2×10^7 Hz for loading frequencies in the range of 0.01-20 Hz. At this temperature, the reduced frequencies have a high uncertainty reflected by its high COVs that fall in the range of 0.3-1.1 for the mixes under analysis. At -10°C , the reduced frequency of U19-HMA has the lowest COV of 0.3 followed by the U25-HMA with a value of 0.8. However, U19-WMA-SonneWarmix and M19-HMA have high COVs of 1.1 and 1.0, respectively. For each mix, the COV of the reduced frequency decreases as the temperature increases to reach a minimum at 25°C being the reference temperature. Then, the COV of reduced frequency increases as the temperature increases to 40°C where it is always higher than that of reduced frequency at 25°C but never exceeding the COV obtained at temperatures below 0°C .

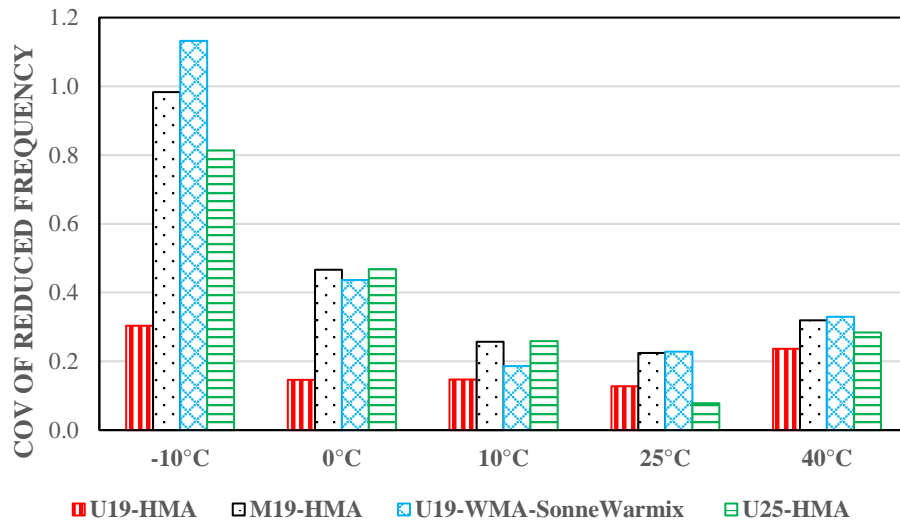


Figure 52. COV of reduced frequencies at different E^* testing temperatures.

The results of the propagation of the uncertainties in the parameters of the $|E^*|$'s sigmoidal function along with that in the parameters of the time-temperature shift factors are presented in Figure 53 in terms of the COV of $|E^*|$ as a function of reduced frequency. For the case of deterministic shift factors, the COV is presented as a continuous curve with respect to the reduced frequency. However, the COV is presented only at reduced frequencies equivalent to possible combinations of testing temperatures and frequencies for the case of probabilistic shift factors. The uncertainty in $|E^*|$ is quantified using both First Order Approximation and Monte Carlo simulations even though the former method might underestimate the COV in $|E^*|$ for values of 0.25 as stated in the previous section. As shown in Figure 53, the COV of $|E^*|$ is not affected whether the shift factors are deterministic or probabilistic regardless of the mix and uncertainty modeling method. The COV of $|E^*|$ has a minor deviation from the COV calculated using the deterministic shift factors especially at high temperature with a difference that does not exceed ± 0.1 . Even though the reduced frequencies have a high COV especially at low temperature, but it has no effect on the uncertainty in $|E^*|$ because the uncertainty in reduced frequency yields $|E^*|$ values whose variability is dominated by the original uncertainty of $|E^*|$ at any given reduced frequency. Thus, the major conclusion that can be drawn from the above observations is that the effect of uncertainties in the shift factor on the mean and COV of $|E^*|$ could be neglected in any probabilistic analysis. The parameters a, b, and c of the shift factor could be assumed to be deterministic with representative values that are estimated by the mean values.

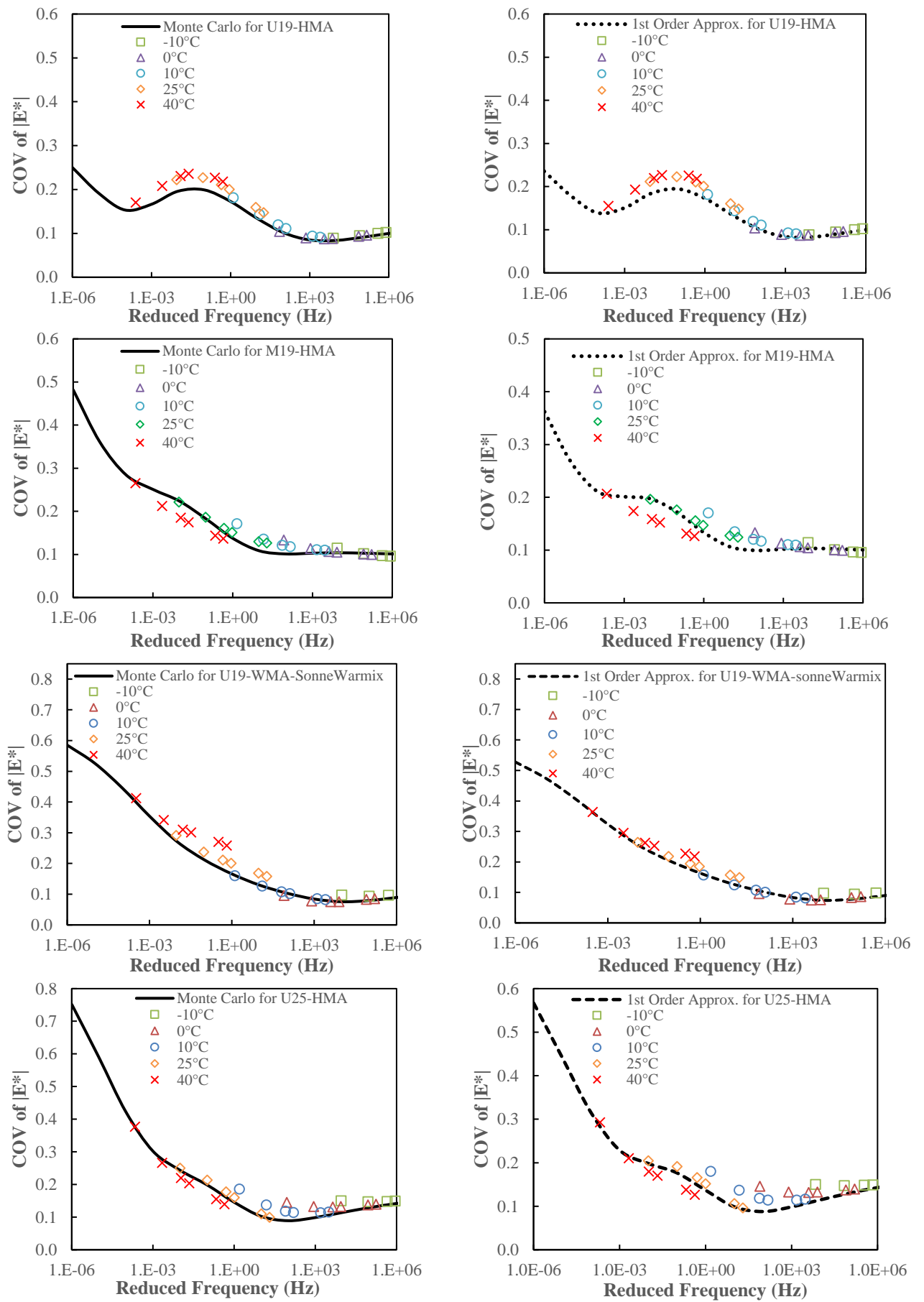


Figure 53. Effect of uncertainty in shift factor model parameters on the COV of $|E^*|$.

6.4.1.6 Effect of Sigmoidal Function Fitting on Uncertainty in $|E^*|$

Researchers have paid significant efforts to represent the $|E^*|$ mastercurve by functional forms that will allow them to readily be applied to the analysis and design of pavements. These fitting functions include the Standard Sigmoidal Function used in this research with four parameters and six parameters as presented by Equation 86 and Equation 72, respectively. These models might exhibit different accuracies in fitting the experimental data. The Standard Sigmoid was adopted as part of the mechanistic-empirical pavement design guide (MEPDG). However, several studies have shown that many asphalt mixtures are not symmetric about the point of maximum gradient, and thus a symmetrical sigmoidal function, like the standard logistic sigmoid, wouldn't be a good universal fitting functional form (Khosravifar et al. 2015, Rowe et al. 2009). Other forms of the sigmoidal function, such as the Generalized Logistic Sigmoid, have thus been suggested (Rowe et al. 2016). However, it has been shown that the choice of the sigmoidal function affects the extrapolated results outside the experimental range especially when following AASHTO TP 79-09 where the experimental range is even more compact (Kim et al. 2015). The predicted $|E^*|$ values at high temperatures and/or low frequencies could change depending on the choice of the fitting function. The aim in this section of the research is not to assess the accuracy of these models but to check whether the selection of the model affects the uncertainty in $|E^*|$ and specifically in the regions of extrapolation.

To conduct this analysis, the $|E^*|$ mastercurve for each replicate of the four mixes is also fitted using the Standard Sigmoidal Function with six parameters and the Generalized Logistic Function which have five parameters. The $|E^*|$ fitting models are referred to as the four, five, and six parameters model. The four parameters model is the one used in the analysis of the inherent uncertainty in $|E^*|$ in the previous sections. Similar to the previous analysis, First Order Approximation and Monte Carlo Simulations were carried out in order to model the uncertainty in the mastercurve of $|E^*|$. The relationships required to conduct the analysis for the 5 parameters model and the 6 parameters model are presented in Table 27 and Table 28, respectively. For each mix, the probabilistic models (mean, standard deviation, and distribution) and the correlation matrix were determined for the parameters of each of the studied sigmoidal functions. The uncertainty in $|E^*|$ is modeled as a function of the random variables (α , β , γ , δ , and λ) and (a, b, c, d, e, and f) for the 5 parameters model and the 6 parameters model, respectively.

Table 27. Relationships used for the First Order Approximation of $|E^*|$ fitted using the Generalized Logistic Function (5 parameters model).

$Y =$	$ E^* = 10^{\frac{\delta + \frac{\alpha}{[1 + \lambda e^{\beta + \gamma \log(fr)]^{1/\lambda}}}}{\lambda}}$
$X_{is} =$	$\delta, \beta, \gamma, \alpha, \text{ and } \lambda$
$E(Y) =$	$E(E^*) = 10^{\frac{\mu_\delta + \frac{\mu_\alpha}{[1 + \mu_\lambda e^{\mu_\beta + \mu_\gamma \log(fr)]^{1/\mu_\lambda}}}}{\lambda}}$
$\frac{\partial E^* }{\partial \delta} =$	$\frac{\ln(10) \cdot 10^{\frac{\delta + \frac{\alpha}{(\lambda e^{\beta + \gamma \log(fr)} + 1)^{1/\lambda}}}}{\lambda}}{\ln(10)}$
$\frac{\partial E^* }{\partial \alpha} =$	$\frac{10^{\frac{\delta + \frac{\alpha}{(\lambda e^{\beta + \gamma \log(fr)} + 1)^{1/\lambda}}}}{\lambda} \cdot \ln(10)}{(\lambda e^{\beta + \gamma \log(fr)} + 1)^{1/\lambda}}$
$\frac{\partial E^* }{\partial \beta} =$	$-\frac{10^{\frac{\delta + \frac{\alpha}{(\lambda e^{\beta + \gamma \log(fr)} + 1)^{1/\lambda}}}}{\lambda} \cdot a e^{\beta + \gamma \log(fr)} \cdot \ln(10)}{(\lambda e^{\beta + \gamma \log(fr)} + 1)^{1/\lambda + 1}}$
$\frac{\partial E^* }{\partial \gamma} =$	$-\frac{10^{\frac{\delta + \frac{\alpha}{(\lambda e^{\beta + \gamma \log(fr)} + 1)^{1/\lambda}}}}{\lambda} \cdot a \cdot e^{\beta + \gamma \log(fr)} \cdot \ln(fr)}{(\lambda e^{\beta + \gamma \log(fr)} + 1)^{1/\lambda + 1}}$
$\frac{\partial E^* }{\partial \lambda} =$	$-10^{\frac{\delta + \frac{\alpha}{(\lambda e^{\beta + \gamma \log(fr)} + 1)^{1/\lambda}}}}{\lambda} \cdot \ln(10) \left(\frac{e^{\beta + \gamma \log(fr)}}{\lambda \cdot (\lambda e^{\beta + \gamma \log(fr)} + 1)^{1/\lambda + 1}} - \frac{\ln(\lambda e^{\beta + \gamma \log(fr)} + 1)}{\lambda^2 \cdot (\lambda e^{\beta + \gamma \log(fr)} + 1)^{1/\lambda}} \right)$

Table 28. Relationships used for the First Order Approximation of $|E^*|$ fitted using the Sigmoidal Function with 6 parameters.

$Y =$	$ E^* = 10^{a + \frac{b}{c + \frac{f}{\exp(d + e \log(fr))}}}$
$X_{is} =$	$a, b, c, d, e, \text{ and } f$
$E(Y) =$	$E(E^*) = 10^{\frac{\mu_a + \frac{\mu_b}{\mu_c + \frac{\mu_f}{\exp(\mu_d + \mu_e \log(fr))}}}}{\lambda}}$
$\frac{\partial E^* }{\partial a} =$	$10^{a + \frac{b}{c + f \cdot \exp(-d - e \log(fr))}} \cdot \ln(10)$
$\frac{\partial E^* }{\partial b} =$	$\frac{10^{a + \frac{b}{c + f \cdot \exp(-d - e \log(fr))}} \cdot \ln(10)}{c + f \cdot \exp(-d - e \log(fr))}$
$\frac{\partial E^* }{\partial c} =$	$-\frac{10^{a + \frac{b}{c + f \cdot \exp(-d - e \log(fr))}} \cdot b \cdot \ln(10)}{(c + f \cdot \exp(-d - e \log(fr)))^2}$
$\frac{\partial E^* }{\partial d} =$	$\frac{10^{a + \frac{b}{c + f \cdot \exp(-d - e \log(fr))}} \cdot b \cdot f \cdot \exp(-d - e \log(fr)) \cdot \ln(10)}{(c + f \cdot \exp(-d - e \log(fr)))^2}$
$\frac{\partial E^* }{\partial e} =$	$\frac{10^{a + \frac{b}{c + f \cdot \exp(-d - e \log(fr))}} \cdot b \cdot f \cdot \log(fr) \cdot \exp(-d - e \log(fr)) \cdot \ln(10)}{(c + f \cdot \exp(-d - e \log(fr)))^2}$
$\frac{\partial E^* }{\partial f} =$	$-\frac{10^{a + \frac{b}{c + f \cdot \exp(-d - e \log(fr))}} \cdot b \cdot \exp(-d - e \log(fr)) \cdot \ln(10)}{(c + f \cdot \exp(-d - e \log(fr)))^2}$

Independent from the uncertainty analysis, the experimental data of the replicates of each mix were pooled and used collectively to conduct a nonlinear regression analysis to fit each of the three models. The nonlinear regression is a developed linear regression technique in which a nonlinear mathematical model is used to describe the relation between the response being $|E^*|$ and the predictor variable which is the reduced frequency in this case. The general form of this regression can be presented by $Y=\eta(x,\beta)+e$, where β is a vector of unknown parameters and e is the residual which is also assumed to be Normal $(0,\sigma^2)$. The fitting of nonlinear regression model is determining the least-squares estimates of the parameters of the nonlinear model (parameters of the Sigmoidal or Logistic Functions). It is similar to that of fitting a linear model but with an explicit formula of estimation where the user is required to provide an initial estimate of each of the parameters to be regressed. The analysis is conducted in R-Studio using the *nls* function.

For all mixes, the estimates of the parameters of the three investigated models have a very small p-value of $2E-16$. This indicates that all the parameters of any of the three models are significant and required to best fit the experimental data using any of these models. Then, the nonlinear regression models were used to compare the goodness of fit and check whether any of the 4, 5, and 6 parameter models is more favorable. Regarding this issue, it is noted here that the adjusted- R^2 value cannot be used as an adequate measure for the goodness of fit in nonlinear models because it is based on the underlying assumption that it is a case of fitting a linear model. It has been shown in literature, from a study done on comparing nine nonlinear models of which five are logistic functions used for pharmacological and biochemical applications, that for the case of nonlinear regression, R^2 will be uniformly high for both very bad and very good models and the use of R^2 and adjusted R^2 to choose the final model will lead to the correct model only 28-43% of the times (Spiess and Neumeier 2010). Thus, the Akaike Information Criterion (AIC), which is widely accepted for the comparison of nonlinear models, is used for model selection. The results of AIC of the three fitted models for each of the mixes is presented in Table 29. Typically, the model with the lowest AIC is the preferred one. Based on the results, the two symmetric sigmoidal models with four and six parameters have exactly the same AIC for the four mixes. This indicates that both models have the same goodness of fit for the $|E^*|$ experimental data. However, the Logistic function with the five parameters have a lower AIC as compared with the two other models for the four mixes indicating that it provides a better fit for the $|E^*|$ mastercurve. However, the difference between AIC of the 5 parameters model and the other model is less than 10 which indicates that the model with 4 parameters and 6 parameters are not weak models and thus these two models can be used (Burnham and Anderson 2003). Therefore, based on the

goodness of fit the three models have the same effect in fitting the data. It is worth noting that this analysis tests the fitted part of the mastercurve with reduced frequency above 10^{-3} Hz and thus it does not examine the model's behavior in the extrapolation region.

Table 29. AIC of the three $|E^*|$ fitting models for four mixes.

Mix	4 Parameters Model	5 Parameters Model	6 Parameters Model
U19-HMA	-583.3	-589.8	-583.3
M19-HMA	-674.7	-673.7	-674.7
U19-WMA-SonneWarmix	-679.3	-687.7	-679.3
U25-HMA	-620.1	-624.1	-620.1

The average $|E^*|$ mastercurves fitted using each of the models are presented in Figure 54 for each of the four mixes. Visually, it can be observed that the $|E^*|$ mastercurves fitted using the three models are exactly the same in the region with reduced frequencies larger than 10^{-3} Hz which corresponds to the region in which data is available from the experiment. This lies within the same conclusions drawn from the nonlinear regression and AIC. However, differences in the fitted mastercurves can be observed in the region of extrapolation i.e. below 10^{-6} - 10^{-3} Hz. As shown in Figure 54, the same mastercurves are extrapolated using the four and six parameters model (symmetrical sigmoidal functions) for any of the mixes. However, a different mastercurve is extrapolated when using the nonsymmetrical Logistic function. In this region and for every mix, extrapolated $|E^*|$ values are always higher for the case of the five parameters model as compared to that of the two other models. It is also notable that the five parameters model gives for the four mixes mastercurves that converge to the same point at very low reduced frequency which is not the case when using the symmetrical fitting models. Thus, the five parameters model provides a good fit in the region in which the data are available from testing. However, this model is not accurate in the extrapolation region where it eliminates the differences between the mixes which implies that it will badly affect performance predictions when used to assess the rutting resistance of asphalt concrete mixes. This implies that the COV of $|E^*|$ in the extrapolation region will be lower when fitting the mastercurve using the 5 parameters model.

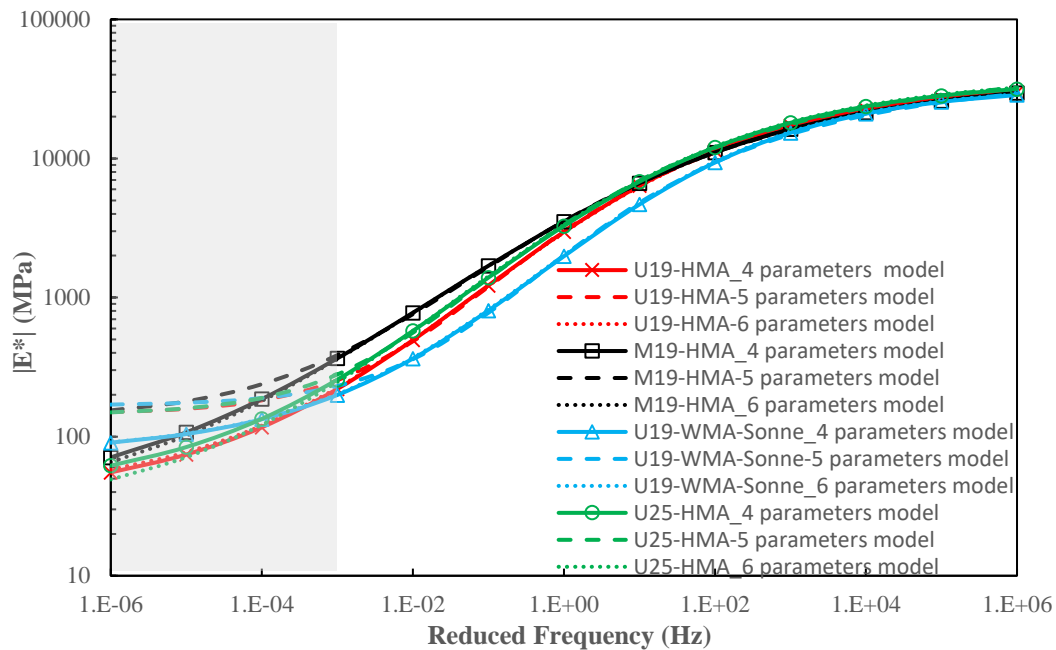


Figure 54. $|E^*|$ mastercurves fitted using three models for the U19-HMA, M19-HMA, U19-WMA-SonneWarmix, and U25-HMA.

The results of quantifying the uncertainty of $|E^*|$ mastercurves fitted using the different models are presented in Figure 55 for the four mixes. The aim of this work is to determine whether selection of the model affects the epistemic portion of $|E^*|$'s uncertainty. For U19-HMA, the mix with the lowest uncertainty not exceeding 0.25 over the entire range of reduced frequencies, the COV is not affected at any region of the mastercurve by the model used to fit it whether it is the symmetrical or non-symmetrical logistic function. However, this is not the case for the other three mixes where the COV in $|E^*|$ obtained using the six parameters model exceeds that of $|E^*|$ obtained using the four parameters model by approximately 0.1 over the entire reduced frequency range of 10^{-3} - 10^6 Hz i.e. the region in which the experimental data is available. As shown in Figure 55-a and Figure 55-b, the COV in $|E^*|$ obtained using both forms of the symmetrical sigmoid (4 parameters and 6 parameter model) converge in the region of extrapolation (for reduced frequencies less than 10^{-3} Hz).

On the other side, the COV of $|E^*|$ fitted using the nonsymmetrical model (5 parameter model) is the same as that by the 4 parameters model of reduced frequency larger than 10^{-3} Hz for M19-HMA, U19-WMA-SonneWarmix, and M19-HMA mixes. However, the uncertainty of $|E^*|$ fitted using this model is significantly smaller than that of $|E^*|$ fitted using either of the symmetrical models in the extrapolation region. As stated earlier, this is expected because the 5 parameters model is forcing all mastercurves to converge at very low reduced frequencies. Thus, it can be concluded that the selection of the $|E^*|$ mastercurve fitting model has an effect on the modeled uncertainty of $|E^*|$. This effect depends on the nature of the model, the region of reduced frequency analyzed, and the type of the mix under

investigation. In general, it is rather having a methodology with high uncertainty and an expected predicted average that is accurate than accepting a methodology with lower uncertainty but with an inaccurate mean. Therefore, all the analysis in this research will proceed based on $|E^*|$ fitted using the four parameters model due to many reasons of which is the fact that it provides acceptable results in the extrapolation region and it is currently the most widely used model to fit $|E^*|$ of asphalt concrete mixes beside that it shares common properties with the two other models when quantifying the COV of $|E^*|$ especially in non-extrapolation regions.

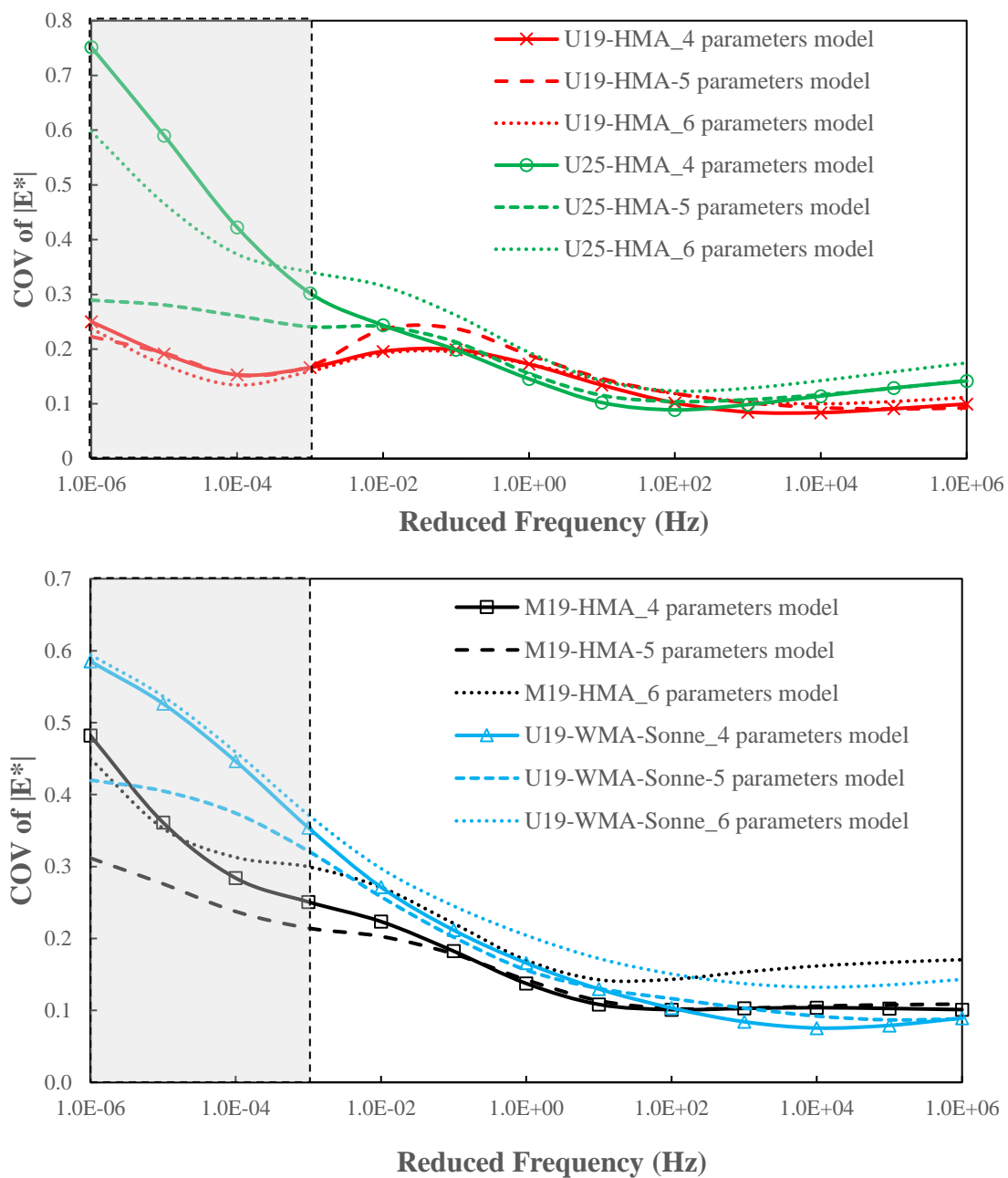


Figure 55. COV of $|E^*|$ mastercurve fitted using three different models for a) U19-HMA and U25-HMA, and b) M19-HMA and U19-WMA-SonneWarmix.

6.4.1.7 Effect of Machine Loading and LVDT Data Acquisition on Uncertainty in $|E^*|$

The roadway towards an accurate characterization of the properties of asphalt concrete entails awareness to issues related to machine compliance and the used instrumentations. It has been reported by previous studies that instrumentation issues in complex modulus testing can result in errors greater than 10% in measured $|E^*|$ (Daniel et al. 2004). The measurement of a material property involves the application and measurement of stress and strains by which a system applies the load and measures its response. The load is applied using a loading frame with a pneumatic or hydraulic actuator and measured using a load cell. The deformations are measured using some types of gauges and transducers where LVDTs mounted on the samples are used for all measurements in this research. Typically, these instruments function based on the fundamentals of electromechanical fields where it can transform mechanical motion into electric signals which are then read and converted to appropriate units of load and displacement. These signals are filtered and conditioned before being passed to the data acquisition system. The collected stress and strain data for $|E^*|$ is fitted using a sinusoidal/haversine function that will account for the noise that might affect the correct amplitudes and phases. Thus, the control and measurement aspects of the testing play an important role in achieving meaningful or appropriate results from the data extracted from the test.

All these issues are considered and accounted for in the instrumentation, acquisition, and data fitting for all the tests conducted in this research. However, it is worth determining whether the quantified uncertainty in $|E^*|$ as per the previous sections is affected by instrumentation or it is solely due to the heterogeneity of asphalt concrete. For that sake and given that the same load is applied for every combination of temperature and frequency, the data of all replicates of the four mixes are pooled to conduct this analysis. For every combination of temperature and frequency, forty data points are analyzed where each of them presents the average load calculated using the last five cycles of each testing sweep. The COVs of the actual applied load are presented as a function of the magnitude of the targeted load as shown in Figure 56. The COV of load presents the variability in applied load from one sample to another and it could also represent the variability entailed by choosing a different bunch of cycles of a given sweep to conduct the analysis required to calculate $|E^*|$. The COV of the load applied by the machine is very small and not exceeding a maximum of 0.03. This indicates that the variability implied by the ability of the machine to apply a given target load is very low and has a minimal effect on the uncertainty of $|E^*|$.

By further analysis of the results, it can be observed that for each temperature, the COV of the applied load follows a clear trend where it decreases as the frequency/load

becomes smaller. At a given temperature, the applied load required to get the required strain level (less than 75 micro-strains) increases as the frequency becomes larger. Even though the COV is very low; however, the variability in the applied load exists and varies systematically.

As the frequency increases at each temperature, the COV of the load increases. Also, as the temperature increases for a given frequency, it can be observed in general that the COV of the load increases as well. So, the variability in the applied load increases as the temperature becomes higher and/or as the loading rate becomes faster. This might be mainly due to errors related to noise, signal conditioning, and filtering whose error typically increases as the load rate becomes faster. In addition, the COV is higher at low magnitudes of load where as the ratio of applied load to capacity decreases, it is harder to control the load as it becomes small compared to the machine's capacity implying a higher error. Further, the error is influenced by the tuning of proportional, integral and derivative (PID) controller used to optimize the system response and its feedback compensator.

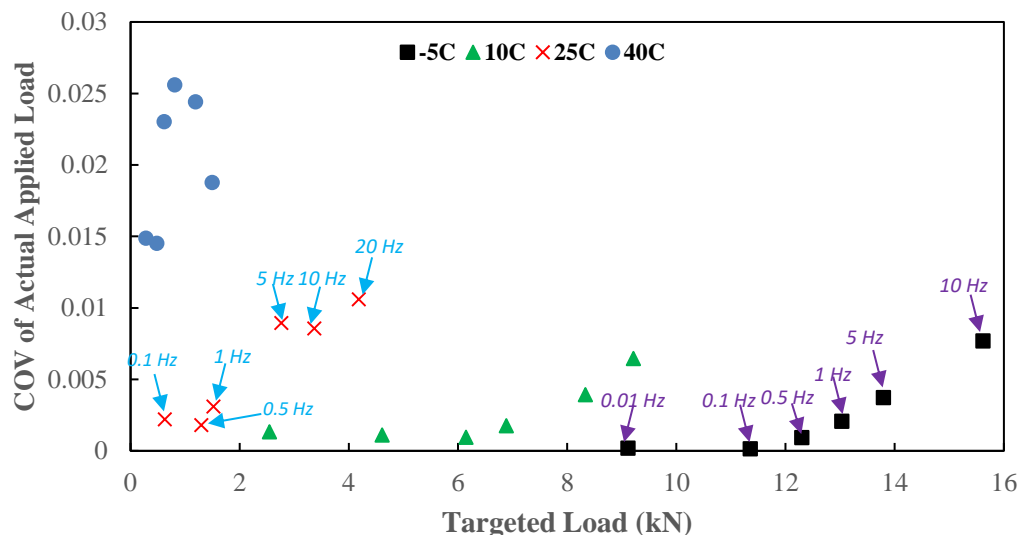


Figure 56. COV of applied load at different frequencies and temperature of E* testing.

Few factors were assumed to affect the uncertainty in $|E^*|$; however, the presented results show that they have no effect. These include:

- The applied number of cycles becomes smaller as the frequency decreases as presented in Table 11. This is done to avoid any damage in the samples being tested where the stiffness of asphalt becomes lower as slower loading rates. So, the smaller number of cycles at smaller frequencies might not influence reaching equilibrium which could be a source of uncertainty in $|E^*|$.
- For all complex modulus tests in this thesis, the data logging rate is fixed to 50 points per cycles regardless of the frequency. This, the number of point per second decreases as the frequency becomes smaller. Even though less points per second are used to fit

the data for low frequencies, the data logging rate has no effect the uncertainty in the load and thus $|E^*|$. So, it is not needed to increase the number of point per cycle being 50 as the frequency becomes smaller.

In addition, the effect of displacement measurement on the uncertainty of $|E^*|$ is studied. This is carried out to check whether there is any variability induced by the LVDTs, its mounting scheme (basically L-mounted assemblies glued on the specimen), data acquisition, and fitting to calculate $|E^*|$. This can't be done based on the data collected from E^* testing of asphalt samples because strain is not an input but a response to a given applied load and thus it is a function of the material's stiffness. Therefore, a simple setup has been designed as shown in Figure 57. This setup constitutes mounting of the same LVDTs used in E^* testing on a hollow steel samples. The LVDTs are mounted by gluing the same L shaped assemblies on the steel sample to measure the deformation over a gauge length of 100 mm (same gauge length used for asphalt testing in this research). The sample is chosen as a hollow steel sample to ensure that the response strain will be in range of 70-75 microstrains which is the same for strain levels targeted in E^* testing. The material is selected as steel because it has low variability especially at such levels of strain. Thus, it is assumed that any detected variability will be due to the LVDTs, displacement fitting, and LVDT's mounting system and especially detecting if the glue is affected by the loading rate and temperature. To achieve this goal, the same testing protocol used in E^* testing of asphalt concrete is performed on the steel sample but with a constant load of 22 kN for all combinations of temperature and frequency. The test implied applying a large number of cycles per sweep beyond that applied in E^* testing of asphalt concrete. For each combination of temperature and frequency, the data of the cycles beyond that applied in E^* testing are fitted. The average of every five cycles are calculated assuring that at least 10 points of average strains are obtained for every combination of frequency and temperature.

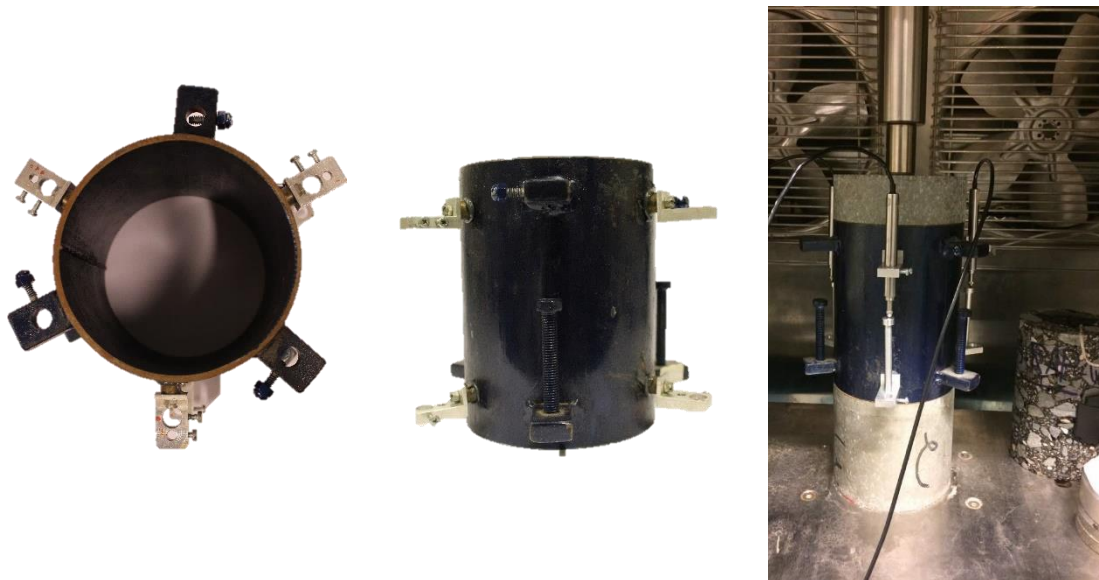


Figure 57. Hollow steel sample used for checking the effect of LVDTs and their mounting setup on the uncertainty in E^* testing.

The results of COV of the measured displacement are presented for every combination of temperature and frequency in Figure 58. It is worth mentioning that the COV of displacement, and namely COV of strain, is scattered without a clear trend with respect to temperature and frequency. The COV of strain is very low and falls in the range of $1.5E-3$ to $4.8E-3$ and thus it can be concluded that neither the LVDTs nor its mounting system (i.e. basically glue) influence the uncertainty in $|E^*|$ or other measured properties of asphalt concrete. Even though the COV is very low and there is not a striking trend that could be observed. However, if one wants to dig deeper in the obtained results, it can be observed that generally a higher COV is obtained at -5°C . This could be mainly due to the possibility of frost at -5°C which might cause more friction hindering the movement of the spring inside the LVDT. Such an effect will be more dominant at slow rates except for 10 Hz where other types of errors might have taken place.

Therefore, it can be concluded that the modeled uncertainty in $|E^*|$ is solely related to the heterogenous composition of asphalt concrete. The uncertainty in $|E^*|$ is not affected by the instrumentation nor machine used for testing. This assures that current practices for conducting E^* does not require any modification to reduce the uncertainty in $|E^*|$. It is worth noting that all the analysis in this research is based on three on-specimen mounted LVDTs. This issue could be addressed in future studied to check whether the use of four LVDTs instead of three affect the results and especially the uncertainty in $|E^*|$.

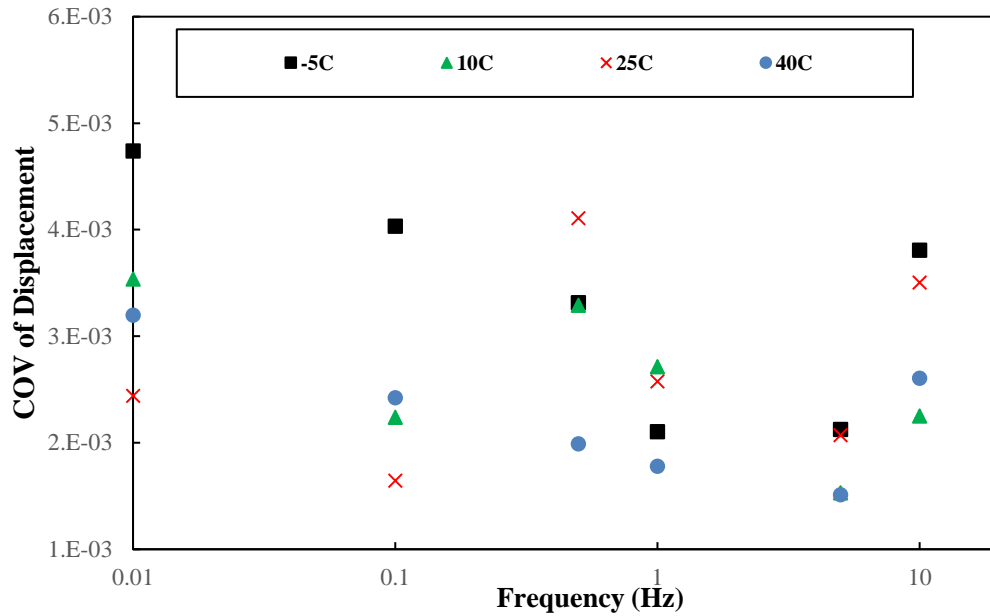


Figure 58. COV of measured displacement using on-specimen mounted LVDTs for a hollow steel sample.

6.4.2 Inherent Uncertainty in $E(t)$ and $D(t)$

6.4.2.1 $E'(w)$, $E(t)$, $D(t)$ Data

In this part, the same experimental data used for quantifying the uncertainty in $|E^*|$ is utilized for quantifying that in $E'(w)$, $E(t)$, and $D(t)$. The quantified uncertainty for $|E^*|$ can be propagated into that of the other LVE functions as a function of reduced time or frequency; however, it is required to present $E(t)$ and $D(t)$ in a probabilistic form i.e. in terms of its Prony series coefficients to be incorporated into convolution integrals to propagate it into the predictions by VECD model. The Prony series of $E(t)$ and $D(t)$ are fitted for each replicate and the uncertainty is quantified in terms of that of each of the Prony coefficients. The conversion of the experimental E^* data to $E(t)$ is done through $E'(w)$ and not $|E^*|$ alone so that it incorporates both the $|E^*|$ and the phase angle components. To study the variability imposed by the phase angle on the different used LVE functions, the inherent uncertainty in $E'(w)$ is investigated. $E'(w)$ is calculated and fitted for each replicate using the standard sigmoidal function with four parameters as used for $|E^*|$ and presented in Equation 88.

$$\log E'(w) = \delta + \frac{\alpha}{1 + e^{\beta + \gamma \log(w_r)}} \quad \text{Equation 88}$$

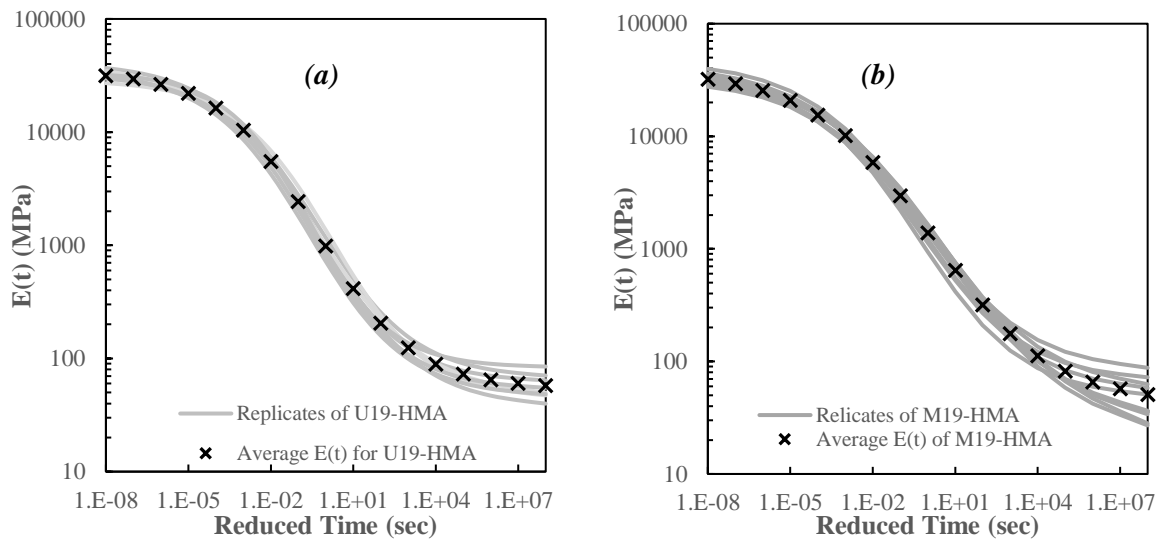
where:

$E'(w)$: storage modulus (MPa)

δ , α , β , and γ : fitting parameters

w_r : Reduced angular frequency (rad/sec) at a reference temperature $T_0 = 25^\circ\text{C}$

$E'(w)$ is required for the conversion into $E(t)$ using both the Approximate method and Exact method as presented earlier. However, $D(t)$ is determined through $E(t)$ that is obtained using the Approximate method. For each replicate, $E(t)$ and $D(t)$ are fitted in the range of 10^{-8} to 10^{+8} seconds using Prony series with 18 coefficients as expressed by Equation 16 and Equation 19, respectively. The relaxation and retardation times have been assumed deterministic with fixed values. However, the regression coefficients of $E(t)$ and $D(t)$ are determined by collocation for certain points of time for the data of each function (Mun et al. 2007). These coefficients vary from one sample to another of the same mix due to the inherent uncertainty that is present in these material properties. The plots presented in Figure 59 and Figure 60 show the scatter of each of these functions around its mean where high variability between the replicates of each mix can be observed at large reduced times. For both $E(t)$ and $D(t)$, this variability shows a high magnitude for the U19-WMA-SonneWarmix and the U25-HMA as compared to U19-HMA. This variability needs to be quantified and modeled to provide a probabilistic Prony representation of each of $E(t)$ and $D(t)$. The variability could be modeled using probabilistic Prony coefficients that can model the uncertainty of $E(t)$ and $D(t)$ at any given reduced time.



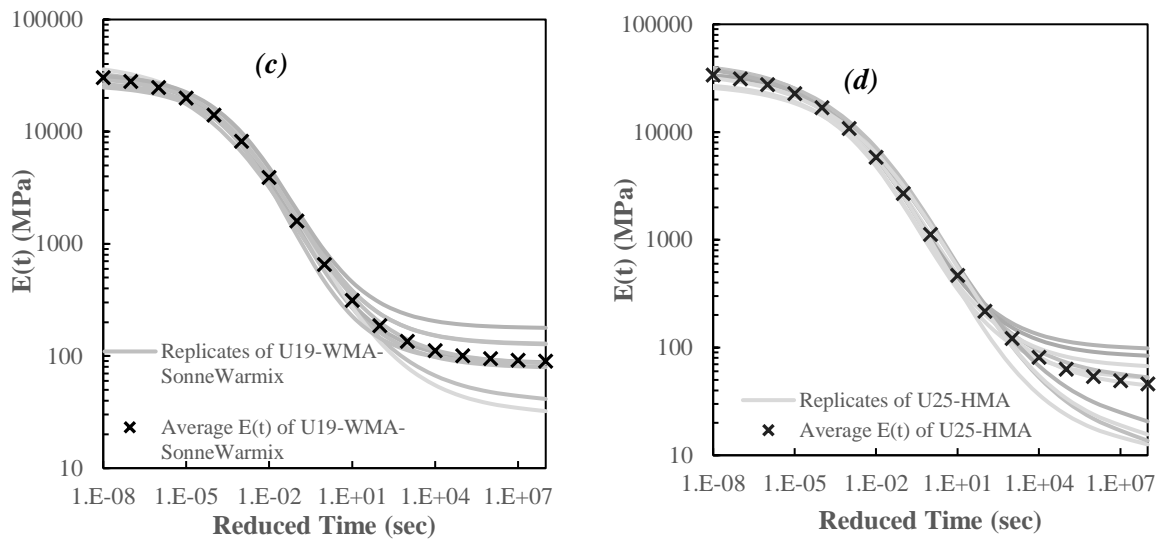


Figure 59. Mastercruves of $E(t)$ replicates and averages for a) U19-HMA, b) M19-HMA, c) U19-WMA-SonneWarmix, and d) U25-HMA.

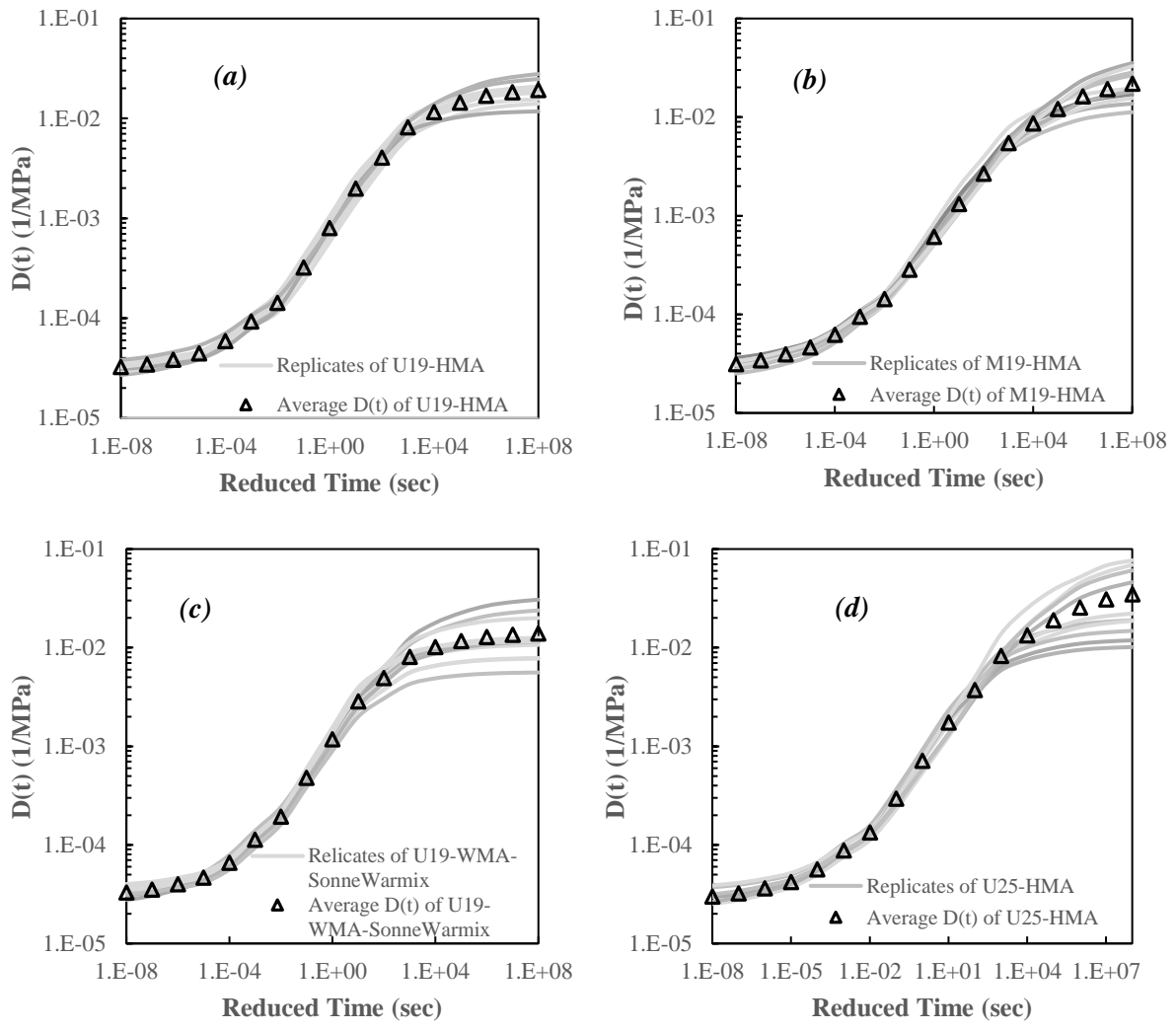


Figure 60. Mastercruves of $D(t)$ replicates and averages for a) U19-HMA, b) M19-HMA, c) U19-WMA-SonneWarmix, and d) U25-HMA.

6.4.2.2 Probabilistic Model of E' , $E(t)$ and $D(t)$

The inherent variability in E' is modeled probabilistically using the same approach followed for $|E^*|$ in the previous sections through the mastercurves' fitted parameters (α , γ , β , and δ) as presented in Equation 88. For each replicate, the parameters of the sigmoidal function of E' are determined and the mean and standard deviation of the parameters of each mix are quantified. In addition, the correlation coefficients for the different pairs of parameters are calculated to define the structure of the covariance matrix as presented in Table 30. Similar to the case of $|E^*|$, the results show that the correlation coefficients between the different pairs of parameters vary in both magnitude and sense from one mix to the another. The same as for the case of $|E^*|$, it can be observed that γ and α exhibit strong positive correlations irrespective of the mix. Also, the couples “ δ - γ ”, “ β - γ ”, and “ β - α ” are observed to be negatively correlated for all mixes. After quantifying the first and second moments, the probabilistic models of the four parameters are finalized by determining their probability distributions. Similar to $|E^*|$, the normal distribution provided a realistic fit of all the model parameters and thus it has been adopted to model the probability distribution of each of α , γ , β , and δ .

Table 30. Components of the Mean Vector, Standard Deviation Vector, and Correlation Matrices For the Fitting Coefficients of $E'(w)$.

Mix		U19-HMA	M19-HMA	U19-WMA-SonneWarmix	U25-HMA
δ	Mean	4.534	4.570	4.520	4.569
	Std Dev.	0.053	0.045	0.057	0.079
α	Mean	-2.782	-2.915	-2.609	-2.922
	Std Dev.	0.151	0.200	0.278	0.366
β	Mean	-0.106	0.131	-0.516	-0.011
	Std Dev.	0.178	0.182	0.170	0.236
γ	Mean	0.574	0.469	0.621	0.546
	Std Dev.	0.045	0.045	0.063	0.054
Correlation Coefficient	δ - δ	1.00	1.00	1.00	1.00
	δ - α	-0.46	0.04	-0.79	-0.63
	δ - β	-0.28	-0.06	0.71	0.27
	δ - γ	-0.43	-0.16	-0.81	-0.58
	α - α	1.00	1.00	1.00	1.00
	α - β	-0.56	-0.90	-0.86	-0.85
	α - γ	0.84	0.89	0.90	0.90
	β - β	1.00	1.00	1.00	1.00
	β - γ	-0.49	-0.92	-0.93	-0.89
	γ - γ	1.00	1.00	1.00	1.00

For each of $E(t)$ and $D(t)$, the inherent variability is modeled probabilistically in terms of the Prony coefficients (E_1, E_2, \dots, E_{17} , and E_∞) and (D_1, D_2, \dots, D_{17} , and D_0), respectively. The

mean and standard deviation for each of the Prony coefficients are calculated for each of the mixes. Also, the correlation coefficients between the different pairs of the Prony coefficients are determined to define the covariance structure represented by a matrix of size 18×18 .

The mean, standard deviation, and a sample subset of the correlation matrix of the obtained Prony coefficients of $E(t)$ are presented in Table 31. Almost the COV of all the coefficients for the four mixes fall in the range of 0.1-0.5 except for E_{inf} for the U25-HMA having a value of 0.72. It varies from one coefficient to the another within the same mix. The COVs of each of Prony coefficients, except E_{inf} , does not show high variability from one mix to another. In addition, the magnitude and sense of the correlation coefficients between the different pairs of Prony coefficients for $E(t)$ do not show a trend as they vary from one mix to the other. For example, the coefficient of correlation between E_8 and E_2 is -0.59 for the U19-HMA but 0.52 for U25-HMA. Some of the pairs are strongly correlated with a magnitude of 0.99 which is especially the case for any coefficient E_i and the coefficients preceding and following it like E_{i-1} and E_{i+1} , respectively. Other pairs of coefficients are weakly correlated with coefficients that are very close to zero like the case between E_{13} and E_2 for M19-HMA and U19-WMA-SonneWarmix. For the same parameters, the correlation coefficients might vary from one mix to the other. Thus, the correlation matrix of the Prony coefficients of $E(t)$ can be considered a property of the investigated mix and it is required in uncertainty propagation to describe the relationship existing between those coefficients.

To complete the probabilistic model of the Prony coefficients, the best-fit probability distribution is checked using the Shapiro-Wilk Normality Test with a significance level of 0.05. The results show that for the coefficients of $E(t)$ corresponding to the four investigated mixes, the normal and lognormal distributions provide an acceptable fit. The selection of the normal or lognormal distribution varies from one coefficient to another and between the mixes as presented in Table 32. In general, it can be observed that the variety of the coefficients of U19-HMA and M19-HMA are best fitted using the lognormal distribution; whereas, that of U19-WMA-SonneWarmix and U25-HMA tends more towards being fitted using the normal distribution.

Table 31. Mean, standard deviation, and part of correlation matrix between the Prony Coefficients of E(t) for the four investigated mixes.

	U19-HMA				M19-HMA				U19-WMA-SonneWarmmix				U25-HMA			
	Average	COV	Correlation with E1	Correlation with E2	Average	COV	Correlation with E1	Correlation with E2	Average	COV	Correlation with E1	Correlation with E2	Average	COV	Correlation with E1	Correlation with E2
E1	1623.9	0.38	1.000	0.996	2355.4	0.22	1.000	0.966	1685.9	0.42	1.000	0.995	2097.1	0.37	1.000	0.990
E2	2528.5	0.31	0.996	1.000	3210.4	0.18	0.966	1.000	2699.6	0.32	0.995	1.000	3059.0	0.30	0.990	1.000
E3	3837.1	0.24	0.973	0.990	4277.0	0.16	0.835	0.949	4174.9	0.22	0.965	0.986	4367.8	0.23	0.943	0.980
E4	5280.7	0.16	0.880	0.918	5202.4	0.14	0.598	0.784	5736.1	0.12	0.804	0.856	5684.0	0.18	0.804	0.877
E5	6202.4	0.11	0.507	0.573	5549.5	0.13	0.321	0.549	6436.5	0.08	0.076	0.161	6383.7	0.14	0.535	0.639
E6	5729.9	0.10	-0.254	-0.196	4958.6	0.12	0.052	0.271	5306.6	0.10	-0.514	-0.454	5765.3	0.11	0.301	0.404
E7	3880.3	0.12	-0.632	-0.628	3589.7	0.13	-0.156	-0.050	3026.1	0.12	-0.511	-0.477	3953.1	0.09	0.395	0.434
E8	1918.0	0.17	-0.545	-0.586	2104.7	0.19	-0.185	-0.211	1263.3	0.13	-0.242	-0.228	2054.3	0.13	0.578	0.517
E9	757.1	0.22	-0.355	-0.417	1040.1	0.28	-0.151	-0.238	455.2	0.15	-0.007	-0.009	866.6	0.21	0.597	0.510
E10	276.2	0.24	-0.193	-0.263	463.4	0.34	-0.120	-0.231	166.6	0.17	0.063	0.053	330.6	0.26	0.591	0.499
E11	105.2	0.23	-0.050	-0.124	200.3	0.37	-0.095	-0.214	66.9	0.18	0.050	0.036	126.2	0.26	0.567	0.477
E12	44.1	0.22	0.080	0.005	89.0	0.36	-0.074	-0.192	29.6	0.19	0.050	0.034	51.5	0.23	0.510	0.428
E13	20.4	0.22	0.199	0.126	42.1	0.34	-0.057	-0.169	14.1	0.19	0.109	0.092	23.0	0.20	0.419	0.353
E14	10.1	0.22	0.305	0.234	21.2	0.32	-0.042	-0.145	7.1	0.20	0.225	0.207	11.1	0.19	0.330	0.282
E15	5.5	0.24	0.422	0.353	12.0	0.31	-0.013	-0.112	3.8	0.22	0.420	0.400	6.0	0.20	0.323	0.285
E16	2.2	0.23	0.384	0.316	4.5	0.30	-0.072	-0.146	1.5	0.21	0.364	0.346	2.3	0.19	0.149	0.131
E17	4.2	0.35	0.648	0.586	11.4	0.32	0.126	-0.002	2.6	0.34	0.818	0.791	4.9	0.28	0.571	0.516
Einf	54.9	0.28	-0.568	-0.539	44.4	0.46	-0.296	-0.059	88.6	0.48	-0.777	-0.779	43.2	0.72	-0.706	-0.617

Table 32. Distribution of the Prony Coefficients of E(t) for the four investigated mixes.

	E1/E2/E3	E4	E5	E6	E7	E8	E9	E10	E11	E12	E13/E14/E15/E16	E17	Einf
U19-HMA	LN	N	N	LN	N	LN	LN	LN	LN	LN	LN	LN	N
M19-HMA	LN	LN	LN	LN	LN	LN	LN	LN	LN	LN	LN	LN	LN
U19-WMA-SonneWarmmix	LN	N	N	N	N	N	N	N	N	N	N	N	LN
U25-HMA	N	N	N	N	N	N	LN	LN	LN	LN	N	LN	N

N=Normal, LN=LogNormal

Similar to the case of E(t), the same exercise is required for the Prony coefficients of D(t). The mean, standard deviation, and the 18x18 correlation matrix are determined for the coefficients of every mix as presented in Table 33. It can be observed that the COVs of each of the coefficients is close for the different mixes. For example, the COV of D6 is 0.15, 0.13,

0.14, and 0.14 for the U19-HMA, the M19-HMA, the U19-WMA-SonneWarmix, and the U25-HMA mix, respectively. This pattern is only violated for the case of D13, D15, and D17 of the U19-WMA-SonneWarmix. For the correlation coefficients, some paris have a very strong correlation with a coefficient of 0.99 while others have no correlation with a coefficient around zero. The magnitude and sense of the correlation coefficients vary depending on both the investigated coefficient and the mix. A pattern of variation between one mix and the other can be observed for some coefficients but not all of them. For example, the correlation coefficient between D1 and D3 is larger than 0.9 for the four mixes, the correlation between D1 and D4 is around 0.8 for all mixes except U25-HMA being 0.5.

In addition, the Shapiro-Wilk Normality Test is conducted to determine the probability distribution that best fit each of the Prony coefficients of $D(t)$. By determining the distribution, the probabilistic model of each of the Prony coefficients is being completely developed which allows the propagation of the uncertainty of each of these coefficients into that of $D(t)$ as a function of reduced time. Similar to $E(t)$ and for all mixes, the normal and lognormal distributions are found to fit the distribution of these coefficients as presented in Table 34. For any of the coefficients, either of the distributions can be used depending to the data of each mix. Thus, it cannot be concluded to assign one distribution to a certain coefficient regardless of the mix type.

Table 33. Mean, standard deviation, and part of correlation matrix between the Prony Coefficients of D(t) for the four investigated mixes.

	U19-HMA				M19-HMA				U19-WMA-SonneWarmix				U25-HMA			
	Average	COV	Correlation with D1	Correlation with D2	Average	COV	Correlation with D1	Correlation with D2	Average	COV	Correlation with D1	Correlation with D2	Average	COV	Correlation with D1	Correlation with D2
D1	6.5E-07	0.23	1.00	1.00	9.6E-07	0.18	1.00	1.00	7.1E-07	0.28	1.00	1.00	7.2E-07	0.18	1.00	1.00
D2	2.6E-06	0.24	1.00	1.00	3.8E-06	0.18	1.00	1.00	2.9E-06	0.29	1.00	1.00	2.8E-06	0.17	1.00	1.00
D3	4.3E-06	0.20	0.94	0.94	5.3E-06	0.13	0.94	0.95	5.3E-06	0.20	0.96	0.96	4.4E-06	0.11	0.92	0.93
D4	4.1E-06	0.28	0.79	0.78	6.1E-06	0.14	0.84	0.85	4.3E-06	0.40	0.83	0.83	4.6E-06	0.12	0.50	0.49
D5	1.7E-05	0.19	0.84	0.85	1.9E-05	0.11	0.71	0.72	2.2E-05	0.15	0.89	0.89	1.7E-05	0.09	0.48	0.50
D6	4.2E-05	0.15	0.74	0.76	3.9E-05	0.13	0.09	0.11	5.9E-05	0.14	0.72	0.73	4.0E-05	0.14	-0.36	-0.34
D7	1.8E-05	0.54	0.87	0.89	3.0E-05	0.14	0.81	0.83	3.8E-05	0.25	0.62	0.63	1.9E-05	0.22	0.60	0.62
D8	2.2E-04	0.19	0.38	0.40	1.7E-04	0.19	-0.23	-0.21	3.6E-04	0.16	0.19	0.20	2.0E-04	0.20	-0.59	-0.56
D9	4.6E-04	0.17	0.33	0.34	3.3E-04	0.19	-0.19	-0.18	6.5E-04	0.17	0.40	0.40	4.2E-04	0.16	-0.39	-0.37
D10	1.6E-03	0.26	-0.11	-0.09	8.2E-04	0.32	-0.42	-0.40	2.4E-03	0.24	0.12	0.12	1.2E-03	0.32	-0.67	-0.65
D11	1.8E-03	0.14	0.53	0.52	1.3E-03	0.16	0.13	0.14	1.5E-03	0.44	0.86	0.85	1.7E-03	0.20	0.50	0.51
D12	6.0E-03	0.18	0.39	0.38	3.9E-03	0.20	0.06	0.07	4.8E-03	0.48	0.77	0.76	6.5E-03	0.38	0.53	0.53
D13	1.2E-03	0.72	0.66	0.64	2.5E-03	0.44	0.85	0.85	1.5E-04	6.91	0.80	0.79	3.7E-03	0.98	0.74	0.73
D14	3.9E-03	0.25	0.60	0.58	4.1E-03	0.32	0.84	0.84	2.7E-03	0.64	0.79	0.78	6.9E-03	0.73	0.67	0.67
D15	1.2E-03	0.86	0.70	0.68	4.4E-03	0.71	0.86	0.85	9.2E-05	11.28	0.76	0.76	6.7E-03	1.21	0.71	0.69
D16	1.5E-03	0.23	0.66	0.64	2.2E-03	0.59	0.89	0.89	1.2E-03	0.59	0.79	0.78	5.0E-03	1.40	0.41	0.41
D17	4.6E-04	1.18	0.73	0.71	3.1E-03	0.87	0.87	0.87	-5.4E-05	-9.54	0.75	0.74	3.9E-03	1.52	0.63	0.60
Do	3.1E-05	0.10	-0.03	-0.06	3.0E-05	0.10	0.48	0.47	3.2E-05	0.11	-0.45	-0.44	2.9E-05	0.16	-0.14	-0.17

Table 34. Distribution of the Prony Coefficients of D(t) for the four investigated mixes.

	D1/D2	D3	D4	D5/D7	D6	D8	D9	D10/D12	D11	D13	D14/Do	D15	D16/D17
U19-HMA	LN	N	N	LN	N	N	LN	LN	LN	N	LN	N	N
M19-HMA	LN	LN	LN	LN	LN	LN	LN	LN	LN	LN	LN	LN	LN
U19-WMA-SonneWarmix	LN	LN	N	LN	LN	LN	LN	LN	N	LN	LN	LN	N
U25-HMA	N	N	N	N	LN	N	N	LN	LN	LN	LN	N	LN

N= Normal and LN= LNormal

6.4.2.3 Modeling of Uncertainty in E' , $E(t)$ and $D(t)$

The probabilistic model describing the uncertainty in the coefficients of the Prony series function allows for the quantification of the inherent variability in $E(t)$ and $D(t)$ for each mix. First Order Approximations and Monte Carlo Simulations with 500,000 realizations of each of the Prony coefficients are conducted to provide realistic estimates of

the mean and COV of each of $E(t)$ and $D(t)$ at any reduced time in the range of 10^{-8} to 10^8 sec using the relationships presented in Table 35.

Table 35. Relationships for First Order Approximation of $E(t)$ and $D(t)$.

Relaxation Modulus	$Y =$	$E(t) = E_{\infty} + \sum_{m=1}^M E_m e^{-t/\rho_m}$
	$X_i s =$	$E_{\infty}, E_1, E_2, \dots, E_{17}$ for $M=17$
	$E(Y) =$	$E(E(t)) = \mu_{E_{\infty}} + \sum_{m=1}^M \mu_{E_m} e^{-t/\rho_m}$
	$\frac{\partial E(t)}{\partial E_{\infty}} =$	1
	$\frac{\partial E(t)}{\partial E_m} =$	e^{-t/ρ_m}
Creep Compliance	$Y =$	$D(t) = D_o + \sum_{m=1}^M D_m [1 - e^{-t/\tau_m}]$
	$X_i s =$	$D_o, D_1, D_2, \dots, D_{17}$ for $M=17$
	$E(Y) =$	$E(D(t)) = \mu_{D_o} + \sum_{m=1}^M \mu_{D_m} [1 - e^{-t/\tau_m}]$
	$\frac{\partial D(t)}{\partial D_o} =$	1
	$\frac{\partial D(t)}{\partial D_m} =$	$1 - e^{-\frac{t}{\tau_m}}$

6.4.2.4 Uncertainty in E' (w)

For the case of E' , the inherent variability is quantified in terms of the four parameters of the sigmoidal function. The uncertainty of E' for all mixes, which is presented by the COV, increases as the reduced angular frequency decreases as presented in Figure 61 for both Monte Carlo simulations and First Order Approximation. The COV curves obtained for each mix using both Monte Carlo and First Approximation are close to each other with a difference obtained only for U25-HMA at low reduced angular frequencies i.e. mix and region with the highest COV. Therefore, First Order Approximation can be relied on in this case to quantify the uncertainty in E' unlike the case of $|E^*|$ where a large difference exists when compared with COV calculated by Monte Carlo especially in the region of extrapolation.

In general, it is observed that the COV of E' is constant for reduced angular frequencies larger than 1000 rad/sec regardless of the type of the mix. As the reduced angular frequency decreases, the COV of E' increases slightly before it becomes steeper at low values of reduced angular frequency and especially in the region of extrapolation. For reduced angular frequencies smaller than 0.1 rad/sec, the uncertainty of E' increases where Monte Carlo simulations yield COVs of 0.22, 0.28, 0.51, 0.63 at 10^{-6} rad/sec for the U19-HMA, M19-HMA, U19-WMA-Sonnewarmix, and U25-HMA, respectively. Therefore, it is expected to have higher effect of the uncertainty on the predicted performance when using E' especially at slow loading rates and/or high temperatures and it becomes more significant when using modified binders or a larger NMA.

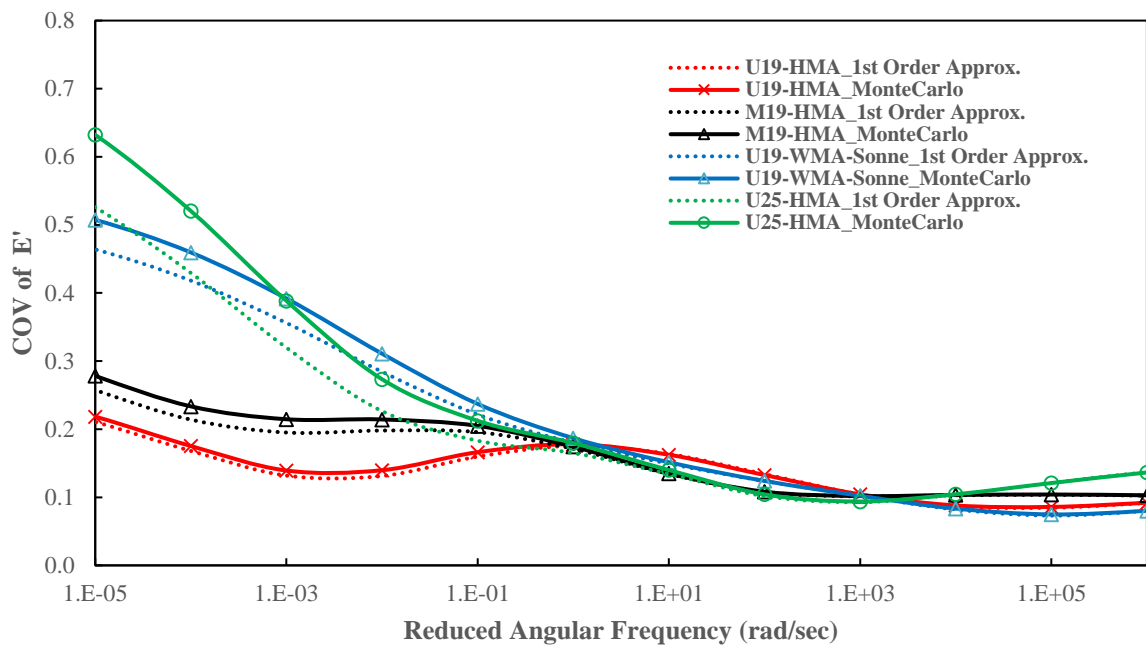


Figure 61. COV of storage modulus mastercurve as a function of reduced angular frequency for the four mixes.

By recalling the definition of E' , it is calculated as the product of $|E^*|$ and cosine of the phase angle at any reduced angular frequency. For comparison, the COV of $|E^*|$ is presented as a function of reduced angular frequency in Figure 62. For each mix, it can be observed that the COV of $|E'|$ follows the same trend as that of $|E^*|$ in terms of its variation with respect to the reduced angular frequency. In addition, the quantified uncertainty of E' is slightly lower than that of $|E^*|$ over the entire domain of angular frequency for each of the four mixes. This reduction in COV is about 0.1 for the M19-HMA, U25-HMA, and U19-WMA-Sonnewarmix and only 0.05 for U19-HMA which has the lowest COV over the entire domain of its mastercurve between 0.1 and 0.2.

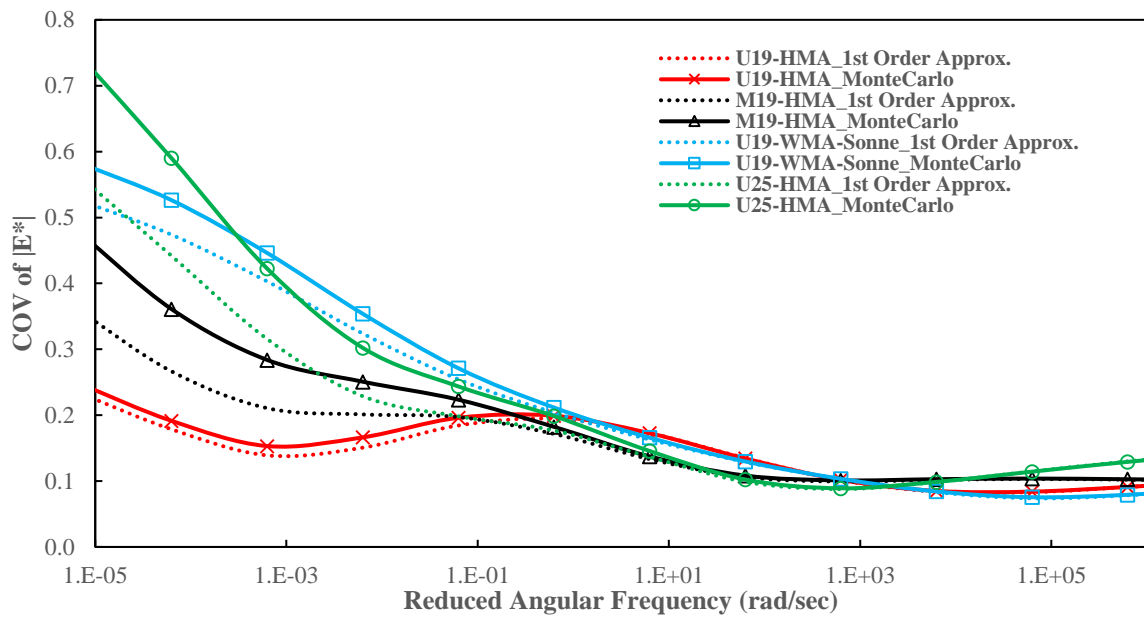
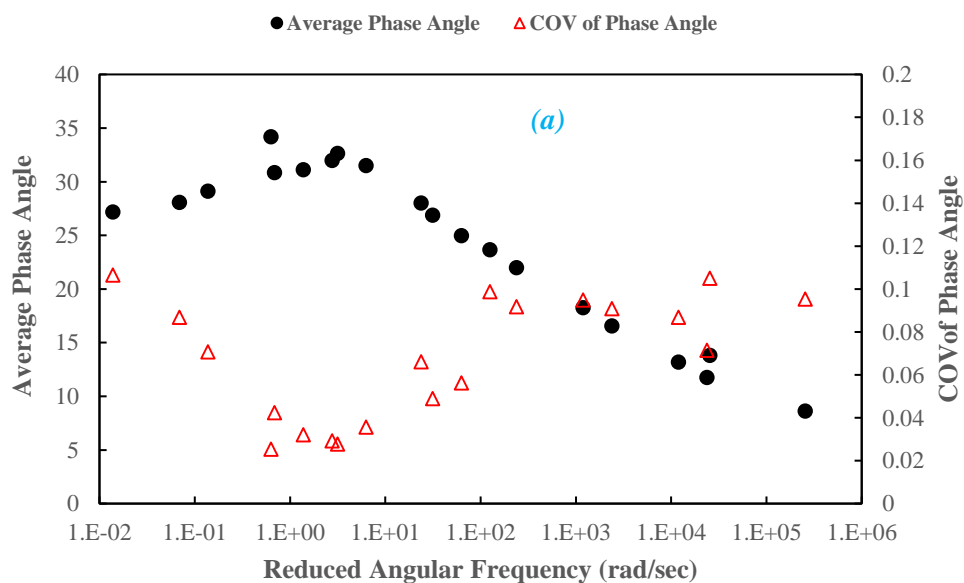


Figure 62. COV of $|E^*|$ mastercurve as a function of reduced angular frequency for the four mixes.

The uncertainty in E' accounts for both the variability in $|E^*|$ and phase angle, ϕ ; however, the results show that the uncertainty in E' is slightly lower than that in $|E^*|$ indicating that ϕ does not play a significant role in imposing more variability in E' . The variability of the phase angle and its cosine over the range of experimental data is shown in Figure 63 for the M19-HMA considered herein for illustration. It can be observed that the phase angle varies in the range of 5° to 35° with a COV ranging between 0.02 and 0.1. However, the cosine of the phase angle as presented in Figure 63-b varies between 0.83 and 0.99 with a very low COV not exceeding 0.03. Thus, E' is basically affected by the uncertainty of the cosine of the phase angle implying a minimal impact on the variability of E' which is basically governed by that of $|E^*|$.



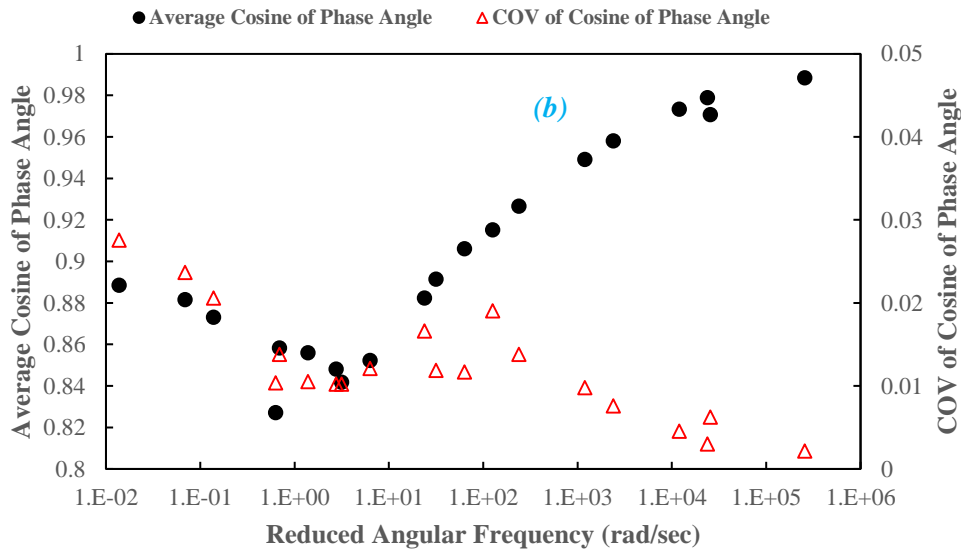


Figure 63. (a) Average and COV of phase angle and b) Average and COV of cosine of phase angle.

6.4.2.5 Uncertainty in $E(t)$

The inherent variability in $E(t)$ is quantified based on the probabilistic models describing the uncertainty in each of the Prony coefficients. Realistic estimates of the mean and COV of $E(t)$ at specified values of reduced time were determined using the simple First Order Approximation technique and the more advanced Monte Carlo simulation technique where 500,000 realizations of each of the 18 Prony coefficients were conducted.

For each mix, the average $E(t)$ mastercurves that are determined from the Monte Carlo simulations and the First Order Approximation method are found to be identical to the average mastercurves of the different replicates. These results show that the Prony series representation of $E(t)$ is realistic and representative of the mixes in this study. The variation of the COV of $E(t)$ as a function of reduced time indicates that the First Order Approximation and the Monte Carlo results yield the same COV irrespective of the range of reduced time. This observation is important since it indicates that the simple First Order Approximation is sufficient for quantifying the uncertainty in $E(t)$ without the need for Monte Carlo simulations which require higher computational efforts.

It is interesting to note that the First Order Approximation failed at providing acceptable results for the case of $|E^*|$ and E' particularly at small reduced frequencies (equivalent to large reduced times) for mixes having high uncertainty as shown in Figure 61 and Figure 62. This can be attributed to the non-linearity of the sigmoidal function used for representing $|E^*|$ and E' which renders the First Order Approximation incapable of modeling the high levels of uncertainty observed and this could be worse for other mixes having higher uncertainties compared to those investigated in this research. The mathematical formulation

leading to $E(t)$ and $D(t)$ seems to have eliminated this complexity resulting in better First Order Approximations for these two parameters.

It is noted that COV of $E(t)$ is also obtained using both the Exact method and Approximate. For all the four mixes, the results yield exactly the same means and COVs regardless of the method in which $E(t)$ is obtained. These results show that the uncertainty of $E(t)$ is not affected by the method used for interconversion.

In general, it can be observed that the COV of $E(t)$ increases as the reduced time increases as presented in Figure 64. For the four mixes, the relatively small COV at small reduced times increases rapidly for reduced times above 10^{-3} sec where it reaches at 10^8 seconds a maximum falling in the range of 0.22-0.66 depending on the type of the mix. It can be observed that COV of $E(t)$ for the M19-HMA mix is always higher than that of the reference mix U19-HMA. The COV of $E(t)$ reaches maxima of 0.22 and 0.26 at 1 seconds and 10^{-8} seconds for U19-HMA compared to 0.33 and 0.39 for M19-HMA. This indicates that the use of a polymer modified binder increases the uncertainty in $E(t)$ given that these two mixes have the same aggregate gradation, same level of air voids, and a very small difference in their asphalt content. Also, by comparing the COV of U19-HMA and U19-WMA-SonneWarmmix, the COV of $E(t)$ is the same for the two mixes for reduced times smaller than 10 seconds, after which that of U19-WMA-SonneWarmmix increases and become much larger reaching a value of 0.47 at 10^{-8} seconds. This shows that the addition of wax as a WMA additive could affect the COV of $E(t)$ at high reduced times i.e. at slow loading rates and/or high temperature. For the U25-HMA mix, the COV of $E(t)$ is slightly higher than that of the other mix at very small reduced times in the range of 10^{-8} - 10^{-3} seconds. For reduced times between 10^{-4} and 10^2 seconds, the COV of $E(t)$ is the same as that of U19-HMA where the two mixes have the same type of binder. For larger reduced time, the COV of $E(t)$ of U25-HMA increases where it becomes larger than of COV of $E(t)$ of all the other mixes. This indicates as the NMAS becomes larger, the COV of $E(t)$ become higher; slightly at low reduced times and significantly at large reduced times. The COV of $E(t)$ in the region of 10^{-2} and 10^2 seconds might be governed by the binder's type whether it is a neat binder or polymer modified. The effect of laboratory mixed additives on the COV of $E(t)$ appear to have an effect at high reduced times.

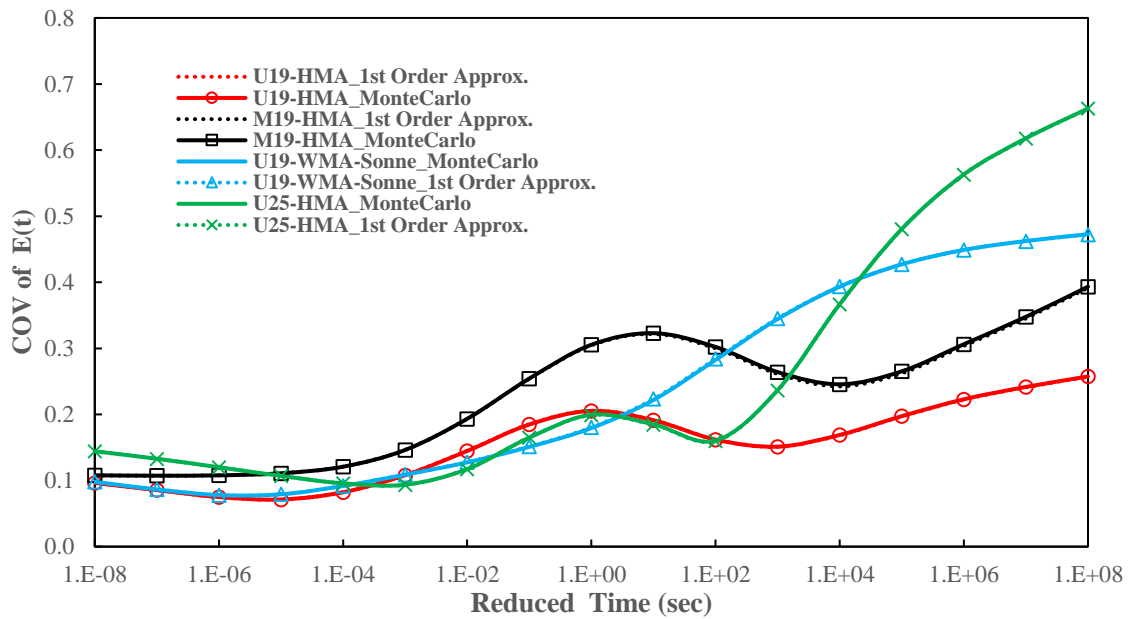


Figure 64. COV quantified by using First Order Approximation and Monte Carlo simulations for $E(t)$ calculated using the Exact method.

When comparing the COV curves of $E(t)$ with that of E' , it can be observed that it is equal for both responses at small reduced times. The behavior of the COV of $E(t)$ compared to E' differs from one mix to the other as the reduced time becomes larger. In general, as the reduced time increases, the COV of $E(t)$ starts to deviate from that of E' for all mixes except the U19-HMA which is the mix with the lowest uncertainty over the entire domain of reduced times analyzed. For the U25-HMA and U19-WMA-SonneWarmix, the COVs of $|E^*|$ and E' exceed that of $E(t)$ at reduced times larger than 5 seconds which is the region in which the NMAS and the WMA additives increase the uncertainty in $|E^*|$, E' , and $E(t)$ as stated earlier. The difference in COVs of $E(t)$ and E' becomes larger with the increase in reduced time for the U25-HMA compared to the U19-WMA-SonneWarmix. However, M19-HMA shows a distinct behavior when comparing the COV of E' and $E(t)$. The COVs are the same at very small and very larger reduced times. The COV of $E(t)$ is higher than that of E' especially in the region of 10^{-2} and 10^2 which is the region attributed to in the previous sections to show the effect of using neat or polymer modified binders on the uncertainties quantified for $|E^*|$, E' , and $E(t)$. The same pattern can be observed for all the mixes in the study. It should be noted that $E(t)$ is converted from E' . Thus, the uncertainty of $E(t)$ is expected to be a function of that of E' .

6.4.2.6 Uncertainty in $D(t)$

The inherent variability in $D(t)$ is quantified through the probabilistic models of the coefficients of its Prony series representation for $D(t)$ converted through $E(t)$. Similar to the case of $E(t)$, the COV is found to be the same using both the First Order Approximation and the Monte Carlo Simulations as presented in Figure 65. For each of the mixes in study, the

mean mastercurves of $D(t)$ calculated by either of the methods are identical to that calculated as the average of the single replicates for each mix. Like other LVE functions, the COV of $D(t)$ is almost constant at small reduced times and it increases with the increase in reduced time where it reaches relatively high values about 0.7 for the U25-HMA.

At reduced times smaller than 10^{-4} seconds, the COV of $D(t)$ is the same for all mixes with NMAS of 19.0 mm and slightly higher for the U25-HMA mixes. As the reduced time increases beyond 10^{-2} seconds, the COV of $D(t)$ increases similarly with the same magnitude for the four mixes reaching a value of 0.2 at 10 seconds. Then, the COV curves deviate from one mix to the other as the reduced time becomes larger. At larger reduced times, the COV of $D(t)$ follows the same pattern as that of the other LVE functions where it reaches the highest for the U25-HMA mix followed by the U19-WMA-Sonne-Warmix and then the M19-HMA with the least for the U19-HMA at a COV not exceeding 0.24. By comparing the COV of $D(t)$ to that of $E(t)$, it can be found out that there is not a significant difference over the entire range of time domain except for the M19-HMA. For the latter mix, the COV of $D(t)$ is smaller than that of $E(t)$ especially at medium to high reduced times.

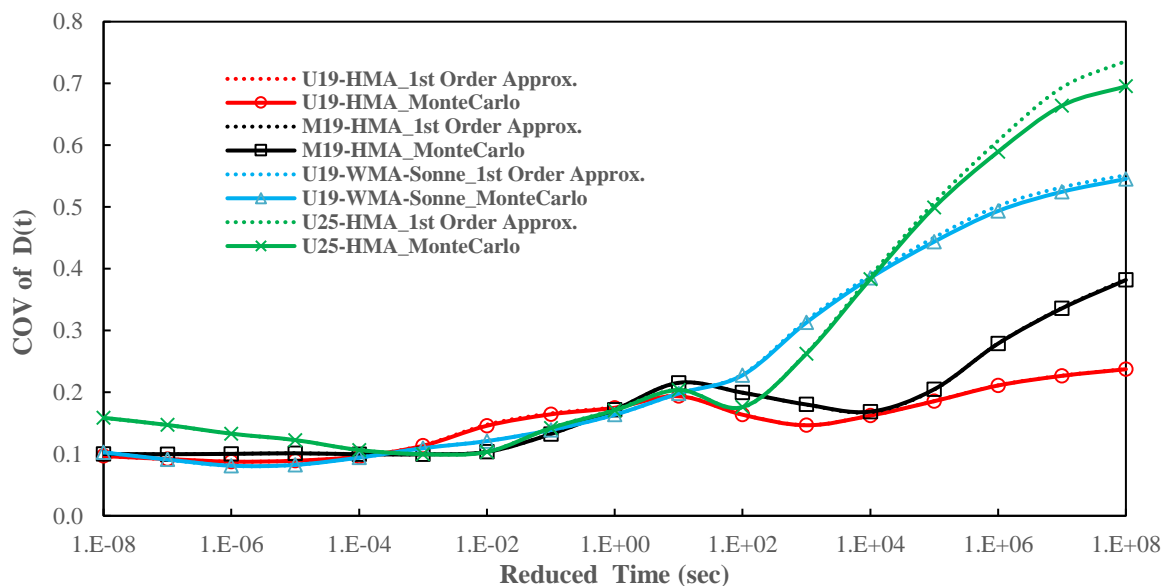


Figure 65. COV of $D(t)$ as a function of reduced time quantified based on First Order Approximation and Monte Carlo Simulations.

By recalling the method of conversion of E^* to $E(t)$ through $D(t)$, it can be found out that the uncertainty in $D(t)$ is not only a function of that of $E(t)$ but its slope too as presented in Equation 30. The slope of $E(t)$, as presented in Figure 66-a, increases as the reduced time become larger till reaching a maximum after which it decreases as the reduced time becomes larger. The slope of $E(t)$ reaches a maximum of 0.38 for all the U19-HMA, U19-WMA-SonneWarmix, and U25-HMA but a lower value of 0.33 for the M19-HMA. In addition, the COV of the slope of $E(t)$ decreases from 0.15-0.2 at a reduced time of 10^{-6} seconds till

reaching a minimum of 0.05 at 1 second at which it increases with a steep slope to reach maximum values in the range of 0.3-0.6 at high reduced times. It can be noted that COV of the slope of $E(t)$ is higher for both U25-HMA and U19-WMA-SonneWarmmix is higher than that of the U19-HMA and the M19-HMA mixes which is the same pattern that can be observed when comparing the COV of $D(t)$. Thus, the COV of $D(t)$ is a function of both $E(t)$ and its slope which explains the trend in COV of $D(t)$ at high reduced times. The decrease in the COV of $D(t)$ for M19-HMA at medium magnitudes of reduced time might be due to the higher values of the mean of slope of $E(t)$ accompanied with a slight increase in its COV in this same region of reduced times.

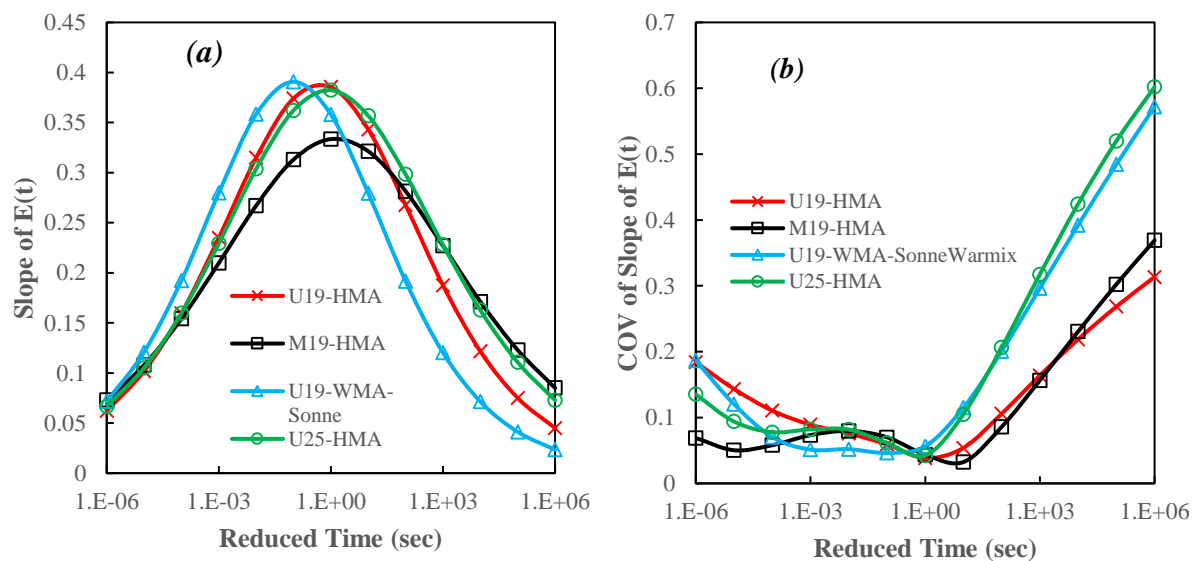
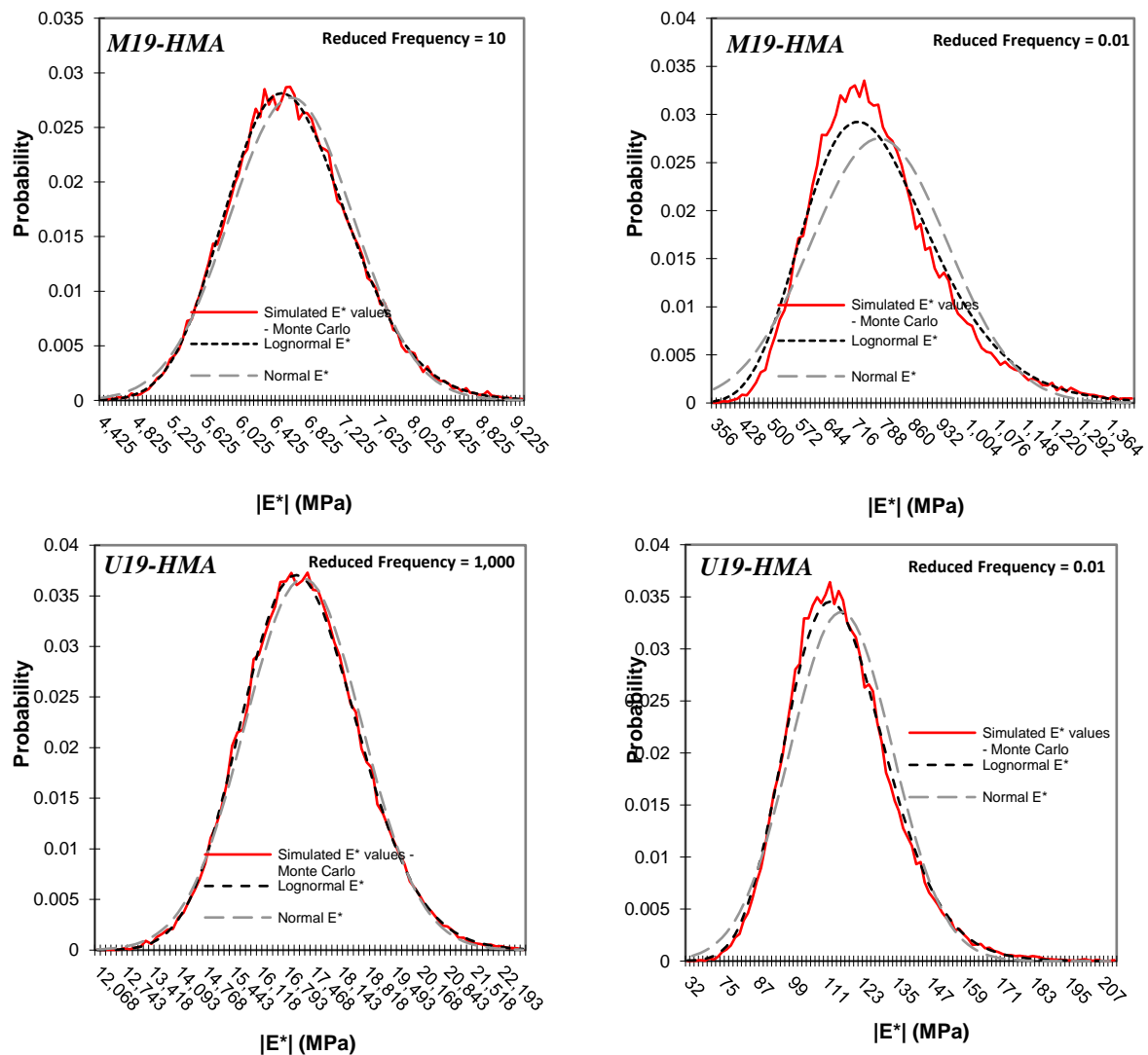


Figure 66. a) Slope of $E(t)$ as a function of reduced time and b) COV of slope of $E(t)$ as a function of reduced time.

6.4.3 Probability Distribution of LVE Functions

To complete the probabilistic model for the each of the LVE functions of the four investigated mixes, the probability distribution of each of these functions is assessed at different reduced times/frequencies. This might not be directly needed for the development of probabilistic mechanistic models especially that $E(t)$ or $D(t)$ will be used in terms of their Prony coefficients whose distributions are already determined. However, some applications that could be addressed in future work requires the distribution of such material properties and not only the mean and standard deviation. As such, the probability distribution functions (PDF) are plotted for the Monte Carlo results to present the uncertainty in $|E^*|$, $E(t)$, and $D(t)$ at different reduced times/frequencies. Sample PDFs are plotted along with the theoretical normal and lognormal distributions for mixes at different reduced frequencies for $|E^*|$ and different reduced times for $E(t)$ as shown in Figure 67 and Figure 68, respectively. Many of the cases especially for $|E^*|$ at high reduced frequencies and $E(t)$ at low reduced times, both the normal and lognormal distribution perfectly fits the data. However, the normal

distribution might not be representative of the actual distribution of data especially for cases of $|E^*|$ and $E(t)$ possessing high COVs i.e. at high reduced times/low reduced frequencies and especially for the case of U25-HMA and U19-WMA-SonneWarmmix. The results show that the lognormal distribution provides the best fit distribution for the cases of both $|E^*|$ and $E(t)$ at any reduced time/frequency and regardless of the type of the mix being analyzed. This has been further checked out using the Shapiro-Wilk Normality test for transformed data in the lognormal scale where the obtained p-values are larger than 0.05 indicating that $\log(|E^*|)$ and $\log(E(t))$ follow a normal distribution i.e. $|E^*|$ and $E(t)$ are lognormally distributed.



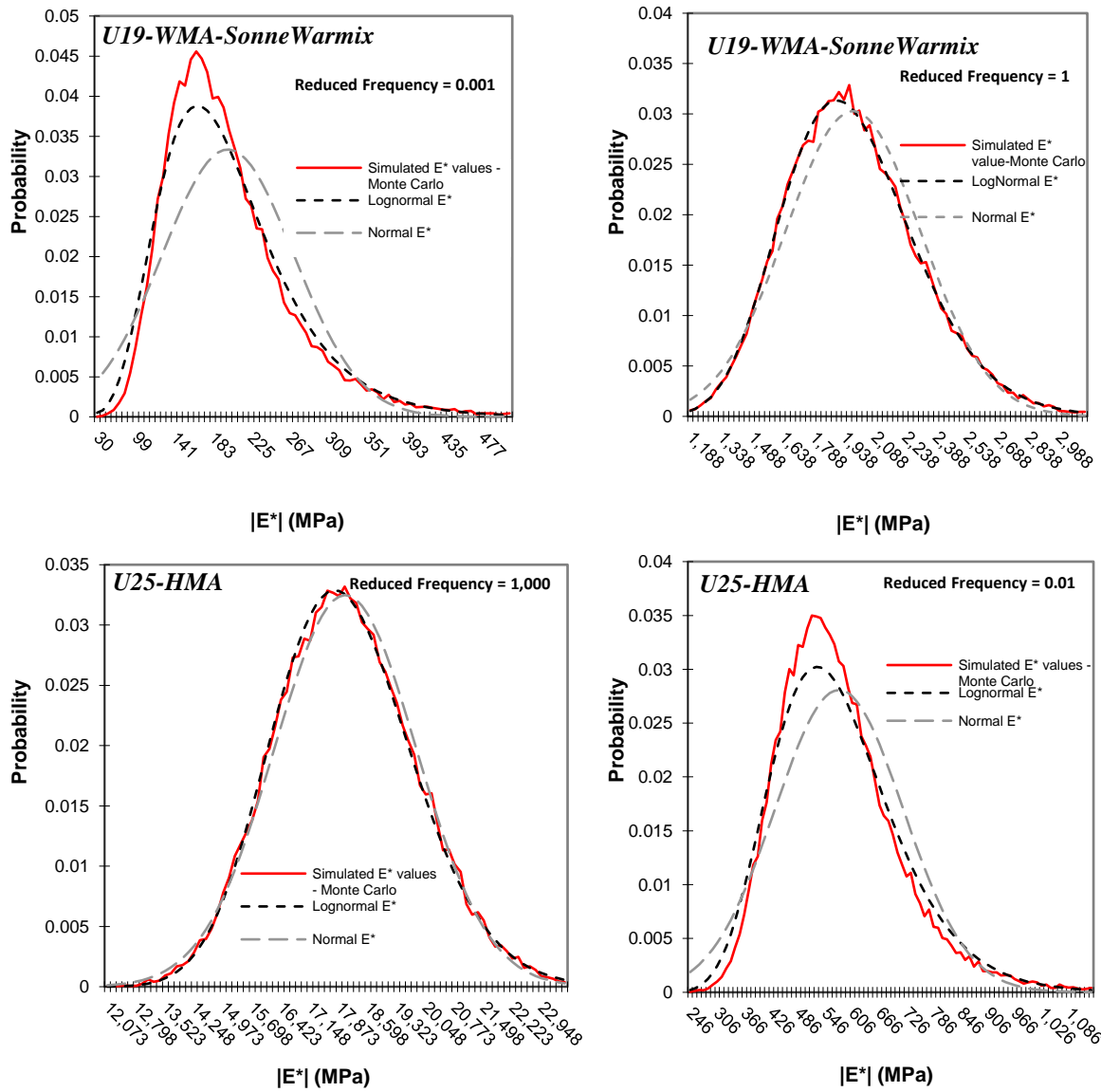
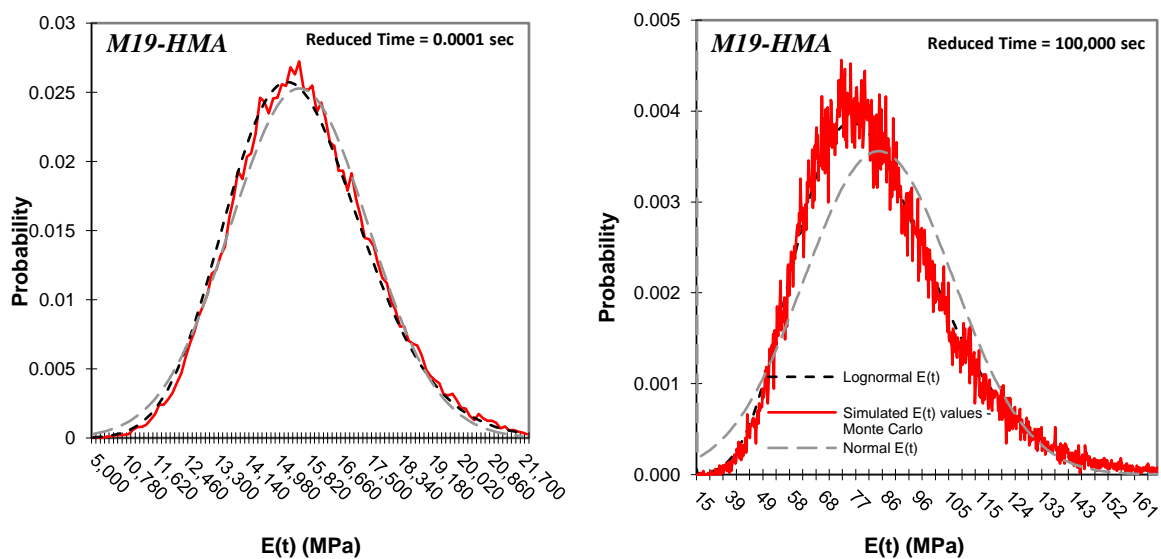


Figure 67. Probability distribution of $|E^*|$ for different reduced frequencies at a reference temperature of 25°C for the four mixes U19-HMA, M19-HMA, U19-WMA-SonneWarmix, and U25-HMA.



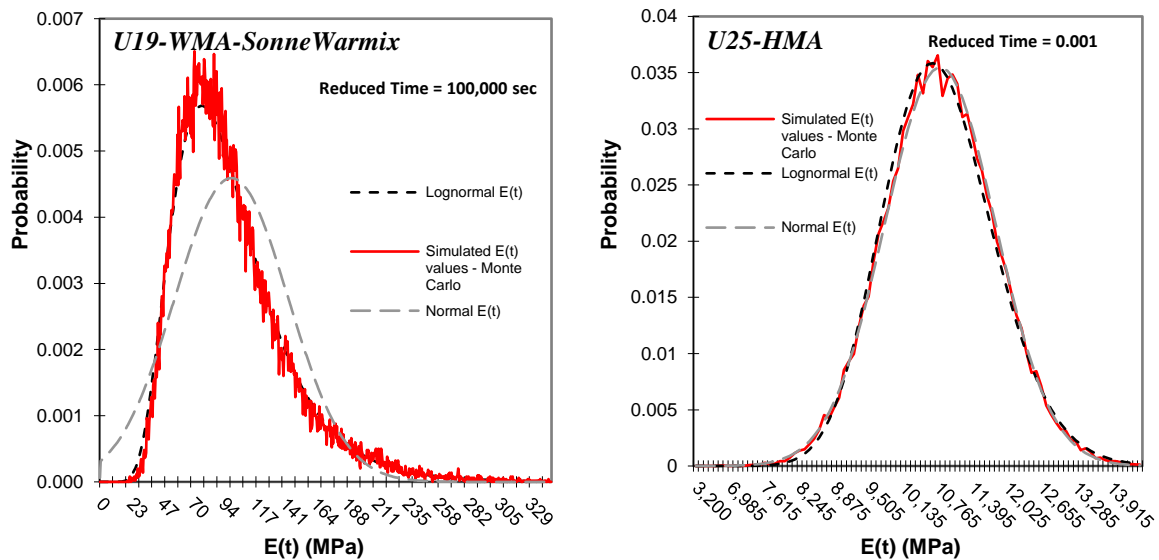


Figure 68. Probability distribution of $E(t)$ for different reduced times at a reference temperature of 25°C for the four mixes U19-HMA, M19-HMA, U19-WMA-SonneWarmix, and U25-HMA.

For the case of $D(t)$, similar results are obtained as shown by the p-values obtained by the Shapiro-Wilk Normality Tests conducted on $D(t)$ and $\log(D(t))$ at different reduced frequencies as presented in Table 36. The test is done to check normality on sample of $D(t)$ realizations extracted normally from the Monte Carlo Simulations. The results show that for the case of M19-HMA and U19-HMA, which are mixes with lower uncertainty compared to the two other mixes, both the Normal and Lognormal distributions can be used to fit the uncertainty in $D(t)$. However, this is applicable for the U25-HMA and U19-WMA-SonneWarmix especially at low reduced times which is the region where $D(t)$ have almost a low constant COV. As the reduced time increases, the p-value decreases to below 0.05 especially for the case of fitting the data by the normal distribution. However, in such cases the p-value for testing the lognormal distribution is high indicating that there isn't a strong evidence to reject the null hypothesis and thus the data can be fitted using this candidate solution. Therefore, it can be concluded that the lognormal distribution serves as an acceptable distribution for fitting the variability in $D(t)$ regardless of the type of the mix being investigated and the reduced time at which $D(t)$ needs to be fitted.

Table 36. p-values from Shapiro-Wilk Normality test for D(t) at different reduced times at a reference temperature of 25°C.

Reduced Time (second)	Distribution	M19-HMA	U19-HMA	U19-WMA-SonneWarmix	U25-HMA
0.00001	Normal	0.43	0.72	0.5	0.08
	Lognormal	0.14	0.87	0.38	0.7
0.001	Normal	0.95	0.59	0.77	0.13
	Lognormal	0.75	0.32	0.97	0.63
0.01	Normal	0.83	0.65	0.91	0.26
	Lognormal	0.78	0.55	0.76	0.91
1	Normal	0.56	0.4	0.37	0.88
	Lognormal	0.55	0.49	0.21	0.83
10	Normal	0.61	0.14	0.22	0.0035
	Lognormal	0.92	0.68	0.22	0.7543
1000	Normal	0.09	0.43	0.0001	0.002
	Lognormal	0.06	0.07	0.92	0.05
100000	Normal	0.41	0.97	0.00003	0.000399
	Lognormal	0.23	0.15	0.84	0.13

6.5 Inherent Uncertainty in Damage Characteristic Curve, C vs. S

6.5.1 Introduction

To develop a probabilistic model for the prediction of viscoelastic strains, it is needed to model and quantify the uncertainties in material properties resulting from both E^* and monotonic testing. The uncertainties in material properties resulting from E^* testing have been thoroughly covered in the previous sections fructifying probabilistic models for the required LVE functions: $|E^*|$, E' , $E(t)$ and $D(t)$ in terms of the fitting parameters of each of them and over the entire range of its mastercurve. To complement this towards a probabilistic VECD model, it is required to quantify and model the inherent uncertainty in the damage characteristic curves as presented in Figure 41. Typically, monotonic tests are conducted which allows for the development of two models to predict damage for any stress input and then predict the pseudostiffness associated with the resulting damage. Therefore, the aim of this part of the research is to model the uncertainty associated in the material properties and models required to predict the pseudostiffness for a given stress input through the damage parameter (S). This will be handled in a stepwise manner by modeling the uncertainty in C vs. S and S vs. Lebesgue Norm of Stress ($Leb(\sigma)$). Then, this will be then aggregated to model the uncertainty in C as a function of $Leb(\sigma)$ directly as S can be considered as an intermediate parameter that relates any input stress to C where the ratio of stress over C (i.e. pseudostrain) is required for predicting the viscoelastic strain over the time domain. When modeling the inherent uncertainty in C vs. $Leb(\sigma)$ and S vs. $Leb(\sigma)$, the stress is considered

deterministic. Also, in modeling the inherent uncertainty in C vs. S , the latter is taken deterministic. It is worth noting that it is sufficient to model the inherent uncertainty directly just for C vs. $\text{Leb}(\sigma)$; however, the inherent uncertainty is modeled for better understanding the problem.

6.5.2 *Inherent Uncertainty in C vs. S*

For each mix, ten replicates are tested using the constant crosshead test at three different rates at 5°C as summarized in Table 21. The rates are selected to be fast enough to ensure that the behavior is viscoelastic without the presence of viscoplasticity. Thus, the data of the replicates of each mix is pooled regardless of the rate being applied thus the inherent uncertainty modeled could account for any variability that might be inferred by the testing rate. Similar to the case of LVE region, deterministic time-temperature shift factors are used in shifting any data required in this part of the research.

6.5.2.1 C vs S Data

By recalling the C vs. S approach, viscoelastic behavior in the absence of viscoplasticity is characterized by Equation 89. Any reduction in the coefficient C , normalized pseudostiffness, is due to damage and thus it can be viewed as the damage effect. C varies from 1 for virgin material to 0 for the case of material in complete failure.

$$C(S) = \frac{\sigma}{I \times \varepsilon_R} = \frac{\sigma}{I \times \int_0^t E(t-\tau) \frac{d\varepsilon}{d\tau} d\tau} \quad \text{Equation 89}$$

The variable S , calculated as the Lebesgue norm of pseudostrain as presented in Equation 57, can be viewed as a global damage parameter (Chehab and Kim 2005). Basically; time, strain, and stress data from the monotonic tests along with $E(t)$ and “ α ” (function of maximum slope of LVE functions) from E^* tests are used to calculate both C and S and then determine their relationship fitted using an exponential function as presented by Equation 58. In addition, since in practice the strain input is unknown, S is related to stress through the Lebesgue norm of stress which can be fitted based on monotonic testing data as per Equation 60. One of the basic benefits of VECD model is the ability to collapse C vs. S curves at temperatures and rates where only the viscoelastic response is present. Typically, specimen-to-specimen variability is accounted for by normalizing the pseudostiffness by the initial pseudostiffness “ I ” where the ratio of pseudostrain to stress at low stress levels, typically below 500 kPa, is 1.0 as there is no damage in the LVE range (Daniel and Kim 2002). In addition, the calculation of pseudostrain requires $E(t)$ where the average $E(t)$ mastercurve is normalized based on $|E^*|$ fingerprint of each specimen used for monotonic testing. Despite

normalizing and fingerprinting, a scatter could be found in the C vs. S curves could show a scatter where the curves at a given temperature might not overlap completely due to the inherent uncertainties associated with stiffness and damage behavior of the replicates of a given mix as presented in Figure 69.

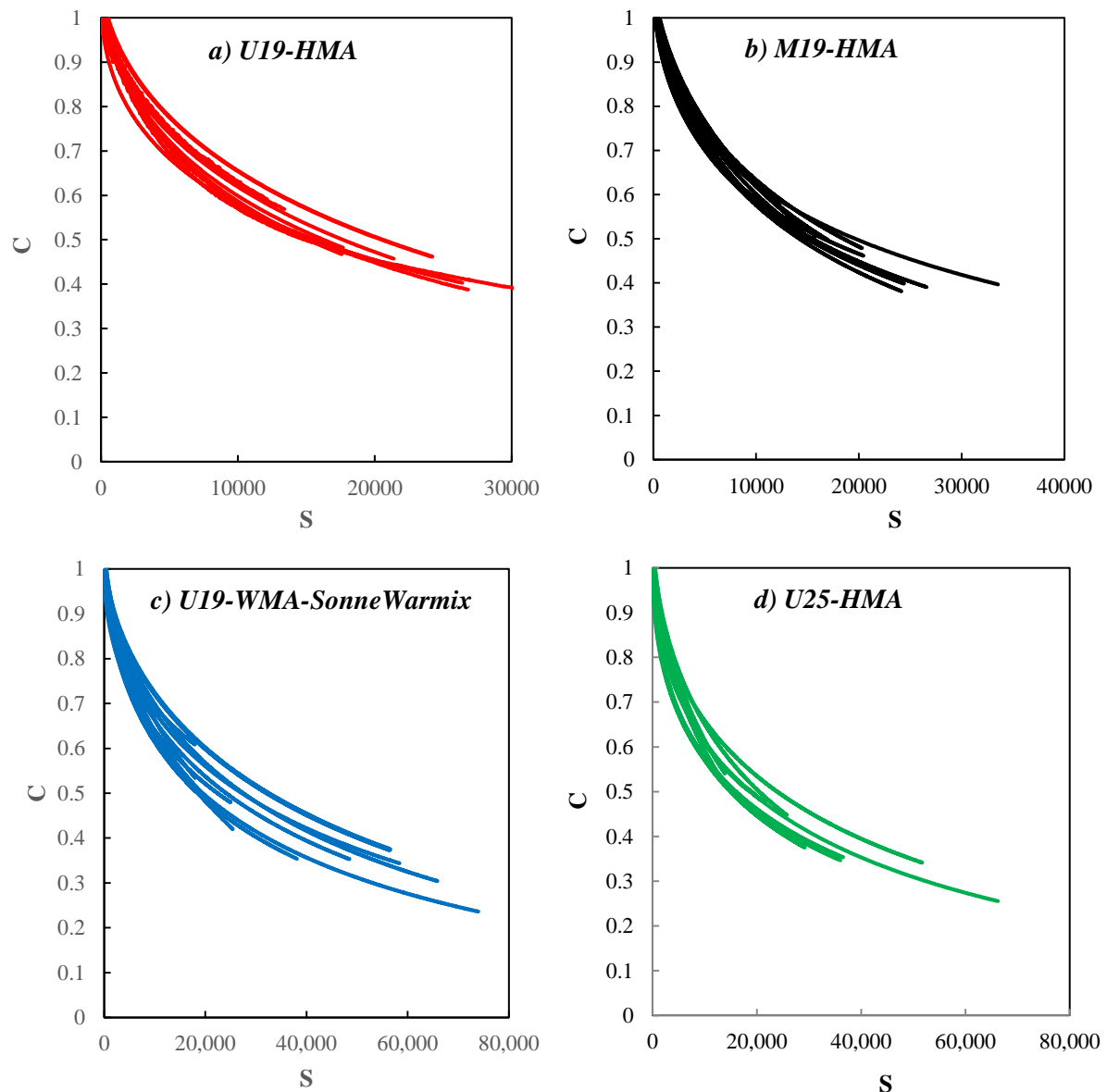


Figure 69. C vs. S plots of replicates tested for each of the ten replicates.

It can be observed that as C drops due to the increase in S, the scatter of C at a given value of S increases. Similarly, the same can be observed that as C drops and for a given value of C, the scatter of S increases. For any mix, the variability is minimal at low values of S because C has a value of 1.0. The plots show that the magnitude of the scatter is mix dependent. At C value of 0.5, S varies in the ranges of 15000-20000, 14500-19000, 19000-32000, and 15500-24300 for the U19-HMA, M19-HMA, U19-WMA-SonneWarmix, and U25-HMA mixes, respectively. This shows that the U19-WMA-SonneWarmix has a higher

variability as compared to the U19-HMA and M19-HMA mixes. Also, the U25-HMA shows a scatter with larger magnitude as compared to U19-HMA. Thus, the mix components affect the inherent uncertainty in C vs. S similar to the case of LVE function.

For the calculations of S, the maximum slope of LVE curve plotted as a function of time in logarithmic scale is required to calculate the parameter “ α ”. This parameter is need to characterize of the failure zone at the crack tip where α is calculated as the reciprocal of the maximum slope. As presented in Table 37 for $|E^*|$ and shown in Figure 66 for E(t), the mean of the maximum slope is around 0.43-0.45 for the U19-HMA, U19-WMA-SonneWarmix, and U25-HMA and about 0.37 for the M19-HMA. By analyzing its uncertainty, the COV of this slope if in the range for 0.04-0.06 for the four mixes based on data of ten replicates for each mix. Due to its low inherent uncertainty and for the sake of simplification, the parameter “ α ” is taken deterministic in the entire analysis.

Table 37. Mean and COV of maximum slope of $|E^*|$ curve based on 10 tested replicates for each mix.

	Mean Maximum Slope	COV of Maximum Slope
U19-HMA	0.437	0.05
M19-HMA	0.369	0.06
U19-WMA-SonneWarmix	0.452	0.06
U25-HMA	0.428	0.04

6.5.2.2 Probabilistic Model of C(S)

For each replicate, C and S are calculated based on data from monotonic test and using a normalized E(t) and a deterministic “ α ” from LVE characterization. For each mix, ten C vs. S curves will be developed and each will be fitted using the exponential model as presented in Equation 58 recalled as the following:

$$C(S) = ae^{b(S)^c}$$

Using this model, the obtained b values has an average falling between -4.0E-03 and -2.0E03 where the normal distribution best fits the data of this parameter. Thus, by simulating realizations of b it is high probable to get values larger than zero which yields wrong and unrealistic values of b. This, could be solved by using the truncated normal distribution that will serve as a conditional distribution restricting the domain of normal distribution to be only in the negative domain. To avoid such complexities, it was decided to modify the model in a way to restrict b to be in the positive domain using the alternative exponential model presented in Equation 90. Using this model, the parameter b is always positive and its variability is fitted using a lognormal distribution which solves the aforementioned problem.

$$C(S) = ae^{-b(S)^c} \quad \text{Equation 90}$$

The uncertainty in the normalized pseudostiffness C as a function of the damage parameter S is characterized in terms of the fitting parameters (a, b, and c) as per Equation

90. For each mix, the probabilistic model of each of the parameters is developed by determining its mean, standard deviation, and probability distribution as presented in Table 38. Also, the correlation coefficients of the pairs a-c, a-b, and b-c are calculated to define the structure of the covariance matrix which is required for uncertainty quantification.

The results show that the parameters a and c have low COVs around 0.03 and 0.1, respectively. However, the parameter b has a higher COV in the range of 0.4-0.7. For the four mixes, parameters a and c follow a normal distribution while parameter b is always lognormally distribution. Moreover, the results of the correlation coefficients show that there is not a pattern describing the magnitude and sense of correlation between a and the parameters b and c for the different investigated mixes. Also, there is not a strong correlation between a and either b or c where it varies between -0.5 and 0.5. However, it can be observed that the parameter b and c possess a strong negative correlation of magnitude around -0.95 regardless of the type of the mix.

It is worth noting that other forms of mathematical equations can be used to fit the C versus S data as the commonly used form $C = 1 - aS^b$ and thus the entire work in the section could be repeated in future works in order to check the effect of the type of model used on the uncertainty in the predicted C values.

Table 38. Mean, standard deviation, probability distribution, and correlation coefficients of parameters fitting the C vs. S curves.

Mix		U19-HMA	M19-HMA	U19-WMA-SonneWarmix	U25-HMA
a	Mean	1.072	1.066	1.057	1.045
	Std Dev.	0.028	0.022	0.027	0.032
	Dist.	Normal	Normal	Normal	Normal
b	Mean	3.74E-03	2.50E-03	3.15E-03	3.99E-03
	Std Dev.	2.53E-03	1.39E-03	1.27E-03	2.25E-03
	Dist.	LogNormal	LogNormal	LogNormal	LogNormal
c	Mean	0.562	0.603	0.554	0.549
	Std Dev.	0.053	0.054	0.044	0.060
	Dist.	Normal	Normal	Normal	Normal
Correlation Coefficient	a-b	0.535	-0.527	0.293	-0.356
	a-c	-0.529	0.563	-0.130	0.394
	b-c	-0.975	-0.977	-0.945	-0.939

6.5.2.3 Modeling of Uncertainty in C(S)

The parameters a, b, and c describing the relationship between C and S are considered as random variables whose uncertainty will be forward propagated to determine the inherent

uncertainty in C for any value of S. Similar to the case of LVE functions, the quantification is carried out using both First Order Approximation and Monte Carlo Simulations. The former method provides the mean and standard deviation of C at any value of S using the relationships in Table 39.

Table 39. Relationships to conduct First Order Approximation for C vs. S.

$Y =$	$C(S) = a \cdot e^{-b \cdot (S)^c}$
$X_i S =$	$a, b, \text{ and } c$
$E(Y) =$	$E(C(S)) = \mu_a \cdot e^{-\mu_b \cdot (S)^{\mu_c}}$
$\frac{\partial C(S)}{\partial a} =$	$e^{-b \cdot (S)^c}$
$\frac{\partial C(S)}{\partial b} =$	$-(S) \cdot a \cdot e^{-b \cdot (S)^c}$
$\frac{\partial C(S)}{\partial c} =$	$-(S)^c \cdot a \cdot e^{-b \cdot (S)^c} \cdot \ln(S)$

Using Monte Carlo simulations, 500,000 realizations of each of the three parameters are generated yielding 500,000 C vs. S curves. This allow for developing the probabilistic model of C as a function of S. One limitation of the models develop is its applicability to S values in the range of 0-25,000 corresponding to a drop in C between 1.0 and 0.4-0.5. This is due to availability of experimental data for the ten replicates of the four mixes in this range as shown in Figure 69.

The mean curves of C vs S obtained from First Order Approximation and Monte Carlo are presented in Figure 70. The results show that Monte Carlo simulations yield the same average values of C for every S as the ones obtained as the average of the replicates from experimental data for the four mixes. However, the mean C vs. S curve obtained by First Order Approximation is lower than that of both Monte Carlo and experimental data with a difference that reaches 10% as C decreases.

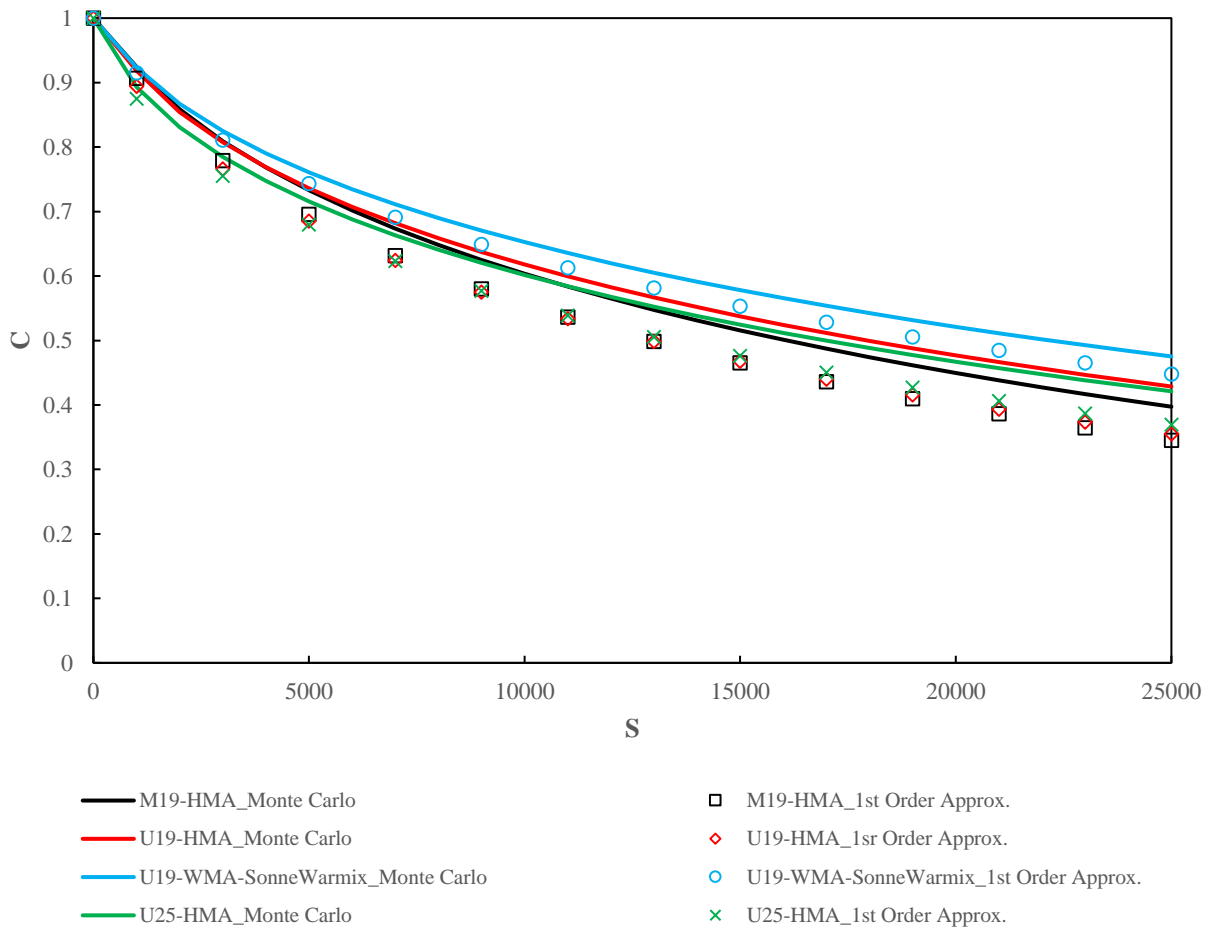


Figure 70. Mean C vs S curves determined by First Order Approximation and Monte Carlo Simulations.

The variation in the COV of C as a function of S is shown in Figure 71. In general, it can be observed that as S increases, the COV of C becomes larger. As the level of damage in asphalt concrete increases, its stiffness becomes lower and it has a higher uncertainty that continues to increase. The COV of C quantified using First Order Approximation is not the same as that estimated by Monte Carlo simulations especially for mixes having a higher level of uncertainty. The COV of C by First Order Approximation is higher than that obtained by the Monte Carlo simulations with a difference reaching 20% at an S of 25,000.

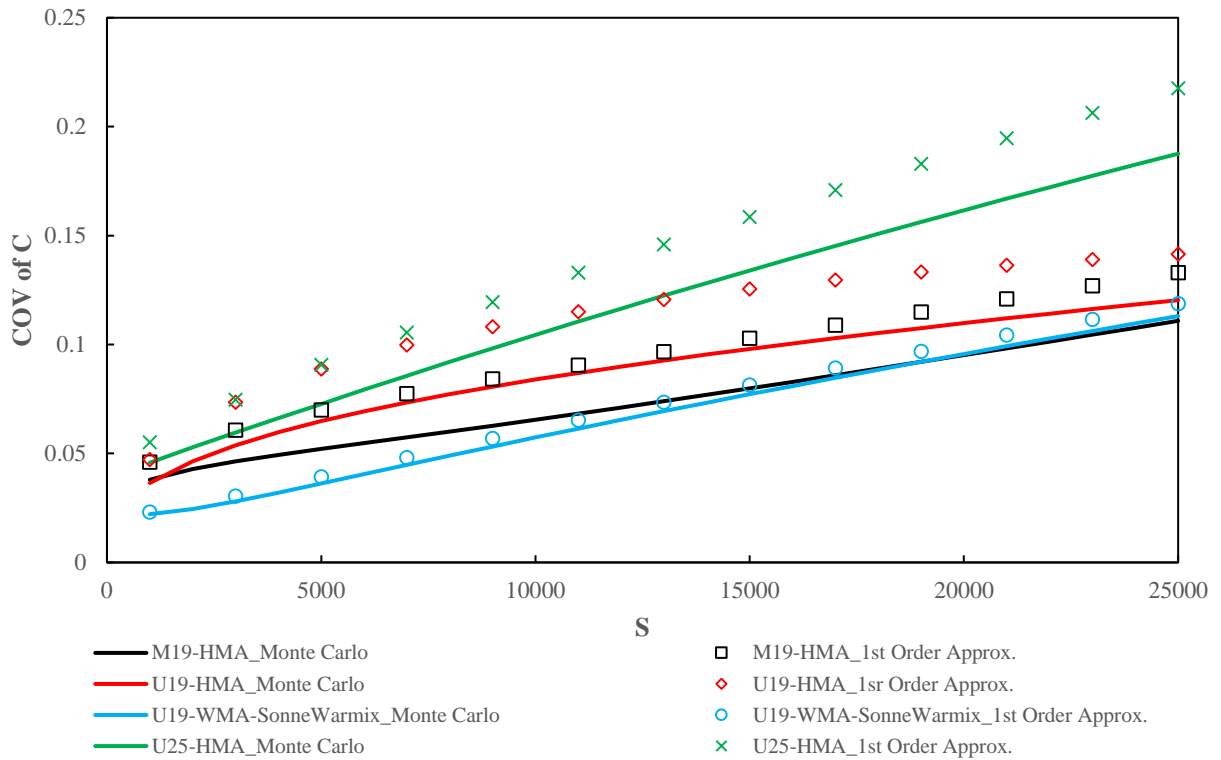


Figure 71. COV of C as a function of S determined by First Order Approximation and Monte Carlo Simulations.

By analyzing the COV of C as function of its mean in Figure 72, it is observed that the First Order Approximation and Monte Carlo simulations give equal COVs. Taking any of the mixes as an example, it is noted that the plots are done for S values in the range of 0-25,000 but the curve of C from First Order Approximation is extended beyond that obtained by Monte Carlo simulations. This indicates that the difference obtained in the COV of C as a function of S is not due to the inability of First Order Approximation to quantify this uncertainty, but due to the inability of this method in properly estimating the mean of C at different S values. This issue can be solved by using Taylor series expansion as shown in Equation 75 and Equation 76.

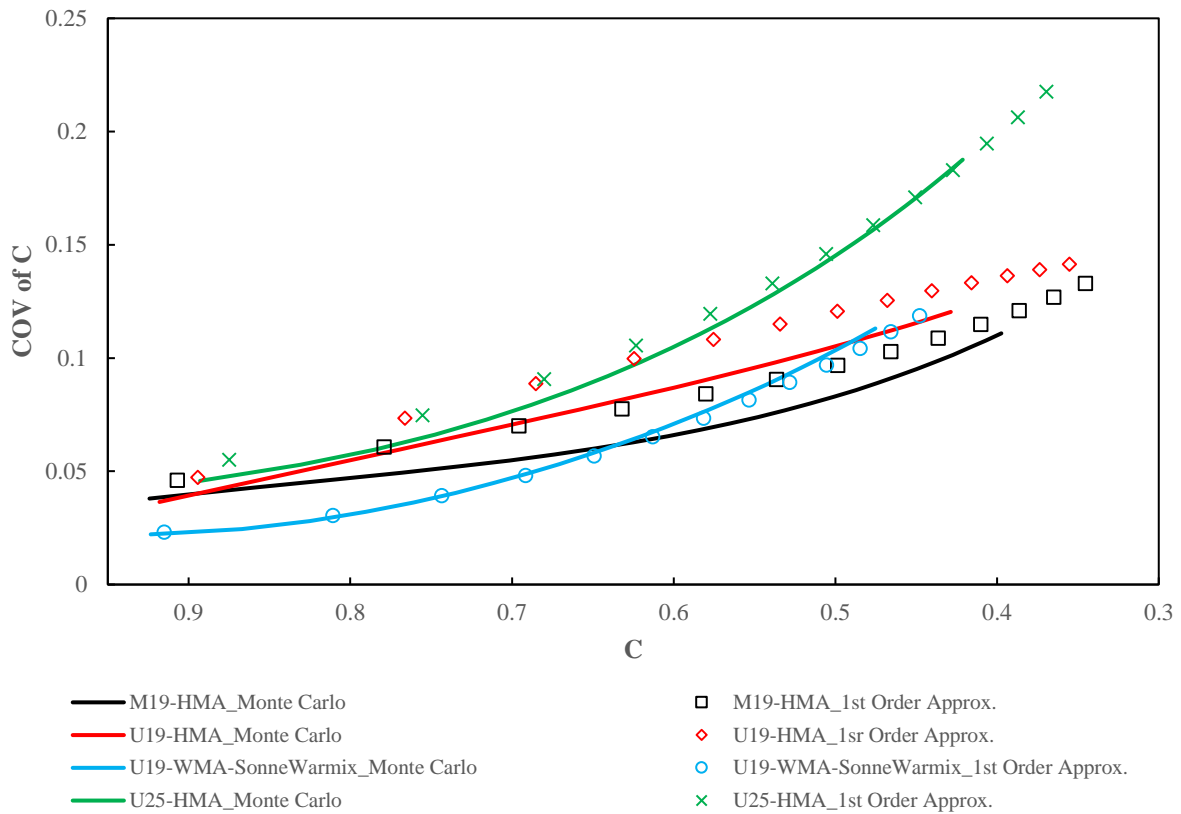


Figure 72. COV of C as a function of its mean determined by First Order Approximation and Monte Carlo Simulations.

The COV of C for the four mixes is about 0.05 for C values of 0.95 where it increases as C drops to 0.45 reaching values in the range of 0.1-0.13 for the U19-HMA, M19-HMA, and U19-WMA-SonneWarmix and a higher value of 0.17 for the U25-HMA mix. For values of C below 0.7, the COV of C for U19-HMA, M19-HMA, and U19-WMA-SonneWarmix converges and increases at the same rate. However, for C values below 0.7, the COV of C increases at a higher rate yielding values higher than that of the three mixes. This, could imply that the COV of C is affected by the NMAS of the investigated mix. The scatter in C as a function of S becomes larger as C decreases where a sample of 250 realizations from Monte Carlo simulations is presented in Figure 73. This scatter, presented by the band of C for a given value of S, is significantly wider for the case of U25-HMA mix as compared to that of the other three mixes. The scatter of C becomes wider at low values of S for the U19-HMA and U25-HMA mixes.

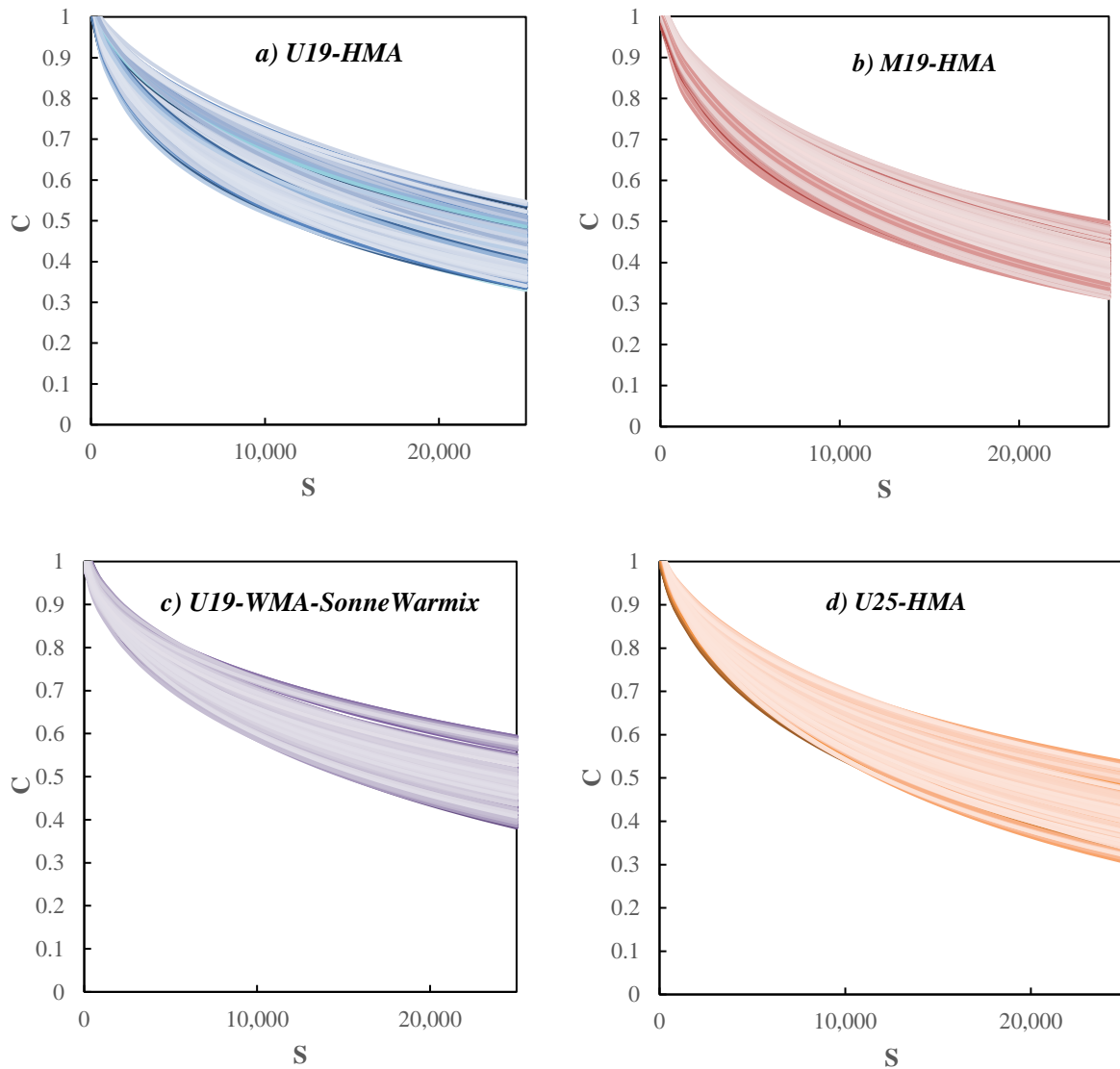


Figure 73. Simulated C vs S curves by Monte Carlo for a) U19-HMA, b) M19-HMA, c) U19-WMA-SonneWarmix, and d) U25-HMA.

6.5.3 Damage as a function of Stress

The uncertainty in S as a function of the Lebesgue norm of stress is quantified and modeled using the same framework and methodology followed for the other material characteristics as shown earlier in this research. The uncertainty of S is modeled for deterministic values of Lebesgue norm of stress referring to deterministic stress input.

6.5.3.1 S vs Stress Data

Based on the data of monotonic testing of the replicates of each mix, S is calculated as the Lebesgue norm of pseudostrain as shown in Equation 57. Inputs from the LVE characterization required for the calculations of pseudostrain and S are considered deterministic as stated earlier. For each mix, the S vs. Lebasque norm of stress are plotted per replica in Figure 74. It can be shown that the plots of the replicates per mix show a scatter

whose magnitude becomes larger with the increase in S (or increase in Lebesgue norm of stress). The M19-HMA mix shows the lower scatter as compared to the other three mixes.

Similar to the case of C vs. S curves, the analysis in this section is limited to Lebesgue norm of stress with values falling in the range of 0-12,000 which corresponds to S of maximum around 25,000 for the four mixes. For each replicate, the S vs. Lebesgue norm of stress is fitted using a series of exponential laws as shown in Equation 91.

$$S(LS(\sigma)) = \sum_{i=1}^3 a_i \cdot e^{b_i \times LS(\sigma)} \quad \text{Equation 91}$$

The number of exponential laws used in this analysis is reduced to three to simplify the probabilistic analysis having six fitting parameters as random variables instead of ten. Therefore, the inherent uncertainty in the six fitting parameters (a_1 , b_1 , a_2 , b_2 , a_3 , and b_3) is forward propagated to model the inherent uncertainty in S .

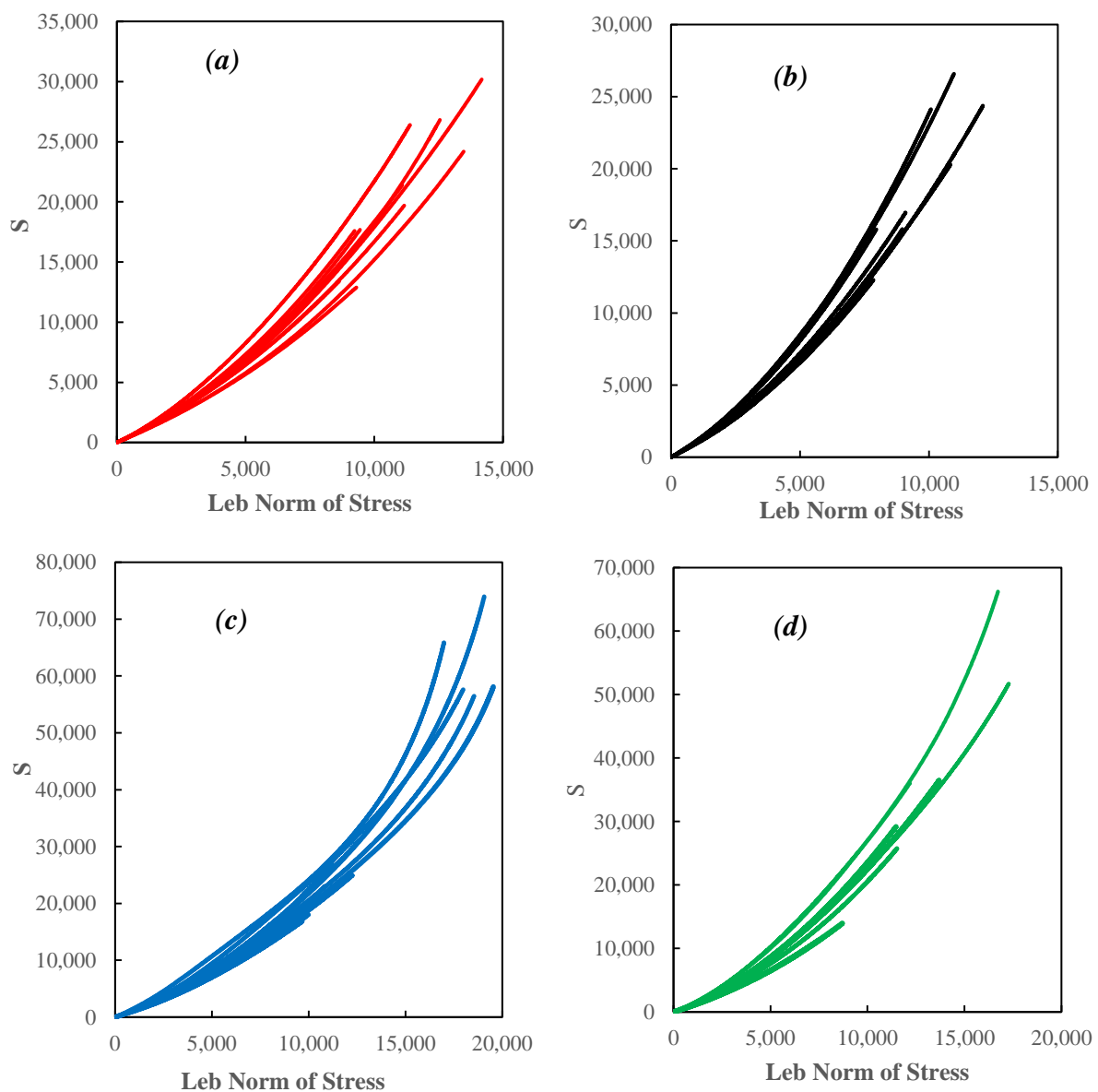


Figure 74. S vs. Lebesgue norm of stress for replicated of the four mixes a) U19-HMA, b) M19-HMA, c) U19-WMA-SonneWarmix, and d) U25-HMA.

6.5.3.2 Probabilistic Model of S vs. Lebesgue Norm of Stress

For each of the mixes, the probabilistic model of the parameters of each mix is developed as presented in Table 40. The mean, standard deviation, and probability distribution for each of these parameters is determined. For the four mixes, the six parameters are found to be well fitted and presented using the normal distribution. The covariance matrix presenting the parameters a_1 , b_1 , a_2 , b_2 , a_3 , and b_3 is complemented by determining the correlation coefficients of the different pairs of these parameters. These coefficients don't show any clear trend in terms of both the sense and magnitude when comparing the different pairs of the coefficients and between one mix and the other. For example, the pair "a1-a3" has a correlation of 0 and -1.0 for U19-HMA and U19-WMA-Sonnewarmix, respectively. Some pairs of the six parameters have a negligible correlation while others are strongly correlated in both senses with magnitudes of 0.96 and -0.99. Thus, it can be concluded that the probabilistic model of the fitting parameters is a property of each investigated mix and not universal for all mixes.

Table 40. Mean, standard deviation, distribution, and correlation coefficients of the parameters fitting S vs. Lebesgue norm of stress for the four mixes.

Mix		U19-HMA	M19-HMA	U19-WMA-SonneWarmix	U25-HMA
a1	Mean	-2271.9	-2304.4	19213.9	-1219.4
	Std Dev.	328.0	306.1	2740.8	133.4
	Dist.	Normal	Normal	Normal	Normal
b1	Mean	1.89E-04	2.40E-04	7.38E-05	2.43E-04
	Std Dev.	1.92E-05	2.49E-05	1.11E-05	1.84E-05
	Dist.	Normal	Normal	Normal	Normal
a2	Mean	12646.01	12144.52	-1.71E-02	10710.41
	Std Dev.	832.64	680.46	3.82E-06	2419.82
	Dist.	Normal	Normal	Normal	Normal
b2	Mean	1.27E-04	1.59E-04	-4.28E-03	1.47E-04
	Std Dev.	8.02E-06	1.34E-05	8.75E-07	1.25E-05
	Dist.	Normal	Normal	Normal	Normal
a3	Mean	-10383.6	-9864.2	-19264.6	-9560.4
	Std Dev.	779.7	660.7	2754.7	2458.2
	Dist.	Normal	Normal	Normal	Normal
b3	Mean	1.65E-05	3.73E-05	-2.09E-06	-4.04E-07
	Std Dev.	6.92E-06	1.52E-05	1.90E-05	2.03E-05
	Dist.	Normal	Normal	Normal	Normal
Correlation Coefficient	a1-b1	0.082	0.717	-0.728	0.326
	a1-b2	0.072	0.550	0.128	0.100
	a1-b3	-0.217	0.399	0.474	-0.423
	a1-a2	-0.397	-0.384	-0.224	0.091
	a1-a3	-0.001	-0.024	-1.000	-0.159
	a2-b1	0.604	-0.473	0.388	0.014
	a2-b2	0.522	-0.546	-0.979	-0.691
	a2-b3	0.487	-0.513	-0.189	0.507
	a2-a3	-0.917	-0.912	0.212	-0.997
	a3-b1	-0.698	0.205	0.719	-0.039
	a3-b2	-0.607	0.358	-0.115	0.676
	a3-b3	-0.440	0.385	-0.483	-0.465
	b1-b2	0.937	0.963	-0.381	0.657
	b1-b3	0.780	0.868	-0.032	-0.129
b2-b3	0.770	0.888	0.035	-0.573	

6.5.3.3 Modeling of Uncertainty in $S(\sigma)$

The uncertainty in the fitting parameters in S is forward propagated to model the inherent uncertainty in S as a function of Lebesgue norm of stress. Both First Order Approximation

and Monte Carlo with 500,000 realizations are utilized for that purpose. The relationships required for First Order Approximation are presented in Table 41.

Table 41. Relationships required for First Order Approximation of S vs. Lebesgue Norm of Stress.

$Y =$	$S(\text{Leb}(\sigma)) = \sum_{i=1}^3 a_i \cdot e^{b_i \times LS(\sigma)}$
$X_{is} =$	$a_1, b_1, a_2, b_2, a_3, \text{ and } b_3$
$E(Y) =$	$E(S) = \sum_{i=1}^3 \mu_{a_i} \cdot e^{\mu_{b_i} \times LS(\sigma)}$
$\frac{\partial S}{\partial a_i} =$ $i = 1, 2, \text{ and } 3$	$e^{b_i \times LS(\sigma)}$
$\frac{\partial S}{\partial b_i} =$ $i = 1, 2, \text{ and } 3$	$a_i \cdot LS(\sigma) \cdot e^{b_i \times LS(\sigma)}$

Both the First Order Approximation and the Monte Carlo simulations give mean S curves that are very close as shown in Figure 75. There is only a slight difference that exists between the mean curves of both methods for the U25-HMA at high values of S. The curves to that calculated as the average of the replicates from experimental testing.

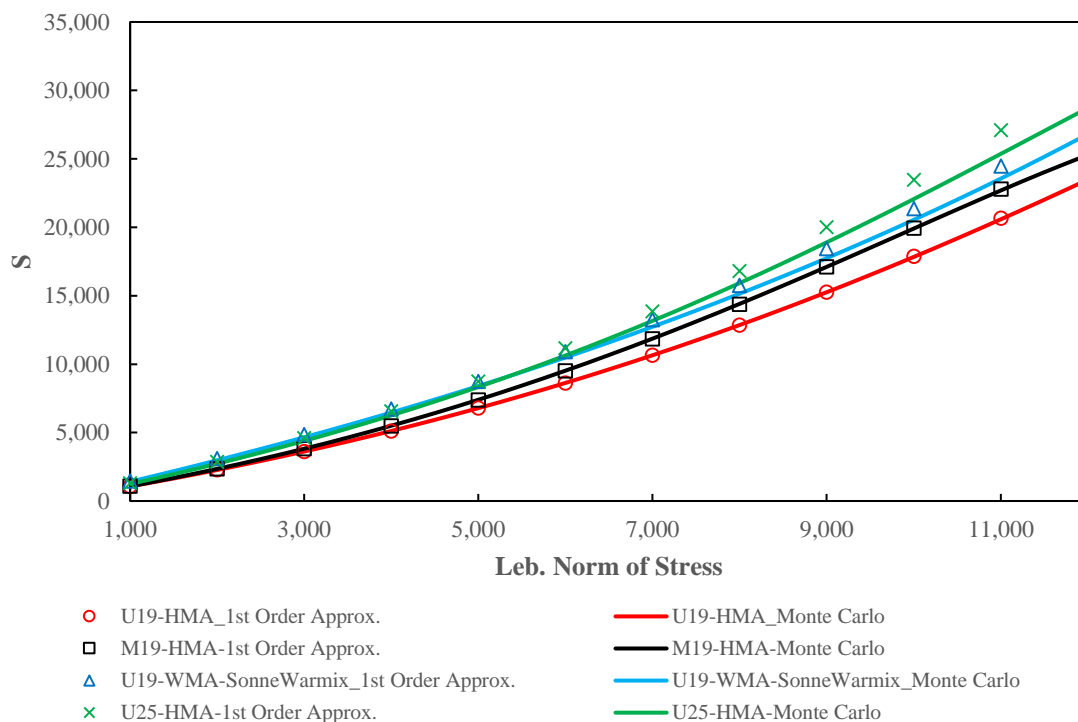


Figure 75. Mean S curves obtained using First Order Approximation and Monte Carlo simulations.

The variation in the COV of S as a function of the Lebesgue norm of stress is presented in Figure 76. Both First Order Approximation and Monte Carlo simulations give close values. This indicates that First Order Approximation can be used for S in case it is not needed to determine the probability distribution of S. The results show that the COV of S is

almost constant and independent on the increase of Lebesgue norm of stress. The COV of S increases from 0.1 to around 0.15 with the increase in Lebesgue norm of stress between 1,000 and 12,500 for the U19-HMA and M19-HMA mixes. However, the COV of S varies around 0.2 and 0.25 for Lebesgue norm of stress between 1,000 and 12,500 for the U19-WMA-SonneWarmix and U25-HMA, respectively. This indicates that the inherent uncertainty in S is independent on Lebesgue norm of stress. Some factors that appears to affect the uncertainty are NMA and WMA additives because the U25-HMA has the highest COV and the COV of S for U19-WMA-SonneWarmix is higher than that of the other mixes. The fact that S has a low and constant COV as a function of the Lebesgue norm of stress, then variability of C might not be highly affected as a function of the Lebesgue norm of stress.

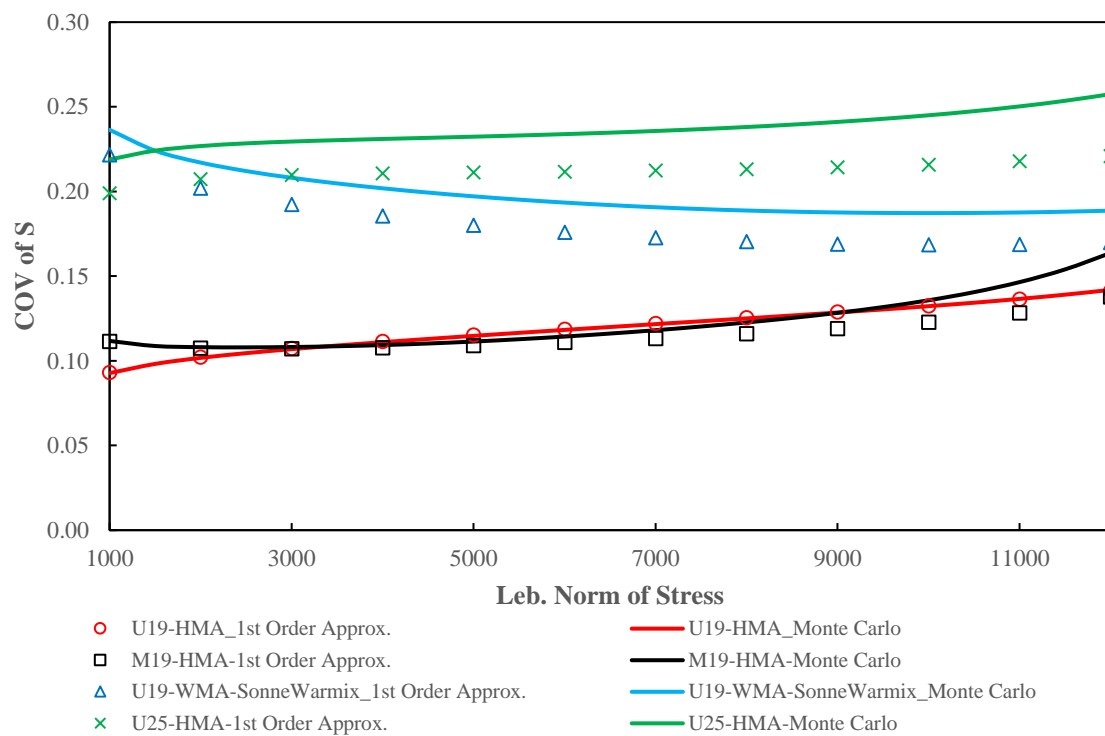


Figure 76. COV of S as a function of Lebesgue norm of stress calculated using First Order Approximation and Monte Carlo simulations.

6.5.4 C as a Function of Lebesgue Norm of Stress

The fitting models of both C vs. S and S vs. Lebesgue norm of stress are aggregated together to model directly the uncertainty of S as a function of Lebesgue norm of stress. For each replicate, the uncertainty in C is modeled as a function of the uncertainty in (a, b, c, a1, b1, a2, b2, a3, and b3) as shown in Equation 92.

$$C = a \cdot e^{-b \cdot (\sum_{i=1}^3 a_i \cdot e^{b_i \times LS(\sigma)})^c} = a \cdot e^{-b \cdot (a_1 \cdot e^{b_1 \times LS(\sigma)} + a_2 \cdot e^{b_2 \times LS(\sigma)} + a_3 \cdot e^{b_3 \times LS(\sigma)})^c}$$

Equation 92

6.5.4.1 Probabilistic Model of C(stress)

The probabilistic model of each of the parameters is the same as determined independently and the previous sections and presented in Table 38 and Table 40. The covariance matrix of these parameters is a 9 by 9 matrix and it is complemented by determining the correlation coefficients of the pairs of the parameters of the two models as presented in Table 42. Similar to the case of C vs. S and S vs. Lebesgue norm of stress there isn't a specific pattern in the magnitude and sense of the correlation coefficients between the different pairs of coefficients and from one mix to another.

Table 42. Correlation coefficients of fitting parameters of C vs. S and S vs. Lebesgue norm of stress.

		a1	b1	a2	b2	a3	b3
U19-HMA	a	-0.055	-0.172	-0.279	0.084	0.322	-0.044
	b	-0.209	0.232	0.498	0.387	-0.455	0.096
	c	0.085	-0.240	-0.473	-0.411	0.481	-0.036
M19-HMA	a	-0.219	-0.086	-0.362	-0.073	0.505	0.267
	b	-0.381	-0.670	0.785	-0.700	-0.692	-0.822
	c	0.400	0.633	-0.760	0.653	0.658	0.795
U19-WMA-SonneWarmix	a	0.248	0.196	0.323	-0.438	-0.263	0.632
	b	-0.011	0.057	-0.029	-0.011	0.006	0.324
	c	0.137	-0.021	-0.025	0.038	-0.135	-0.129
U25-HMA	a	-0.349	-0.353	-0.691	0.274	0.712	-0.217
	b	0.495	0.015	0.348	-0.265	-0.391	-0.345
	c	-0.577	0.080	-0.436	0.338	0.481	0.396

6.5.4.2 Modeling of Uncertainty in C(Leb(stress))

The uncertainty in C as a function of the Lebesgue norm of stress is modeled similar to that of the previous properties. First order Approximation is conducted as per the relationship presented in Table 43. In addition, 500,000 realizations of C for designated values of Lebesgue norm of stress are simulated using Monte Carlo simulations.

Similar to the results of the previous sections, the quantified uncertainty in C is almost the same as a function of both Lebesgue norm of stress and S. The same magnitude, trend in sorting of the mixes, and difference between Monte Carlo simulations and First Order approximations are obtained for given values of Lebesgue norm of stress and S correspond to

these designated values. This indicates that the uncertainty in S at a given value of Lebesgue norm of stress has a minimal effect on the uncertainty in C . Therefore, it is valid to model the uncertainty in C directly as a function of the Lebesgue norm of stress.

The mean curve of C vs. Lebesgue norm of stress obtained by Monte Carlo simulations is similar to that obtained as the average of the replicates of experimental data. As shown in Figure 77, the mean of C is underestimated using the First Order Approximation where this could be solved by considering the mean estimate resulting from Taylor expansion as shown in Equation 76. Similar to the case of C vs S , the inherent uncertainty in C increases as the Lebesgue norm of stress becomes larger for the four investigated mixes as presented in Figure 78. As the Lebesgue norm of stress increases, C drops from an initial value of 1.0 where this will be associated with an increase in the uncertainty in C .

Table 43. Relationships required for First Order Approximation of C vs. Lebesgue norm of stress.

$Y =$	$C = a \cdot e^{-b \cdot (\sum_{i=1}^3 a_i \cdot e^{b_i \times LS(\sigma)})^c} = a \cdot e^{-b \cdot (a_1 \cdot e^{b_1 \times LS(\sigma)} + a_2 \cdot e^{b_2 \times LS(\sigma)} + a_3 \cdot e^{b_3 \times LS(\sigma)})^c}$
$X_{is} =$	$a, b, c, a_1, b_1, a_2, b_2, a_3, \text{ and } b_3$
$E(Y) =$	$E(C) = \mu_a \cdot e^{-\mu_b \cdot (\sum_{i=1}^3 \mu_{a_i} \cdot e^{b_i \times LS(\sigma)})^c}$
$\frac{\partial C}{\partial a} =$	$e^{-b \cdot (a_1 \cdot e^{b_1 \times LS(\sigma)} + a_2 \cdot e^{b_2 \times LS(\sigma)} + a_3 \cdot e^{b_3 \times LS(\sigma)})^c}$
$\frac{\partial C}{\partial b} =$	$-a \cdot e^{-b \cdot (a_1 \cdot e^{b_1 \times LS(\sigma)} + a_2 \cdot e^{b_2 \times LS(\sigma)} + a_3 \cdot e^{b_3 \times LS(\sigma)})^c} \cdot (a_1 \cdot e^{b_1 \times LS(\sigma)} + a_2 \cdot e^{b_2 \times LS(\sigma)} + a_3 \cdot e^{b_3 \times LS(\sigma)})^c$
$\frac{\partial C}{\partial c} =$	$-a \cdot b \cdot e^{-b \cdot (a_1 \cdot e^{b_1 \times LS(\sigma)} + a_2 \cdot e^{b_2 \times LS(\sigma)} + a_3 \cdot e^{b_3 \times LS(\sigma)})^c} \cdot \ln(a_1 \cdot e^{b_1 \times LS(\sigma)} + a_2 \cdot e^{b_2 \times LS(\sigma)} + a_3 \cdot e^{b_3 \times LS(\sigma)}) \cdot (a_1 \cdot e^{b_1 \times LS(\sigma)} + a_2 \cdot e^{b_2 \times LS(\sigma)} + a_3 \cdot e^{b_3 \times LS(\sigma)})^c$
$\frac{\partial C}{\partial a_i} =$ $i = 1, 2, 3$	$-a \cdot b \cdot c \cdot e^{-b \cdot (a_1 \cdot e^{b_1 \times LS(\sigma)} + a_2 \cdot e^{b_2 \times LS(\sigma)} + a_3 \cdot e^{b_3 \times LS(\sigma)})^c} \cdot e^{b_i \times LS(\sigma)} \cdot (a_1 \cdot e^{b_1 \times LS(\sigma)} + a_2 \cdot e^{b_2 \times LS(\sigma)} + a_3 \cdot e^{b_3 \times LS(\sigma)})^{c-1}$
$\frac{\partial C}{\partial b_i} =$ $i = 1, 2, 3$	$-a \cdot b \cdot c \cdot a_i \cdot LS(\sigma) \cdot e^{b_i \times LS(\sigma)} \cdot e^{-b \cdot (a_1 \cdot e^{b_1 \times LS(\sigma)} + a_2 \cdot e^{b_2 \times LS(\sigma)} + a_3 \cdot e^{b_3 \times LS(\sigma)})^c} \cdot (a_1 \cdot e^{b_1 \times LS(\sigma)} + a_2 \cdot e^{b_2 \times LS(\sigma)} + a_3 \cdot e^{b_3 \times LS(\sigma)})^{c-1}$

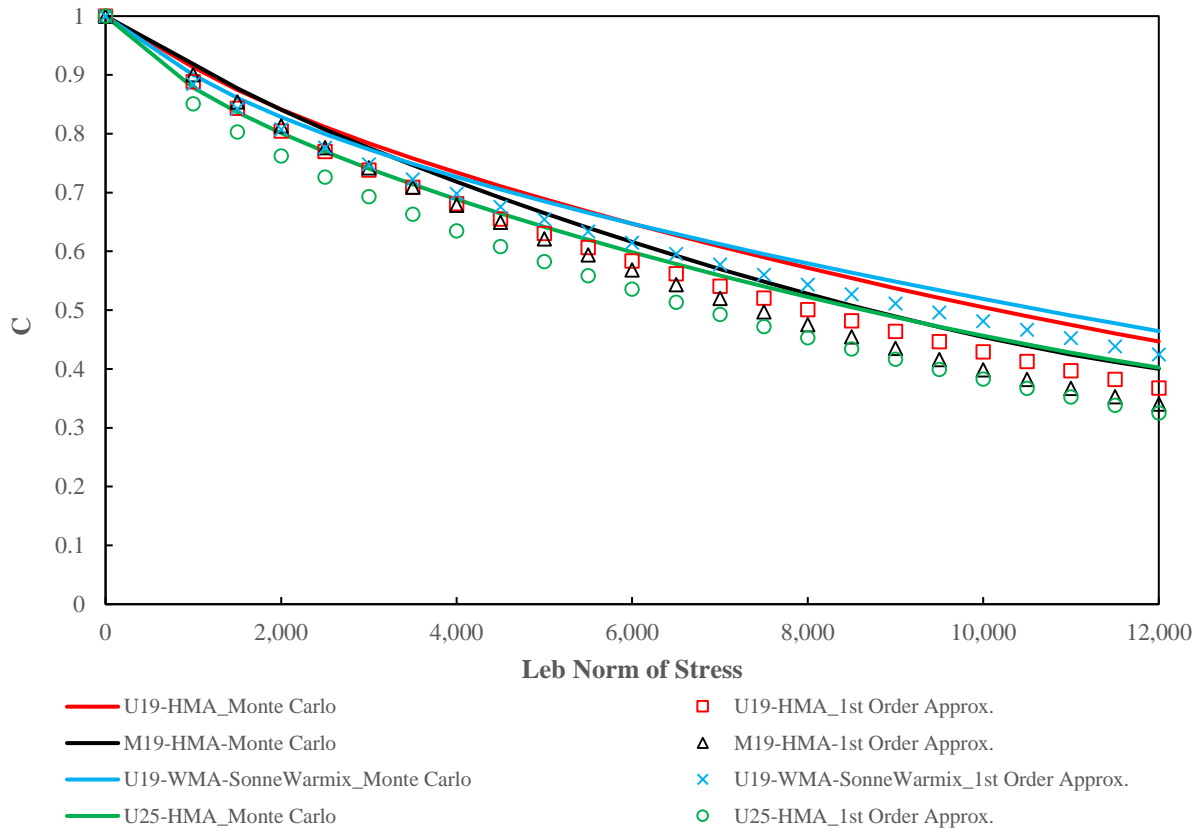


Figure 77. Mean of C vs. Lebesgue Norm of Stress evaluated by the First Order Approximation and Monte Carlo Simulation for the four mixes.

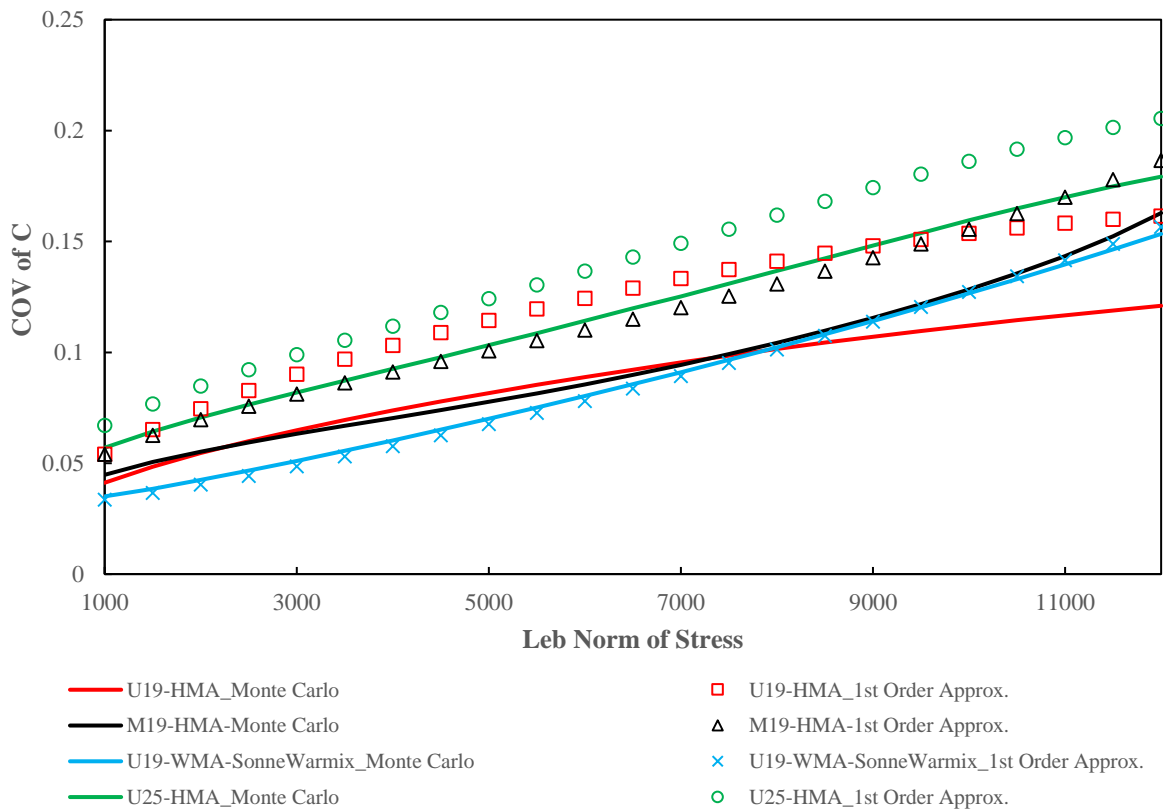


Figure 78. COV of C as a function of Lebesgue norm of stress evaluated using First Order Approximation and Monte Carlo simulations for the four mixes.

By plotting the uncertainty of C as function of the mean of C , Monte Carlo and First Order Approximation yield similar results. Thus, the difference in results of First Order Approximation and Monte Carlo simulations as shown in Figure 78 is mainly due to the shortening of First Order Approximation in estimating the mean of C which can be resolved as stated. Therefore, the simple First Order Approximation is a valid tool that can be used to quantify the uncertainty in C . As C drops from 1 to 0.4, its uncertainty increases from 0 to a value in the range of 0.1-0.15 for the four investigated mixes. Whether comparing the COV of C as a function of either mean C or Lebesgue norm of stress, it can be observed that the U25-HMA possess a higher curve as that of the reference mix U19-HMA. The mixes U19-WMA-SonneWarmix and M19-HMA have the same COV as that of U19-HMA for Lebesgue norm of stress values up to 8,000. Beyond that point the uncertainty of C for those two mixes exceed that of U19-HMA. This indicates that components of the asphalt mix influence the uncertainty in predicted C similar to the case of LVE functions but at different magnitudes. The low values in the uncertainty in C might indicate the strength of the C vs S approach and its methodology in properly presented the damage characteristics of asphalt concrete mixes and accounting for uncertainties that it might possess. Even though, the magnitude of the COV of C is low (below 0.15 for a reduction of C from 1.0 to 0.4), the significance of this uncertainty should be checked through forward propagating it to predict the strain response for a given stress profile and temperatures as to be presented in the following sections.

CHAPTER 7

PREDICTION OF PROBABILISTIC VISCOELASTIC STRAINS

7.1 Propagation Methodology

As presented earlier and extensively in this dissertation, the uncertainties of the different components of the VECD model are characterized and quantified. This work yielded a probabilistic model for each of the LVE functions ($|E^*|$, E' , $E(t)$, and $D(t)$) and a probabilistic damage characteristic curve (ultimately C as a function of stress). The uncertainties of all these components are forward propagated to predict a probabilistic viscoelastic strain for any stress input profile and at any temperature. Thus, a probabilistic viscoelastic continuum damage model (P-VECD) is developed where it requires the probabilistic models for each of $D(t)$, C vs. S , and S vs. Lebesgue norm of stress. These properties are aggregated through the convolution integral to predict the viscoelastic strains. The nature of the convolution integral implies that a very high computational effort is required to simulate a large number of realizations of the predicted viscoelastic strains for a given stress profile at a given temperature and at any time. Therefore, 500 realizations of each of $D(t)$, C vs S , and S vs Lebesgue Norm of stress are selected randomly from the Monte Carlo simulations of each of these functions. These realizations are mapped randomly to simulate 500 realizations of viscoelastic strains for any given stress profile. The computations required for the predictions of the P-VECD are carried out using an algorithm coded in R-Studio and presented in the Appendix of this dissertation.

7.2 Input Data: Stress History and Material Properties

The magnitude of the viscoelastic strains to be predicted is a function of the stress (or loading) input and temperature. The stress input could be of any form including monotonic loading at any rate, cyclic loading with different frequencies, random loading regimes with different forms of loading modes, magnitudes, rates, resting periods, and number of cycles. In this dissertation and for illustrating purposes, the stress profile is selected to be of a ramp form similar to the response of the specimens tested in the constant crosshead rate tests and used for the development of the VEPCD model at earlier stages. For this purpose, three different stress profiles are selected as shown in Figure 79. The three profiles are selected randomly to have different rates, different temperatures, and different maximum applied stresses. Given that the VECD model and similarly the P-VECD are developed at 5°C, the time domain of each stress profile is transferred to the reduced time domain at 5°C. This

yields a stress increasing up nonlinearly to reach 5000 kPa at 180 seconds for the stress profile at 5°C, 2000 kPa at a reduced time of 2000 seconds for the stress profile at 25°C, and 1,000 kPa at a reduced time of 400,000 seconds for the stress profile at 35°C. These profiles has been selected to assure that the corresponding average C value at maximum stress and reduced time of each of the three profiles does not drop below 0.4 which is limit for which P-VECD models are developed in this research. In addition, the stress profile at 35°C was selected to have a slow rate where stress is applied up to a reduced time of 400,000 seconds to assure that domains with high COVs for D(t) are accounted for in this analysis.

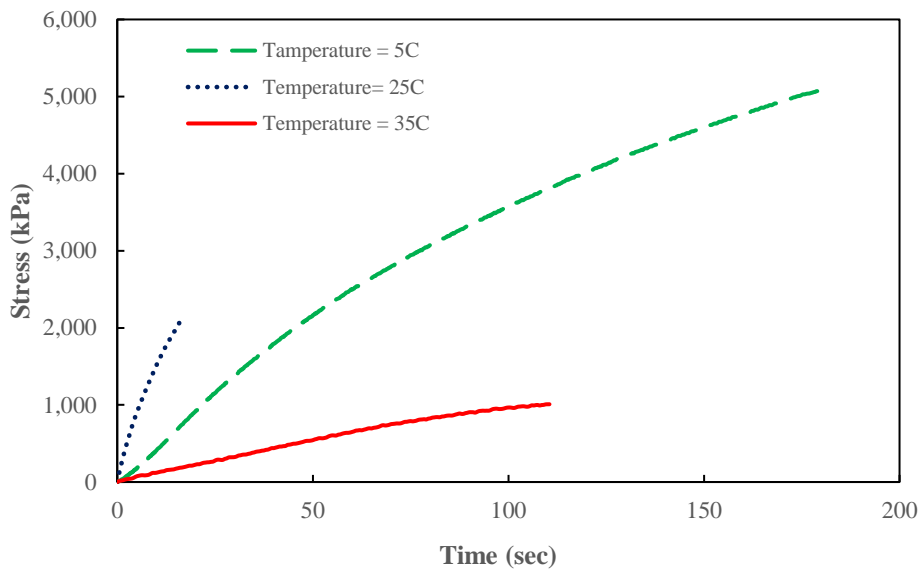


Figure 79. Different investigated stress inputs as a function of actual time at 5°C, 25°C, and 35°C.

For each stress profile, the Lebesgue Norm of stress is calculated for the case of each mix to serve as an immediate parameter to compute the damage parameter “S” and its corresponding “C” values over the entire domain reduced times in the analysis. This is carried out for each of the four mixes U19-HMA, M19-HMA, U19-WMA-SonneWarmmix, and U25-HMA as presented in Figure 80, Figure 81, and Figure 82 for the stress profiles at 5°C, 25°C, and 35°C, respectively. For any given time, it can be observed that the Lebesgue Norm of Stress is always lower for the case of M19-HMA as compared to the other three mixes. This difference is mainly due to the variation in parameter “ α ” between M19-HMA and the other mixes where in this analysis “ α ” is taken to be the average of 10 replicates of each mix. In addition, the time-temperature shift factors for each mix are taken deterministic as the average of 10 replicates to calculate the reduced times. For each case of stress input, the pseudostiffness “C” is calculated using the parameters of the C vs S model and S vs Lebesgue norm of stress of the 500 realizations extracted from Monte Carlo Simulations of each mix. For each of the three stress profiles, the data of 500 curves of C vs Lebesgue Norm of Stress is calculated for the case of each of the four mixes.

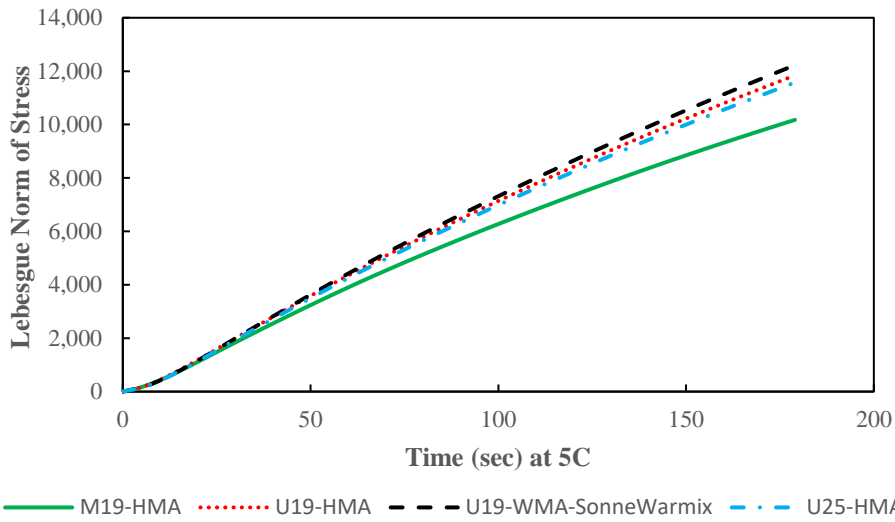


Figure 80. Lebesgue norm of the investigated stress profile as a function of time at 5°C for the cases of U19-HMA, M19-HMA, U19-WMA-SonneWarmmix, and U25-HMA.

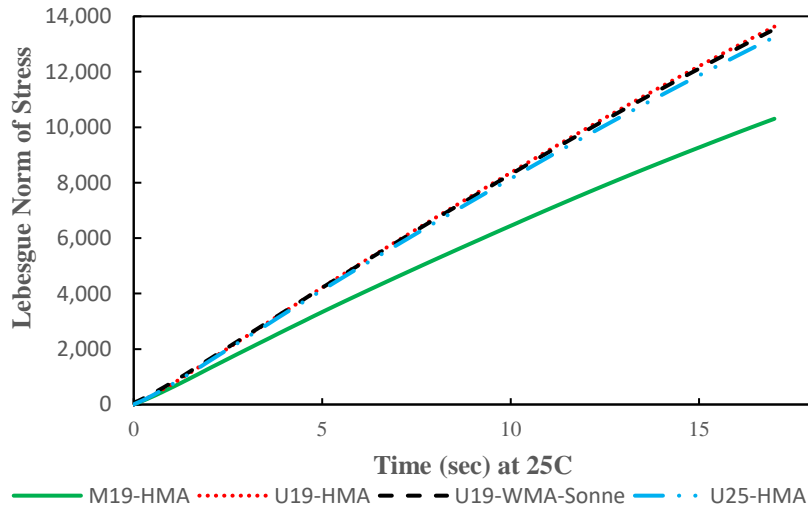


Figure 81. Lebesgue norm of the investigated stress profile as a function of time at 25°C for the cases of U19-HMA, M19-HMA, U19-WMA-SonneWarmmix, and U25-HMA.

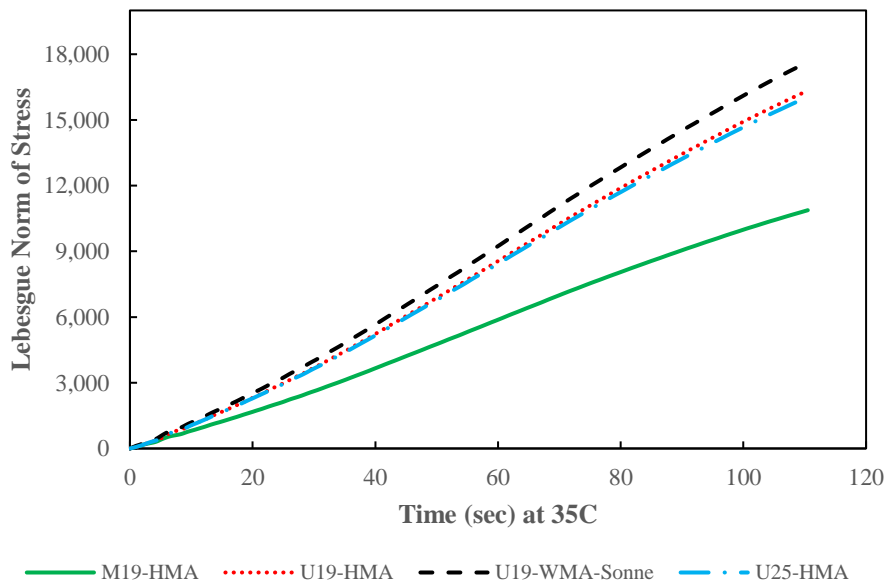


Figure 82. Lebesgue norm of the investigated stress profile as a function of time at 35°C for the cases of U19-HMA, M19-HMA, U19-WMA-SonneWarmmix, and U25-HMA.

In addition, the P-VECD model requires having probabilistic $D(t)$ mastercurves developed at a reduced time of 5°C . This is achieved by extracting 500 realizations of the Prony coefficients corresponding to $D(t)$ mastercurves simulated using the Monte Carlo method. The extracted $D(t)$ mastercurves plotted as a function of reduced time at a reference temperature of 5°C are shown in Figure 83. The scatter around the mean appears to be low at small reduced times and increases as the reduced time becomes larger especially for the case of U19-WMA-SonneWarmmix and U25-HMA. It is worth noting that for the investigated stress profiles, the uncertainty to be propagated in the P-VECD is that of $D(t)$ for values of reduced time smaller than 400,000 second.

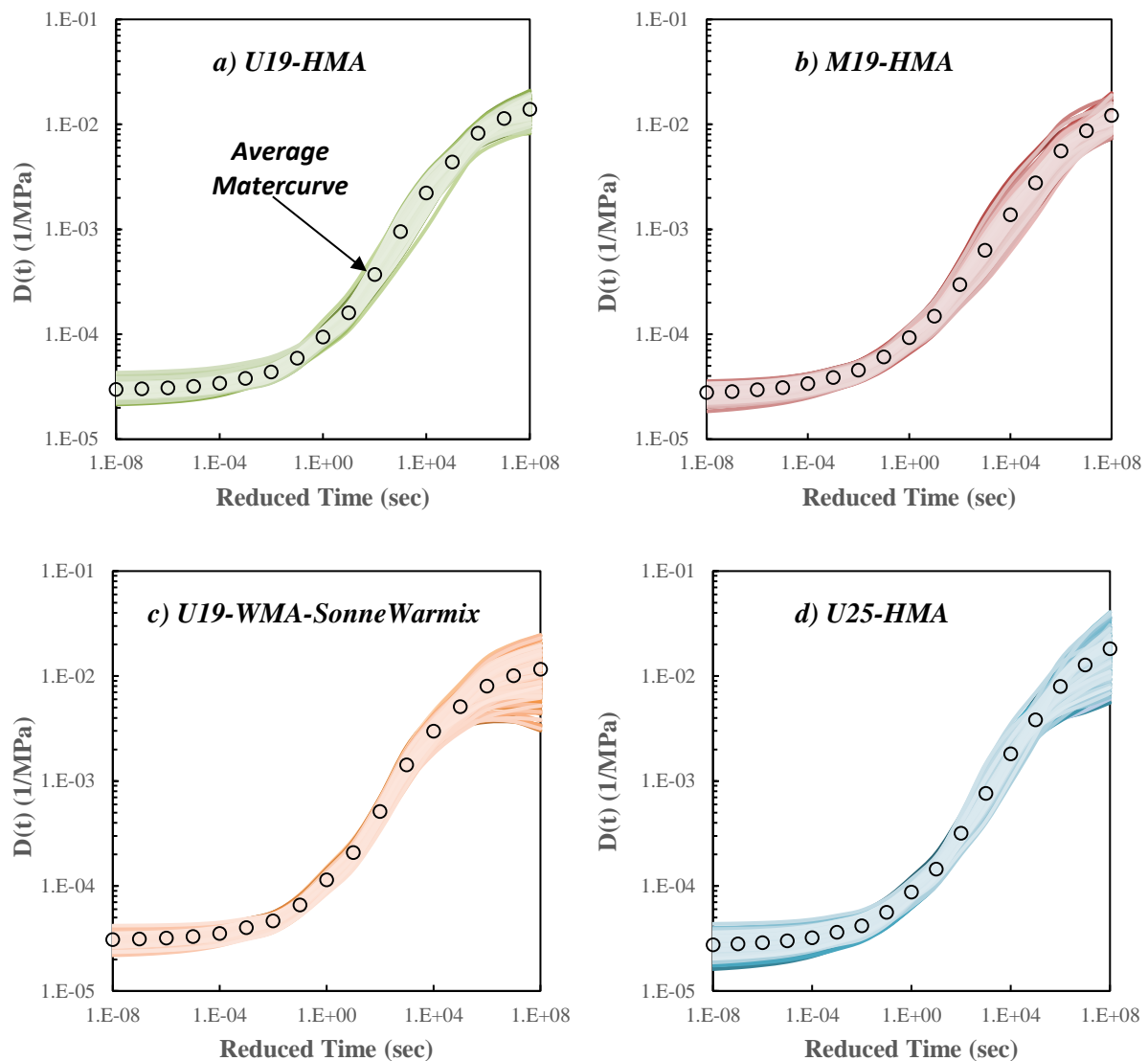


Figure 83. A sample of simulated $D(t)$ mastercurves from Monte Carlo Realizations plotted as a function of reduced time at 5°C and extracted for the prediction of probabilistic viscoelastic strains.

7.3 Predicted Viscoelastic Strains: Deterministic and Probabilistic solutions

7.3.1 Results of the P-VECD Model Predictions

The 500 realizations of C vs Stress and those of $D(t)$ are matched randomly leading to 500 combinations presenting probable material characteristics required for P-VECD model. For each of these cases, the viscoelastic strain is predicted where its mean and COV are calculated for each mix as presented in Figure 84, Figure 85, and Figure 86 for the analyzed stress profiles at 5°C, 25°C, and 35°C, respectively. It can be observed that the predicted viscoelastic strain increases rapidly at the initial/instantaneous portion of the application of stress before it continues to increase but at a much gradual/shallow slope. In parallel with that, it can be observed that the COV of the predicted viscoelastic strains possesses a similar behavior where it rises rapidly just after the application of the load beyond which it increases very slightly with the increase in the predicted viscoelastic strains. This pattern can be observed for all the cases of the predicted probabilistic viscoelastic strains regardless of the mix type and the analyzed stress profile.

The three analyzed stress profiles are selected such that at the C value is approximately around 0.4 at the end of the load application. This could imply that the predicted probabilistic viscoelastic strains are within the same order of magnitude at the end of the loading time where it evolves around 0.01 for the three cases. Thus, any difference between the predicted viscoelastic strain of the four mixes will be due to the difference in predicted C values and difference in properties related to LVE characterization and mainly $D(t)$ and the time-temperature shift factors. Based on that the uncertainty will be mainly affected by uncertainty of C vs Lebesgue norm of stress which has a maximum of 0.2 and that of $D(t)$ up to a reduced time of 400,000 second where it increases from 0.1 at low reduced times up to 0.2-0.4 depending on the investigated mix.

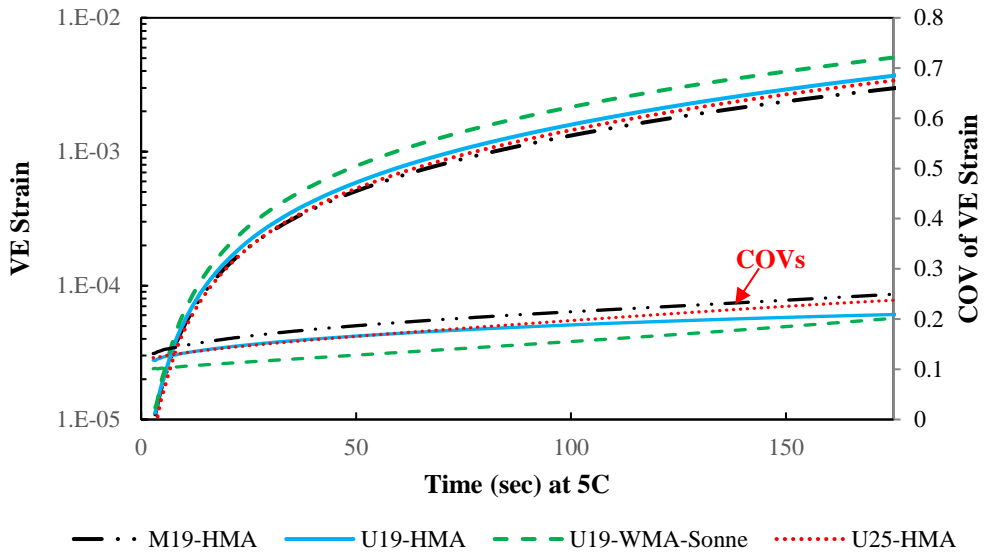


Figure 84. Predicted probabilistic viscoelastic strain means and COVs for case of stress input at 5°C for M19-HMA, U19-HMA, U19-WMA-SonneWarmmix, and U25-HMA.

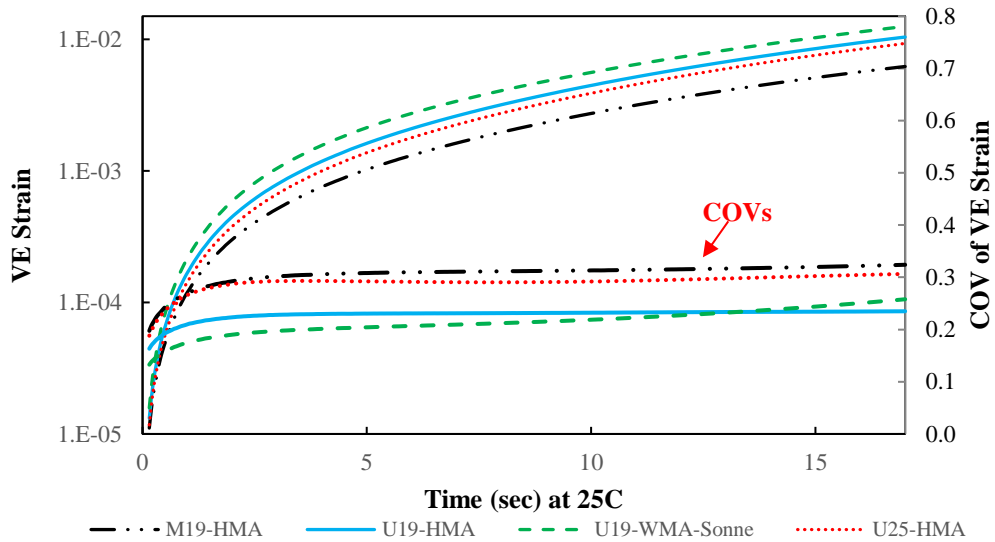


Figure 85. Predicted probabilistic viscoelastic strain means and COVs for case of stress input at 25°C for M19-HMA, U19-HMA, U19-WMA-SonneWarmmix, and U25-HMA.

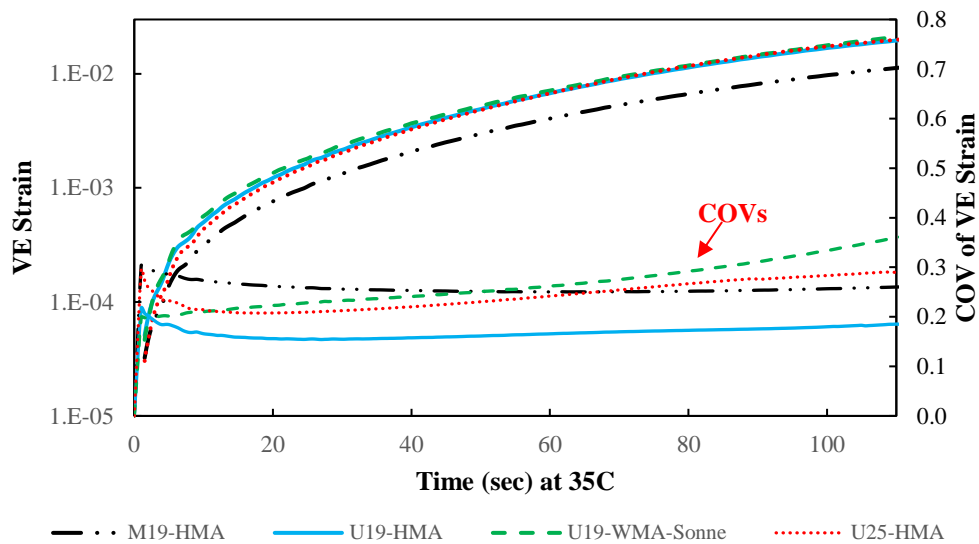


Figure 86. Predicted probabilistic viscoelastic strain means and COVs for case of stress input at 5°C for M19-HMA, U19-HMA, U19-WMA-SonneWarmix, and U25-HMA.

For the case of the stress profile at 5°C, the COV of the predicted viscoelastic strain increases from an initial value of 0.12 to around 0.22 at time/reduced time of 170 second. However, the COV of the predicted viscoelastic strain is around 0.28 for the stress profile at 25°C and around 0.31 for the stress profile at 35°C. This shows that temperature and basically the uncertainty in $D(t)$ as a function of reduced time increase the uncertainty of the predicted viscoelastic strain. The uncertainty of the predicted viscoelastic strain at any time is mainly due to the high uncertainty at the initial/instantaneous portion of time just after the application of the load. This uncertainty can be assumed to be mostly constant as C drops down to values of 0.4.

It can be also observed that the COV of the predicted viscoelastic strains becomes different from one mix to the other as the temperature increases or as the range of the reduced time becomes larger to reach a value of C of 0.4. For the three stress profiles, the COV of the predicted viscoelastic strain is always higher for the case of M19-HMA and U25-HMA compared to that of the U19-HMA. The COV of the predicted viscoelastic strain of U19-WMA-SonneWarmix is equal to that of U19-HMA at small reduced times but exceeds it as the reduced time becomes larger. For case of the stress profile at 5°C, the COV of predicted viscoelastic strain of M19-HMA and U25-HMA is about 10% higher than that of U19-HMA and U19-WMA-SonneWarmix. This difference increases to 25% for the case of the stress profile at 25°C. However, for the case of stress profile at 35°C, the COV of predicted viscoelastic strain for M19-HMA and U25-HMA is 65% higher than that for the case of the U19-HMA mix. For U19-WMA-SonneWarmix, the COV is almost 100% higher than that of the U19-HMA especially at high reduced times. Therefore, the uncertainty in the predicted

viscoelastic strain is just a reflection of that in LVE and damage characteristic properties where it becomes larger as the reduced time become larger, as the NMAS increases, and/or when using a modified binder. It is worth noting that the uncertainty in the predicted viscoelastic strains for the mix with WMA additive is significantly higher than that of the other mixes especially at high reduced times similar to the case of LVE functions as shown in the earlier sections.

7.3.2 Probability Distribution of Predicted Probabilistic Viscoelastic Strains

To complete the requirements of the P-VECD model, it is required to determine the probability distribution of the predicted viscoelastic strains for the different analyzed case studies. The predictions of the P-VECD are random variables with a mean, standard deviation, and a distribution. For a given stress profile applied for any type of asphalt concrete mixture, the mean and standard deviation vary over the domain of time predictions and thus the best fit distribution might possess the same behavior. To test this hypothesis, two candidate probability distributions are tested using the Shapiro-Wilk Normality Test. Therefore, predicted viscoelastic strains using the P-VECD model at different times of each of the investigated test profiles are tested for normality. Also, the same data is transformed to the logarithmic scale where the Shapiro-Wilk Normality Test is used to test the hypothesis whether the transformed data is Normally distributed or not and thus implying if the original data is lognormally distribution or not. The test is conducted for the predicted viscoelastic strains at different points of time being 10, 25, 50, 100, and 150 seconds for the investigated test profile at 5°C where the resulting p-values are presented in Table 44. In addition, the p-values resulting from the Shapiro-Wilk Normality Test at times of 20, 40, 60, 80, and 100 seconds are presented in Table 45 for the investigated stress input at 35°C. In this case the tested null hypothesis is that the data is Normally distributed. For a chosen alpha value or level of significance of 0.05, a p-value less than 0.05 indicates that the null hypothesis is rejected and the data is not Normally distributed. The results show that for the case of the investigated stress profile at 5°C, almost both the Normal and Lognormal distributions can be used to fit the predicted viscoelastic strains. However, the p-value for the testing of the Lognormal distribution is significantly higher than that of the p-value for the Normal distribution for all times and for the case of the four mixes. On the other hand, the hypothesis testing for the distribution of the predicted viscoelastic strains at most times of the investigated stress input at 35°C yield very low p-values less than 0.05 when testing for Normality. However, the p-value is always larger than 0.05 at all times and for all the mixes when testing for fitting the data by the Lognormal distribution. Therefore, it can be concluded

that the predicted viscoelastic strains by P-VECD model are best fit using the Lognormal distribution.

Table 44. *p*-values by Shapiro-Wilk Normality Test for predicted viscoelastic strains for the investigated stress input at 5°C for the four mixes.

		t=10 sec	t=25 sec	t=50 sec	t=100 sec	t=150 sec
M19-HMA	Normal	0.053	0.135	0.288	0.430	0.369
	LogNormal	0.179	0.453	0.708	0.724	0.613
U19-HMA	Normal	0.310	0.368	0.300	0.386	0.413
	LogNormal	0.380	0.490	0.360	0.401	0.453
U19-WMA-SonneWarmix	Normal	0.453	0.152	0.053	0.012	0.004
	LogNormal	0.990	0.916	0.563	0.522	0.260
U25-HMA	Normal	0.183	0.060	0.049	0.075	0.153
	LogNormal	0.700	0.526	0.575	0.654	0.501

Table 45. *p*-values by Shapiro-Wilk Normality Test for predicted viscoelastic strains for the investigated stress input at 35°C for the four mixes.

		t=20 sec	t=40 sec	t=60 sec	t=80 sec	t=100 sec
M19-HMA	Normal	0.000	0.001	0.003	0.005	0.009
	LogNormal	0.889	0.847	0.938	0.942	0.948
U19-HMA	Normal	0.012	0.034	0.042	0.085	0.045
	LogNormal	0.065	0.071	0.103	0.177	0.146
U19-WMA-SonneWarmix	Normal	0.065	0.099	0.075	0.127	0.198
	LogNormal	0.022	0.064	0.043	0.048	0.089
U25-HMA	Normal	0.003	0.045	0.092	0.053	0.026
	LogNormal	0.498	0.943	0.895	0.747	0.680

7.3.3 Number of Realizations Required for P-VECD Model

The results in the previous section for the P-VECD model are based on 500 predictions of viscoelastic strains. Thus, the presented mean, COVs, and distribution at any time are the results of a population of 500 points. However, in all the previous sections the probabilistic analysis and uncertainty quantification are based on 500,000 realizations from Monte Carlo simulations. For the prediction of viscoelastic strain is timely and thus the implementation of a large number of simulations requires a very high computational effort. Therefore, in this research 500 realizations of each of D(t), C vs. S curve parameters, and S vs. Lebesgue Norm of Stress parameters are randomly extracted from 500,000 realizations of Monte Carlo simulations of each of the characteristics for the four mixes. However, to validate the conclusions related to the predicted viscoelastic strains by the P-VECD model, it is worth checking the variability in the predicted results as a function of the required number of realizations to be considered for the development of the P-VECD model. In order to accomplish this task, the viscoelastic strains are predicted in response to the previously

investigated stress profile at 5°C using a different number of realizations varying between 3 and 10,000. Thus, it is required to check the number of simulations required to give valid and realistic simulated results. In the case of the deterministic VECD, the answer would be simply once. However, for the P-VECD this would be more complex. This task is carried out in order to check whether 500 simulations are enough for yielding realistic predictions by the P-VECD model without further inducing more error due to the scarcity of the number of simulations/realizations. Therefore, it is recommended to have enough number of points to yield realistic predictions but with minimal computational efforts.

The effect of the number of simulations used for the development of the P-VECD on the variability of the predicted viscoelastic strains are calculated at different times of 10, 25, 50, 75, 100, and 150 second and presented for U19-HMA, M19-HMA, U19-WMA-SonneWamix, and U25-HMA in Figure 87, Figure 88, Figure 89, and Figure 90, respectively. The results show that the COV of the predicted viscoelastic strain is unstable for small numbers of simulations below 100 at any time. The COV calculated using a small number of simulations can be observed to be significantly either lower or higher than the stabilized COV. Taking the case of the reference mix U19-HMA i.e. the mix with the lowest uncertainty, it can be observed that for example at t=100 second the COV decreases from a value of 0.27 for the case of 3 simulations to a 0.17 when calculated using 20 simulations. Then, this COV increases slightly to a value of 0.20 for the case of 40 simulations before it decreases to stabilize at 0.18 after 100 simulations. However, for the case of U25-HMA which is a mix with higher uncertainties, the COV at time of 100 second increases from 0.1 to 0.23 as the number of simulations increase from 3 to 40. This COV slightly decreases as the number of simulations increases to stabilize at a value of 0.197 for a number of simulations of 500. It is also observed that higher fluctuations occur for the cases with low number of simulations for the U19-WMA-SonneWarmix as compared to the other mixes. For the case of all mixes, the COV of the predicted viscoelastic strains has a COV at 500 simulations that is within a range of error not exceeding 5% when calculating the COV of the predicted viscoelastic strains based on 10,000 simulations. This indicates the development of a realistic P-VECD requires a number of simulations equal to or great than 500. As the number of simulations approaches 500, the results of the P-VECD predictions converge to a stable solution that is slightly improved by simulations but at a high computational cost.

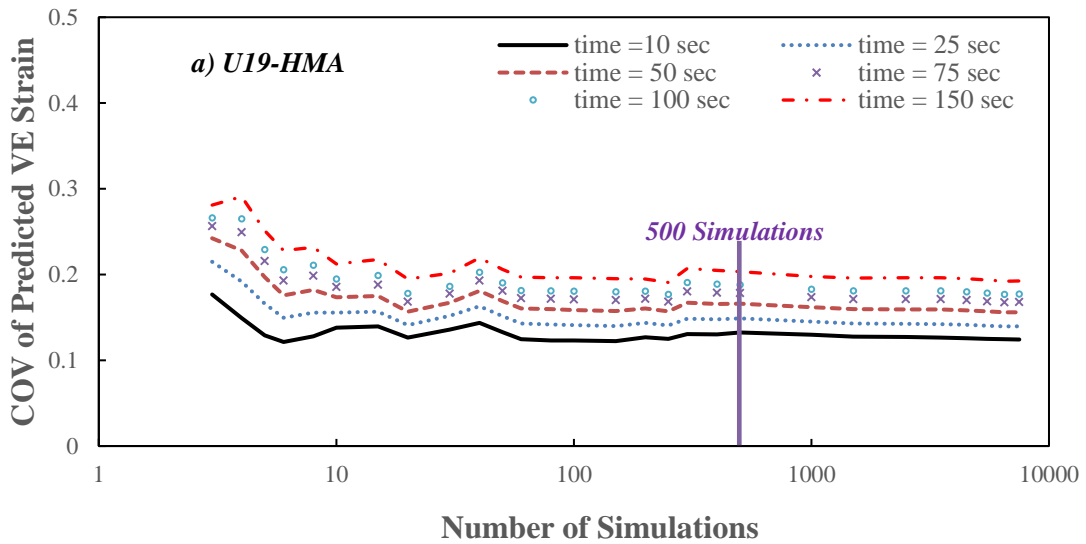


Figure 87. COV of predicted viscoelastic strains across the 10,000 simulations of the P-VECD model for U19-HMA.

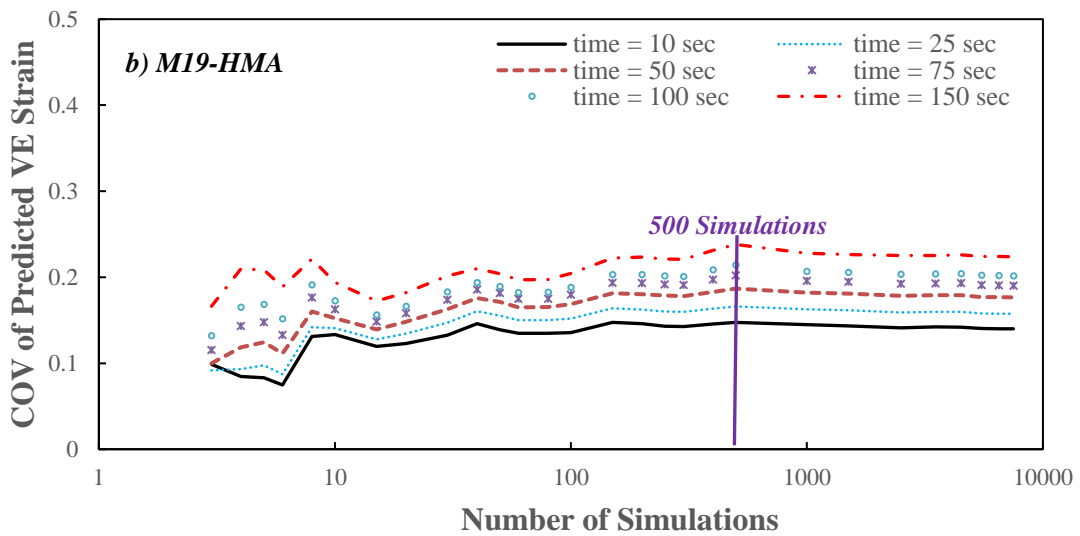


Figure 88. COV of predicted viscoelastic strains across the 10,000 simulations of the P-VECD model for M19-HMA.

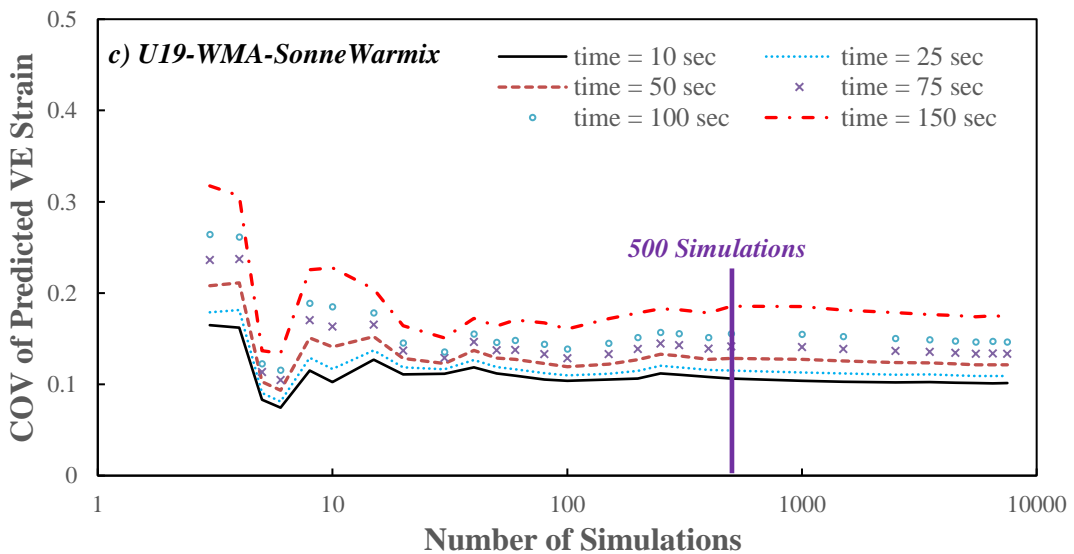


Figure 89. COV of predicted viscoelastic strains across the 10,000 simulations of the P-VECD model for U19-WMA-SonneWarmix.

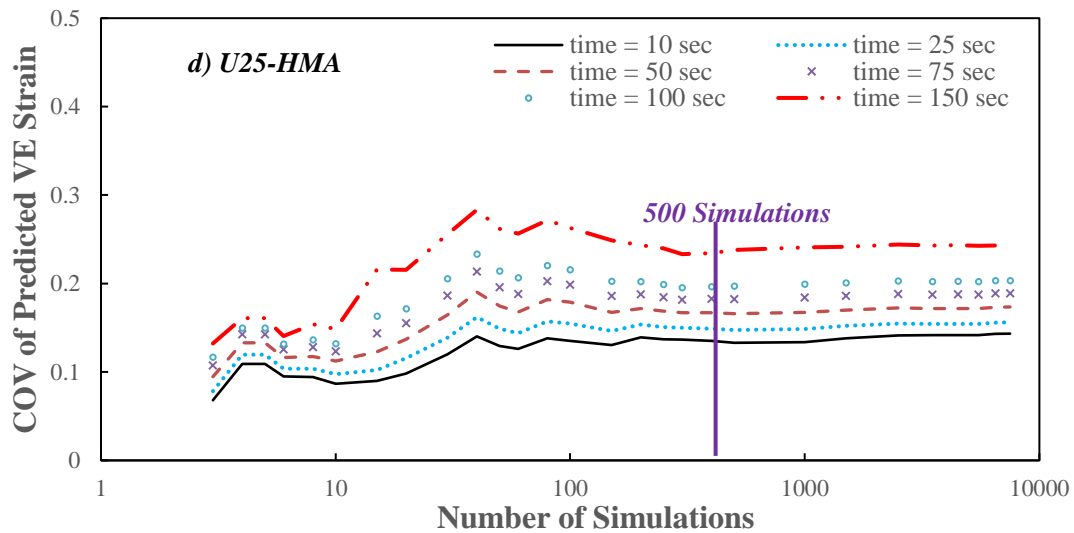


Figure 90. COV of predicted viscoelastic strains across the 10,000 simulations of the P-VECD model for U19-WMA-SonneWarmix.

7.4 Comparison of Results of Deterministic VECD AND P-VECD Results

The results of the P-VECD models of each of the mixes for the three investigated stress profiles allow for the development of the 68% and 95% confidence intervals which typically correspond to the ranges of \pm one and two standard deviations from the mean, respectively. These intervals provide an estimated range of values of the predicted viscoelastic strains for a specific mix in response to a given stress profile. It provides a tool for assessing how confident or certain that the true population mean of the predicted viscoelastic strain falls within a given range. Typically, the width of these intervals will be a function of the considered confidence level, variability of the estimated parameter, and the size of the sample used in the estimations of the statistical parameters of the investigated population. In the case of this study, the confidence level is defined as 68% and 95% and the samples size is the same in all cases being 500. Thus, the difference in the width of the confidence interval at any specific time for the same stress profile will be a function of the variability of the properties of the investigated asphalt concrete mix. Thus, the confidence intervals will present the inherent uncertainty in the predicted viscoelastic strains.

The developed 68% and 95% confidence intervals for the predicted viscoelastic strains using the P-VECD model are presented in Figure 91, Figure 92, and Figure 93 for the previously investigated stress profiles at 5°C, 25°C, and 35°C, respectively. It can be observed that for the same stress profile, the width of the confidence intervals at a given point in time varies from one mix to another. In addition, it can be observed that for the same mix the width of the confidence interval (both 68% and 95%) at the end of the analysis period becomes larger for stress profiles at higher temperatures. It is noticed that for the same mix the three stress profiles are chosen to yield same C value at the point of time corresponding to

the end of the analysis. This indicates that as reduced time increases and/or the mix have higher uncertainties especially in its LVE properties the width of the confidence intervals becomes larger. Therefore, it can be concluded that estimates of the mean value of the predicted viscoelastic strain fall in wider regions especially for mixes whose properties possess higher variabilities and for cases with larger analyzed reduced times.

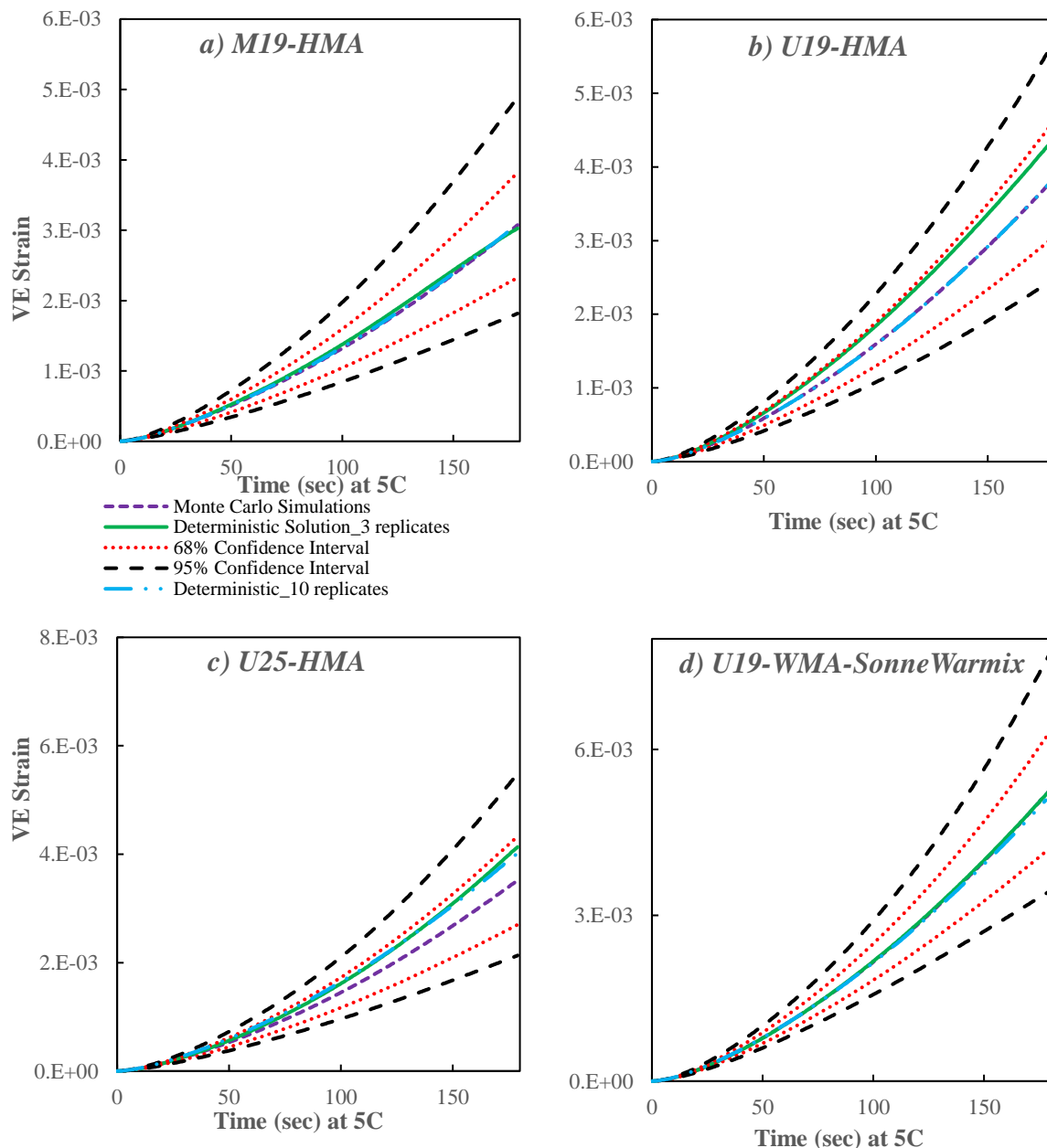


Figure 91. Predicted viscoelastic strains in response to the investigated stress profile at 5°C calculated using deterministic VECD and P-VECD model along with its 68% and 95% confidence intervals for a) M19-HMA, b) U19-HMA, c) U25-HMA, and d) U19-WMA-SonneWarmmix.

Two deterministic solutions are calculated for each of the investigated cases for the four mixes U19-HMA, M19-HMA, U19-WMA-SonneWarmmix, and U25-HMA. One of these solutions represent the common practice case where the predictions are based on the material

properties determined for three replicates tested for E^* and another three replicates tested using the monotonic test. The second investigated deterministic solution represent the predictions of the viscoelastic strains based on ten replicates tested in E^* and another ten replicates tested using the monotonic test. The results show that the deterministic solution based on ten replicates is almost close or equal to the solution obtained from the P-VECD models for almost all analyzed cases. The difference appears only for the case of the predicted viscoelastic strain of the U25-HMA mix where the deterministic solution falls in the region within one standard deviation from the mean obtained using the P-VECD model. The closer the deterministic solution to the predicted mean by the P-VECD model would be better; however, obtaining such difference is expected especially that the mean viscoelastic strain curve herein is an unknown population parameter expected to fall in this range. The case that it is not close to the mean curve obtained by the P-VECD model suggests that it can be considered as an accurate but a less precise estimate of the population parameter.

On the other side, it can be observed that the deterministic solution from three replicates has a scatter around the mean obtained from the P-VECD models for all cases of the 12 combinations of mix types and stress profiles. The deterministic solution can be observed to be either very close, close, or apart from the probabilistic mean but within the limits of the developed confidence intervals. This is expected due to the modeled uncertainty in the material properties and thus in that of the predicted viscoelastic strains. Thus, it is required to take into account the uncertainties associated with predicted viscoelastic strains especially when using the outputs of such advanced material characterization models as inputs for structural models required to calculate stresses and strains within pavement systems. A single value of the predicted viscoelastic strain will be considered when depending on the deterministic solution which might underestimate the probable viscoelastic strain in many cases and thus affect the reliability of designed pavements. -

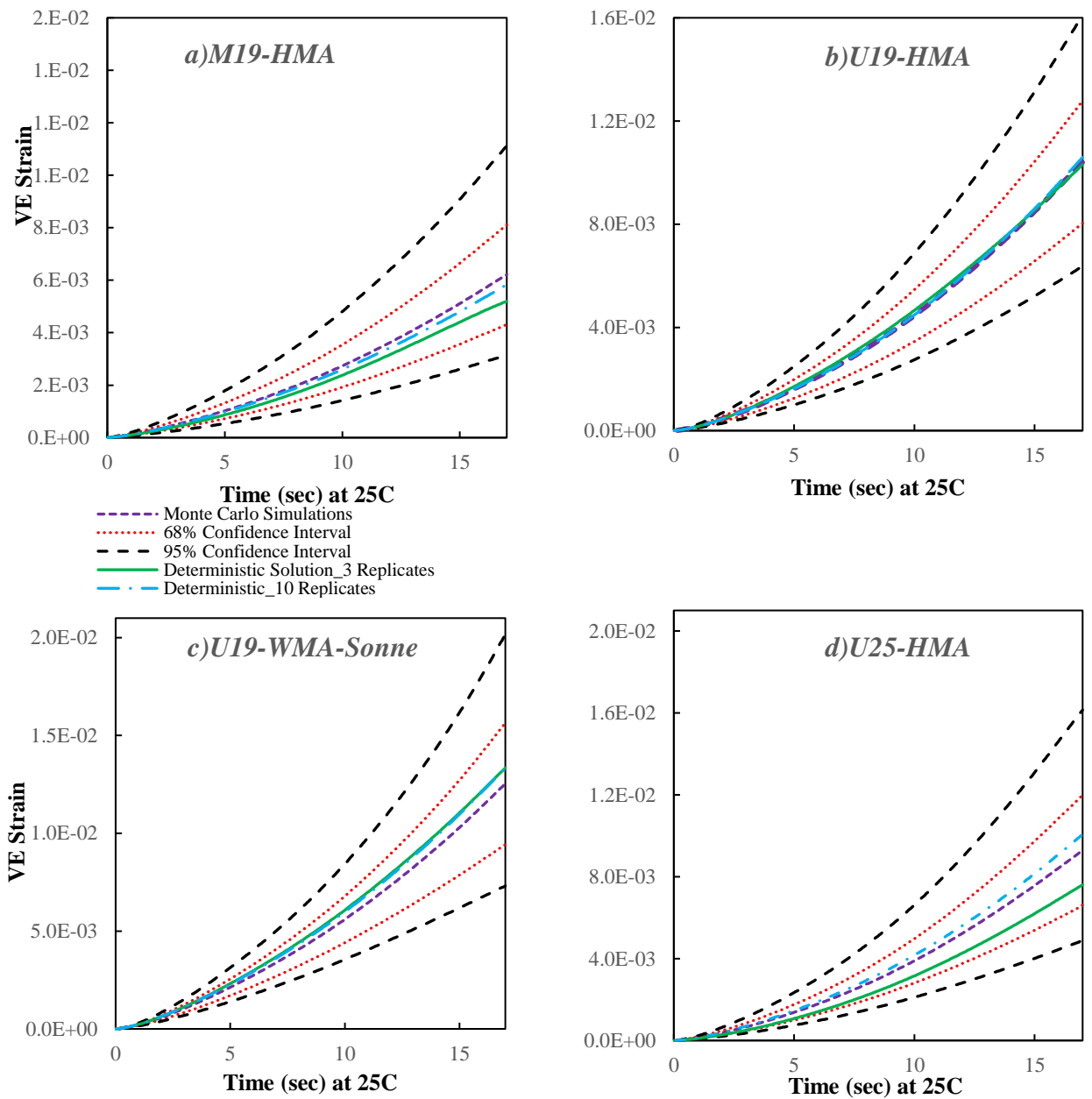


Figure 92. Predicted viscoelastic strains in response to the investigated stress profile at 25°C calculated using deterministic VECD and P-VECD model along with its 68% and 95% confidence intervals for a) M19-HMA, b) U19-HMA, c) U19-WMA-SonneWarmix and d) U25-HMA.

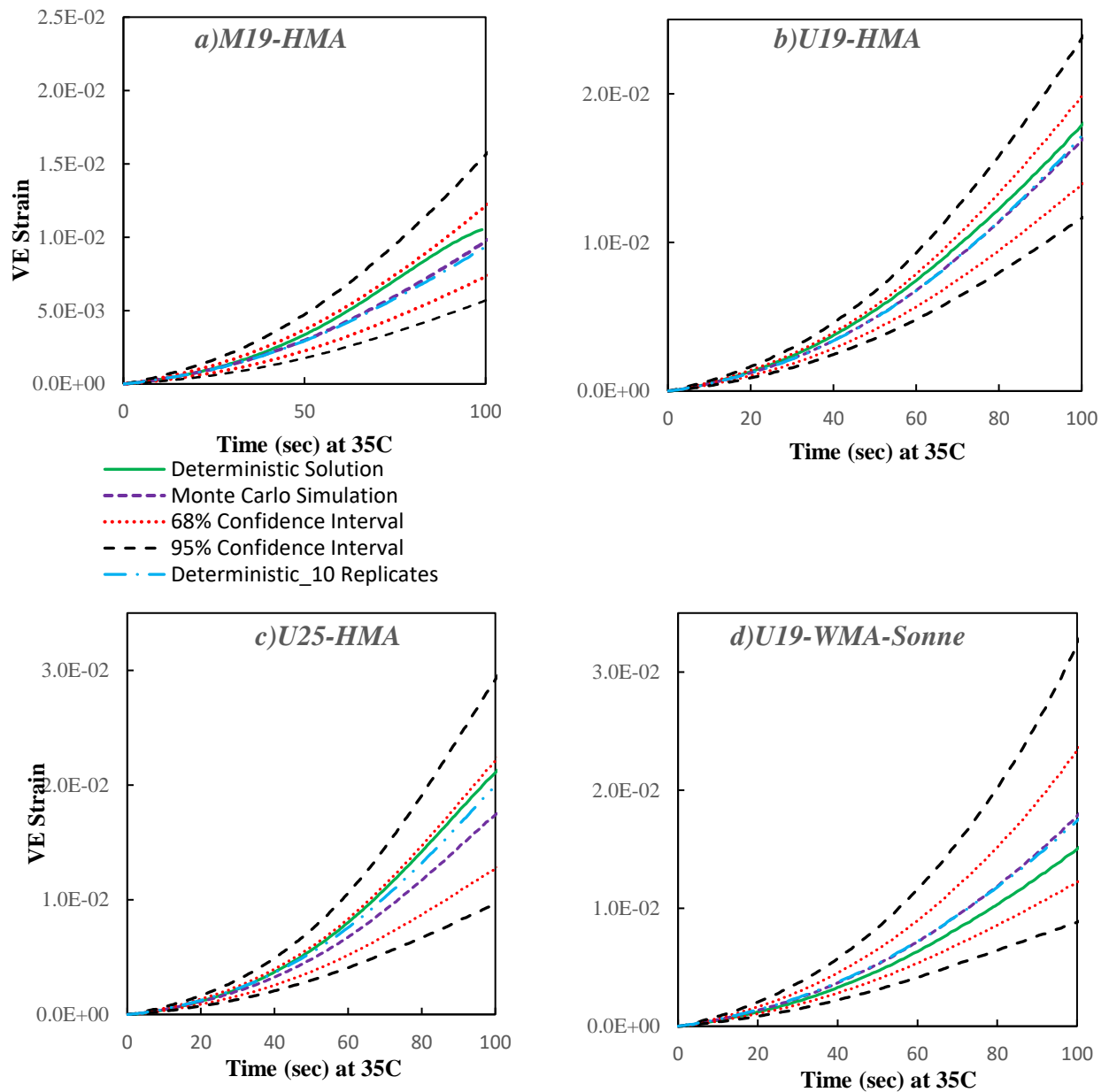


Figure 93. Predicted viscoelastic strains in response to the investigated stress profile at 35°C calculated using deterministic VECD and P-VECD model along with its 68% and 95% confidence intervals for a) M19-HMA, b) U19-HMA, c) U25-HMA, and d) U19-WMA-SonneWarmix.

The mean, standard deviation, and the distribution of the predicted viscoelastic strain for all the investigated stress profiles are determined as a result of the P-VECD model. This allows for the calculation of the probability that the viscoelastic strain at any time exceeds that predicted using the case of common practice presented as the deterministic solution from three replicates. Knowing that the predicted viscoelastic strain follows a lognormal distribution at any time of prediction and for any combination of the investigated stress profiles and mix, a sample of these probabilities are calculating. For example, the probability that the viscoelastic strain exceeds that of the deterministic solution is estimated at a time of 100 seconds of the investigated stress profile at 5°C. This probability is found to be 19.1%,

43.9%, 45.7%, and 23.4% for the U19-HMA, M19-HMA, U19-WMA-SonneWarmix, and U25-HMA, respectively. Similarly, such a probability is calculated at a time of 15 second for the stress profile of 25°C where it is found to be 44.6%, 51.7%, 34%, and 70.1% for the U19-HMA, M19-HMA, U19-WMA-SonneWarmix, and U25-HMA, respectively. At a time of 100 second for the investigated stress profile of 35°C, the probability is calculated as 32%, 33.8%, 64.2%, and 20.4% for the M19-HMA, U19-HMA, U19-WMA-SonneWarmix, and U25-HMA, respectively. The results show that the probability of the predicted viscoelastic strains exceeds the values of the deterministic solutions may be as low as 19% and as high as 70%. The analysis of these probabilities show that there is not a specific trend in variation from one mix to another and according to temperature of the asphalt concrete. This is expected as long as the estimate mean of the viscoelastic strain falls within the limits of the confidence intervals. The probabilities show that the deterministic solution could significantly underestimate the viscoelastic strain in response to a given stress input. Thus, it is needed to consider a P-VECD model to better represent the actual behavior of asphalt concrete mixes.

7.5 Use of Global Damage Characteristic Curve for Predicting Viscoelastic Strains

7.5.1 Development of Global Damage Characteristic Curve

The results of the previous parts show that the predicted viscoelastic strains for a given stress response have a significant level of uncertainty. This uncertainty is forward propagated and it a result of the uncertainty in LVE material properties and damage characteristic curves presented by both the C versus S curve and the S versus Lebesgue norm of stress curve, jointly referred to as C versus stress curves. In addition, damage characteristic curves of the four mixes for which the P-VECD models are developed show a difference but not a huge one even though the mixes have different components included unmodified neat binder, polymer modified binder, WMA additive, and different aggregate sizes. Therefore, the apparently limited different between the different damage characteristic curves and the significant uncertainty in those curves sheds the light on assessing the sensitivity of C versus stress curves on the predictions of the viscoelastic strains for a given stress profile. This is carried out in this study through the construction of global damage characteristic curve.

The global damage characteristic curve involved the development of a global C versus S and a global S versus Lebesgue norm of stress curves. These curves are referred to herein as global but in the context of the mixes in this research. To achieve this task, the data used for the development of the damage characteristic curves of the P-VECD model of each of the mixes U19-HMA, M19-HMA, U19-WMA-SonneWarmix, and U25-HMA are pooled

together. This implies having 40 “C versus S” curves and 40 “S versus Lebesgue norm of stress curves”. The global C versus stress curves are calculated and fitted as the average of these 40 curves regardless of the type of the mix. The developed global “C versus S” and “S versus Lebesgue norm of stress curves” are presented in Figure 94 and Figure 95, respectively.

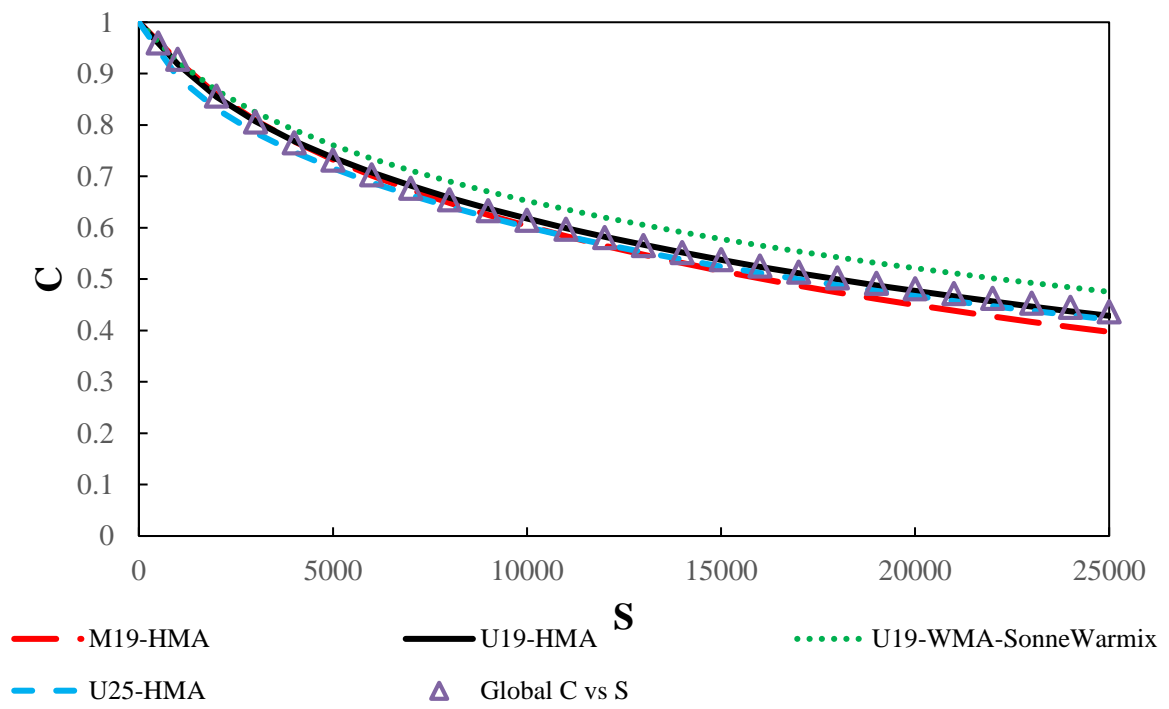


Figure 94. Mix-specific and global C vs S curves calculated based on the four mixes: U19-HMA, M19-HMA, U19-WMA-SonneWarmix, and U25-HMA.

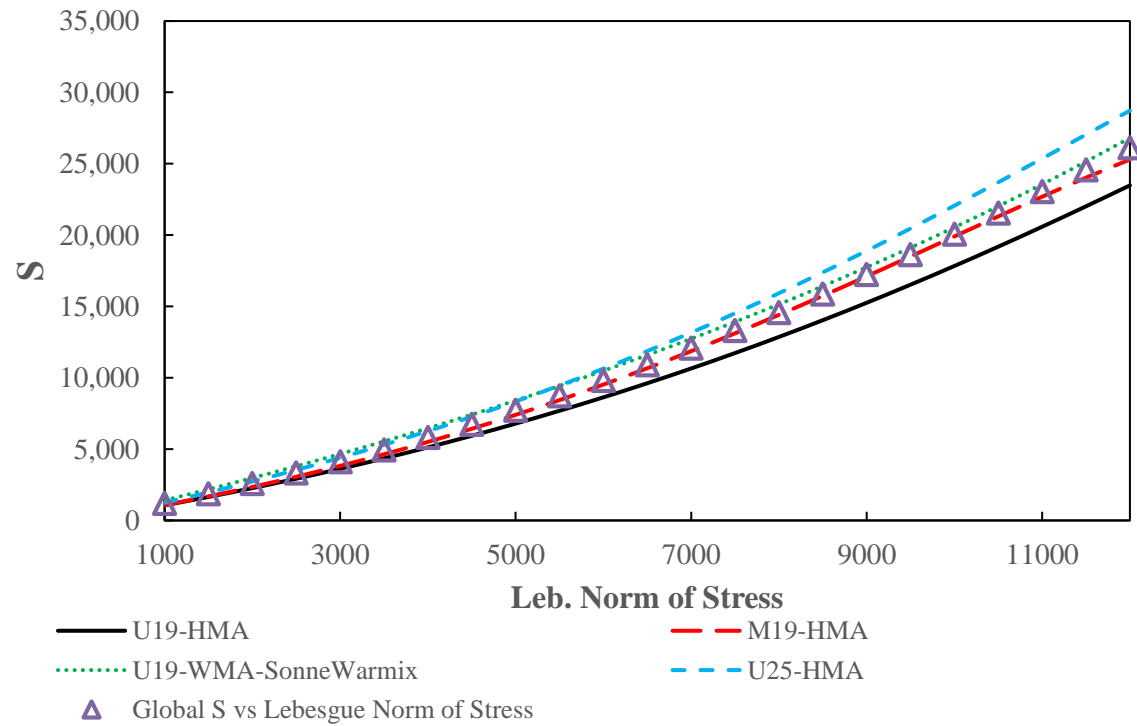


Figure 95. Mix-specific and global S vs Lebesgue Norm of Stress curves calculated based on the four mixes: U19-HMA, M19-HMA, U19-WMA-SonneWarmix, and U25-HMA.

7.5.2 Verification of Using a Global Damage Characteristic Curve

The concept of using a global C versus stress relationship relies on a hypothesis that these curves characterize the general behavior of the reduction in the pseudostiffness of asphalt concrete resulting from the accumulation of damage under given loading conditions. Thus, the assumption of a global C versus stress relationship instead of mix specific relationships provides a simplification for the prediction of viscoelastic strains in a fast and with a limited testing efforts. Thus, the viscoelastic strain will be predicted as the response of input stress profiles for different mixes where the global C versus stress relationship will be used along with $D(t)$ specific to the mix under investigation. Thus, the simplification of the VECD model testing herein assumes that the C versus stress relationship characterizes the behavior but $D(t)$ presents the properties of every specific mix.

The global C versus stress relationship is developed using the data of the four mixes U19-HMA, M19-HMA, U19-WMA-SonneWarmix, and U25-HMA. For each of these mixes, the viscoelastic strain is predicted using the global C vs stress and compared to the solution obtained using the mix specific relationships for the previously investigated three stress profiles. The followed modeling strategy involves the consideration of mix specific $D(t)$ calculated as the average of three tested replicates in E^* . The actual deterministic and probabilistic solutions of the viscoelastic strains along with the prediction based on the global C versus stress curves are presented in Figure 96, Figure 97, and Figure 98 for the investigated stress profiles at temperatures of 5°C, 25°C, and 35°C, respectively. The results show that the predicted viscoelastic strains using the global C versus stress relationships are very close that predicted by the P-VECD models for the cases of the three investigated stress profiles for the four mixes. The obtained viscoelastic strain curves are even closer to the probabilistic solutions than that of the deterministic solution involving mix specific C versus stress relationships. Therefore, it can be concluded that so far the usage of a global C vs stress curve for a set of mixes having common sources of materials might yield a realistic, accurate, and precise solution that is almost equal to that of the P-VECD model.

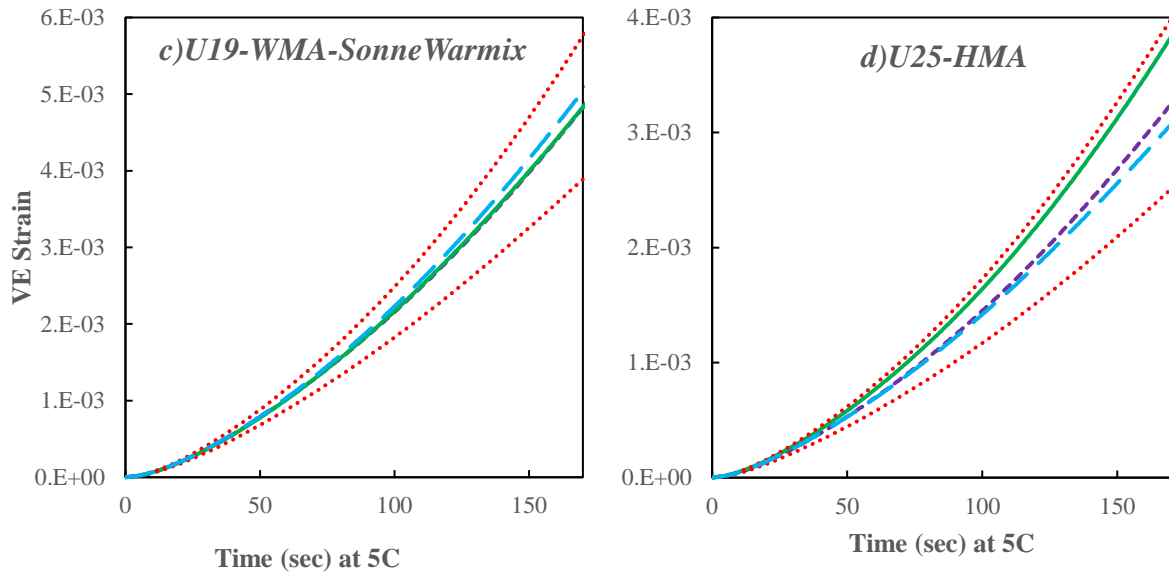
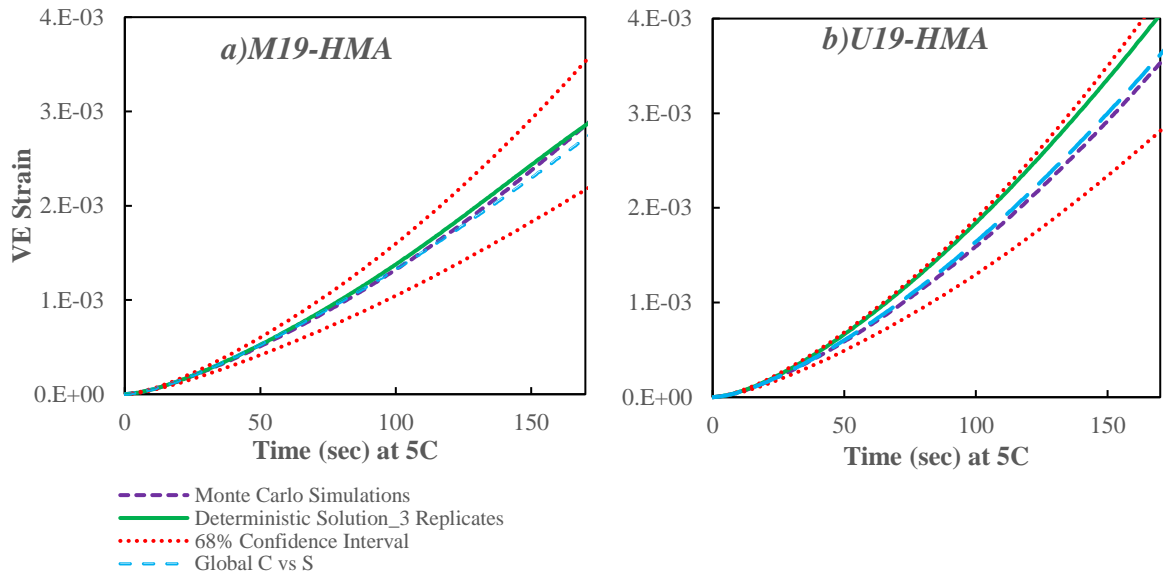
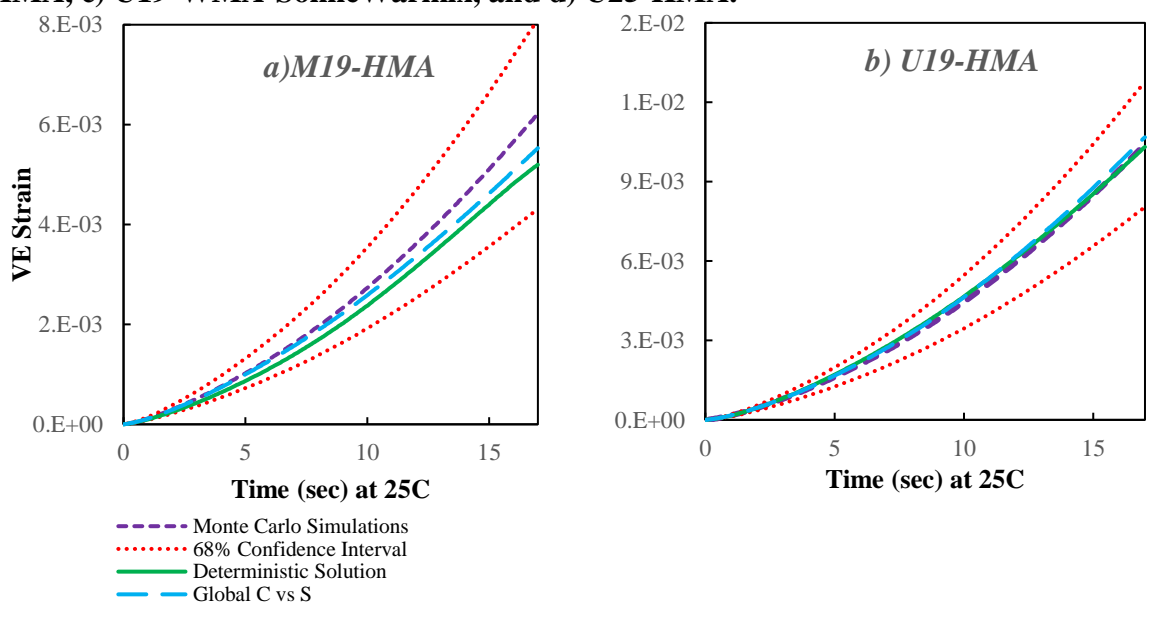


Figure 96. Predicted viscoelastic strains calculated using Global damage characteristic curve in response for the investigated stress profile at 5°C for a) M19-HMA, b) U19-HMA, c) U19-WMA-SonneWarmix, and d) U25-HMA.



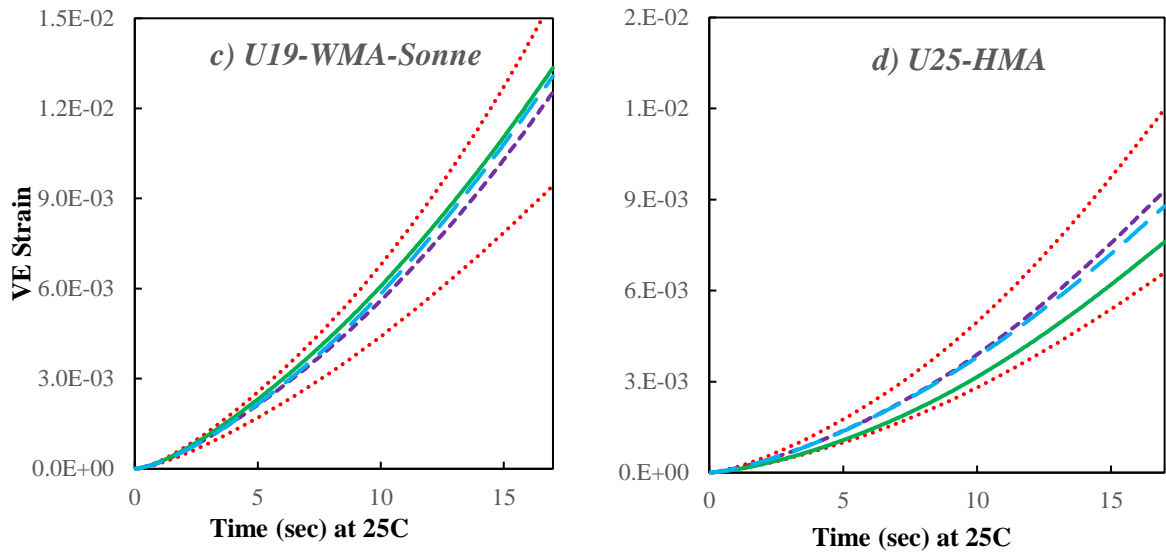
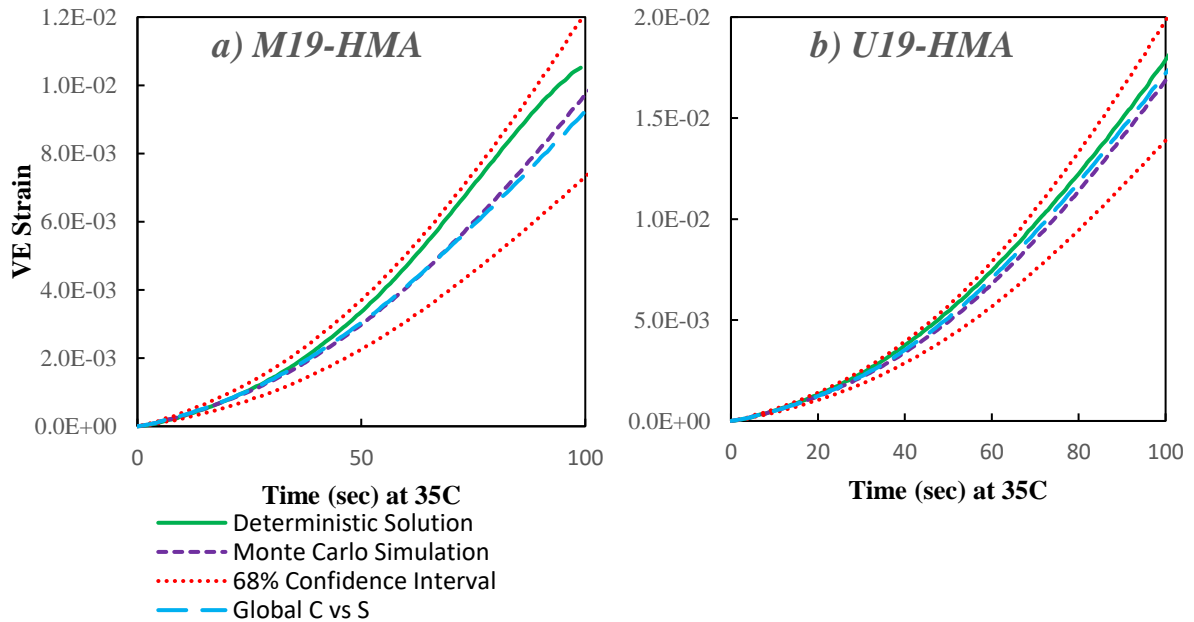


Figure 97. Predicted viscoelastic strains calculated using Global damage characteristic curve in response for the investigated stress profile at 25°C for a) M19-HMA, b) U19-HMA, c) U19-WMA-SonneWarmix, and d) U25-HMA.



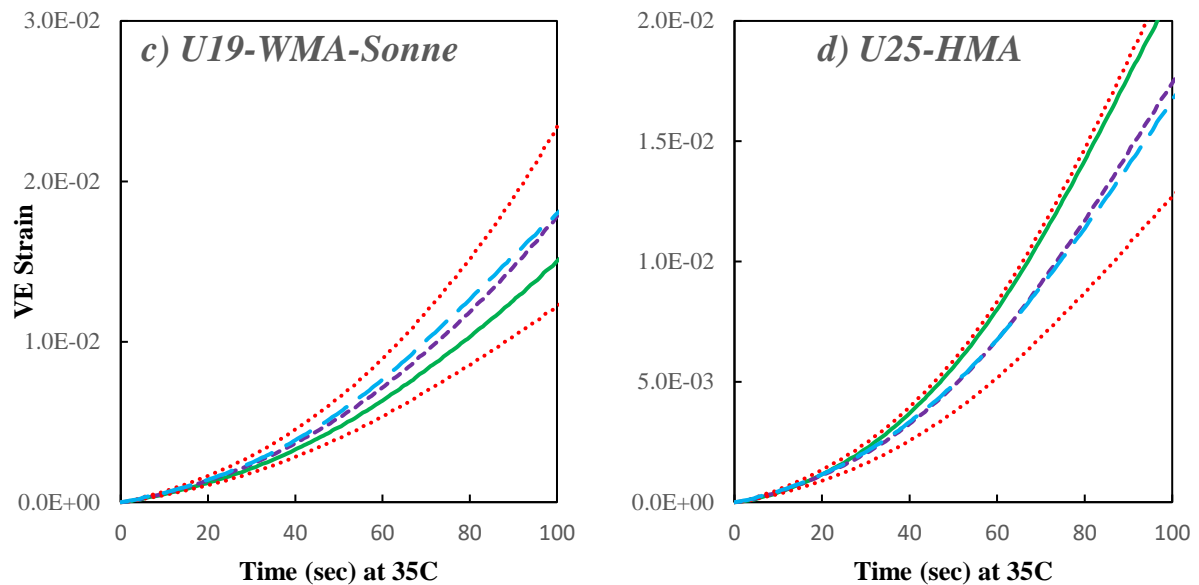


Figure 98. Predicted viscoelastic strains calculated using Global damage characteristic curve in response for the investigated stress profile at 35°C for a) M19-HMA, b) U19-HMA, c) U19-WMA-SonneWarmix, and d) U25-HMA.

7.5.3 Validation of Using a Global C vs Stress Relationship

The predicted viscoelastic strains do not show a significant difference when calculated using mix-specific and global C versus stress relationships for the cases of each of the mixes: U19-HMA, M19-HMA, U19-WMA-SonneWarmix, and U25-HMA. The predictions of viscoelastic strains using a global C vs stress relationship is realistic in the case of mixtures used to develop the global relationship. However, this needs to be further addressed to study the validity of using a global C versus stress relationship for prediction of viscoelastic strains for mixes other than those used to develop the global relationships. To address this task, some of the mixes used in the assessment of WMA mixes is considered to predict their response using both the developed C versus stress relationships and each mix's specific properties. The mixes considered in this context are M19-WMA-Rediset, M19-WMA-Sasobit, U19-HMA-Fibers, U19-WMA-SonneWarmix-Fibers, U25-WMA-Rediset, and U25-WMA-Advera. These mixes incorporate a variety of factors that include different types of WMA additives, with or without fibers, different types of binders, different mixing and compaction temperatures, and different aggregates sizes. It is notable that these six mixes along with the previous four used to develop the global C versus stress relationships have different mix components but all have the following common factors:

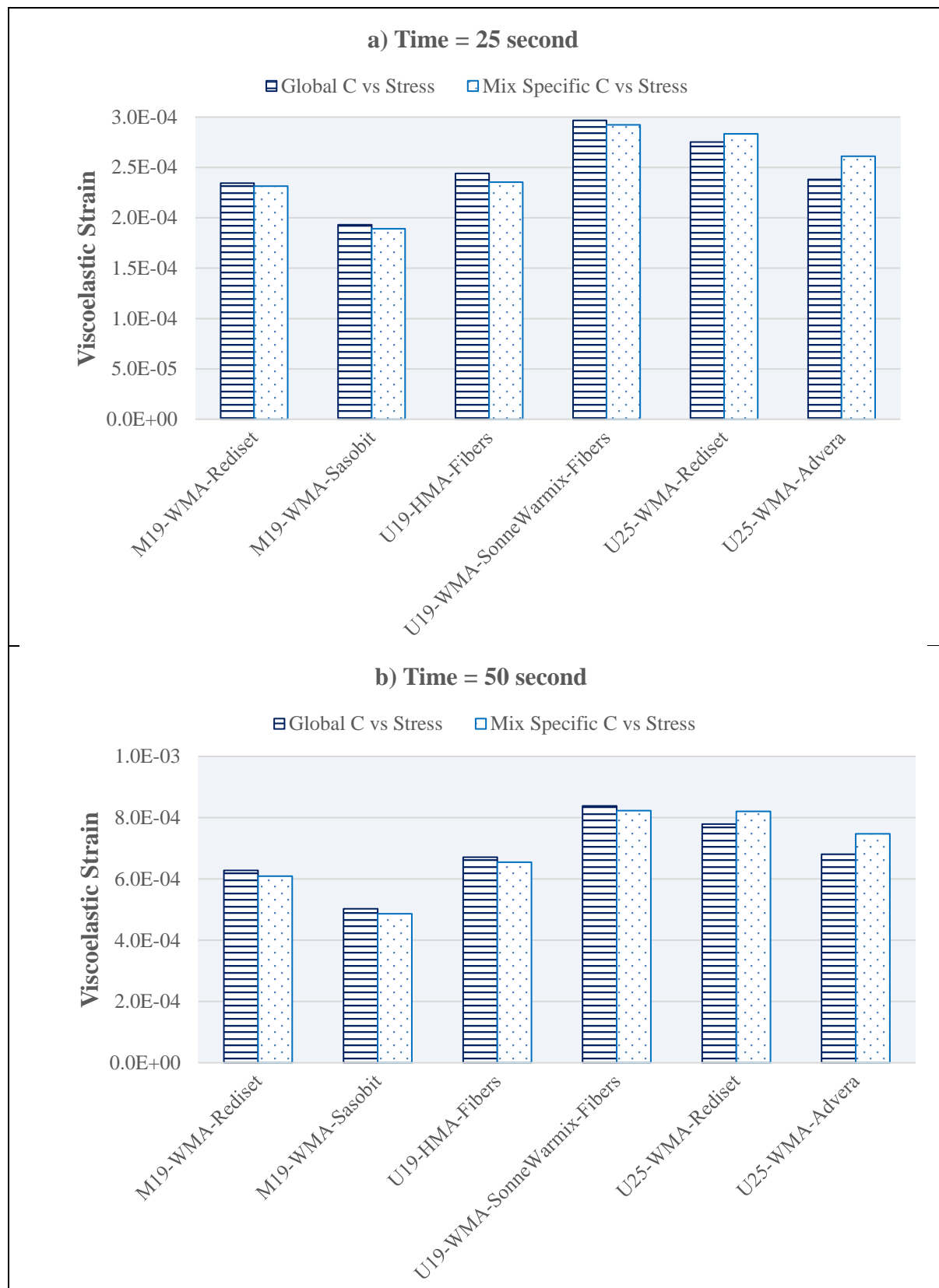
- All the ten mixes have the same type and source of aggregates.
- Mixes with modified binder have the same source and type of binder
- Mixes with unmodified binder have the same source and type of binder

- All samples of these mixes are mixed, compacted, and tested in the same laboratory
- All the replicates of these mixes are tested in compression state
- All replicates of the ten mixes have the same level of air voids

For illustration, the viscoelastic strain is predicted in response to the previously investigated stress profile at 5°C. This is carried out using both mix specific and global C versus stress relationships. The results for the six mixes used for validation are presented at selected times of 25, 50, 100, and 150 second as presented in Figure 99. The results of both predictions per mix are very close where the global C versus stress relationships yield predicted viscoelastic strains that are within $\pm 10\%$ of the mean predicted viscoelastic strain using the mix's specific C versus stress relationships. The viscoelastic strain predicted using the global C versus stress relationship could be either larger or smaller than that predicted using the mix specific relationships depending on the investigated mix. The results are consistent for all mixing regardless of the time of analysis and thus regardless of the magnitude of the predicted strain, the value of C, and reduced time.

It can be concluded that it is possible to use a global C versus stress relationship for the prediction of viscoelastic strains. This is validated in this study for three different control mixes with different components added to modify the functionality of such mixes. Therefore, the validity of using the global C versus stress relationship is recommended as a simplification especially when assessing mixes that could have the same materials but with only few components vary. This is a valid case in projects in which viscoelastic strains are needed to be predicted and compared for mixing incorporating certain types of additives such as fibers and WMA additives, different binder types, and different aggregate gradations. Therefore, the global C versus stress relation can be done by testing crosshead samples for the reference mixes and thus used for predictions of the modified mixes. Thus, such mixes will require only characterizing their LVE properties mainly $D(t)$, " α ", and the time-temperature shift factors. So, the global C versus stress could be used when comparing mixes of same category so that it will reduce the required number of tests to be conducted implying less effort, less time, and less need for resources. However, the conclusion herein needs to be validated in future studies for other categories of mixes implying different sources of materials and different levels of air voids. In addition, this could open the door for the development and assessment of a universal C versus stress relationship by building and testing a database of C versus stress relationship for the compression state from mixes worked on at different countries around the world, with totally different materials, and by

different research groups. This could be helpful in assessing a further simplification whether a unique universal C versus stress curve could be used to predict viscoelastic strains with a minimal effect on the accuracy of the responses to be predicted.



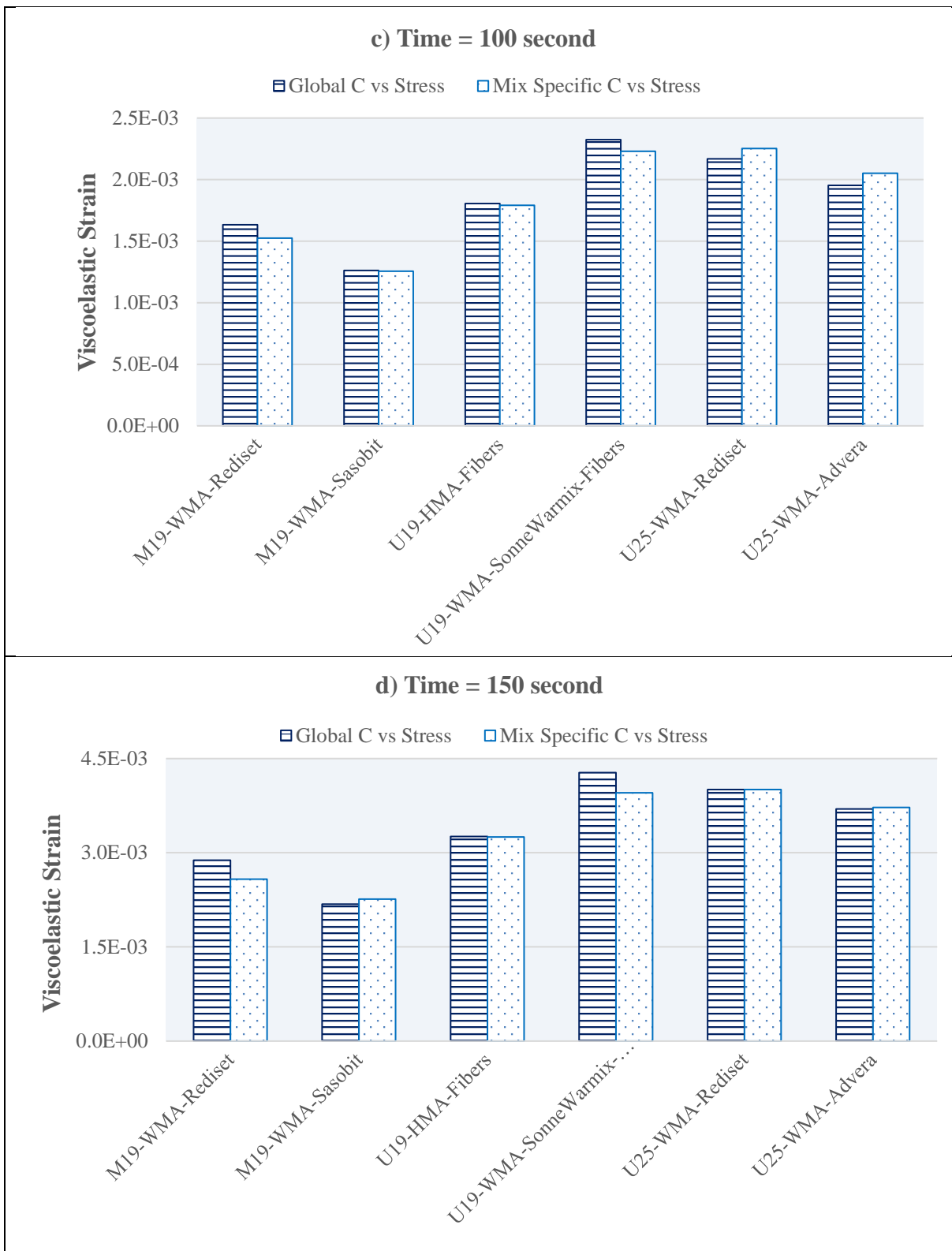
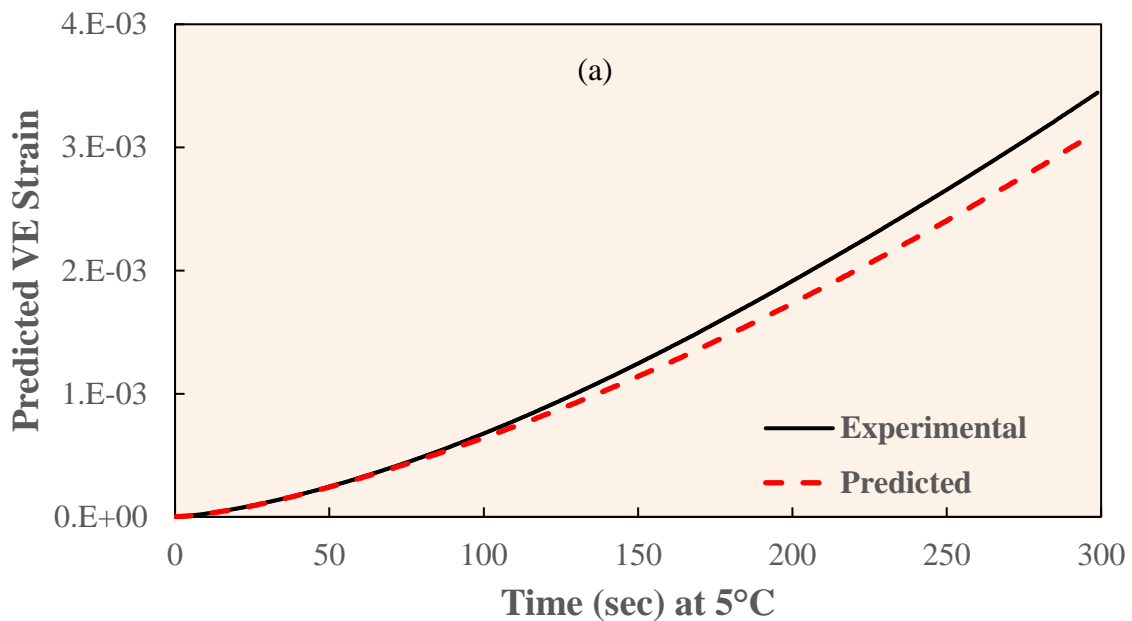


Figure 99. Viscoelastic strains calculated in response to the investigated stress profile at 5°C for different mixes using both the damage characteristic curves specific to each mix and the developed global relations for a) Time = 25 second, b) Time = 50 second, c) Time = 100 second, and d) Time = 150 second.

Furthermore, the usage of a global damage vs. stress relationship is validated using experimental data of U25-WMA-Sasobit-RAP mix which is a mix with an aggregate gradation of a NMAS of 25.0 mm, a wax-based WMA additive, unmodified binder, and RAP

replacing 15% by weight of the total mix as described in the Appendix. The usage of the global damage vs. stress relationship is validated by comparing the predicted viscoelastic strains using this relationship with the strains measured for two samples tested by applying a constant crosshead rates. The two samples are tested at 5°C at rates of 0.00005 ϵ /sec and 0.000025 ϵ /sec which are conditions selected to ensure the absence of viscoplasticity. Thus, for each of these replicates the viscoelastic strain is predicted for the stress profile of each one at 5°C using the developed global C vs. L(σ) relationship. The results, as presented in Figure 100, show that the viscoelastic strains predicted using the global C vs LS(σ) relationships are very close to the on-specimen viscoelastic measured strains. The measured and predicted strains are very close with a slight difference not exceeding 10% especially at high levels of damage without a significant pattern obtained for the two tested replicates. Therefore, this further validates the usage of a global C vs. LS(σ) relationships especially that the mixture used contains components different from those of the mixes used for the development of these global relationships.



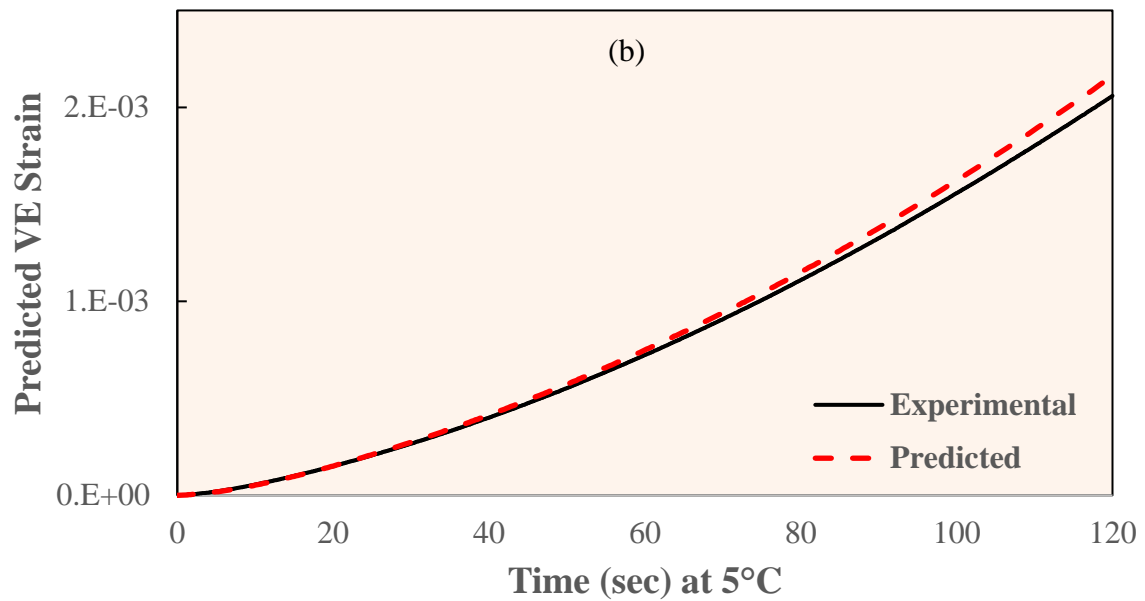


Figure 100. Measured and predicted viscoelastic strains using global damage vs. stress relationships for tested replicates of U25-WMA-Sasobit-RAP at 5°C and rates of a) 0.000025 ϵ /sec and b) 0.00005 ϵ /sec.

In addition, the effectiveness of using global C vs LS(σ) relationships is validated for a different mode of loading other than that of monotonic testing similar to that of the tests used for the calibration of the VECD model. For this purpose, the viscoelastic strain is predicted for the random cyclic stress profile as used earlier and presented in Figure 28. The viscoelastic strain is predicted in response to this stress profile at 5°C using both the U25-WMA-Sasobit-RAP mix-specific and global relationships as presented in Figure 101. The results show that the viscoelastic strains predicted using the global relationships is very close to that predicted using the mix-specific relationships in both the loading and unloading regimes. This shows that using global C vs stress relationships is also valid for different modes of loading and not only that used to calibrate them.

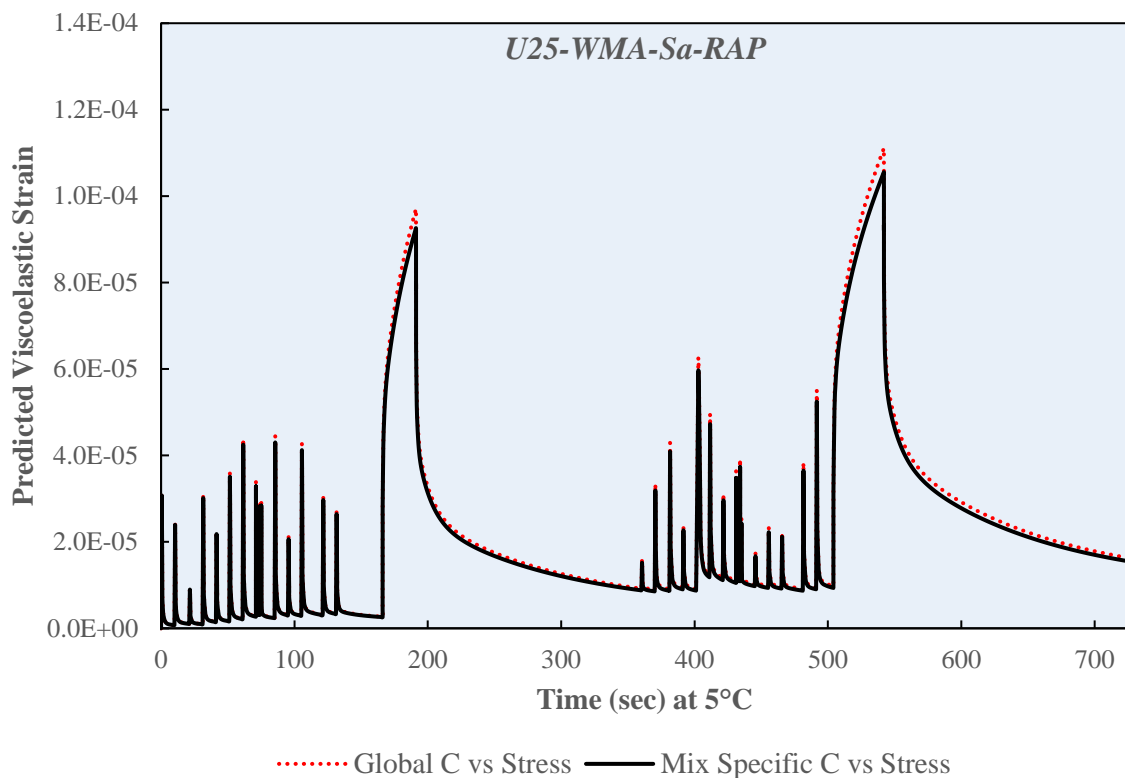
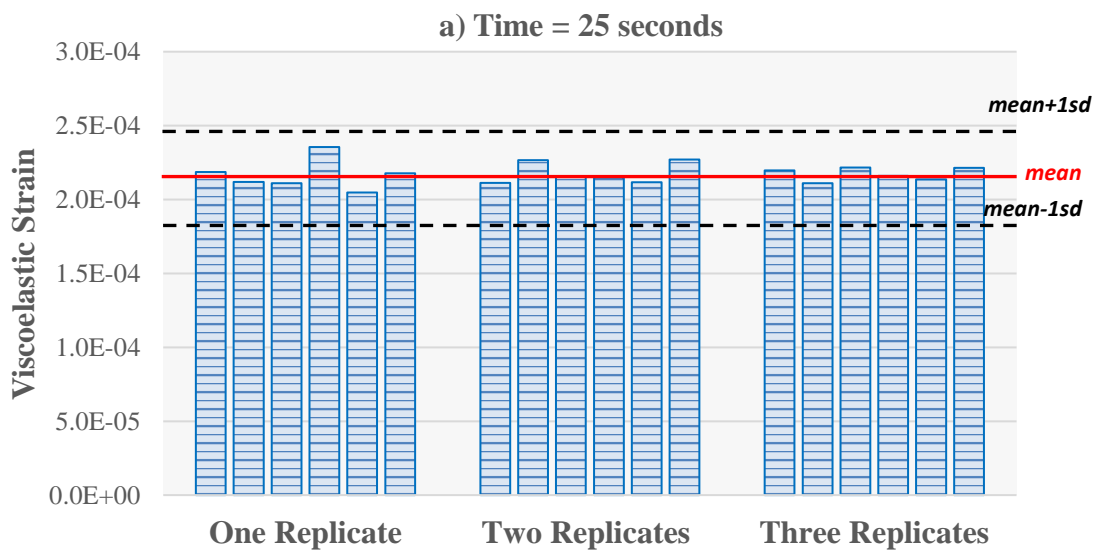


Figure 101. Viscoelastic strains in response to random stress profile predicted using mix-specific and global C vs stress relationships.

7.6 Effect of Number of Replicates of Crosshead Test on The Predicted Viscoelastic Strains

The investigated mechanistic models are not new to develop where the VECD model has been worked on by several research groups since many years ago. However, efforts have been paid throughout the years in order to improve such models and simplify them so that they can be easily applied and used to assess the mechanistic behavior of asphalt concrete. One of the questions that could be asked regarding the VECD model is what number of replicates is least required to be tested in monotonic testing to develop the damage characteristic properties of asphalt concrete yet giving realistic results with a minimum effort. As stated earlier, the current common practice requires determining the damage characteristic curves as the average of three replicates tested using the monotonic tests. Several factors investigated in this study trigger the investigation of minimizing the effort required to develop a VECD model. These factors include the uncertainty observed in the prediction by the P-VECD model, the closeness of the damage characteristic curves of the different investigated mixes, and the applicability of the use of global C versus stress curves to predict realistic viscoelastic strains like that obtained by P-VECD models. Similar to the case of analyzing the use of global C versus stress curves, the LVE properties will be kept consistent

as the current practice where all related properties are calculated and determined as the average of three E^* tested replicates. Therefore, the VECD model is developed using C versus stress relationships calculated from one, two, and three monotonic tested replicates. For illustration purposes, this exercise is carried out for the case of U19-HMA where the viscoelastic strains are predicted in response to the previously investigated stress profile at 5°C . For each of the VECD models to be developed based on one, two, and three replicates tested by the monotonic test, the required number of replicates is extracted randomly from the ten tested replicates and used for the development of the P-VECD model. For each case of the VECD models, six realizations are considered where the viscoelastic strains are predicted for each case as presented in Figure 102 at selected times of 25, 50, 100, and 150 second along with the results obtained from the P-VECD with the limits of \pm one standard deviation around it. Graphically, the results show that whether the C versus stress is calculated based on testing on, two, or three monotonic samples, the predicted viscoelastic strains are scatters around the mean estimated using the P-VECD model. For all the 18 cases, the deterministic viscoelastic strains fall within the range of \pm one standard deviation from the probabilistic mean. The scatter of the deterministic viscoelastic strains around that predicted by the P-VECD model becomes larger as the time increases where this is due to the increase in the COV of the predicted viscoelastic strains as shown in the previous sections of this research work. This shows that using a C versus S curve and a S versus Lebesgue norm of stress curves resulting from a minimal number of samples as low as one might yield realistic predictions by the VECD model.



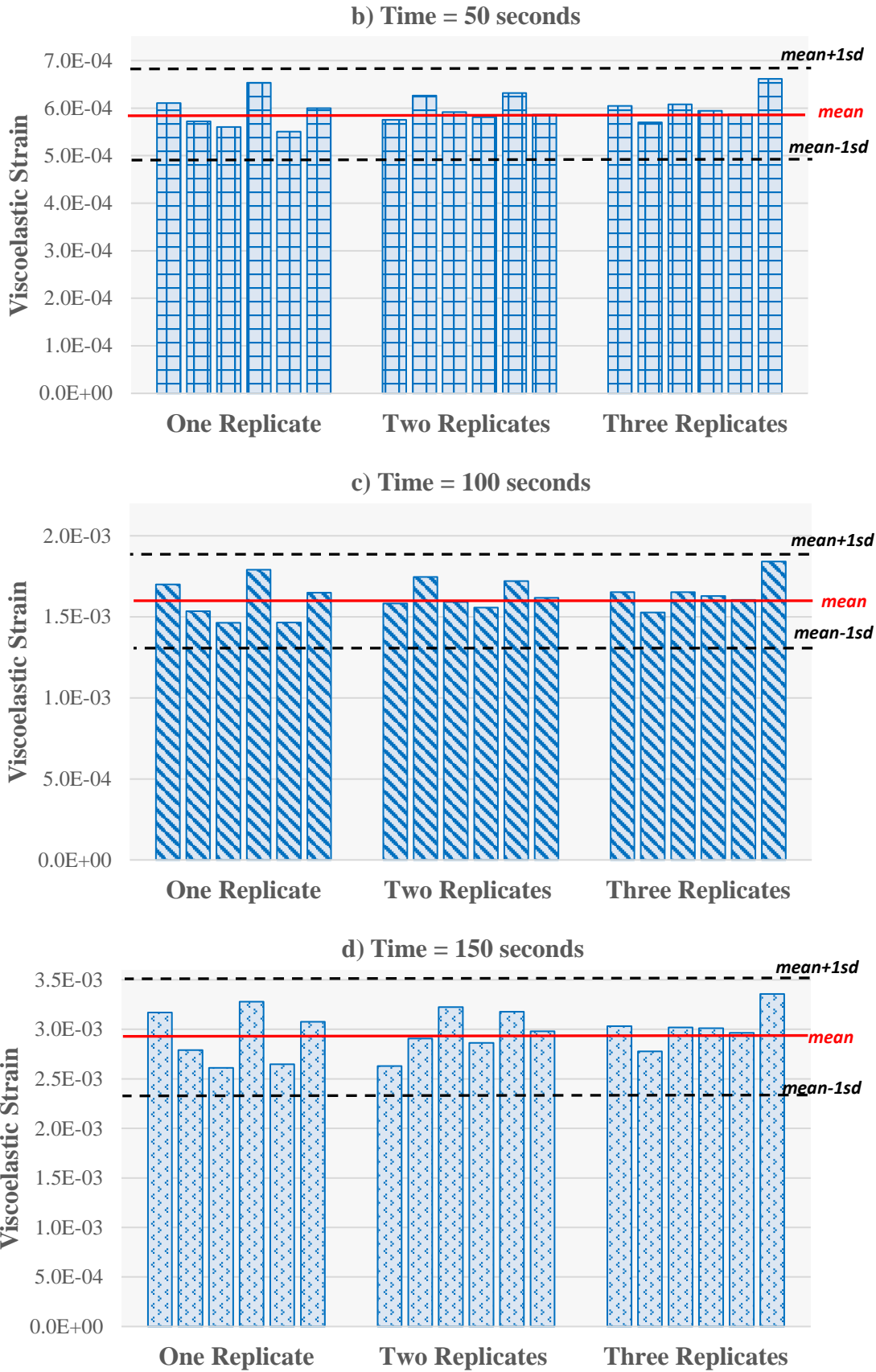


Figure 102. Predicted viscoelastic strains in response to the investigated stress profile at 5C using damage characteristic curves calculated based on one, two, and three tested replicates at a) time = 25 second, b) time = 50 second, c) time = 100 second, and d) time = 150 second.

To further assess the possibility of adopting only one or two monotonic samples, a suit of statistical tests is conducted where the number of replicates is considered as a treatment effect whose deviation from the overall mean needs to be assessed. One way analysis of variance (ANOVA) is conducted to test the following hypothesis:

- H_0 : The population means of viscoelastic strains predicted using one, two, and three monotonic replicates are equal.
- H_a : At least two population means are NOT equal.

The results of the hypothesis testing are presented in Table 46 where the p-value falls in the range of 0.69-0.98 which is higher than the level of significance of 0.05 and thus fail to reject H_0 where there is not a strong evidence that the means are different. Therefore, the mean predicted viscoelastic strains based on C versus stress relationships from one, two, and three replicates are statistically equal. This is further assessed by conducting the multiple comparison Tukey HSD test where the obtain p-values are greater than 0.05 assuring the results obtained from the one-way ANOVA. The p-values obtained for the pairwise comparison of the means obtained from two and three replicates is higher than that obtained for the case of comparing the means obtained from one and three replicates This indicates that it is more evident that the C versus stress from two replicates yields more realistic results as compared to case of a single sample even though they are statistically equal. In addition, the variances of the predicted viscoelastic strains obtained for the three investigated treatments is assessed. The F-test is a well-known test that can be used for that purpose; however, it cannot be used in this case because we have more than two groups to be compared. Therefore, the Bartlett's test statistic is conducted to assess the equality of the variances obtained because of using C versus stress from one, two, and three monotonic samples. This test is applicable because more than two groups need to be compared and for the case of more than three measurements per group. The tests yield p-values in the range of 0.07-0.2 which is larger than an alpha value of 0.05 indicating the variances are equal. The p-value decreases as the time increases indicating that the evidence of failing to reject the null hypothesis becomes less strong which is due to the presence of higher uncertainty in the predicted viscoelastic strains as the time increases as indicated in the previous sections. Therefore, it can be concluded that it is possible to simplify the process of the development of VECD models by using only one or two monotonic samples without affecting the accuracy nor the precision of the obtained results.

Table 46. p-values from statistical analysis results for predicted viscoelastic strains using damage characteristic curves calculated from one, two, and three replicates.

Time (second)	Bartlett Test of Homogeneity of Variances	One-Way ANOVA	TukeyHSD		
			One- two	Two- Three	One- three
25	0.20	0.98	0.99	0.99	0.99
50	0.13	0.87	0.86	0.95	0.97
100	0.08	0.95	0.97	0.99	0.95
150	0.07	0.69	0.76	0.99	0.70

CHAPTER 8

MODELING OF THE INHERENT UNCERTAINTY IN LVE FUNCTIONS FROM FIELD AND MULTI-LABORATORY DATA

8.1 Introduction

Understanding the difference between the behavior of mixtures produced in the laboratory and that of plant-produced mixtures is of interest to researchers in the paving industry, in order to better assess anticipated field performance at a mix design level (Cooper III 2011, Rahbar-Rastegar and Daniel 2016, Xiao et al. 2014). Numerous factors lead to differences between plant and laboratory mixed samples that can impact the properties of asphalt mixes. These factors include different handling, heating, and storage conditions of asphalt binder whereby in the lab it is stored in small cans at room temperature, while in the plant it is stored in enclosed heated systems. Likewise, the handling, mixing and heating methods of asphalt mixes differ between lab and plant. Other significant factors include segregation of aggregates, breakdown of aggregates during stockpiling and processing, and differences in added amounts of mineral fillers in the plants. Studies have shown differences in the stiffness of laboratory and plant produced samples, with lab mixes having higher stiffness on average/in general. Thus, it is important to investigate and quantify the effects that are induced by plant conditions on the uncertainty of the properties of asphalt mixes. This is carried out by examining and comparing the uncertainties in LVE properties of two categories of asphalt mix test specimens: lab mixed, lab compacted (LMLC) specimens and plant mixed, lab compacted (PMLC). The data of U19-HMA, M19-HMA, U25-HMA, and U19-WMA-SonneWarmix represent LMLC samples while PMLC samples are represented by a new suit of mixes defined/identified as Set I in the following sections. In addition, the effect of laboratory equipment, testing protocols, and different test operators are assessed on another suit of LMLC specimens for a set of mixes referred to as Set II in the following sections.

8.2 Inherent Uncertainty in $|E^*|$

8.2.1 *Dynamic Modulus Data*

In this section of the research, the quantification of the inherent uncertainty for each of $|E^*|$, $E'(w)$, $E(t)$, and $D(t)$ was achieved using six HMA mixes whose properties are shown in Table 47. These mixes were divided into two data sets:

- Set I consists of test replicates from three mixes collected from a paving project. These mixes have the same aggregates gradations as the other 19.0 mm and 25.0 mm HMA and WMA mixes previously investigated in this research.
- Set II consists of test replicates from three mixes published in NCHRP 9-29 Report 702 (Bonaquist 2011). In that study, three prefabricated replicates from each mix were sent to eight laboratories to be tested, resulting in a total number of 24 test replicates for each mix. These eight laboratories are accredited by AASHTO for hot-mix asphalt testing presenting agency labs, commercial labs, and research labs.

Table 47. Properties of the mixes used to quantify the inherent uncertainty of |E*|.

Mix description and designation	Set I			Set II		
	Mix 1	Mix 2	Mix 3	Mix 1	Mix 2	Mix 3
	19mm Fuel Resistant (FR) HMA	25mm mix HMA	19mm HMA	Coarse-graded 9.5mm HMA	12.5mm SMA	Fine-graded 25.0mm HMA
Asphalt binder grade	PG 76-16			PG 64-22	PG 76-22	PG 64-22
Design asphalt content, %	4.0	3.8	4.0	5.5	6.5	4.7
Design air voids, AV %	4.0			3.9	5.0	3.6
Design voids in mineral aggregate, VMA %	13.5	12.6	13.4	15.9	18.2	15.4
Design voids filled with asphalt, VFA %	70.0	68.3	70.2	75.5	72.5	76.6
Sieve size, mm	Aggregate gradation, % passing					
37.5	100	100	100	100	100	100
25.0	100	94	100	100	100	98
19.0	96	80	96	100	100	90
12.5	79	71	79	100	98	79
9.5	69	66	69	95	81	68
4.75	48	50	48	52	30	50
2.36	30	34	30	38	18	36
1.18	20	22	20	28	14	25
0.6	14	14	14	20	13	17
0.3	9	10	9	12	12	11
0.15	7	7	7	7	9	8
0.075	4.2	4.5	4.2	4.9	8.3	5.2
Number of E* replicates	38	11	8	24	24	24

Loose samples of the three mixes from Set I were collected from the field during construction. The asphalt content of these samples, designed at a target air void level of 4.0%, was checked and assured to fall within $\pm 0.3\%$ of the optimum asphalt content of each of these mixes as shown for the 19.0 mm FR mix of Set I in Figure 103. The optimum asphalt content was selected a QA/QC criterion for accepting the quality of the produced asphalt concrete mixture based on the specification of that specific paving project. That is a performance-related specification where binder/asphalt content is often used as a criterion in QA/QC and pay factor analysis in the context of rutting. The advantage of this test is its relatively low cost. While value of binder content serves as a good indicator of the quality of the mix production, it is not an adequate indicator of the mix's performance over its service life. The quality of the mix's performance is dependent on many variables in mix production, laying and compaction. It is worth noting that relying solely on one volumetric property is simply not enough to forecast the performance of the mix. Typically, specifications set a target binder content and an allowable margin of error. For the case of the 19.0 mm FR mix, the required optimum asphalt content is 4.0% with an acceptable error of $\pm 0.25\%$. The QA/QC practices of this project require dividing it in batches where each batch represents the amount of asphalt mix produced per day typically consisting of 5,000-10,000 ton. Tested samples from each batch indicate that the binder content falls within the acceptable range of 3.75-4.25%, as shown in Figure 103, where theoretically and in the context of the project from which the samples were collected, it indicates an acceptable quality for the produced asphalt concrete mix. The analysis of the two other mixes of Set I shows similar results.

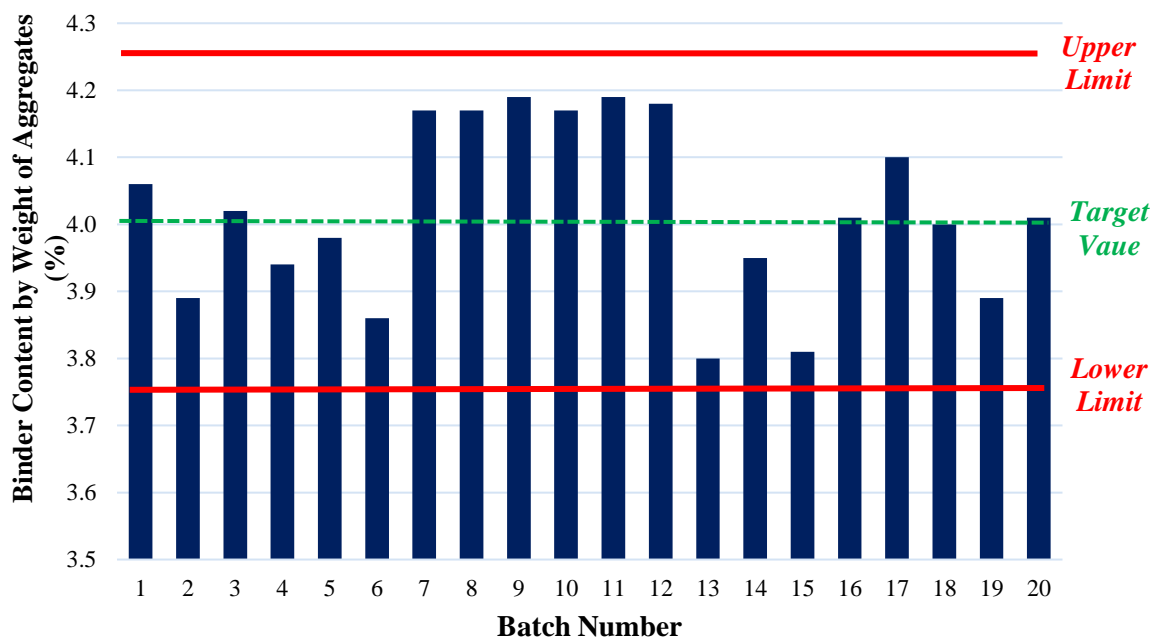


Figure 103. Binder content of different batches of 19.0 mm FR mix of Set I.

Replicates of each mix of Set I were compacted in the same lab using a Superpave Gyrotory Compactor at the same compaction temperature required in the field targeting a cored sample of $4\pm 0.5\%$ air voids. Core samples were 100 mm in diameter and 150 mm in height. Specimens were then instrumented and tested for $|E^*|$ in accordance with AASHTO TP79 in compression mode at frequencies of 20, 10, 1, 0.1, and 0.01 Hz at 4°C , 20°C and 40°C .

The replicates of each of the mixes of Set I were tested at two laboratories (i.e. Lab A and Lab B) by different operators. Thus, the covered inherent uncertainties will include the effect of multi-laboratory testing. However, a hypothesis testing was conducted to check if there is a significant difference in the means of the replicates tested at each of the two laboratories. The t-test was conducted to evaluate the following null hypothesis:

- Null Hypothesis (H_0) : $\mu_{Lab A} = \mu_{Lab B}$
- Alternative Hypothesis (H_A) : $\mu_{Lab A} \neq \mu_{Lab B}$

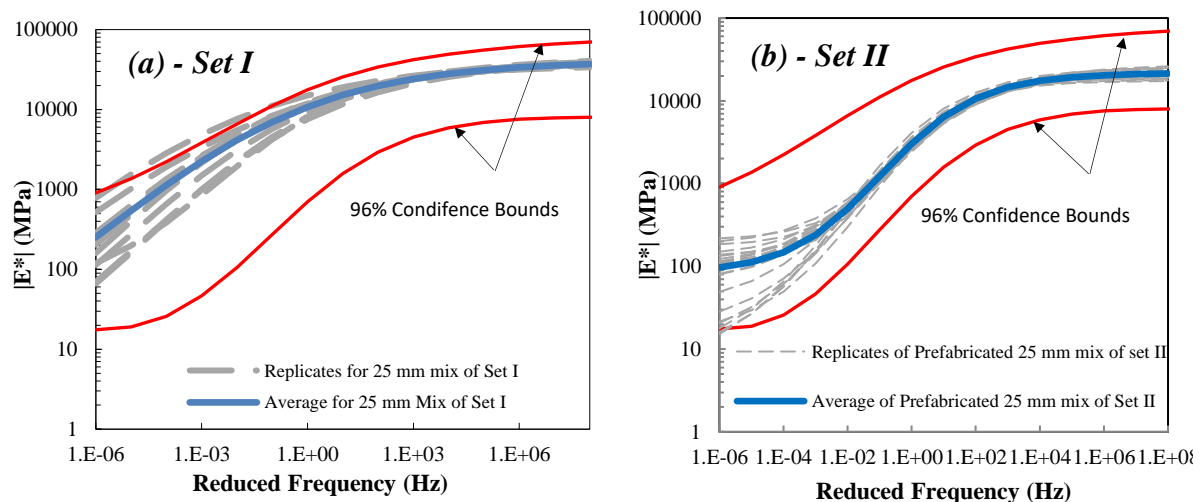
The t-test was conducted at all possible combinations of testing frequencies and temperature yielding an average p-value = 0.4135 indicating there is no evidence to reject the null hypothesis at the 95% significance level. The means of the results from the two laboratories are statistically equal. In addition, an F-test was conducted to check if there is a significant difference in the uncertainties between the two labs. This F-test studies if the variances between the two labs are different or not through the following null hypothesis:

- Null Hypothesis (H_0) : $var_{Lab A} = var_{Lab B}$
- Alternative Hypothesis (H_A) : $var_{Lab A} \neq var_{Lab B}$

The F-test shows that there is no evidence to reject the null hypothesis at the 95% significance level. It can thus be assumed that the variance of the two labs is equal and there is no laboratory-induced variability. Therefore, the data can be pooled and analyzed as one sample coming from a single population.

For Set II, the replicates of the mixes were prepared in accordance with AASHTO PP60 with a target air voids of $7.0\pm 1.0\%$, and $|E^*|$ was also tested in accordance with AASHTO TP79 at frequencies of 10, 1, 0.1, and 0.01 Hz at 4°C , 20°C and 40°C . The raw data of each of the tested replicates was taken from Appendices B and C of the aforementioned report. For each of the mixes of Set II, the data corresponding to the 24 replicates were pooled in the statistical analysis of the inherent variability despite the fact that the 24 replicates were tested in eight labs. The pooling is justified given the fact that all specimens were prefabricated in one laboratory and that the average $|E^*|$ master curves of the three replicates (for any given mix) did not show biases due to the differences in the testing laboratories.

For each replicate in Sets I and II, $|E^*|$ master curve was fitted at a reference temperature of 20°C as presented in Figure 104-a and Figure 104-b, respectively. For each replicate, the parameters α , γ , β , and δ using the 4 parameter sigmoidal function, presented earlier by Equation 87, were determined along with the shift factors. For each mix, an average $|E^*|$ master curve that represents the average of the replicates is also presented. A visual comparison between the mean $|E^*|$ master curves of the two sets indicates that the average curves for mixes in Set I are consistently higher than the average curves in Set II. This is expected given the significant differences in the asphalt mix characteristics (particularly stiffness) of the two sets. Irrespective of the mix properties, results in Figure 104 indicate that there exists scatter/variability that is clearly exhibited in the $|E^*|$ curves of the different replicates around the average curve of any given mix. The scatter is minimal at relatively high values of reduced frequency and increases systematically as the reduced frequency decreases. This implies that the inherent variability of $|E^*|$ is expected to be higher in the lower range of reduced frequencies. Visual observation of the scatter indicates that the magnitude of the variability in $|E^*|$ at relatively small reduced frequencies changes and seems to be correlated with the NMAS. For the mixes with the larger NMAS of 25 mm and 19 mm, the inherent variability in $|E^*|$ seems to be higher than the variability exhibited in the mixes having smaller NMAS of 12.5 mm and 9.5 mm. To quantify the magnitude of the inherent variability in $|E^*|$ master curves of the replicates (Figure 104) relative to the universal variability that is expected to exist in $|E^*|$ master curves (Kahil et al.), the 96% confidence bounds in $|E^*|$ as determined in Kahil et al. are presented in Figure 104 (a and b). The results indicate that the 96% confidence bound interval constitutes a realistic representation of the upper and lower bounds of the universal variability in $|E^*|$, since the master curves of the vast majority of the replicates in Set I and Set II fell within the 96% confidence bound interval.



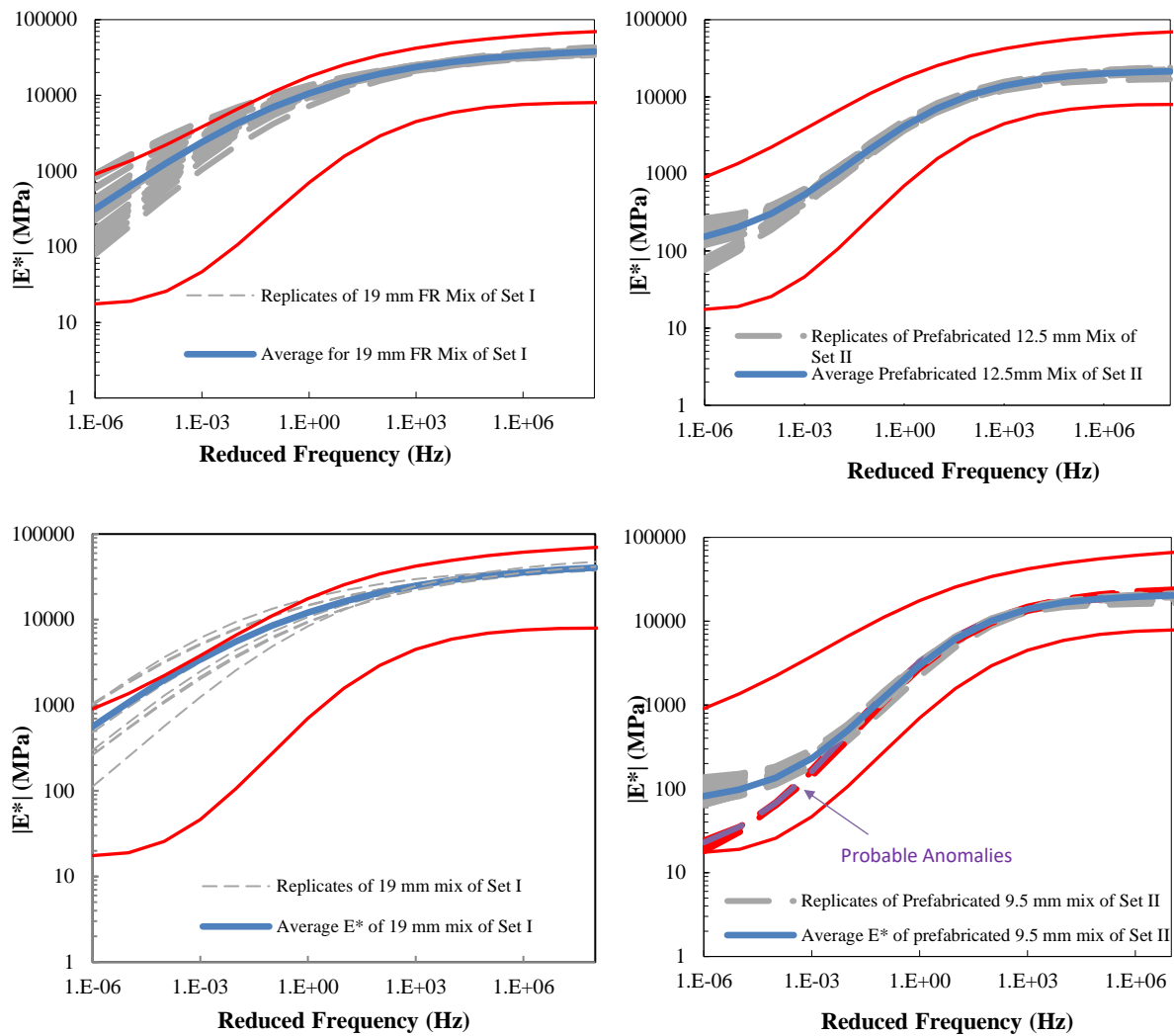


Figure 104. Best fit sigmoidal functions for $|E^*|$ of replicates in (a) Set I and (b) Set II mixes.

8.2.2 Probabilistic Model of $|E^*|$ Master Curve

Similar to the case of the mixes prepared in the lab in the previous parts of this research, the inherent variability in $|E^*|$ is modeled probabilistically through the parameters α , γ , β , and δ of the $|E^*|$ master curve. The uncertainties in the parameters a , b , and c of the shift factor will be neglected given that the contribution of these parameters to the total uncertainty of $|E^*|$ was earlier found to be negligible. For each of the replicates under study, the parameters of the sigmoidal function were determined. The mean and standard deviation for each parameter was consequently calculated for any given mix. The correlation coefficients that define the covariance structure between the different pairs of parameters was also determined. The mean vector, standard deviation vector, and correlation matrix of the four parameters are presented in Table 48 for all the mixes analyzed in this study. Results indicate that the correlation coefficients between the different pairs of the four parameters vary in magnitude and sense similar to the case of U19-HMA, M19-HMA, U25-HMA, and U19-

WMA-SonneWarmix investigated earlier. It can be observed that δ and α exhibit strong negative correlations irrespective of the mix and set. Also, β and γ are observed to be positively correlated for all mixes.

The statistical data presented in Table 48 defines the first two moments (mean and covariance) of the model parameters. To complete the probabilistic model for the inherent variability in $|E^*|$, knowledge about the probability distributions of the parameters is required. In addition to conducting the Shapiro-Wilk Normality Test, the cumulative distribution functions (CDF) were determined for each of the four parameters. Theoretical normal and lognormal CDFs were then investigated as candidates for modeling the variability in the random variables: α , γ , β , and δ . Example plots showing the actual and theoretical CDFs are presented in Figure 105 for the 19 mm mix of Set I which has 38 $|E^*|$ master curve replicates. The CDFs in Figure 105 indicate that the normal distribution provides a realistic fit of all model parameters. Consequently, the normal distribution will be adopted in this study to model α , γ , β , and δ . Thus, whether asphalt concrete is laboratory or plant mixes, the parameters fitting the sigmoidal functions of their $|E^*|$ mastercurves can be fit using the normal distribution.

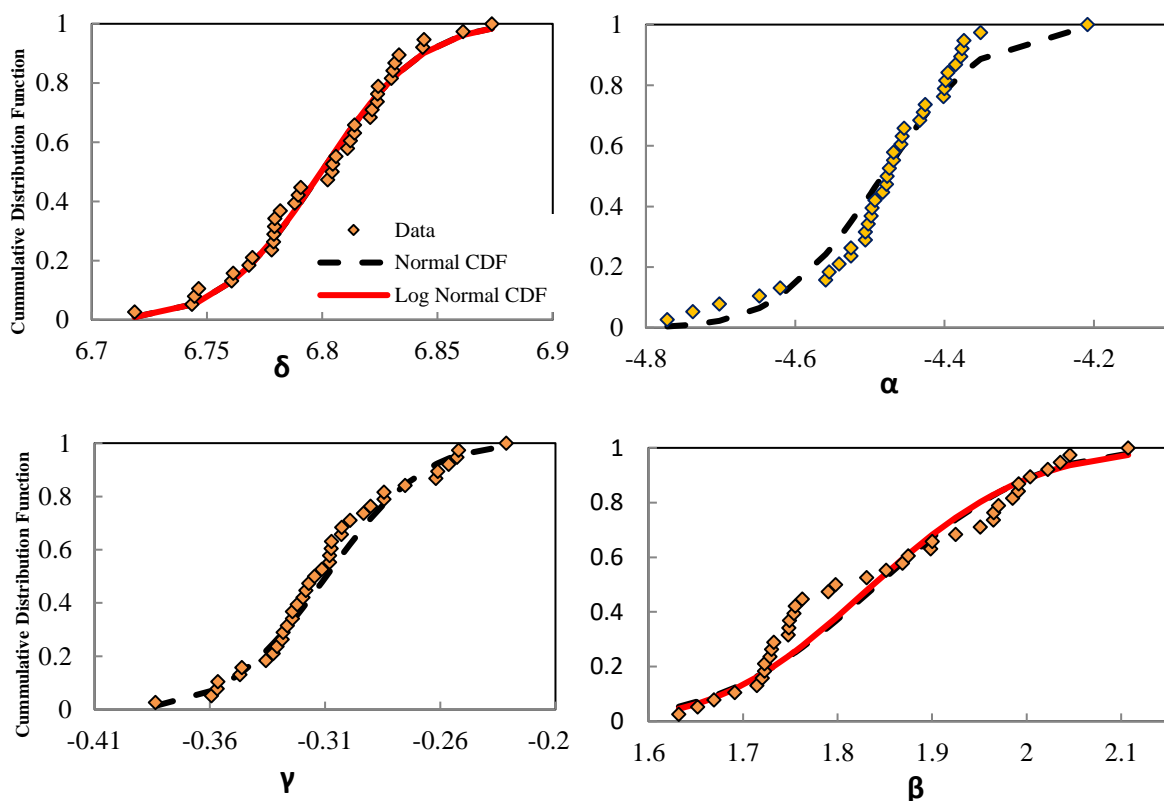


Figure 105. Cumulative distribution functions for the parameters: δ , α , γ , and β .

Table 48. Components of the mean vector, standard deviation vector, and correlation matrices for the fitting coefficients of $|E^*|$ for the mixes under study.

Mix		δ		α		β		γ		Correlation Coefficient									
		Mean	Std Dev.	Mean	Std Dev.	Mean	Std Dev.	Mean	Std Dev.	δ - δ	δ - α	δ - β	δ - γ	α - α	α - β	α - γ	β - β	β - γ	γ - γ
Set I	25 mm	2.470	0.441	4.303	0.460	-1.846	0.268	0.347	0.057	1.00	-1.00	0.71	0.87	1.00	-0.69	-0.88	1.00	0.74	1.00
	19 mm FR	6.800	0.034	-4.483	0.109	1.842	0.130	-0.309	0.034	1.00	-0.33	-0.59	0.33	1.00	0.25	0.06	1.00	0.33	1.00
	19 mm	6.840	0.041	-4.507	0.062	1.880	0.277	-0.281	0.021	1.00	-0.54	-0.73	-0.26	1.00	0.25	-0.13	1.00	0.38	1.00
Set II - Prefabricated	9.5 mm	4.037	0.142	2.431	0.166	-0.640	0.112	0.657	0.048	1.00	-0.99	0.69	0.81	1.00	-0.64	-0.86	1.00	0.44	1.00
	12.5 mm	4.052	0.335	2.456	0.360	-0.842	0.192	0.522	0.050	1.00	-1.00	0.95	0.86	1.00	-0.94	-0.88	1.00	0.88	1.00
	25 mm	3.898	0.488	2.600	0.528	-0.674	0.259	0.659	0.088	1.00	-1.00	0.94	0.82	1.00	-0.94	-0.84	1.00	0.71	1.00

8.2.3 Modeling of Uncertainty In $|E^*|$

The probabilistic model describing the uncertainty in the parameters of the sigmoidal function allows for the quantification of the inherent variability in $|E^*|$ for each mix by Monte Carlo Method and First Order Approximation. Monte Carlo Simulations consisting of 500,000 realizations of each parameter in the sigmoidal function were conducted to provide realistic estimates of the mean and COV of $|E^*|$ at specified values of reduced frequencies ranging from 10^{-6} to 10^6 Hz.

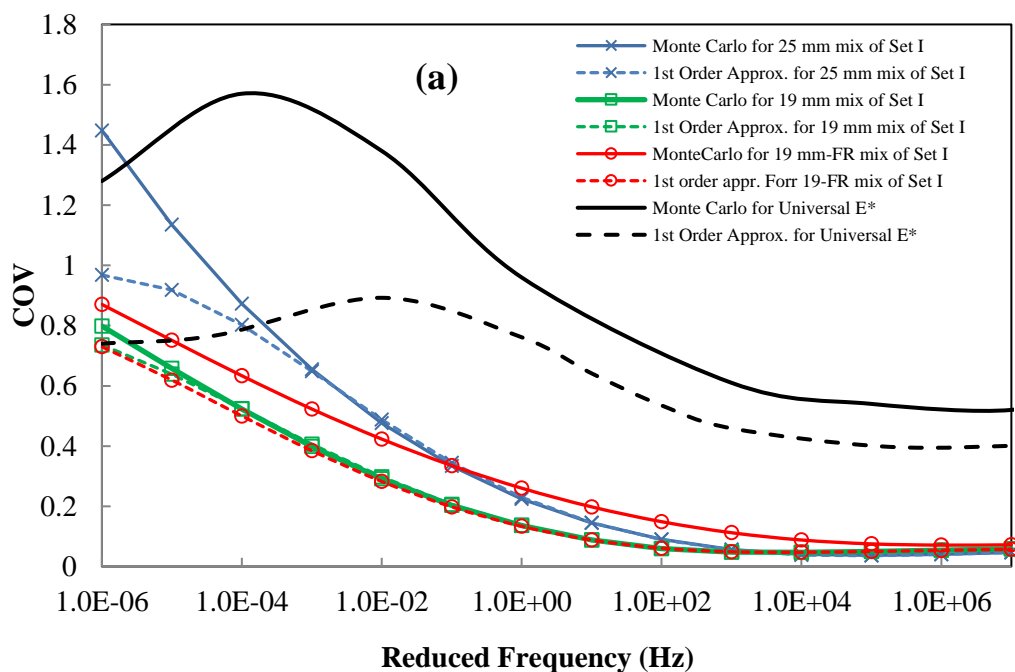
8.2.4 Results

As expected from earlier results, the average $|E^*|$ master curves that were determined from the Monte Carlo simulations for each mix in the two data sets were found to be identical to the average master curves of the different test replicates shown in Figure 104. Like the case of lab-mixed samples, the First Order Approximation yield a slight difference in the mean $|E^*|$ mastercurve at small reduced frequencies. The variation of the COV of $|E^*|$ with reduced frequency is plotted on Figure 106(a) and Figure 106(b) for mixes of Set I and Set II, respectively. Results in Figure 106 indicate that the COV of $|E^*|$ increases as the reduced frequency decreases indicating that the inherent variability of $|E^*|$ is governed by the asphalt temperature and loading frequency which is consistent with previous conclusions regarding the lab-mixes samples.

For all asphalt mixes and data sets, the COV of $|E^*|$ at high reduced frequencies (10^2 to 10^6 Hz) seems to vary in the narrow range around 0.1. These COV values are considered to be small and indicate a very low degree of inherent variability in $|E^*|$. These values are the same as that of lab-mixed samples indicating that the inherent uncertainty of $|E^*|$ is almost independent of the mixing process. For reduced frequencies that are smaller than 100 Hz, the uncertainty in $|E^*|$ increases drastically with decreases in the reduced frequency, reaching maximum COV values of 1.45 in some mixes at the lowest reduced frequencies analyzed. These observations indicate very high inherent variability levels in $|E^*|$ at high temperatures

and low frequencies where higher levels of deformation are incorporated. The increase of the inherent uncertainty with the decrease in the reduced frequency is expected to be due to the dominance of the aggregates' influence and the decrease in the number of loading cycles at low reduced frequencies (i.e. 100 cycles at 10 Hz versus 15 cycles at 0.1Hz). For the lower frequencies, steady state may not be fully achieved in the last 5 or 6 cycles of testing at 0.1 Hz.

A thorough analysis of the COVs in Figure 106 indicates that the magnitude of the inherent variability in $|E^*|$ in the medium to low reduced frequency range is a function of the NMAS in the mix. For example, results from mixes in Set I indicate that the 25mm mix shows a higher COV (~ 1.45 at 10^{-6} Hz) compared to that of the 19mm mixes (~ 0.8 and 0.9 at 10^{-6} Hz). A similar trend is observed in results in Set II where the COV at 10^{-6} Hz is found to decrease from 1.36 for the 25mm mix to 0.6 for the 12.5 mm mix. For the 9.5 mm mix in Set II, results indicate that 4 replicates out of a total of 24 replicates that were tested had $|E^*|$ master curves that were inconsistent with the other replicates. In this research, these replicates are considered as anomalies and are not included in the probabilistic model. When these cases are excluded, the Monte Carlo simulations indicate a relatively low COV value of 0.25 for $|E^*|$ at a reduced frequency of 10^{-6} Hz. The variation of the COV of $|E^*|$ with NMAS is presented in Figure 107. Results indicate a strong correlation between the two parameters with the inherent variability in $|E^*|$ decreasing as NMAS decreases.



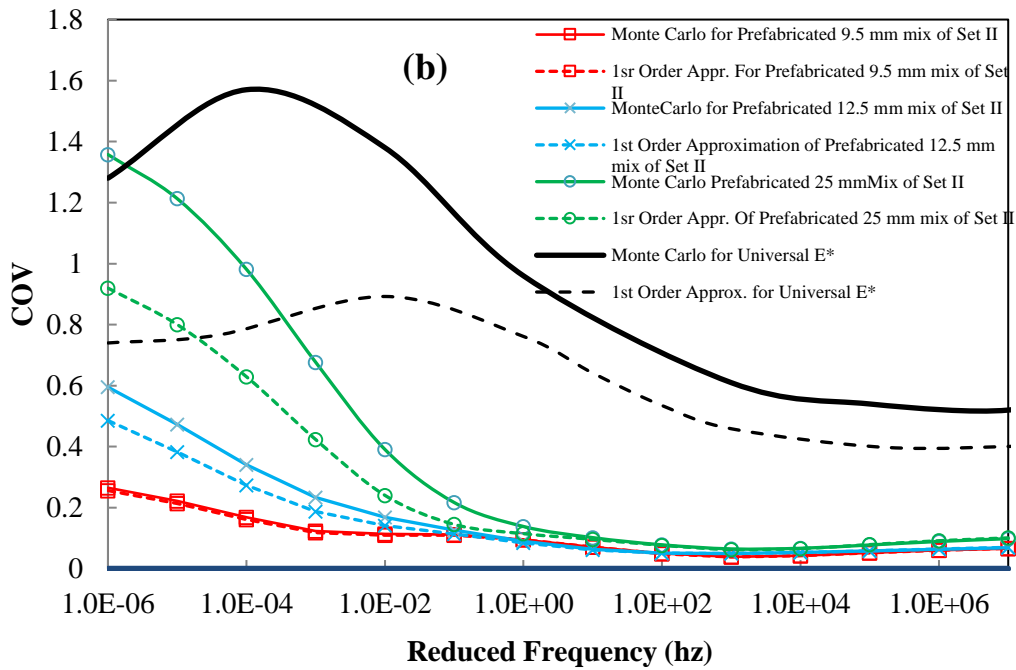


Figure 106. (a) COV of $|E^*|$ as a function of reduced frequency for mixes of Set I compacted at a level of 4.0% air voids, (b) COV of $|E^*|$ as a function of reduced frequency for prefabricated mixes of Set II compacted at a level of 7.0% air voids.

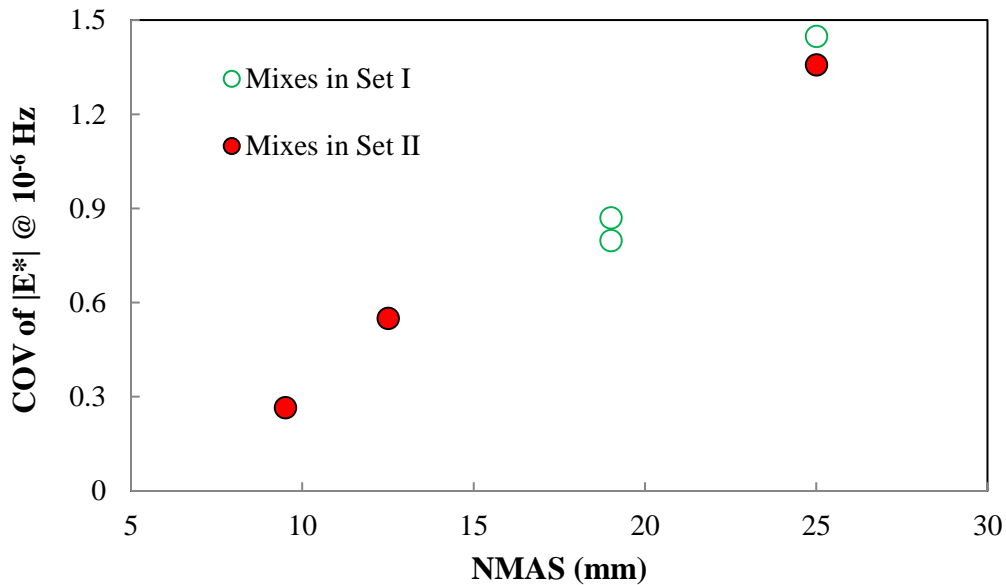


Figure 107. Correlation between COV of $|E^*|$ and NMA5 at very low reduced frequencies.

Since one of the objectives of this section of the research is to quantify the contribution of the uncertainty due to inherent variability to the total uncertainty in $|E^*|$, the universal COVs that were quantified in Kahil et al. are presented in Figure 1 versus reduced frequency. The universal COVs reflect the universal uncertainty in $|E^*|$, which includes in it the contributions of inherent variability and model uncertainty. Results of Figure 1 indicate that in the high reduced frequency range, the COVs due to inherent variability in $|E^*|$ as deduced from the 6 mixes analyzed in this study constitute less than 10% of the universal

uncertainty in $|E^*|$. For the medium to low reduced frequency range, the contribution of the uncertainty due to inherent variability increases to 25% to 100% of the universal uncertainty, depending on the properties of the mix analyzed (mainly NMAS). It could be concluded that for mixes with relatively large NMAS and at very low reduced frequencies, the inherent variability of $|E^*|$ could approach that of the universal uncertainty, indicating that spatial variability will dominate the total uncertainty in $|E^*|$. It should be noted that differences in mix properties (different types of aggregates, different gradations, different types of binder, different binder content, and different air voids level) between the 25 mm mix in Set I (air void level $4.0\pm 0.5\%$) and Set II (air void level $7.0\pm 1.0\%$) did not affect the inherent uncertainty in $|E^*|$ significantly. Thus, it can be concluded that the uncertainty of $|E^*|$ is mainly affected by the NMAS of the mix.

For applications involving reliability-based design, information that is limited to the mean and COV of $|E^*|$ is not sufficient. There is a need for establishing the probability distribution that would best model the uncertainty of $|E^*|$. The results of the Monte Carlo simulations were used to investigate the probability distribution of $|E^*|$. For this purpose, histograms showing the uncertainty in $|E^*|$ as obtained from the Monte Carlo analyses were plotted versus theoretical normal or lognormal distributions in Figure 108. A representative case that involves the 25mm mix in Set I is presented in Figure 108 for illustration. Results indicate that the normal distribution could provide a realistic model of $|E^*|$ for limited cases at relatively high reduced frequencies where the uncertainty in $|E^*|$ is relatively small and the histograms are relatively symmetrical. However, as the reduced frequency decreases, the $|E^*|$ histograms tend to become skewed to the right. For these cases, a lognormal distribution is required to model the uncertainty in $|E^*|$. These observations are valid for all the other mixes that are analyzed in this research as well as the universal $|E^*|$ presented in Kahil et al..

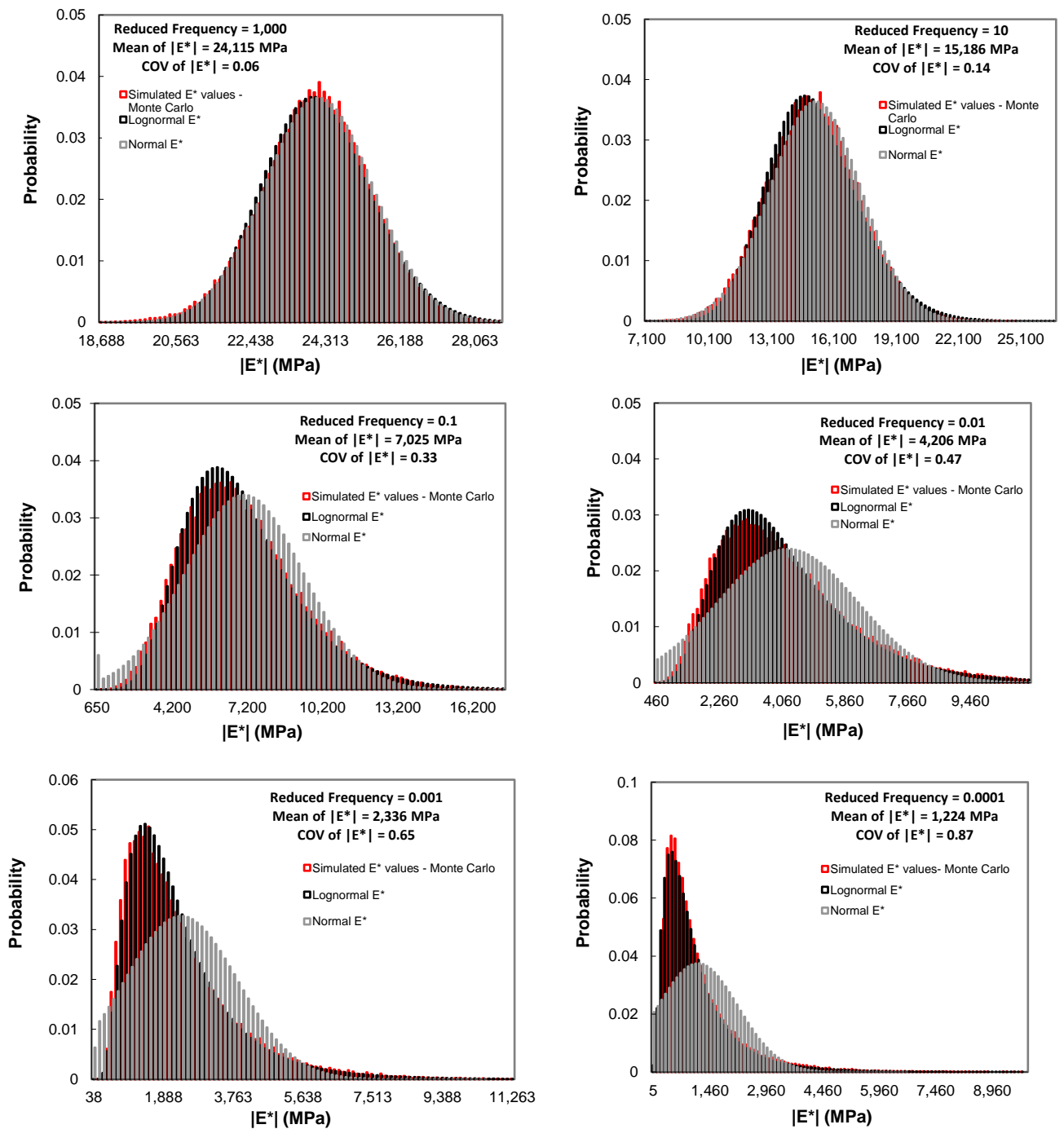


Figure 108. Histograms of simulated $|E^*|$ values compared to theoretical distributions for the 25mm mix.

8.2.5 Rut Depth Prediction

To illustrate the impact of the inherent variability in $|E^*|$ on performance prediction, a simple example incorporating the rut depth (RD) of a pavement section was simulated. The rut depth, rather than fatigue cracking, was considered to address cases involving high temperatures and/or slow traffic. In these cases, the $|E^*|$ that is relevant corresponds to low reduced frequencies, which were shown in the previous sections to possess higher and varying uncertainties. The simulated $|E^*|$ values for the 19 mm-FR and the 25 mm mixes of

Set I were used in order to predict the asphalt concrete rut depth of a typical pavement section with 10,000,000 ESALS. The section consists of a 20 cm thick asphalt concrete layer with a 38.1cm granular base layer and a subgrade of a resilient modulus of 100 MPa. These mixes were paved at an area with hot climatic condition represented by the following five climatic characteristics:

- Mean annual temperature: 28°C
- Mean monthly air temperature standard deviation: 5.83°C
- Mean annual wind speed: 12.6 km/hr
- Mean annual sunshine: 61%
- Mean cumulative rainfall depth: 16.4 cm

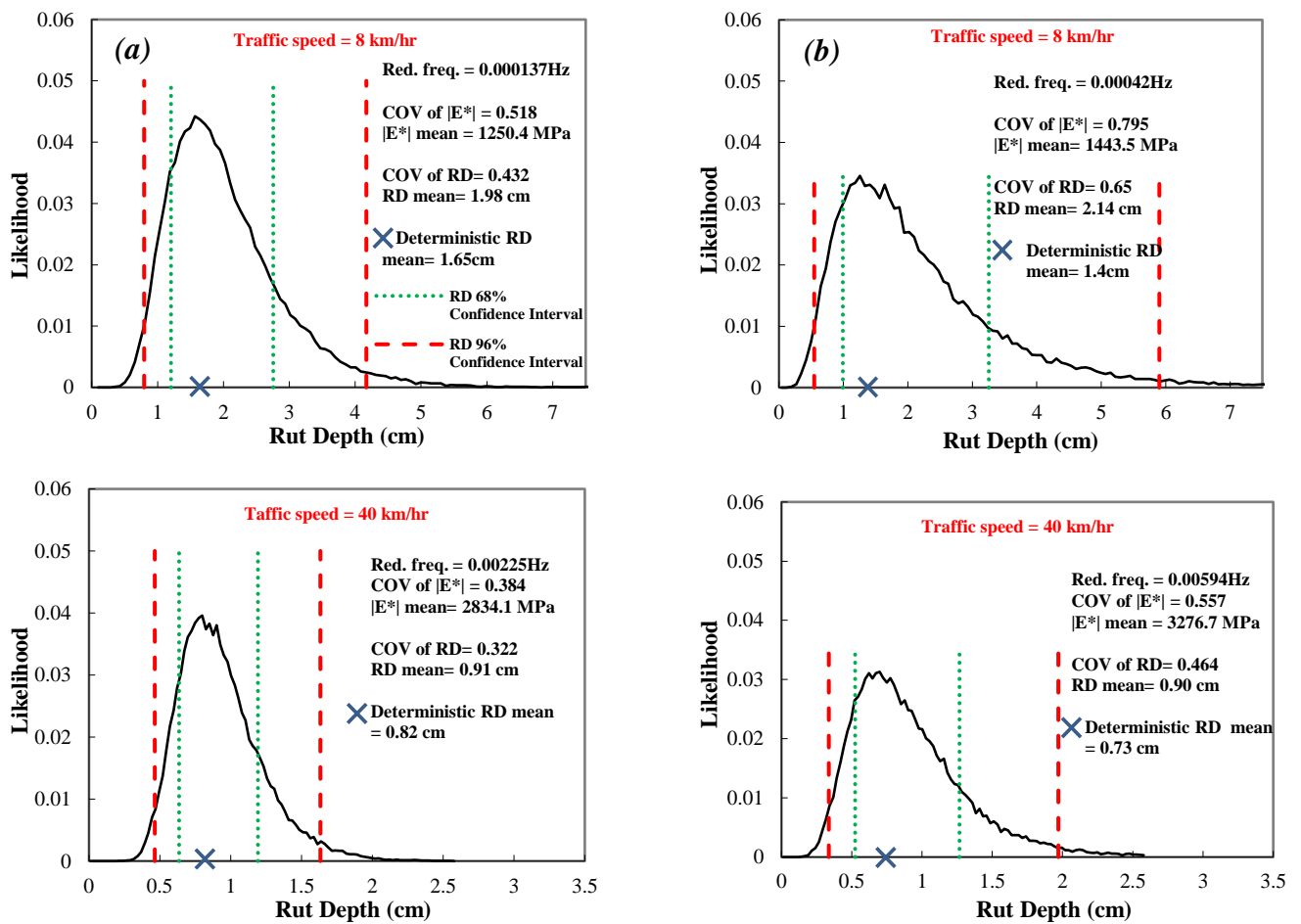
The Microsoft Excel-based tool for quality related specifications by NCHRP 09-22 was used in order to determine the effective temperature and frequency. In this context, the effective temperature is defined as the single testing temperature of asphalt at which a certain rut depth is obtained within a given pavement system characterizing the impact of the environmental conditions from a seasonal temperature cycle (El-Basyouny and Jeong 2009). The effective frequency presents the effect of traffic speed within a given pavement system. These parameters were determined for the case of each mix simulating design speeds of 8km/hr (5mph), 40km/hr (25mph), and 105km/hr (65mph) to present slow moving vehicles at intersections, normal speed at residential streets, and fast moving vehicles at interstate and other major arterials, respectively. The effective temperature and frequency for each case were used to calculate the reduced frequency which is required to determine the effective $|E^*|$ value. For each reduced frequency, the COV of $|E^*|$ is calculated using the models presented in Figure 106 so that this quantified uncertainty will be propagated into the simulated rut depth. The effective $|E^*|$ has been shown to be related to the rut depth through the following calibrated model by NCHRP 9-22 (Jeong 2010):

$$Rut\ Depth = 1.076 E_{eff}^{*-0.85} \quad \text{Equation 93}$$

where rut depth is expressed in inches, and E_{eff}^* in (10^{-5}) psi.

500,000 realizations of $|E^*|$ were simulated to assess the uncertainty in the resulting rut depth as indicated in Figure 109(a) and Figure 109(b) for the 19mm-FR mix and the 25mm mix, respectively. It is shown that as the traffic speed decreases (reduced frequency decreases), the effective $|E^*|$ decreases and the uncertainty in $|E^*|$ increases, leading to larger uncertainties in the predicted rut depth. An investigation of the results leads to the following observations with regards to the probability distribution of rut depth: (1) as the traffic speed

or reduced frequency decreases, the skewness of the probability distribution increases, (2) as the uncertainty of $|E^*|$ increases, the 68% and 96% confidence intervals of rut depth become wider and the COV of rut depth increases significantly, (3) for the same traffic speed, the 25mm mix results in a higher uncertainty in the predicted rut depth, and (4) the rut depth calculated deterministically is consistently lower than that simulated by the average of the Monte Carlo simulations and this difference increases as the COV of $|E^*|$ increases. These results show that the quantification of the inherent uncertainties in $|E^*|$ is critical for any reliability-based analysis that aims at estimating the probability of exceeding a target rut depth. This effect has a high significance on rut depths for the cases of hot weather and slow speed where rutting would be the most critical and dominant distress. Thus, accounting for the inherent variability of $|E^*|$ is of importance for QA/QC applications and for the proper implementation of performance based specifications.



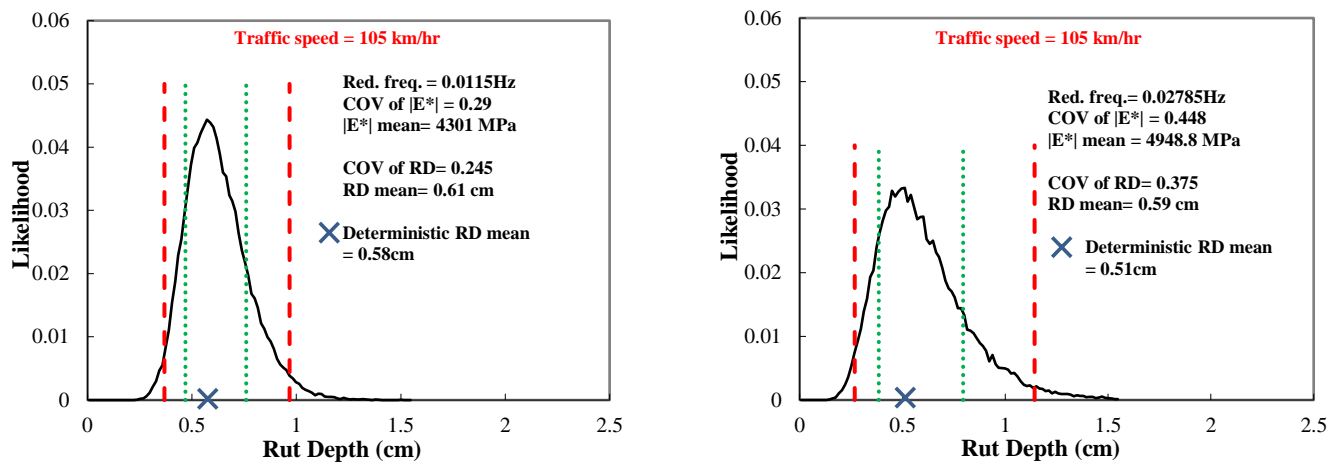


Figure 109. Probabilistic Simulation of Rut Depth for hot climate case with slow moving, normal, and fast-moving traffic (a) 19mm FR mix (b) 25mm mix.

8.2.6 Conclusions

The inherent variability in $|E^*|$ was characterized across the full spectrum of the $|E^*|$ master curve through the analysis of $|E^*|$ data of six different mixes. Monte Carlo simulations were used to propagate the uncertainties of the sigmoidal model coefficients to determine the mean, COV, and probability distribution in $|E^*|$ as function of reduced frequency. Also, the inherent uncertainty in $|E^*|$ was propagated through forward modeling to characterize the uncertainty in the predicted rut depth for a set of pavement sections. Based on these simulations and analyses, the following conclusions can be drawn:

- The COV of $|E^*|$ due to inherent variability assumes relatively small values (0.05 to 0.075) for cases with reduced frequencies that are larger than 10^2 Hz. For reduced frequencies that are in the medium to low range, the uncertainty in $|E^*|$ increases dramatically indicating that the inherent uncertainty of $|E^*|$ is a function of the reduced frequency; i.e., testing temperature and frequency.
- Results from the six mixes analyzed indicate that the magnitude of the inherent variability as reflected in the COV of $|E^*|$ is strongly correlated to the NMAS. For the very low frequency range ($\sim 10^{-6}$ Hz), the COV of $|E^*|$ decreases from a high value of approximately 1.4 for NMAS of 25mm to a low value of approximately 0.25 for mixes with NMAS of 9.5mm. The uncertainty of $|E^*|$ is independent of the air voids level of the specimens being tested.
- The probability distribution of $|E^*|$ was found to be highly skewed, particularly for the relatively low reduced frequency range and mixes with a large NMAS. The lognormal distribution was found to provide an acceptable model of the uncertainty in $|E^*|$ and is recommended for use in any reliability-based analyses involving the use of $|E^*|$.

8.3 Inherent Uncertainty in E(t) and D(t)

8.3.1 E'(w), E(t), D(t) Data

In this part, the same experimental data of the mixes of Set I and Set II used for quantifying the uncertainty in |E*| is utilized for quantifying that in E'(w), E(t), and D(t). The data of mixes in Set I and Set II are used as presented in Table 47. The Prony series of E(t) and D(t) are fitted for each replicate and the uncertainty is quantified in terms of that of each of the Prony coefficients. The conversion of the experimental E* data to E(t) is done through E'(w) and not |E*| alone so that it incorporates both the stiffness and phase angle components. To study the variability imposed by the phase angle on the different used LVE functions, the inherent uncertainty in E'(w) is investigated. E'(w) is calculated and fitted for each replicate using the sigmoidal function presented in Equation 94.

$$\log E'(w) = \delta + \frac{\alpha}{1 + e^{\beta - \gamma \log(w_r)}} \quad \text{Equation 94}$$

where:

E'(w): storage modulus (MPa or psi)

δ , α , β , and γ : fitting parameters

w_r : Reduced angular frequency (rad/sec) at a reference temperature $T_0 = 20^\circ\text{C}$

E'(w) is required for the conversion into E(t) using both the Approximate method and Exact method as presented earlier. However, D(t) is determined through E(t) that is obtained using the Approximate method. For each replicate, E(t) and D(t) are fitted in the range of 10^{-8} to 10^{+8} seconds using Prony series with 18 coefficients as expressed by Equation 16 and Equation 19, respectively. The averages of the resulting Prony coefficients for E(t) calculated using the Approximate method are presented along with their COVs in Table 49 for the mixes of both Set I and Set II. The presented COVs show that there is not a specific pattern for the variability among these coefficients between one mix and the other; also, the COV varies from one coefficient to the other. The plots of E(t) are presented in Figure 110 which show variability within the same mix especially at large reduced times. In addition, the plots of the converted D(t) mastercurves for each of the replicates in the study are presented in Figure 110. It can be observed that high variabilities appear at large reduced times for all the mixes at different magnitudes between one mix and the other.

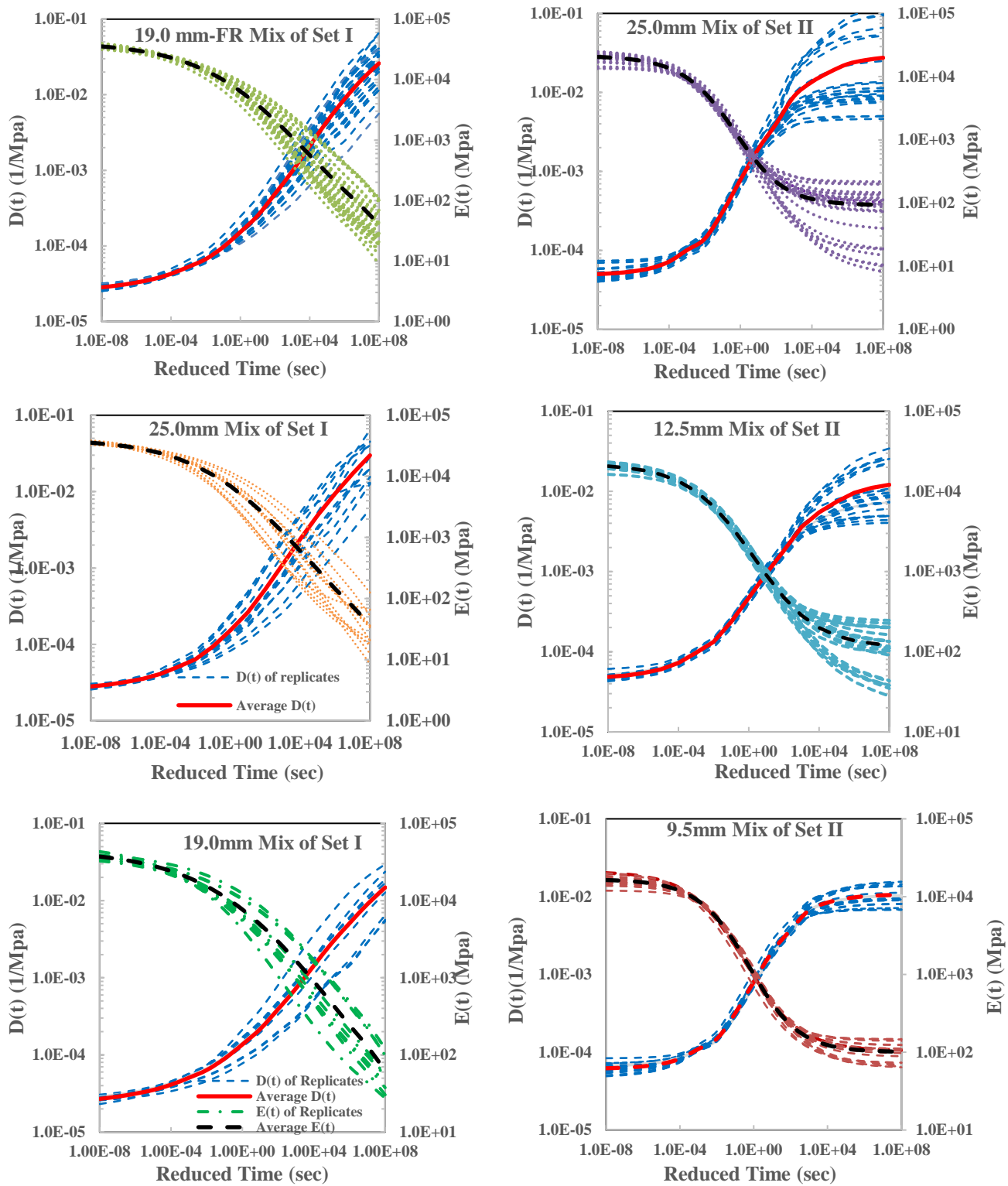


Figure 110. E(t) and D(t) mastercurves for mixes of Set I and Set II at 20°C.

Table 49. The averages and COVs for Prony coefficients for E(t) calculated using the Approximate method at 20°C for mixes of Set I and Set II.

	Set I						Set II					
	Mix 1		Mix 2		Mix 3		Mix 1		Mix 2		Mix 3	
	Average	COV	Average	COV	Average	COV	Average	COV	Average	COV	Average	COV
E1	1927.93	0.18	1666.60	0.24	2195.45	0.27	233.58	0.57	670.46	0.26	471.48	0.61
E2	2467.33	0.16	2205.18	0.20	2720.67	0.26	456.18	0.51	1076.10	0.21	843.06	0.53
E3	3099.38	0.15	2871.84	0.17	3306.25	0.25	875.65	0.45	1681.49	0.16	1477.11	0.44
E4	3747.53	0.14	3606.46	0.16	3868.05	0.23	1608.79	0.37	2477.69	0.11	2454.75	0.34
E5	4300.97	0.13	4294.45	0.15	4307.66	0.19	2679.41	0.26	3304.62	0.08	3664.77	0.24
E6	4603.91	0.12	4741.54	0.13	4508.12	0.15	3692.42	0.12	3750.98	0.06	4478.72	0.12
E7	4504.88	0.10	4730.14	0.09	4376.07	0.08	3533.24	0.06	3372.45	0.05	3862.14	0.10
E8	3949.04	0.08	4167.67	0.07	3895.58	0.07	2079.62	0.10	2310.80	0.07	2140.50	0.15
E9	3055.25	0.09	3206.32	0.15	3156.47	0.17	819.89	0.14	1242.05	0.12	833.87	0.18
E10	2077.83	0.16	2155.42	0.28	2320.72	0.29	273.76	0.15	570.08	0.15	281.70	0.19
E11	1256.94	0.28	1278.17	0.41	1552.95	0.41	94.45	0.16	247.30	0.17	98.01	0.20
E12	690.64	0.42	678.09	0.54	948.68	0.53	36.15	0.18	109.24	0.17	37.70	0.24
E13	358.97	0.57	332.13	0.67	541.85	0.62	15.30	0.21	51.79	0.18	16.15	0.29
E14	172.39	0.69	148.37	0.78	278.58	0.69	6.72	0.24	24.63	0.20	7.19	0.34
E15	98.20	0.80	75.47	0.76	164.36	0.71	3.49	0.29	15.74	0.23	3.93	0.39
E16	18.12	0.91	12.96	1.85	33.09	0.91	0.89	0.26	2.31	0.22	0.90	0.40
E17	66.33	0.85	44.66	0.66	108.94	0.64	1.89	0.41	13.15	0.29	2.43	0.49
E_{inf}	5.67	0.40	5.03	0.78	6.38	0.53	92.68	0.39	112.60	0.57	90.67	0.67

8.3.2 Probabilistic Model of E', E(t) and D(t)

The inherent variability in E' is modeled probabilistically using the same approach followed for |E*| through α , γ , β , and δ of the fitted mastercurves because both of these material functions are presented by the same form of the sigmoidal function. For each replicate, the parameters of the sigmoidal function of E' are determined and thus the mean and standard deviation of the parameters of each mix are quantified. Also, the correlation coefficients for the different pairs of parameters are calculated to define the structure of the covariance matrix presented in Table 50. The results show that the correlation coefficients between different pairs of the parameters have almost the same sense for all the mixes but with varying magnitudes. It can be observed that a strong negative correlation and a strong positive correlation are exhibited between the pairs “ α - β ” and “ β - γ ” of all the mixes, respectively. The correlation coefficients for the different pairs of α , γ , β , and δ do not exhibit the same magnitude and sense for the cases of |E*| and E'(w). After quantifying the first and second moments, the probabilistic models of these parameters are finalized by determining the probability distributions of each of the four parameters. Similar to the case |E*| for all mixes in this dissertation, the normal distribution provides a realistic fit of all the model

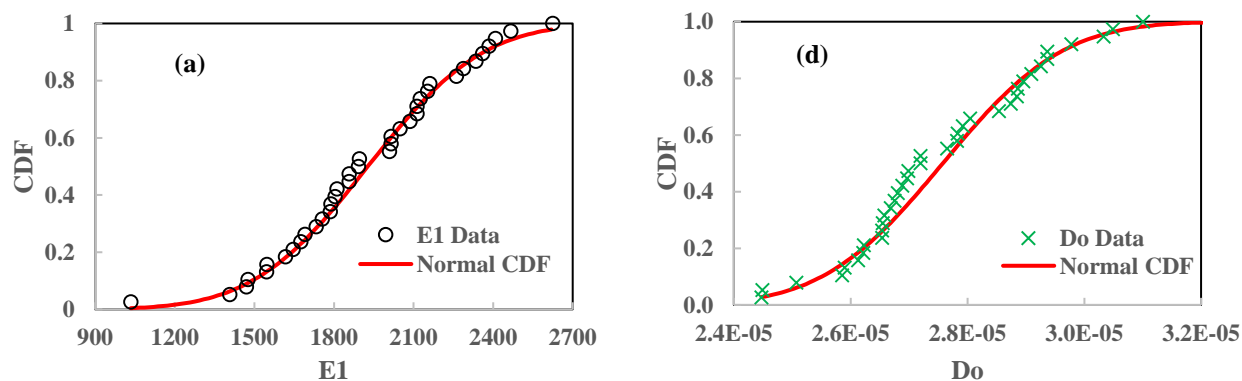
parameters and thus it has been adopted to model the probability distribution of each of α , γ , β , and δ .

Table 50. Components of the mean vector, standard deviation vector, and correlation matrices for the fitting coefficients of storage modulus for the mixes under study.

Mix	δ		α		β		γ		Correlation Coefficient										
	Mean	Std Dev.	Mean	Std Dev.	Mean	Std Dev.	Mean	Std Dev.	δ - δ	δ - α	δ - β	δ - γ	α - α	α - β	α - γ	β - β	β - γ	γ - γ	
Set I	19 mm FR	6.783	0.032	-3.913	0.217	1.407	0.188	-0.334	0.040	1.000	-0.109	-0.315	0.321	1.000	-0.554	-0.555	1.000	0.681	1.000
	25 mm	6.772	0.029	-4.130	0.456	1.538	0.360	-0.344	0.043	1.000	0.155	-0.134	0.438	1.000	-0.834	-0.593	1.000	0.770	1.000
	19 mm	6.816	0.043	-3.920	0.292	1.462	0.325	-0.307	0.031	1.000	-0.097	-0.408	0.091	1.000	-0.637	-0.835	1.000	0.640	1.000
Set II	9.5 mm	6.381	0.062	-2.301	0.263	0.020	0.209	-0.733	0.077	1.000	-0.456	-0.088	0.807	1.000	-0.747	-0.795	1.000	0.449	1.000
	12.5 mm	6.503	0.037	-2.378	0.332	0.289	0.233	-0.545	0.053	1.000	-0.682	0.614	0.738	1.000	-0.941	-0.867	1.000	0.920	1.000
	25 mm	6.483	0.085	-2.529	0.513	0.011	0.306	-0.686	0.112	1.000	-0.663	0.467	0.917	1.000	-0.930	-0.798	1.000	0.638	1.000

For the cases of $E(t)$ and $D(t)$, the mean and standard deviation for each of the 18 Prony coefficients are calculated for each of the mixes in Set I and Set II. Also, the correlation coefficients between the different pairs of the Prony coefficients are calculated. The magnitude and sense of the correlation coefficients between the different pairs of Prony coefficients for $E(t)$ and $D(t)$ have not shown a trend; however, it varies from one mix to the other in the cases of both $E(t)$ and $D(t)$. Some pairs of coefficients are strongly correlated with a magnitude of 0.99 while other pairs are weakly correlated with coefficients that are almost 0. For pairs that are negatively correlated, the magnitude of correlation falls in the range of -0.9 and 0.

To complete the probabilistic model of the Prony coefficients, the best-fit probability distribution is checked using the Shapiro-Wilk Normality Test with a significance level of 0.05. For some coefficients of $E(t)$ and $D(t)$, the normal and lognormal distributions provide an acceptable fit. However, other coefficients do not follow normal or lognormal distributions. The cumulative distribution function (CDF) of each these coefficients indicates that a large number of data points are accumulated within certain bounds of the data as shown in Figure 111 (c and f) which was not the case for lab-mixed samples as shown earlier for U19-HMA, M19-HMA, U19-WMA-SonneWarmix, and U25-HMA. In such cases, Hermite Polynomials of the 5th order could be used to model the distributions (Najjar 2005). Figure 111 shows a sample of the distribution fitting for the Prony coefficients of $E(t)$ and $D(t)$ of the 19.0mm mix-Set I.



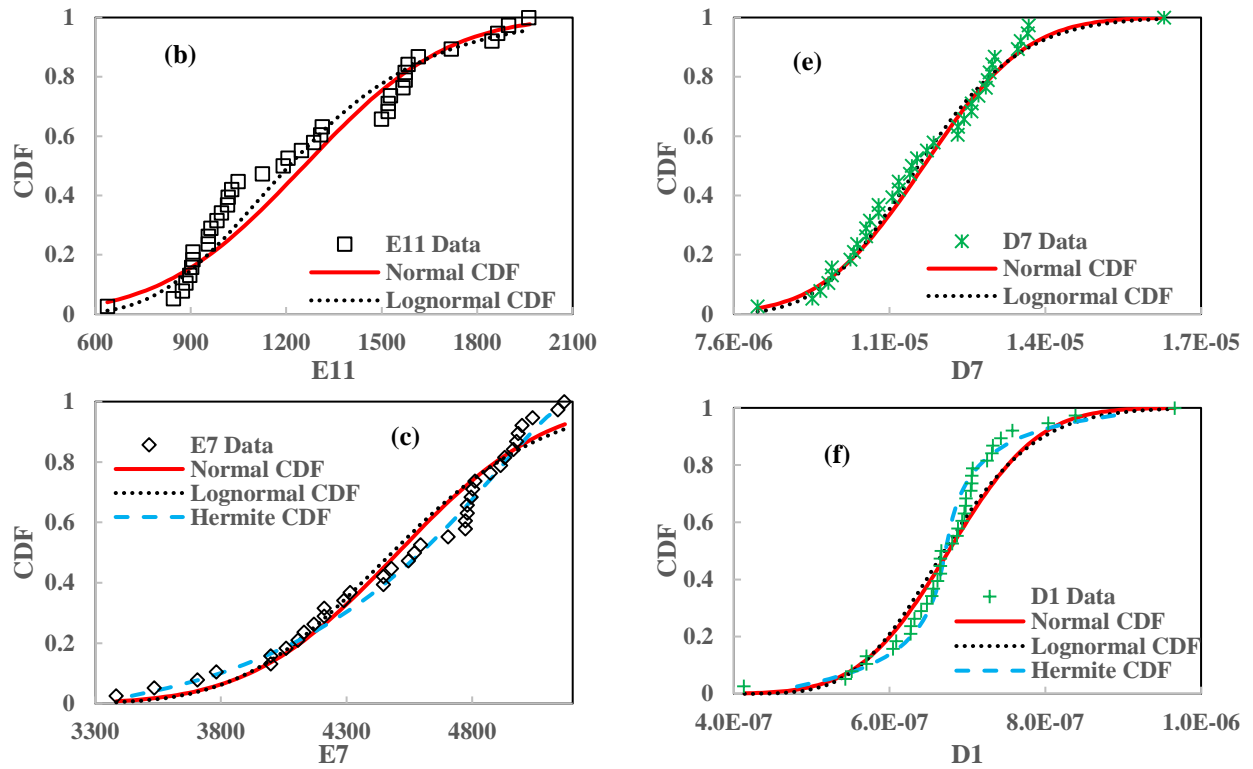


Figure 111. Cumulative distribution functions of sample parameters referring to E(t) and D(t) of 19mm-FR Mix of Set I: a) E1 having normal distribution as best fit, b) E11 having log normal as best fit, c) E7 having the 5th order Hermite polynomial as the best fit, d) Do having normal distribution as best fit, e) D7 having log normal as best fit, and f) D1 having the 5th order Hermite polynomial as the best fit.

The Hermite Polynomials can be used in order to form a transform function between a variate of a non-normal distribution to that with a standard normal distribution. Hermite Polynomials can be defined as:

$$H_i(u) = e^{\frac{u^2}{2}} \frac{d^i}{du^i} [f_u(u)] \quad \text{Equation 95}$$

where: u = variable with a standard normal distribution

i = order of the Hermite Polynomial

These polynomials can be expressed by a recurrence relation as:

$$H_{i+1}(u) = -H_i(u) - iH_{i-1}(u) \quad \text{Equation 96}$$

where: $H_0(u) = 1.0$

$$H_1(u) = -u$$

$$H_2(u) = u^2 - 1$$

$$H_3(u) = -u^3 + 3u$$

$$H_4(u) = u^4 - 6u^2 + 3$$

$$H_5(u) = -u^5 + 10u^3 - 15u$$

The variate with a non-normal probability distribution is mapped with a standard normal probability distribution using the Gaussian transform function expressed by Equation 97. This function can be expressed as a linear combination of Hermite Polynomials for any random variable with a finite variance presented by Equation 98.

$$Y = \varphi_Y(u) \quad \text{Equation 97}$$

$$Y = \sum_{i=0}^{\infty} \frac{\Psi_i}{i!} H_i(u) \quad \text{Equation 98}$$

where:

Ψ_i = coefficients of the transform function

The Hermite Polynomial transfer function can be expressed in the following form:

$$Y \cong \mu_Y + \frac{\sigma_Y}{\sqrt{1 + \sum_{i=2}^n \frac{(\Psi_i)^2}{i!}}} \left[H_1(u) + \sum_{i=2}^n \frac{(\Psi_i)}{i!} H_i(u) \right] \quad \text{Equation 99}$$

where:

$$\Psi_0 = \mu_Y$$

$$\Psi_1 = \frac{\sigma_Y}{\sqrt{1 + \sum_{i=2}^n \frac{(\Psi_i/\Psi_1)^2}{i!}}} \quad \text{Equation 100}$$

For the coefficients following neither the normal nor the lognormal distributions, the 5th order Hermite Polynomial is fitted to best present its distribution and thus complete the probabilistic model of each of the Prony Coefficients. The results show that there is not a clear trend in the distribution of each of the coefficients of the cases of E(t) and D(t) where the distribution varies from one mix to the other.

The required probability distribution of each coefficient is dependent on the mix as shown in Table 51. The results show that for the same mix and the same response function, each of the Prony coefficients can follow a distribution and it is not the case that all the coefficients follow the same one. For example, the coefficient E15 is best fitted with a normal, lognormal, and 5th Hermite Polynomials for the 25.0mm mix-Set II, 12.5mm mix-Set II, and the three mixes of Set I, respectively.

Table 51. Mean, Standard Deviation, Distribution, and Part of Correlation Matrix Between the Prony Coefficients of Each of E(t) and D(t) for Two of The Investigated Mixes.

	19 mm-FR Mix of Set I					25 mm Mix of Set II				
	Average	COV	Dist.	Correlation with E1	Correlation with E2	Average	COV	Dist.	Correlation with E1	Correlation with E2
E1	1927.9	0.177	N	1.000	0.973	471.5	0.613	N	1.000	0.996
E2	2467.3	0.161	N	0.973	1.000	843.1	0.529	N	0.996	1.000
E3	3099.4	0.150	N	0.887	0.970	1477.1	0.441	N	0.978	0.992
E4	3747.5	0.142	N	0.745	0.878	2454.7	0.344	N	0.928	0.957
E5	4301.0	0.134	N	0.558	0.733	3664.8	0.242	5th HP	0.805	0.852
E6	4603.9	0.122	5th HP	0.334	0.537	4478.7	0.124	5th HP	0.486	0.547
E7	4504.9	0.102	5th HP	0.054	0.267	3862.1	0.097	N	-0.343	-0.342
E8	3949.0	0.079	N	-0.342	-0.174	2140.5	0.148	LogN	-0.216	-0.242
E9	3055.3	0.086	N	-0.601	-0.629	833.9	0.180	LogN	0.159	0.147
E10	2077.8	0.161	N	-0.398	-0.557	281.7	0.189	logN	0.351	0.365
E11	1256.9	0.281	Log N	-0.223	-0.421	98.0	0.195	N	0.329	0.372
E12	690.6	0.424	5th HP	-0.121	-0.330	37.7	0.238	N	0.223	0.282
E13	359.0	0.571	5th HP	-0.056	-0.270	16.1	0.295	N	0.197	0.260
E14	172.4	0.694	5th HP	-0.019	-0.234	7.2	0.341	N	0.212	0.276
E15	98.2	0.798	5th HP	0.019	-0.196	3.9	0.393	N	0.348	0.408
E16	18.1	0.908	5th HP	-0.020	-0.232	0.9	0.397	5th HP	-0.013	0.058
E17	66.3	0.847	5th HP	0.063	-0.150	2.4	0.491	N	0.591	0.635
Einf	5.7	0.402	N	-0.176	-0.038	90.7	0.674	5th HP	-0.696	-0.671
	Average	COV	Dist.	Correlation with D1	Correlation with D2	Average	COV	Dist.	Correlation with D1	Correlation with D2
D1	6.74E-07	0.133	5th HP	1.000	0.993	4.53E-07	0.436	N	1.000	1.000
D2	2.42E-06	0.135	5th HP	0.993	1.000	1.79E-06	0.412	N	1.000	1.000
D3	2.57E-06	0.121	N	0.778	0.843	3.01E-06	0.328	N	0.983	0.988
D4	3.85E-06	0.108	LogN	0.866	0.914	5.07E-06	0.251	N	0.971	0.977
D5	6.87E-06	0.152	Log N	0.408	0.507	1.28E-05	0.245	N	0.911	0.923
D6	1.15E-05	0.191	Log N	0.178	0.286	3.92E-05	0.156	LogN	0.688	0.708
D7	1.13E-05	0.138	Log N	0.554	0.642	4.46E-06	2.534	N	0.643	0.655
D8	3.51E-05	0.277	N	-0.023	0.089	2.04E-04	0.165	N	0.158	0.186
D9	6.14E-05	0.344	N	-0.108	0.002	4.81E-04	0.145	LogN	0.205	0.212
D10	8.69E-05	0.354	LogN	-0.044	0.067	1.40E-03	0.240	N	-0.400	-0.382
D11	2.83E-04	0.443	N	-0.215	-0.108	1.68E-03	0.456	LogN	0.592	0.582
D12	4.50E-04	0.590	5th HP	-0.195	-0.091	7.46E-03	0.892	5th HP	0.509	0.491
D13	1.28E-03	0.560	5th HP	-0.280	-0.177	2.53E-03	2.093	5th HP	0.515	0.492
D14	2.56E-03	0.473	N	-0.260	-0.160	6.00E-03	1.263	5th HP	0.496	0.474
D15	4.74E-03	0.923	5th HP	-0.354	-0.257	4.33E-03	2.269	5th HP	0.428	0.404
D16	7.79E-03	0.543	5th HP	-0.249	-0.168	1.94E-03	1.089	5th HP	0.522	0.501
D17	1.37E-02	0.669	5th HP	-0.274	-0.201	2.09E-03	2.462	5th HP	0.416	0.392
Do	2.76E-05	0.059	N	-0.010	-0.076	4.97E-05	0.202	5th HP	-0.759	-0.753

N = Normal distribution, LogN= Lognormal distribution, and 5th HP= 5th Order Hermite Polynomial

8.3.3 Modeling of Uncertainty

The probabilistic model describing the uncertainty in the coefficients of the Prony series function allows for the quantification of the inherent variability in E(t) and D(t) for each mix. First Order Approximations and Monte Carlo Simulations with 500,000 realizations of each of the Prony coefficients are conducted to provide realistic estimates of the mean and COV of each of E(t) and D(t) at any reduced time in the range of 10^{-8} to 10^8 sec.

8.3.3.1 Uncertainty in $E'(w)$

For the case of E' where the inherent variability is quantified in terms of the four parameters of the sigmoidal function, the quantified uncertainty is the same as that of $|E^*|$. The uncertainty of E' for all mixes, which is presented by the COV, increases as a function of reduced time as presented in Figure 112. Also, the same conclusion can be drawn as that for $|E^*|$ for the variation of the uncertainty as a function of the NMAS. For reduced times above 10 sec, the uncertainty of E' increases as the NMAS becomes larger. The uncertainty of E' follows almost a plateau for low reduced times, but then increases where it reaches a value of 0.25, 0.65, 0.85, and 1.4 at 10^6 sec for the 9.5 mm, 12.5 mm, 19.0 mm, and 25.0 mm mixes respectively. So, the effect of the uncertainty is expected to become more significant having a higher influence on the predicted performance for mixes with higher NMAS, at slow loads, and/or hot weather.

The uncertainty in E' has to account for both the variability in $|E^*|$ and phase angle; however, the results show that the uncertainty in E' is the same as that in $|E^*|$. This shows that E' is affected by the variability in $|E^*|$ and not the phase angle. By recalling the definition of E' , it refers to the multiplication of $|E^*|$ by the cosine of the phase angle where the former is much greater in magnitude than the cosine of the phase angle. For example at a high reduced frequency of 1000 Hz, the phase angle varies in small ranges of 8.8° to 10.3° , 9° to 11.5° , and 6° to 10° for the 12.5 mm mix of Set II, 25 mm mix of Set I, and the 19 mm FR mix of Set I, respectively. Thus, for each of these mixes the cosine of the phase angle falls in the ranges: 0.984 to 0.988, 0.98 to 0.988, and 0.985 to 0.995 which is almost about 1 and thus has no or minimal contribution compared to that of the variability in $|E^*|$ on E' . Similarly at a low reduced frequency of 0.001 Hz, the phase angle of each of these mixes fall in the ranges of 21° to 30° , 19° to 31° , and 22° to 30° for the 12.5 mm mix of Set II, 25 mm mix of Set I, and the 19 mm FR mix of Set I, respectively. This shows that also the variability in the phase angle increases as the reduced frequency decreases but still has a minimal contribution to the uncertainty in E' .

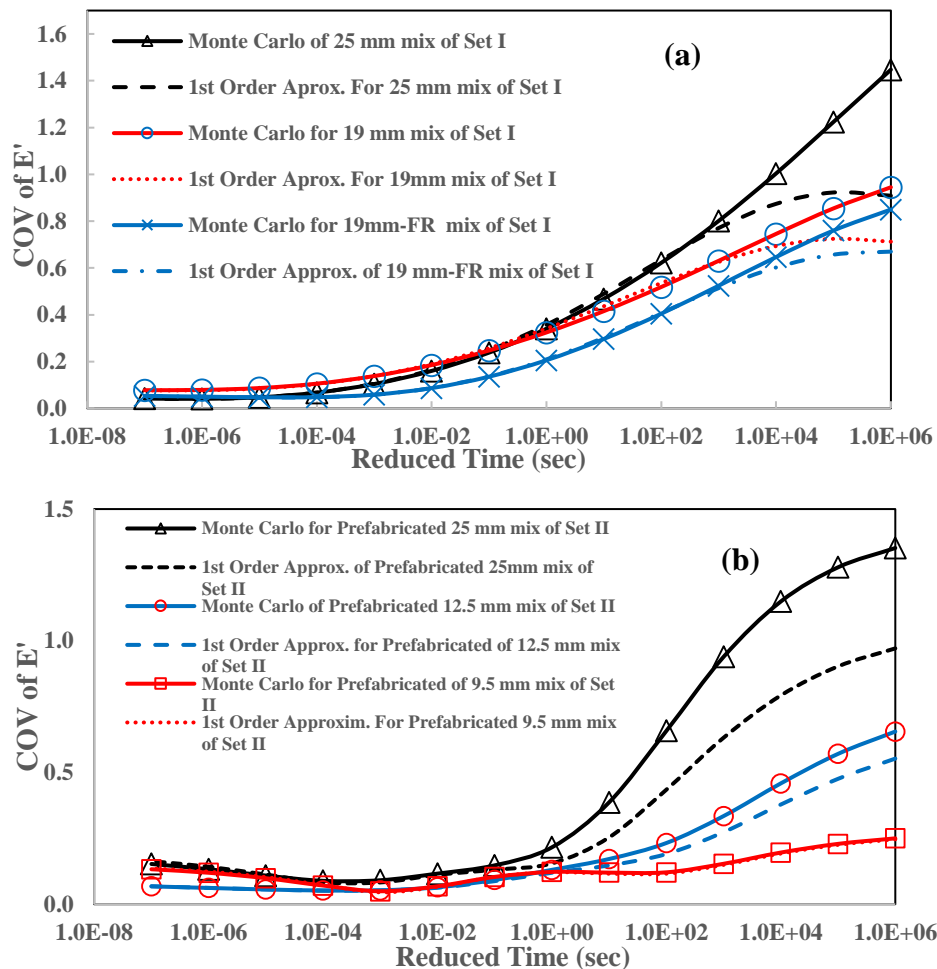


Figure 112 (a) COV of E' as a function of reduced time for mixes of Set I, (b) COV of E' as a function of reduced time for mixes of Set II.

8.3.3.2 Uncertainty in $E(t)$

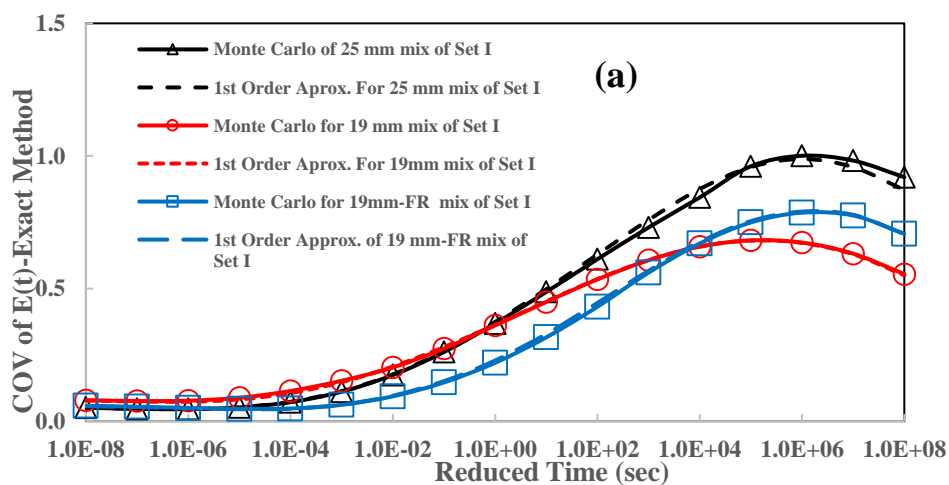
The inherent variability in $E(t)$ for each mix is quantified based on the probabilistic models describing the uncertainty in each of the Prony coefficients. The First Order Approximation and Monte Carlo simulations with 500,000 realizations of each of the 18 Prony coefficients were conducted to provide realistic estimates of the mean and COV of $E(t)$ at specified values of reduced times between 10^{-8} and 10^8 sec. The $E(t)$ converted from E^* data using both the Approximate and Exact methods is investigated to check whether the selected method has a contribution to the quantified uncertainty or not.

For all the mixes in the study, the results show that the Approximate and the Exact method provides exactly the same $E(t)$ mastercurves. Similar results are shown for other mixes by previous research studies (Mun et al. 2007). For each mix and for both methods, the average $E(t)$ master curves that are determined from the Monte Carlo simulations and the First Order Approximation method are found to be identical to the average master curves of

the different replicates. These results shows that the Prony series representation of E(t) is realistic and representative of the six mixes in study.

On the other hand, the uncertainty of E(t) calculated using both the Approximate and Exact methods is presented by COV as function of reduced time as shown in Figure 113 and Figure 114 for mixes of Set I and Set II, respectively. For each mix, the calculated COV curves as a function of reduced time are identical whether E(t) is calculated using the Approximate Method or the Exact Method as shown in Figure 113 (a and b) and Figure 114 (a and b) for the mixes of Set I and Set II, respectively. This result is important as it shows that the uncertainty of E(t) is not affected by the method used to convert the E* data into E(t). Thus, it can be concluded that both interconversion methods yield exactly the same average E(t) mastercurves with the same level of uncertainty as a function of reduced time. This shows that either method can be used along with Prony series representation to provide realistic estimate of the mean E(t) at any reduced time in the range of 10^{-8} and 10^8 sec without affecting the level of uncertainty inherited in the calculated response.

In addition, the results show that the First Order Approximation Method and the Monte Carlo simulations yield the same COV all over the investigated range of reduced time between 10^{-8} and 10^8 sec. This shows that for E(t) calculated by either interconversion methods and presented by Prony Series, any of the uncertainty modeling techniques (First Order Approximation or Monte Carlo Simulations) can be used in order provide a realistic estimate of the mean mastercurve and COVs as a function of reduced time. This observation is important since it indicates that the simple First Order Approximation is sufficient for quantifying the uncertainty in E(t) without the need for Monte Carlo simulations which require higher computational efforts.



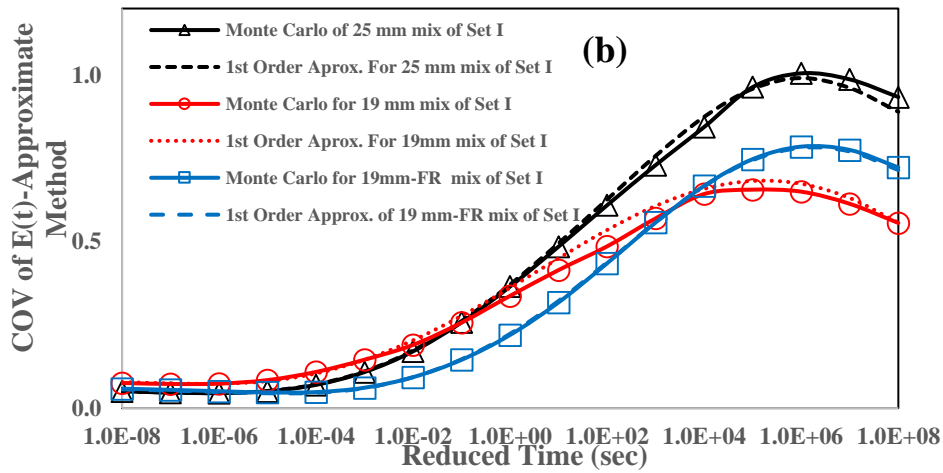


Figure 113 (a) COV of $E(t)$ calculated using the Approximate Method for mixes of Set I as a function of reduced time, (b) COV of $E(t)$ calculated using the Exact Method for mixes of Set I as a function of reduced time.

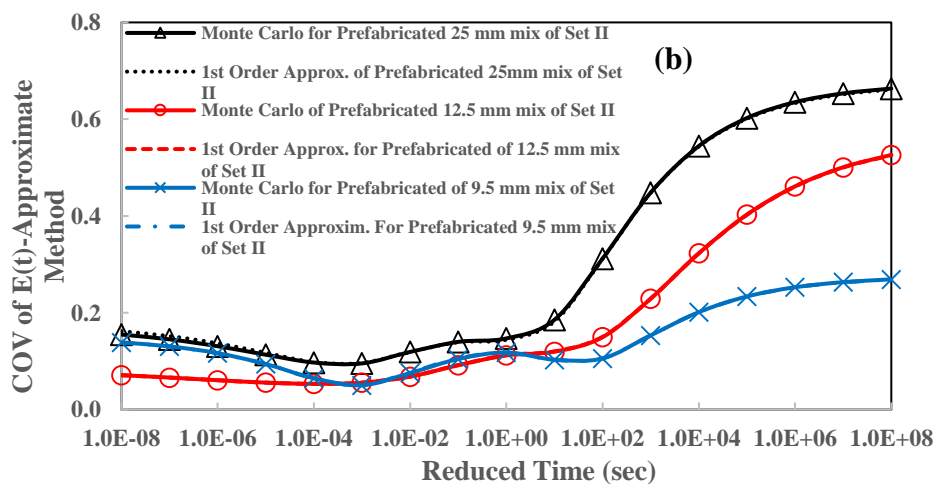
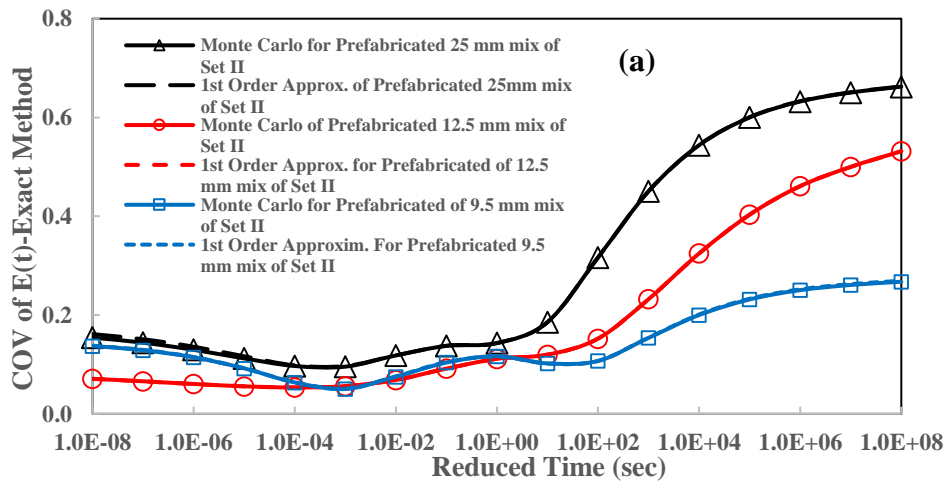


Figure 114. (a) COV of $E(t)$ calculated using the Approximate Method for mixes of Set II as a function of reduced time, (b) COV of $E(t)$ calculated using the Exact Method for mixes of Set II as a function of reduced time.

It is remarkable that this is not the case of $|E^*|$ and E' as a significant difference on COVs starts to appear as the COV becomes high i.e. at high reduced times and/or mixes with large NMAS as shown in Figure 106 and Figure 112. This can be attributed to the high non-linearity of the sigmoidal function used for presenting $|E^*|$ and E' which renders the First Order Approximation incapable of quantifying high levels of uncertainty.

In general, it can be observed that the COV of $E(t)$ increases as the reduced time increases. For mixes of Set I, the COV almost follows a plateau before starting to increase for reduced time above 10^{-3} sec where it reaches a peak in the range of 0.6-1.0 at high reduced time between 10^4 and 10^6 sec after which it starts to drop down. For this set of mixes, it can be observed that the 25 mm mix has higher COVs than the 19.0 mm mixes. For Set II, COVs of the 25 mm and 9.5 mm decrease slightly from 0.15 to approximately 0.1 as the reduced time increases from 10^{-8} to 10^{-3} sec. In this range of reduced time, the COV of $E(t)$ for the 12.5 mm mix of Set II is almost constant similar to the case of all mixes of Set I. One similarity between the 12.5 mm mix of Set II and the mixes of Set I is that all has a PG 76 binder which is stiffer than that of the 25.0 mm and 9.5 mm mixes of Set I being of PG 64. So, the higher and descending COVs at very low reduced times might be attributed to the type of binder; however, such a conclusion needs further assessment using more mixes. For all mixes of Set II, the COV increases significantly as the reduced time increases above 10^{-3} sec to reach values of 0.66, 0.53, and 0.38 for the 25.0 mm mix, the 12.5 mm, and the 9.5 mm mix, respectively. Also, it can be observed that the COV of the 25 mm mix is higher than that of the other 2 mixes at all reduced times and in role that of the 12.5 mm mix is higher than that of the 9.5 mm mix at reduced times above 10 seconds.

When comparing the COV curves of $E(t)$ compared to that of E' , it can be observed that it is equal for both responses at low reduced times. However, as the reduced time increases, the COVs of $E(t)$ start to deviate from that of E' beyond a reduced time of 0.1 sec where the COVs in $|E^*|$ and E' exceed that of $E(t)$. This difference is observed to increase as the reduced time increases and/or the NMAS becomes larger. For example, for the 25 mm mix of Set II, the COV of $E(t)$ is 0.63 which is less than that of E' being 1.4 at 10^6 sec. The same pattern can be observed for all the mixes in the study. It is noted that $E(t)$ is converted from E' using either the Approximate or the Exact methods, thus the uncertainty of $E(t)$ should be a function of that of E' . By recalling Equation 22 and Equation 23 for converting E' to $E(t)$ using the Approximate method, the analysis of the results of the local log-log slope of $E'(w)$ shows that it has COV that varies with reduced time where it can range between 0.1 and 1.0. When this uncertainty is propagated forward into the reciprocal of the adjustment function “ λ ” using the mathematical formulation with the cosine and gamma function, it

yields a very low COV for λ ranging between 0.0008 and 0.04 depending on the mix and the reduced time. Thus, the uncertainty in $E(t)$ is a function of that in $E'(w)$ and the very low COV of the reciprocal of λ whose mean value ranges between 0.85 and 0.99 depending on the reduced time under study. The mathematical formulation of $E(t)$ along with the low COV in the reciprocal of λ may lead to the drop in the COV of $E(t)$ compared to E' and $|E^*|$ at high reduced times.

Despite of the method used for converting the E^* data into $E(t)$ and whether the 1st Order Approximation Method or Monte Carlo Simulation is used to quantify the uncertainty, it is found that $E(t)$ has high COVs especially as the reduced time increases. Thus, it is important to take this variability into account to check its effect through forward modeling on the predicted VE and VP strains.

8.3.3.3 Uncertainty in D(t)

$D(t)$ is converted from $E(t)$ using the Approximate Method and thus it is needed to check how the uncertainty in $E(t)$ is propagated into $D(t)$. The inherent variability in $D(t)$ presented by the COV is quantified through the probabilistic models of the coefficients of the Prony series representation defining this response function. Similar to the case of $E(t)$, the COV is the same whether it is calculated using the 1st Order Approximation Method or the Monte Carlo Simulations. For each of the mixes in study, the mean mastercurve calculated by either methods through the probabilistic models of the Prony coefficients is identical to that calculated as the average of the single replicates for each mix.

Like other LVE functions, the uncertainty in $D(t)$ increases with the increase in reduced time where it reaches relatively high values above 0.8 for some of the investigated mixes at high reduced times as shown in Figure 115. For each set of mixes, the COV of $D(t)$ can be observed to be the same for all the mixes at low reduced times. In general, the COV curves deviate from one mix to the other as the reduced time increases. This is clearer for the case of mixes of Set II where it can be observed that for reduced times larger than 10 sec, the COV becomes larger for mixes with higher NMAAS and this difference increases as the reduced time increases. Such behavior is not observed for mixes of Set I as shown in Figure 115-a in which the COV of $D(t)$ is constant (around 0.06) for reduced times below 10^4 sec. It increases to reach high values of 0.7 before it becomes constant or slightly decreases as the reduced times exceeds 10^4 sec. It increases to reach high values about 0.7 before it becomes constant or slightly decreases as the reduced times exceeds 10^4 sec. This difference in behavior in mixes of Set I and Set II might be due to factors other than NMAAS and reduced time. This need to be further investigated in future studies and such factors may include air

voids level and binder type. These factors are highlighted because mixes of Set I has an air void level of 4.0% while that of Set II has 7.0%. This could be an influencing factor because the difference in the COV for mixes in Set I is much lower than that of the mixes in Set II. Additionally, the binder type could be an influencing factor because the 25.0mm and 19.0mm mixes of Set I have almost the same COV as one common factor between them is the same type of polymer modified binder.

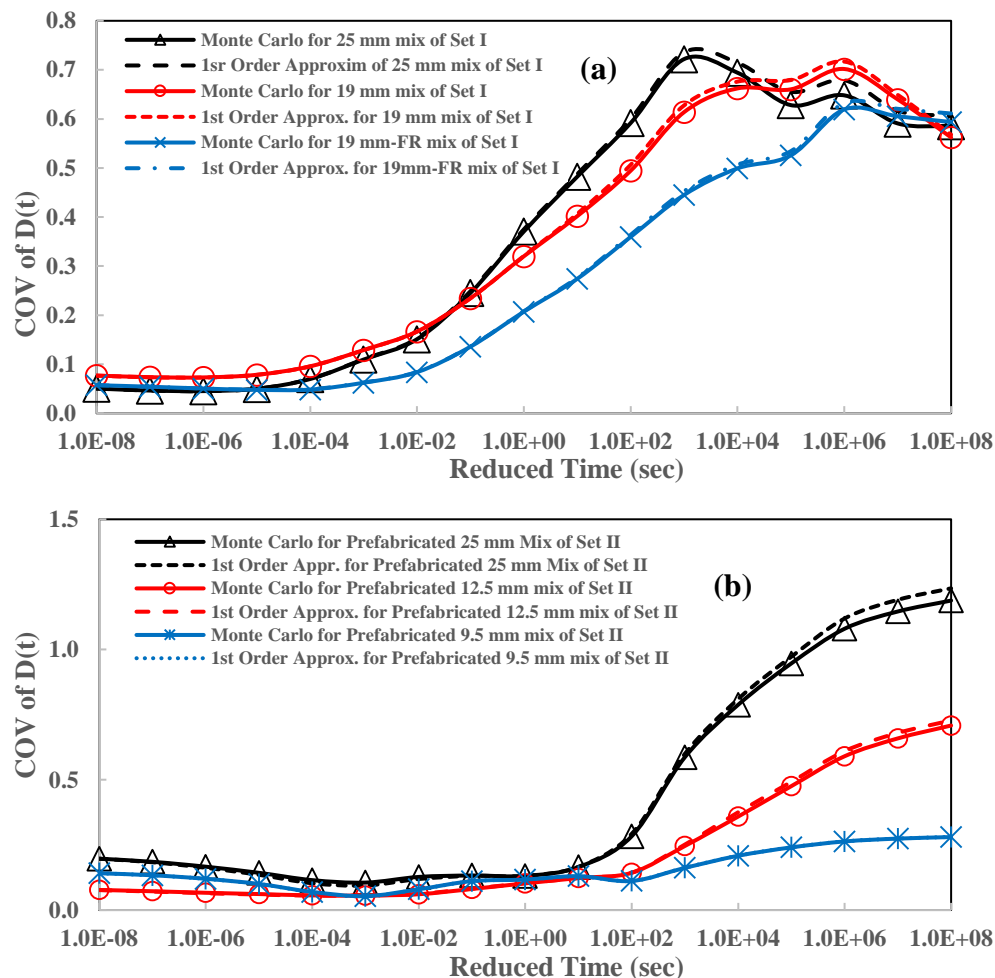


Figure 115. (a) COV of D(t) for mixes of Set I as a function of reduced time, (b) COV of D(t) for mixes of Set II as a function of reduced time.

The COV of D(t) is compared with that of E(t) because the inherent uncertainty in E(t) is propagated into that of D(t). For mixes of Set I, the COV of D(t) is the same as that of E(t) but it becomes lower at high reduced times of 1000 sec and 1sec for the 25.0 mm mix and the 19.0 mm mix, respectively. For the mixes in Set II, the 9.5 mm mix has almost the same low COV for both D(t) and E(t). For the 12.5 mm and the 25.0 mm mix, the COVs of E(t) and D(t) are the same up to 1000 sec above which that of D(t) becomes much higher. Consequently, it can be concluded that the comparison of the COV of D(t) to that of E(t) is mix dependent with no clear trends. More importantly, if the D(t) of the 25.0mm mix of Set I is compared to that of Set II, it can be found that the COVs are much higher for the mixes of

Set II at large reduced times. Therefore, the uncertainty in $D(t)$ is not strongly correlated to the NMAAS as it is the case of $|E^*|$. The NMAAS might have an effect but it might be overshadowed by the uncertainties of other factors. By recalling Equation 30 which is used for converting $E(t)$ to $D(t)$:

$$E(t)D(t) = \frac{\sin(m\pi)}{m\pi}$$

Equation 30

It can be observed that the uncertainty in $D(t)$ is affected by that of $E(t)$ where “ m ” is determined by fitting $E(t)$ to local power representations. The analysis of the uncertainty in the slope of $E(t)$ at two large reduced times of 10^4 and 10^6 sec (where differences occur between COV of $E(t)$ and $D(t)$) shows that it varies between mixes as shown in Figure 116. It can be observed that the COV of the slope of $E(t)$ is much lower for the mixes of Set I as compared to Set II. Within the same set, the 25.0 mm mix has a higher COV than the others. This shows that the COV in the slope of $E(t)$ is a function of NMAAS; however, it is also a function of other factors which might include the level of air voids and type of binder that varies between Set I and II. By relating the effect of variability in the slope of $E(t)$ on the COV of $D(t)$, the results show that the latter is a function of COVs of both $E(t)$ and its slope. The COV in $E(t)$ is higher for mixes in Set I than Set II; however, this behavior is inverted for the case of $D(t)$ where the mixes in Set II have a higher COV. This might be due to the effect of uncertainty in the slope of $E(t)$ which is propagated through interconversion into $D(t)$. The low COVs in the slope of $E(t)$ for mixes of Set I might lead to the drop in COV in $D(t)$ compared to $E(t)$, and the high COVs in slope of $E(t)$ might be the reason for the rise in the COV of $D(t)$ compared to $E(t)$.

By comparing the variability at high reduced times for the two 25.0mm mixes, the mix of Set I has higher COV for $E(t)$, lower COV for slope of $E(t)$, and higher COV for $D(t)$. This assures that variability in $D(t)$ is not only a function of NMAAS but on variability of $E(t)$ and its slope. The latter might be affected by other physical factors like air voids and binder type as stated earlier.

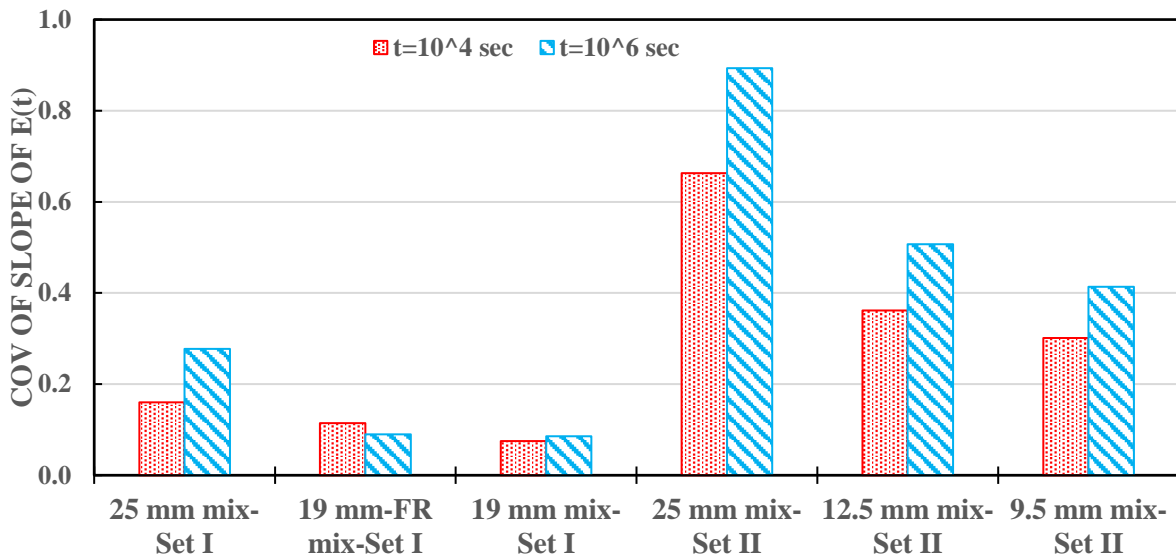


Figure 116. The COV of the slope of E(t) at reduced times of 10⁴ and 10⁶ sec for the mixes of Set I and Set II.

8.3.4 Probability Distribution of E(t) and D(t)

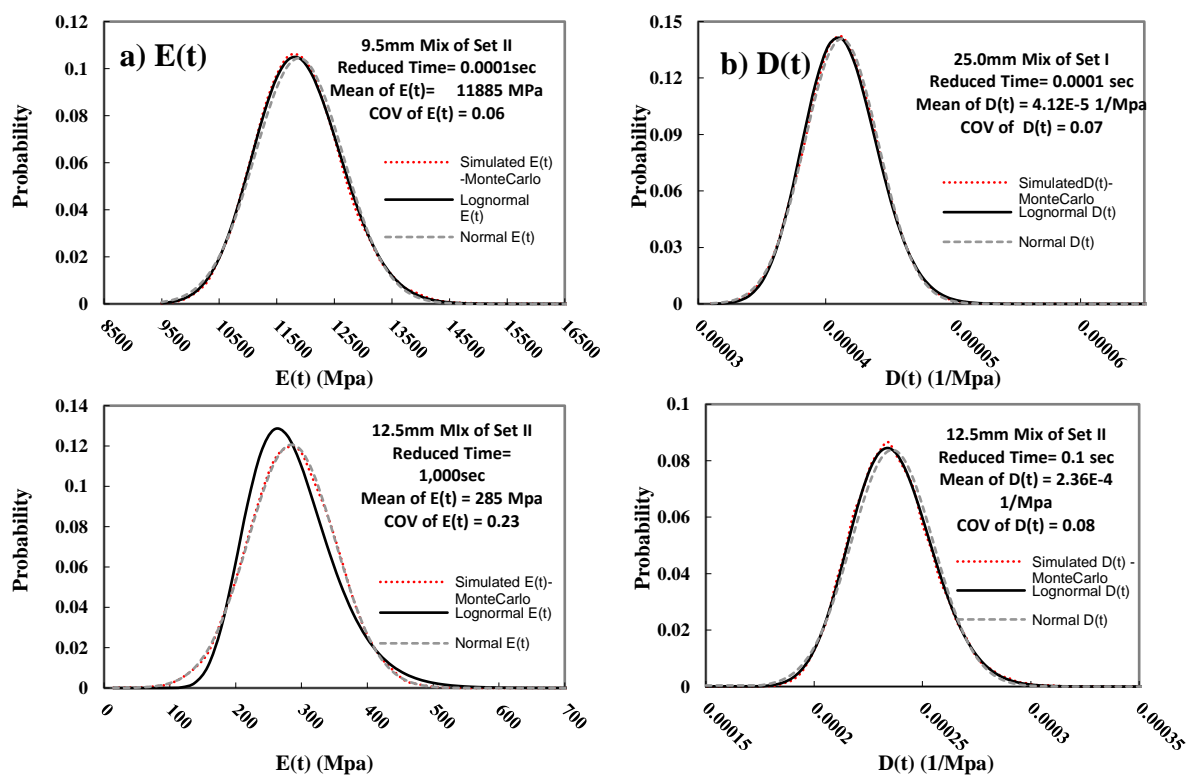
For some applications, the incorporation of either E(t) or/and D(t) within a probabilistic based analysis requires knowing its distribution and not only its mean and COV. It is needed to know the probability distribution that best represents the uncertainty in each of these response functions. The probability distribution functions (pdf) are plotted for the results simulated using Monte Carlo at different reduced times to present the uncertainty in E(t) and D(t). Based on the results of modeling the probability distributions of |E*|, the normal and lognormal are tested as candidate distributions for E(t) and D(t). Sample PDFs are plotted along with the theoretical normal and lognormal distributions for mixes of Set I and Set II at different reduced time where a sample of these plots is presented in Figure 117.

The results in Figure 117 show that different probability distributions are required to model the uncertainty in E(t) and D(t). For the 9.5mm and 12.5mm mixes of Set II, E(t) follows a normal distribution at all reduced times. Also, a lognormal distribution is observed to fit the E(t) data for the 25.0mm mix of Set I at all reduced times. However in the case of 19mm-FR mix of Set I and 25.0mm mix of Set II, although E(t) follows a normal distribution for reduced times below 10sec, it is not the case for larger reduced times with high values of E(t) COVs. For a reduced time of 100sec, the truncated normal distribution can be used to fit the data of the 25.0 mm mix but not the 19.0mm-FR mix. In fact, results indicate the presence of many cases (particularly at very large reduced times) where the PDF exhibits a steep increase at low values of E(t) before it decreases slowly with a positively skewed tail. The

19.0mm-FR mix shown in Figure 117 is an example of such cases where neither the normal nor the lognormal distributions could adequately model the uncertainty in $E(t)$.

Similarly, no universal probability distribution could be model the uncertainty in $D(t)$ at different reduced times. Results show that the $D(t)$ follows a normal distribution at any reduced time for the 19.0 mm-FR mix and a lognormal distribution for both the 25.0 mm and 12.5 mm mixes of Set II. For the 9.5 mm mix of Set II, a lognormal distribution is the best fit for the data at small reduced times and normal distribution for large reduced times. For the 25.0 mm mix of Set II, $D(t)$ has a normal distribution for reduced times below 10 second, a lognormal distribution for reduced times up to 1000 second, and then the data follows neither distributions, with a PDF that has a steep increase at low values of $D(t)$ up to a given peak and then the data becomes highly skewed to the right. In the case of distributions with arbitrary shapes especially at reduced times with high COVs, the Hermite Polynomials are recommended to be used in order to model such distributions.

Based on the above, it can be concluded that the distributions of $E(t)$ and $D(t)$ are mix dependent. It is worth noting that the probability distributions of $E(t)$ and $D(t)$ are needed in cases where single values of $E(t)$ and $D(t)$ are required. Otherwise, for viscoplastic modeling for example, the uncertainty could be propagated through Prony coefficients where $E(t)$ and $D(t)$ will be modeled in the form of their Prony series representation.



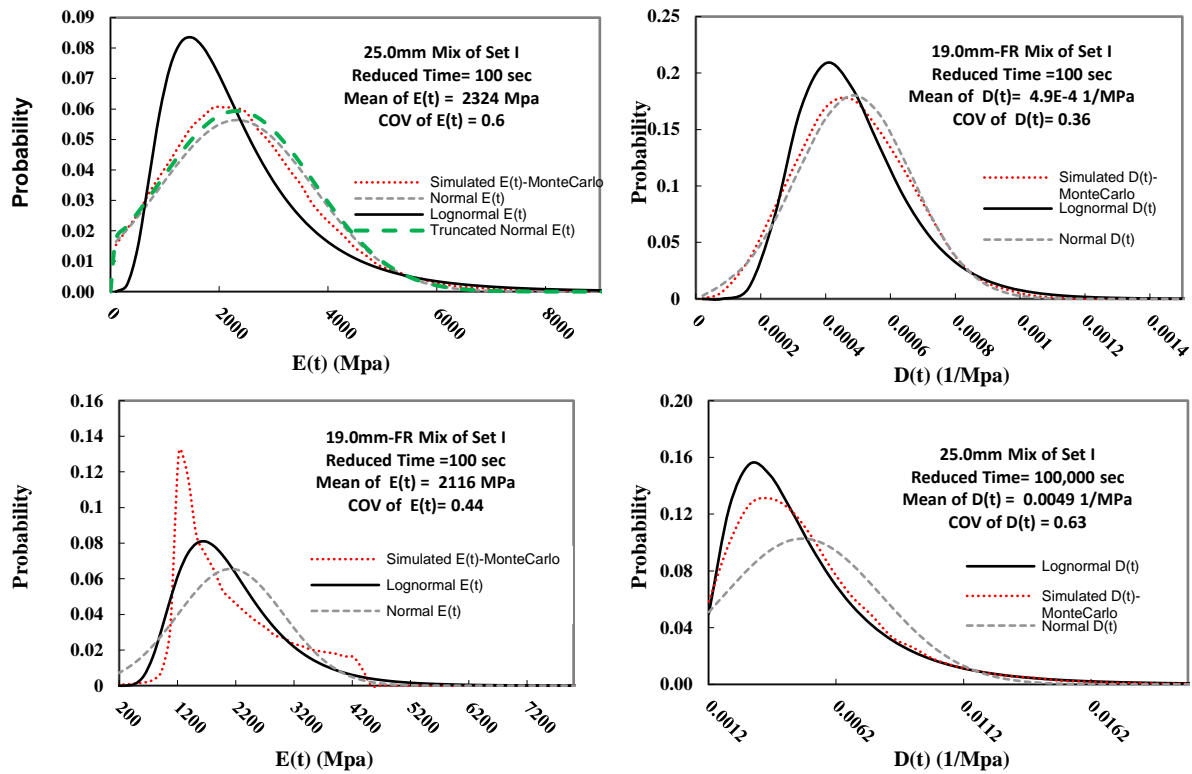


Figure 117. Probability distribution functions of simulated data for a) E(t) and b) D(t) at for selected mixes and reduced times.

8.3.5 Case Study

To illustrate the importance of quantifying inherent uncertainty in LVE functions, a simple case study is presented regarding the prediction of the tensile strain (ϵ_t) for a a three-layered pavement system as illustrated in Figure 118. The strain is measured under the center of the load at the bottom of the AC layer consisting of the 19.0mm-FR mix of Set I.

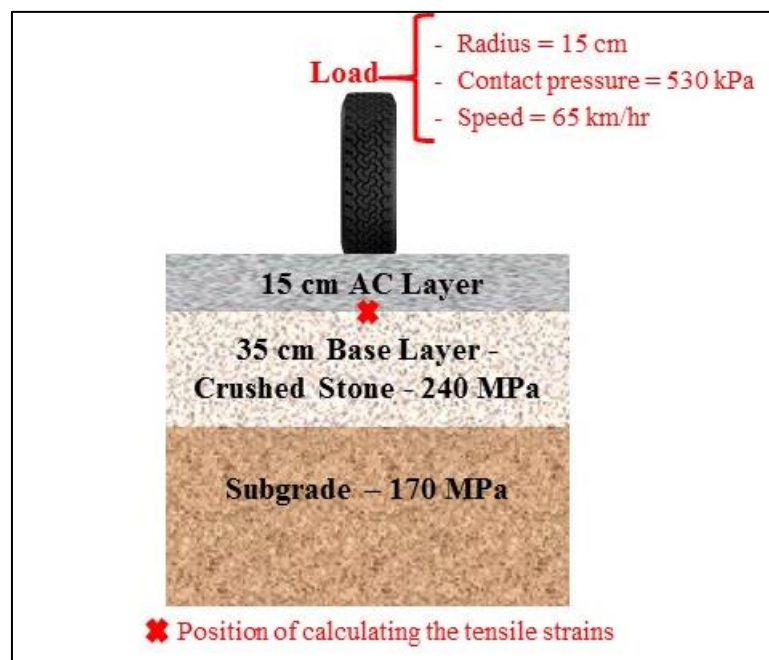


Figure 118. Illustration of the case study used for the calculation of the tensile strains under the load at the bottom of AC layer within a three-layered pavement system.

The program Kenlayer is used for this analysis in which the AC is characterized as a LVE material through the mastercurve of $D(t)$ (Huang 1993). The base and subgrade are considered to be linear elastic with a Poisson ratio of 0.35 and 0.45, respectively. A suite of 300 runs are conducted with corresponding $D(t)$ mastercurves selected from Monte Carlo simulations. Three different pavement temperatures of 10°C, 20°C, and 35°C are considered in this case study in order to investigate the effect of the uncertainty in $D(t)$ at different reduced times.

The predicted deterministic and probabilistic ε_t calculated for the case in which AC properties are assumed to be uncertain are presented in Table 39. For each of the three pavement temperatures under consideration, the predicted deterministic ε_t and the mean of the probabilistic ε_t are found to be approximately equal. For the probabilistic case, as the pavement's temperature increases, the COV of ε_t increases due to a likely increase in the COV of $D(t)$ as the reduced time increases. The prediction of the allowable number of load repetitions N_f is carried out using the transfer function developed by the Asphalt Institute for 20% of area cracked as shown in Equation 101.

$$N_f = 0.0796\varepsilon_t^{-3.291}|E^*|^{-0.854} \quad \text{Equation 101}$$

where: ε_t = tensile strain and $|E^*|$ is dynamic modulus calculated at a given pavement temperature and load speed.

The deterministic and probabilistic solutions, calculated using 50,000 realizations of $|E^*|$ and ε_t , are presented in Table 52. The predicted deterministic and probabilistic (mean) N_f are approximately equal in the cases of pavement temperature of 10°C and 20°C, with COVs of 0.2 and 0.3, respectively. However, a slight variation of 18% in the mean N_f between the deterministic and probabilistic solutions can be observed at the high temperature of 35°C at which N_f possesses a relatively high COV of 0.7. Thus, the variability in N_f has a similar trend as that of ε_t as a function of the pavement's temperature but at different magnitudes due to the mathematical formulations used for the calculation of N_f . The results of the Shapiro-Wilk Normality Test show that N_f has a lognormal distribution which is highly skewed to the right.

Table 52. Predicted tensile strains and corresponding number of cycles to failure in fatigue using deterministic and probabilistic analyses.

	10°C	20°C	35°C
Deterministic ϵ_t	51.5 $\mu\epsilon$	69.8 $\mu\epsilon$	132.5 $\mu\epsilon$
Probabilistic ϵ_t	Mean: 51.7 $\mu\epsilon$ COV: 0.05	Mean: 70.4 $\mu\epsilon$ COV: 0.07	Mean: 134.2 $\mu\epsilon$ COV: 0.15
Deterministic N_f	44.2 million	28.1 million	9.2 million
Probabilistic N_f	Mean: 44.6million COV: 0.2	Mean: 29.5million COV: 0.3	Mean: 10.9million COV: 0.7

The probabilistic approach to solving the problem allows for quantifying the inherent risks in the pavement design. In fact, one can quantify the probability of unsatisfactory performance (defined as the probability of achieving 20% cracking for N_f less than the deterministic design N_f) to be in the range of 53-55% for the three cases under investigation. These probabilities are relatively large indicating a relatively high and potentially unacceptable risk of unsatisfactory performance for the designed pavement. The probabilistic solution allows for calculating the number of allowable load repetitions that would result in a smaller and more acceptable probability of unsatisfactory performance. If such an analysis is conducted assuming a probability of unsatisfactory performance of 10%, it could be shown that the number of allowable load repetitions for this pavement is reduced, leading to decreases in the order of 20, 34, and 60% in the service life of these pavements for the cases of 10°C, 20°C, and 35°C, respectively. On the other hand, if the same design number of repetitions is to be maintained while reducing the required probability of unsatisfactory performance to 10%, then the design asphalt thickness has to be increased by 0.8 cm, 1.25 cm, and 2.25 cm for the 10°C, 20°C, and 35°C cases, respectively. The relatively larger difference in the required thickness for the cases with higher design temperatures is attributed to the relatively larger COV of the LVE functions as the reduced time becomes higher.

The results indicate that the quantification of the uncertainty in $D(t)$ and its forward propagation into number of load repetitions to failure has a significant effect on the predicted pavement life. The quantification and modeling of the uncertainties in $D(t)$ can be considered to be critical for any reliability-based analysis that aims at estimating the probability of not achieving a target N_f . Although the calculated probabilities account only for the variability in the properties of the AC layer (basically $D(t)$ and $|E^*|$), the results indicated relatively high risks of unsatisfactory performance. Such probabilities could be used to refine the design of

the pavement within a probabilistic framework which can incorporate other sources of uncertainties. Thus, accounting for the inherent variability of LVE response functions is of importance for QA/QC applications and for the proper implementation of performance based specifications.

8.3.6 Conclusions

Based on this work, the following conclusions are drawn:

- The COV of E' is the same as that of $|E^*|$ but different from that of $E(t)$ especially at high reduced times.
- The COV of both $E(t)$ and $D(t)$ possess relatively low and equal values at small reduced times. The values of COV increase with differences appearing as the reduced time increases.
- Although E^* , $E(t)$, and $D(t)$ can be determined from one another using interconversion techniques, the inherent variability varies from one function to the other.
- The inherent variability in $E(t)$ is independent of the interconversion method used.
- For both $E(t)$ and $D(t)$, the same COV curves are obtained both Monte Carlo Simulations and First Order Approximation.
- Unlike $|E^*|$, the inherent uncertainty in $E(t)$ and $D(t)$ is not only a function of the NMAS but on other factors that need to be further investigated in future studies. These might include type of binder and level of air voids.
- $E(t)$ and $D(t)$ may follow a normal or lognormal distribution depending on the mix type and reduced time. Nevertheless, neither of these distributions can be used at reduced times with high COVs as the distribution will have an arbitrary shape.
- The uncertainty in $D(t)$ has a significant effect on the distribution and variability of the predicted number of loads to failure in fatigue cracking.

8.4 Effect of Plant-Mixing and Multi-Laboratory Testing on Uncertainty in LVE Functions

In this section of the dissertation, E^* data for six different mixes are analyzed by modeling the uncertainty of each of the LVE functions of these mixes. These mixes represent two sets: plant produced mixes for Set I and multi-laboratory testing for mixes of Set II. The work herein takes the modeling of the uncertainty in LVE functions one step further to provide a better discretization of real asphalt concrete properties that will be placed in the field. This is achieved by considering the variability in E^* data resulting from testing the same mix in different laboratories having different testing equipment and different operators. The composition of the mixes investigated for the stated purpose is different than that of the

four mixes designed and thoroughly analyzed in the scope of this dissertation, namely: U19-HMA, M19-HMA, U25-HMA, and U19-WMA-SonneWarmmix. It is worth noting that those four mixes have the same aggregate type, source, and gradation as those of Set I.

As shown earlier and highlighted in Figure 119 and Figure 120, the uncertainty in $|E^*|$ of plant-produced mixes has generally higher magnitudes than that of mixes produced in the laboratory. The difference is notable especially at small reduced frequencies below 0.1 Hz. At a reduced frequency of 10^{-6} Hz, the COV of $|E^*|$ of M19-HMA is 0.4 which is almost half that of both 19.0 mm mixes of Set I. The COV of $|E^*|$ of these three 19.0 mm mixes is comparable as all have same aggregate type and gradation and are produced with polymer modified binders. The COV of $|E^*|$ of the 19.0 mm FR mix is slightly higher than that of the 19.0 mm mix of the same set. This may be due to the addition of fuel resistance additive as stated earlier. A similar trend is observed for the uncertainty in $|E^*|$ for the 25.0 mm mix of Set I as compared to that of U25-HMA; however, the difference is of higher order than that observed in the suite of the 19.0 mm mix. At a reduced frequency of 10^{-6} Hz, $|E^*|$ of U25-HMA possesses a COV of 0.6 while that of the 25.0 mm mix of Set I has a much higher COV around 1.4. Although these mixes do not have the same binder type, this does not justify the significant difference in uncertainty (more than the double for Set I). It is also evident that air void content does not have a considerable effect on the uncertainty in $|E^*|$. Uncertainty is much higher for mixes with air void content of 4.0% (Set I) than it is for mixes with air void content of $7.0 \pm 1\%$ (M19-HMA and U25-HMA), which does not lead to a conclusive inference on the effect of air voids.

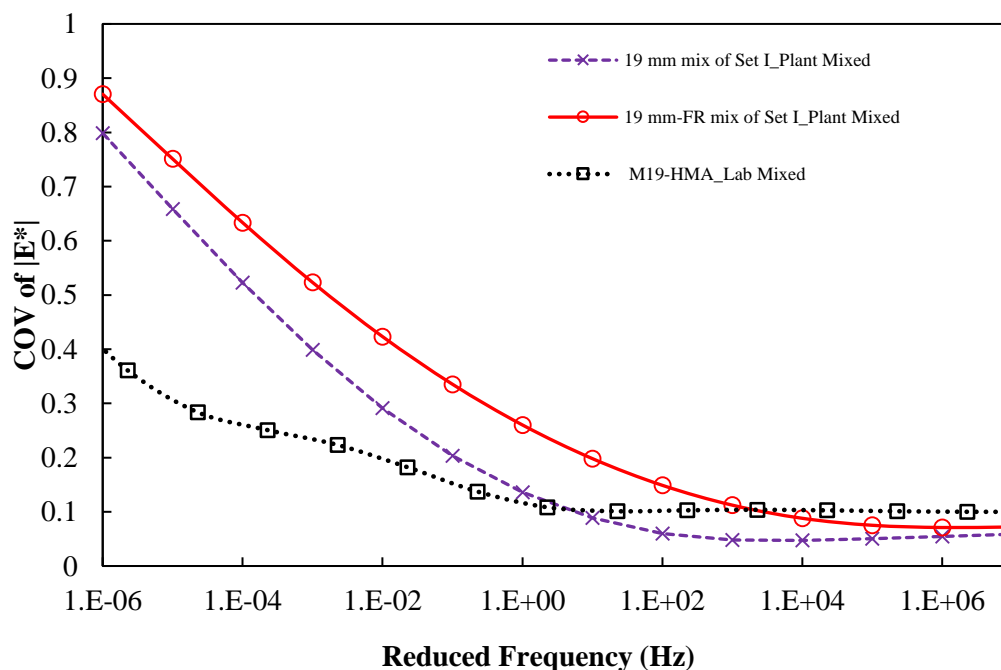


Figure 119. COV of $|E^*|$ as a function of reduced frequency at 20°C based on Monte Carlo Simulations for the 19.0 mm mixes that are plant and laboratory mixed.

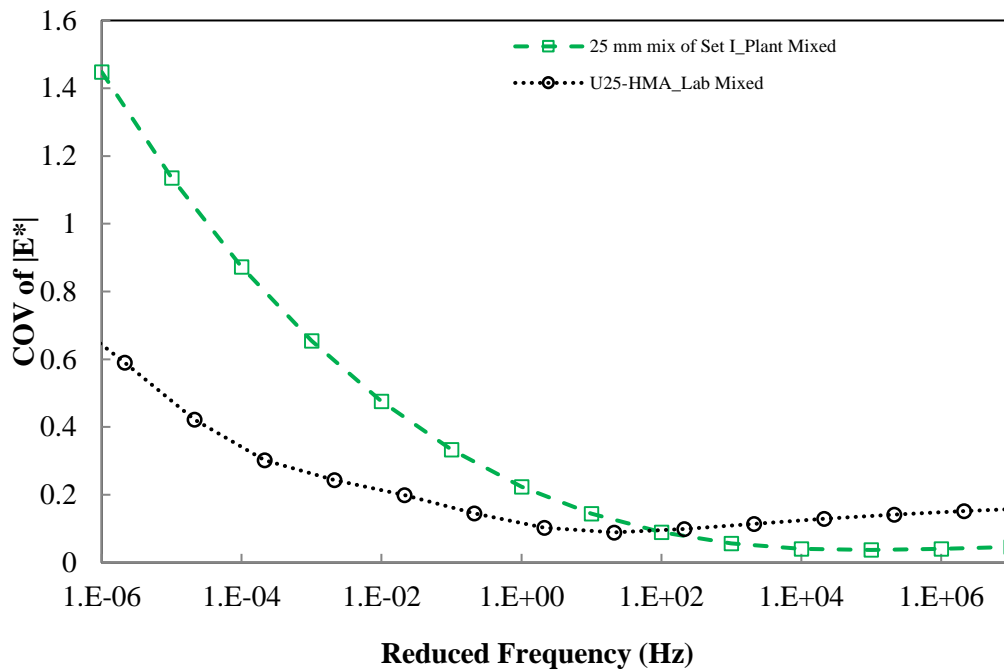


Figure 120. COV of $|E^*|$ as a function of reduced frequency at 20°C based on Monte Carlo Simulations for the 25.0 mm mixes that are plant and laboratory mixed

Multiple factors may play a role in yielding higher uncertainties in $|E^*|$ for plant mixed asphalt concrete replicates, especially at low reduced frequencies corresponding to high temperatures and/or slow loading rates. One of these factors is the variability in the actual asphalt content of the samples being tested. For lab-mixed samples, there is a higher control on the weight of asphalt binder added per sample where the margin of error is within $\pm 0.5\%$ of the total weight of asphalt binder. The margin of error for plant mixed samples, on the other hand, reaching $\pm 7\%$ of the total asphalt binder corresponding to the $\pm 0.25\%$ tolerance of the optimum asphalt binder content, as shown in Figure 103. Thus, variability in asphalt content within the tested specimens could be a major source for boosting the uncertainty in $|E^*|$ especially at low reduced frequencies equivalent to high temperature and/or slow loading rates. The effect of variability in asphalt content is dominant in high temperature and/or slow loading rates when asphalt is less stiff and its viscous behavior is more apparent on the uncertainty. The uncertainty in $|E^*|$ will be further exaggerated/pronounced in other cases where a higher tolerance of asphalt binder is accepted, such as tolerance values of 0.4%, 0.5%, and 0.6% adopted by States of Delaware, Indiana, and Kansas, respectively (Cooper III 2011). Another factor that has an impact on E^* uncertainty is the phenomenon of short-term aging of asphalt mixes, which differs between laboratory and plants. Although the aging protocol of the lab is designed to mimic the actual conditions of the plant and field as much as possible, yet differences exist and can be a significant source of uncertainty in the properties of asphalt concrete. In laboratory, the tested asphalt concrete sample weighs a few

kilograms and is placed in a pan at an even thickness ranging between 25 mm and 50 mm and stirred for a period of one hour to ensure uniform aging of the entire mix. A similar aging process cannot be achieved in a plant as asphalt concrete is placed in large amounts in storage silos or trucks, where and ageing may not be consistent throughout the asphalt mix, i.e., the portion of the asphalt concrete mix at the surface is likely to be more aged than the portion of the mix at the center of the silo. Thus, properties of the same asphalt concrete mix may be different between samples taken from same batch or truck. The sampling technique can be an additional source of uncertainty. Sampling should be representative of the actual construction process; therefore, samples must be taken directly from the plant, from loaded trucks, and from the paved roadway behind the paver. To reduce uncertainty, the sampling technique has to be unbiased, representing all possible elements of the material being sampled, and accounted for accordingly in the analysis of test results.

Another major source that contributes to boosting uncertainty for field mixes is the variation in the aggregate gradation from one batch to another and from one sample to another. For laboratory mixed samples, aggregates are weighed exactly as required for every sieve size. However, the field conditions and the impossibility of sieving thousands of tons of aggregates impose highly probable variations, and thus, aggregate gradation is not controlled per sieve size. Typically, QA/QC acceptance measures and job mix formulas provide contractors and asphalt plants with a range of tolerance for the percentage by weight of aggregates for each sieve size. Moreover, segregation and degradation of aggregates might occur in stockpiling and storage processes leading to an additional source of variability. The difference in COV of $|E^*|$ between laboratory and field appears to be higher for the case of the 25.0 mm mixes as compared to that of the 19.0 mm mixes. This indicates that the uncertainty in $|E^*|$ further increases between laboratory and plant mixes as the NMAS becomes larger. This aligns with the findings of Rahbar-Rastegar and Daniel that laboratory mixes are stiffer than field mixes and that this difference is larger for 19.0 mm compared to 9.5 mm and 12.5 mm mixes (2016).

As shown in Figure 119 and Figure 120, the COV of $|E^*|$ is slightly higher for laboratory mixed samples compared to plant mixed samples at high reduced frequencies larger than 1000 Hz. For the 19.0 mm mixes, the COV of $|E^*|$ is 0.05-0.07 and 0.1 for the plant mixed and laboratory mixed samples, respectively. The difference is higher for the case of the 25.0 mm mixes, where the COV is 0.15 and 0.05 for the laboratory and field mixed samples, respectively. This does not match the trend observed at lower reduced frequencies for which the magnitude of the difference is much higher. It is worth noting that for laboratory mixed samples, E^* values were obtained at four temperatures of -5°C, 5°C, 25°C, and 40°C; however,

plant mixed samples of mixes in Set I and Set II were tested at three temperatures 4°C, 20°C, and 40°C. As such, experimental data corresponding to high reduced frequencies is not available for plant mixed samples. Therefore, the uncertainty at high reduced frequencies for plant mixes might be reduced due to symmetrical nature of the four-parameter sigmoidal function used to fit the data. The sigmoidal function leads to the convergence of the mastercurve based on the $|E^*|$ values acquired from testing at lower reduced frequencies, i.e. high temperatures, and masks part of the uncertainty imposed by the material at high reduced frequencies, i.e., lower temperatures.

Similar to the case of $|E^*|$, the observed uncertainty for plant mixed samples is forward propagated into $E(t)$ and $D(t)$. The COVs of $E(t)$ and $D(t)$ for the 19.0 mm mix for the plant and laboratory mixed samples are presented in Figure 121 and Figure 122, respectively. The COVs of both $D(t)$ and $E(t)$ are higher for plant mixed samples compared to that of laboratory mixed samples at high reduced times, i.e., high temperatures. The same behavior of laboratory mixed and plant mixed samples and reasoning for comparing the respective uncertainty in $|E^*|$ is applicable for $E(t)$ and $D(t)$.

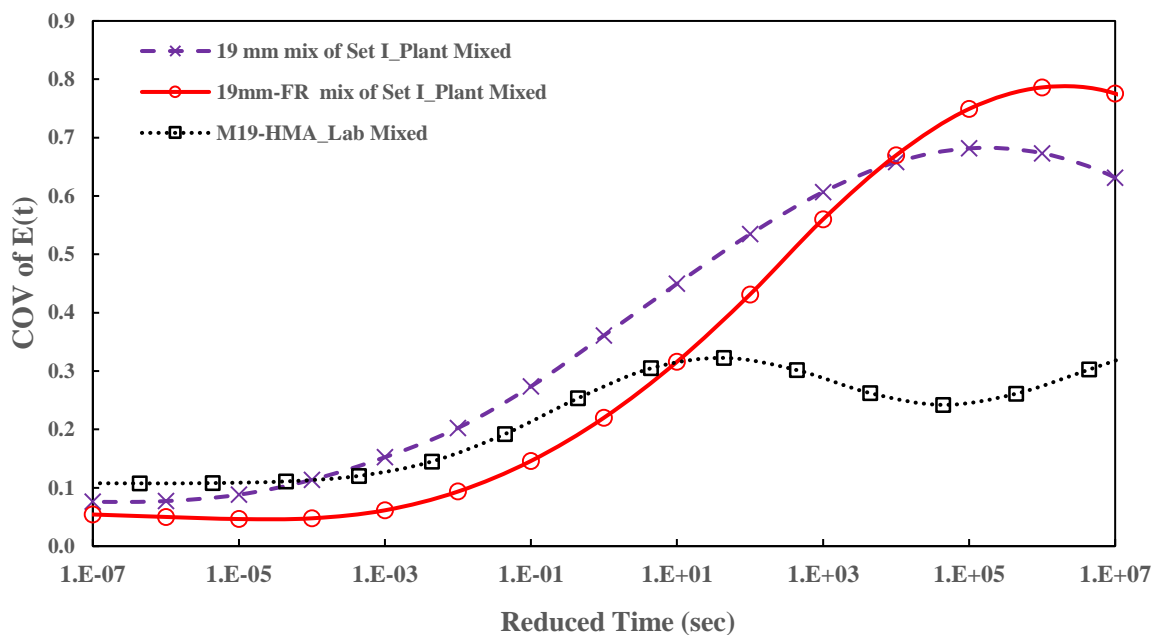


Figure 121. COV of $E(t)$ as a function of reduced frequency at 20°C based on Monte Carlo Simulations for the 19.0 mm mixes that are plant and laboratory mixed.

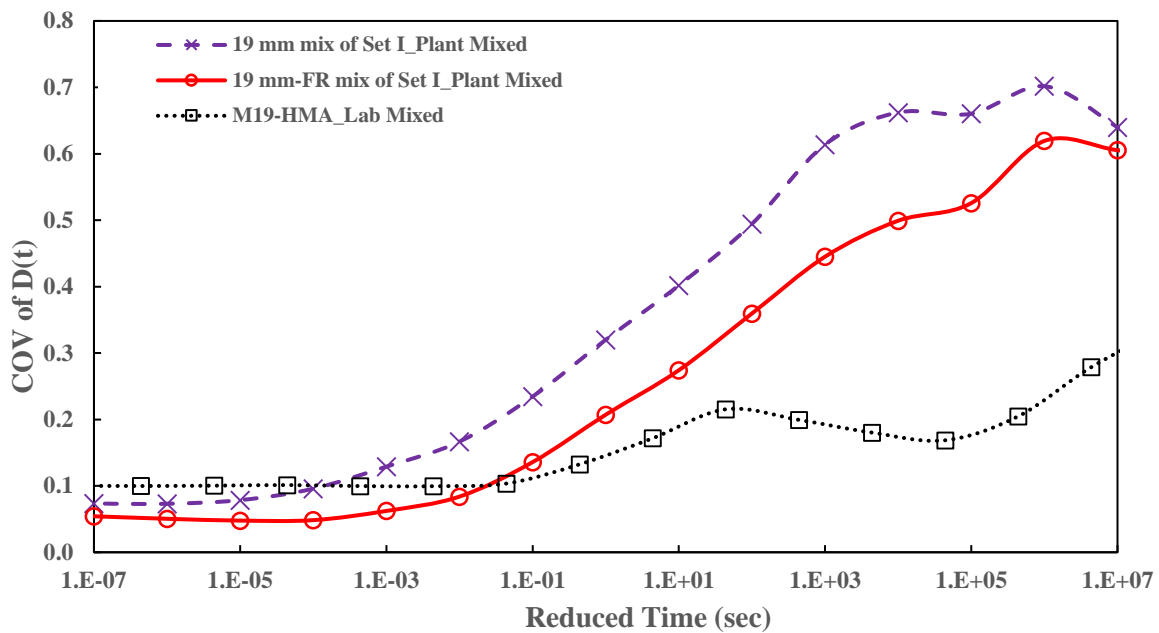


Figure 122. COV of $D(t)$ as a function of reduced frequency at 20°C based on Monte Carlo Simulations for the 19.0 mm mixes that are plant and laboratory mixed.

Based on the presented results, QA/QC procedures must account for the type of specimens being tested. The performance prediction of constructed pavements must consider the variability of the material characteristic properties used and must also account for further uncertainties imposed by the conditions of plant mixing as compared to laboratory mixing. This variability needs to be further investigated in future studies where uncertainties of material properties measured for laboratory mixed and plant mixed samples are accounted for in a reliability-based framework for performance prediction. Given that both types of samples yield the same COV at large reduced frequencies, it is recommended for QA/QC practices to conduct $|E^*|$ testing at combinations of temperature and frequency with corresponding reduced frequencies equal to or greater than 10 Hz for a reference temperature of 20°C. In addition, future work should target providing specifications for $|E^*|$ where tolerances account for the nature or the mix, i.e., whether the mix is plant-produced or laboratory-produced, the mix's NMAS, and the reduced frequency at which it is tested.

On the other hand, it should be noticed that mixes of Set II are represented by samples that are laboratory mixed and laboratory compacted but tested at eight different laboratories. Regardless of the type of the specimens, the COV of $|E^*|$ is high for the three investigated mixes and its magnitude is comparable to that of samples of Set I representing plant mixed, laboratory compacted samples. This indicates that testing in many laboratories using different pieces of equipment and by different operators may be an important source significantly affecting the variability in measured LVE properties. Thus, it is highly important to assure that for QA/QC practices, a proper control and training should be done to assure that no further

uncertainty will be imposed due to different testing protocols, inconsistency in used equipment, distinct operator's practices, and uncontrolled human errors.

Future work will require modeling the uncertainty in LVE functions for more mixes produced both in the lab and the field. This is required to better understand and thoroughly define the influence of plant production conditions on the uncertainty in asphalt concrete properties within a reliability-based framework for performance prediction of constructed pavements.

CHAPTER 9

CONCLUSIONS AND FUTURE WORK

9.1 Summary and Conclusions

The work presented in this research covered aspects related to three different fields mainly: sustainability of asphalt concrete mixes through the assessment of WMA, advanced material characterization and modeling of the behavior of asphalt concrete, and probabilistic modeling of the inherent uncertainties in the properties of asphalt mixes. It is believed that the work herein contributes to each one of these fields. This research provides a framework for accurate and realistic characterization of HMA and WMA mixes using advanced material models and a probabilistic approach. This is carried out mechanistically through the modeling of the viscoelastic and viscoplastic behavior of asphalt concrete in the compression state. In addition, the uncertainties in the linear viscoelastic function are modeled and quantified for a variety of mixes with different components. For this purpose, an extensive experimental program is conducted with a large number of tested replicates that is believed sufficient to conduct a statistical analysis especially that review of literature shows a scarcity in data for conducting such an analysis. The probabilistic modeling of asphalt concrete properties is based on mechanical models to characterize these properties besides the use of statistical, mathematical, and computational techniques. A major benefit of this work is yielding more realistic predictions through the incorporation of the uncertainties in material properties rendering the current state purely deterministic models towards becoming probabilistic which paves the roadway towards a full reliability-based assessment of pavements.

A variety of WMA additives are used with different types of asphalt binders to assess the mechanical behavior of WMA in compression state. The major contribution of this work are summarized by the following:

- The viscoelastic and viscoplastic continuum damage models used for characterization of HMA mixes are applicable for WMA mixes.
- At a time that LVE properties and damage characteristic curves can be used to assess different types of mixes, the realistic and accurate comparison of different mixes requires the use of all these measured and develop material properties in the prediction of the response of each of the mixes to a given stress profile.

- The effect of WMA additives on the mechanical properties of asphalt mixes in compression state is dependent on the type of binder used (i.e. unmodified vs. polymer modified binder) and the temperature considered in the analysis.
- Based on the developed viscoelastoplastic models, the different WMA additives show a light effect on the predicted strains compared to control HMA mixes when used with modified binder at a low temperature of 5°C and with unmodified binder at 35°C.
- The predicted total strain is significantly higher than control mixes for various types of WMA additives used with modified asphalt binder at high temperature of 35°C and with unmodified asphalt binder a low temperature of 5°C.
- At time the wax based additive Sasobit shows minimal effect on the performance of asphalt concrete in compression when assessed based on the viscoelastic model, it induced high viscoplastic strains compared to that of the control HMA mixes.
- Compared to other WMA additives and based on viscoelastoplastic models, Advera shows the most favourable results when used with modified binder; however, the performance of mixes with Sasobit and Rediset is more favourable for the case of unmodified binder.
- For the materials used in the Arabian Gulf region, it is recommended to use WMA mixes without any change in the asphalt content. The mixing and compaction temperature can be reduced constantly among all contractors by 20°C and 35°C for modified and un-modified binders, respectively.
- The effect adding aramid and polypropylene fibers provides an improvement to the mixes' performance in the compression state when used with a wax based WMA additive.
- The improvement of the performance of mix due to the introduction of aramid and polypropylene fibers with SonneWarmix has to be further investigated and validated among the other WMA additives in study.

In addition, the investigation of the uncertainties in asphalt concrete mixes shows that such uncertainties are significant. They are dependent on several factors related to the specific mix under investigation and the loading conditions for which they are assessed including temperature, loading rate, and stress magnitude. These uncertainties are dependent on the properties for which they are modeled and could be affected by several factors including production conditions of the asphalt concrete, variabilities due to testing at different

laboratories, and analysis methods incorporating different mathematical models and simulation techniques. The following major conclusions could be drawn:

- Results from mixes analyzed indicate that the magnitude of the inherent variability as reflected in the COV of $|E^*|$ is strongly correlated to the NMAS.
- The COV of $|E^*|$, $E(t)$, and $D(t)$ increases as the temperature increases and/or the loading rate becomes slower.
- The COV of E' is the same as that of $|E^*|$ but different from that of $E(t)$ especially at high reduced times.
- For the results of the same lab, the COV in LVE properties is due to natural variability in the asphalt concrete and it is not affected by any factors related to the loading machine or data acquisition.
- The selection of the type of Logistic function plays an important role on the uncertainty of LVE functions especially in the extrapolation region where experimental data is not available.
- The effect of uncertainties in the shift factor on the mean and COV of LVE functions could be neglected in any probabilistic analysis.
- The COV of both $E(t)$ and $D(t)$ possess relatively low and equal values at small reduced times. The values of COV increase with differences appearing as the reduced time increases.
- Although E^* , $E(t)$, and $D(t)$ can be determined from one another using interconversion techniques, the inherent variability varies from one function to the other.
- The inherent variability in $E(t)$ is independent of the interconversion method used.
- For both $E(t)$ and $D(t)$, the same COV curves are obtained both Monte Carlo Simulations and First Order Approximation.
- Unlike $|E^*|$, the inherent uncertainty in $E(t)$ and $D(t)$ is not only a function of the NMAS but on other factors that need to be further investigated in future studies. These might include type of binder and level of air voids.
- $E(t)$ and $D(t)$ may follow a normal or lognormal distribution depending on the mix type and reduced time. Nevertheless, neither of these distributions can be used at reduced times with high COVs as the distribution will have an arbitrary shape which is especially the case for plant mixed samples.

Beside modeling and quantifying the uncertainty in LVE functions, the uncertainties in the damage characteristic curves are modeled. The uncertainty is modeled in a stepwise manner

for C vs S curves and S vs Lebesgue Norm of stress curves where the aggregation of the uncertainties of these two models together yield the same results as modeling the uncertainty in C directly as a function of the Lebesgue Norm of stress. The COV of C is found to increase as C drops due to the application of load and thus accumulation of damage. The values in the uncertainty in C are relatively low (<0.2) which might indicate the strength of the C vs S approach and its methodology in properly presented the damage characteristics of asphalt concrete mixes and accounting for uncertainties that it might possess. Even though, the magnitude of the COV of C is low, the significance of this uncertainty should be checked through forward propagating it to predict the strain response for a given stress profile and temperatures. Thus, uncertainties LVE functions and damage characteristic curves are forward propagated within the framework of the developed P-VECD model which yield a probabilistic predicted viscoelastic strains. The major conclusion of this part of the research is summarized as the following:

- The uncertainty in the predicted viscoelastic strain is just a reflection of that in LVE and damage characteristic properties where it becomes larger as the reduced time become larger, as the NMA increases, and/or when using a modified binder.
- It is worth noting that the uncertainty in the predicted viscoelastic strains for the mix with WMA additive is significantly higher than that of the other mixes especially at high reduced times similar to the case of LVE functions as shown in the earlier sections.
- The predicted viscoelastic strains by P-VECD model are best fit using the Lognormal distribution.
- The number of realizations for P-VECD model to yield accurate and realistic results is at least 500 simulations.
- The results show that the probability of the predicted viscoelastic strains exceeds the values of the deterministic solutions may be as low as 19% and as high as 70%. The analysis of these probabilities show that there is not a specific trend in variation from one mix to another and according to temperature of the asphalt concrete.
- The probabilities show that the deterministic solution could significantly underestimate the viscoelastic strain in response to a given stress input.
- Based on P-VECD model results, it is possible to use a global C versus stress relationship for the prediction of viscoelastic strains as a simplification for the development of VECD models especially when assessing mixes that could have

the same materials but with only few components vary. This is a valid case in projects in which viscoelastic strains are needed to be predicted and compared for mixing incorporating certain types of additives such as fibers and WMA additives, different binder types, and different aggregate gradations. This could be helpful in assessing a further simplification whether a unique universal C versus stress curve could be used to predict viscoelastic strains with a minimal effect on the accuracy of the responses to be predicted.

- Based on P-VECD results, it is possible to simplify the process of the development of VECD models by using only one or two monotonic samples without affecting the accuracy nor the precision of the obtained results.

9.2 Recommendations for Future Work

Overall, the results of this research are promising in terms of providing a mechanistic characterization of different WMA technologies and in terms of exploring the uncertainties in advanced material characterization models of asphalt concrete. These conclusions and findings of this research shed the light on many aspects that are required to be addressed in future studies. Thus, this work should serve as a basis that requires continuation in different areas that include:

- Assessment of WMA mixes using another viscoplastic models that could take the effect of aggregate interlock into consideration. Such models will be more realistic in characterizing the behavior of asphalt concrete mixes at high temperature in the compression state.
- Further assessment of the considered HMA and WMA mixes based on multiaxial level by repeating the conducted tested but under different confining pressures.
- Study the rheological properties of the different asphalt binders with and without WMA additives. These properties should incorporate conducting the complex shear modulus test and multiple stress creep and recovery test for unaged and aged samples. The determined properties could better show the effect of WMA additives on the short term and long term aging of the binder. In addition, the properties of the binder will be matched with that of the mix in order to better understand the effect of WMA additives on the mechanical performance of the mixes.
- Investigate on a microscopic level whether there is any portion of aramid and polypropylene fibers getting dissolved in the asphalt binder during mixing and

thus plays a role in improving the properties of the binder. This will assure whether fibers have a mechanical role in reinforcing of the mixes or exceeds that to partially modifying the binder.

- Investigate different mixing methodologies to assure a proper dispersion of fibers within the mix during production.
- The results from the assessment of WMA mixes should be further investigated to assess the sustainability of WMA through a life cycle environmental and economic costs analysis that cover the sustainability aspects of WMA based on material production, construction, and maintenance/rehabilitation to be determined based on different performance indices that include linear viscoelastic properties, viscoelastic predictions, and viscoelastoplastic predictions for given pavement study cases.
- Assessment of WMA mixes based on VEPCD models developed in tension state in order to study the effect of various WMA additives on the fatigue life of asphalt concrete.
- Conducted a detailed study with a variety of mixes produced in the laboratory and the plant to quantify and model the uncertainty in various material properties including linear viscoelastic behavior, viscoelastic behavior, and viscoplastic behavior. This work should investigate factors related to field production with high effect on uncertainty with suggestions on how to reduce uncertainties of asphalt concrete properties during production and construction.
- Incorporate the modeled uncertainties to develop a more realistic QA/QC criteria for asphalt concrete paving projects.
- Develop a probabilistic viscoplastic model and incorporate it with the introduced P-VECD model to yield a full probabilistic model for characterizing the viscoelastoplastic behavior of asphalt concrete.
- Validate the development and usage of a global damage characteristic curve of asphalt concrete mixes using data developed by research groups for mixes using all over the world. This could serve as an important step for the simplification in the efforts required for the development of VECD models.
- The introduced P-VECD model framework is developed in the compression state but exactly the same procedure and methodology could be adopted for VECD models in tension state which could be of high importance for a probabilistic assessment of the fatigue life of asphalt concrete mixes.

REFERENCES

- Abbas, A., E. Masad, T. Papagiannakis and T. Harman (2007). "Micromechanical modeling of the viscoelastic behavior of asphalt mixtures using the discrete-element method." International Journal of Geomechanics **7**(2): 131-139.
- Aguiar-Moya, J. P. and J. A. Prozzi (2011). Development of reliable pavement models, Southwest Region University Transportation Center, Center for Transportation Research, University of Texas at Austin.
- Aguiar-Moya, J. P. and J. A. Prozzi (2011). Effect of field variability of design inputs on the MEPDG. Transportation Research Board 90th Annual Meeting.
- Aguiar-Moya, J. P., J. A. Prozzi and L. Manuel (2012). Framework for Reliability Analysis of Pavement Structures Using Mechanistic-Empirical Pavement Design Guide. Transportation Research Board 91st Annual Meeting.
- Al-Qadi, I. L., H. Wang, J. Baek, Z. Leng, M. Doyen and S. Gillen (2012). "Effects of curing time and reheating on performance of warm stone-matrix asphalt." Journal of Materials in Civil Engineering **24**(11): 1422-1428.
- Alavi, M., E. Hajj, A. Hanz and H. Bahia (2012). "Evaluating Adhesion Properties and Moisture Damage Susceptibility of Warm-Mix Asphalts: Bitumen Bond Strength and Dynamic Modulus Ratio Tests." Transportation Research Record: Journal of the Transportation Research Board(2295): 44-53.
- Azari, H., G. Al-Khateeb, A. Shenoy and N. Gibson (2007). "Comparison of Simple Performance Test| E*| of Accelerated Loading Facility Mixtures and Prediction| E*|: Use of NCHRP 1-37A and Witczak's New Equations." Transportation Research Record: Journal of the Transportation Research Board.
- Bahia, H., D. Hanson, M. Zeng, H. Zhai, M. Khatri and R. Anderson (2001). NCHRP Report 459: Characterization of Modified Asphalt Binders in Superpave Mix Design. . Washington, D. C., TRB, National Research Council.
- Bai, F., X. Yang and G. Zeng (2016). "A stochastic viscoelastic–viscoplastic constitutive model and its application to crumb rubber modified asphalt mixtures." Materials & Design **89**: 802-809.
- Bonaquist, R. (2011). "NCHRP Report 691." Mix Design Practices for Warm Mix Asphalt.
- Bonaquist, R. F. (2011). Precision of the dynamic modulus and flow number tests conducted with the asphalt mixture performance tester, Transportation Research Board.
- Bower, N., H. Wen, S. Wu, K. Willoughby, J. Weston and J. DeVol (2016). "Evaluation of the performance of warm mix asphalt in Washington state." International Journal of Pavement Engineering **17**(5): 423-434.
- Brown, E. R., P. S. Kandhal, F. L. Roberts, Y. R. Kim, D.-Y. Lee and T. W. Kennedy (2009). Hot mix asphalt materials, mixture design, and construction, NAPA Research and Education Foundation.
- Burnham, K. P. and D. Anderson (2003). "Model selection and multi-model inference." A Pratical informatio-theoric approach. Springer **1229**.

- Buss, A., R. C. Williams and S. Schram (2016). "Evaluation of moisture susceptibility tests for warm mix asphalts." Construction and Building Materials **102**: 358-366.
- Button, J. W., C. Estakhri and A. Wimsatt (2007). A synthesis of warm mix asphalt, Texas Transportation Institute, Texas A & M University System College Station, TX.
- Caro, S., D. Castillo and E. Masad (2015). "Incorporating the heterogeneity of asphalt mixtures in flexible pavements subjected to moisture diffusion." International Journal of Pavement Engineering **16**(5): 432-444.
- Caro, S., D. Castillo and M. Sánchez-Silva (2013). "Methodology for modeling the uncertainty of material properties in asphalt pavements." Journal of Materials in Civil Engineering **26**(3): 440-448.
- Castillo, D. and S. Caro (2014). "Probabilistic modeling of air void variability of asphalt mixtures in flexible pavements." Construction and Building Materials **61**: 138-146.
- Chang, C.-H., Y.-K. Tung and J.-C. Yang (1994). "Monte Carlo simulation for correlated variables with marginal distributions." Journal of Hydraulic Engineering **120**(3): 313-331.
- Chehab, G. and Y. Kim (2009). Interrelationships among asphalt concrete stiffnesses, McGraw-Hill Construction, Columbus, OH: 139-160.
- Chehab, G., Y. Kim, R. Schapery, M. Witzak and R. Bonaquist (2002). "Time-temperature superposition principle for asphalt concrete with growing damage in tension state." Journal of the Association of Asphalt Paving Technologists **71**.
- Chehab, G., Y. Kim, R. Schapery, M. Witzak and R. Bonaquist (2003). "CHARACTERIZATION OF ASPHALT CONCRETE IN UNIAXIAL TENSION USING A VISCOELASTOPLASTIC CONTINUUM DAMAGE MODEL (WITH DISCUSSION)." Journal of the Association of Asphalt Paving Technologists **72**.
- Chehab, G. R. (2002). "Characterization of asphalt concrete in tension using a viscoelastoplastic model."
- Chehab, G. R. and Y. R. Kim (2005). "Viscoelastoplastic continuum damage model application to thermal cracking of asphalt concrete." Journal of materials in civil engineering **17**(4): 384-392.
- Ching, J. (2011). Practical Monte Carlo based reliability analysis and design methods for geotechnical problems, INTECH Open Access Publisher.
- Chowdhury, A. and J. W. Button (2008). A review of warm mix asphalt, Texas Transportation Institute, the Texas A & M University System.
- Cooper III, S. B. (2011). "Evaluation of Volumetric and Mechanistic Properties of Asphalt Mixtures: Laboratory vs. Field."
- Cucalon, L. G., F. Yin, A. E. Martin, E. Arambula, C. Estakhri and E. S. Park (2015). "Evaluation of Moisture Susceptibility Minimization Strategies for Warm-Mix Asphalt: Case Study." Journal of Materials in Civil Engineering **28**(2): 05015002.

- D'Angelo, J. A., E. E. Harm, J. C. Bartoszek, G. L. Baumgardner, M. R. Corrigan, J. E. Cowser, T. P. Harman, M. Jamshidi, H. W. Jones and D. E. Newcomb (2008). Warm-mix asphalt: European practice.
- Daniel, J. S., G. R. Chehab and Y. R. Kim (2004). "Issues affecting measurement of the complex modulus of asphalt concrete." Journal of materials in civil engineering **16**(5): 469-476.
- Daniel, J. S. and Y. R. Kim (2002). "Development of a simplified fatigue test and analysis procedure using a viscoelastic, continuum damage model (with discussion)." Journal of the Association of Asphalt Paving Technologists **71**.
- Das, P. K., Y. Tasmemir and B. Birgisson (2012). "Low temperature cracking performance of WMA with the use of the Superpave indirect tensile test." Construction and Building Materials **30**: 643-649.
- Dilip, D. M., P. Ravi and G. S. Babu (2013). "System reliability analysis of flexible pavements." Journal of Transportation Engineering **139**(10): 1001-1009.
- El-Basyouny, M. and M. Jeong (2009). "Effective temperature for analysis of permanent deformation and fatigue distress on asphalt mixtures." Transportation Research Record: Journal of the Transportation Research Board(2127): 155-163.
- El-Basyouny, M. and M. Jeong (2010). "Probabilistic performance-related specifications methodology based on mechanistic-empirical pavement design guide." Transportation Research Record: Journal of the Transportation Research Board(2151): 93-102.
- Elseifi, M. A., I. L. Al-Qadi and P. J. Yoo (2006). "Viscoelastic modeling and field validation of flexible pavements." Journal of engineering mechanics **132**(2): 172-178.
- Estakhri, C., J. Button and A. E. Alvarez (2010). Field and laboratory investigation of warm mix asphalt in Texas.
- Ghanem, R. (2013). Uncertainty Quantification. The 3rd International Workshop on Moisture-Induced Damage in Asphalt Mixtures, Texas A&M at Qatar.
- Ghanem, R., D. Higdon and H. Owhadi (2016). "Introduction to Uncertainty Quantification."
- Gibson, N. H. (2006). "A viscoelastoplastic continuum damage model for the compressive behavior of asphalt concrete."
- Gudipudi, P. P. and B. S. Underwood (2016). "Reliability Analysis of Fatigue Life Prediction from the Viscoelastic Continuum Damage Model." Transportation Research Record: Journal of the Transportation Research Board(2576): 91-99.
- Gudipudi, P. P. and B. S. Underwood (2017). "Use of Fine Aggregate Matrix Experimental Data in Improving Reliability of Fatigue Life Prediction of Asphalt Concrete: Sensitivity of This Approach to Variation in Input Parameters." Transportation Research Record: Journal of the Transportation Research Board(2631): 65-73.
- Haggag, M., W. Mogawer and R. Bonaquist (2011). "Fatigue evaluation of warm-mix asphalt mixtures: Use of uniaxial, cyclic, direct tension compression test." Transportation Research Record: Journal of the Transportation Research Board(2208): 26-32.

- Hamdar, Y., H. Kassem, I. Srour and G. Chehab (2015). "Performance-Based Specifications for Sustainable Pavements: A Lean Engineering Analysis." Energy Procedia **74**: 453-461.
- Hamzah, M. O., B. Golchin, A. Jamshidi and E. Chailleux (2015). "Evaluation of Rediset for use in warm-mix asphalt: a review of the literatures." International Journal of Pavement Engineering **16**(9): 809-831.
- Harrigan, E. T. (2012). "Guidelines for Project Selection and Materials Sampling, Conditioning, and Testing in WMA Research Studies." Transportation Research Board Research Results Digest **370**
- Hilton, H. H., J. Hsu and J. S. Kirby (1991). "Linear viscoelastic analysis with random material properties." Probabilistic Engineering Mechanics **6**(2): 57-69.
- Huang, Y. H. (1993). Pavement analysis and design.
- Jamrah, A. and M. E. Kutay (2015). "Investigation of Different Methods for Obtaining Asphalt Mixture Creep Compliance for Use in Pavement Mechanistic–Empirical Design Software." Transportation Research Record: Journal of the Transportation Research Board(2524): 100-109.
- Jeong, M. G. (2010). "Manual of practice HMA quality assurance spreadsheet program using measured values of E^* and d ." Transportation Research Board.
- Kahil, N. S., S. S. Najjar and G. Chehab (2015). "Probabilistic Modeling of Dynamic Modulus Master Curves for Hot-Mix Asphalt Mixtures." Transportation Research Record: Journal of the Transportation Research Board(2507): 90-99.
- Kalita, K. and P. Rajbongshi (2015). "Variability characterisation of input parameters in pavement performance evaluation." Road Materials and Pavement Design **16**(1): 172-185.
- Kaloush, K., K. P. Biligiri, W. A. Zeiada, C. Rodezno, S. Dwivedi, J. Reed and C. Cary (2008). "Evaluation of FORTA Fiber-Reinforced Asphalt Mixtures Using Advanced Material Characterization Tests–Evergreen Drive, Tempe, Arizona."
- Kassem, H., G. Chehab and G. Saad (2015). "An FEM-predictive tool for simulating the cooling characteristics of freshly paved asphalt concrete layers." International Journal of Pavement Engineering **16**(2): 157-167.
- Katicha, S. (2007). "Analysis of Hot Mix Asphalt (HMA) Linear Viscoelastic and Bimodular Properties Using Uniaxial Compression and Indirect Tension (IDT) Tests."
- Khosravifar, S., A. Farzaneh, I. Haider and C. W. Schwartz (2015). Advantages of Non-Symmetric Sigmoidal Function in Construction 2 of Dynamic Modulus Master Curves of Asphalt Mixtures 3. Transportation Research Board 94th Annual Meeting.
- Kim, H. B. and S. H. Lee (2002). "Reliability-based design model applied to mechanistic empirical pavement design." KSCE Journal of Civil Engineering **6**(3): 263-272.
- Kim, J., H. S. Lee and N. Kim (2010). "Determination of shear and bulk moduli of viscoelastic solids from the indirect tension creep test." Journal of engineering mechanics **136**(9): 1067-1075.

- Kim, M., L. N. Mohammad and M. A. Elseifi (2015). "Effects of various extrapolation techniques for abbreviated dynamic modulus test data on the MEPDG rutting predictions." Journal of Marine Science and Technology **23**(3): 353-363.
- Kim, Y. and J. Daniel (1997). "Development of a Mechanistic Fatigue Prediction Model for Aging Asphalt-Aggregate Mixtures." Final Report submitted to Western Research Institute.
- Kim, Y. R. (2008). Modeling of asphalt concrete.
- King, M. H. (2004). "Determination of Dynamic Moduli in Uniaxial Compression for North Carolina Hot Mix Asphalt Concrete."
- Lee, H.-J. and Y. R. Kim (1998). "Viscoelastic continuum damage model of asphalt concrete with healing." Journal of Engineering Mechanics **124**(11): 1224-1232.
- Lee, S.-J., G. Zi, S. Mun, J. S. Kong and J.-H. Choi (2015). "Probabilistic prognosis of fatigue crack growth for asphalt concretes." Engineering Fracture Mechanics **141**: 212-229.
- Lemaitre, J. (2012). A course on damage mechanics, Springer Science & Business Media.
- Mahoney, J. P., A. W. Backus and J. Walter (2000). "QA Specification Practices." Washington State Transportation Center (TRAC), Seattle, WA.
- Maji, A. and A. Das (2008). "Reliability considerations of bituminous pavement design by mechanistic–empirical approach." International Journal of Pavement Engineering **9**(1): 19-31.
- Martin, A. E., E. Arambula, F. Yin, L. G. Cucalon, A. Chowdhury, R. Lytton, J. Epps, C. Estakhri and E. S. Park (2014). Evaluation of the moisture susceptibility of WMA technologies, Transportation Research Board.
- Martin, A. E., E. Arambula, F. Yin and E. S. Park (2016). Validation of Guidelines for Evaluating the Moisture Susceptibility of WMA Technologies.
- Masad, E., E. Kassem and D. Little (2011). "Characterization of asphalt pavement materials in the State of Qatar: a case study." Road Materials and Pavement Design **12**(4): 739-765.
- Mehrez, L., M. Darabi, R. Ghanem, E. Masad and D. Little (2014). Modeling and propagation of stochastic linear viscoelastic material properties of asphalt mixtures in pavement structures. 9th International Conference on Structural Dynamics, Portugal.
- Mehrez, L., E. Kassem, E. Masad and D. Little (2014). "Stochastic identification of linear-viscoelastic models of aged and unaged asphalt mixtures." Journal of Materials in Civil Engineering **27**(4): 04014149.
- Mogawer, W. S., A. J. Austerman, E. Kassem and E. Masad (2011). "Moisture damage characteristics of warm mix asphalt mixtures." Journal of the Association of Asphalt Paving Technologists **80**.
- Mohammad, L. N., M. Elseifi, S. B. Cooper III and A. Raghavendra (2013). "Levels of variability in volumetric and mechanical properties of asphalt mixtures." Journal of Materials in Civil Engineering **25**(10): 1424-1431.

Mun, S., G. R. Chehab and Y. R. Kim (2007). "Determination of time-domain viscoelastic functions using optimized interconversion techniques." Road materials and pavement design **8**(2): 351-365.

Najjar, S. S. (2005). "The importance of lower-bound capacities in geotechnical reliability assessments."

Newcomb, D., A. E. Martin, F. Yin, E. Arambula, E. S. Park, A. Chowdhury, R. Brown, C. Rodezno, N. Tran and E. Coleri (2015). Short-term laboratory conditioning of asphalt mixtures.

Nowak, A. S. and K. R. Collins (2012). Reliability of structures, CRC Press.

Park, S. and Y. R. Kim (1999). "Interconversion between relaxation modulus and creep compliance for viscoelastic solids." Journal of materials in civil engineering **11**(1): 76-82.

Park, S. W., Y. R. Kim and R. A. Schapery (1996). "A viscoelastic continuum damage model and its application to uniaxial behavior of asphalt concrete." Mechanics of Materials **24**(4): 241-255.

Prowell, B. D., G. C. Hurley and B. Frank (2011). Warm-mix asphalt: Best practices, National Asphalt Pavement Association Lanham, Md, USA.

Rahbar-Rastegar, R. and J. S. Daniel (2016). "Laboratory versus plant production: impact of material properties and performance for RAP and RAS mixtures." International Journal of Pavement Engineering: 1-12.

Rowe, G., G. Baumgardner and M. Sharrock (2016). Functional forms for master curve analysis of bituminous materials. Proceedings of the 7th international RILEM symposium ATCBM09 on advanced testing and characterization of bituminous materials.

Rowe, G., S. Khoee, P. Blankenship and K. Mahboub (2009). "Evaluation of aspects of E* test by using hot-mix asphalt specimens with varying void contents." Transportation Research Record: Journal of the Transportation Research Board(2127): 164-172.

Rubio, C., G. Martínez, L. Baena and F. Moreno (2012). "Warm mix asphalt: an overview." Journal of Cleaner Production **24**: 76-84.

Saadeh, S., E. Masad and D. Little (2007). "Characterization of asphalt mix response under repeated loading using anisotropic nonlinear viscoelastic-viscoplastic model." Journal of Materials in Civil Engineering **19**(10): 912-924.

Sadek, H. (2015). Mechanistic-based characterisation of fatigue resistance of alternative mix designs, University of Liverpool.

Sadek, H., E. Masad, H. Al-Khalid and O. Sirin (2016). "Probabilistic analysis of fatigue life for asphalt mixtures using the viscoelastic continuum damage approach." Construction and Building Materials **126**: 227-244.

Sadeq, M., H. Al-Khalid, E. Masad and O. Sirin (2016). "Comparative evaluation of fatigue resistance of warm fine aggregate asphalt mixtures." Construction and Building Materials **109**: 8-16.

- Sadeq, M., E. Masad, H. Al-Khalid and O. Sirin (2015). "Assessment of linear and nonlinear viscoelastic responses of warm-mix asphalt binders." Bituminous Mixtures and Pavements VI: 27.
- Safaei, F., J.-s. Lee, L. A. H. d. Nascimento, C. Hintz and Y. R. Kim (2014). "Implications of warm-mix asphalt on long-term oxidative ageing and fatigue performance of asphalt binders and mixtures." Road Materials and Pavement Design **15**(sup1): 45-61.
- Schapery, R. (1984). "Correspondence principles and a generalized J integral for large deformation and fracture analysis of viscoelastic media." International Journal of Fracture **25**(3): 195-223.
- Schapery, R. and S. Park (1999). "Methods of interconversion between linear viscoelastic material functions. Part II—an approximate analytical method." International Journal of Solids and Structures **36**(11): 1677-1699.
- Schwartz, C., N. Gibson and R. Schapery (2002). "Time-temperature superposition for asphalt concrete at large compressive strains." Transportation Research Record: Journal of the Transportation Research Board(1789): 101-112.
- Shakiba, M., R. Al-Rub, M. Darabi, T. You, E. Masad and D. Little (2013). "Continuum coupled moisture-mechanical damage model for asphalt concrete." Transportation Research Record: Journal of the Transportation Research Board(2372): 72-82.
- Sharma, H. and A. K. Swamy (2016). "Development of probabilistic fatigue curve for asphalt concrete based on viscoelastic continuum damage mechanics." International Journal of Pavement Research and Technology **9**(4): 270-279.
- Simo, J. and T. Hughes (1998). Computational Inelasticity. New York, Springer
- Simsiriwong, J., R. W. Sullivan and H. H. Hilton (2014). Master Creep Compliance Curve for Random Viscoelastic Material Properties. Challenges In Mechanics of Time-Dependent Materials and Processes in Conventional and Multifunctional Materials, Volume 2, Springer: 41-47.
- Singh, P. and A. K. Swamy (2017). "Probabilistic characterisation of damage characteristic curve of asphalt concrete mixtures." International Journal of Pavement Engineering: 1-10.
- Smith, A. (2007). Advera WMA Zeolite. WMA Technical Working Group. PQ Corporation Presentation, Hunt Valley, USA.
- Solaimanian, M., T. W. Kennedy and R. B. McGennis (1999). The South Central Superpave Center Summary Report.
- Spieß, A.-N. and N. Neumeyer (2010). "An evaluation of R2 as an inadequate measure for nonlinear models in pharmacological and biochemical research: a Monte Carlo approach." BMC pharmacology **10**(1): 6.
- Sullivan, T. J. (2015). Introduction to uncertainty quantification, Springer.
- Superpave (1996). "Superpave Mix Design." Asphalt Institute, Lexington, KY Superpave Series No. 2 (SP-2).

- Tang, W. H. and A. Ang (2007). Probability Concepts in Engineering: Emphasis on Applications to Civil & Environmental Engineering, Wiley.
- Tashman, L. and M. A. Elangovan (2008). Dynamic Modulus Test-Laboratory Investigation and Future Implementation in the State of Washington.
- Thyagarajan, S., B. Muhunthan, N. Sivaneswaran and K. Petros (2011). "Efficient simulation techniques for reliability analysis of flexible pavements using the mechanistic-empirical pavement design guide." Journal of Transportation Engineering **137**(11): 796-804.
- Timm, D. H., D. E. Newcomb, B. Birgisson and T. V. Galambos (1999). "Incorporation of Reliability in Minnesota Mechanistic-Empirical Pavement Design."
- Underwood, B. S. (2011). Multiscale constitutive modeling of asphalt concrete.
- Underwood, B. S. and Y. R. Kim (2012). "Comprehensive evaluation of small strain viscoelastic behavior of asphalt concrete." Journal of Testing and Evaluation **40**(4): 1-11.
- Underwood, B. S., Y. R. Kim and M. N. Guddati (2010). "Improved calculation method of damage parameter in viscoelastic continuum damage model." International Journal of Pavement Engineering **11**(6): 459-476.
- Underwood, B. S., T. Yun and Y. R. Kim (2010). "Experimental investigations of the viscoelastic and damage behaviors of hot-mix asphalt in compression." Journal of Materials in Civil Engineering **23**(4): 459-466.
- Uzan, J. (1996). "ASPHALT CONCRETE CHARACTERIZATION FOR PAVEMENT PERFORMANCE PREDICTION (WITH DISCUSSION)." Journal of the Association of Asphalt Paving Technologists **65**.
- Uzan, J., A. Sides and M. Perl (1985). "Viscoelastoplastic model for predicting performance of asphaltic mixtures." Transportation Research Record(1043).
- Vavrik, W. R. (2002). Bailey method for gradation selection in hot-mix asphalt mixture design, Transportation Research Board, National Research Council.
- Wang, L. (2010). Mechanics of Asphalt: Microstructure and Micromechanics: Microstructure and Micromechanics, McGraw Hill Professional.
- Wax, S. (2005). Roads and Trials with Sasobit®.
- West, R., C. Rodezno, G. Julian, B. Prowell, B. Frank, L. V. Osborn and T. Kriech (2014). Field performance of warm mix asphalt technologies.
- Xiao, F., B. Putman and S. Amirkhanian (2014). "Plant and Laboratory Compaction Effects on Performance Properties of Plant-Foamed Asphalt Mixtures Containing RAP." Journal of Materials in Civil Engineering **27**(9): 04014240.
- Yin, F. and L. G. Cucalon (2011). "Laboratory conditioning protocols for warm-mix asphalt."
- Yun, T. and Y. R. Kim (2011). "Modeling of viscoplastic rate-dependent hardening-softening behavior of hot mix asphalt in compression." Mechanics of time-dependent materials **15**(1): 89-103.

Yun, T., B. S. Underwood and Y. R. Kim (2009). "Time-temperature superposition for HMA with growing damage and permanent strain in confined tension and compression." Journal of Materials in Civil Engineering **22**(5): 415-422.

Zaumanis, M. (2014). Warm Mix Asphalt. Climate Change, Energy, Sustainability and Pavements, Springer: 309-334.

Zhao, Y. (2002). "Permanent deformation characterization of asphalt concrete using a viscoelastoplastic model."

Zhao, Y. and Y. Kim (2003). "Time-temperature superposition for asphalt mixtures with growing damage and permanent deformation in compression." Transportation Research Record: Journal of the Transportation Research Board(1832): 161-172.

Zhou, F., S. Hu, G. Das, R. Lee, T. Scullion and G. Claros (2012). "Successful High RAP Mixes Designed with Balanced Rutting and Cracking Requirements." Asphalt Paving Technology-Proceedings Association of Asphalt Technologists **81**: 477.

APPENDIX

1- Specimen Preparation Protocols And Data Log Sheets

BATCHING SHEET

Project:		Specimen ID:	
Mix Type/ Description:		Computer file:	
		Date:	Time:
Specimen Type:		Aggregate Type(s):	
% AC:	Weight & Type of Binder:	Specimen weight:	
Balance	Capacity: _____ Sensitivity: _____ Leveled: _____ Fans affecting reading are off: _____	Bowl	Clean and dry: _____ Weight Empty: _____

Mix Gradation of aggregates				
	Sieve Size	% Cumulative Retained Mass	Cumulative Retained Mass	Batched Cumulative Retained Mass
Coarse	1"			
	3/4"			
	1/2"			
	3/8"			
	# 4			
Fine	# 8			
	# 16			
	# 30			
	# 50			
	# 100			
	# 200			
Filler	Pan			
	Total	100.0		

Final Weight of Bowl +aggregates:	
Aluminum foil placed:	Batch labeled:

Signature: _____

Batching

EQUIPMENT NEEDED:

1. Scoop
2. Flat-bottom pans/bowls
3. Balance: 10 kg balance with sensitivity of 0.1 g (SP-2 allows the usage of balance sensitive to 1g)
4. Aluminum foil
5. Permanent marker
6. Batching sheet
- 7.

PROCEDURE:

1. Prepare batching sheet showing the batch weights of each aggregate component (type and size)
2. Zero the balance and take the weight of the empty bowl used, and then re-zero it again.
3. For each aggregate component, scoop from the bucket the quantity needed.
 - Look at the # on the side of the bucket to find the type and size of aggregate.
 - Pile the aggregates on one side of the bowl this will allow to easily extract out the excess without taking out any other aggregate components.
4. Do not re-zero the balance after each component, but weigh the other component up to the cumulative weight showed on the batching sheet.
5. Mix the aggregates thoroughly with the same scoop used.
6. Take the weight of the bowl filled with the aggregates.
7. Cover the bowl with aluminum foil and label the foil with the specimen ID.
8. Make sure to fill all the needed data in the batching sheet of each specimen.

Mixing

EQUIPMENT NEEDED:

1. Oven, thermostatically controlled, for heating aggregates, asphalt, and equipment.
2. Bucket mixer for Superpave samples / Dough mixer for Marshal samples (check if gmm and compacted samples should be mixed using the same mixer)
3. Stopwatch
4. Infrared thermometer with k-type thermocouple
5. Balance: 10-kg capacity with a sensitivity of 0.1 gram.
6. Mixing spoon, bowl/bucket, and whip
7. Asphalt spoon (ladle spoon)
8. Spatula
9. Shallow round-bottom pan.
10. Torch
11. Paper towels
12. Oven gloves
13. Safety Glasses

PROCEDURE:

1. Place bowls containing aggregates in the oven at 15°C higher than mixing temperature for at least 4 hours, preferably overnight.
2. Heat mixing bowl/bucket and all utensils at 15°C higher than mixing temperature for at least 2 hours.
3. Heat the asphalt binder in the oven at 15°C higher than mixing temperature for 2 hours. Keep the can open while heating.
4. Remove the mixing bowl and all other utensils from the oven.
5. Remove the aggregates from the oven and form a crater in the middle of the aggregates.
6. Place the bowl having the aggregates on the balance beside the hot plates and zero it.
7. Pour the required amount of asphalt into the crater in the bowl.
 - Use paper towels to extract the excess amount of asphalt.

8. Mix quickly with the spoon to blend the aggregate with the asphalt and make sure that most fines are blended with the binder.
9. Introduce the mix into the bucket or mixing bowl.
(ASTM D6925 requires placing aggregates in mixing bowl/bucket, then add the binder).
10. Attach the bowl/bucket to the mixing machine.
11. Set the mechanical mixer to a minimum speed for 1 minute.
 - Make sure you wear safety glasses during the mixing procedure.
 - When using the dough mixer, make sure to push the bowl up to ensure that the aggregates on the bottom will also be mixed.
 - When using the bucket mixer, assist the mixing by holding the whip at the center or by blending the aggregates in the bucket using the mixing spoon.
12. After a minute stop the mechanical mixer and scrape the bowl with the spatula to get the fine aggregates mixed in.
13. Check the temperature: in case lower than the mixing temperature, use the torch for heating the bottom of the bucket/bowl.
14. Mix for a second minute while heating if needed.
15. Visually inspect to see that all the aggregates are coated with asphalt. When all the aggregates are coated with asphalt remove the bowl/bucket from the mixer.
16. Remove the whip from the mechanical mixer and scrap off all fine aggregates into the bowl using a spatula.
17. With the spatula scrap the fine particles on the inside sides of the bowl and distribute them evenly throughout the mix.
18. Pour the mix into a shallow round-bottom pan and with the spatula scrap the mixing bowl to get all the fine aggregates and mix them evenly throughout the mix.
19. Spread the mix into the pan at an even thickness ranging between 25 mm and 50 mm in order to be ready for short term aging (for both mixes that will be used for Gmm or for compaction (MS-2, page 52)).

Repeat the procedure for other batches, but note that:

- If the same mixing bowl/bucket and whip is to be used again, they should be free from fine particles (as much as you can). They can be rubbed using wire brush.
- Reheat the mixing bowl/bucket, mixer whip, and spatula at 15°C higher than mixing temperature for about 15 minutes.
- A new mixing spoon should be used that has already been placed in the oven
- In case same asphalt can is to be used, place it again in the oven during this time.

Short Term Aging

All mixes need to be short term aged when in its loose state before compaction or any other testing.

Equipment

- Oven, thermostatically controlled, for heating aggregates, asphalt, and equipment.

Procedure:

1. Place the mix and pan in the oven at a temperature equal to the specified compaction temperature ± 5 °C for a period of 2 hours ± 5 minutes.
2. Stir the mix after 60 ± 5 min to maintain uniform conditioning.

In case sample will be used for Gmm: After aging, keep stirring/mixing the sample frequently until it cools down.

Notes:

- Experience has shown that aggregates having more than 2% (water) absorption should be aged for four hours to allow additional asphalt absorption to occur (MS-2, page 52).

Mixing And Short Term Aging Sheet

Project: _____	Specimen ID: _____	Computer file: _____
-----------------------	---------------------------	-----------------------------

<u>Placement in Oven</u>		
Batch	Utensils	Asphalt binder
Date: _____	_____	Type: _____
Time: _____	Date: _____	Time & date: _____
Temperature of oven: _____	Time: _____	Can size: _____

<u>Mixing:</u>			
Balance	Capacity: _____ Sensitivity: _____ Leveled: _____ 	Fans and air conditions are turned off: _____	
Time: _____	Weight of binder	Mixer used:	Thermometer used:
Date: _____	added: _____		
Temperature when mix is added to the mixing bowl/bucket:	Temperature after one minute of mixing:	Temperature at end of mixing:	Torch used: When: _____
Remarks: _____ _____			

<u>Short Term Aging:</u>			
Date: _____			
Time of putting pan in oven:	Temperature of oven:	Stirring time:	Time removed from oven:

Signature: _____

Compaction

EQUIPMENT:

1. Superpave Gyrotory Compactor (SGC)
 - Ram Pressure: 600 kPa
 - Gyration Angle: 1.25 Deg.
 - Gyration Speed: 30 gyrations/minute
2. Mold of inner diameter of 150 mm.
3. Metal plate: 150 mm diameter (for ServoPac)
4. Compaction papers: 150 mm diameter
5. Infrared thermometer
6. Scoop, spoon, and spatula

PROCEDURE:

Before starting any compaction, make sure to check that level of oil for the compactor and that the compactor has been recently calibrated.

1. While the mix is in short-term aging, place the compaction mold assembly, scoop, spoon, and spatula in the oven at the required compaction temperature $\pm 5^{\circ}\text{C}$ for a minimum of 45 minutes prior to the compaction.
2. Connect the compactor's laptop and open a new compaction file specifying all the required parameters including:
 - Desired end point: Specimen Height, Revolutions Number, or Superpave Gyrotory Compactive Effort.
 - Header information: Specimen ID, project name, percent binder, mass of specimen, and Gmm.
 - Mold diameter.
 - Specimen height range.
 - File name and location to be saved in.
3. At the end of the conditioning period, remove the loose mix sample, the compaction mold assembly, and required utensils from the oven.
4. Place a paper disk inside the mold to aid separation of the specimen from the base plate after compaction.

5. Quickly place the mixture into the mold. Take care to minimize segregation of the mixture in the mold. After pouring half the mix into the mold, scrape with a spatula so that the mix settles down and creates more room for the second half; make sure that the spatula penetrates to the bottom of the mold.
6. After the mixture has been completely loaded into the mold, level the mix, and place a paper disk on the mixture to avoid material adhering to the ram head.
7. Load the compaction mold into the SGC and initiate the compaction process.
8. Center the mold under the loading ram and start the system so that the ram extends down to the mold cylinder and contacts the specimen. The ram will stop when the pressure reaches 600kPa.
9. Apply the angle of gyration and start the gyratory compaction until reaching the desired end point.
10. Remove the mold from the compactor.
11. After a suitable cooling period, extrude the compacted specimen from the mold and remove the top compaction paper.
 - The purpose of the cooling period is to ensure that the specimen will not deform when it is extruded. Cooling may be facilitated using a fan.
12. Mark the specimen with its ID name, top, and bottom.
13. Flip the specimen onto a pan and remove the second paper.
14. Place the extruded specimen on a flat surface in an area where it can cool, undisturbed, to room temperature.
15. Place the mold, plates, and spatula back in the oven for fabrication of other specimens.
16. Collect the data file of the height measurements for each gyration.

General Notes

1. All compacted specimens need to be packed in zip lock bags after they cool down to room temperatures.
2. The compacted specimens should be stored in the same way they are compacted (top vs. bottom).
3. The storage should be in a dark environment.

Compaction Sheet

Project:	Specimen ID:
Computer file:	Compaction file:
Date:	Time:

End Point:

- Specimen Height:** _____ mm
- Revolution Number:** _____
- Superpave Gyrotory Compactive Effort:** _____

**Specimen Height Range: (0 - 300 mm) (0 -75 mm) (50 - 125 mm) (100 – 175 mm)
(150 – 225 mm)**

Temperature at the beginning of compaction: _____

Angle of Compaction:

Vertical Pressure:

Specimen labeled and top/bottom indicated:_____

Remarks:

Signature: _____

Gmm Testing Sheet

Project:	Specimen ID:
Computer file:	Mix Description:
Date:	Time:

- **Date of sample mixing :**
- **Date of sample curing :**

Balance	Capacity: _____ Sensitivity: _____ Leveled: _____	Fans and air conditions are turned off: _____
----------------	---	---

- **Weight of flask empty:** _____
- **Weight of sample :** _____
- **Time of putting sample on vibrator:** _____
- **Time of removing sample from vibrator:** _____
- **Weight of flask+ sample + water:** _____
- **Temperature of water:** _____
- **Weight of flask + water:** _____
- **Date of Calibration of flask:** _____
- **Temperature correction factor:** _____

Signature: _____

Gmb Testing Sheet/Volumetric Samples

Project:	Specimen ID:
Computer file:	Mix Description:
Date:	Time:

- **Date of sample mixing** :
- **Date of sample compaction** :
- **ASTM Method Used** :

Balance	Capacity: _____ Sensitivity: _____ Leveled: _____	Fans and air conditions are turned off: _____
----------------	---	---

- **Dry Weight in air, A** : _____
- **Mass of Specimen submerged in water, C:** _____
- **Temperature of water:** _____
- **SSD mass in air, B:** _____

Thickness 1	Thickness 2	Thickness 3	Thickness 4

Comments:

Absorption = $\frac{B-A}{B-C} \times 100 =$ _____

Signature: _____

Gmb Testing Sheet/E* Samples

Project:	Specimen ID:
Computer file:	Mix Description:
Date:	Time:
Date of sample mixing:	Date of sample compaction:

Compacted Sample

Balance	Capacity: _____ Sensitivity: _____ Leveled: _____	Fans and air conditions are turned off: _____	
Dry Weight in air, A:		Mass submerged in water, C:	
SSD mass in air, B:		Temperature of water:	
Height 1:	Height 2:	Height 3:	Height 4:


Coring and Sawing

Date and time:			
Height 1:	Height 2:	Height 3:	Height 4:
Comments:			

Cored and Sawed Sample

Balance	Capacity: _____ Sensitivity: _____ Leveled: _____	Fans and air conditions are turned off: _____	
Date and time:		Washed:	
Mass of Coated specimen under water, E :		Temperature of water:	
Mass of Dry coated, D:		Dry Weight in air, A:	

Sample Preparation for Complex Modulus

Date and time of gluing:	<div style="display: flex; flex-direction: column; align-items: center;"> <div style="text-align: left; margin-bottom: 10px;"><u>Left Side of the Chamber</u></div>  <div style="display: flex; justify-content: space-between; width: 100%; margin-top: 10px;"> <u>Door</u> <u>Door</u> </div> </div>
Time of mounting LVDTs:	
LVDTs used:	
Type of Glue used:	

Mixing, Short Term Aging, and Compaction Sheet

Project: _____	Specimen ID: _____	Computer file: _____	
<u>Placement in Oven</u>		<u>Balance</u>	
Batch and Utensils	Asphalt binder		
Date: _____	Type: _____	Capacity: _____	
Time: _____	Time & date:	Sensitivity: _____	
Temperature of oven:	_____	Leveled: _____	
_____	Can size: _____	Fans and air conditions are turned off:	
_____	_____	_____	
<u>Mixing:</u>			
Time: _____	Weight of binder	Mixer used:	Thermometer
Date: _____	added: _____		used:
Temperature when mix is added to the mixing bowl/bucket:	Temperature after one minute of mixing:	Remarks:	
<u>Short Term Aging:</u>			
Date: _____		Oven Used: _____	
Time of putting pan in oven:	Temperature of oven:	Stirring time:	Time removed from oven:
<u>Compaction</u>			
Date and time: _____		Compaction	
file: _____			
<u>End Point:</u>			
○ Specimen Height: _____ mm → Number of gyrations performed: _____			
Specimen Height Range: (0 - 300 mm) (0 - 75 mm) (50 - 125 mm) (100 - 175 mm) (150 - 225 mm)			
Temperature at the beginning of compaction:		Specimen labeled and top/bottom indicated: _____	

Angle of Compaction: _____			
Vertical Pressure: _____			

--	--

Complex Modulus Testing

Project:	Sample:	File:	
Target Temperature			
Time of turning on the chamber:			
Time of start of testing			
Exact temperature when test is started:			

Template file used for temp1: _____

Template file used for temp2: _____

Template file used for temp3: _____

Template file used for temp4: _____

Testing Notes:

PID Tuning Parameters for E* Testing

Temp(°C)	FREQ(Hz)	P	I	D
-5	10	2500	10	5000
	5	2500	0	5000
	1	2500	0	5000
	0.5	5000	2	1200
	0.1	5000	5	4000
	0.01	5000	0	3000
10	10	3500	10	5400
	5	2500	0	5000
	1	3500	0	5000
	0.5	4000	2	1200
	0.1	4000	10	3000
	0.01	4000	0	3000
25	20	3400	0	2000
	10	4500	1	5800
	5	3600	1	5000
	1	4500	2	5000
	0.5	5000	2	1200
	0.1	3000	1	2000
40	20	5000	0	2500
	10	2500	0	2500
	5	3000	0	2000
	1	4000	0	2000
	0.5	5000	0	1200
	0.1	1800	10	1200

2- R CODES

CALCULATION OF PSEUDOSTRAINS/ PIECEWISE LINEAR METHOD

```

#piecewise linear
Data= read.csv("C:/Input_PseudoStrainCalculation.csv", header=T)
#Data is input in a CSV (comma-separated-values)file.
#Name of file is "Input_PseudoStrainCalculation"
#Data is stored in a tabular form of 6 columns
#Column 1 has "Time" as header and have time steps. Time is in seconds.
#Column 2 has "Strain" as header and strain corresponding to every point in time
#Column 3 has "Stress" as header and stress corresponding to every point in time.
Stress is in "kPa"
#Column 4 has "Einf" as header and has only one row presenting the Einfinity
coefficient of the Prony series
#Column 5 has "Em" as header and has 17 entries presenting the Prony coefficients
#Column 6 has "taws" as header and has 17 entries presenting the relaxation times

time= Data$Time
strain= Data$Strain
stress=Data$Stress
Einf=Data$Ee[1]
Em=head(Data$coef,17)
taws=head(Data$taw,17)

n=length(time)
pseudostrain=rep(NA,n)
c=rep(NA,n-1)

pseudostrain[1]=0
c[1]=(strain[2]-strain[1])/(time[2]-time[1])
B=Einf*(time[2]-time[1])
for (k in 1:17)
{B=B+Em[k]*taws[k]*(-exp(-time[2]/taws[k]))-Em[k]*taws[k]*(-exp(-
time[1]/taws[k]))}
pseudostrain[2]=B*c[1]
for(i in 3:n)
{
temp=rep(NA,i-1)
for(j in 1:i-1)
{
c[j]=(strain[j+1]-strain[j])/(time[j+1]-time[j])
b=Einf*(-time[j]+time[j+1])

```

```

for(k in 1:17)
  {b=b+Em[k]*taws[k]*(-exp(-(time[i]-time[j])/taws[k]))-Em[k]*taws[k]*(-exp(-
(time[i]-time[j+1])/taws[k]))}
  temp[j]=b*c[j]
}

pseudostrain[i]=sum(temp)*1000
}
plot(stress~pseudostrain)

```

CALCULATION OF PSEUDO STRAINS/ STATE VARIABLES METHOD

#To calculate pseudostrain referring to strain measured by each LVDT of a given sample.

```

Data= read.csv("C:/Pseudo1.csv", header=T)
time= Data$Time
step=time[2]-time[1]
strain= Data$Strain
stress=Data$Stress
Einf=Data$Ee[1]
Em=head(Data$coef,17)
taws=head(Data$taw,17)

```

```

N=length(time)
B=N-1
pseudostrain=rep(NA,N)

```

```

No=rep(NA,B)
N1=rep(NA,B)
N2=rep(NA,B)
N3=rep(NA,B)
N4=rep(NA,B)
N5=rep(NA,B)
N6=rep(NA,B)
N7=rep(NA,B)
N8=rep(NA,B)
N9=rep(NA,B)
N10=rep(NA,B)
N11=rep(NA,B)
N12=rep(NA,B)
N13=rep(NA,B)
N14=rep(NA,B)
N15=rep(NA,B)
N16=rep(NA,B)
N17=rep(NA,B)
No[1]=0
N1[1]=0
N2[1]=0
N3[1]=0
N4[1]=0
N5[1]=0
N6[1]=0

```

```

N7[1]=0
N8[1]=0
N9[1]=0
N10[1]=0
N11[1]=0
N12[1]=0
N13[1]=0
N14[1]=0
N15[1]=0
N16[1]=0
N17[1]=0
pseudostrain[1]=0

for(n in 1:B)
{
  No[n+1]=Einf*(strain[n+1]-strain[1])
  N1[n+1]=exp(-step/taws[1])*N1[n]+Em[1]*(exp(-step/(2*taws[1])))*(strain[n+1]-
strain[n])
  N2[n+1]=exp(-step/taws[2])*N2[n]+Em[2]*(exp(-step/(2*taws[2])))*(strain[n+1]-
strain[n])
  N3[n+1]=exp(-step/taws[3])*N3[n]+Em[3]*(exp(-step/(2*taws[3])))*(strain[n+1]-
strain[n])
  N4[n+1]=exp(-step/taws[4])*N4[n]+Em[4]*(exp(-step/(2*taws[4])))*(strain[n+1]-
strain[n])
  N5[n+1]=exp(-step/taws[5])*N5[n]+Em[5]*(exp(-step/(2*taws[5])))*(strain[n+1]-
strain[n])
  N6[n+1]=exp(-step/taws[6])*N6[n]+Em[6]*(exp(-step/(2*taws[6])))*(strain[n+1]-
strain[n])
  N7[n+1]=exp(-step/taws[7])*N7[n]+Em[7]*(exp(-step/(2*taws[7])))*(strain[n+1]-
strain[n])
  N8[n+1]=exp(-step/taws[8])*N8[n]+Em[8]*(exp(-step/(2*taws[8])))*(strain[n+1]-
strain[n])
  N9[n+1]=exp(-step/taws[9])*N9[n]+Em[9]*(exp(-step/(2*taws[9])))*(strain[n+1]-
strain[n])
  N10[n+1]=exp(-step/taws[10])*N10[n]+Em[10]*(exp(-step/(2*taws[10])))*(strain[n+1]-
strain[n])
  N11[n+1]=exp(-step/taws[11])*N11[n]+Em[11]*(exp(-step/(2*taws[11])))*(strain[n+1]-
strain[n])
  N12[n+1]=exp(-step/taws[12])*N12[n]+Em[12]*(exp(-step/(2*taws[12])))*(strain[n+1]-
strain[n])
  N13[n+1]=exp(-step/taws[13])*N13[n]+Em[13]*(exp(-step/(2*taws[13])))*(strain[n+1]-
strain[n])
  N14[n+1]=exp(-step/taws[14])*N14[n]+Em[14]*(exp(-step/(2*taws[14])))*(strain[n+1]-
strain[n])
  N15[n+1]=exp(-step/taws[15])*N15[n]+Em[15]*(exp(-step/(2*taws[15])))*(strain[n+1]-
strain[n])
  N16[n+1]=exp(-step/taws[16])*N16[n]+Em[16]*(exp(-step/(2*taws[16])))*(strain[n+1]-
strain[n])
  N17[n+1]=exp(-step/taws[17])*N17[n]+Em[17]*(exp(-step/(2*taws[17])))*(strain[n+1]-
strain[n])

pseudostrain[n+1]=1000*(No[n+1]+N1[n+1]+N2[n+1]+N3[n+1]+N4[n+1]+N5[n+1]+N6[

```

```
n+1]+N7[n+1]+N8[n+1]+N9[n+1]+N10[n+1]+N11[n+1]+N12[n+1]+N13[n+1]+N14[n+1]
+N15[n+1]+N16[n+1]+N17[n+1])
}
```

```
Data$pseudostrain=pseudostrain
plot(stress~pseudostrain)
```

```
write.csv(Data,"D:/Mlx-Sample-ID_of_LVDT.csv")
```

CALCULATION OF VISCOELASTIC STRAINS

```
Data= read.csv("C:/Input Data.csv",header=T)
```

```
time= Data$Time
stress=Data$Stress
a=Data$StressOverC
```

```
Do=Data$Do[1]
Dm=head(Data$coef,17)
taws=head(Data$taw,17)
```

```
n=length(time)
c=rep(NA,n-1)
```

```
VEstrain=rep(NA,n)
```

```
VEstrain[1]=0
```

```
c[1]=(a[2]-a[1])/(time[2]-time[1])
B=Do*(time[2]-time[1])
```

```
for (k in 1:17)
{ B=B+Dm[k]*(time[2]+taws[k]*exp(-(time[2])/taws[k]))
Dm[k]*((time[1])+taws[k]*exp(-(time[1])/taws[k]))}
```

```
VEstrain[2]=B*c[1]
```

```
for(i in 3:n)
```

```
{
temp=rep(NA,i-1)
for(j in 1:i-1)
{
c[j]=(a[j+1]-a[j])/(time[j+1]-time[j])
b=Do*(-time[j]+time[j+1])
for(k in 1:17)
{ b=b+Dm[k]*((time[i]-time[j])+taws[k]*exp(-(time[i]-time[j])/taws[k]))-
Dm[k]*((time[i]-time[j+1])+taws[k]*exp(-(time[i]-time[j+1])/taws[k]))}
temp[j]=b*c[j]
}
}
```

```
VEstrain[i]=sum(temp)
```

```

}

Data$VEstrain=VEstrain/1000
plot(Data$VEstrain~time)

write.csv(Data, "D:/VEstrain.csv")

```

CALCULATION OF PROBABLISTIC VISCOELASTIC STRAINS

```

Data1= read.csv("C:/Users/Hussein Kassem/Desktop/Probabilistic VE Strain
Prediction/U19-WMA-Sonne/U19-WMA-CX@35@0.0001/StiffnessDamage.csv")

data.matrix(Data1)
a1=Data1[,1]
b1=Data1[,2]
a2=Data1[,3]
b2=Data1[,4]
a3=Data1[,5]
b3=Data1[,6]
a=Data1[,7]
b=Data1[,8]
c=Data1[,9]

Data2= read.csv("C:/Users/Hussein Kassem/Desktop/Probabilistic VE Strain
Prediction/U19-WMA-Sonne/U19-WMA-CX@35@0.0001/StressInput.csv")
time=Data2$Time
stress=Data2$Stress
LS=Data2$LBStress
size=length(time)

StressOVERC=matrix(, nrow = size, ncol = 500)

for(q in 1:500)
{
  StressOVERC[1,q]=0
  for (v in 2:size)
  {
    StressOVERC[v,q]=stress[v]/(a[q]*exp(-
b[q]*((a1[q]*exp(b1[q]*LS[v])+a2[q]*exp(b2[q]*LS[v])+a3[q]*exp(b3[q]*LS[v]))^c[q])))
  }
}

Data3= read.csv("C:/Users/Hussein Kassem/Desktop/Probabilistic VE Strain
Prediction/U19-WMA-Sonne/U19-WMA-CX@35@0.0001/PronyData.csv")
data.matrix(Data3)

```

```

tawss=c(0.00000001,0.0000001,0.000001,0.00001,0.0001,0.001,0.01,0.1,1,10,100,1000,10
000,100000,1000000,10000000,100000000,rep(NA,size-17))

Dn=matrix(, nrow = 500, ncol = 18)
Dn=Data3

m=matrix(, ncol = 500, nrow = size)
for(s in 1:500)
{
  #continued
  Ds=c(Dn[s,1],Dn[s,2],Dn[s,3],Dn[s,4],Dn[s,5],Dn[s,6],Dn[s,7],Dn[s,8],Dn[s,9],Dn[s,10],D
n[s,11],Dn[s,12],Dn[s,13],Dn[s,14],Dn[s,15],Dn[s,16],Dn[s,17],rep(NA,size-17))
  Do=c(Data3[s,18],rep(NA,size-1))
  StressOverC=StressOVERC[,s]
  Data= data.frame(time, stress, LS, StressOverC,tawss,Ds,Do)

  time= Data$time
  stress=Data$stress
  a=Data$StressOverC

  Do=Data$Do[1]
  Dm=head(Data$Ds,17)
  taws=head(Data$tawss,17)

  n=length(time)
  c=rep(NA,n-1)
  VEstrain=rep(NA,n)
  VEstrain[1]=0

  c[1]=(a[2]-a[1])/(time[2]-time[1])
  B=Do*(time[2]-time[1])
  for (k in 1:17)
  {B=B+Dm[k]*(time[2]+taws[k]*exp(-(time[2])/taws[k]))-
Dm[k]*((time[1])+taws[k]*exp(-(time[1])/taws[k]))}
  VEstrain[2]=B*c[1]

  for(i in 3:n)
  {
    temp=rep(NA,i-1)

    for(j in 1:i-1)
    {
      c[j]=(a[j+1]-a[j])/(time[j+1]-time[j])
      b=Do*(-time[j]+time[j+1])
      for(k in 1:17)
      {b=b+Dm[k]*((time[i]-time[j])+taws[k]*exp(-(time[i]-time[j])/taws[k]))-
Dm[k]*((time[i]-time[j+1])+taws[k]*exp(-(time[i]-time[j+1])/taws[k]))}
      temp[j]=b*c[j]
    }
    VEstrain[i]=sum(temp)
  }
}

```

```

Data$VEstrain=VEstrain/1000
plot(Data$VEstrain~time)

write.csv(Data, paste0(s,".csv"))
m[,s]=VEstrain/1000
}
data.frame(m)
write.csv(m,"Predicted VE Strain_#of realization.csv")

```

9.3 CODE FOR MONTE CARLO SIMULATIONS: CASE OF C VS S

```

#average of random variables
mean.b <- c(1.0719,0.003742,0.5616436)

#covariance matrix
sigma.b <- matrix (c(0.00080595,0.00003842,-0.00079634,
                    0.00003842,0.00000640,-0.00013153,
                    -0.00079634,-0.00013153,0.00281633),3,3)

# Parameter b has a lognormal distribution
mean_b=0.003742
sd_b= 0.002530
cov_b=sd_b/mean_b
sdlog_b=sqrt(log(1+cov_b^2))
meanlog_b=log(mean_b)-sdlog_b^2/2

bM1 <- rmvnorm(n=100000,mean=mean.b,sigma=sigma.b)

a=bM1[,1]
b1=bM1[,2]
c=bM1[,3]
b=exp(qnorm(pnorm((b1-mean_b)/sd_b))*sdlog_b+meanlog_b)
S=c(1000,2000,3000,4000,5000,6000,7000,8000,9000,10000,11000,12000,13000,14000,1
5000,16000,17000,18000,19000,20000,21000,22000,23000,24000,25000)
C1000=a*exp(-b*(S[1]^c))
C2000=a*exp(-b*(S[2]^c))
C3000=a*exp(-b*(S[3]^c))
C4000=a*exp(-b*(S[4]^c))
C5000=a*exp(-b*(S[5]^c))
C6000=a*exp(-b*(S[6]^c))
C7000=a*exp(-b*(S[7]^c))
C8000=a*exp(-b*(S[8]^c))
C9000=a*exp(-b*(S[9]^c))
C10000=a*exp(-b*(S[10]^c))
C11000=a*exp(-b*(S[11]^c))
C12000=a*exp(-b*(S[12]^c))
C13000=a*exp(-b*(S[13]^c))
C14000=a*exp(-b*(S[14]^c))
C15000=a*exp(-b*(S[15]^c))
C16000=a*exp(-b*(S[16]^c))

```

```

C17000=a*exp(-b*(S[17]^c))
C18000=a*exp(-b*(S[18]^c))
C19000=a*exp(-b*(S[19]^c))
C20000=a*exp(-b*(S[20]^c))
C21000=a*exp(-b*(S[21]^c))
C22000=a*exp(-b*(S[22]^c))
C23000=a*exp(-b*(S[23]^c))
C24000=a*exp(-b*(S[24]^c))
C25000=a*exp(-b*(S[25]^c))
muC=rep(0,25)
covC=rep(0,25)
muC[1]=mean(C1000)
muC[2]=mean(C2000)
muC[3]=mean(C3000)
muC[4]=mean(C4000)
muC[5]=mean(C5000)
muC[6]=mean(C6000)
muC[7]=mean(C7000)
muC[8]=mean(C8000)
muC[9]=mean(C9000)
muC[10]=mean(C10000)
muC[11]=mean(C11000)
muC[12]=mean(C12000)
muC[13]=mean(C13000)
muC[14]=mean(C14000)
muC[15]=mean(C15000)
muC[16]=mean(C16000)
muC[17]=mean(C17000)
muC[18]=mean(C18000)
muC[19]=mean(C19000)
muC[20]=mean(C20000)
muC[21]=mean(C21000)
muC[22]=mean(C22000)
muC[23]=mean(C23000)
muC[24]=mean(C24000)
muC[25]=mean(C25000)
covC[1]=sd(C1000)/muC[1]
covC[2]=sd(C2000)/muC[2]
covC[3]=sd(C3000)/muC[3]
covC[4]=sd(C4000)/muC[4]
covC[5]=sd(C5000)/muC[5]
covC[6]=sd(C6000)/muC[6]
covC[7]=sd(C7000)/muC[7]
covC[8]=sd(C8000)/muC[8]
covC[9]=sd(C9000)/muC[9]
covC[10]=sd(C10000)/muC[10]
covC[11]=sd(C11000)/muC[11]
covC[12]=sd(C12000)/muC[12]
covC[13]=sd(C13000)/muC[13]
covC[14]=sd(C14000)/muC[14]
covC[15]=sd(C15000)/muC[15]
covC[16]=sd(C16000)/muC[16]

```



```
covC[17]=sd(C17000)/muC[17]
covC[18]=sd(C18000)/muC[18]
covC[19]=sd(C19000)/muC[19]
covC[20]=sd(C20000)/muC[20]
covC[21]=sd(C21000)/muC[21]
covC[22]=sd(C22000)/muC[22]
covC[23]=sd(C23000)/muC[23]
covC[24]=sd(C24000)/muC[24]
covC[25]=sd(C25000)/muC[25]
```

```
Data=data.frame(a,b,c,C1000,C2000,C3000,C4000,C5000,C6000,C7000,C8000,C9000,C10000,C11000,C12000,C13000,C14000,C15000,C16000,C17000,C18000,C19000,C20000,C21000,C22000,C23000,C24000,C25000)
```

```
write.csv(Data,"D:/Data_U19HMA_C_Eigenvalues.csv")
```

```
Summary=data.frame(S,covC,muC,IQRC)
```

```
write.csv(Summary,"D:/Summary_U19HMA_C.csv")
```

3- ASSESSING THE EFFECT OF THE ADDITION OF RAP ON |E*| OF WMA

Reclaimed Asphalt Pavement

The reclaimed asphalt pavement (RAP) used in this research was collected from a locally milled asphalt pavement after 20 years of service. This RAP was initially made of unmodified binder and limestone aggregates. The asphalt content of three replicates of RAP was measured using the extraction method as per ASTM D2172. It has an average asphalt content of 7.0% of its total weight with an aggregate gradation as presented in the following table:

Aggregate gradation of limestone aggregates of RAP.

SIEVE SIZE (MM)	% PASSING
12.5	100.0
9.5	91.0
4.75	55.6
2.36	28.2
1.18	12.7
0.6	5.5
0.3	2.3
0.15	0.9
0.075	0.4
PAN	0.0

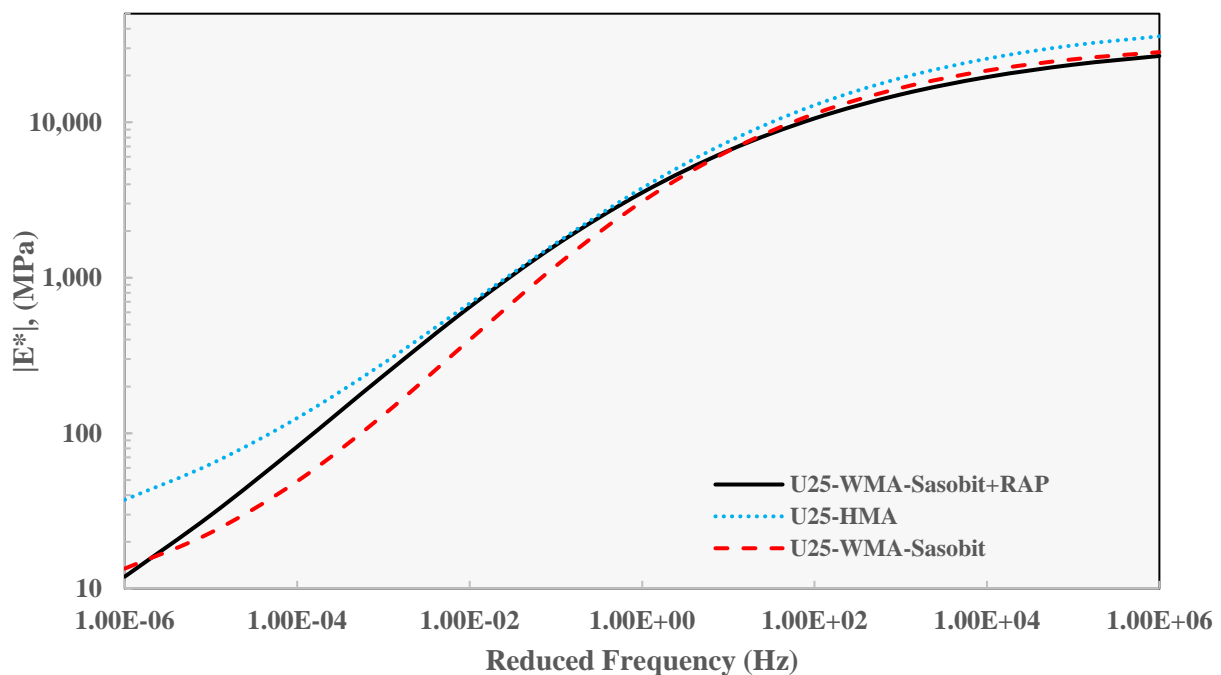
Design of Mixes with RAP

The effect of the addition of RAP on WMA mixes was assessed by incorporating it in the mix with unmodified binder and Sasobit. RAP was added to the mix without changing the aggregate gradation and thus mix design trials were conducted to determine the asphalt content that gives a 4.0% air void level while taking into account that part of the RAP's binder will be blended with the virgin binder. This step was conducted for the HMA mix with unmodified binder and 25.0 mm gradation, where the 15% RAP reduced the amount of required virgin binder from 3.5% to 2.3%. The amount of RAP was selected to be 15% to avoid any need to change the mix design process, especially that higher amounts of RAP

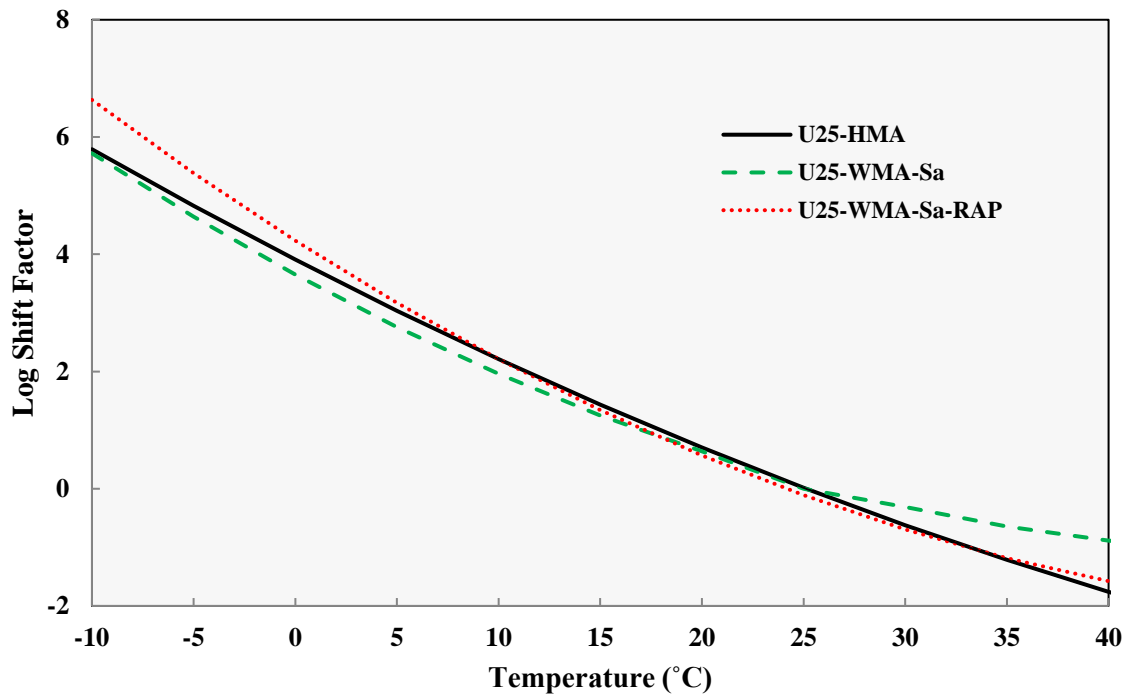
require the reduction in the grade of the virgin binder used for better mixing between virgin binder and the stiffer recycled binder (Brown et al. 2009). For the WMA with Sasobit of a dosage of 1% by weight of binder and 15% RAP, the same %AC of 2.3% is used to achieve 4% air voids at a compaction temperature reduced by 35°C. However, the addition of RAP required that the mixing temperature should be reduced by only 20°C instead of 35°C in order to ensure a proper coating of the virgin aggregates. RAP is heated at the mixing temperatures for a period of three hours before mixing where they are not placed overnight with virgin aggregates to avoid any further aging of the RAP's binder (Zhou et al. 2012).

Dynamic Modulus Testing

The E^* testing of three replicates for each mix shows that the addition of RAP to WMA mixes with Sasobit and unmodified binder is able to improve the mix's stiffness at reduced frequencies in the range of 10^{-5} to 1 Hz. This can compensate for the reduction of stiffness due to the addition of WMA additives to mixes with unmodified binder. In addition, the addition of RAP slightly decreases the mix' stiffness at high reduced frequencies as shown in the figure below. Thus, WMA with Sasobit and unmodified binder can incorporate 15% by weight as RAP without negatively affecting the mix's performance. For WMA with RAP, the time-temperature shift factors are increased especially at low temperatures in comparison to the control HMA mix and the WMA mix without RAP.



$|E^*|$ mastercurves at a reference temperature of 25°C for HMA and WMA-Sasobit mixes with and without RAP having an unmodified binder and a 25.0 mm aggregate gradation.



Time-Temperature shift factors to construct $|E^*|$ for HMA and WMA-Sasobit mixes with and without RAP made of unmodified binder and a 25.0 mm aggregate gradation.

4- COMPLEX MODULUS DATA

This section of the appendix presents raw data of the different replicates for E* testing of the mixes involved in this study.

Sample ID	Air Voids %	Testing Temperature °C	Testing Frequency Hz	E* MPa	Phase Angle degrees
M19-HMA-1	7.0	-7.3	10	35628.9	5.3
			5	34802.1	5.3
			1	31978.9	6.2
			0.5	30553.9	6.6
			0.1	27195.5	8.2
			0.01	22307.1	10.9
		10.5	10	17858.2	13.81
			5	16072.1	15.31
			1	12252.7	18.85
			0.5	10693.2	20.42
			0.1	7590.73	24.45
			0.01	4342.67	30.17
		24.6	20	8820.7	22.6
			10	7506.3	24.6
			5	6227.5	26.7
			1	3915.5	32.1
			0.5	3125.0	33.8
			0.1	1792.7	36.1
		41.1	20	2725.1	31.2
			10	2245.4	30.0
			5	1689.3	30.2
			1	1013.8	28.7
			0.5	834.2	28.2
			0.1	510.0	27.6

Sample ID	Air Voids %	Testing Temperature °C	Testing Frequency Hz	E* MPa	Phase Angle degrees
M19-HMA-2	6.8	-11.8	10	32845.1	4.4
			5	32174.9	4.5
			1	29870.5	5.0
			0.5	28743.2	5.2
			0.1	26124.5	6.5
			0.01	22058.4	4.0
		10.4	10	15272.7	12.9
			5	14031.1	14.4
			1	10689.0	17.6
			0.5	9333.7	19.5
			0.1	6638.8	23.8
			0.01	3812.6	28.2
		25.0	20	8006.1	22.7
			10	6914.3	24.4
			5	5844.5	26.8
			1	3549.7	31.8
			0.5	2813.7	34.3
			0.1	1720.7	36.8
		40.0	20	2555.3	30.7
			10	2245.3	29.8
			5	1715.8	29.8
			1	1009.3	28.0
			0.5	825.0	27.3
			0.1	470.2	26.8

Sample ID	Air Voids %	Testing Temperature °C	Testing Frequency Hz	E* MPa	Phase Angle degrees
M19-HMA-3	7.1	-9.3	10	28915.6	4.8
			5	27977.5	5.5
			1	25789.6	6.5
			0.5	24486.4	6.6
			0.1	21788.8	8.5
			0.01	17846.2	12.6
		10	10	14579.2	14.5
			5	13194.8	16.1
			1	9948.4	19.8
			0.5	8703.5	21.0
			0.1	6209.6	25.6
			0.01	3503.0	31.0
		25.4	20	7217.8	25.1
			10	6321.8	26.5
			5	5346.6	29.0
			1	3400.6	35.0
			0.5	2772.5	36.9
			0.1	2456.5	40.9
		41.3	20	2255.3	31.0
			10	1950.7	30.4
			5	1501.0	30.0
			1	878.5	27.9
			0.5	713.1	27.7
			0.1	421.3	27.5

Sample ID	Air Voids %	Testing Temperature °C	Testing Frequency Hz	E* MPa	Phase Angle degrees
M19-HMA-4	6.5	-9.6	10	31608.1	4.7
			5	30848.9	4.4
			1	28633.9	5.4
			0.5	27245.7	6.3
			0.1	24668.5	7.3
			0.01	19798.3	12.8
		6.8	10	20372.1	10.4
			5	18924.1	11.2
			1	15479.6	14.3
			0.5	14013.6	15.7
			0.1	10958.4	18.7
			0.01	7118.7	24.3
		25.0	20	8923.8	21.4
			10	7548.9	23.3
			5	6369.1	25.3
			1	4010.8	30.0
			0.5	3211.1	31.7
			0.1	1914.1	34.0
		41.1	20	2960.0	31.0
			10	2391.6	31.0
			5	1868.0	30.8
			1	1084.9	30.5
			0.5	859.0	29.5
			0.1	487.1	28.3

Sample ID	Air Voids %	Testing Temperature °C	Testing Frequency Hz	E* MPa	Phase Angle degrees
M19-HMA-5	6.8	-8.1	10	31955.3	3.6
			5	31265.2	5.2
			1	28726.7	6.3
			0.5	27493.5	6.5
			0.1	24625.6	8.2
			0.01	18546.2	15.3
		8.1	10	19155.2	11.5
			5	17655.2	12.9
			1	13877.7	16.6
			0.5	12206.0	17.8
			0.1	8827.6	22.1
			0.01	5017.0	28.4
		25.0	20	8135.3	22.9
			10	6705.8	24.8
			5	5534.3	26.8
			1	3212.6	31.5
			0.5	2503.1	32.7
			0.1	1360.6	33.9
		40.4	20	2960.0	31.0
			10	2391.6	31.0
			5	1868.0	30.8
			1	1084.9	30.5
			0.5	859.0	29.5
			0.1	487.1	28.3

Sample ID	Air Voids %	Testing Temperature °C	Testing Frequency Hz	E* MPa	Phase Angle degrees
M19-HMA-6	7.5	-8.2	10	28250.3	4.1
			5	27358.3	5.5
			1	25075.9	6.2
			0.5	24211.1	7.1
			0.1	21509.4	8.2
			0.01	18342.0	15.3
		8.1	10	15145.9	12.8
			5	13710.7	14.3
			1	10559.6	18.0
			0.5	9316.4	20.3
			0.1	6610.3	23.8
			0.01	3785.9	29.4
		25	20	6751.1	23.7
			10	5859.6	25.1
			5	4865.2	27.0
			1	2870.9	32.0
			0.5	2292.9	32.1
			0.1	1284.8	33.5
		40.6	20	2351.5	31.9
			10	1896.6	30.0
			5	1469.6	29.7
			1	869.7	27.1
			0.5	691.7	25.8
			0.1	397.8	25.3

Sample ID	Air Voids %	Testing Temperature °C	Testing Frequency Hz	E* MPa	Phase Angle degrees
M19-HMA-7	6.7	-8.2	10	37307.0	4.2
			5	35210.2	5.7
			1	32036.5	6.7
			0.5	30806.8	7.3
			0.1	27037.9	9.2
			0.01	18679.5	15.3
		8.4	10	21780.2	11.4
			5	19545.5	14.2
			1	14928.0	17.8
			0.5	13237.9	19.4
			0.1	9396.3	23.4
			0.01	5337.6	29.0
		25.0	20	9079.7	23.7
			10	7393.4	25.2
			5	6143.8	27.1
			1	3679.4	31.6
			0.5	2917.8	32.5
			0.1	1662.9	33.6
		41.4	20	2619.1	32.0
			10	2144.9	30.9
			5	1669.7	30.3
			1	995.6	28.2
			0.5	808.7	27.3
			0.1	477.8	27.2

Sample ID	Air Voids %	Testing Temperature °C	Testing Frequency Hz	E* MPa	Phase Angle degrees
M19-HMA-8	6.8	-7.6	10	28501.8	5.4
			5	26715.6	5.7
			1	24476.9	7.1
			0.5	23220.0	7.9
			0.1	19925.6	9.7
			0.01	15175.0	12.8
		8.5	10	16313.7	12.5
			5	15142.8	14.0
			1	11626.9	17.8
			0.5	10248.3	19.5
			0.1	7153.3	23.8
			0.01	3907.2	29.8
		25.0	20	6786.4	28.7
			10	5679.6	27.8
			5	4599.7	29.5
			1	2589.9	33.5
			0.5	2012.3	34.3
			0.1	1066.1	35.7
		42.2	20	1964.2	33.5
			10	1576.1	32.3
			5	1188.2	31.8
			1	677.9	29.2
			0.5	524.5	27.9
			0.1	288.8	25.8

Sample ID	Air Voids %	Testing Temperature °C	Testing Frequency Hz	E* MPa	Phase Angle degrees
M19-HMA-9	6.8	-8.7	10	30868.4	5.2
			5	29923.3	5.6
			1	27352.1	6.5
			0.5	26234.3	6.8
			0.1	23067.3	8.4
			0.01	18774.5	12.7
		7.6	10	18279.4	11.2
			5	16737.7	12.2
			1	13611.3	14.8
			0.5	12283.8	16.3
			0.1	9434.9	19.8
			0.01	6060.8	27.4
		25.0	20	7407.0	23.0
			10	6402.2	24.6
			5	5314.5	26.6
			1	3278.9	31.5
			0.5	2601.5	33.2
			0.1	1537.2	35.1
		40.0	20	2665.5	32.3
			10	2235.2	32.4
			5	1789.1	33.2
			1	1046.4	33.0
			0.5	825.6	32.9
			0.1	467.5	33.1

Sample ID	Air Voids %	Testing Temperature °C	Testing Frequency Hz	E* MPa	Phase Angle degrees
M19-HMA-10	6.8	-7.0	10	32831.9	5.8
			5	31724.3	5.9
			1	28745.9	7.2
			0.5	27393.2	7.9
			0.1	24074.7	9.4
			0.01	19509.0	12.2
		9.1	10	18456.2	12.4
			5	16840.0	13.7
			1	13197.9	16.6
			0.5	11737.0	18.9
			0.1	8597.6	22.4
			0.01	5346.5	27.8
		25.0	20	9011.4	22.2
			10	7769.8	24.1
			5	6457.0	26.0
			1	3903.7	30.5
			0.5	3133.9	31.8
			0.1	1824.0	33.5
		40.6	20	2901.1	30.7
			10	2384.0	29.9
			5	1861.0	29.3
			1	1116.4	27.6
			0.5	885.6	26.8
			0.1	510.7	25.5

Sample ID	Air Voids %	Testing Temperature °C	Testing Frequency Hz	E* MPa	Phase Angle degrees
M19-WMA-Advera-1	6.8	-9.8	10	37345.3	6.0
			5	36212.3	5.6
			1	33592.5	5.5
			0.5	31787.9	6.1
			0.1	28190.6	8.3
			0.01	22740.7	10.6
		4.9	10	21222.6	10.8
			5	19428.9	12.2
			1	15768.3	14.8
			0.5	14071.5	16.4
			0.1	10487.5	20.7
			0.01	6693.1	27.1
		25.5	20	7340.1	25.4
			10	6375.4	27.3
			5	5234.2	29.5
			1	3133.4	35.6
			0.5	2455.7	36.8
			0.1	1490.6	40.0
		41.3	20	2177.4	33.7
			10	2067.5	33.1
			5	1574.3	33.7
			1	1004.4	32.4
			0.5	878.2	33.3
			0.1	465.6	29.8

Sample ID	Air Voids %	Testing Temperature °C	Testing Frequency Hz	E* MPa	Phase Angle degrees
M19-WMA-Advera-2	6.8	-10.5	10	37034.1	5.3
			5	35887.1	5.1
			1	32845.6	6.2
			0.5	30842.4	6.2
			0.1	27244.4	8.6
			0.01	22006.7	11.3
		5.8	10	20392.6	12.2
			5	18542.4	13.4
			1	14524.5	16.7
			0.5	12894.4	18.5
			0.1	9315.7	22.8
			0.01	5244.8	30.7
		25.2	20	6766.7	26.6
			10	5570.1	28.4
			5	4418.8	29.8
			1	2489.0	33.4
			0.5	1931.5	33.9
			0.1	1029.5	33.1
		41.2	20	1743.2	32.7
			10	1514.2	30.9
			5	1102.7	29.4
			1	642.3	25.3
			0.5	518.5	23.8
			0.1	305.6	22.0

Sample ID	Air Voids %	Testing Temperature °C	Testing Frequency Hz	E* MPa	Phase Angle degrees
M19-WMA-Rediset-1	7.1	-9.2	10	28929.1	4.6
			5	28233.8	5.4
			1	25666.4	6.4
			0.5	24637.3	6.9
			0.1	21544.1	8.8
			0.01	17930.7	15.0
		9.6	10	15394.7	13.6
			5	13865.1	15.1
			1	10575.5	18.8
			0.5	9272.4	20.7
			0.1	6503.9	24.8
			0.01	3554.2	30.7
		25.0	20	7116.3	23.3
			10	5980.2	24.9
			5	4982.6	26.7
			1	2911.1	31.6
			0.5	2298.5	32.9
			0.1	1234.0	35.2
		39.3	20	2250.5	33.1
			10	2096.5	34.8
			5	1512.9	34.4
			1	846.9	32.8
			0.5	650.5	30.4
			0.1	338.8	30.3

Sample ID	Air Voids %	Testing Temperature °C	Testing Frequency Hz	E* MPa	Phase Angle degrees
M19-WMA-Rediset-2	6.8	-9.5	10	33227.7	6.6
			5	32707.7	8.6
			1	29936.7	11.7
			0.5	28776.9	12.7
			0.1	25931.0	13.3
			0.01	21273.8	14.8
		10.2	10	16837.7	15.1
			5	15157.7	16.4
			1	11470.7	20.5
			0.5	9879.1	22.1
			0.1	6747.8	26.9
			0.01	3604.4	32.1
		25.0	20	6999.7	23.9
			10	5954.2	25.9
			5	4870.4	28.0
			1	2791.1	32.8
			0.5	2151.3	33.5
			0.1	1130.1	34.6
		40.7	20	1972.2	33.7
			10	1688.9	31.3
			5	1234.2	31.0
			1	703.4	27.1
			0.5	565.5	25.4
			0.1	317.7	24.8

Sample ID	Air Voids %	Testing Temperature °C	Testing Frequency Hz	E* MPa	Phase Angle degrees
M19-WMA-Rediset-3	7.2	-9.1	10	26040.0	5.8
			5	25063.4	5.9
			1	22516.4	7.2
			0.5	21509.9	7.8
			0.1	18766.4	9.7
			0.01	14824.4	14.7
		8.6	10	13885.5	13.8
			5	12519.5	15.5
			1	9633.5	18.9
			0.5	8370.2	20.8
			0.1	5826.9	25.3
			0.01	3210.5	31.7
		25.8	20	5769.8	26.0
			10	4874.1	28.0
			5	3995.4	29.7
			1	2293.4	34.6
			0.5	1796.8	35.5
			0.1	997.3	37.1
		40.1	20	1922.2	35.7
			5	1444.6	36.5
1	878.3		33.8		
0.5	792.1		35.6		

Sample ID	Air Voids %	Testing Temperature °C	Testing Frequency Hz	E* MPa	Phase Angle degrees
M19-WMA-Sasobit-1	7.0	-11.0	10	37776.1	4.7
			5	37023.4	7.8
			1	34199.4	8.1
			0.5	33276.2	8.4
			0.1	29664.7	9.2
			0.01	25252.0	7.5
			5.7	10	21952.1
		5		20510.2	11.1
		1		16708.5	13.4
		0.5		15285.2	15.0
		0.1		11734.1	18.6
		0.01		7431.6	23.5
		25.0	20	9072.0	21.3
			10	7888.1	22.8
			5	6724.7	26.2
			1	4311.2	31.8
			0.5	3516.0	33.5
			0.1	2145.0	37.2
			41.5	20	2840.1
		10		2572.8	31.5
5	1950.6	31.7			
1	1150.1	30.4			
0.5	925.9	29.9			
0.1	557.2	29.8			

Sample ID	Air Voids %	Testing Temperature °C	Testing Frequency Hz	E* MPa	Phase Angle degrees
M19-WMA-Sasobit-2	7.2	-8.2	10	27518.8	5.6
			5	26695.3	6.7
			1	24266.6	7.9
			0.5	23322.5	8.0
			0.1	20543.9	9.4
			0.01	16740.1	13.4
		4.9	10	18152.9	10.2
			5	16934.0	11.1
			1	13777.0	13.7
			0.5	12502.0	15.2
			0.1	9652.8	18.7
			0.01	6235.1	24.5
		25.8	20	6953.5	24.0
			10	6043.7	25.2
			5	5121.8	26.8
			1	3112.9	31.7
			0.5	2498.7	32.5
			0.1	1507.2	35.2
		41.0	20	2450.6	28.8
			10	2194.9	27.9
			5	1728.0	28.7
			1	1092.8	27.2
			0.5	911.3	27.4
			0.1	568.4	29.1

Sample ID	Air Voids %	Testing Temperature °C	Testing Frequency Hz	E* MPa	Phase Angle degrees
M19-WMA-Sasobit-3	6.5	-7.8	10	27632.2	6.8
			5	28283.6	11.5
			1	26899.2	11.0
			0.5	23394.7	10.5
			0.1	20954.6	13.4
			0.01	17543.9	13.7
		5.3	10	19255.3	10.3
			5	17704.8	11.2
			1	14452.1	14.0
			0.5	13013.5	14.8
			0.1	9984.6	18.0
			0.01	6558.8	23.4
		24.4	20	8079.5	21.8
			10	7079.7	23.7
			5	5980.0	24.9
			1	3770.0	30.6
			0.5	3062.7	31.9
			0.1	1984.0	34.4
		38.0	20	3053.3	30.8
			10	2980.3	30.9
			5	2490.7	32.0
			1	1482.6	32.6
			0.5	1244.3	33.7
			0.1	872.0	36.2

Sample ID	Air Voids %	Testing Temperature °C	Testing Frequency Hz	E* MPa	Phase Angle degrees
U19-HMA-1	7.2	-6.5	10	33632.3	6.3
			5	32343.9	8.1
			1	28913.1	9.2
			0.5	27216.8	9.5
			0.1	23125.6	11.7
			0.01	17260.1	17.5
		10.5	10	15466.9	15.8
			5	13803.8	17.8
			1	10163.6	22.3
			0.5	8622.8	24.3
			0.1	5681.9	29.3
			0.01	2763.6	34.3
		25.0	20	9153.5	27.6
			10	7613.4	29.6
			5	5540.4	32.0
			1	2771.3	36.3
			0.5	2107.4	36.3
			0.1	1059.3	35.5
		42.5	20	1523.4	31.2
			10	1054.7	30.6
			5	864.3	29.1
			1	528.4	24.8
			0.5	434.7	23.7
			0.1	250.8	22.3

Sample ID	Air Voids %	Testing Temperature °C	Testing Frequency Hz	E* MPa	Phase Angle degrees
U19-HMA-2	6.6	-6.0	10	30117.5	6.4
			5	28905.6	7.5
			1	25663.8	8.8
			0.5	24398.4	9.7
			0.1	21015.5	11.8
			0.01	15748.5	16.8
		10.2	10	15850.8	15.1
			5	14251.9	16.6
			1	10440.5	21.2
			0.5	8993.6	23.4
			0.1	5985.8	29.0
			0.01	2900.8	36.1
		25.0	20	7247.3	27.1
			10	5946.8	29.1
			5	4743.1	31.3
			1	2569.7	36.0
			0.5	1929.7	37.0
			0.1	959.6	37.0
		40.2	20	2056.0	33.3
			10	1431.5	33.8
			5	1086.0	31.6
			1	622.7	28.0
			0.5	497.9	26.7
			0.1	297.9	25.9

Sample ID	Air Voids %	Testing Temperature °C	Testing Frequency Hz	E* MPa	Phase Angle degrees
U19-HMA-3	6.8	-6.6	10	31414.2	7.5
			5	29708.6	6.0
			1	26415.7	7.4
			0.5	24475.7	8.4
			0.1	20792.0	10.8
			0.01	15865.8	16.7
		9.7	10	14740.5	15.4
			5	13289.2	17.7
			1	9627.9	22.5
			0.5	8232.8	25.0
			0.1	5288.5	29.8
			0.01	2536.6	34.7
		25.0	20	6621.1	27.0
			10	5316.8	29.1
			5	4133.8	31.2
			1	2220.1	35.4
			0.5	1653.4	35.9
			0.1	802.9	34.7
		40.2	20	1767.7	33.5
			10	1273.5	33.3
			5	922.3	31.1
			1	535.4	26.4
			0.5	425.5	25.1
			0.1	247.9	23.7

Sample ID	Air Voids %	Testing Temperature °C	Testing Frequency Hz	E* MPa	Phase Angle degrees
U19-HMA-4	7.2	-10	10	37541.4	3.6
			5	36840.3	5.0
			1	33652.2	5.7
			0.5	32384.2	5.9
			0.1	28554.8	8.3
			0.01	23575.8	8.3
		8.4	10	18031.8	13.0
			5	16049.4	14.2
			1	12373.8	17.8
			0.5	10931.6	19.8
			0.1	7912.6	24.5
			0.01	4408.2	31.7
		25.0	20	7849.0	24.8
			10	6644.2	26.5
			5	5421.6	28.8
			1	3092.8	33.3
			0.5	2357.1	34.2
			0.1	1187.7	35.4
		39.1	20	2578.1	34.3
			10	1975.3	33.4
			5	1448.6	33.3
			1	795.5	29.8
			0.5	602.0	27.9
			0.1	311.8	26.5

Sample ID	Air Voids %	Testing Temperature °C	Testing Frequency Hz	E* MPa	Phase Angle degrees
U19-HMA-5	6.8	-9.2	10	31661.0	4.7
			5	30907.9	4.8
			1	27923.6	6.1
			0.5	26985.1	6.0
			0.1	24242.3	7.7
			0.01	20697.7	6.6
		7.2	10	20636.9	11.1
			5	18697.2	12.0
			1	15050.8	15.6
			0.5	13099.4	17.0
			0.1	9401.4	21.7
			0.01	5354.6	29.7
		25.0	20	8106.1	25.6
			10	7057.8	29.2
			5	5872.2	31.8
			1	3510.7	36.6
			0.5	2779.2	37.9
			0.1	1572.8	39.1
		42	20	2326.3	37.7
			10	1874.7	36.2
			5	1401.7	34.8
			1	804.1	31.2
			0.5	624.3	29.6
			0.1	336.0	26.6

Sample ID	Air Voids %	Testing Temperature °C	Testing Frequency Hz	E* MPa	Phase Angle degrees
U19-HMA-6	7.2	-8.4	10	37359.0	5.2
			5	36671.2	6.4
			1	33215.9	6.7
			0.5	31527.2	8.4
			0.1	27484.7	9.8
			0.01	22213.7	16.5
		9.0	10	20271.3	13.0
			5	18359.5	15.4
			1	13888.1	19.7
			0.5	12004.7	21.2
			0.1	8284.7	26.1
			0.01	4190.1	30.9
		25.0	20	8208.1	26.2
			10	6920.2	29.0
			5	5455.6	31.7
			1	3007.9	36.1
			0.5	2280.5	36.9
			0.1	1139.5	37.0
		39.0	20	2559.8	35.5
			10	1922.1	34.5
			5	1378.6	34.2
			1	748.0	30.2
			0.5	570.3	28.8
			0.1	300.0	27.0

Sample ID	Air Voids %	Testing Temperature °C	Testing Frequency Hz	E* MPa	Phase Angle degrees
U19-HMA-7	7.2	-8.0	10	43357.3	11.1
			5	42231.0	10.6
			1	38936.8	14.4
			0.5	37010.4	12.9
			0.1	32521.6	17.6
			0.01	24770.6	14.4
		9.0	10	24950.3	13.1
			5	22816.9	14.7
			1	17722.8	18.4
			0.5	15359.7	20.6
			0.1	10921.5	24.9
			0.01	6077.1	32.0
		25.0	20	10015.6	24.5
			10	8367.7	26.6
			5	6861.5	29.3
			1	3999.8	34.2
			0.5	3061.1	34.8
			0.1	1608.2	35.8
		39.5	20	2938.6	34.5
			10	2010.3	32.0
			5	1642.3	33.1
1	903.7		30.2		
0.5	687.5		29.1		
0.1	361.8		26.9		

Sample ID	Air Voids %	Testing Temperature °C	Testing Frequency Hz	E* MPa	Phase Angle degrees
U19-HMA-8	7.2	-8.9	10	30761.0	5.8
			5	30199.7	5.2
			1	27642.4	6.2
			0.5	26613.8	6.3
			0.1	23707.2	8.7
			0.01	19919.3	9.4
		9.5	10	17917.3	13.9
			5	16608.0	15.6
			1	12733.4	19.7
			0.5	11252.8	22.4
			0.1	7903.5	27.2
			0.01	4171.0	34.5
		25.0	20	8043.1	27.0
			10	6622.8	29.2
			5	5250.8	31.6
			1	2801.7	36.6
			0.5	2105.6	37.1
			0.1	1017.8	36.5
		39.0	20	2126.9	36.3
			10	1591.9	34.1
			5	1128.9	33.2
1	624.4		28.2		
0.5	481.3		25.9		
0.1	262.6		23.5		

Sample ID	Air Voids %	Testing Temperature °C	Testing Frequency Hz	E* MPa	Phase Angle degrees
U19-HMA-9	7.1	-8.6	10	35102.3	4.7
			5	34041.8	5.6
			1	31217.2	6.4
			0.5	29749.5	7.1
			0.1	25888.9	8.8
			0.01	19840.6	14.4
		7.6	10	18609.7	13.4
			5	16769.6	14.9
			1	12970.8	18.5
			0.5	11308.7	20.4
			0.1	8046.6	24.4
			0.01	4394.3	31.6
		25.0	20	7340.2	25.4
			10	6130.0	27.5
			5	4888.8	29.6
			1	2740.5	34.3
			0.5	2082.9	34.6
			0.1	1044.6	34.4
		40.6	20	1932.8	34.0
			10	1526.7	32.3
			5	1130.4	31.3
			1	651.8	27.2
			0.5	510.2	25.6
			0.1	285.6	23.5

Sample ID	Air Voids %	Testing Temperature °C	Testing Frequency Hz	E* MPa	Phase Angle degrees
U19-HMA-10	6.8	-9.4	10	28670.2	4.3
			5	27802.2	4.2
			1	25841.0	5.8
			0.5	24703.8	5.6
			0.1	22408.7	7.6
			0.01	19009.9	9.8
		8.7	10	18114.4	11.2
			5	16930.3	12.7
			1	13545.1	16.3
			0.5	12207.0	17.7
			0.1	9109.2	21.9
			0.01	5479.3	28.9
		25.0	20	9442.9	22.7
			10	8200.4	24.2
			5	6849.2	26.5
			1	3976.4	31.5
			0.5	3079.2	32.8
			0.1	1588.5	34.7
		42.0	20	2888.2	33.4
			10	2239.0	32.9
			5	1610.5	33.6
			1	873.6	29.4
			0.5	661.5	27.8
			0.1	357.0	25.8

Sample ID	Air Voids %	Testing Temperature °C	Testing Frequency Hz	E* MPa	Phase Angle degrees
U19-HMA-11	7.2	-7.0	10	28139.8	6.1
			5	26637.9	5.4
			1	24244.6	6.8
			0.5	22873.6	7.3
			0.1	19812.3	8.8
			0.01	15531.6	11.2
		6.0	10	16128.6	11.8
			5	15005.8	13.3
			1	11904.3	16.1
			0.5	10649.8	17.9
			0.1	8015.7	21.2
			0.01	4793.9	30.0
		25.0	20	6785.0	24.5
			10	5858.6	26.1
			5	4836.1	28.1
			1	2803.7	33.2
			0.5	2189.7	34.5
			0.1	1172.8	36.2
		39.4	20	2202.3	32.7
			10	1711.8	31.9
			5	1266.4	32.1
			1	705.4	29.7
			0.5	544.6	28.2
			0.1	296.4	26.4

Sample ID	Air Voids %	Testing Temperature °C	Testing Frequency Hz	E* MPa	Phase Angle degrees
U19-HMA-Fibers-1	6.4	-7.1	10	29916.0	4.8
			5	28722.7	6.1
			1	26108.1	7.5
			0.5	24699.7	7.1
			0.1	21375.3	9.7
			0.01	16466.0	15.8
		10.5	10	15480.5	16.1
			5	14062.8	17.5
			1	10532.9	22.0
			0.5	9272.7	23.9
			0.1	6258.8	28.9
			0.01	3317.1	36.3
		25.0	20	8375.8	25.8
			10	7116.8	28.9
			5	5723.8	31.7
			1	3242.2	36.1
			0.5	2454.8	37.3
			0.1	1321.5	37.4
		41.6	20	3093.6	30.7
			10	2337.4	30.7
			5	1818.6	30.0
			1	1093.1	25.1
			0.5	893.6	23.3
			0.1	337.7	23.9

Sample ID	Air Voids %	Testing Temperature °C	Testing Frequency Hz	E* MPa	Phase Angle degrees
U19-HMA-Fibers-2	7.0	-5.2	10	35444.5	5.6
			5	33357.4	7.8
			1	29669.1	9.2
			0.5	27912.0	9.7
			0.1	23484.9	12.5
			0.01	18148.5	18.3
		10.0	10	15952.4	15.1
			5	14582.1	17.0
			1	10759.0	21.5
			0.5	9319.0	23.8
			0.1	6247.8	28.6
			0.01	3095.7	34.7
		25.0	20	7300.5	27.3
			10	5991.2	29.9
			5	4709.8	32.5
			1	2541.8	37.5
			0.5	1893.3	38.1
			0.1	986.4	38.0
		40.1	20	2227.2	35.5
			10	1615.1	35.2
			5	1201.0	34.8
			1	672.8	31.9
			0.5	537.0	31.3
			0.1	328.6	31.2

Sample ID	Air Voids %	Testing Temperature °C	Testing Frequency Hz	E* MPa	Phase Angle degrees
U19-HMA-Fibers-3	7.1	-6.1			
			10	26217.5	6.3
			1	22061.6	7.9
			0.5	20782.5	8.6
			0.1	17413.3	10.9
			0.01	12519.1	16.8
		9.3	10	13587.1	14.1
			5	12402.5	16.1
			1	9255.1	20.1
			0.5	8018.0	22.1
			0.1	5538.5	27.3
			0.01	2871.1	34.0
		25.2	20	6007.6	26.0
			10	5040.8	27.9
			5	4022.4	29.7
			1	2190.4	32.9
			0.5	1677.6	33.7
			0.1	866.8	33.1
		40.2	20	1705.9	31.1
			10	1267.3	30.6
			5	1014.2	29.7
			1	594.0	25.6
			0.5	476.5	24.1
			0.1	261.6	21.5

Sample ID	Air Voids %	Testing Temperature °C	Testing Frequency Hz	E* MPa	Phase Angle degrees
U19-HMA-Fibers-4	6.5	-5.8	10	27713.8	5.8
			5	26457.0	6.5
			1	23476.8	8.1
			0.5	22065.2	8.6
			0.1	18815.0	11.9
			0.01	13663.4	14.5
		9.1	10	16645.2	15.4
			5	14965.0	17.1
			1	11090.7	21.4
			0.5	9574.9	23.7
			0.1	6447.1	29.2
			0.01	3160.0	35.1
		25.0	20	7019.0	26.0
			10	5754.8	28.1
			5	4537.7	30.3
			1	2433.2	34.1
			0.5	1835.6	34.3
			0.1	920.4	32.8
		40.3	20	1810.9	31.9
			10	1289.9	31.4
			5	1006.5	29.5
			1	570.2	23.4
			0.5	442.8	21.2
			0.1	249.8	19.8

Sample ID	Air Voids %	Testing Temperature °C	Testing Frequency Hz	E* MPa	Phase Angle degrees
U19-WMA-SonneWarmix-1	6.4	-4.8	10	32141.3	5.8
			5	30919.5	6.9
			1	27512.1	8.5
			0.5	25818.1	9.9
			0.1	21714.9	12.1
			0.01	15775.8	20.2
		9.6	10	16643.0	15.8
			5	14918.7	18.0
			1	10853.5	22.3
			0.5	9345.6	24.9
			0.1	6084.6	30.2
			0.01	2896.2	34.9
		25.0	20	6626.0	29.6
			10	5142.8	32.1
			5	3941.6	34.3
			1	2011.1	37.1
			0.5	1501.0	37.3
			0.1	727.7	35.7
		41.3	20	1526.8	35.4
			10	1100.7	35.5
			5	907.8	33.8
			1	524.8	29.3
			0.5	417.2	28.6
			0.1	263.7	27.6

Sample ID	Air Voids %	Testing Temperature °C	Testing Frequency Hz	E* MPa	Phase Angle degrees
U19-WMA-SonneWarmix-2	6.6	-5.5	10	31495.9	6.4
			5	30392.0	7.8
			1	26851.4	8.8
			0.5	25714.9	9.0
			0.1	21964.9	11.6
			0.01	16134.5	18.4
		10	10	16613.0	16.7
			5	14960.3	18.6
			1	10906.2	23.5
			0.5	9345.3	25.8
			0.1	6088.5	31.0
			0.01	2818.2	36.4
		25.0	20	7541.3	29.5
			10	6024.6	32.4
			5	4649.4	34.7
			1	2341.3	38.2
			0.5	1744.2	38.5
			0.1	869.1	38.0
		40	20	2702.2	33.0
			10	1945.9	33.0
			5	1591.3	30.7
			1	956.0	27.1
			0.5	778.2	26.6
			0.1	451.4	26.2

Sample ID	Air Voids %	Testing Temperature °C	Testing Frequency Hz	E* MPa	Phase Angle degrees
U19-WMA-SonneWarmix-3	7.1	-5.6	10	26822.7	5.3
			5	26088.5	7.1
			1	23014.8	8.9
			0.5	21940.9	9.8
			0.1	18464.3	12.6
			0.01	13497.5	18.4
		11.1	10	13073.4	17.2
			5	11366.3	19.2
			1	7922.7	24.2
			0.5	6479.9	26.7
			0.1	3843.5	32.1
			20	5281.9	30.2
		25.0	10	4072.1	32.9
			5	2982.1	35.1
			1	1421.5	36.9
			0.5	1041.8	35.6
			0.1	513.7	31.3
			20	1391.0	33.1
		38.8	10	942.3	33.1
			5	759.0	29.9
			1	450.8	24.1
			0.5	364.0	22.8
			0.1	206.8	19.2

Sample ID	Air Voids %	Testing Temperature °C	Testing Frequency Hz	E* MPa	Phase Angle degrees
U19-WMA-SonneWarmix-4	6.5	-11.3	10	33899.0	3.4
			5	32688.9	4.5
			1	30167.1	5.6
			0.5	29201.4	6.6
			0.1	25970.3	7.7
			0.01	21255.6	10.6
		4	10	22172.9	11.3
			5	20252.8	13.0
			1	16070.9	16.3
			0.5	14107.6	18.6
			0.1	10115.0	23.6
			0.01	5733.8	25.3
		25.0	20	5849.9	29.3
			10	4616.5	32.4
			5	3466.7	34.6
			1	1681.2	37.7
			0.5	1240.6	36.4
			0.1	582.3	34.1
		40.0	20	1475.2	36.0
			10	1130.5	32.8
			5	818.5	31.2
			1	481.4	25.9
			0.5	382.9	24.4
			0.1	215.3	22.8

Sample ID	Air Voids %	Testing Temperature °C	Testing Frequency Hz	E* MPa	Phase Angle degrees
U19-WMA-SonneWarmix-5	6.5	-10	10	31771.7	5.5
			5	30928.8	5.6
			1	28229.0	6.3
			0.5	27134.0	7.2
			0.1	23868.8	9.2
			0.01	18855.3	12.9
		6.2	10	18657.3	13.2
			5	16929.8	15.2
			1	12763.0	19.6
			0.5	11318.1	21.8
			0.1	7689.7	27.0
			0.01	3749.3	34.6
		25.0	20	5970.4	29.0
			10	4674.0	31.4
			5	3508.1	33.7
			1	1748.1	35.4
			0.5	1306.2	34.5
			0.1	637.5	31.1
		39.5	20	1457.8	34.1
			10	1136.2	30.6
			5	819.9	28.5
			1	501.0	22.5
			0.5	400.7	21.3
			0.1	226.3	19.5

Sample ID	Air Voids %	Testing Temperature °C	Testing Frequency Hz	E* MPa	Phase Angle degrees
U19-WMA-SonneWarmix-6	7.1	-8.0	10	34628.3	5.2
			5	33829.1	5.8
			1	30533.9	6.9
			0.5	29042.4	7.9
			0.1	25373.3	9.6
			0.01	20492.8	12.2
		7.2	10	13924.6	14.9
			5	12725.5	16.9
			1	9470.6	20.9
			0.5	8227.0	23.2
			0.1	5547.8	28.6
			0.01	2802.8	34.8
		25.0	20	5054.7	29.9
			10	4046.9	31.6
			5	3120.3	33.4
			1	1608.8	35.1
			0.5	1221.2	34.2
			0.1	620.7	31.7
		39.7	20	1403.8	34.3
			10	1023.4	30.7
			5	737.1	28.8
			1	437.3	24.1
			0.5	343.8	22.8
			0.1	213.3	22.7

Sample ID	Air Voids %	Testing Temperature °C	Testing Frequency Hz	E* MPa	Phase Angle degrees
U19-WMA-SonneWarmix-7	7.0	-8.5	10	25846.3	3.9
			5	25073.9	4.7
			1	22914.4	6.0
			0.5	22001.8	7.0
			0.1	19317.8	8.8
			0.01	15695.9	12.2
		5.7	10	16718.0	11.9
			5	15560.0	13.3
			1	12398.6	17.7
			0.5	11002.0	19.0
			0.1	7731.1	24.4
			0.01	4290.9	32.4
		25.0	20	6367.2	28.6
			10	5184.1	30.7
			5	4085.9	33.1
			1	2109.1	36.6
			0.5	1657.2	38.5
			0.1	838.4	36.2
		40.9	20	1701.5	38.5
			10	1301.3	35.0
			5	1018.2	33.7
			1	637.2	29.0
			0.5	504.2	27.8
			0.1	304.1	26.9

Sample ID	Air Voids %	Testing Temperature °C	Testing Frequency Hz	E* MPa	Phase Angle degrees
U19-WMA-SonneWarmix-8	6.7	1.3	10	28290.6	9.7
			5	26704.7	11.1
			1	22000.8	14.0
			0.5	19981.4	15.8
			0.1	15312.6	19.3
			0.01	8997.4	27.4
		10.4	10	16933.5	16.6
			5	14912.9	18.2
			1	10743.8	23.1
			0.5	9083.4	25.6
			0.1	5826.7	31.0
		25.0	20	6783.1	29.1
			10	5388.0	32.0
			5	4104.3	34.5
			1	2058.7	37.6
			0.5	1532.4	36.9
			0.1	741.9	34.6
		40.0	20	1678.2	37.0
			10	1276.8	33.7
			5	950.7	32.1
			1	580.8	27.7
0.5	667.5		29.8		
0.1	434.4		25.6		

Sample ID	Air Voids %	Testing Temperature °C	Testing Frequency Hz	E* MPa	Phase Angle degrees
U19-WMA-SonneWarmix-9	7.6	-9.5	10	30675.1	5.4
			5	29648.9	5.3
			1	27215.5	6.2
			0.5	26013.5	7.1
			0.1	22693.1	8.8
			0.01	18114.0	11.2
			7.1	10	17638.8
		5		15994.4	14.5
		1		12099.0	18.5
		0.5		10424.8	20.7
		0.1		7210.8	25.8
		0.01		3723.3	32.7
		25.0	20	7044.1	27.9
			10	5545.7	30.1
			5	4310.2	32.4
			1	2208.9	35.2
			0.5	1650.5	34.8
			0.1	770.2	32.9
		40.6	20	1762.9	34.4
			10	1369.9	31.3
			5	1000.1	29.7
1	612.9		23.2		
0.5	503.3		20.5		
0.1	301.6		17.4		

Sample ID	Air Voids %	Testing Temperature °C	Testing Frequency Hz	E* MPa	Phase Angle degrees
U19-WMA-SonneWarmix-10	7.6	-8.9	10	38020.9	5.3
			5	35346.4	5.4
			1	30590.2	6.8
			0.5	28858.4	7.2
			0.1	24965.3	9.3
			0.01	19663.4	12.7
		5.7	10	21724.4	11.9
			5	19592.0	13.4
			1	15298.2	17.5
			0.5	13308.3	20.0
			0.1	9407.9	26.4
			0.01	4867.8	34.6
		25.0	20	6537.8	30.3
			10	5219.9	32.5
			5	4025.6	34.3
			1	2054.6	37.5
			0.5	1539.2	36.5
			0.1	775.3	33.4
		42.0	20	1410.9	35.3
			10	1075.7	31.5
			5	765.1	30.5
			1	430.8	26.5
			0.5	331.1	25.5
			0.1	173.1	24.0

Sample ID	Air Voids %	Testing Temperature °C	Testing Frequency Hz	E* MPa	Phase Angle degrees
U19-WMA-SonneWarmix-11	7.0	-7.3	10	32546.3	6.6
			5	31097.7	7.0
			1	28243.4	8.6
			0.5	26915.8	9.0
			0.1	23187.7	11.3
			0.01	18267.0	16.9
		8.0	10	18561.3	14.2
			5	16860.1	15.3
			1	12779.0	19.4
			0.5	11110.8	22.1
			0.1	7475.7	26.9
			0.01	3615.9	34.6
		25.0	20	6847.3	27.9
			10	5438.4	31.0
			5	4151.2	32.9
			1	2083.4	36.9
			0.5	1545.1	36.5
			0.1	721.4	34.7
		41.4	20	1340.4	34.7
			10	1029.5	31.0
			5	754.2	29.3
			1	458.0	23.9
			0.5	367.6	22.2
			0.1	231.9	20.9

Sample ID	Air Voids %	Testing Temperature °C	Testing Frequency Hz	E* MPa	Phase Angle degrees
U19-WMA-Sonne Warmix-12	6.6	-6.3	10	29983.0	5.1
			5	28960.0	6.4
			1	26045.8	7.6
			0.5	24566.3	8.3
			0.1	21338.2	10.1
			0.01	15709.9	13.5
		7.8	10	15977.9	14.3
			5	14510.3	16.0
			1	10912.3	19.9
			0.5	9409.5	22.0
			0.1	6353.1	27.4
			0.01	3106.6	34.0
		25.0	10	4388.7	32.1
			5	3301.7	34.1
			1	1619.0	35.6
			0.5	1199.0	33.8
			0.1	566.3	29.8
		40.4	20	1737.6	33.3
			10	1321.4	29.5
			5	952.9	27.2
			1	605.7	21.5
0.5	366.4		20.6		
0.1	228.8		18.8		

Sample ID	Air Voids %	Testing Temperature °C	Testing Frequency Hz	E* MPa	Phase Angle degrees
U19-WMA-Sonne Warmix-Fibers-1	6.7	-6.4	10	30761.3	6.6
			5	29545.1	6.5
			1	26233.2	8.5
			0.5	24666.3	8.6
			0.1	21007.1	11.3
			0.01	15555.9	18.6
			10.7	10	15279.1
		5		13613.7	17.7
		1		9941.2	22.6
		0.5		8335.2	24.6
		0.1		5395.7	29.3
		0.01		2509.9	35.5
		25.0		20	7170.8
			10	5780.4	28.7
			5	4594.8	30.7
			1	2470.3	34.8
			0.5	1837.8	35.3
			0.1	904.2	34.4
		38.5	20	2244.7	33.0
			10	1568.2	34.3
			5	1198.7	32.8
			1	648.1	28.2
			0.5	501.9	26.7
			0.1	255.1	23.9

Sample ID	Air Voids %	Testing Temperature °C	Testing Frequency Hz	E* MPa	Phase Angle degrees
U19-WMA-SonneWarmix-Fibers-2	7.2	-7.5	10	23613.8	4.7
			5	23011.2	5.6
			1	20811.4	7.4
			0.5	19720.6	8.2
			0.1	17090.6	10.2
			0.01	12999.1	14.6
		10.3	10	13146.7	15.5
			5	11794.9	17.3
			1	8628.9	22.1
			0.5	7414.8	24.5
			0.1	4922.5	29.9
			0.01	2336.3	36.8
		25.0	20	5946.1	28.4
			10	4773.6	30.5
			5	3706.7	32.5
			1	1884.8	36.4
			0.5	1402.1	36.6
			0.1	671.8	35.6
		39.8	20	1613.2	37.2
			10	1106.0	36.9
			5	885.4	34.0
			1	545.7	27.6
			0.5	461.5	26.3
			0.1	311.2	25.6

Sample ID	Air Voids %	Testing Temperature °C	Testing Frequency Hz	E* MPa	Phase Angle degrees
U19-WMA-SonneWarmix-Fibers-3	6.6	-7.1	10	27280.5	5.6
			5	26407.5	5.7
			1	23856.2	7.0
			0.5	22751.4	7.9
			0.1	19799.8	9.6
			0.01	15778.4	13.5
		9.6	10	16661.0	15.5
			5	15101.2	17.7
			1	11273.3	22.4
			0.5	9643.0	24.5
			0.1	6288.2	30.1
			0.01	2987.0	35.6
		25.0	20	7094.6	29.3
			10	5753.7	31.4
			5	4457.2	33.3
			1	2297.4	36.9
			0.5	1694.6	37.8
			0.1	842.0	36.3
		39.0	20	4185.3	30.3
			10	3009.9	28.8
			5	2490.0	25.3
			1	1630.0	19.3
			0.5	1360.2	17.6
			0.1	865.0	15.0

Sample ID	Air Voids %	Testing Temperature °C	Testing Frequency Hz	E* MPa	Phase Angle degrees
U19-WMA-SonneWarmix-Fibers-4	7.1	-4.6	10	29205.0	7.0
			5	27832.3	7.3
			1	24358.6	9.2
			0.5	22495.9	10.2
			0.1	18665.3	13.2
			0.01	13004.5	19.0
		11.7	10	13546.5	19.0
			5	11928.2	21.3
			1	8216.2	26.7
			0.5	6852.0	28.9
			0.1	4070.6	34.6
		25.0	20	6333.8	33.4
			10	5047.1	35.7
			5	3887.2	37.6
			1	1925.1	39.8
			0.5	1434.7	39.4
			0.1	710.8	37.9
		40.2	20	1588.7	34.5
			10	1086.5	33.9
			5	874.0	30.8
			1	503.9	26.3
			0.5	395.5	25.4
			0.1	215.0	25.0

Sample ID	Air Voids %	Testing Temperature °C	Testing Frequency Hz	E* MPa	Phase Angle degrees
U25-HMA-1	7.1	-3.3	10	34637.2	5.6
			5	32983.1	7.5
			1	29033.0	9.4
			0.5	27322.6	10.5
			0.1	23014.6	12.7
			0.01	15566.9	20.2
			10.0	10	21635.8
		5		19494.8	16.2
		1		14635.0	20.1
		0.5		12556.7	21.8
		0.1		8534.1	27.0
		0.01		4333.8	35.3
		24.9		20	8382.8
			10	7028.2	27.3
			5	5714.4	30.1
			1	3231.7	35.7
			0.5	2405.4	37.1
			0.1	2557.7	38.9
			40.2	20	2331.0
		10		1793.5	38.2
		5		1259.5	39.4
		1		626.9	37.8
		0.5		457.4	37.5
		0.1		208.4	35.5

Sample ID	Air Voids %	Testing Temperature °C	Testing Frequency Hz	E* MPa	Phase Angle degrees
U25-HMA-2	6.6	-4.5	10	36195.1	6.9
			5	35323.3	8.1
			1	31770.2	9.3
			0.5	29910.0	10.0
			0.1	25510.9	12.3
			0.01	20459.2	16.1
		10.4	10	22181.3	14.3
			5	20118.7	15.6
			1	15478.2	19.6
			0.5	13292.1	21.6
			0.1	9220.8	26.5
			0.01	4843.9	34.3
		25.5	20	9550.0	24.9
			10	7950.8	27.2
			5	6556.3	29.6
			1	3877.6	34.8
			0.5	3054.9	37.1
			0.1	1745.9	39.3
		41.2	20	2498.6	37.4
			10	1938.7	36.8
			5	1368.3	37.7
			1	699.4	36.8
			0.5	522.5	36.1
			0.1	275.4	35.1

Sample ID	Air Voids %	Testing Temperature °C	Testing Frequency Hz	E* MPa	Phase Angle degrees
U25-HMA-3	7.1	-5.4	10	32727.9	6.2
			5	31615.8	6.3
			1	28204.8	8.4
			0.5	26512.3	9.2
			0.1	22401.3	10.7
			0.01	16057.8	18.2
		10.2	10	18573.5	14.2
			5	16653.4	15.3
			1	12614.9	19.4
			0.5	11080.7	21.2
			0.1	7730.9	26.2
			0.01	4349.4	33.2
		25.4	20	8574.4	24.2
			10	7285.5	26.3
			5	5994.4	28.9
			1	3554.1	34.3
			0.5	2808.2	36.7
			0.1	1745.5	41.2
		38.6	20	2858.8	35.9
			10	2178.3	38.5
			5	1584.4	38.7
			1	831.7	39.1
			0.5	692.9	38.5
			0.1	519.0	37.2

Sample ID	Air Voids %	Testing Temperature °C	Testing Frequency Hz	E* MPa	Phase Angle degrees
U25-HMA-4	6.7	-5.3	10	28644.3	4.8
			5	27507.5	6.0
			1	24774.9	6.9
			0.5	23417.4	7.5
			0.1	20258.1	9.8
			0.01	15332.6	14.1
		11.7	10	16040.0	14.3
			5	14670.8	15.6
			1	11064.9	19.9
			0.5	9494.5	21.6
			0.1	6615.6	26.6
			0.01	3442.5	33.1
		25.0	20	8790.9	23.6
			10	7463.2	24.4
			5	6133.5	26.8
			1	3623.1	32.0
			0.5	2790.5	33.5
			0.1	1437.7	34.7
		38.4	20	3368.0	32.5
			10	2651.9	32.5
			5	1969.8	33.1
			1	1069.9	30.8
			0.5	833.1	28.6
			0.1	433.2	25.8

Sample ID	Air Voids %	Testing Temperature °C	Testing Frequency Hz	E* MPa	Phase Angle degrees
U25-HMA-5	7.8	-7.0	10	26721.0	5.4
			5	25964.6	5.9
			1	23399.6	6.7
			0.5	22488.2	7.4
			0.1	19801.2	9.3
			0.01	15862.6	13.4
		5.0	10	19204.7	11.3
			5	17749.3	12.4
			1	14163.1	15.5
			0.5	12748.4	16.9
			0.1	9380.8	21.7
			0.01	5442.7	29.8
		25.0	20	7047.3	25.7
			10	5887.4	27.9
			5	4709.6	30.5
			1	2549.2	34.1
			0.5	1939.6	34.6
			0.1	956.9	34.3
		38.3	20	2247.0	34.9
			10	1709.8	33.8
			5	1221.4	33.3
			1	669.9	29.4
			0.5	512.6	28.2
			0.1	280.0	26.0

Sample ID	Air Voids %	Testing Temperature °C	Testing Frequency Hz	E* MPa	Phase Angle Degrees
U25-HMA-6	7.5	-6.9	10	34836.1	5.7
			5	33935.8	5.3
			1	30493.1	7.1
			0.5	29410.3	7.1
			0.1	25946.0	8.9
			0.01	20711.6	12.0
		7.0	10	22241.4	10.9
			5	20810.3	12.6
			1	16785.1	16.2
			0.5	15133.6	18.2
			0.1	11283.4	22.9
			0.01	6123.5	29.8
		25.0	20	9113.0	25.2
			10	7300.1	27.3
			5	5783.2	29.6
			1	3183.7	34.5
			0.5	2384.8	35.1
			0.1	1165.4	35.1
		42.5	20	1782.9	33.1
			10	1369.5	30.5
			5	1006.1	29.2
			1	602.6	24.5
			0.5	475.6	22.4
			0.1	280.3	20.2

Sample ID	Air Voids %	Testing Temperature °C	Testing Frequency Hz	E* MPa	Phase Angle degrees
U25-HMA-7	6.9	-8.0	10	41331.8	4.9
			5	40059.8	5.6
			1	36490.1	7.3
			0.5	34655.4	7.6
			0.1	30304.1	9.3
			0.01	24057.9	12.3
		5.4	10	26391.7	11.3
			5	24005.7	13.0
			1	19315.1	16.0
			0.5	17035.0	17.5
			0.1	12703.6	22.0
			0.01	7655.2	28.4
		25.0	20	8918.2	25.3
			10	7244.1	27.7
			5	5799.4	29.8
			1	3207.8	34.7
			0.5	2425.9	34.6
			0.1	1186.8	34.4
		41.0	20	2324.4	34.0
			10	1754.4	32.1
			5	1271.5	31.2
			1	737.9	26.2
			0.5	572.1	24.2
			0.1	317.4	21.9

Sample ID	Air Voids %	Testing Temperature °C	Testing Frequency Hz	E* MPa	Phase Angle Degrees
U25-HMA-8	7.7	-6.5	10	33370.6	4.9
			5	32384.6	6.7
			1	29261.2	7.2
			0.5	27901.3	7.7
			0.1	24158.4	9.5
			0.01	18789.5	15.9
		5.0	10	23025.3	10.9
			5	21261.8	11.8
			1	17052.8	14.6
			0.5	15176.2	16.9
			0.1	11304.0	21.1
			0.01	6374.0	31.0
		25.0	20	7481.3	27.0
			10	6148.2	28.9
			5	4911.8	31.2
			1	2679.6	35.6
			0.5	2012.2	36.3
			0.1	989.2	35.0
		41.8	20	2026.4	35.0
			10	1507.5	32.7
			5	1079.3	31.3
			1	612.6	25.9
			0.5	476.6	23.8
			0.1	281.3	20.8

Sample ID	Air Voids %	Testing Temperature °C	Testing Frequency Hz	E* MPa	Phase Angle degrees
U25-HMA-9	6.5	-6.8	10	25912.1	4.9
			5	25187.3	5.5
			1	22659.4	6.5
			0.5	21633.1	7.3
			0.1	18925.9	9.0
			0.01	15123.4	13.8
		6.0	10	18357.1	9.8
			5	17085.9	11.4
			1	13898.8	14.2
			0.5	12452.4	16.0
			0.1	9605.5	19.7
			0.01	6241.3	25.8
		25.0	20	7870.0	23.1
			10	6781.2	25.3
			5	5546.0	27.7
			1	3137.0	32.6
			0.5	2402.6	33.7
			0.1	1265.8	34.5
		40.4	20	2718.8	33.6
			10	2060.8	33.0
			5	1498.7	33.0
			1	827.8	29.3
			0.5	632.6	27.8
			0.1	356.3	26.4

Sample ID	Air Voids %	Testing Temperature °C	Testing Frequency Hz	E* MPa	Phase Angle Degrees
U25-HMA-10	7.1	-4.4	10	31624.2	6.7
			5	30014.9	7.4
			1	26423.3	9.4
			0.5	24728.7	10.5
			0.1	20322.4	13.2
			0.01	14836.4	18.8
		6.4	10	21826.1	12.4
			5	19709.7	14.8
			1	15315.2	18.3
			0.5	13316.8	20.5
			0.1	9373.6	25.2
			0.01	5016.4	32.8
		25.0	20	8433.9	26.5
			10	7217.8	28.6
			5	5779.7	30.5
			1	3198.3	35.8
			0.5	2429.8	36.8
			0.1	1219.1	37.0
		40	20	2579.5	35.1
			10	1956.2	33.9
			5	1422.0	33.3
			1	805.6	29.2
			0.5	628.6	27.8
0.1	354.9		25.3		

Sample ID	Air Voids %	Testing Temperature °C	Testing Frequency Hz	E* MPa	Phase Angle degrees
U25-WMA-Advera-1	6.7	-4.7	10	33083.5	5.0
			5	31825.1	7.0
			1	28100.8	9.6
			0.5	26487.0	10.2
			0.1	22334.1	13.4
			0.01	16552.2	18.1
		9.8	10	18526.9	15.8
			5	16783.3	18.2
			1	12185.2	23.6
			0.5	10355.8	26.3
			0.1	6619.3	32.9
			0.01	2937.5	42.1
		25.0	20	7506.0	30.7
			10	6144.1	32.8
			5	4725.2	35.5
			1	2352.7	39.7
			0.5	1682.3	41.3
			0.1	722.3	41.6
		41.1	20	1664.4	42.1
			10	1301.1	42.2
			5	912.7	42.6
			1	484.8	42.9
			0.5	361.5	42.4

Sample ID	Air Voids %	Testing Temperature °C	Testing Frequency Hz	E* MPa	Phase Angle Degrees
U25-WMA-Advera-2	7.5	-4.4	10	25650.1	7.1
			5	24880.4	8.2
			1	21912.5	10.1
			0.5	20799.9	11.3
			0.1	17683.8	13.5
			0.01	12013.0	20.8
		10.5	10	15247.8	16.4
			5	13590.9	17.9
			1	9747.6	23.3
			0.5	8302.1	25.7
			0.1	5364.3	31.5
			0.01	2535.1	38.0
		25.0	20	6717.7	29.1
			10	5461.8	30.6
			5	4207.7	33.6
			1	2216.5	36.9
			0.5	1604.8	37.3
			0.1	748.6	36.8
		38.2	20	1515.1	34.0
			10	1185.8	34.7
			5	922.8	34.2
			1	576.3	32.8
			0.5	456.4	31.5
			0.1	261.8	31.8

Sample ID	Air Voids %	Testing Temperature °C	Testing Frequency Hz	E* MPa	Phase Angle degrees
U25-WMA-Advera-3	6.4	-4.7	10	30970.4	4.8
			5	29843.8	6.4
			1	26392.1	7.9
			0.5	25013.7	8.6
			0.1	21335.6	11.3
			0.01	15845.0	18.1
		10.7	10	16792.5	15.3
			5	15165.9	17.2
			1	11027.6	22.1
			0.5	9372.5	24.6
			0.1	6055.5	29.7
			0.01	2761.8	34.3
		26.0	20	8073.8	25.6
			10	6580.1	28.1
			5	5226.4	30.6
			1	2777.6	36.0
			0.5	2046.1	36.9
			0.1	992.3	37.0
		37.3	20	3452.0	36.9
			10	2621.9	37.2
			5	1965.1	36.8
			1	1109.5	33.9
			0.5	876.3	31.9
			0.1	627.8	24.7

Sample ID	Air Voids %	Testing Temperature °C	Testing Frequency Hz	E* MPa	Phase Angle Degrees
U25-WMA-Rediset-1	7.2	-5.7	10	33801.7	6.0
			5	32763.4	6.0
			1	29132.6	7.7
			0.5	27763.1	8.6
			0.1	23750.5	11.1
			0.01	18434.5	17.0
		12.3	10	14015.5	17.6
			5	12417.7	19.6
			1	8642.5	25.2
			0.5	7151.2	27.6
			0.1	4286.6	32.6
			0.01	1728.3	35.6
		25	20	6450.3	28.9
			10	4890.1	31.8
			5	3597.8	34.4
			1	1644.1	37.8
			0.5	1130.2	37.8
			0.1	478.1	36.5
		37.5	20	3054.4	43.9
			10	2051.4	42.2
			5	1539.0	39.9
			1	980.3	32.9
			0.5	837.2	30.2
			0.1	683.8	21.8

Sample ID	Air Voids %	Testing Temperature °C	Testing Frequency Hz	E* MPa	Phase Angle degrees
U25-WMA-Rediset-2	7.2	-6.3	10	30616.7	4.2
			5	28807.5	6.9
			1	25394.1	8.1
			0.5	23439.9	9.3
			0.1	19312.1	12.6
			0.01	12578.4	19.2
		10.0	10	14923.7	15.8
			5	13116.1	17.9
			1	9200.0	23.0
			0.5	7500.6	26.0
			0.1	4450.9	30.5
			0.01	1664.4	33.1
		26.7	20	7493.2	33.7
			10	5828.4	33.4
			5	4194.9	37.1
			1	2148.8	37.5
			0.5	1650.0	35.6
			0.1	865.1	32.5
		37	20	3709.4	35.4
			10	2760.9	32.4
			5	2087.6	30.6
			1	1241.5	25.3
			0.5	1035.2	23.1
			0.1	970.2	15.7

Sample ID	Air Voids %	Testing Temperature °C	Testing Frequency Hz	E* MPa	Phase Angle Degrees
U25-WMA-Rediset-3	6.9	-5	10	29812.6	6.2
			5	28515.8	6.7
			1	25182.3	8.8
			0.5	23709.0	9.3
			0.1	20213.3	12.5
			0.01	15516.3	19.6
		11.4	10	15872.6	16.3
			5	14278.3	18.0
			1	10331.0	22.9
			0.5	8619.3	25.6
			0.1	5482.6	31.1
			0.01	2441.4	36.1
		25.4	20	7341.9	28.7
			10	5811.3	31.7
			5	4408.2	34.1
			1	2151.2	38.6
			0.5	1524.2	38.7
			0.1	677.5	37.5
		37.5	20	3654.4	39.2
			10	3117.0	35.7
			5	2524.9	32.4
			1	1514.0	28.4
			0.5	1310.6	25.0
			0.1	1088.5	15.2

Sample ID	Air Voids %	Testing Temperature °C	Testing Frequency Hz	E* MPa	Phase Angle degrees
U25-WMA-Sasobit-1	7.1	-3.1	10	24787.0	5.9
			5	23819.5	6.8
			1	21030.7	8.5
			0.5	19872.3	9.4
			0.1	16771.0	11.8
			0.01	11915.6	17.7
		12.8	10	14053.8	15.7
			5	12779.5	17.6
			1	9277.6	22.0
			0.5	7885.3	24.1
			0.1	5038.1	28.2
			0.01	2257.5	31.7
		25.8	20	7150.1	25.6
			10	5793.0	28.3
			5	4513.3	30.6
			1	2284.3	35.5
			0.5	1614.0	36.6
			0.1	733.4	37.7
		37.7	20	5829.6	33.5
			10	4583.9	32.9
			5	3517.7	31.3
			1	1872.6	28.4
			0.5	1501.6	25.6
			0.1	860.0	22.2

Sample ID	Air Voids %	Testing Temperature °C	Testing Frequency Hz	E* MPa	Phase Angle Degrees
U25-WMA-Sasobit-2	7.5	-5.5	10	27904.9	5.1
			5	26695.0	5.5
			1	23827.9	6.9
			0.5	22355.6	7.7
			0.1	18944.0	10.3
			0.01	13803.0	18.1
		11.1	10	15118.3	15.6
			5	13397.9	17.3
			1	9810.1	21.5
			0.5	8249.0	23.9
			0.1	5254.0	29.6
			0.01	2336.1	35.6
		28.4	20	6056.6	27.8
			10	4862.3	30.5
			5	3796.8	32.7
			1	1934.0	36.2
			0.5	1408.5	36.6
			0.1	656.8	35.6
		39.7	20	3396.2	35.4
			10	2616.3	34.4
			5	2008.2	32.0
			1	1198.9	26.7
			0.5	968.0	24.5
			0.1	585.1	22.2

Sample ID	Air Voids %	Testing Temperature °C	Testing Frequency Hz	E* MPa	Phase Angle degrees
U25-WMA-Sasobit-3	7.0	-5.0	10	29208.5	3.5
			5	28380.3	5.3
			1	25732.1	6.4
			0.5	24629.0	7.0
			0.1	21782.0	9.0
			0.01	17364.5	13.2
		13.2	10	15071.1	14.8
			5	13476.4	16.6
			1	10036.5	21.0
			0.5	8538.7	22.9
			0.1	5699.9	28.2
			0.01	2666.1	33.9
		26.8	20	10871.9	30.3
			10	8637.8	33.1
			5	6667.8	35.4
			1	3473.0	39.4
			0.5	2537.3	40.1
			0.1	1318.3	39.8
		38.0	20	3363.5	33.5
			10	2490.3	34.7
			5	1848.1	34.8
			1	918.5	33.9
			0.5	701.6	32.0
			0.1	497.8	32.7